frontiers | Research Topics

Combined EEG in research and diagnostics: Novel perspectives and improvements

Edited by
Kamran Avanaki, Morten Mørup, Camillo Porcaro and Oscar Arias-Carrion

Published in
Frontiers in Neuroscience

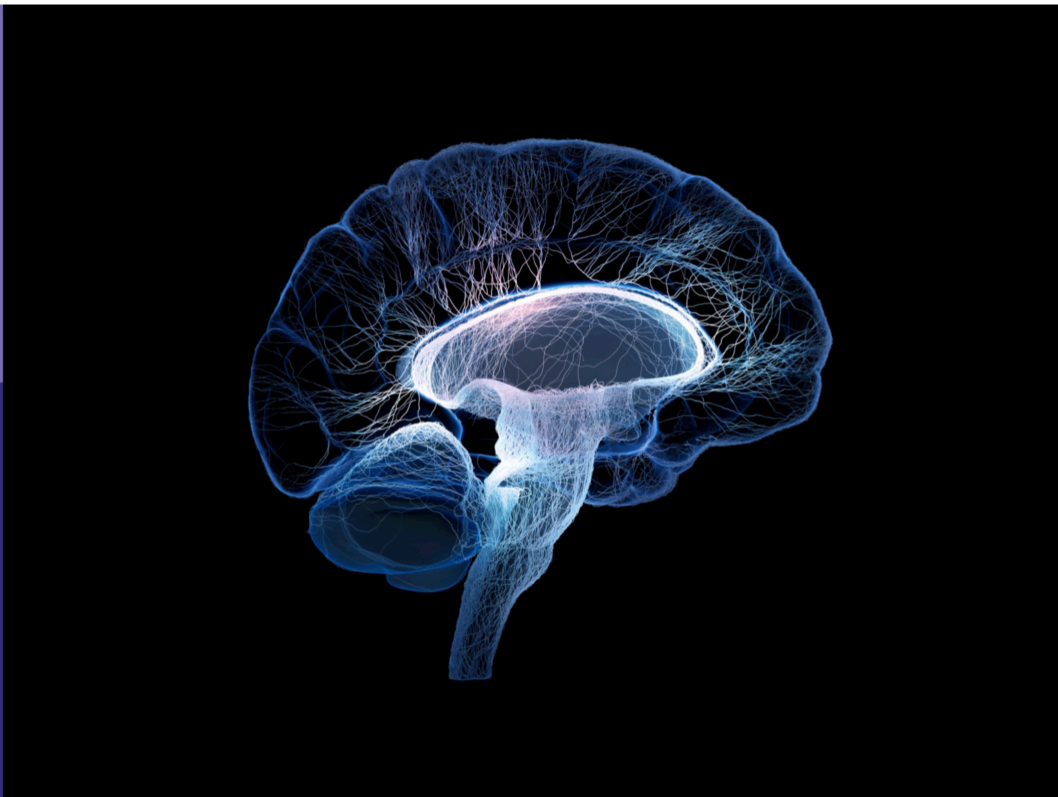

ISSN 1664-8714
ISBN 978-2-83251-799-4
DOI 10.3389/978-2-83251-799-4

About Frontiers

Frontiers is more than just an open access publisher of scholarly articles: it is a pioneering approach to the world of academia, radically improving the way scholarly research is managed. The grand vision of Frontiers is a world where all people have an equal opportunity to seek, share and generate knowledge. Frontiers provides immediate and permanent online open access to all its publications, but this alone is not enough to realize our grand goals.

Frontiers journal series

The Frontiers journal series is a multi-tier and interdisciplinary set of open-access, online journals, promising a paradigm shift from the current review, selection and dissemination processes in academic publishing. All Frontiers journals are driven by researchers for researchers; therefore, they constitute a service to the scholarly community. At the same time, the *Frontiers journal series* operates on a revolutionary invention, the tiered publishing system, initially addressing specific communities of scholars, and gradually climbing up to broader public understanding, thus serving the interests of the lay society, too.

Dedication to quality

Each Frontiers article is a landmark of the highest quality, thanks to genuinely collaborative interactions between authors and review editors, who include some of the world's best academicians. Research must be certified by peers before entering a stream of knowledge that may eventually reach the public - and shape society; therefore, Frontiers only applies the most rigorous and unbiased reviews. Frontiers revolutionizes research publishing by freely delivering the most outstanding research, evaluated with no bias from both the academic and social point of view. By applying the most advanced information technologies, Frontiers is catapulting scholarly publishing into a new generation.

What are Frontiers Research Topics?

Frontiers Research Topics are very popular trademarks of the *Frontiers journals series*: they are collections of at least ten articles, all centered on a particular subject. With their unique mix of varied contributions from Original Research to Review Articles, Frontiers Research Topics unify the most influential researchers, the latest key findings and historical advances in a hot research area.

Find out more on how to host your own Frontiers Research Topic or contribute to one as an author by contacting the Frontiers editorial office: frontiersin.org/about/contact

Combined EEG in research and diagnostics: Novel perspectives and improvements

Topic editors
Kamran Avanaki — University of Illinois at Chicago, United States
Morten Mørup — Technical University of Denmark, Denmark
Camillo Porcaro — Università degli Studi di Padova, Italy
Oscar Arias-Carrion — Hospital General Dr. Manuel Gea Gonzalez, Mexico

Citation
Avanaki, K., Mørup, M., Porcaro, C., Arias-Carrion, O., eds. (2023). *Combined EEG in research and diagnostics: Novel perspectives and improvements*. Lausanne: Frontiers Media SA. doi: 10.3389/978-2-83251-799-4

Table of contents

frontiers | Frontiers in Neuroscience

TYPE Editorial
PUBLISHED 16 February 2023
DOI 10.3389/fnins.2023.1152394

Editorial: Combined EEG in research and diagnostics: Novel perspectives and improvements

Camillo Porcaro[1,2,3]*, Kamran Avanaki[4], Oscar Arias-Carrion[5] and Morten Mørup[6]

[1]Department of Neuroscience and Padova Neuroscience Center, University of Padua, Padua, Italy, [2]Institute of Cognitive Sciences and Technologies—National Research Council, Rome, Italy, [3]Centre for Human Brain Health and School of Psychology, University of Birmingham, Birmingham, United Kingdom, [4]University of Illinois at Chicago, Chicago, IL, United States, [5]Unidad de Trastornos del Movimiento y Sueño, Hospital General Dr. Manuel Gea González, Mexico City, Mexico, [6]Technical University of Denmark, Lyngby, Denmark

OPEN ACCESS

EDITED AND REVIEWED BY
Vince D. Calhoun,
Georgia State University, United States

*CORRESPONDENCE
Camillo Porcaro
✉ camillo.porcaro@unipd.it

SPECIALTY SECTION
This article was submitted to
Brain Imaging Methods,
a section of the journal
Frontiers in Neuroscience

RECEIVED 27 January 2023
ACCEPTED 31 January 2023
PUBLISHED 16 February 2023

CITATION
Porcaro C, Avanaki K, Arias-Carrion O and Mørup M (2023) Editorial: Combined EEG in research and diagnostics: Novel perspectives and improvements.
Front. Neurosci. 17:1152394.
doi: 10.3389/fnins.2023.1152394

KEYWORDS

EEG-fMRI, EEG-MEG, EEG-based BCI, EEG-TMS, EEG-tES, EEG-fNIRS

Editorial on the Research Topic
Combined EEG in research and diagnostics: Novel perspectives and improvements

In neuroscience, electroencephalography and neuroimaging techniques are widely used to improve our understanding of brain mechanisms and to identify biomarkers for the most diverse neurological pathologies (Tulay et al., 2019). However, electro-magnetoencephalography (E-MEG) and neuroimaging techniques, such as functional magnetic resonance imaging (fMRI), are complementary [i.e., EEG/MEG techniques have an excellent temporal resolution at the expense of their spatial resolution and vice versa for fMRI or other neuroimaging techniques such as single-photon emission computed tomography (SPECT), positron emission tomography (PET) and functional near-infrared spectroscopy (fNIRS)]. Furthermore, the complementarity of these techniques has led to the development of multimodal integration (Tulay et al., 2019).

In recent decades, technological advances have allowed researchers to integrate different electrophysiological and neuroimaging techniques more efficiently to provide optimal spatial and temporal resolution. With its excellent spatial resolution and portability, EEG is often combined with other methods, such as fMRI (Ostwald et al., 2010, 2011, 2012; Porcaro et al., 2010, 2011) or fNIRS, transcranial magnetic stimulation (TMS) (Giambattistelli et al., 2014; Tecchio et al., 2023), and transcranial electrical stimulation (tES) (Porcaro et al., 2019b), to enhance the understanding of the brain functions underlying brain processes in healthy and pathological conditions (Buss et al., 2019). Moreover, EEG combined with non-invasive brain stimulation (NIBS) such as TMS, or tES can be used as a potential treatment and monitoring of brain pathologies (Napolitani et al., 2014; Cottone et al., 2018; Porcaro et al., 2019b). EEG, coupled with proper and advanced mathematical methods, can provide markers for neurodegenerative diseases and facilitate their diagnosis (Tecchio et al., 2015; Smits et al., 2016; Marino et al., 2019; Porcaro et al., 2019a, 2020, 2022a,b,c).

This Research Topic gives an overview of the current knowledge of EEG combined with other techniques for research and diagnostic purposes through 11 articles by 65 authors, which contain two reviews, eight original research papers and one method (Total views: 30,624; as of 27 Jan 2023).

One of the reviews focuses on investigating brain disorders using tES in combination with non-invasive neuroimaging techniques. The review highlights shortcomings and provides a comprehensive guideline for further investigation (Yang et al.). In particular, EEG and fNIRS were selected as noninvasive neuroimaging modalities in this systematic review. Nine brain disorders were investigated in this review, including Alzheimer's disease, depression, autism spectrum disorder, attention-deficit hyperactivity disorder, epilepsy, Parkinson's disease, stroke, schizophrenia, and traumatic brain injury. This review showed that most of the articles (82.6%) employed transcranial direct current stimulation (tDCS) as an intervention method with modulation parameters of 1 mA intensity (47.2%) for 16–20 min (69.0%) duration of stimulation in a single session (36.8%). The author concluded that future work needs to investigate a closed-loop tES with monitoring by neuroimaging techniques to achieve personalized therapy for brain disorders.

The second review includes a flow chart of questions that researchers can consider when deciding whether to record EEG and fMRI separately or simultaneously (Scrivener). Overall, this article aims to equip new researchers with the resources needed to make an informed decision regarding the necessity of simultaneous EEG-fMRI. As multi-modal neuroimaging requires additional time, equipment, and financial resources, it is essential to consider the recording options available thoroughly. Furthermore, ongoing technological and methodological developments continue to facilitate the successful application of combined EEG-fMRI to answer questions about the brain and behavior with increasing precision.

In addition to the reviews, eight original studies analyze the combination of electrophysiological techniques. While some studies focused on combining EEG and Electromyography (EMG) others combined electro- and magnetoencephalography (E-MEG). One of the studies combining EEG and EMG (Zhao et al.) showed robust relationships between EEG and EMG signals that might be of some interest for analyzing neuromotor disorders, such as Parkinson's disease, to identify neural correlates of abnormal gait. In another study, the authors (Pascarella et al.) have developed a new measure named normalized compression distance (NCD) to measure cortico-muscular synchronization using EEG and EMG data. A third study employed a coupled tensor decomposition to extract the signal sources from MEG-EEG during intermittent photic stimulation (IPS). There, Coupled Semi-Algebraic framework for approximate CP decomposition *via* SImultaneous matrix diagonalisation (C-SECSI) was able to separate physiologically meaningful oscillations of visually evoked brain activity from background signals. The component frequencies are able to identify either an entrainment to the respective visual stimulation frequency, its first harmonic, or an oscillation in the individual alpha band or theta band. A reciprocal relationship between alpha and theta band oscillations is present in the group analysis of both EEG and MEG data. The coupled tensor decomposition using the C-SECSI framework is a robust, powerful method for the unsupervised extraction and separation of meaningful sources from multidimensional biomedical measurement data (Naskovska et al.). Finally, another study combined EEG and MEG data using microstates modeled from subject- and modality-specific archetypes that represent distinct topographic maps between which the brain continuously traverses. The implemented method successfully models scale and polarity invariant data, such as microstates, accounting for intersubject and intermodal variability. Furthermore, the model is readily extendable to other modalities ensuring component correspondence while elucidating spatiotemporal signal variability (Olsen et al.).

The utility of electroencephalography for diagnostics is further highlighted both considering Alzheimer's disease (AD) and Stroke. For AD, topological features of networks constructed for each EEG channel based on weighted visibility graphs were considered in Yu et al. and deep learning computer vision models were applied to image representations of topographic and spectral properties of the EEG in Jeong et al.. For stroke, the properties of EEG microstates, including changes in functional connectivity patterns were explored in Hao et al.. Additionally, the use of EEG for the quantification of treatment effect is investigated in the context of remote ischemic preconditioning (RIPC) in Li et al., whereas a modeling framework based on fNIRS as a complementary approach to EEG is proposed for the discrimination of single trial task responses for brain computer interfaces (BCI) in Zhang et al..

Overall, this Research Topic shows the fronts in combining EEG with other techniques to study dynamic brain functions or changes from a temporal and spatial perspective. These include technical possible study design, data acquisition, and data analysis to improve human health by combining advanced brain technologies with cutting-edge science and original bio-medical insight. This challenge requires creative problem-solving, precision and a lot of imagination. There is a big challenge in removing artifacts to perform fully continuous EEG-fMRI/TMS/tDCS/tES recordings. This will be the mainstay of multimodal functional brain imaging. Neuroimaging-techniques is an area that needs further research and validation of algorithms.

Finally, clinical applications have thus far been limited. In the future, combined neuroimaging studies will help neuroscientists to extract neuro-information underlying sensory and cognitive activity in healthy and pathological conditions.

Author contributions

All authors contributed to the article and approved the submitted version.

Funding

This work was partly supported by the Department of excellence 2018–2022 initiative of the Italian Ministry of Education (MIUR) awarded to the Department of Neuroscience–University of Padua [MART_ECCELLENZA18_01].

Acknowledgments

The editors appreciate the contributions of all authors to this Research Topic, the constructive comments of all the reviewers, and the editorial support from Frontiers throughout the publication process.

Conflict of interest

The authors declare that the research was conducted in the absence of any commercial or financial relationships that could be construed as a potential conflict of interest.

Publisher's note

References

Buss, S. S., Fried, P. J., and Pascual-Leone, A. (2019). Therapeutic noninvasive brain stimulation in Alzheimer's disease and related dementias. *Curr. Opin. Neurol.* 32, 292–304. doi: 10.1097/WCO.0000000000000669

Cottone, C., Cancelli, A., Pasqualetti, P., Porcaro, C., Salustri, C., and Tecchio, F. (2018). A new, high-efficacy, noninvasive transcranial electric stimulation tuned to local neurodynamics. *J. Neurosci.* 38, 586–594. doi: 10.1523/JNEUROSCI.2521-16.2017

Giambattistelli, F., Tomasevic, L., Pellegrino, G., Porcaro, C., Melgari, J. M., Rossini, P. M., et al. (2014). The spontaneous fluctuation of the excitability of a single node modulates the internodes connectivity: a TMS-EEG study. *Hum. Brain Mapp.* 35, 1740–1749. doi: 10.1002/hbm.22288

Marino, M., Liu, Q., Samogin, J., Tecchio, F., Cottone, C., Mantini, D., et al. (2019). Neuronal dynamics enable the functional differentiation of resting state networks in the human brain. *Hum.* Brain Mapp. *40, 1445–1457. doi: 10.1002/hbm.24458*

Napolitani, M., Bodart, O., Canali, P., Seregni, F., Casali, A., Laureys, S., et al. (2014). Transcranial magnetic stimulation combined with high-density EEG in altered states of consciousness. *Brain Inj.* 28, 1180–1189. doi: 10.3109/02699052.2014.920524

Ostwald, D., Porcaro, C., and Bagshaw, A. P. (2010). An information theoretic approach to EEG-fMRI integration of visually evoked responses. *Neuroimage.* 49, 498–516. doi: 10.1016/j.neuroimage.2009.07.038

Ostwald, D., Porcaro, C., and Bagshaw, A. P. (2011). Voxel-wise information theoretic EEG-fMRI feature integration. *Neuroimage.* 55, 1270–1286. doi: 10.1016/j.neuroimage.2010.12.029

Ostwald, D., Porcaro, C., Mayhew, S. D., and Bagshaw, A. P. (2012). Eeg-fmri based information theoretic characterization of the human perceptual decision system. *PLoS ONE.* 7. doi: 10.1371/journal.pone.0033896

Porcaro, C., Balsters, J. H., Mantini, D., Robertson, I. H., and Wenderoth, N. (2019a). P3b amplitude as a signature of cognitive decline in the older population: An EEG study enhanced by Functional Source Separation. *Neuroimage.* 184, 535–546. doi: 10.1016/j.neuroimage.2018.09.057

Porcaro, C., Cottone, C., Cancelli, A., Rossini, P. M., Zito, G., and Tecchio, F. (2019b). Cortical neurodynamics changes mediate the efficacy of a personalized neuromodulation against multiple sclerosis fatigue. Sci. *Rep.* 9, 1–10. doi: 10.1038/s41598-019-54595-z

Porcaro, C., Marino, M., Carozzo, S., Russo, M., Ursino, M., Ruggiero, V., et al. (2022a). Fractal dimension feature as a signature of severity in disorders of consciousness: An EEG study. *Int. J. Neural Syst.* 32, 2250031. doi: 10.1142/S0129065722500319

Porcaro, C., Mayhew, S. D., Marino, M., Mantini, D., and Bagshaw, A. P. (2020). Characterisation of haemodynamic activity in resting state networks by fractal analysis. *Int. J. Neural Syst.* 30, S0129065720500616. doi: 10.1142/S0129065720500616

Porcaro, C., Nemirovsky, I. E., Riganello, F., Mansour, Z., Cerasa, A., Tonin, P., et al. (2022b). Diagnostic developments in differentiating unresponsive wakefulness syndrome and the minimally conscious state. *Front. Neurol.* 12. doi: 10.3389/fneur.2021.778951

Porcaro, C., Ostwald, D., and Bagshaw, A. P. F. (2010). Functional source separation improves the quality of single trial visual evoked potentials recorded during concurrent EEG-fMRI. *Neuroimage.* 50, 112–123. doi: 10.1016/j.neuroimage.2009.12.002

Porcaro, C., Ostwald, D., Hadjipapas, A., Barnes, G. R., and Bagshaw, A. P. (2011). The relationship between the visual evoked potential and the gamma band investigated by blind and semi-blind methods. *Neuroimage.* 56, 1059–1071. doi: 10.1016/j.neuroimage.2011.03.008

Porcaro, C., Vecchio, F., Miraglia, F., Zito, G., and Rossini, P. M. (2022c). Dynamics of the "cognitive" brain wave P3b at rest for Alzheimer dementia prediction in mild cognitive impairment. *Int. J. Neural Syst.* 32, 2250022. doi: 10.1142/S0129065722500228

Smits, F. M., Porcaro, C., Cottone, C., Cancelli, A., Rossini, P. M., and Tecchio, F. (2016). Electroencephalographic fractal dimension in healthy ageing and Alzheimer's disease. *PLoS ONE.* 11, e0149587. doi: 10.1371/journal.pone.0149587

Tecchio, F., Cancelli, A., Cottone, C., Ferrucci, R., Vergari, M., Zito, G., et al. (2015). Brain plasticity effects of neuromodulation against multiple sclerosis fatigue. *Front. Neurol.* 6, 141. doi: 10.3389/fneur.2015.00141

Tecchio, F., Giambattistelli, F., Porcaro, C., Cottone, C., Mutanen, T. P., Pizzella, V., at al. (2023). Effective intracerebral connectivity in acute stroke: A TMS-EEG study. *Brain Sci.* 13, 233. doi: 10.3390/brainsci13020233

Tulay, E. E., Metin, B., Tarhan, N., and Arikan, M. K. (2019). Multimodal neuroimaging: basic concepts and classification of neuropsychiatric diseases. *Clin. EEG Neurosci.* 50, 20–33. doi: 10.1177/1550059418782093

frontiers in Neuroscience

ORIGINAL RESEARCH
published: 09 April 2020
doi: 10.3389/fnins.2020.00261

Coupled CP Decomposition of Simultaneous MEG-EEG Signals for Differentiating Oscillators During Photic Driving

Kristina Naskovska[1], Stephan Lau[2,3], Alexey A. Korobkov[1,4], Jens Haueisen[2] and Martin Haardt[1]*

[1] Communications Research Laboratory, Ilmenau University of Technology, Ilmenau, Germany, [2] Institute of Biomedical Engineering and Informatics, Ilmenau University of Technology, Ilmenau, Germany, [3] School of Computer Science, Australian Institute for Machine Learning, The University of Adelaide, Adelaide, SA, Australia, [4] Institute for Radio-Electronics and Telecommunications, Department for Radio-Electronic and Telecommunication Systems, Kazan National Research Technical University named after A.N Tupolev-KAI, Kazan, Russia

Edited by:
Morten Mørup,
Technical University of Denmark,
Denmark

Reviewed by:
Maarten De Vos,
University of Oxford, United Kingdom
Gareth Barnes,
University College London,
United Kingdom

***Correspondence:**
Jens Haueisen
jens.haueisen@tu-ilmenau.de

Specialty section:
This article was submitted to
Brain Imaging Methods,
a section of the journal
Frontiers in Neuroscience

Received: *17 June 2019*
Accepted: *09 March 2020*
Published: *09 April 2020*

Citation:
Naskovska K, Lau S, Korobkov AA, Haueisen J and Haardt M (2020) Coupled CP Decomposition of Simultaneous MEG-EEG Signals for Differentiating Oscillators During Photic Driving.
Front. Neurosci. 14:261.
doi: 10.3389/fnins.2020.00261

Magnetoencephalography (MEG) and electroencephalography (EEG) are contemporary methods to investigate the function and organization of the brain. Simultaneously acquired MEG-EEG data are inherently multi-dimensional and exhibit coupling. This study uses a coupled tensor decomposition to extract the signal sources from MEG-EEG during intermittent photic stimulation (IPS). We employ the Coupled Semi-Algebraic framework for approximate CP decomposition via SImultaneous matrix diagonalization (C-SECSI). After comparing its performance with alternative methods using simulated benchmark data, we apply it to MEG-EEG recordings of 12 participants during IPS with fractions of the individual alpha frequency between 0.4 and 1.3. In the benchmark tests, C-SECSI is more accurate than SECSI and alternative methods, especially in ill-conditioned scenarios, e.g., involving collinear factors or noise sources with different variances. The component field-maps allow us to separate physiologically meaningful oscillations of visually evoked brain activity from background signals. The frequency signatures of the components identify either an entrainment to the respective stimulation frequency or its first harmonic, or an oscillation in the individual alpha band or theta band. In the group analysis of both, MEG and EEG data, we observe a reciprocal relationship between alpha and theta band oscillations. The coupled tensor decomposition using C-SECSI is a robust, powerful method for the extraction of physiologically meaningful sources from multidimensional biomedical data. Unsupervised signal source extraction is an essential solution for rendering advanced multi-modal signal acquisition technology accessible to clinical diagnostics, pre-surgical planning, and brain computer interface applications.

Keywords: alpha band, electroencephalography, frequency entrainment, magnetoencephalography, simultaneous diagonalization, steady-state evoked response, tensor, theta band

1. INTRODUCTION

Magnetoencephalography (MEG) and electroencephalography (EEG) are contemporary methods to investigate the function and organization of the brain. They, respectively, measure the magnetic flux and the electric potential at the head surface that are generated by simultaneous neuronal activity inside the brain. MEG-EEG data are inherently multi-dimensional, typically including the dimensions time, space (channels), modality (MEG, EEG), participant, and experimental condition. Simultaneously acquired MEG and EEG signals capture aspects of the same electric activity over time and can, therefore, exhibit coupling.

Tensor algebra has applications in signal processing, data analysis, blind source separation, and many more (Cichocki et al., 2015). The multidimensional signals are decomposed into rank one components according to the Canonical Polyadic (CP) decomposition (Kolda and Bader, 2009). Roemer and Haardt (2008, 2013) present a Semi-Algebraic framework for approximate CP decomposition via SImultaneous matrix diagonalization (SECSI) for the efficient and robust computation of the an approximate low-rank CP decomposition of noise corrupted data.

Many combined signal processing applications benefit from a coupled analysis based on the coupled CP decomposition (Becker et al., 2012; Acar et al., 2013, 2015; Rivet et al., 2015; Naskovska et al., 2017b; Sørensen and De Lathauwer, 2017a; Zou et al., 2017). The coupled CP decomposition jointly decomposes heterogeneous tensors that have at least one factor matrix in common. Detailed analysis of the computation of the coupled CP decomposition based on Alternating Least Squares (ALS) is presented in Farias et al. (2016) and Cohen et al. (2016). Farias et al. (2016) and Cohen et al. (2016) show that the computation of the coupled CP decomposition based on ALS is sensitive to different noise variances in the different tensors. An extension of the SECSI framework (Roemer and Haardt, 2008, 2013) to the coupled SECSI (C-SECSI) framework is proposed in Naskovska and Haardt (2016). The C-SECSI framework efficiently approximates the coupled CP decomposition of two noisy tensors that have at least one mode in common even in ill-posed scenarios, e.g., if the columns of a factor matrix are highly correlated. Moreover, the C-SECSI framework offers adjustable complexity-accuracy trade-offs and efficiently decomposes tensors with different noise variances without performance degradation.

Human scalp EEG signals contain characteristic frequencies, which can be partly related to cognitive processes. Their power and synchronization can vary with wakefulness, attention, age, disease, and in response to a sensory input (Klimesch, 1999). The dominant frequency peak in the spectrum is called the alpha rhythm and is traditionally expected between 7.5 and 12.5 Hz in adults (Klimesch, 1999). The second strongest is the theta rhythm, typically between 4 and 7.5 Hz. Whereas the frequencies of alpha and theta covary, their band powers are related to each other in a reciprocal way (Klimesch, 1999). Both, alpha and theta bands, are specifically related to cognitive and memory performance. Good performance at rest is associated with a tonic increase in alpha together with a decrease in theta. During event processing, a strong decrease in alpha together with an increase in theta indicates good performance (Klimesch, 1999). Desynchronization in the lower alpha band indicates attention, whereas a desynchronization in the upper alpha band is associated with semantic memory performance. Synchronization of theta reflects episodic memory and successful encoding of new information (Klimesch, 1999).

Intermittent photic stimulation (IPS) is a stimulation of the brain with repetitive light flashes that can drive oscillations in the brain. This is called the photic driving (PD) effect. The PD effect is widely used to assess effects of medication and for neurological diagnostics of, for example, epilepsy (Kalitzin et al., 2002). IPS can cause a frequency entrainment and a resonance effect. Frequency entrainment is characterized by the synchronization of brain rhythms to the photic stimulation (da Silva, 1991; Notbohm et al., 2016). The resonance effect is characterized by an increased amplitude of brain rhythms, such as alpha and theta, when the stimulation frequency coincides with their intrinsic frequencies. Photic driving has been reported to appear with stimulation frequencies up to 90 Hz (Herrmann, 2001). The strongest resonance appears around the individual alpha frequency (Mangan et al., 1993; Klimesch, 1999; Herrmann, 2001; Lazarev et al., 2001). A secondary resonance can be observed in the individual theta band of adults (Mangan et al., 1993; Klimesch, 1999) and more pronounced in children and adolescents (Klimesch, 1999; Lazarev et al., 2001).

Schwab et al. (2006) have performed the first investigation of frequency entrainment using simultaneously recorded MEG and EEG signals during IPS with frequency fractions of the individual alpha rhythm of each participant. In a subsequent comparable experiment, Salchow et al. (2016) have shown that a strong alpha resonance exists for a rod-type photo-receptor cell input at stimulation frequencies close to the individual alpha frequency peak and in the theta band. In this study, we consider the same experiment as in Salchow et al. (2016) using a time-frequency transformation (Wacker et al., 2011).

The objective of this study is to extract and differentiate signal sources from simultaneous MEG-EEG recordings during intermittent photic stimulation using a coupled tensor decomposition. We evaluate the capability of the proposed approach by comparing it to alternative methods using simulated benchmark data.

2. METHODS

2.1. Tensor Algebra and Notation

Scalars are denoted either as capital or lower-case italic letters A, a. Vectors, matrices, and tensors are denoted as bold-faced lower-case $\boldsymbol{a}$, capital $\boldsymbol{A}$, and bold-faced calligraphic letters $\boldsymbol{\mathcal{A}}$, respectively. The superscripts $^{\mathrm{T}}$, $^{\mathrm{H}}$,$^{-1}$, and $^{+}$ denote transposition, Hermitian transposition, matrix inversion, and Moore-Penrose pseudo matrix inversion, respectively. The operators $\|.\|_{\mathrm{F}}$ and $\|.\|_{\mathrm{H}}$ symbolize the Frobenius norm and the higher order norm, respectively. Moreover, an n-mode product between a tensor $\boldsymbol{\mathcal{A}} \in \mathbb{C}^{I_1 \times I_2 \ldots \times I_N}$ and a matrix $\boldsymbol{B} \in \mathbb{C}^{J \times I_n}$ is denoted by $\boldsymbol{\mathcal{A}} \times_n \boldsymbol{B}$, for $n = 1, 2, \ldots N$ (Kolda and Bader, 2009).

A super-diagonal or or identity N-way tensor with dimensions $R \times R \ldots \times R$ is denoted as $\mathcal{I}_{N,R}$. The n-mode unfolding of a tensor $\boldsymbol{\mathcal{A}}$ is symbolized as $[\boldsymbol{\mathcal{A}}]_{(n)}$, and the n-th 3-mode slice is denoted with $\boldsymbol{A}_n = \boldsymbol{\mathcal{A}}_{(.,.,n)}$. Fundamental tensor algebra concepts and definitions are provided in Kolda and Bader (2009), De Lathauwer et al. (2000), Cichocki et al. (2015), Comon et al. (2009), and Sidiropoulos et al. (2017).

The CP tensor decomposition is an extension of the Singular Value Decomposition (SVD) to multidimensional arrays (tensors). It decomposes a tensor into the minimum number of rank one components. For a low-rank tensor $\boldsymbol{\mathcal{X}}_0 \in \mathbb{C}^{M_1 \times M_2 \times M_3}$ with rank R the CP decomposition is

$$\boldsymbol{\mathcal{X}}_0 = \boldsymbol{\mathcal{I}}_{3,R} \times_1 \boldsymbol{F}_1 \times_2 \boldsymbol{F}_2 \times_3 \boldsymbol{F}_3,$$

where $\boldsymbol{F}_1 \in \mathbb{C}^{M_1 \times R}$, $\boldsymbol{F}_2 \in \mathbb{C}^{M_2 \times R}$, and $\boldsymbol{F}_3 \in \mathbb{C}^{M_3 \times R}$ are the factor matrices (Kolda and Bader, 2009; Cichocki et al., 2015). In contrast to the SVD, the factor matrices resulting from the CP decomposition are not necessarily unitary, implying that the underling rank one components are not orthogonal to one another. Moreover, the CP decomposition is essentially unique under mild conditions.

Due to the uniqueness properties, the factor matrices of a CP decomposition can be identified up to a permutation and one complex scaling ambiguity per column. There are many different types of algorithms for the computation of the CP decomposition that can be categorized as follows: Alternating Least Squares (ALS), Gradient Descent (GD), Quasi-Newton and Nonlinear Least Squares (NLS) based algorithms as well as semi-algebraic approaches.

If two low-rank noiseless tensors $\boldsymbol{\mathcal{X}}_0^{(1)} \in \mathbb{C}^{M_1 \times M_2^{(1)} \times M_3^{(1)}}$ and $\boldsymbol{\mathcal{X}}_0^{(2)} \in \mathbb{C}^{M_1 \times M_2^{(2)} \times M_3^{(2)}}$ have the first mode in common, then they have a coupled CP decomposition defined as

$$\begin{aligned}\boldsymbol{\mathcal{X}}_0^{(1)} &= \boldsymbol{\mathcal{I}}_{3,R} \times_1 \boldsymbol{F}_1 \times_2 \boldsymbol{F}_2^{(1)} \times_3 \boldsymbol{F}_3^{(1)} \\ \boldsymbol{\mathcal{X}}_0^{(2)} &= \boldsymbol{\mathcal{I}}_{3,R} \times_1 \boldsymbol{F}_1 \times_2 \boldsymbol{F}_2^{(2)} \times_3 \boldsymbol{F}_3^{(2)},\end{aligned} \tag{1}$$

where, $\boldsymbol{F}_1 \in \mathbb{C}^{M_1 \times R}$, $\boldsymbol{F}_2^{(i)} \in \mathbb{C}^{M_2^{(i)} \times R}$ and $\boldsymbol{F}_3^{(i)} \in \mathbb{C}^{M_3^{(i)} \times R}$, $i = 1, 2$ are the factor matrices and R is the rank of the tensors. The coupled CP decomposition has even more relaxed uniqueness conditions than the CP decomposition. Some uniqueness properties for the coupled CP decomposition are available in Sørensen et al. (2015) and Zou et al. (2017).

The coupled CP decomposition jointly analyzes heterogeneous data sets or signals and identifies their shared underlying components. The facts that the heterogeneous signals can have different nature and dimensions and that the uniqueness properties are relaxed make the coupled CP decomposition a very practical tool for array (Sørensen et al., 2015, 2018; Sørensen and De Lathauwer, 2017a,b), audio (Zou et al., 2017), and biomedical signal progressing (Becker et al., 2012; Acar et al., 2013, 2015; Papalexakis et al., 2014; Rivet et al., 2015; Naskovska et al., 2017a,b; Van Eyndhoven et al., 2017).

Another extension of the SVD to multidimensional arrays is the higher order SVD (HOSVD) or Multi-linear SVD (De Lathauwer et al., 2000). The factor matrices resulting from the HOSVD are unitary matrices and they represent a unitary basis of the n-mode unfolding of the tensor, for $n = 1, \ldots N$ (for N-way tensors). Similar to the concept of truncated SVD, for a noise corrupted tensor a truncated HOSVD can be defined. The truncated HOSVD is a practical tool for noise suppression, dimension reduction, and signal subspace estimation (Haardt et al., 2008).

In case of noise corrupted tensors the truncated coupled HOSVD,

$$\boldsymbol{\mathcal{X}}^{(1)} = \boldsymbol{\mathcal{X}}_0^{(1)} + \boldsymbol{\mathcal{N}}^{(1)} \approx \boldsymbol{\mathcal{S}}^{[s],(1)} \times_1 \boldsymbol{U}_1^{[s]} \times_2 \boldsymbol{U}_2^{[s],(1)} \times_3 \boldsymbol{U}_3^{[s],(1)} \tag{2}$$

$$\boldsymbol{\mathcal{X}}^{(2)} = \boldsymbol{\mathcal{X}}_0^{(2)} + \boldsymbol{\mathcal{N}}^{(2)} \approx \boldsymbol{\mathcal{S}}^{[s],(2)} \times_1 \boldsymbol{U}_1^{[s]} \times_2 \boldsymbol{U}_2^{[s],(2)} \times_3 \boldsymbol{U}_3^{[s],(2)}, \tag{3}$$

can be calculated jointly, for the common mode using the economy-size SVD,

$$\left[\, [\boldsymbol{\mathcal{X}}^{(1)}]_{(1)} \;\; [\boldsymbol{\mathcal{X}}^{(2)}]_{(1)} \,\right] = \boldsymbol{U}_1^{[s]} \cdot \boldsymbol{\Sigma}_1^{[s]} \cdot \boldsymbol{V}_1^{[s]\mathrm{H}}.$$

In (2) and (3), $\boldsymbol{\mathcal{S}}^{[s],(1)}$ and $\boldsymbol{\mathcal{S}}^{[s],(2)} \in \mathbb{C}^{R \times R \times R}$ are the truncated core tensors and the loading matrices $\boldsymbol{U}_1^{[s]} \in \mathbb{C}^{M_1 \times R}$, $\boldsymbol{U}_2^{[s],(i)} \in \mathbb{C}^{M_2^{(i)} \times R}$ and $\boldsymbol{U}_3^{[s],(i)} \in \mathbb{C}^{M_3^{(i)} \times R}$ have unitary columns and span an estimate of the column space of the n-mode unfolding of $\boldsymbol{\mathcal{X}}^{(i)}$, for $n = 1, 2, 3$ and $i = 1, 2$, respectively.

2.2. Computation of the Coupled CP Decomposition

In order to compute the factors corresponding to the coupled CP decomposition, the existing algorithms for the computation of the CP decomposition have to be modified. For instance, the ALS algorithm can be extended to a coupled ALS (C-ALS) by taking into account that the common factor matrix can be jointly computed by means of concatenation. Another weighted version of the coupled ALS using normalization that can even support hybrid and noisy coupling is proposed in Farias et al. (2016). For the purpose of dimensionality reduction a compression based on the HOSVD can be used as a preprocessing step for ALS (Cohen et al., 2016). These ALS based algorithms are easy to implement, however, they have no convergence guarantee and can require many iterations.

Alternatively, the coupled CP decomposition can be computed based on a line search. The line search based algorithm CCP-MINF is available in Tensorlab 3.0 (Vervliet et al., 2016). Additionally, a NLS-based algorithm is available in Tensorlab 3.0 (Vervliet et al., 2016). The CCP-NLS algorithm is an iterative algorithm that computes updates of the factor matrices based on a Newton descent, which includes a linear approximation of the Hessian. A further approach is the semi-algebraic computation of the CP decomposition, which involves converting the CP model into a simultaneous matrix decomposition (SMD) followed by diagonalization in order to obtain the factor matrices (Sørensen et al., 2015; Naskovska and Haardt, 2016). The coupled SECSI algorithm (Naskovska and Haardt, 2016) is an efficient extension of SECSI (Roemer and Haardt, 2008, 2013; Roemer et al., 2012) that uses the tensor structure to construct not only one but the full set of possible SMDs jointly for both tensors.

The C-SECSI approach provides an estimate of the factor matrices using the joint HOSVD followed by the whole set of possible SMDs. Eight initial estimates of the factor matrices I, . . . , VIII are obtained, if the two tensors have one factor matrix in common (Naskovska and Haardt, 2016). The computation of only two initial estimates of the factor matrices of two tensors $\boldsymbol{\mathcal{X}}^{(1)}$ and $\boldsymbol{\mathcal{X}}^{(2)}$ that have the first mode in common is visualized in **Figure 1**. These estimates are depicted by the two parallel branches in **Figure 1**, as well as an indication whether they are estimated from a transform matrix, from the diagonalized tensor, estimated via Least Squares (LS) or a joint LS fit. Note that these two estimates are obtained by diagonalizing the third mode of the core tensors resulting from the joint HOSVD, where $\boldsymbol{T}_1$ and $\boldsymbol{T}_2$ represent the transform matrices. Similarly, another two estimates of the factor matrices are obtained by diagonalizing the second mode of the core tensors. The diagonalization along the first mode (common mode) results in another four SMDs. However, since the common mode is in the diagonal elements, these SMDs cannot be combined. Therefore, they are solved separately and result in four additional initial estimates of the factor matrices.

From all these initial estimates of the factor matrices the one of major interest is the common factor matrix $\hat{\boldsymbol{F}}_1$. The first four estimates of the common factor matrix (from $\hat{\boldsymbol{F}}_{1,\mathrm{I}}$ to $\hat{\boldsymbol{F}}_{1,\mathrm{IV}}$) are obtained either from the common transform matrices or via a joint LS fit. On the other hand, the last four estimates (from $\hat{\boldsymbol{F}}_{1,\mathrm{V}}$ to $\hat{\boldsymbol{F}}_{1,\mathrm{VIII}}$) are separately obtained from the diagonal elements of the diagonalized tensor. Therefore, the first four solutions are coupled and the last four are uncoupled. The final solution is then chosen for each of the tensors separately based on a heuristic that uses an accuracy-complexity trade-off (Roemer and Haardt, 2013; Naskovska and Haardt, 2016). Here, we use the reconstructed paired solutions (REC PS), with which the final solution is selected out of the eight estimates I − VIII based on the reconstruction error (Roemer and Haardt, 2013). The reconstruction error is calculated according to

$$e_{\mathrm{rec}} = \frac{\left|\left|\hat{\boldsymbol{\mathcal{X}}} - \boldsymbol{\mathcal{X}}\right|\right|_{\mathrm{H}}^2}{||\boldsymbol{\mathcal{X}}||_{\mathrm{H}}^2},$$

where $\hat{\boldsymbol{\mathcal{X}}}$ denotes the estimated tensor and $\boldsymbol{\mathcal{X}}$ denotes the input tensor. Note that when $\boldsymbol{\mathcal{X}}$ is a noisy observation as in **Figures 14, 15**, i.e., $\boldsymbol{\mathcal{X}} = \boldsymbol{\mathcal{X}}_0 + \boldsymbol{\mathcal{N}}$, we refer to this refer to this error as residual and denote it as RES.

To evaluate the reliability of the C-SECSI framework, we check whether the same (coupled) solution is chosen for both tensors (Naskovska et al., 2017a). Therefore, we define the reliability in percent

$$\mathrm{REL} = \left(1 - \frac{1}{2} \cdot \frac{\left|\left|\hat{\boldsymbol{F}}_1^{(2)} \cdot \boldsymbol{P} - \hat{\boldsymbol{F}}_1^{(1)}\right|\right|_{\mathrm{F}}^2}{\left|\left|\hat{\boldsymbol{F}}_1^{(1)}\right|\right|_{\mathrm{F}}^2}\right) \cdot 100\%, \tag{4}$$

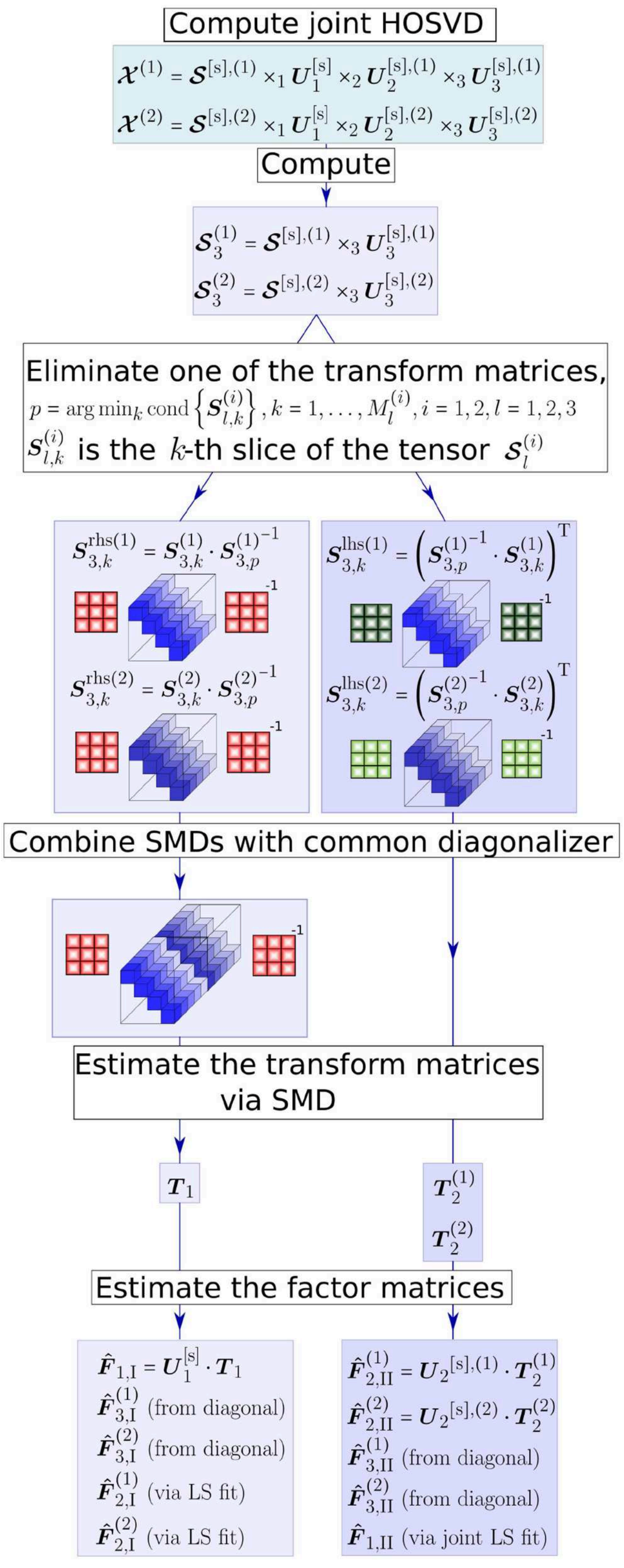

FIGURE 1 | The C-SECSI framework for the computation of the coupled CP decomposition of two tensors $\boldsymbol{\mathcal{X}}^{(1)}$ and $\boldsymbol{\mathcal{X}}^{(2)}$ that have the first mode in common.

as a similarity measure of the final estimates of the common factor matrices. Here, $\boldsymbol{P}$ is a permutation matrix of size $R \times R$ that resolves the permutation ambiguity of the CP decomposition. Moreover, $\hat{\boldsymbol{F}}_1^{(1)}$ and $\hat{\boldsymbol{F}}_1^{(2)}$ are the final estimates of the common mode assigned to the tensors $\boldsymbol{\mathcal{X}}^{(1)}$ and $\boldsymbol{\mathcal{X}}^{(2)}$, respectively. This reliability measure has a maximum if the final estimates result from a coupled solution and the assumed rank is correctly approximated. Therefore, the reliability can be used to control the tensor rank of the coupled approximate CP decompositions. Note that for tensor rank one the reliability is always 100%. This is due to the fact that for rank one tensors the C-SECSI framework does not calculate any SMD. In this case, only one final estimate of the factor matrices is provided directly from the joint truncated HOSVD.

2.3. Measured MEG-EEG Signals

With ethics approval (Faculty of Medicine of the Friedrich-Schiller-University Jena, Germany), simultaneous MEG-EEG was performed on 12 healthy participants, aged between 21 and 42 years (median 26 years) during stimulation with flickering light (Salchow et al., 2016). The light stimulus was delivered through optical fibers from light emitting diodes outside the recording room. Light diffusers approximately 10 cm in front of the participants eyes provided a luminance of 0.0003 cd/m^2. Throughout the exposure, the eyes of the participants were closed. The MEG provided 102 magnetometers and the EEG used 128 electrodes.

The purpose of the experiment was to investigate the behavior and interactions of oscillators in the healthy brain by systematically probing them with a controlled visual stimulation input. The frequency is a principle parameter of an oscillator. Therefore, a series of frequencies covering the alpha and theta bands was used to sample the brain's response pattern across the frequency dimension. The measured response is expected to contain multiple superimposed sources, some of which will be oscillatory. In a first step, the individual alpha rhythm was measured during 60 s of MEG at rest. The individual alpha frequencies f_α were then calculated by means of the averaged Discrete Fourier Transform (DFT) from the occipital MEG channels. The resulting alpha frequencies for Participants 1 to 12 are, in this order, 9.6, 10.7, 10.4, 10.8, 10.7, 10.8, 7.5, 10.8, 11.0, 10.7, 12.2, and 10.3 Hz.

IPS was then conducted at frequencies of $f_s = [0.40\ 0.45\ 0.50\ 0.55\ 0.60\ 0.70\ 0.80\ 0.90\ 0.95\ 1.00\ 1.05\ 1.10\ 1.30\ 1.60\ 1.90\ 1.95\ 2.00\ 2.05\ 2.10\ 2.30] \cdot f_\alpha$. However, because there was no evidence of entrainment for stimulation frequencies larger than $1.30 \cdot f_\alpha$ (Salchow et al., 2016), we used only the first 13 stimulation frequencies in this study, i.e., from $0.40 \cdot f_\alpha$ until $1.30 \cdot f_\alpha$.

Each stimulation frequency was performed in 30 stimulation trains, each consisting of 40 periods with an pulse/cycle duration of 0.5. Between each train there was a resting period of four seconds. From one frequency block to the next one, there was a resting period of 30 s. To avoid an ordering effect, the sequence of the stimulation frequencies was permuted and not known to the participant. Further details regarding the experiment including an analysis are provided in Salchow et al. (2016).

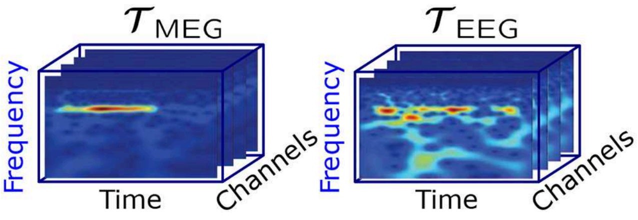

FIGURE 2 | Visualization of the MEG and EEG tensor per participant and stimulation frequency.

2.4. Signal Processing and Decomposition

The MEG and EEG signals were averaged for each stimulation frequency. A small number of non-functional EEG channels were excluded, which were typically at the inferior posterior edge of the EEG caps, where the variable head shape and/or thick hair layer results in the cap being too loose to fixate the electrodes and stabilize the electrolyte gel. These channels were identified based on their non-physiological signals, e.g., constant value, very strong noise or large artifacts. One technically faulty MEG sensor was excluded.

A complex Morlet wavelet decomposition was used to obtain an estimate of the instantaneous frequencies across the stimulation time range of the MEG and EEG signals. Wavelet frequencies of 1,000/256 Hz, 1,000/255 Hz,. . ., 1,000/1 Hz were used during the decomposition. The wavelet coefficients between 3.77 Hz (1,000/265 Hz) and 15.15 Hz (1,000/66 Hz) were selected for the further analysis, thereby including the alpha and theta band. **Figure 2** shows an example of the wavelet coefficients for each of the MEG and EEG channels arranged as slices in a three-way tensor.

As a result we have different complex tensors with dimensions frequency × time × channels for each stimulation frequency, measurement mode (MEG or EEG) and participant. The frequency and time dimensions correspond to the discretized values resulting directly from the wavelet transform. The frequency dimension contains 200 discrete frequency values from 3.77 Hz (1,000/265 Hz) to 15.15 Hz (1,000/66 Hz). The time dimension, however, varies from around 5,000 ms up to 20,000 ms depending on the corresponding stimulation frequency. Furthermore, the channel dimension represents the number of MEG and EEG channels, which varies across participants and conditions.

Next, the MEG and EEG signal tensors were jointly analyzed with the C-SECSI framework for each participant and stimulation frequency, respectively. The coupled CP decompositions were originally computed for different ranks. However, the reliability and the residual indicated that the tensor rank is overestimated for values equal to or larger than three (Naskovska et al., 2017a). Therefore, we assumed a tensor rank of two, $\hat{R} = 2$. We assumed that the frequency mode is common for both, the MEG and the EEG signal tensor. Before the computation of the coupled

CP decomposition, each of the tensors was normalized by calculating

$$\mathcal{T}_{\mathrm{MEG}}' = \frac{\mathcal{T}_{\mathrm{MEG}}}{\|\mathcal{T}_{\mathrm{MEG}}\|_{\mathrm{H}}} \quad \text{and} \quad \mathcal{T}_{\mathrm{EEG}}' = \frac{\mathcal{T}_{\mathrm{EEG}}}{\|\mathcal{T}_{\mathrm{EEG}}\|_{\mathrm{H}}}.$$

This normalization of the tensors made the different amplitude scales and units (fT and μV) of the MEG and EEG signals compatible.

2.5. Analysis of Components

The joint MEG-EEG signal decomposition based on the coupled CP decomposition resulted in three factor matrices for the MEG and three factor matrices for the EEG signal tensor [c.f. Equation (1)] for each participant and each stimulation frequency. Each factor matrix consisted of two columns corresponding to the two components due to the assumed rank $\hat{R} = 2$.

The stimulation experiment provides us with a known reproducible visual response pattern that exhibits physiological integrity. However, the success of an individual experiment depends on the attention and compliance of the participant and varies across the series of repetitive stimulation. We aim to analyze the response of the brain to visual stimulation and, therefore, we need to determine the experiments in which that response was in fact successfully stimulated. For this purpose, the topographic distributions of the signals (field-maps) were labeled independently by three experienced professionals (SL, UG, DS). The measured MEG and EEG signals were converted to field-maps by calculating the root of the mean of the square (RMS) of the values in each channel. The components were displayed as field-maps by taking the channel factor matrix. We used three categories: (1) containing primarily only visual response patterns, (2) containing some visual response patterns and some other activity, and (3) containing no visual response patterns. For each participant, the labeler identified the participant-specific variation of the visual response pattern in position, orientation, symmetry and amplitude due to individual cortical folding, head shape and EEG cap/MEG placement. This could most easily be observed for stimulation close to the individual alpha frequency, where the response was typically strong and clear. Each labeler then labeled all data of that participant sequentially. The labeling sets were unified with a majority vote (if all three raters different, use Category 2). A majority was obtained in 96% of cases, including 88% perfect agreement and 8% with a deviation of one category step by one of the three labelers, e.g., if the dataset is between two categories. Note that this labeling takes into account the spatial characteristics of visual response signals and is more specific than a simple amplitude or power threshold in the alpha frequency band. Secondly, it accommodates the inclusion of sources with frequencies other than the alpha frequency, especially in the theta band.

For the group analysis of the brain oscillations during successful photic stimulation without confounding factors, we use only Category 1. For each component, the principal frequency, i.e., the maximum of the frequency signature, was determined as the obtained frequency of this component.

In order to separate the components reflecting recruitment to the stimulation frequency from other components, we differentiate two groups: The recruited group contains the components, whose obtained frequency is very close to the stimulation frequency or its second harmonic (Herrmann, 2001; Lazarev et al., 2001) with a maximum deviation of $\pm 0.05 f_s$ and $\pm 0.05 \cdot 2 \cdot f_s$, respectively. The non-recruited group consists of the remaining components. All frequencies are expressed in fractions of the individual alpha frequency of the participant to account for the inter-individual differences (Klimesch, 1999).

3. RESULTS

3.1. Benchmark Performance With Simulations

In order to systematically compare the C-SECSI decomposition approach with other methods (Roemer and Haardt, 2008, 2013; Cichocki et al., 2015) on the algorithmic level, we use a set of simulations covering a broad range of tensor properties.

3.1.1. Reliability

Figure 3 visualizes the typical reliability as a function of the assumed rank $\hat{R}$. These curves result from Monte Carlo simulations with 1,000 realizations, for real valued tensors of dimensions $8 \times 8 \times 8$, which spans open a tensor space with sufficient points per dimension to include complex multidimensional patterns. The entries of the factor matrices are drawn from a zero-mean Gaussian random process with variance one. Afterwards, the tensors are computed according to the coupled CP decomposition in Equation (1), allowing us to control the exact rank of the tensors. Additionally, a white Gaussian noise was added resulting in SNR_1 (Signal to Noise Ratio) and SNR_2.

$$\mathrm{SNR}_1 = 10 \log_{10} \left(\frac{\left\| \mathcal{X}_0^{(1)} \right\|_{\mathrm{H}}^2}{\left\| \mathcal{N}^{(1)} \right\|_{\mathrm{H}}^2} \right) \quad \mathrm{SNR}_2 = 10 \log_{10} \left(\frac{\left\| \mathcal{X}_0^{(2)} \right\|_{\mathrm{H}}^2}{\left\| \mathcal{N}^{(2)} \right\|_{\mathrm{H}}^2} \right)$$

The SNR values in the simulations have been chosen to include realistic levels during physiological measurements, such as −0.5 dB for brain signals below noise level, 0 dB for brain signals at noise level and 5 dB for brain signals above noise but still impacted by it. The true tensor rank and the corresponding SNRs are indicated in the legend, while the assumed rank $\hat{R}$ is varied from two to six, given that several brain regions can be involved in performing a cognitive function. The true tensor rank for each curve is additionally indicated with a marker above the curves. It is clear that we have a reliability maximum when the assumed rank equals the correct tensor rank. Moreover, the SNR influences the reliability measure due to the dependency of the estimates on the SNR.

Figure 4 depicts the reliability when the two tensors have different numbers of components. For instance, for the blue curve the first tensor has rank 4, while the second tensor has rank

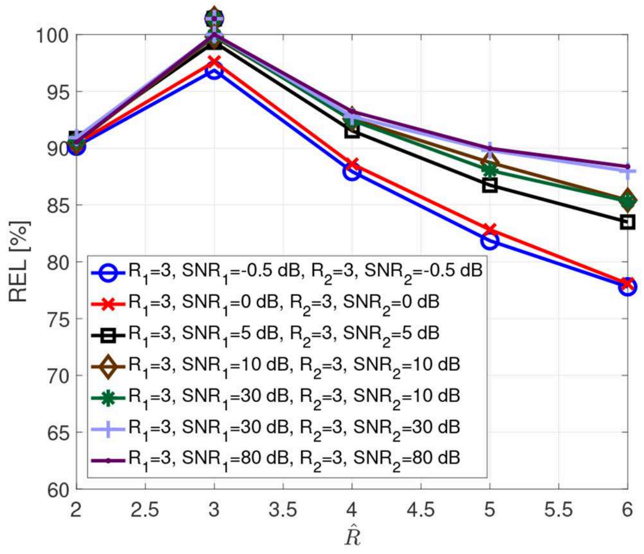

FIGURE 3 | Reliability as a function of the assumed rank $\hat{R}$ for different SNRs.

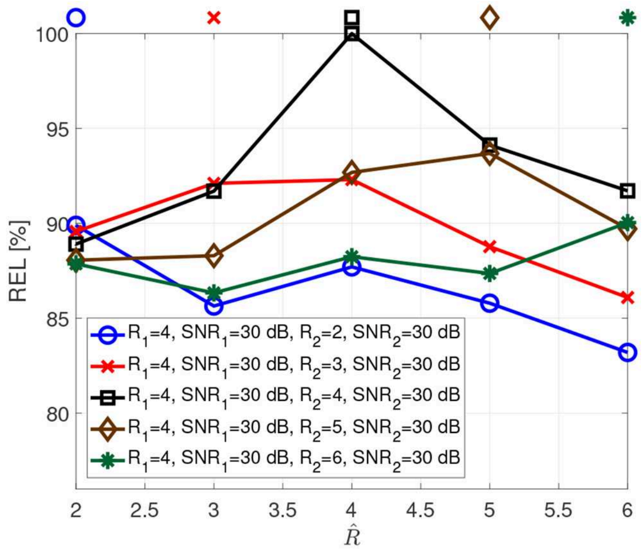

FIGURE 4 | Reliability as a function of the assumed rank $\hat{R}$ for different ranks.

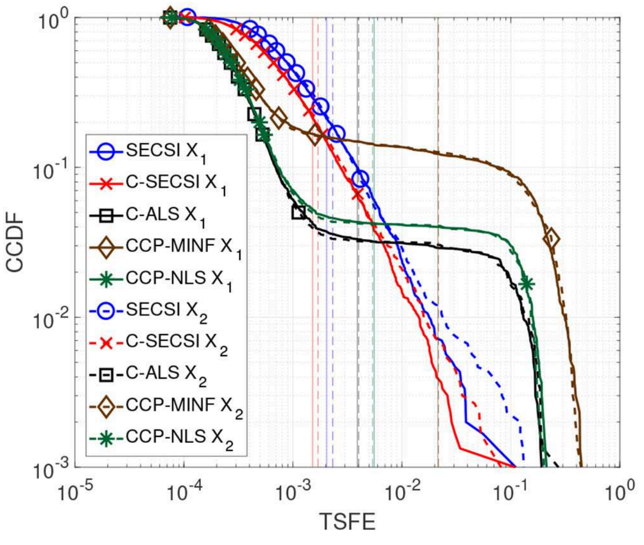

FIGURE 5 | CCDF of the TSFE for real-valued tensors $\boldsymbol{\mathcal{X}}_1$ and $\boldsymbol{\mathcal{X}}_2$ with dimensions 40 × 4 × 10, tensor rank $R_1 = R_2 = 3$, factor matrices with mutually correlated columns designed as sine functions, and $\text{SNR}_1 = \text{SNR}_2 = 25$ dB.

2. This implies that the tensors share only two components, and the first tensor has two additional components. In this case, the reliability has local maxima for both ranks.

3.1.2. Accuracy

When performing a signal analysis using the CP decomposition, we are interested in the factor matrices, because their columns represent the signatures of the underlying components for the corresponding dimensions. Therefore, an important measure for the comparison of the algorithms is the total squared factor error (TSFE)

$$\text{TSFE} = \frac{1}{N}\sum_{n=1}^{N} \min_{\boldsymbol{P}\in\mathcal{M}_{\text{PD}}(R)} \frac{\left|\left|\hat{\boldsymbol{F}}_n \cdot \boldsymbol{P} - \boldsymbol{F}_n\right|\right|_{\text{F}}^2}{||\boldsymbol{F}_n||_{\text{F}}^2},$$

where $\mathcal{M}_{\text{PD}}(R)$ is a set of permutation matrices $\boldsymbol{P}$ of size $R \times R$, R is the tensor rank, and N is the tensor dimensionality.

In **Figure 5** we compare the performance of C-SECSI (Naskovska and Haardt, 2016), SECSI (Roemer and Haardt, 2013), C-ALS, CCDP-NLS and CCDP-MINF (Vervliet et al., 2016) for two real-valued tensors of size 40 × 4 × 10, $R_1 = R_2 = 3$, with first mode in common. The three signatures of the first factor matrix represent the first 40 samples of sine functions, $\sin(2\pi t f_1 + \frac{\pi}{3})$, $\sin(2\pi t f_2)e^{t10\text{Hz}}$, and $\sin(2\pi t f_3)e^{-t3\text{Hz}}$ with $f_1 = 10$ Hz, $f_2 = 20$ Hz, and $f_3 = 30$ Hz, which are in the physiological frequency range for brain signals. The second and the third factor matrices are drawn from a zero-mean Gaussian random process with variance one. Moreover, the third factor matrices have collinear columns with a correlation factor of 0.9. The Complementary Cumulative Distribution Function (CCDF) of the TSFE for a SNR equal to 25 dB is depicted in **Figure 5**. The vertical lines represent the mean value of the error for each curve. SECSI and C-SECSI do not have outliers even for such an ill-conditioned scenario in contrast to the other algorithms.

The total mean squared factor errors (TMSFE) for different noise variances when using the uncoupled SECSI framework vs. the C-SECSI framework are presented in **Figure 6**. Both tensors $\boldsymbol{\mathcal{X}}_1$ and $\boldsymbol{\mathcal{X}}_2$ with common first mode have dimensions $40 \times 4 \times 10$ and tensor ranks $R_1 = R_2 = 3$. The tensors are designed in the same manner as for **Figure 5**. However, only the third factor matrix of the second tensor $\boldsymbol{\mathcal{X}}_2$ has mutually correlated columns

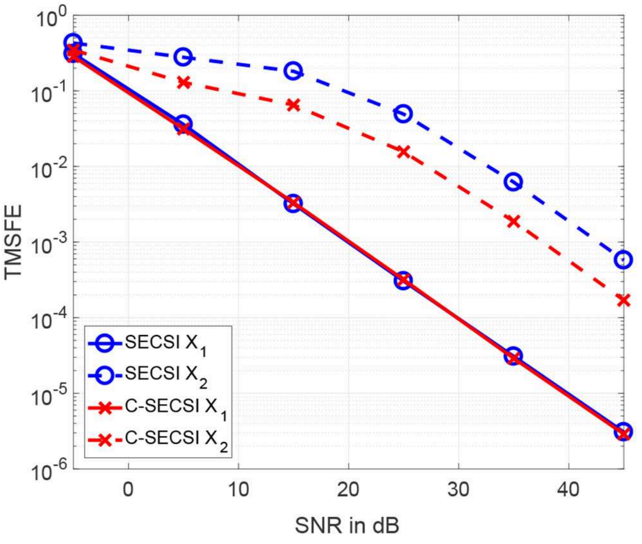

FIGURE 6 | TMSFE as a function of the SNR for complex-valued tensors $\mathcal{X}_1$ and $\mathcal{X}_2$ with dimensions 4 × 8 × 7, tensor rank $R_1 = R_2 = 3$, where the second tensor has third factor matrix with mutually correlated columns.

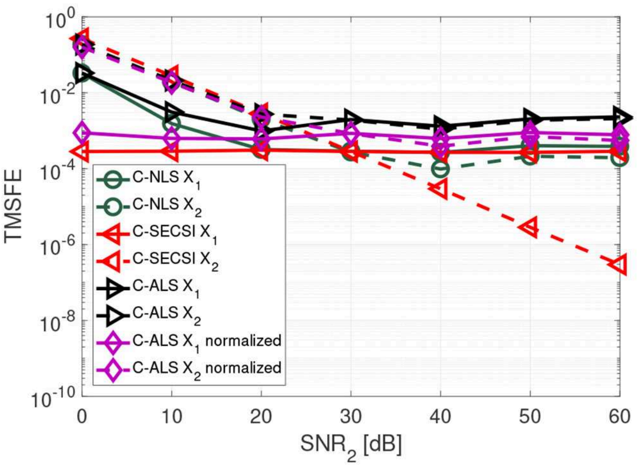

FIGURE 7 | TMSFE as a function of the SNR_2 for complex-valued tensors $\mathcal{X}_1$ and $\mathcal{X}_2$ with dimensions 3 × 8 × 7, tensor rank $R_1 = R_2 = 3$, and $\text{SNR}_1 = 30$ dB.

with a correlation coefficient of $\rho = 0.98$. This highly correlated factor matrix causes the tensor $\mathcal{X}_2$ to be ill-conditioned. The **Figure 6** shows that using the coupled algorithm improves the estimation accuracy of the ill-conditioned tensor without corrupting the well-conditioned tensor.

3.1.3. Normalization

In **Figure 7** we show that the C-SECSI framework, unlike other algorithms, can jointly decompose coupled tensors even if they are affected by noise with different variance. The tensors $\mathcal{X}_1$ and $\mathcal{X}_2$ with common first mode have dimensions 3 × 8 × 7, and tensor ranks $R_1 = R_2 = 3$. The factor matrices contain complex values drawn from a zero mean circularly symmetric complex Gaussian random process with variance one. The first tensor has a constant SNR_1 of 30 dB, while the SNR_2 of the second tensor is varied from 0 to 60 dB. These results are averaged over 3,000 realizations. "C-ALS normalized" denotes the C-ALS algorithm with additional normalization with respect to the different noise variances. C-SECSI outperforms the "C-ALS normalized."

Further details on the importance of normalization and compression with the HOSVD for ALS are available in Cohen et al. (2016). However, the results in **Figure 7** show that normalization with respect to the noise variance is not required when computing the coupled CP decomposition using the C-SECSI framework.

3.2. Decomposition of Measured MEG-EEG Data

3.2.1. Visual Response Rates

The labeling of visual response topographies in the RMS field-maps shows that 74% of the MEG measurements and 89% of the EEG measurements contain some visual response pattern (Categories 1 and 2). After the decomposition, there is some visual response pattern in at least one of the components in 73% of MEG measurements and 96% of EEG measurements. Clear visual response patterns (Category 1) are observed in 42% of the MEG data sets before the decomposition and 63% after the decomposition. Of the EEG data sets, 72% show clear visual response patterns before the decomposition and 85% after the decomposition. Within the components exhibiting a clear visual response pattern (Category 1), 32% of MEG components and 49% of EEG components belong to the recruited group, meaning that their dominant frequency matches the stimulation frequency or its first harmonic. The remaining data sets formed the non-recruited group, containing signal sources that had a dominant frequency that was different from the stimulation frequency.

3.2.2. Characteristics of Estimated Components

The estimated factor matrices from the coupled CP decomposition for Participant 1 and stimulation frequency $1.1 f_\alpha$ are shown in **Figure 8**. Additionally, the figure depicts the field-maps of the RMS of the measured signal for both, MEG and EEG (column 1). The RMS field-maps represent the power distribution of the measured signals before the decompositions. Columns 2 and 3 show the field-maps for the channel signatures for components 1 and 2, respectively. The frequency and time signatures are provided in columns 4 and 5. The stimulation with $1.1 f_\alpha$ produces the strongest response for Participant 1. Note that f_α is estimated from a resting state measurement and may, therefore, slightly differ during PD. In the RMS maps of MEG and EEG, we can see a clear occipital activation due to the PD (visual response Category 1). Both components are located in the occipital area as well and present two frequencies or narrow frequency distributions close to the individual alpha frequency of 9.6 Hz. Component 2 is common between the MEG and the EEG signals and matches closely the stimulation frequency (recruited). In the time domain (column 5) it is dominant and displays an onset, plateau, and offset phase. Component 1 is a visual response as well, but has a different obtained frequency

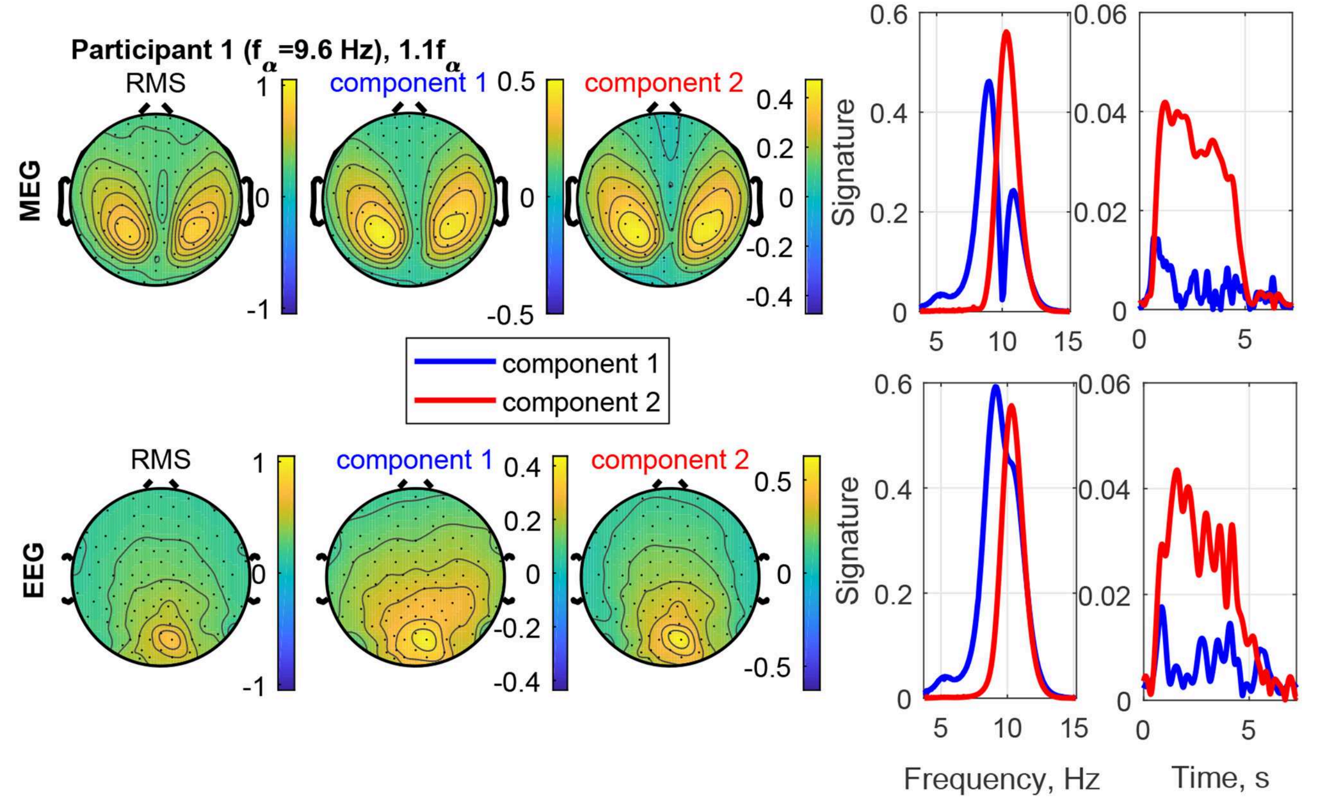

FIGURE 8 | RMS, channel, frequency, and time signature for Participant 1 and stimulation frequency $1.1f_\alpha$.

(non-recruited) that is closer to the individual alpha frequency. In the time domain it is stronger in the onset phase of the stimulation train and diminishes after that.

The result of stimulating the same participant with $0.55f_\alpha$, in the theta band, is shown in **Figure 9**. This stimulation produced an increased response as well, which was not as strong as that of $1.1f_\alpha$. The two components are both in the occipital region, show visual response patterns, and are both of comparable strength over the time course. **Figure 10** shows the input frequency distribution of the MEG over time (bottom left) of an indicative channel (top right), the time signatures of the resulting components aligned above and the frequency signatures aligned on the right. Component 1 presents closely the stimulation frequency (recruited), which is visible in the frequency distribution during the stimulation train. Component 2 presents closely the harmonic $2 \cdot 0.55f_\alpha$ of the stimulation frequency (recruited). **Figure 11** shows that both of these frequencies appear in the MEG and EEG signals. Component 1 of the EEG signal extends more centrally (**Figure 9**, row 2 column 2), which is consistent with the topography of theta band activity (Klimesch, 1999, p. 180).

Figure 12 shows an example of the separation of a visual response from a superimposed other source in Participant 1 at the stimulation frequency $0.7f_\alpha$. The field-map of the MEG signals shows no clear visual response pattern (visual response Category 3). However, Component 2 reveals the visual response at the stimulation frequency (recruited). The other, more complex and temporally variable source is found in Component 1. **Figure 13** shows the frequency distributions of the input MEG signal of a frontal channel primarily capturing the activity of Component 1 (left sub-figure) and an input MEG channel primarily capturing the activity in Component 2 (right sub-figure). The components reflect the primary frequency aspects, keeping in mind that the decomposition captures the primary aspects present across channels and time. The time signature of Component 2 matches the stimulation train, which further confirms that it is a stimulation response. The time signature of Component 2 is irregular and present after the stimulation train. This further confirms that it is not a direct stimulation response. The decomposition of the EEG signals differentiates two sources, which are both at the stimulation frequency (recruited). Component 1 is confined to the occipital region and dominates the time course, while Component 2 (red) includes a small fraction of activity in the theta band, extends more central and is more distributed.

The components of unsuccessful stimulation experiments, during which no consistent visual response could be elicited (data not shown), isolate the main patterns in the respective frequency distribution. These may be transient in time or only present at a short time point on the time axis, which is captured by the time signatures. The topographies of the signals and components

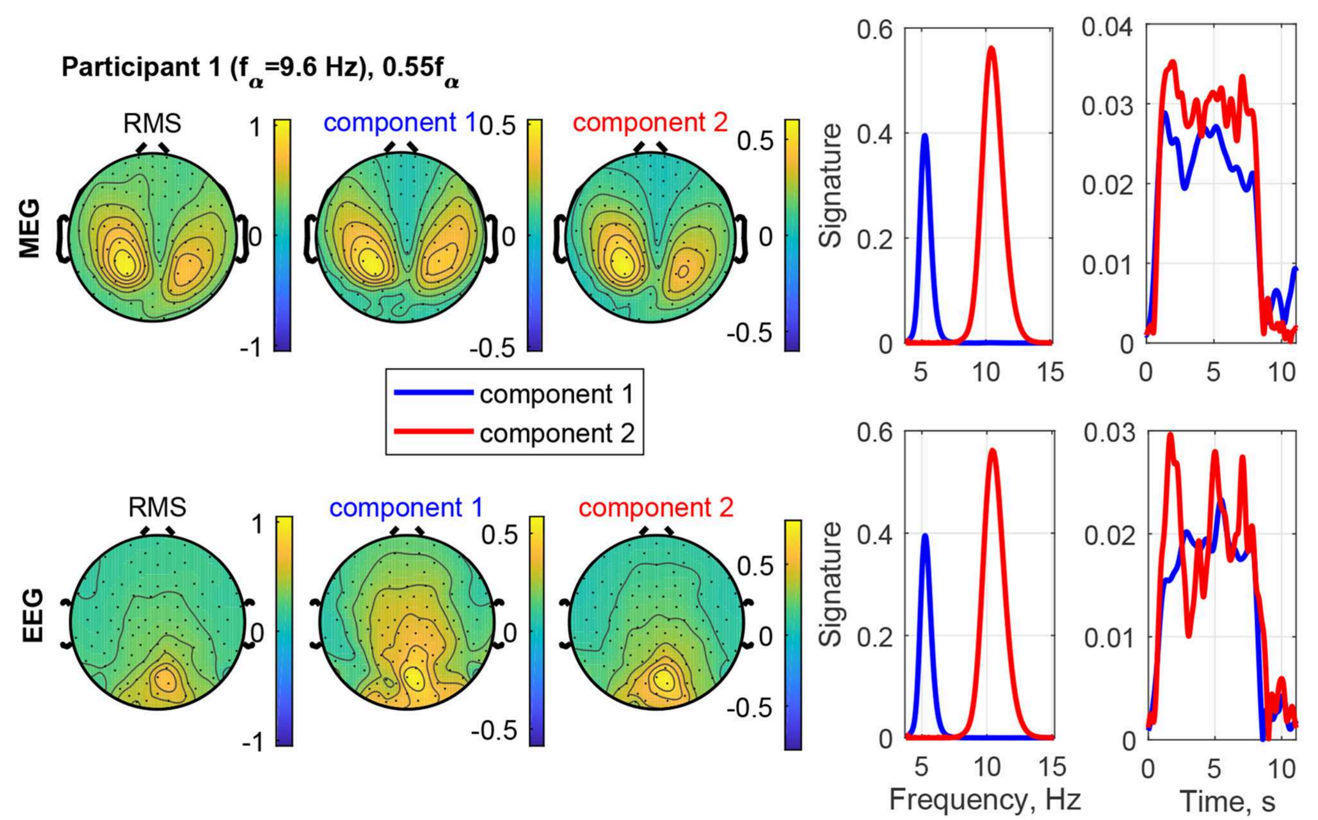

FIGURE 9 | RMS, channel, frequency, and time signature for Participant 1 and stimulation frequency $0.55f_\alpha$.

are broader and not restricted to the occipital regions of the visual cortex. The signals may be generated by resting-state brain rhythms.

3.2.3. Group Analysis of Obtained Frequencies

In order to evaluate the responses of all participants together, we take the obtained frequencies, the maxima of the frequency signatures, of only the components with primarily only visual response patterns (Category 1) and differentiate the two conditions, recruited and non-recruited components. The MEG group analysis is shown in **Figure 14** and the EEG group analysis in **Figure 15**. The second and third rows show the component weights as violin plots with the median curve, while the fourth row shows the corresponding reliability distribution and the fifth row shows the residual for each stimulation frequency.

The upper plots of both, **Figures 14**, **15**, depict two dashed reference lines each representing the stimulation frequency f_s and its harmonic $2f_s$. Components very close to this line are recruited (marker X) and all others non-recruited (marker O). The results show that entrainment can appear for all of the stimulation frequencies up $1.1f_\alpha$, although in each participant only a subset of stimulation experiments was successful in producing an entrainment.

The non-recruited components (dotted line denotes median) most commonly show frequencies of $(0.4 \pm 0.1)f_\alpha$ for stimulation frequencies between $0.4f_\alpha - 1.0f_\alpha$. Between stimulation frequencies $1.0f_\alpha - 1.3f_\alpha$, response frequencies around $(1.0 \pm 0.05)f_\alpha$ are more common. Few components appear outside this pattern with response frequencies of $(0.6 - 0.7)f_\alpha$. Note that the non-recruited components appear during flicker stimulation and have a clear visual response pattern. The group analysis identifies two reoccurring response frequency ranges of $(0.4 \pm 0.1)f_\alpha$, a theta band response, and $(1.0 \pm 0.05)f_\alpha$, an alpha band response.

It is important to note that in the components of a single measurement there are only either recruited components or non-recruited components, not both. The only rare exceptions are cases, in which the response frequency changed mid-way in the series of trials and both were superimposed during averaging. In all data sets with clear visual response pattern (Category 1) without recruitment, either the alpha or the theta band response is present, not both. Rare exceptions are again where the response frequency changes mid-way in the series of trials and both are superimposed during averaging.

The weights represent the power of each component using its norm and indicate its dominance. The violin plots of the weights in **Figures 14**, **15** show that the recruited components are dominant compared to the non-recruited frequencies. A comparatively high reliability and a low residual give strongest confidence in the components and their obtained frequencies

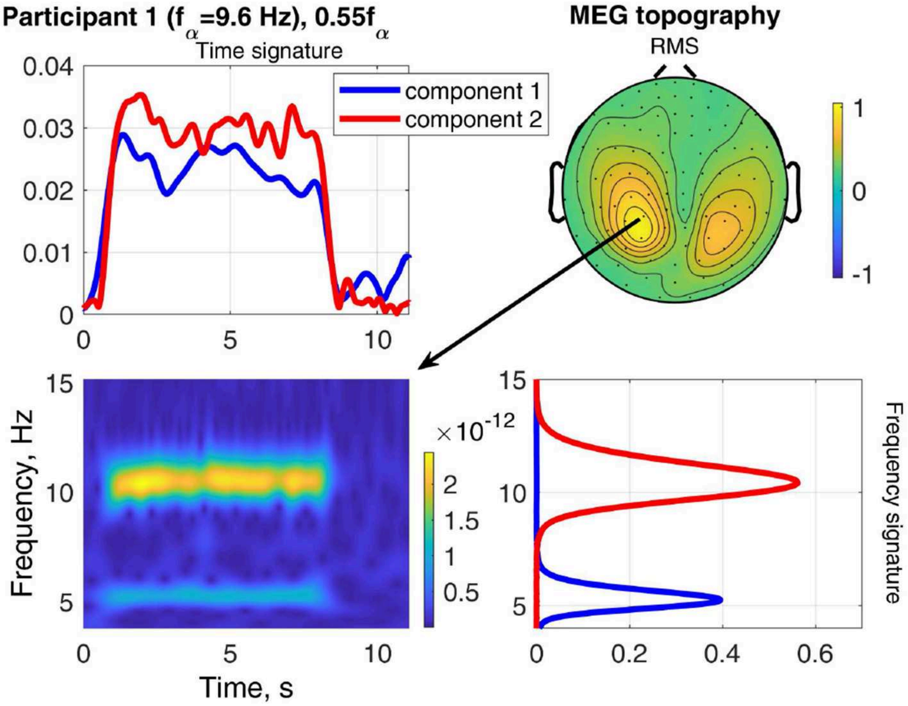

FIGURE 10 | Relation between frequency distribution (bottom left) of an indicative MEG channel (top right) and the time (top left) and frequency (bottom right) signatures of the components of Participant 1 at stimulation frequency 0.55f_α.

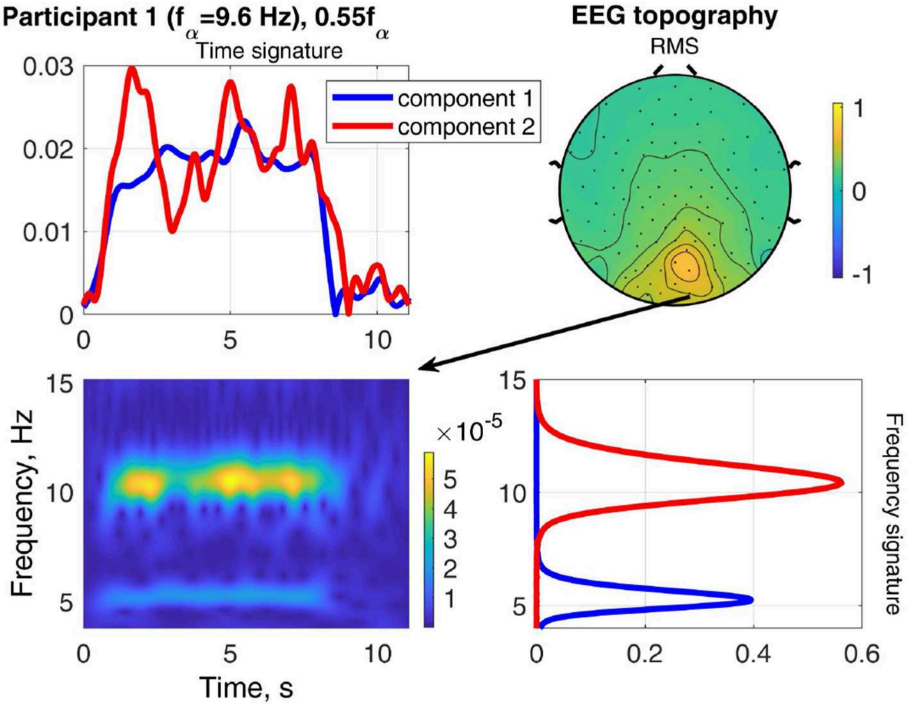

FIGURE 11 | Relation between frequency distribution (bottom left) of an indicative EEG channel (top right) and the time (top left) and frequency (bottom right) signatures of the components of Participant 1 at stimulation frequency 0.55f_α.

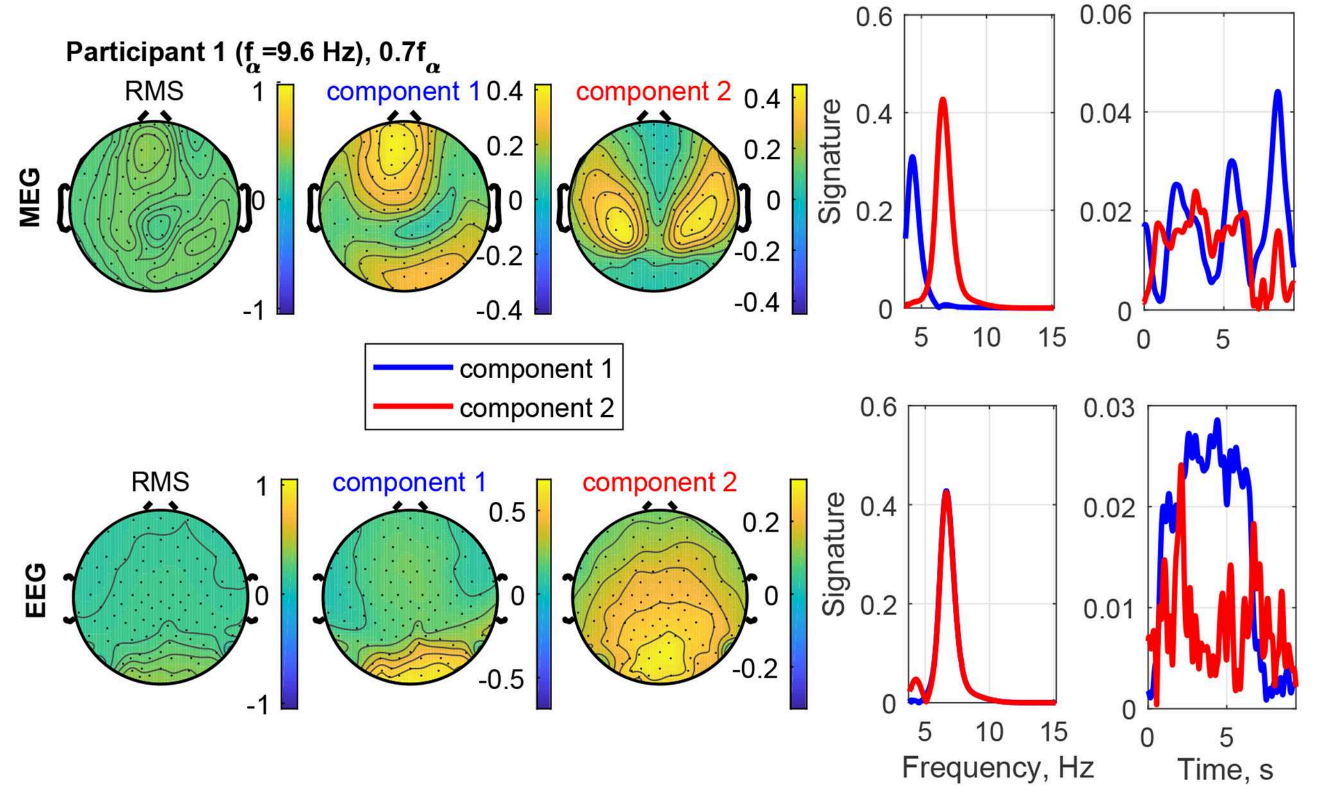

FIGURE 12 | RMS, channel, frequency, and time signature for Participant 1 and stimulation frequency $0.7f_\alpha$.

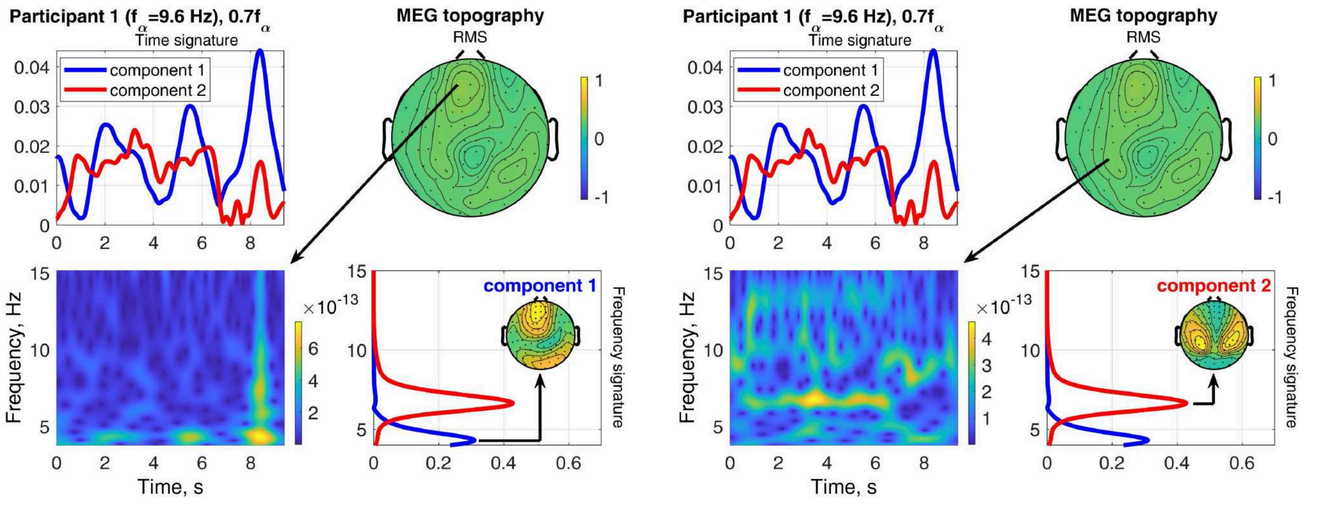

FIGURE 13 | Relation between frequency distributions of one indicative MEG channel of component 1 (left sub-figure) as well as one indicative MEG channel of component 2 (right sub-figure) and the time and frequency signatures of Participant 1 at stimulation frequency $0.7f_\alpha$.

for stimulation frequencies around $0.5f_\alpha$ and f_α. This is where the MEG and EEG signals have two components in common (REL = 100%). For the rest of the stimulation frequencies, the MEG and EEG signals have only one common component.

4. DISCUSSION

4.1. Evaluation of C-SECSI Approach

We propose to compute the coupled CP decomposition based on the C-SECSI framework (Naskovska and Haardt, 2016). The

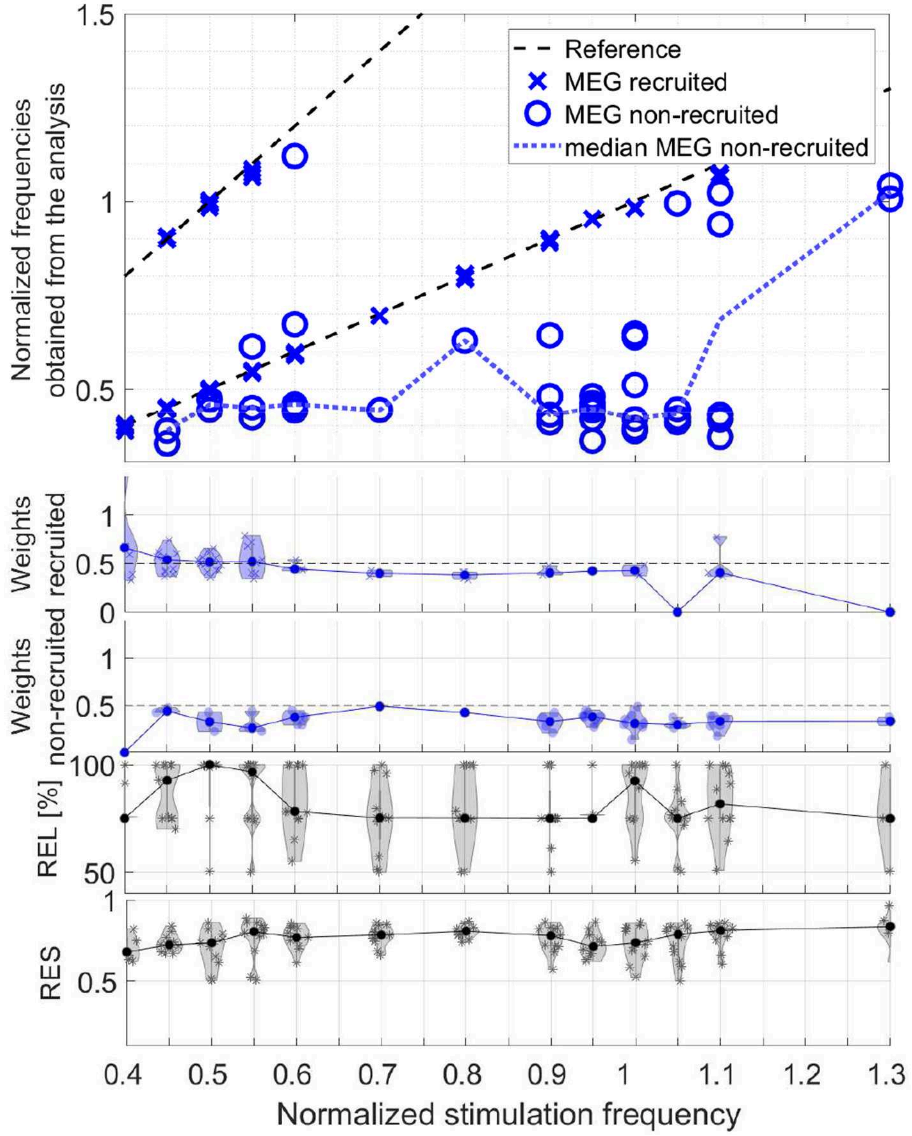

FIGURE 14 | Scatter plot of the normalized frequencies obtained from the analysis for MEG data, violin plots of the weights of the recruited and non-recruited components, reliability, and residual as function of the normalized stimulation frequency.

C-SECSI framework for three-way tensors with one mode in common computes eight initial estimates, four of which are coupled and four uncoupled. The final estimate is then chosen based on the minimum reconstruction error for both tensors independently. Therefore, C-SECSI computes the coupled CP decomposition under the constraint that one of the modes is coupled, but it still computes uncoupled estimates. This is very practical for the analysis of biomedical data, where the coupling is assumed but not yet proven. Moreover, for comparing the independently chosen final estimates we have defined the coupling reliability in Equation (4). The benchmark results (**Figures 3**, **4**) show that the reliability measure can be used to control the rank estimate of the coupled decomposition. This is a very important feature of C-SECSI, because the rank estimate is a very challenging problem, especially for noisy measurement signals. The C-SECSI framework has higher accuracy in ill-conditioned scenarios such as computing the coupled CP decomposition with a collinear factor. In both accuracy tests (**Figures 5**, **6**), we obtained a higher accuracy than with the traditional SECSI framework proposed in Roemer and Haardt (2008, 2013) and alternative methods. Another advantage of the C-SECSI framework is that it can decompose tensors that are corrupted by noise with different variances without any additional normalization or estimation of the SNR (**Figure 7**).

4.2. Decomposition of MEG-EEG Data

The application of the coupled CP decomposition to simultaneously recorded MEG-EEG signals demonstrates its capability of extracting physiologically meaningful signal sources, in this case oscillators during photic driving. The coupled CP

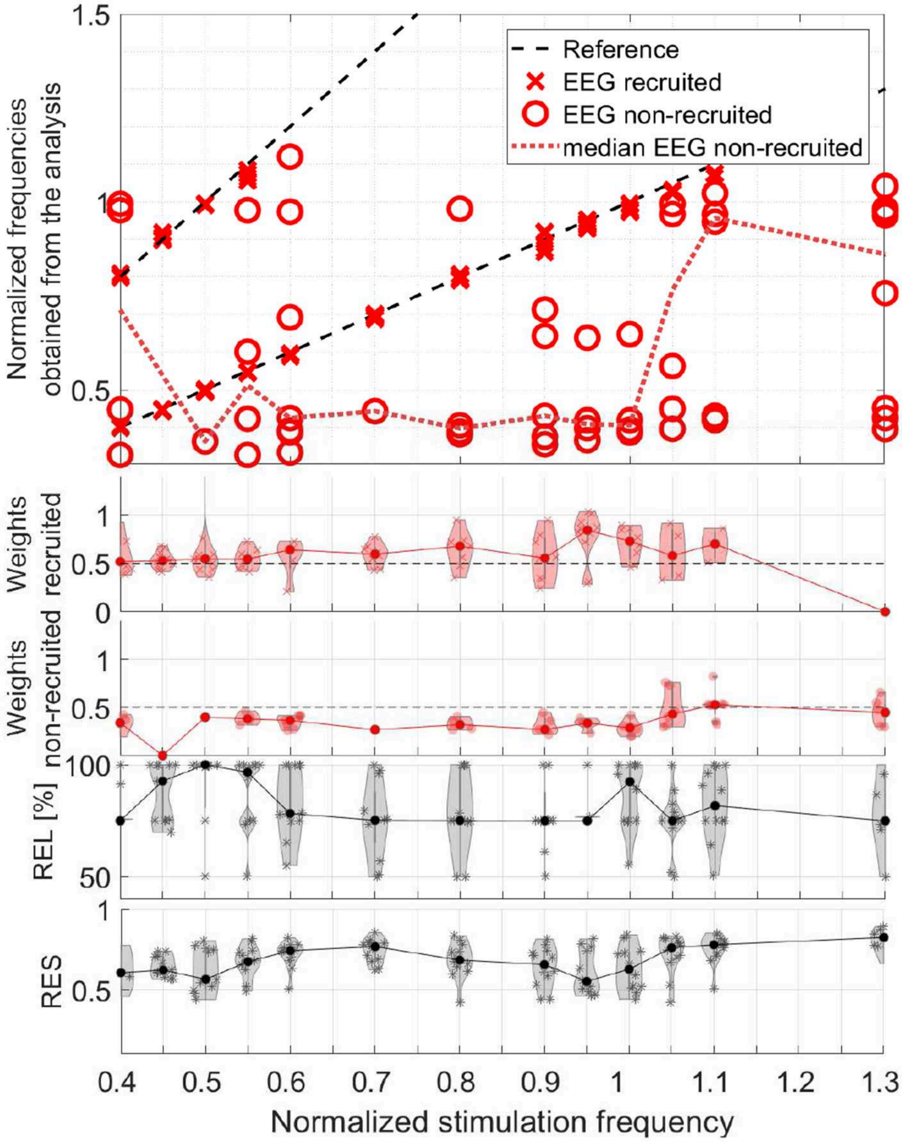

FIGURE 15 | Scatter plot of the normalized frequencies obtained from the analysis for EEG data, violin plots of the weights of the recruited and non-recruited components, reliability, and residual as function of the normalized stimulation frequency.

decomposition allows us to decompose these multidimensional heterogeneous signals into their most prominent components and residual signal. Small overestimations of the rank lead to less prominent signal patterns being extracted from the residual and represented as a component. The underlying components are extracted while preserving the original multidimensional structure of the signals (frequency × time × channels, c.f. **Figure 2**) under the assumption that they have a common frequency mode.

4.2.1. Field-Maps

The overall rate of response in terms of a spatial activation pattern in the field-maps is comparable to preceding studies (Schwab et al., 2006; Salchow et al., 2016), which used entrainment measures to detect responses. This study, however, includes all frequencies within the wavelet frequency window around the alpha and theta band. We found a high response rate close to the individual alpha frequency, an intermediate rate in the theta band, and a low response rate otherwise. This is in agreement with Salchow et al. (2016), Schwab et al. (2006), and Halbleib et al. (2011). The EEG data present more frequent response patterns than the MEG data. This could be due to the different sensitivities to the angles and the depths of the sources in the brain (Hunold et al., 2016).

The tensor decomposition with rank 2 extracts the two primary components of the data in frequency × time × channel space and, thereby, eliminates further sources that could otherwise confound the analysis. The component topographies are either physiologically meaningful, i.e., representing a visual response, or represented some other clearly distinguishable source of similar strength. This allows us to isolate the stimulus response. In turn, this substantially improves the identifiability of visual response patterns in MEG components and to a lesser degree in EEG components. The example in **Figure 12** demonstrates how a visual response component can be uncovered and isolated from an unclear MEG data set.

4.2.2. Time Courses

The time signatures of the recruited components demonstrate the three phases: onset, plateau, and offset (e.g., **Figure 9**). This is in good agreement with previous studies (Schwab et al., 2006; Salchow et al., 2016). However, the decomposition additionally allows us to separate signal components with a weaker or instable time course (e.g., **Figure 12**). Further, it highlights changes over time, such as a component that is only present during the onset phase and diminishes after that (e.g., MEG in **Figure 8**). This component-wise time course display allows the user to gain insight into the stationarity and effectiveness of the stimulation experiment.

4.2.3. Frequencies

The decomposition of the data tensor allows us to extract the main components with their frequency signatures. In this stimulation experiment, the frequency signatures primarily contain one or sometimes two peaks, which reflect the resonance to the stimulation frequency and/or intrinsic frequencies within the alpha and theta bands. Note that in general, each frequency signature can contain multiple frequency contributions, if they are related to each other in the data tensor. MEG and EEG signals do not always have all frequency components in common, this can be explained by the different sensitivities to the angles and the depths of the sources in the brain (Hunold et al., 2016) and has been observed in preceding tensor decomposition studies (Naskovska et al., 2017a,b).

The decomposition is able to separate sources at different frequencies that show the same or a similar topographical distribution in the field-map, even if the frequency peaks partly overlap (e.g., **Figure 8**). The existence of such similar topographies, indicating a similar physical distribution of the activity in the brain, during the plateau phase for different frequencies has been reported and described in more detail by Halbleib et al. (2011). The strongest resonance frequency peak during stimulation is in many cases slightly above the alpha frequency peak at rest, i.e., $1f_\alpha - 1.1f_\alpha$. This can be understood from the observation that the signal contribution to the alpha band above the peak frequency, the upper alpha, and the signal contribution below the peak, the lower alpha, respond independently (Klimesch, 1999). Our results indicate that the strongest resonance in this case may be produced by stimulation in the upper alpha range. A desynchronization of the lower alpha band is associated with attention (Klimesch, 1999). The attention of the participant may, therefore, play a role in the composition of the power distribution in the alpha band as well. In the example in **Figure 8**, Component 2 (red) reflects the resonance frequency in the upper alpha range, while Component 1 (blue) reflects the remaining signal contributions to the alpha band, primarily in the lower alpha range. The separation is more pronounced in the MEG data than the EEG data in this case.

During stimulation with a frequency of approximately $f_s = 0.5f_\alpha$, we can differentiate two components, one with a frequency peak at the stimulation frequency f_s and one with its harmonic $2f_s \approx f_\alpha$, e.g., in **Figure 9**. This is in agreement with Salchow et al. (2016), who determined alpha entrainment from the $2f_s \approx f_\alpha$ peak amplitude. The critical feature of this case is that the frequency peaks match closely the stimulation frequency and its harmonic (dashed lines in **Figures 14**, **15**).

4.3. Oscillators During Photic Stimulation

4.3.1. Recruitment

The unsupervised tensor decomposition of MEG-EEG signals isolates components that are characterized by one frequency peak, respectively, which is sustained through all or part of the stimulation train. These can be understood as oscillations. Within the components displaying clear visual response topographies (Category 1), approximately one third of the MEG components and approximately half of the EEG components are recruited to the stimulation frequency or its first harmonic (**Figures 14**, **15**). This concurs with the entrainment reported in previous studies (Mangan et al., 1993; Klimesch, 1999; Herrmann, 2001; Schwab et al., 2006; Salchow et al., 2016). Using photopic stimulation conditions, Herrmann (2001) additionally describes entrainment for higher harmonics. The observation that in a single experiment we can only observe either a recruited oscillation or a non-recruited oscillation, but not both, suggests that the oscillators underlying the non-recruited oscillations are entrained to the stimulation frequency in the recruited case. This is supported by Wacker et al. (2011) and Halbleib et al. (2011), who point out that these recruited oscillations are not purely synchronized stimulus responses, but reflect a driven oscillator in the brain that maintains the oscillation for several cycles after the stimulation has ended. Notbohm et al. (2016) further strengthen this hypothesis using jittered flash stimulation experiments.

4.3.2. Intrinsic Oscillations

The successful visual stimulation also identifies components with non-recruited frequencies, which are approximately two thirds of the MEG components and approximately half of the EEG components. These can be considered intrinsic oscillations (da Silva, 1991), because they are produced without a match in stimulation frequency and occur across participants. They appear primarily in two frequency bands, $0.9f_\alpha - 1.1f_\alpha$, the alpha band, and $0.3f_\alpha - 0.5f_\alpha$, the theta band (**Figures 14**, **15**). Although MEG and EEG have partly different sensitivities, the group analysis across participants of both modalities confirm this finding. The presence of alpha band responses during stimulation with other frequencies is confirmed by Herrmann (2001). Theta band oscillations during photic stimulation have been described in children (Lazarev et al., 2001) and in students (19–24 years; Mangan et al., 1993) similar to our participants.

4.3.3. Resonance

The response amplitude in the tensor components resonates for stimulation frequencies in the alpha band and the theta band. Resonance is also observed for stimulation close to half of the individual alpha frequency, which may partly coincide with the theta band response. The resonance to stimulation in the alpha band and half of it is in good agreement with existing literature (Herrmann, 2001; Schwab et al., 2006; Salchow et al., 2016). The resonance in the theta band is confirmed and described by Mangan et al. (1993), Lazarev et al. (2001), and Klimesch (1999). In agreement with these studies, our results show that the resonance extends to stimulation frequencies that are a small fraction above and below the respective intrinsic frequency peak.

4.3.4. Connections

The observation that in the non-recruited case we observe either a component in the alpha band or a component in the theta band, not both, indicates a reciprocal relation between the two bands. In fact, such a reciprocal relation in band power has been reported in the EEG literature and summarized in a comprehensive review by Klimesch (1999). Our study confirms this observation in MEG signals. da Silva (1991) hypothesizes that the brain contains a system of connected neural oscillators with individual resonance frequencies that respond to photic driving. Our results support this hypothesis and suggest alpha and theta oscillators that can resonate with photic driving. When an entrainment to a stimulation frequency takes place, then the recruited frequencies dominate the signals.

4.4. Future Work and Applications

The time-frequency-channel tensor in this study translates well to other studies in neuroscience in that it uses typical data dimensions of time, e.g., a measurement, channels, e.g., a set or array of sensors, and a series of features or parameters, e.g., frequencies. The decomposition method can be applied to the unsupervised discovery of patterns in data of exploratory studies in the future. The component analysis can be extended by performing source reconstructions of the components. This could reveal the locations of the underlying brain activity regions. It could also allow for quantitative measures of the physiological integrity of the components. This may help in providing new insight into the brain's organization and function. Future work could involve higher-order tensors, for example, by including the participant as one dimension of a population tensor. The necessary cross-participant co-registration and normalization should be investigated and validated.

The tensor decomposition approach can be of high practical value when integrated into brain-computer-interfaces, such as a speller application for paralyzed users (Rezeika et al., 2018). Such spellers detect user selections from the brain's response to steady state visual stimulation. Using the selections, the user can navigate through a list of letters on a screen and produce a message. Another practical use is in neurofeedback systems, which decompose and display features of the measured brain activity on-line to the user and allow the user to train control over beneficial brain states. In the clinical setting, it can augment and further contribute to diagnostics. It can lead to improved treatment outcome of brain disorders, for example, by locating epileptic network nodes in the epileptic brain.

Beyond neuroscience, the tensor decomposition method is highly applicable to machine learning tasks in big data in general, specifically the discovery of multi-dimensional patterns (Stoudenmire, 2018; Klus and Gelβ, 2019).

5. CONCLUSION

The tensor decomposition with C-SECSI is able to separate physiologically meaningful oscillations of visually evoked brain activity from background signals. The component frequencies identify either an entrainment to the respective visual stimulation frequency or its first harmonic, or an oscillation in the individual alpha band or theta band. In the group analysis of both, MEG and EEG data, a reciprocal relationship between alpha and theta band oscillations is present. The coupled tensor decomposition using the C-SECSI framework is a robust, powerful method for the unsupervised extraction and separation of meaningful sources from multidimensional biomedical measurement data.

DATA AVAILABILITY STATEMENT

The datasets generated for this study are available on request to the corresponding author.

ETHICS STATEMENT

The studies involving human participants were reviewed and approved by Faculty of Medicine of the Friedrich-Schiller-University Jena, Germany. The patients/participants provided their written informed consent to participate in this study.

AUTHOR CONTRIBUTIONS

All authors designed the research. KN, AK, and MH developed the decomposition method. KN, SL, and AK performed the data analysis. All authors contributed to the scientific discussion. SL and KN compiled the paper with contributions from all other authors.

FUNDING

This work was supported by the German Research Foundation (DFG) HA 2899/23-1 and the Internal Excellence Initiative of Ilmenau University of Technology. We acknowledge support for the Article Processing Charge by the German Research Foundation and the Open Access Publication Fund of Ilmenau University of Technology.

ACKNOWLEDGMENTS

The authors would like to thank Uwe Graichen (UG) and Daniel Strohmeier (DS) for independently labeling the measurements.

REFERENCES

Acar, E., Bro, R., and Smilde, A. K. (2015). Data fusion in metabolomics using coupled matrix and tensor factorizations. *Proc. IEEE* 103, 1602–1620. doi: 10.1109/JPROC.2015.2438719

Acar, E., Rasmussen, M. A., Savorani, F., Næs, T., and Bro, R. (2013). Understanding data fusion within the framework of coupled matrix and tensor factorizations. *Chemometr. Intell. Lab.* 129, 53–63. doi: 10.1016/j.chemolab.2013.06.006

Becker, H., Comon, P., and Albera, L. (2012). "Tensor-based preprocessing of combined EEG/MEG data," in *Proceedings of the IEEE 20th European Signal Processing Conference (EUSIPCO)* (Bucharest), 275–279.

Cichocki, A., Mandic, D., Phan, A., Caiafa, C., Zhou, G., Zhao, Q., et al. (2015). Tensor decompositions for signal processing applications: from two-way to multiway. *IEEE Sig. Proc. Mag.* 32, 145–163. doi: 10.1109/MSP.2013.2297439

Cohen, J. E., Farias, R. C., and Comon, P. (2016). "Joint tensor compression for coupled canonical polyadic decompositions," in *Proceedings of the IEEE 24th European Signal Processing Conference (EUSIPCO)* (Budapest), 2285–2289. doi: 10.1109/EUSIPCO.2016.7760656

Comon, P., Luciani, X., and de Almeida, A. L. F. (2009). Tensor decompositions, alternating least squares and other tales. *J. Chemometr.* 23, 393–405. doi: 10.1002/cem.1236

da Silva, F. L. (1991). Neural mechanisms underlying brain waves: from neural membranes to networks. *Electroencephalogr. Clin. Neurophysiol.* 79, 81–93. doi: 10.1016/0013-4694(91)90044-5

De Lathauwer, L., de Moor, B., and Vandewalle, J. (2000). A multilinear singular value decomposition. *SIAM J. Matrix Anal. A.* 21, 1253–1278. doi: 10.1137/S0895479896305696

Farias, R. C., Cohen, J. E., and Comon, P. (2016). Exploring multimodal data fusion through joint decompositions with flexible couplings. *IEEE Trans. Sig. Proc.* 64, 4830–4844. doi: 10.1109/TSP.2016.2576425

Haardt, M., Roemer, F., and Del Galdo, G. (2008). Higher-order SVD based subspace estimation to improve the parameter estimation accuracy in multi-dimensional harmonic retrieval problems. *IEEE Trans. Sig. Proc.* 56, 3198–3213. doi: 10.1109/TSP.2008.917929

Halbleib, A., Gratkowski, M., Schwab, K., Ligges, C., Witte, H., and Haueisen, J. (2011). Topographic analysis of engagement and disengagement of neural oscillators in photic driving: a combined electroencephalogram/magnetoencephalogram study. *J. Clin. Neurophysiol.* 29, 33–41. doi: 10.1097/WNP.0b013e318246ad6e

Herrmann, C. S. (2001). Human EEG responses to 1-100 Hz flicker: resonance phenomena in visual cortex and their potential correlation to cognitive phenomena. *Exp. Brain Res.* 137, 346–353. doi: 10.1007/s002210100682

Hunold, A., Funke, M., Eichardt, R., Stenroos, M., and Haueisen, J. (2016). EEG and MEG: sensitivity to epileptic spike activity as function of source orientation and depth. *Physiol. Meas.* 37, 1146–1162. doi: 10.1088/0967-3334/37/7/1146

Kalitzin, S., Parra, J., Velis Lopes, D. N., and da Silva, F. H. (2002). Enhancement of phase clustering in the EEG/MEG gamma frequency band anticipates transitions to paroxysmal epileptic form activity in epileptic patients with known visual sensitivity. *IEEE Trans. Biomed. Eng.* 49, 1279–1286. doi: 10.1109/TBME.2002.804593

Klimesch, W. (1999). EEG alpha and theta oscillations reflect cognitive and memory performance: a review and analysis. *Brain Res. Rev.* 19, 169–195. doi: 10.1016/S0165-0173(98)00056-3

Klus, S., and Gelβ, P. (2019). Tensor-based algorithms for image classification. *Algorithms* 12:240. doi: 10.3390/a12110240

Kolda, T., and Bader, B. (2009). Tensor decompositions and applications. *SIAM Rev.* 51, 455–500.

Lazarev, V. V., Simpson, D. M., Schubsky, B. M., and de Azevedo, L. C. (2001). Photic driving in the electroencephalogram of children and adolescents: harmonic structure and relation to the resting state. *Braz. J. Med. Biol. Res.* 34, 1573–1584. doi: 10.1590/S0100-879X2001001200010

Mangan, G. L., Pellett, O., Colrain, I. M., and Bates, T. C. (1993). Photic driving and personality. *Pers. Indiv. Differ.* 15, 329–340. doi: 10.1016/0191-8869(93)90224-Q

Naskovska, K., and Haardt, M. (2016). "Extension of the semi-algebraic framework for approximate CP decompositions via simultaneous matrix diagonalization to the efficient calculation of coupled CP decompositions," in *Proceedings of the 50th Asilomar Conference on Signals, Systems and Computers* (Pacific Grove, CA), 1728–1732.

Naskovska, K., Korobkov, A. A., Haardt, M., and Haueisen, J. (2017a). "Analysis of the photic driving effect via joint EEG and MEG data processing based on the coupled CP decomposition," in *Proceedings of the IEEE 25th European Signal Processing Conference (EUSIPCO)* (Kos), 1285–1289.

Naskovska, K., Lau, S., Aboughazala, A., Haardt, M., and Haueisen, J. (2017b). "Joint MEG-EEG signal decomposition using the coupled SECSI framework: validation on a controlled experiment," in *Proceedings if the 2017 IEEE 7th International Workshop on Computational Advances in Multi-Sensor Adaptive Processing (CAMSAP)* (Curacao), 360–364.

Notbohm, A., Kurths, J., and Herrmann, C. S. (2016). Modification of brain oscillations via rhythmic light stimulation provides evidence for entrainment but not for superposition of event-related responses. *Front. Hum. Neurosci.* 10:10. doi: 10.3389/fnhum.2016.00010

Papalexakis, E. E., Mitchell, T. M., and Sidiropoulos, N. D. (2014). "Turbo-SMT accelerating coupled sparse matrix-tensor," in *Proceedings of the 2014 SIAM International Conference on Data Mining* (Philadelphia, PA), 118–126. doi: 10.1137/1.9781611973440.14

Rezeika, A., Benda, M., Stawicki, P., Gembler, F., Saboor, A., and Volosyak, I. (2018). Brain-computer interface spellers: a review. *Brain Sci.* 8:57. doi: 10.3390/brainsci8040057

Rivet, B., Duda, M., Guérin-Dugué, A., Jutten, C., and Comon, P. (2015). "Multimodal approach to estimate the ocular movements during EEG recordings: a coupled tensor factorization method," in *Proceedings of the 37th Annual International Conference of the IEEE Engineering in Medicine and Biology Society (EMBC)* (Milan), 6983–6986. doi: 10.1109/EMBC.2015.7319999

Roemer, F., and Haardt, M. (2008). "A closed-form solution for parallel factor (PARAFAC) analysis," in *Proceedings of the 2008 IEEE International Conference on Acoustics, Speech and Signal Processing* (Las Vegas, NV), 2365–2368. doi: 10.1109/ICASSP.2008.4518122

Roemer, F., and Haardt, M. (2013). A semi-algebraic framework for approximate CP decomposition via simultaneous matrix diagonalization (SECSI). *Signal Process.* 93, 2722–2738. doi: 10.1016/j.sigpro.2013.02.016

Roemer, F., Schroeter, C., and Haardt, M. (2012). "A semi-algebraic framework for approximate CP decompositions via joint matrix diagonalization and generalized unfoldings," in *Proceedings of the 46th Asilomar Conference on Signals, Systems and Computers (ASILOMAR)* (Pacific Grove, CA), 2023–2027. doi: 10.1109/ACSSC.2012.6489396

Salchow, C., Strohmeier, D., Klee, S., Jannek, D., Schiecke, K., Witte, H., et al. (2016). Rod driven frequency entrainment and resonance phenomena. *Front. Hum. Neurosci.* 10:413. doi: 10.3389/fnhum.2016.00413

Schwab, K., Ligges, C., Jungmann, T., Hilgenfeld, B., Haueisen, J., and Witte, H. (2006). Alpha entrainment in human electroencephalogram and magnetoencephalogram recordings. *Neuroreport* 17, 1829–1833. doi: 10.1097/01.wnr.0000246326.89308.ec

Sidiropoulos, N. D., De Lathauwer, L., Fu, X., Huang, K., Papalexakis, E. E., and Faloutsos, C. (2017). Tensor decomposition for signal processing and machine learning. *IEEE Trans. Sig. Proc.* 65, 3551–3582. doi: 10.1109/TSP.2017.2690524

Sørensen, M., and De Lathauwer, L. (2017a). Multidimensional harmonic retrieval via coupled canonical polyadic decomposition— I: Model and identifiability. *IEEE Trans. Sig. Proc.* 65, 517–527. doi: 10.1109/TSP.2016.2614796

Sørensen, M., and De Lathauwer, L. (2017b). Multidimensional harmonic retrieval via coupled canonical polyadic decomposition - part II: algorithm and multirate sampling. *IEEE Trans. Sig. Proc.* 65, 528–539. doi: 10.1109/TSP.2016.2614797

Sørensen, M., Domanov, I., and De Lathauwer, L. (2015). Coupled canonical polyadic decompositions and (coupled) decompositions in multilinear rank-($L_{r,n}, L_{r,n}, 1$) terms - part II: algorithms. *SIAM J. Matrix Anal. Appl.* 36, 496–522. doi: 10.1137/140956853

Sørensen, M., Domanov, I., and De Lathauwer, L. (2018). Coupled canonical polyadic decompositions and multiple shift-invariance in array processing. *IEEE Trans. Sig. Proc.* 66, 3665–3680. doi: 10.1109/TSP.2018.2835423

Stoudenmire, E. M. (2018). Learning relevant features of data with multi-scale tensor networks. *Quantum Sci. Technol.* 3:034003. doi: 10.1088/2058-9565/aaba1a

Van Eyndhoven, S., Hunyadi, B., De Lathauwer, L., and Van Huffel, S. (2017). "Flexible fusion of electroencephalography and functional magnetic resonance imaging: revealing neural-hemodynamic coupling through structured matrix-tensor factorization," in *Proceedings of the IEEE 24th European Signal Processing Conference (EUSIPCO)* (Kos), 26–30.

Vervliet, N., Debals, O., Sorber, L., van Barel, M., and De Lathauwer, L. (2016). *Tensorlab 3.0*. Available online at: http://www.tensorlab.net (accessed March 1, 2016).

Wacker, M., Galicki, M., Putsche, P., Milde, T., Schwab, K., Haueisen, J., et al. (2011). A time-variant processing approach for the analysis of alpha and gamma MEG oscillations during flicker stimulus generated entrainment. *IEEE Trans. Biomed. Eng.* 58, 3069–3077. doi: 10.1109/TBME.2011.2160640

Zou, L., Chen, X., Ji, X., and Wang, Z. J. (2017). Underdetermined joint blind source separation of multiple datasets. *IEEE Access* 5, 7474–7487. doi: 10.1109/ACCESS.2017.2695497

Conflict of Interest: The authors declare that the research was conducted in the absence of any commercial or financial relationships that could be construed as a potential conflict of interest.

frontiers in Neuroscience

ORIGINAL RESEARCH
published: 21 July 2020
doi: 10.3389/fnins.2020.00641

Identification of Alzheimer's EEG With a WVG Network-Based Fuzzy Learning Approach

Haitao Yu[1]*, Lin Zhu[1], Lihui Cai[1], Jiang Wang[1], Jing Liu[2]*, Ruofan Wang[3] and Zhiyong Zhang[4]

[1] School of Electrical and Information Engineering, Tianjin University, Tianjin, China, [2] Department of Neurology, Tangshan Gongren Hospital, Tangshan, China, [3] School of Information Technology Engineering, Tianjin University of Technology and Education, Tianjin, China, [4] Department of Pathology, Tangshan Gongren Hospital, Tangshan, China

A novel analytical framework combined fuzzy learning and complex network approaches is proposed for the identification of Alzheimer's disease (AD) with multichannel scalp-recorded electroencephalograph (EEG) signals. Weighted visibility graph (WVG) algorithm is first applied to transform each channel EEG into network and its topological parameters were further extracted. Statistical analysis indicates that AD and normal subjects show significant difference in the structure of WVG network and thus can be used to identify Alzheimer's disease. Taking network parameters as input features, a Takagi-Sugeno-Kang (TSK) fuzzy model is established to identify AD's EEG signal. Three feature sets—single parameter from multi-networks, multi-parameters from single network, and multi-parameters from multi-networks—are considered as input vectors. The number and order of input features in each set is optimized with various feature selection methods. Classification results demonstrate the ability of network-based TSK fuzzy classifiers and the feasibility of three input feature sets. The highest accuracy that can be achieved is 95.28% for single parameter from four networks, 93.41% for three parameters from single network. In particular, multi-parameters from the multi-networks set obtained the best result. The highest accuracy, 97.12%, is achieved with five features selected from four networks. The combination of network and fuzzy learning can highly improve the efficiency of AD's EEG identification.

Keywords: Alzheimer's disease, EEG, TSK fuzzy model, weighted visibility graph, feature select, multiple network

Edited by:
Kamran Avanaki,
Wayne State University, United States

Reviewed by:
Zhaohong Deng,
Jiangnan University, China
Rayyan Manwar,
Wayne State University, United States

****Correspondence:***
Haitao Yu
htyu@tju.edu.cn
Jing Liu
liujingtsh@163.com

Specialty section:
This article was submitted to Brain Imaging Methods, a section of the journal Frontiers in Neuroscience

Received: *11 February 2020*
Accepted: *25 May 2020*
Published: *21 July 2020*

Citation:
Yu H, Zhu L, Cai L, Wang J, Liu J, Wang R and Zhang Z (2020) Identification of Alzheimer's EEG With a WVG Network-Based Fuzzy Learning Approach. Front. Neurosci. 14:641. doi: 10.3389/fnins.2020.00641

INTRODUCTION

Currently, Alzheimer's disease (AD) is becoming a common and serious disease due to organic neurodegenerative and progressive lesions in the brain. The patients always show some typical clinical presentations, particularly in the aspect of cognitive dysfunction such as deficient episodic memory and disabled remembering (Smailovic et al., 2018). The clinical diagnosis of AD currently adopts scale assessment, such as Mini-mental State Examination (MMSE), Montreal Cognitive Assessment (MoCA), activities of daily living (ADL), and physiological detection of cerebrospinal fluid. Patients with severe AD can be observed to have changes in brain structure, such as encephalatrophy, through brain functional imaging. Yang et al. applied magnetic resonance imaging (MRI) to detect the cerebral changes of blood flow and oxygenation in AD and mild cognitive impairment (MCI) subjects, and showed its powerful ability to distinguish from normal controls (Yang et al., 2010). Hiroshi's study has demonstrated progression of atrophy mapping upstream to Braak's stages of neurofibrillary tangle deposition in AD. The main cause of organic brain lesions in AD is considered to be the loss of neurons and synapses (Brenner et al., 1988). It has been suggested that the loss of both synapses and neural pathways leads to a decrease in brain functional connectivity and influences electrical signals of the brain, so it is feasible to diagnose neurotic disease by electroencephalogram (EEG). EEG, which can measure the brain's voltage fluctuations with high temporal resolution, contains plenty of physiological information, and there is growing evidence that EEG may contribute to early recognition of AD patients.

The conventional EEG visual inspection is one of methods widely used in neurological assessment. Numerous previous studies have reported the disappearance of alpha EEG activities, particularly in posterior brain regions, through unaided viewing (Matsuda, 2013; Wang et al., 2015; Horvath et al., 2018). It has also been reported that visual EEG scores of ADs show a strong correlation with dementia severity (Kowalski et al., 2001). In the study of de Waal et al. (de Waal et al., 2011), AD patients with early onset are more likely to show severe diffuse slowing characteristic than those with later onset, which is consistent with the clinical manifestations of AD. In addition, studies have quantified the complexity of electrophysiological activities and reported declined complexity of EEG in AD patients (Cao et al., 2016). The change on the AD brain is also reflected in the perturbations of EEG synchronization. As EEG signals are irregular and non-stationary complex signals, traditional visual inspection is not sufficient for AD EEG identification (Buzsaki and Draguhn, 2004; de Waal et al., 2011; Cao et al., 2016). To address this issue, complex network theory is introduced into AD diagnosis, which aims to describe human brain from a global perspective (Palop et al., 2006; Nimmrich et al., 2015; Cao et al., 2016; Gao et al., 2019).

Over the past few years, more and more researchers have begun to adopt the attractive idea of using complex network methods to characterize the dynamic features of complex systems (Zou et al., 2019). This novel approach is the thorough combination of two frontier research fields, analysis methods of non-linear time series (Hively et al., 2000; Costa et al., 2002, 2005) and complex networks theory (Brown et al., 2004; Boccaletti et al., 2006). Zhang et al. have constructed complex networks with strength of temporal correlation between time series and reported that the behavior information (chaotic or fractal) of time series directly correlate with the topological structures (Zhang and Small, 2006). As an effective tool to get insight into the brain function, the brain network analysis has been widely applied in AD research. The healthy brain was found to work with network properties such as small-worldness, hubness, and rich-clubs, while the AD brain operated with less optimal network topologies (Meunier et al., 2010; Blinowska and Kaminski, 2013; Martijn and van den Heuvel, 2013; Wang et al., 2014, 2016; Deng et al., 2015). Loss of small-world features (toward random network topology) can be observed in functional network constructed from EEG and functional magnetic resonance imaging data (Stam et al., 2007; He and Evans, 2010; Tahaei et al., 2012; Reid and Evans, 2013). Numerous EEG studies have consistently demonstrated decreased functional connections in the higher frequency bands of AD patients compared to controls (Tijms et al., 2013; van Straaten et al., 2014).

Compared to other approaches of constructing complex networks through time sequence, visibility graph (VG) algorithms can better integrate the basic features of time series. Lacasa et al. and Liu et al. converted time series into graphs and extracted the topological features using graph theory methods (Lacasa et al., 2008; Liu et al., 2010). They pointed out that the irregularity of time sequence can be characterized by the network topology. For instance, the periodic sequence can be transformed into regular lattice, while the chaotic series corresponds to random graphs. Subsequent researches began to introduce VG method into the EEG study of neurological diseases, and found features extracted from VG networks can be effectively used as mathematical markers in neurodegenerative diagnosis. VG algorithm was first applied in related research in AD by Ahmadlou et al. They reported that complexity of EEGs computed by VGs can be used in the distinguishing between AD and control EEGs (Ahmadlou et al., 2010).

The VG can only express the existence of edges between different time nodes, but not the strength of the edges. Therefore, Supriya et al. have proposed to combine the weighted edge with the horizontal visibility graph, which are not applicable to all complex network graphs (Supriya et al., 2016). Addressing the limitations of above approaches, Zhu et al. have improved the weighted visibility graph (WVG) algorithm by specifying radian function as the criterion for calculating edge weights in all kinds of complex network, and obtained promising results in the detection of epilepsy (Zhu et al., 2014). Also, studies have shown that the visualization method can preserve the characteristics like reduction of complexity (Polikar et al., 2007; Czigler et al., 2008) and slowing of rhythm (Dauwels et al., 2011; Cao et al., 2015; McBride et al., 2015) in patients with AD. WVG networks retain more structural information of the time series, which is more conducive for AD identification, compared to connectivity networks. Therefore, we apply the WVG method on the feature extraction of Alzheimer's disease. A variety of different parameters are extracted from the visibility graph, and used to further investigate which parameter can be used for diagnosing AD.

After quantitative analysis of complex WVG networks, the valuable information about the time series has been extracted. The machine learning generally approaches the extracted features for training the model and then applies them in signal detection. Traditional machine learning methods, including decision tree, random forests, k-nearest neighbor (KNN), Naive Bayes (NB), logistic regression, and so on (Siegelmann and Holzman, 2010; Hramov et al., 2019), have been widely used in the detection of neurological diseases. However, for systems with highly non-linear characteristics, models that built based on these methods do not characterize real models and be utilized in classification well. With this consideration, a rule-based fuzzy model is proposed and has been widely used in many fields like computer vision, natural language processing, and enhanced learning, achieving remarkable results (Gu et al., 2017). Takagi-Sugeno-Kang (TSK) method is proposed to build a model established by using fuzzy mathematics language to describe some characteristics and internal relations of fuzzy phenomena. Compared with traditional classifiers that lack transparency, TSK can be used in multiple features classification and shows a superior model interpretability, which is defined as the ability to better understand the decision strategies of response functions in a human-interpretable manner in order to interpret internal relationships (Deng et al., 2018). In current applications of machine learning, such interpretability has received wide attention and is considered to be crucial.

In this paper, multiple networks are constructed based on multi-channel EEG, with each EEG channel able to be transformed into one-layer network. Then a number of different network features are extracted from them, which is too much for input feature vectors. In order to explore this problem, some feature selection approaches will be utilized to choose features, and the influence of different screening methods on the final classification results will also be tried. The parameters will be divided into three groups—single parameter from multi-network, multi-parameter from single network, and multi-parameter from multi-network—to observe the difference between the classification results of fuzzy models trained with different types of features. The structure of rest paper is as follows: section Methods and materials is devoted to describing the experimental design, including data collection and subject condition. Meanwhile, the principle of mathematical graph methods and Takagi-Sugeno-Kang (TSK) model adopted in paper are also explained in this part. In section Experimental Results, we performed a statistical analysis of the results and implemented AD recognition based on the proposed framework. Section Conclusion and Discussion includes a discussion of the application and advantages of the proposed model, as well as future work.

MATERIALS AND METHODS

Subjects and EEG Recordings

EEG recordings are collected from AD subjects and control subjects, respectively. The AD group included 30 confirmed AD patients who are diagnosed with mini-mental state examination (MMSE) scores are between 12 and 15. The diagnosis results meet the National Institute on Aging-Alzheimer's Association criteria. All of them have not used antipsychotic drugs, antidepressants, dopamine blockers, or excessive amounts of alcohol, and don't have other neurological or psychiatric disorders or any other serious illness. The AD group includes 18 females and 12 males, whose ages range from 74 to 78. The control group consisted of 30 healthy subjects of matched ages, ranging from 70 to 76 years old, and includes 10 females and 20 males. The MMSE scores of them are between 28 and 30. In order to avoid the impact on EEG activity, all subjects will be prohibited from using neuroactive drugs before the experiment. The data adopted in this paper is from our previous study (Wang et al., 2016), which is approved by the Ethics Committee of Tangshan Gongren Hospital and was conducted in accordance with the Declaration of Helsinki. In addition, all the subjects in this experiment gave informed consent.

A 16-channel EEG monitoring system (Solar2000B) is adopted. The EEG channels have 10 MΩ input impedance with bandwidth as 0.08–300 Hz. In order to obtain low-frequency signals that meet the analysis requirements, the low-pass filtering range is set to 0.08–50 Hz. Studies have demonstrated that the EEG amplitude across different bands tends to stabilize when the scalp-electrode impedance is <10 kΩ, so electrode impedance in our experiments is set to 3 kΩ. The international 10–20 system, which consists of 16 electrodes, is adopted as electrode distribution in the scalp (surface) EEG recordings, and the linked earlobe A1 and A2 are used as reference. EEGs are recorded by Symtop amplifier (model: UEA–B; frequency: 1,024 Hz; electrode impedance: 3 k).

During the experiment, the subjects stayed in a semi-dark quiet room and were told to keep awake with eyes closed. The EEG recording process was kept to at least 30 min for each subject. In order to eliminate the impact of nervousness, anxiety, and head movement, a 10-min EEG is selected from each recorded EEG epoch. Sharp transient artifacts caused by eye movement and muscle artifacts, as well as segments with voltage exceeding 150uV, are also removed. Next, fifteen epochs without artifacts with an 8-s long duration for each ($15 * 8\,\text{s} = 120\,\text{s}$) were chosen for each subject's EEG, which are suitable for weighted visibility graph construction.

WVG Methods

The EEG signal is the electrical signal of the brain neurons measured on the surface of the cerebral cortex or scalp. It has obvious non-stationary, non-linear, and dynamic characteristics. The VG method provides a way to research the underlying dynamics of EEG data (Lacasa et al., 2008; Deng et al., 2018). Since the VG can inherit the dynamic nature of creating time series data, this technique has the characteristics of describing time series from the perspective of graph theory. The VG algorithm was originally applied in the field of robot motion planning, architectural design, and topographic descriptions of geographical space (Lozano-Pérez and Wesley, 1979; Turner et al., 2001; Lacasa et al., 2009; Jiang et al., 2017; Zou et al., 2019). This algorithm combined the mutual visible relationship of the point and obstacles in the two-dimensional landscape with the computational geometry framework. The literature study reveals that WVG can also be used in EEG data analysis to convert non-stationary, one-dimensional time series into two-dimensional viewable views for analysis. Different channels of EEG signals can reflect the electrophysiological information from different regions of the brain, so each single channel can obtain single complex network and multi-layer networks can be obtained through multi-channel EEG. The schematic diagram of constructing brain network by WVG method is shown in **Figure 1**.

In the construction of a WVG from a univariate EEG data $\{x_i\}_{i=1}^{N}$ with $x_i = x(t_i)$, individual observations are considered as vertices. Thus, the weighted adjacency matrix **W** can be obtained

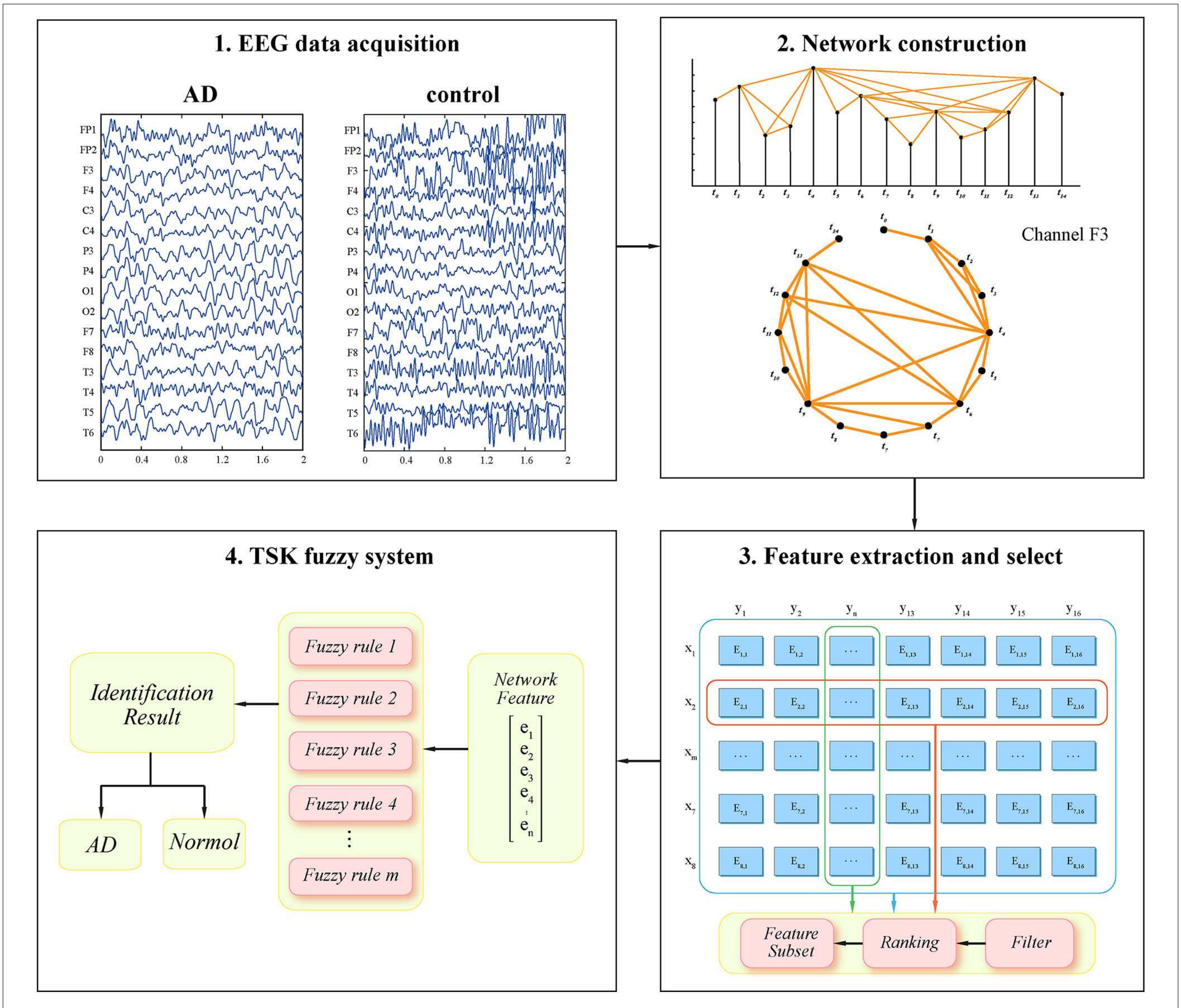

FIGURE 1 | The framework of our method for classifying the AD patients in EEG signals. First multichannel EEG signals of two types of subjects are acquired and a preliminary analysis was performed. Second, we construct the WVG network based on each EEG channel. Third, the features are extracted and further ranked based on feature select method. Finally, we combine the network theory with a fuzzy rule-based system to identify AD pattern with the selected network topological properties.

with size of $N \times N$. Nodes of WVG network are defined by time points $\{t_i\}, i = 1, 2, ...N$ and each edge in this network is defined by the connection between two time points (Zou et al., 2019). Two nodes are defined as connected if the criterion

$$\frac{x(t_i) - x(t_k)}{t_k - t_i} > \frac{x(t_i) - x(t_j)}{t_k - t_i} \tag{1}$$

is fulfilled for all time points t_k with $t_i < t_k < t_j$. Then the absolute value of edge weight between two nodes are determined as

$$w_{i,j} = \arctan \frac{x(t_i) - x(t_j)}{t_i - t_j}, i < j \tag{2}$$

Feature Extraction and Select

The topology of the network is quantified based on the multiple complex networks obtained with WVG method. In order to statistically analyze the characteristics of AD networks and control networks, we calculate the clustering coefficient, average weighted degree, graph index complexity, network entropy, degree distribution index, modularity, local efficiency, and average path length as eight different topological characteristics.

Clustering Coefficient

The clustering coefficient is a measure to quantify how tightly connected the neighbor is around a node (Rubinov and Sporns, 2010). For a network G with N nodes, the connectivity between nodes i and j is $a_{i,j}$ ($a_{i,j}$=1 if the connection exists or $a_{i,j}$=0 if not), the weight of connection are $w_{i,j}$ ($w_{i,j} \in [0, 1]$). For a weighted network, the local clustering coefficient of node i is defined as:

$$C(i) = \frac{1}{s_i (K_i - 1)} \sum_{j,h \in G} \frac{\left(w_{i,j} + w_{i,h}\right)}{2} a_{i,j} \, a_{i,h} \, a_{j,h} \tag{3}$$

where s_i, the strength of the node i, is defined as:

$$s_i = \sum_{j \in G_i} w_{i,j} \tag{4}$$

And G_i represents the nodes set of node i neighborhoods. Further define the clustering coefficient of the whole network as:

$$C = \frac{1}{N} \sum_{i \in G_i} C(i) \tag{5}$$

Average Weighted Degree

Average Weighted Degree is an important parameter for distinguishing networks with different topologies. The average weighted degree of the network can be obtained through averaging weights of the incident links on all the nodes in the network (Supriya et al., 2016):

$$wd = \frac{1}{N} \sum_{i \in G_i} s_i \tag{6}$$

where s_i is described above in function (4).

Graph Index Complexity

Kim et al. have introduced graph index complexity as a new feature into the diagnosis of patients with AD by quantifying the complexity of the image graph (Kim and Wilhelm, 2008; Wang et al., 2016). With the largest eigenvalue of the adjacency matrix of a graph with n nodes presented as $\lambda_{\max}$ (Blinowska and Kaminski, 2013). The graph index complexity is defined as follows:

$$c_{\lambda_{\max}} = 4c(1 - c) \tag{7}$$

where

$$c = \frac{\lambda_{\max} - 2\cos(\pi/(n+1))}{n - 1 - 2\cos(\pi/(n+1))} \tag{8}$$

Degree Distribution Index

The degree distribution $P_{\deg}(k)$ is often used to classify complex networks, which can be formed by counting how many nodes have each degree. In this paper, a probability distribution object is obtained by fitting the Poisson distribution to the degree distribution vector. The degree distribution $P_{\deg}(k)$ is defined as

$$P_{\deg}(k) = \frac{\lambda^k}{k!} e^{-\lambda} \tag{9}$$

The degree distribution index is defined as the λ values of the fitting distribution (Stephen and Toubia, 2009).

Network Entropy

The network entropy can be computed straightforwardly based on the degree distribution as

$$S = -\sum_k P_{\deg}(k) \log P_{\deg}(k) \tag{10}$$

Modularity

Modularity is a quality feature that can measure the quality of the clusters (communities), which are obtained by dividing the network partition (Supriya et al., 2016). The modularity Q of this weighted network is defined as:

$$Q = \frac{1}{2m} \sum_{i,j} \left(a_{i,j} - \frac{k_i k_j}{2m}\right) \delta(C_i, C_i) \tag{11}$$

where $m = \frac{1}{2} \sum_{i,j \in G} w_{i,j}$ is the sum weights of all links in the network, $k_i = \sum_{j \in G} w_{i,j}$ is the sum weight of the links attached to node i, C_i represents the community which vertex i is assigned to, the function $\delta\left(C_i, C_j\right)$ is 1 if nodes i and j belong to the same community and 0 otherwise. In this paper, we used the Louvain method (Blondel et al., 2008) to distribute nodes into different communities. This method is divided into two steps. In the first step, each node is added into the neighbor communities to determine the one which can maximize the modularity gain ΔQ. In second step, a new network is reconstructed whose node is defined as the small community found in the first step, and whose weights of new links are given by the sum weight of the links between nodes in the corresponding two old communities. Those two steps will be repeated iteratively until the maximum of modularity is accomplished and there is no more movement of nodes. The modularity gain ΔQ is defined as (Zhaohong et al., 2013):

$$\Delta Q = \left[\frac{\Sigma_{\text{in}} + k_{i,\text{in}}}{2m} - \left(\frac{\Sigma_{\text{tot}} + k_i}{2m}\right)^2\right] - \left[\frac{\Sigma_{\text{in}}}{2m} - \left(\frac{\Sigma_{\text{tot}}}{2m}\right)^2 - \left(\frac{k_i}{2m}\right)^2\right] \tag{12}$$

where Σ_{in} represents the sum of all the links weights inside community C, Σ_{tot} is the sum of the weights of the links attached to nodes in C, k_i is the sum of the weights of the links attached to node i, $k_{i,\text{in}}$ is the sum of the weights of the links from i to nodes in C, and m is the sum weights of all links in the network.

Local Efficiency

Local efficiency, as a node-specific measure, is defined to measure the density of the subnetwork composed of the neighborhood of the node i. Local efficiency of ith node is given as

$$E_{loc}(i) = \frac{1}{N_{G_i}\left(N_{G_i} - 1\right)} \sum_{i,j \in G, i \neq j} l_{i,j} \tag{13}$$

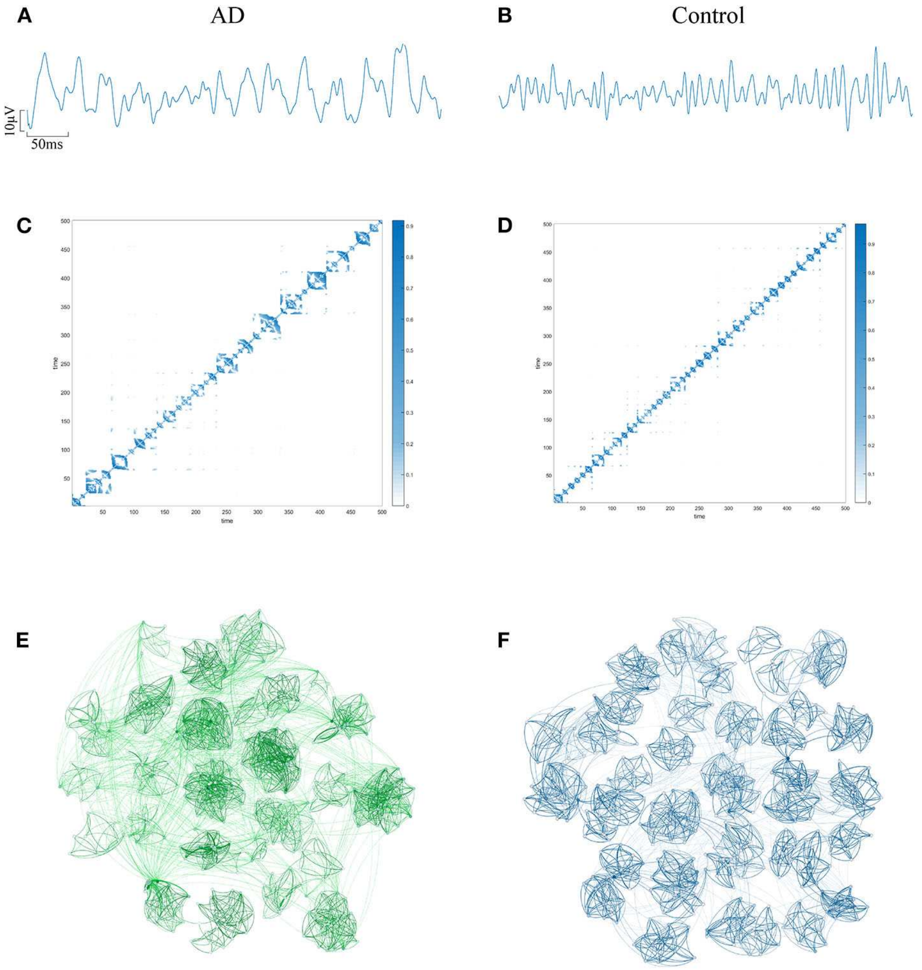

FIGURE 2 | An example of converting EEG signal from an AD subject and a control subject into a WVG. EEG signals of FP1 channel from AD **(A)** subject and control **(B)** subject with 5s length. The adjacency matrixes of the converted WVGs respectively for AD **(C)** subject and control **(D)** subject. Schematic diagram of complex networks corresponding to WVGs of AD **(E)** subject and control **(F)** subject.

Where $l_{i,j}$ is the shortest distance between i and j, and N_{G_i} is the number of the neighborhood of node i. Local network efficiency is the average of the local efficiency of all nodes

$$E_{loc}=\frac{1}{N}\sum_{i}E_{loc}\left(i\right) \tag{14}$$

Average Path Length

Average path length is a vital index to measure information transmission ability of networks. It can be used to evaluate the connectivity of the global functional network, including local and remote connection. The average path L is defined as:

$$L=\frac{1}{N\left(N-1\right)}\sum_{i,j,i\neq j}l_{i,j} \tag{15}$$

TSK Fuzzy Model

Given an original input dataset $\mathbf{X}=\{\mathbf{x}_1,\mathbf{x}_2,...,\mathbf{x}_n\} \in \mathbf{R}^d$ and the corresponding class label $\mathbf{Y}=\left\{\mathbf{y}_1,\mathbf{y}_2,...,\mathbf{y}_n\right\}$ ($y_{i,j} = 1$ when the ith sample belongs to jth class; otherwise, $y_{i,j} = 0$), the kth fuzzy inference rules are often defined as

$$R^k: \text{IF } x_1 \text{ is } A_1^k \wedge x_2 \text{ is } A_2^k \wedge \ldots \wedge x_d \text{ is } A_d^k, \text{THEN}$$
$$f_k\left(\mathbf{x}\right)=\beta_0^k+\beta_1^k x_1+...+\beta_d^k x_d, \text{k}=1,...,\text{K}$$

Where $\mathbf{x} = [x_1,x_2,...,x_d]^T$ is input vector of each rule, K is the number of fuzzy rules, A_i^k are Gaussian antecedent fuzzy sets subscribed by the input variable x_i of Rule k, $\wedge$ is a fuzzy conjunction operator, $f_k\left(\mathbf{x}\right)$ is a linear function about the inputs, and β_i^k are linear parameters.

With each rule is premised on the sample vector $\mathbf{x}$, the output of a TSK fuzzy system is expressed as

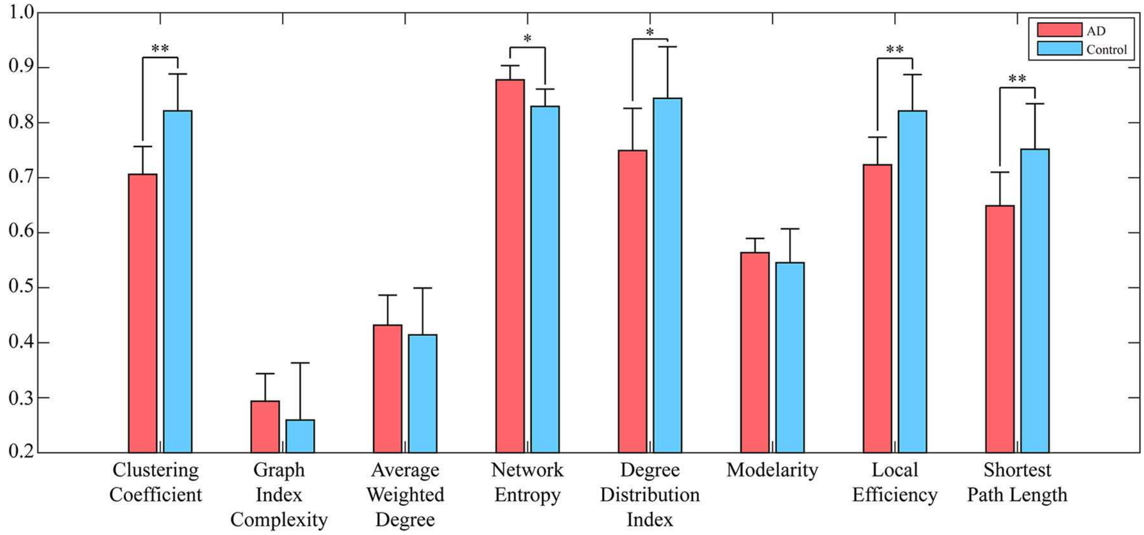

FIGURE 3 | Network parameters (averaged across subjects) of both AD networks and control networks. Error bars represent standard error across subjects. The degree of significant difference is calculated by Analysis of Variance (ANOVA) across all subjects. **A significant correlation ($p_c \leq 0.01$ corrected for multiple comparisons across tiles). *A trend ($p_c \leq 0.05$).

$$\tilde{y} = \sum_{k=1}^{K} \frac{\mu_k(\mathbf{x}) f_k(\mathbf{x})}{\sum_{k'=1}^{K} \mu_{k'}(\mathbf{x})} = \sum_{k=1}^{K} \tilde{\mu}_k(\mathbf{x}) f_k(\mathbf{x}) \tag{16}$$

where

$$\mu_k(\mathbf{x}) = \prod_{i=1}^{d} \mu_{A_i^k}(x_i) \tag{17}$$

is the fuzzy membership function and

$$\tilde{\mu}_k(\mathbf{x}) = \frac{\mu_k(\mathbf{x})}{\sum_{k'=1}^{K} \mu_{k'}(\mathbf{x})} \tag{18}$$

is the normalized fuzzy membership function of the antecedent parameters of the kth fuzzy rule. While $\mu_{A_i^k}(x_i)$ is Gaussian membership function for fuzzy set A_i^k that can be expressed as

$$\mu_{A_i^k}(x_i) = \exp\left(-\frac{\left(x_i - c_i^k\right)^2}{\delta_i^k}\right) \tag{19}$$

where c_i^k is kth cluster center parameters, which can be calculated with the classical fuzzy c-means (FCM) clustering algorithm (Bezdek et al., 1984):

$$c_i^k = \frac{\sum\limits_{j=1}^{N} u_{jk} x_{ji}}{\sum\limits_{j=1}^{N} u_{jk}} \tag{20}$$

and the width parameter δ_i^k can be estimated by (Zhaohong et al., 2013):

$$\delta_i^k = \frac{h \cdot \sum\limits_{j=1}^{N} u_{jk}\left(x_{ji} - c_i^k\right)^2}{\sum\limits_{j=1}^{N} u_{jk}} \tag{21}$$

where the element $u_{jk} \in [0, 1]$ denotes the fuzzy membership of nth input sample $\mathbf{x}_n$ to the kth cluster ($k = 1, 2, ..., K$), h is a constant called the scale parameter.

For an input sample $\mathbf{x}_n$, let

$$\mathbf{x}_{n,e} = \left(1, {\mathbf{x}_n}^T\right)^T \tag{22}$$

$$\tilde{x}_n^k = \tilde{\mu}^k(\mathbf{x}_n)\,\mathbf{x}_e \tag{23}$$

$$\rho(\mathbf{x}_n) = \left(\left(\tilde{x}_n^1\right)^T, \left(\tilde{x}_n^2\right)^T, ..., \left(\tilde{x}_n^K\right)^T\right)^T \in R^{K(d+1)} \tag{24}$$

TABLE 1 | Classification results with each single parameter from single network layer is taken as input feature.

	x_1	x_2	x_3	x_4	x_5	x_6	x_7	x_8
y_1	0.6218	0.5546	0.5618	0.6543	0.5654	0.5457	0.5721	0.5904
y_2	0.5925	0.6550	0.5086	0.6368	0.5275	0.5364	0.5721	0.6893
y_3	0.6225	0.5482	0.5454	0.6454	0.6214	0.5596	0.5996	0.5243
y_4	0.6718	0.4779	0.5514	0.5632	0.6464	0.5229	0.5800	0.6146
y_5	0.5754	0.5918	0.5507	0.6343	0.5443	0.5382	0.5868	0.5982
y_6	0.6600	0.5718	0.5582	0.5486	0.5536	0.5625	0.5675	0.6386
y_7	0.5721	0.5793	0.5086	0.7893	0.6211	0.5779	0.5964	0.5293
y_8	0.5461	0.5550	0.6279	0.5957	0.6207	0.5679	0.5818	0.5679
y_9	0.7925	0.6671	0.6446	0.54	0.5454	0.7446	0.7182	0.5768
y_{10}	0.5271	0.3804	0.5811	0.6625	0.5504	0.5693	0.5225	0.5479
y_{11}	0.5157	0.425	0.5304	0.5107	0.5257	0.5275	0.5179	0.5075
y_{12}	0.6996	0.6832	0.6193	0.7432	0.6789	0.7904	0.745	0.7386
y_{13}	**0.7996**	0.6411	0.5664	0.5586	0.6325	0.7218	0.69	0.5343
y_{14}	0.5279	0.515	0.5082	0.5218	0.5314	0.5464	0.5379	0.5107
y_{15}	0.5625	0.4011	0.5071	0.5529	0.365	0.6868	0.3814	0.3789
y_{16}	0.7489	0.5479	0.5082	0.5486	0.54	0.6979	0.6175	0.4589

$$\beta^k = \left(\beta_0^k, \beta_1^k, ..., \beta_d^k\right)^T \tag{25}$$

$$\beta_g = \left(\left(\beta^1\right)^T, \left(\beta^2\right)^T, ..., \left(\beta^K\right)^T\right)^T \tag{26}$$

then the output value $\tilde{y}_n$ of a TSK fuzzy classifier for sample $\mathbf{x}_n$ can be expressed as

$$\tilde{y}_n = {\beta_g}^T \rho\left(\mathbf{x}_n\right) \tag{27}$$

Learning Algorithm

Given a training dataset $D_S = \left\{\mathbf{x}_i, \mathbf{y}_i | \mathbf{x}_i \in R^d, \mathbf{y}_i \in R^C, i = 1, ..., N_S\right\}$, where C is the number of classes, the consequent parameter β_g can be learned by using generalized hidden-mapping ridge regression (GHRR) (Deng et al., 2014; Tian et al., 2019). The objective function is:

$$\min_{\beta_g} J\left(\beta_g\right) = \frac{1}{2}\sum_{j=1}^{C}\sum_{i=1}^{N_S}\left\|{\beta_{g,j}}^T\mathbf{x}_{g,i} - y_{i,j}\right\|^2 + \frac{\lambda}{2}\sum_{j=1}^{C}{\beta_{g,j}}^T\beta_{g,j} \tag{28}$$

where is the consequent parameter vector of the jth class is represented by $\beta_{g,j}$, λ is a regularization parameter controls the complexity of the classifier, and the tolerance of error λ can be set manually or determined by cross-validation. The optimal consequent parameters, $\beta_{g,j}$, can be computed by setting the derivatives of J with regard to each $\beta_{g,j}$ is 0 and the solution is (Yu et al., 2020):

TABLE 2 | Classification results with the set of single parameter from multiple networks is taken as input feature vector.

Method	Best input vector length	Accuracy	Sensitivity	Specificity
CFS	4	0.9211	0.9375	0.9091
DGUFS	3	0.7971	0.8974	0.6667
Fisher	4	0.9528	0.9491	0.9583
FSV	6	0.9430	0.9406	0.9449
LLCFS	9	0.9431	0.9223	0.9600
mRMR	6	0.8706	0.7971	0.9091

$$\beta_{g,j} = \left(\lambda_1\mathbf{I}_{(d+1)*K\times(d+1)*K} + \sum_{i=1}^{N_S}\mathbf{x}_{g,i}{\mathbf{x}_{g,i}}^T\right)^{-1}\sum_{i=1}^{N_S}\mathbf{x}_{g,i}y_{i,j} \tag{29}$$

EXPERIMENTAL RESULTS

The EEG of AD patients implies a large amount of information that cannot be visually expressed from the waveform. Research shows that the visualization algorithm can express the hidden information in the form of images. In order to verify whether the AD brain's electrical features can be represented by WVG, we first select the same channel EEG from an AD patient and a control subject. Two episodes with a length of 500 data points (as shown in **Figures 2A,B**) are further intercepted, and converted to WVG. The result is shown in **Figures 2C,D**. Studies have reported that it's easy to detect a diffuse slowing in the EEG of AD patients with the naked eye (Micanovic and Pal, 2014). This diffuse slowing feature is well-preserved in WVG, and WVG of AD patients can be clearly observed in more communities, indicating the feasibility of WVG method for AD detection. For further observation of the topological feature of the WVG network, the two adjacency matrixes are represented as network structure diagrams that shown in **Figures 2E,F**. The dots in figure represent all network nodes and the network edges are represented by curves, and the shade of the curve color can directly reflect the weighted value of the edges. It can be observed that the different communities in the WVG network of normal people are generally similar in size and the distributions of connections are uniform. The community structure of the networks obtained by the WVG method is more irregular for AD patients. Most nodes are concentrated in a small part of communities, and the connection between communities is also closer. The result indicates that the electrophysiological signals of AD brains are more unstable, with fluctuations that are stronger. Research on single channel reveals that the WVG network of AD and normal people are significantly difference. Next, we will transform all 16 channels into multi-networks ($\{y_n\}(1 \leq n \leq 16)$) and each layer of network can be obtained from each channel. We further considered which parameters are selected to quantify this difference.

To reduce the computing time and to retain as much information as possible, the EEG signal is divided into many

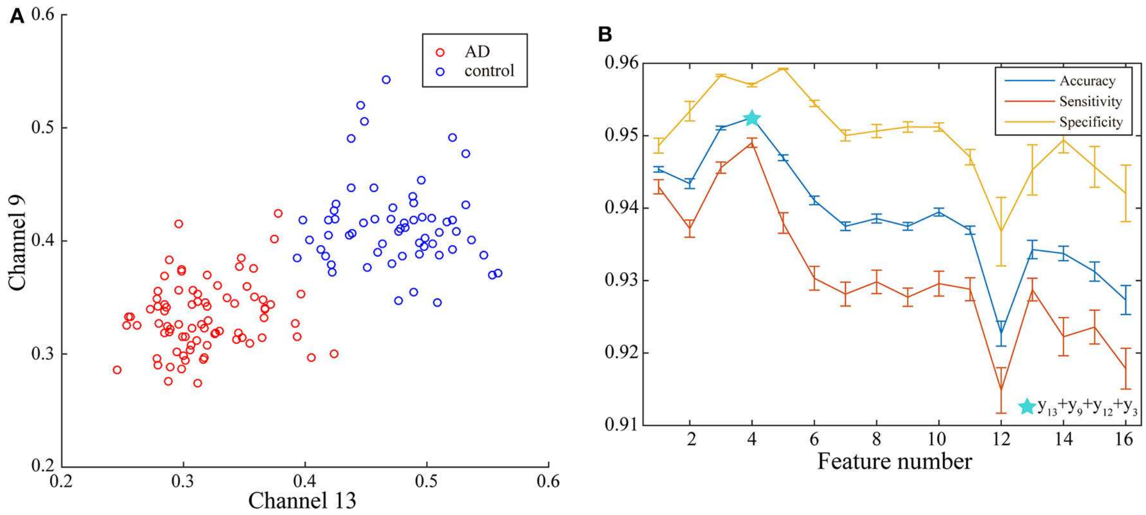

FIGURE 4 | (A) Joint distribution of clustering coefficient obtained from WVG network transformed from Channel 13 and Channel 9. **(B)** Classification results when the number of input features is from 1 to 16, which is obtained under single parameter (clustering coefficient) from multi-networks set and ordered through feature selection method.

episodes through sliding windows with lengths of 500 data points. Since the size of the converted WVG network is consistent with the length of EEG series, a series of adjacency matrixes of size 500 × 500 are finally obtained. Next, we calculate clustering coefficient (x_1), graph index complexity (x_2), average weighted degree (x_3), network entropy (x_4), degree distribution index (x_5), modularity (x_6), local efficiency (x_7), and average path length (x_8) of each WVG network of both AD and control. Above parameters can be obtained from each different network layers, which can be considered as different features. Since there is a considerable difference in the magnitude of the values of different parameters, the calculated result is normalized to 0∼1. All windows of each person were further averaged, and then a statistical analysis was performed based on each person. As shown in **Figure 3**, parameters of all subjects are statistically analyzed and the parameters that are significantly different for AD group and control group are marked with ∗. The values of clustering coefficient, local efficiency, and shortest path length of the AD group are significantly lower than that of controls with $p < 0.01$. Meanwhile, the degree distribution entropy of AD group is higher than that of controls with $p < 0.05$ while the degree distribution lambda of AD group is lower than that of controls with $p < 0.05$.The obtained results demonstrate that network topological parameters can be used to detect AD.

Through statistical analysis, it's obvious that some of the above parameters can clearly distinguish AD from the control group. In order to further verify the effect of these parameters on AD recognition, these parameters will be used as input features of the training fuzzy classifier. In each training process, we randomly select 80% of the original data to form training datasets which can be used for ten-fold cross-validation (10-CV), with 90% (90% × 80%) utilized for model training and 10% (10% × 80%) for constructing a validation set. The above procedure is repeated 10 times to cover the entire training set and finally determine the optimal hyperparameters of the TSK model. The remaining 20% of all data is tested as the testing data with determined hyperparameters. For each different input feature or feature vector, the classification results (accuracy, sensitivity, specificity) are averaged after training for 50 times.

The construction of each WVG network is based on a single time series, so 16 WVGs are obtained from 16-channel EEG used in this paper. These WVG networks contain different electrophysiological information of neurons in different brain regions. However, in the existing studies, the parameters extracted from WVG networks constructed by different brain regions' EEG were usually regarded as the same class of features, so the differences between brain regions were ignored. Therefore, we consider the 16 WVG networks as different networks and combine them into a multi-layer network. In order to verify whether the underlying dynamic information of these network layers are different, the classification is first performed with a single feature as input. Each parameter extracted from each single network layer transformed from different channels is used as the single input feature for model training, and the classification results are shown in **Table 1** with optimal classification result is bolded. It can be observed that for the same network parameter extracted from different network layers, the classification results are significantly different. The difference in classification accuracy of the same parameter from different network can even reach 28.39% for average weighted degree ($\left\{\left(x_3, y_k\right)\right\}, k = 1, ..., 16$), indicating that the dynamic information that contained in EEG of different brain regions does have significant differences and parameters of different layers maybe independent from each other. This finding shows that the network characteristics of the multi-network composed of WVG network layers can be used as independent input features for the classifier.

The input feature vector consisting of multiple parameters is used for fuzzy system training. The classification will be performed based on the following three feature sets [as shown

TABLE 3 | Classification results with the set of multiple parameters from single network is taken as input feature vector.

Method	Best input vector length	Accuracy	Sensitivity	Specificity
CFS	3	0.9259	0.9434	0.9091
DGUFS	4	0.8734	0.8772	0.8696
Fisher	2	0.8969	0.9259	0.8696
FSV	3	0.9341	0.9379	0.9321
LLCFS	6	0.9009	0.9091	0.8929
mRMR	5	0.7937	0.7692	0.8197

in **Figure 1**(3)]: (1) Single parameter from multi-networks: When ensuring that the classifier input is the same parameter, select different network layers for parameter extraction and combination. (2) Multi-parameters from single network: In the case of one single network layer, different parameters are extracted and selected for combination as a classifier input. (3) Multi-parameters from multi-network: All parameters extracted from all network layers are used as different input features to the classifier. Then for each set, various feature select methods including Correlation-based Feature Selection (CFS) (Guyon et al., 2002), Dependence Guided Unsupervised Feature Selection (DGUFS) (Zhu et al., 2017), Fisher (Gu et al., 2012), Feature Selective Validation (FSV) (Bradley and Mangasarian, 1999), Locality-Constrained Linear Coding Feature Select (LLCFS) (Zeng and Cheung, 2011), and minimum-redundancy maximum-relevance (mRMR) (Peng et al., 2005) are used to sort the features to obtain the feature sequence for each set. According to the obtained feature sequence, select the different number of features in order (i.e., the first one feature, the first two features, the first three features...) to component the input vectors for the TSK model training process. In the feature select process (as shown in **Figure 1**), the methods of Feature Selection Library (FSLib) are adopted for determining feature input vectors of TSK. All the algorithms are implemented with MATLAB 2016b.

First, case 1 is described as an example, and the structure of TSK is also described in details in following. As the clustering coefficient ($\{(x_1, y_{13})\}$) reached a highest accuracy of 79.96% in **Table 1**, local efficiency from all network layers ($\{(x_1, y_k)\}, k = 1, ..., 16$) is adopted for feature selection and multi-input classification. The orders of the features are obtained by various sorting feature selection algorithms. After the ranking of network parameters, we choose input feature vectors with different lengths as inputs of TSK model and calculate classification results (accuracy, sensitivity, and specificity), respectively. The optimal length of input vectors and classification results are shown in **Table 2**. It can be observed that with different feature select methods, the length of the feature vectors with the optimal classification result is different. Besides, the sensitivity is higher than the specificity for the feature vectors filtrated by CFS and DGUFS methods, while the others are opposite. It shows that the change of the feature used for training will affect the properties of the trained model. As for the parameter set of clustering coefficients extracted from multiple networks, the Fisher method can be used to achieve the optimal classification result. The classification process with Fisher method are further explored.

With the applying of Fisher algorithm, the order of the parameters is obtained as (x_1, y_{13}), (x_1, y_9), (x_1, y_{12}), (x_1, y_3), (x_1, y_1), (x_1, y_2), (x_1, y_1), (x_1, y_6), (x_1, y_{10}), (x_1, y_8), (x_1, y_5), (x_1, y_{15}), (x_1, y_7), (x_1, y_4), (x_1, y_{14}), (x_1, y_6). The joint distribution of the first two channels under the ranking is illustrated to verify the effectiveness of the same network parameter of WVG network transformed from different channels as the multi-input for classification. The result is shown in **Figure 4A** with each point represents a subject. It's obviously that AD subjects display significant differences from controls, which also demonstrate that local efficiencies, respectively, of channel 9 and channel 13 are effective to classify AD and controls. These two parameters can also get the best classification results when multi-network clustering coefficient is taken as single parameter input. However, the optimal parameters obtained by feature selection are not completely consistent with those that are optimal for the classification result when a single parameter is used as input. This indicates that the information of a single brain region cannot be used as a direct feature to distinguish patients with AD, but the implicit information of different brain regions can complement each other. In the above ranking order, five rules TSK classifiers are used with the number of classifier inputs is from 1 to 16 in order, and the final classification results under cross-validation are listed in **Figure 4B**. As the length of input feature vector increases, the accuracy reaches a maximum of 95.28% at four inputs and then begins to decrease.

In this part, the framework of the TSK is also described in details based on the selected optimal combination feature. The input vector **x** consists of the clustering coefficients of channel 13((x_1, y_{13})), channel 9((x_1, y_9)), channel 12((x_1, y_{12})), and channel 3((x_1, y_3)). Membership functions can be linguistically expressed using a fuzzy linguistic description including "*very low,*" "*low,*" "*medium,*" "*high,*" and "*very high.*" Each membership function of different features corresponds to different description in ascending order of the values of centers. To provide further explanation, the clustering coefficient of channel 13 is interpreted as an example. We define the gaussian model as a membership function, and each rule will get a set of antecedent parameter (centers, standard variance), respectively, which are (0.3990 0.0031) for Rule 1, (0.3956 0.0030) for Rule 2, (0.4165 0.0032) for Rule 3, (0.4052 0.0031) for Rule 4, and (0.4040 0.0030) for Rule 5. By the permutation of these five centers of each rule, membership functions can be described with fuzzy linguistic description: Rule 1 is "*very low,*" Rule 2 is "*very high,*" Rule 3 is "*low,*" Rule 4 is "*medium,*" and Rule 5 is "*high.*" The other four features can also be fuzzy and described similarly. Therefore, with the linguistic expressions and the corresponding linear function the fuzzy rule can be given as follows:

R^1 : IFy_{13} is ***very low*** $\wedge$ y_9 is ***very low*** $\wedge$ y_{12} is ***medium*** $\wedge$ y_3 is ***very low***,

$$\text{THEN } f_1(\mathbf{x}) = \begin{bmatrix} 0.4975 - 0.1872y_{13} + 0.1615y_9 + 0.1515y_{12} + 0.2134y_3 \\ -0.1385 - 0.0959y_{13} - 0.0738y_9 - 0.0514y_{12} - 0.1147y_3 \end{bmatrix},$$

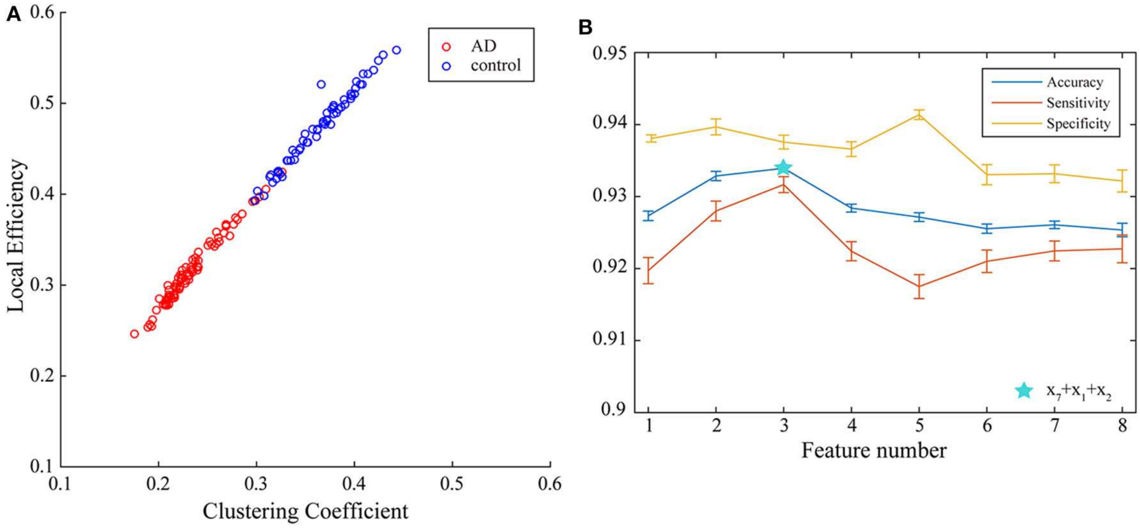

FIGURE 5 | (A) Joint distribution of clustering coefficient and local efficiency obtained from WVG network obtained from Channel 13. **(B)** Classification results when the number of input features is from 1 to 8, which is obtained under multi-parameters from single network (y_{13}) set and ordered through feature selection method.

R^2 : IFy_{13} is ***very high*** $\wedge$ y_9 is ***very high*** $\wedge$ y_{12} is ***very low*** $\wedge$ y_3 is ***very high***,

$$\text{THEN } f_2(\mathbf{x}) = \begin{bmatrix} -1.99\text{e-}4 + 1.59\text{e-}5y_{13} - 9.79\text{e-}5y_9 - 2.13\text{e-}5y_{12} + 2.03\text{e-}4y_3 \\ 0.0013 + 3.34\text{e-}4y_{13} + 4.12\text{e-}4y_9 + 2.65\text{e-}4y_{12} + 1.15\text{e-}4y_3 \end{bmatrix},$$

R^3 : IF y_{13} is ***low*** $\wedge$ y_9 is ***low*** $\wedge$ y_{12} is ***high*** $\wedge$ y_3 is ***low***,

$$\text{THEN } f_3(\mathbf{x}) = \begin{bmatrix} 0.2508 - 0.0485y_{13} + 0.0555y_9 + 0.0167y_{12} + 0.1049y_3 \\ -0.0039 - 0.0195y_{13} - 0.0095y_9 - 0.0572y_{12} - 0.0341y_3 \end{bmatrix},$$

R^4 : IF y_{13} is ***medium*** $\wedge$ y_9 is ***high*** $\wedge$ y_{12} is ***very high*** $\wedge$ y_3 is ***medium***,

$$\text{THEN } f_4(\mathbf{x}) = \begin{bmatrix} -0.0536 - 0.0429y_{13} - 0.0341y_9 - 0.0765y_{12} - 2.05\text{e-}4y_3 \\ 0.2071 + 0.0872y_{13} + 0.0759y_9 + 0.1244y_{12} + 0.0450y_3 \end{bmatrix},$$

R^5 : IF y_{13} is ***high*** $\wedge$ y_9 is ***medium*** $\wedge$ y_{12} is ***low*** $\wedge$ y_3 is ***high***,

$$\text{THEN } f_5(\mathbf{x}) = \begin{bmatrix} 0.0130 + 0.0016y_{13} - 0.0020y_9 + 0.0025y_{12} + 0.0041y_3 \\ 2.47\text{e-}4 + 0.0026y_{13} + 0.0017y_9 + 0.0011y_{12} + 4.33\text{e-}5y_3 \end{bmatrix}.$$

The fuzzy system that has been learned based on these five rules above, the example with an input of [0.2098 0.2106 0.3585 0.2264] is given to further explain the mechanism of testing process. Inputs of the identification process based on the trained fuzzy system are the network features of an AD patient, and the decision output is the prediction of label vector. The sum of the five calculated rule-based outputs is $f = [0.8940\ 0.00956]^T$, then the maximal element in f is set to 1 while others to 0 for handling the decision output. Finally, AD patient can be identified based on the final value of the output $y = \begin{bmatrix}1 & 0\end{bmatrix}^T$.

Next, multi-parameters from single network are also used as input set for the classifier together. The classification results obtained by various feature select methods and the optimal lengths of input feature vectors are shown in **Table 3**. The parameters selected by FSV method can be used to form the vector to obtain the optimal classification result, and the sorted parameters are further analyzed in detail. The features in order obtained through the FSV algorithm is (x_7, y_{13}), (x_1, y_{13}), (x_2, y_{13}), (x_3, y_{13}), (x_8, y_{13}), (x_5, y_{13}), (x_6, y_{13}), (x_4, y_{13}). Clustering coefficients ((x_7, y_{13})) and local efficiencies ((x_1, y_{13})) are chosen to verify the feasibility of the classification, and the image is shown in **Figure 5A**. It is clear that there is a significant difference between the AD and the control group. The TSK classification is applied to all feature input groups. As shown in **Figure 5B**, the classification accuracy reaches a maximum value of 93.41% when the first three features are taken as input vector. The optimal combination obtained by the feature sorting method is local efficiency (x_7), clustering coefficient (x_1), and graph complexity index (x_2). The graph complexity index has a low discrimination between AD and the control group, and the TSK models trained with graph complexity index extracted from each network layer as single input have low classification accuracy. However, the image complexity index can supplement the clustering coefficient and local efficiency, indicating that the redundancy between some parameters from same network layer is small, which is of great significance as a feature of model training. Through the above classification results, multi-parameters, and multi-networks can both be applied to the TSK classification, and they are not the same type as input sets for model training.

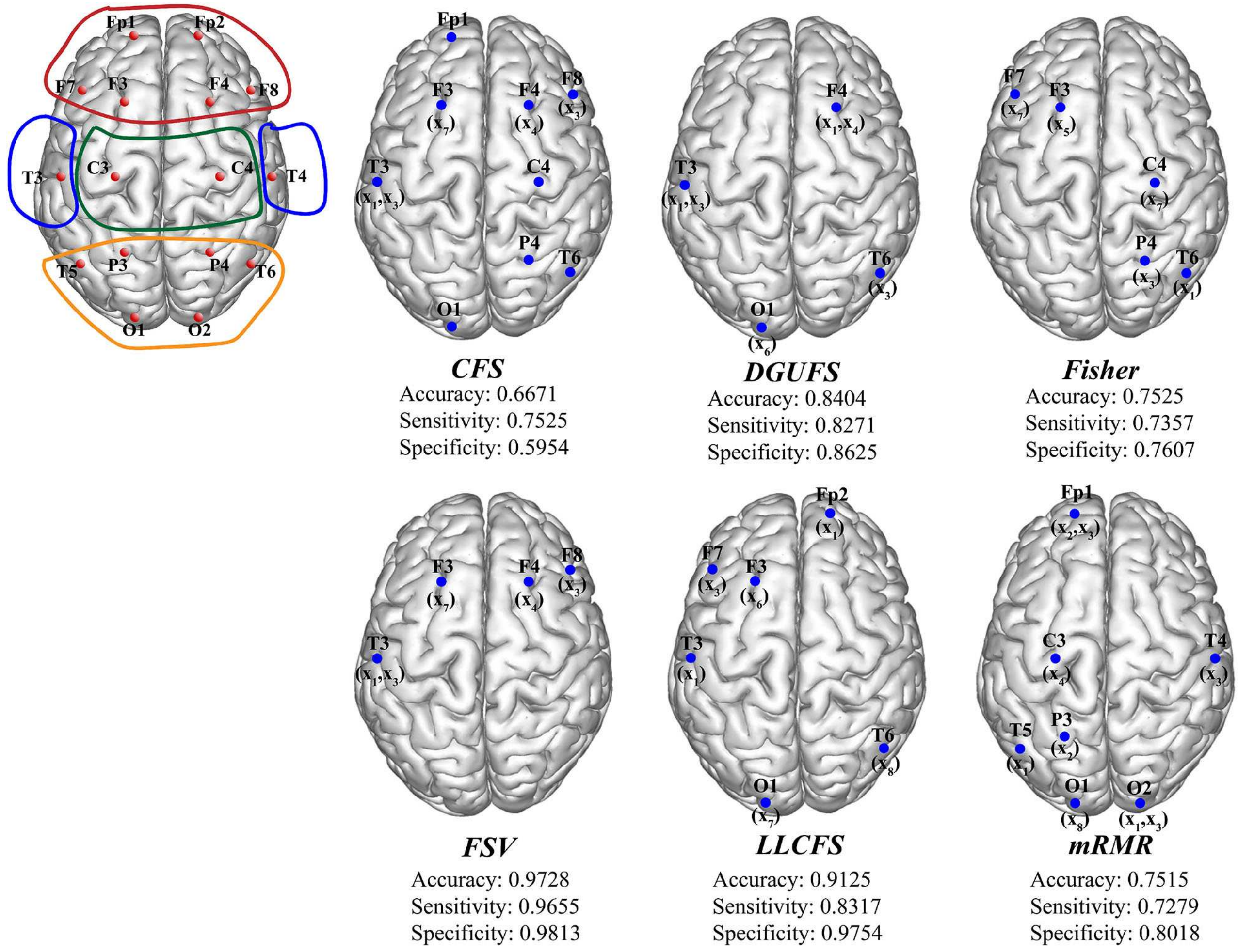

FIGURE 6 | The schematic diagram of channel position with the frontal lobe is marked within red lines, the temporal lobe in blue, the parietal lobe in green, and the occipital lobe in orange. The optimal parameters and corresponding classification results under different feature select methods.

Finally, the multi-parameters from multi-networks are used for training. We further applied different feature select methods on this input set, and find the best feature input vectors, respectively. **Figure 6** provides the methods and corresponding classification results. The brain area enclosed by the red line is the frontal lobe, the blue is the temporal lobe, the green is the parietal lobe, and the orange is the occipital lobe. It can be observed that the parameters that are filtered by different methods are more common to be extracted from the network layers of the frontal EEG. This suggests that information in the frontal lobe is more effective in identifying AD patients. Damage to the frontal lobe of the brain, which plays a prominent role in thinking and behavior, can lead to forgetfulness, delayed behavior, and distraction. Meanwhile, signals from other brain regions also play an important role in AD recognition, indicating that AD disease has a global impact on the brain. The best result of multi-parameters from multi-networks set are selected through FSV method, which up to 97.28%. The combination is $\left\{\left(x_7, y_3\right), \left(x_3, y_{13}\right), \left(x_1, y_{13}\right), \left(x_3, y_{12}\right), \left(x_4, y_4\right)\right\}$. The accuracy rate with set 3 is improved compared with set 1 and set 2, indicating that it is of certain significance to take multiple parameters extracted from multiple networks as different features.

CONCLUSION AND DISCUSSION

This paper proposes a multi-input machine learning method that combines fuzzy classifier and WVG to identify AD patient's EEG. In order to improve the interpretability and recognition accuracy of the model, complex network theory and TSK fuzzy system model is adopted. A WVG network layer is constructed using a single channel EEG. The multi-parameters obtained from multiple networks can be used as independent input features for model training, and the TSK model based on fuzzy rules is used to classify AD EEG with better interpretability.

We considered three types of classification input sets: multi-parameters from single network, single parameter from multi-networks, and multi-parameters from multi-networks. These three types of inputs are, respectively, applied as the training set of the learning of the TSK model. The experimental results show that the fuzzy model-based system model can achieve optimal performance with multi-parameters from multi-networks as classification input set, and the accuracy is up to 97.83%. Meanwhile, the optimal input numbers are different for the three types of input sets proposed in this paper. The best input combination is 5 input features in the input set of multi-parameters from multi-networks.

The current clinical techniques of AD identification, mainly including the scale assessing, cerebrospinal fluid examination, and the observation of atrophy of gray matter through the brain functional imaging, are difficult to obtain reliable diagnostic markers. It is also difficult to find obvious organic changes in the early stage of AD. We propose an AD diagnostic model that combines the TSK fuzzy model with complex network obtained by WVG method and propose three different kinds of training input sets, which provides a new method for the search of AD EEG biomarkers. Compared with traditional methods, the AD identification approach proposed in this paper, has lower implementation difficulty and higher accuracy.

EEG, which is commonly considered to have significant chaotic characteristics, cannot be well-evaluated with linear analysis. The WVG method used in this paper can transform the one-dimensional time series into images and extract the underlying information contained in electrophysiological activities of different brain regions. In contrast with other network construction methods like synchronous network, the WVG networks obtained by each EEG channel are independent of each other. Thus, more network features can be found and effective biomarkers can be obtained from kinds of feature sets with WVG (Zhu et al., 2014). The classification results show that this WVG method is very effective for feature extraction of AD recognition. In future works it will be combined with multi-layer network theory, further discussing the correlation between different channels with constructing multi-layer network. In past research we confirmed the feasibility of the multi-layer network scheme, and extracted the multiplex clustering coefficient and multiplex participation coefficient (Cai et al., 2020). Future work will consider both the implicit characteristics of single channels and the information integration between multiple channels.

We propose three different kinds of feature sets and prove that the optimal parameter vectors can be obtained from the set multi-parameters from multi-networks. This finding indicates that simultaneously considering different networks and different parameters as disparate features has obvious help for the acquisition of AD biomarkers. At the same time, the classification results show that the excessive features as input is not conducive to the optimization of the classification model, so it is necessary to reduce the feature dimension. Too much feature increase may lead to the overfitting of the learning model, and even the increase of invalid features may lead to the decrease of the accuracy based on test set (Guyon et al., 2002). Therefore, the application of feature selection plays an important role in improving the accuracy of fuzzy learning models.

In this paper, we combined the identification model combining feature selection approaches with machine learning. Researchers can effectively reduce the number of EEG channels, and the difficulty of data collection will be significantly reduced. Meanwhile, with the reduction of the parameters, it can be easier to improve the efficiency of the AD recognition process. Compared with traditional manual diagnosis, machine learning methods have higher reliability, and improved recognition accuracy. Especially, the TSK method has higher interpretability and robustness by integrating the advantages of fuzzy rules and membership functions. There are still some limitations in our research. We used a variety of feature selection methods, but a feature selection method suitable for the highly interpretable TSK model is necessary to be considered. Future work may focus on how to select features more efficiently and accurately to achieve higher classification accuracy.

DATA AVAILABILITY STATEMENT

The datasets generated for this study are available on request to the corresponding author.

ETHICS STATEMENT

The studies involving human participants were reviewed and approved by the Ethics committee of Tangshan Gongren hospital. The patients/participants provided their written informed consent to participate in this study.

AUTHOR CONTRIBUTIONS

HY: article writing, design of methods, and article correction. LZ: article writing, processing and analysis of data, and design of methods. LC: design of methods and data analysis. JW: data analysis and article review. JL: data collection. RW: article review and correction. ZZ: data collection. All authors contributed to the article and approved the submitted version.

FUNDING

This work was supported by Tianjin Natural Science Foundation (Grant No. 19JCYBJC18800), Tangshan Science and Technology Project (Grant Nos. 18130208A and 19150205E), Hebei Science and Technology Project (Grant No. 18277773D), and Natural Science Foundation of Tianjin Municipal Science and Technology Commission (Grant No. 13JCZDJC27900).

REFERENCES

Ahmadlou, M., Adeli, H., and Adeli, A. (2010). New diagnostic EEG markers of the Alzheimer's disease using visibility graph. *J. Neural Transm.* 117, 1099–1109. doi: 10.1007/s00702-010-0450-3

Bezdek, J. C., Ehrlich, R., and Full, W. (1984). FCM: the fuzzy c-means clustering algorithm. *Comput. Geosci.* 10, 191–203. doi: 10.1016/0098-3004(84)90020-7

Blinowska, K. J., and Kaminski, M. (2013). Functional brain networks: random, "small world" or deterministic? *PLoS ONE* 8:e78763. doi: 10.1371/journal.pone.0078763

Blondel, V. D., Guillaume, J.-L., Lambiotte, R., and Lefebvre, E. (2008). Fast unfolding of communities in large networks. *J. Stat. Mech Theory Exp.* 10:P10008. doi: 10.1088/1742-5468/2008/10/p10008

Boccaletti, S., Latora, V., Moreno, Y., Chavez, M., and Hwang, D. (2006). Complex networks: Structure and dynamics. *Phys. Rep.* 424, 175–308. doi: 10.1016/j.physrep.2005.10.009

Bradley, P., and Mangasarian, O. (1999). "Feature selection via concave minimization and support vector machines," in *Machine Learning Proceedings of the Fifteenth International Conference* (San Francisco, CA).

Brenner, R. P., Reynolds, C. F., and Ulrich, R. F. (1988). Diagnostic efficacy of computerized spectral versus visual EEG analysis in elderly normal, demented and depressed subjects. *Electroencephalogr. Clin. Neurophysiol.* 69, 110–117. doi: 10.1016/0013-4694(88)90206-4

Brown, K. S., Hill, C. C., Calero, G. A., Myers, C. R., Lee, K. H., Sethna, J. P., et al. (2004). The statistical mechanics of complex signaling networks: nerve growth factor signaling. *Phys. Biol.* 1, 184–195. doi: 10.1088/1478-3967/1/3/006

Buzsaki, G., and Draguhn, A. (2004). Neuronal oscillations in cortical networks. *Science* 304, 1926–1929. doi: 10.1126/science.1099745

Cai, L., Wei, X., Liu, J., Zhu, L., Wang, J., Deng, B., et al. (2020). Functional integration and segregation in multiplex brain networks for Alzheimer's disease. *Front. Neurosci.* 14:51. doi: 10.3389/fnins.2020.00051

Cao, L., Wang, J., Cao,Y., Deng, B., and Yang, C. (2016). "LPVG analysis of the EEG activity in Alzheimer's disease patients," in *2016 12th World Congress on Intelligent Control and Automation (WCICA)* (Guilin: IEEE). doi: 10.1109/WCICA.2016.7578491

Cao, Y., Cai, L., Wang, J., Wang, R., Yu, H., Cao, Y., et al. (2015). Characterization of complexity in the electroencephalograph activity of Alzheimer's disease based on fuzzy entropy. *Chaos* 25:083116. doi: 10.1063/1.4929148

Costa, M., Goldberger, A. L., and Peng, C. K. (2002). Multiscale entropy analysis of complex physiologic time series. *Phys. Rev. Lett.* 89:068102. doi: 10.1103/PhysRevLett.89.068102

Costa, M. D., Goldberger, A. L., and Peng, C. K. (2005). Broken asymmetry of the human heartbeat: loss of time irreversibility in aging and disease. *J. Electrocardiol.* 38, 1–206. doi: 10.1016/j.jelectrocard.2005.06.076

Czigler, B., Csikos, D., Hidasi, Z., Anna Gaal, Z., Csibri, E., Kiss, E., et al. (2008). Quantitative EEG in early Alzheimer's disease patients - power spectrum and complexity features. *Int. J. Psychophysiol.* 68, 75–80. doi: 10.1016/j.ijpsycho.2007.11.002

Dauwels, J., Srinivasan, K., Ramasubba Reddy, M., Musha, T., Vialatte, F. B., Latchoumane, C., et al. (2011). Slowing and loss of complexity in Alzheimer's EEG: two sides of the same coin? *Int. J. Alzheimers. Dis.* 2011:539621. doi: 10.4061/2011/539621

de Waal, H., Stam, C. J., Blankenstein, M. A., Pijnenburg, Y. A., Scheltens, P., and van der Flier, W. M. (2011). EEG abnormalities in early and late onset Alzheimer's disease: understanding heterogeneity. *J. Neurol. Neurosurg. Psychiatr.* 82, 67–71. doi: 10.1136/jnnp.2010.216432

Deng, B., Liang, L., Li, S., Wang, R., Yu, H., Wang, J., et al. (2015). Complexity extraction of electroencephalograms in Alzheimer's disease with weighted-permutation entropy. *Chaos* 25:043105. doi: 10.1063/1.4917013

Deng, Z., Choi, K. S., Jiang, Y., and Wang, S. (2014). Generalized hidden-mapping ridge regression, knowledge-leveraged inductive transfer learning for neural networks, fuzzy systems and kernel methods. *IEEE Trans. Cybern.* 44, 2585–2599. doi: 10.1109/TCYB.2014.2311014

Deng, Z., Xu, P., Xie, L., Choi, K. S., and Wang, S. (2018). Transductive joint-knowledge-transfer TSK FS for recognition of epileptic EEG signals. *IEEE Trans. Neural Syst. Rehabil. Eng.* 26, 1481–1494. doi: 10.1109/TNSRE.2018.2850308

Gao, Z., Wang, X., Yang, Y., Mu, C., Cai, Q., Dang, W., et al. (2019). EEG-based spatio-temporal convolutional neural network for driver fatigue evaluation. *IEEE Trans. Neural Netw. Learn. Syst.* 30, 2755–2763. doi: 10.1109/TNNLS.2018.2886414

Gu, Q., Li, Z., and Han, J. (2012). "Generalized fisher score for feature selection," in *Proceedings of the Twenty-Seventh Conference on Uncertainty in Artificial Intelligence (UAI'11)* (Arlington, VA: AUAI Press), 266–273.

Gu, X., Chung, F.-L., and Wang, S. (2017). Bayesian Takagi–Sugeno–Kang Fuzzy classifier. *IEEE Trans. Fuzzy Syst.* 25, 1655–1671. doi: 10.1109/tfuzz.2016.2617377

Guyon, I., Weston, J., Barnhill, S., and Vapnik, V. (2002). Gene selection for cancer classification using support vector machines. *Mach. Learn.* 46, 389–422. doi: 10.1023/a:1012487302797

He, Y., and Evans, A. (2010). Graph theoretical modeling of brain connectivity. *Curr. Opin. Neurol.* 23, 341–350. doi: 10.1097/WCO.0b013e32833aa567

Hively, L. M., Protopopescu, V. A., and Gailey, P. C. (2000). Timely detection of dynamical change in scalp EEG signals. *Chaos* 10, 864–875. doi: 10.1063/1.1312369

Horvath, A., Szucs, A., Csukly, G., Sakovics, A., Stefanics, G., and Kamondi, A. (2018). EEG and ERP biomarkers of Alzheimer's disease: a critical review. *Front. Biosci.* 23, 183–220. doi: 10.2741/4587

Hramov, A. E., Maksimenko, V., Koronovskii, A., Runnova, A. E., Zhuravlev, M., Pisarchik, A. N., et al. (2019). Percept-related EEG classification using machine learning approach and features of functional brain connectivity. *Chaos* 29:093110. doi: 10.1063/1.5113844

Jiang, W., Wei, B., Tang, Y., and Zhou, D. (2017). Ordered visibility graph average aggregation operator: An application in produced water management. *Chaos* 27:023117. doi: 10.1063/1.4977186

Kim, J., and Wilhelm, T. (2008). What is a complex graph? *Phys. A* 387, 2637–2652. doi: 10.1016/j.physa.2008.01.015

Kowalski, J. W., Gawel, M., Pfeffer, A., and Barcikowska, M. (2001). The diagnostic value of EEG in Alzheimer disease: correlation with the severity of mental impairment. *J. Clin. Neurophysiol.* 18, 570–575. doi: 10.1097/00004691-200111000-00008

Lacasa, L., Luque, B., Ballesteros, F., Luque, J., and Nuno, J. C. (2008). From time series to complex networks: the visibility graph. *Proc. Natl. Acad. Sci. U.S.A.* 105, 4972–4975. doi: 10.1073/pnas.0709247105

Lacasa, L., Luque, B., Luque, J., and Nuño, J. C. (2009). The visibility graph: a new method for estimating the Hurst exponent of fractional Brownian motion. *EPL* 86, 30001–30005. doi: 10.1209/0295-5075/86/30001

Liu, C., Zhou, W.-X., and Yuan, W.-K. (2010). Statistical properties of visibility graph of energy dissipation rates in three-dimensional fully developed turbulence. *Phys. Stat. Mech. Appl.* 389, 2675–2681. doi: 10.1016/j.physa.2010.02.043

Lozano-Pérez, T., and Wesley, M. A. (1979). An algorithm for planning collision-free paths among polyhedral obstacles. *Commun. ACM* 22, 560–570. doi: 10.1145/359156.359164

Martijn, P., and van den Heuvel, O. S. (2013). Network hubs in the human brain. *Trends Cogn. Sci.* 17, 683–696

Matsuda, H. (2013). Voxel-based morphometry of brain MRI in normal aging and Alzheimer's disease. *Aging Dis* 4, 29–37. doi: 10.1016/j.tics.2013.09.012

McBride, J. C., Zhao, X., Munro, N. B., Jicha, G. A., Schmitt, F. A., Kryscio, R. J., et al. (2015). Sugihara causality analysis of scalp EEG for detection of early Alzheimer's disease. *Neuroimage Clin.* 7, 258–265. doi: 10.1016/j.nicl.2014.12.005

Meunier, D., Lambiotte, R., and Bullmore, E. T. (2010). Modular and hierarchically modular organization of brain networks. *Front. Neurosci.* 4:200. doi: 10.3389/fnins.2010.00200

Micanovic, C., and Pal, S. (2014). The diagnostic utility of EEG in early-onset dementia: a systematic review of the literature with narrative analysis. *J. Neural Transm.* 121, 59–69. doi: 10.1007/s00702-013-1070-5

Nimmrich, V., Draguhn, A., and Axmacher, N. (2015). Neuronal network oscillations in neurodegenerative diseases. *Neuromolecular Med.* 17, 270–284. doi: 10.1007/s12017-015-8355-9

Palop, J. J., Chin, J., and Mucke, L. (2006). A network dysfunction perspective on neurodegenerative diseases. *Nature* 443, 768–773. doi: 10.1038/nature05289

Peng, H., Long, F., and Ding, C. (2005). Feature selection based on mutual information: criteria of max-dependency, max-relevance, and min-redundancy. *IEEE Trans. Pattern Anal. Mach. Intell.* 27, 1226–1238. doi: 10.1109/TPAMI.2005.159

Polikar, R., Topalis, A., Green, D., Kounios, J., and Clark, C. M. (2007). Comparative multiresolution wavelet analysis of ERP spectral bands using an ensemble of classifiers approach for early diagnosis of Alzheimer's disease. *Comput. Biol. Med.* 37, 542–558. doi: 10.1016/j.compbiomed.2006.08.012

Reid, A. T., and Evans, A. C. (2013). Structural networks in Alzheimer's disease. *Eur. Neuropsychopharmacol.* 23, 63–77. doi: 10.1016/j.euroneuro.2012.11.010

Rubinov, M., and Sporns, O. (2010). Complex network measures of brain connectivity: uses and interpretations. *Neuroimage* 52, 1059–1069. doi: 10.1016/j.neuroimage.2009.10.003

Siegelmann, H. T., and Holzman, L. E. (2010). Neuronal integration of dynamic sources: Bayesian learning and Bayesian inference. *Chaos* 20, 037112. doi: 10.1063/1.3491237

Smailovic, U., Koenig, T., Kareholt, I., Andersson, T., Kramberger, M. G., Winblad, B., et al. (2018). Quantitative EEG power and synchronization correlate with Alzheimer's disease CSF biomarkers. *Neurobiol. Aging* 63, 88–95. doi: 10.1016/j.neurobiolaging.2017.11.005

Stam, C. J., Jones, B. F., Nolte, G., Breakspear, M., and Scheltens, P. (2007). Small-world networks and functional connectivity in Alzheimer's disease. *Cereb. Cortex* 17, 92–99. doi: 10.1093/cercor/bhj127

Stephen, A. T., and Toubia, O. (2009). Explaining the power-law degree distribution in a social commerce network. *Soc. Netw.* 31, 262–270. doi: 10.1016/j.socnet.2009.07.002

Supriya, S., Siuly, S., Wang, H., Cao, J., and Zhang, Y. (2016). Weighted visibility graph with complex network features in the detection of epilepsy. *IEEE Access* 4, 6554–6566. doi: 10.1109/access.2016.2612242

Tahaei, M. S., Jalili, M., and Knyazeva, M. G. (2012). Synchronizability of EEG-based functional networks in early Alzheimer's disease. *IEEE Trans. Neural Syst. Rehabil. Eng.* 20, 636–641. doi: 10.1109/TNSRE.2012.2202127

Tian, X., Deng, Z., Ying, W., Choi, K. S., Wu, D., Qin, B., et al. (2019). Deep multi-view feature learning for EEG-based epileptic seizure detection. *IEEE Trans. Neural Syst. Rehabil. Eng.* 27, 1962–1972. doi: 10.1109/TNSRE.2019.2940485

Tijms, B. M., Wink, A. M., de Haan, W., van der Flier, W. M., Stam, C. J., Scheltens, P., et al. (2013). Alzheimer's disease: connecting findings from graph theoretical studies of brain networks. *Neurobiol. Aging* 34, 2023–2036. doi: 10.1016/j.neurobiolaging.2013.02.020

Turner, A., Doxa, M., O'Sullivan, D., and Penn, A. (2001). From Isovists to Visibility Graphs: A Methodology for the Analysis of Architectural Space. *Environ. Plan. B* 28, 103–121. doi: 10.1068/b2684

van Straaten, E. C., Scheltens, P., Gouw, A. A., and Stam, C. J. (2014). Eyes-closed task-free electroencephalography in clinical trials for Alzheimer's disease: an emerging method based upon brain dynamics. *Alzheimers. Res. Ther.* 6:86. doi: 10.1186/s13195-014-0086-x

Wang, J., Yang, C., Wang, R., Yu, H., Cao, Y., and Liu, J. (2016). Functional brain networks in Alzheimer's disease: EEG analysis based on limited penetrable visibility graph and phase space method. *Phys. A Stat. Mechan. Appl.* 460, 174–187. doi: 10.1016/j.physa.2016.05.012

Wang, R., Wang, J., Li, S., Yu, H., Deng, B., and Wei, X. (2015). Multiple feature extraction and classification of electroencephalograph signal for Alzheimers' with spectrum and bispectrum. *Chaos* 25:013110. doi: 10.1063/1.4906038

Wang, R., Wang, J., Yu, H., Wei, X., Yang, C., and Deng, B. (2014). Decreased coherence and functional connectivity of electroencephalograph in Alzheimer's disease. *Chaos* 24:033136. doi: 10.1063/1.4896095

Yang, W., Xia, H., Xia, B., Lui, L. M., and Huang, X. (2010). "ICA-based feature extraction and automatic classification of AD-related MRI data," in *Sixth International Conference on Natural Computation* (Yantai: IEEE).

Yu, H., Lei, X., Song, Z., Liu, C., and Wang, J. (2020). Supervised network-based fuzzy learning of EEG signals for Alzheimer's disease identification. *IEEE Trans. Fuzzy Syst.* 28, 60–71. doi: 10.1109/tfuzz.2019.2903753

Zeng, H., and Cheung, Y. M. (2011). Feature selection and kernel learning for local learning-based clustering. *IEEE Trans. Pattern Anal. Mach. Intell.* 33, 1532–1547. doi: 10.1109/TPAMI.2010.215

Zhang, J., and Small, M. (2006). Complex network from pseudoperiodic time series: topology versus dynamics. *Phys. Rev. Lett.* 96:238701. doi: 10.1103/PhysRevLett.96.238701

Zhaohong, D., Yizhang, J., Kup-Sze, C., Fu-Lai, C., and Shitong, W. (2013). Knowledge-leverage-based TSK Fuzzy System modeling. *IEEE Trans. Neural Netw. Learn. Syst.* 24, 1200–1212. doi: 10.1109/TNNLS.2013.2253617

Zhu, G., Li, Y., and Wen, P. P. (2014). Epileptic seizure detection in EEGs signals using a fast weighted horizontal visibility algorithm. *Comput. Methods Programs Biomed.* 115, 64–75. doi: 10.1016/j.cmpb.2014.04.001

Zhu, P., Zhu, W., Hu, Q., Zhang, C., and Zuo, W. (2017). Subspace clustering guided unsupervised feature selection. *Pattern Recognit.* 66, 364–374. doi: 10.1016/j.patcog.2017.01.016

Zou, Y., Donner, R. V., Marwan, N., Donges, J. F., and Kurths, J. (2019). Complex network approaches to nonlinear time series analysis. *Phys. Rep.* 787, 1–97. doi: 10.1016/j.physrep.2018.10.005

Conflict of Interest: The authors declare that the research was conducted in the absence of any commercial or financial relationships that could be construed as a potential conflict of interest.

frontiers
in Neuroscience

REVIEW
published: 26 March 2021
doi: 10.3389/fnins.2021.629323

Systemic Review on Transcranial Electrical Stimulation Parameters and EEG/fNIRS Features for Brain Diseases

Dalin Yang[1], *Yong-Il Shin*[2] *and Keum-Shik Hong*[2]*

[1] School of Mechanical Engineering, Pusan National University, Busan, South Korea, [2] Department of Rehabilitation Medicine, Pusan National University School of Medicine, Pusan National University Yangsan Hospital, Yangsan-si, South Korea

Background: Brain disorders are gradually becoming the leading cause of death worldwide. However, the lack of knowledge of brain disease's underlying mechanisms and ineffective neuropharmacological therapy have led to further exploration of optimal treatments and brain monitoring techniques.

Objective: This study aims to review the current state of brain disorders, which utilize transcranial electrical stimulation (tES) and daily usable noninvasive neuroimaging techniques. Furthermore, the second goal of this study is to highlight available gaps and provide a comprehensive guideline for further investigation.

Method: A systematic search was conducted of the PubMed and Web of Science databases from January 2000 to October 2020 using relevant keywords. Electroencephalography (EEG) and functional near-infrared spectroscopy were selected as noninvasive neuroimaging modalities. Nine brain disorders were investigated in this study, including Alzheimer's disease, depression, autism spectrum disorder, attention-deficit hyperactivity disorder, epilepsy, Parkinson's disease, stroke, schizophrenia, and traumatic brain injury.

Results: Sixty-seven studies (1,385 participants) were included for quantitative analysis. Most of the articles (82.6%) employed transcranial direct current stimulation as an intervention method with modulation parameters of 1 mA intensity (47.2%) for 16–20 min (69.0%) duration of stimulation in a single session (36.8%). The frontal cortex (46.4%) and the cerebral cortex (47.8%) were used as a neuroimaging modality, with the power spectrum (45.7%) commonly extracted as a quantitative EEG feature.

Conclusion: An appropriate stimulation protocol applying tES as a therapy could be an effective treatment for cognitive and neurological brain disorders. However, the optimal tES criteria have not been defined; they vary across persons and disease types. Therefore, future work needs to investigate a closed-loop tES with monitoring by neuroimaging techniques to achieve personalized therapy for brain disorders.

Keywords: transcranial electrical stimulation, transcranial direct current stimulation, transcranial alternation stimulation, transcranial random noise stimulation, electroencephalography, functional near-infrared spectroscopy, brain disease

Edited by:
Oscar Arias-Carrion,
Hospital General Dr. Manuel Gea Gonzalez, Mexico

Reviewed by:
Chia-Wei Sun,
National Chiao Tung University, Taiwan
Estate M. Sokhadze,
University of South Carolina, United States

***Correspondence:**
Keum-Shik Hong
kshong@pusan.ac.kr

Specialty section:
This article was submitted to Brain Imaging Methods, a section of the journal Frontiers in Neuroscience

Received: *14 November 2020*
Accepted: *25 February 2021*
Published: *26 March 2021*

Citation:
Yang D, Shin Y-I and Hong K-S (2021) Systemic Review on Transcranial Electrical Stimulation Parameters and EEG/fNIRS Features for Brain Diseases. Front. Neurosci. 15:629323. doi: 10.3389/fnins.2021.629323

INTRODUCTION

Brain disorders represent a collection of syndromes characterized by abnormalities in memory, sensation, behavior, and even personality. Neurological disorders are the second leading cause of death worldwide (Feigin et al., 2019). The burden is recognized as a global public health challenge and will increase in the next few decades (Feigin et al., 2020). As reported by the World Health Organization, there are approximately 800,000 deaths from suicide each year (approximately one death every 40 s) due to mental health issues (World Health Organization, 2018). Through decades of research, health professionals have developed a set of systematic criteria for diagnosing brain disorders, together with pharmaceutical and psychological treatments; however, understanding of the neural substrates and mechanisms involved in these diseases is limited (Chou and Chouard, 2008). In addition, reliable neurological biomarkers for identifying brain disorders are insufficient (Chou and Chouard, 2008). Moreover, certain brain disorders remain substantially unaffected by neuropharmacological therapy (Ciullo et al., 2020), and the treatment options are far from optimal in terms of efficacy and specificity. Therefore, it is essential to find alternative therapies for brain disorders that are efficient in clinical practice.

Brain stimulation has been widely applied due to its ability to modulate brain plasticity in neuropsychiatric patients (Davis and Smith, 2019; Kim E. et al., 2020; Yoo et al., 2020). Typically, brain stimulation methods have been classified as invasive or noninvasive brain stimulation (NIBS). The invasive brain stimulation approach (i.e., pharmacological intervention, targeted microsimulation, optogenetics, etc.) has been commonly applied in animal models (Polanía et al., 2018). It can be used to demonstrate the relationships of its targets to brain function with high spatial precision (e.g., cell-type effect). NIBS provides a way to modulate brain function without opening the skull. Thus, many human studies have employed NIBS to explore the causal relationship between neurological function and behavior. Two mainstay NIBS approaches have emerged to treat brain disorders in the clinical context: transcranial magnetic stimulation (TMS) and transcranial electrical stimulation (tES). The principle underlying these two modalities is based on electromagnetism and harnesses weak electrical current stimulation. More specifically, TMS can depolarize neurons by generating a strong current, and tES can influence ion channels and gradients to modulate neuronal membrane potential (Fregni and Pascual-Leone, 2007). Comparing the spatial effectiveness of NIBS with other methods, TMS and tES, the best-known stimulation modalities, can generate relatively large magnetic and electrical fields in the brain. A third promising NIBS method, transcranial focused ultrasound stimulation (tFUS), provides a solution for the low degree of spatial localization in tES and TMS by projecting the acoustic intensity field beam into brain tissues (Pasquinelli et al., 2019). However, further investigation of neurophysiological foundations is required before applying tFUS as a safe therapy in daily routine (Polanía et al., 2018). Therefore, TMS and tES are the current primary noninvasive brain stimulation methods. Both modalities affect brain function by modulating the excitation or inhibition of interneuron circuits. Generally, tES can maintain a longer outlasting effect of neural excitability than can TMS (Schulz et al., 2013). In addition, tES offers the possibility of designing a reliable sham/placebo condition for double-blind controlled clinical trials since short-term tingling sensations gradually fade away after the onset of stimulation (Nitsche et al., 2008). Moreover, tES has the advantages of lower cost, portability, and ease of application. The temporal and spatial resolutions of various brain intervention methods are compared in **Figure 1**.

Conventionally, there are three tES modalities: transcranial direct stimulation (tDCS), transcranial alternating current stimulation (tACS), and transcranial random noise stimulation (tRNS) (Brunyé, 2018; Bikson et al., 2019). The delivery method of the current is the main difference among the three modalities. tDCS typically transfers a homogeneous direct current ranging from 1 to 2 mA from the electrodes (i.e., two or more) on the scalp to modulate brain activation (Vosskuhl et al., 2018; Yaqub et al., 2018; Brunyé et al., 2019). In the tACS case, the current is delivered in an oscillating manner with a particular frequency and stimulation amplitude. tRNS differs from tDCS and tACS. The current amplitude for tRNS is randomly applied with a normal distribution around a specific mean strength. The principle of tACS and tRNS is the modulation of ongoing neural oscillations and the induction of the neuroplastic effect by using appropriate parameter values. tDCS is used to influence neuronal excitability by membrane polarization; for example, the anode causes depolarization, and the cathode results in hyperpolarization. The effect depends on various stimulation parameters, such as polarity, stimulation duration, intensity level, and the subject's brain state. To date, there are no clear criteria or quantitative assessment techniques to provide guidelines for tES in terms of modulation duration and intensity or the locations where electrodes should be placed.

Neuroimaging refers to the use of magnetic and other techniques to understand the living brain system, which can reflect the properties of function, structure, or change in the brain in terms of temporal (i.e., functional imaging) and spatial localization (i.e., structural and functional imaging) (Li et al., 2018; Yin et al., 2019). Neuroimaging is commonly used to diagnose neuropsychiatric disorders and evaluate effects following therapy (i.e., brain stimulation) and includes techniques such as structural magnetic resonance imaging (MRI), functional magnetic resonance imaging (fMRI), single-photon emission computed tomography (SPECT), positron emission tomography (PET), functional near-infrared spectroscopy (fNIRS), and electroencephalography (EEG) (Naseer and Hong, 2015; Hong and Khan, 2017; Hong et al., 2020). Typically, MRI, fMRI, SPECT, and PET can offer an excellent spatial resolution for brain state examinations. However, these assessments can only be performed in restricted environments due to equipment size (i.e., bulkiness or lack of mobility) (Hong and Yaqub, 2019). Moreover, some techniques (e.g., PET and SPECT) require the insertion of radioactive tracers, limiting repeated measurements, especially for children and pregnant women (Irani et al., 2007). In addition, these systems, including MRI and fMRI, are costly,

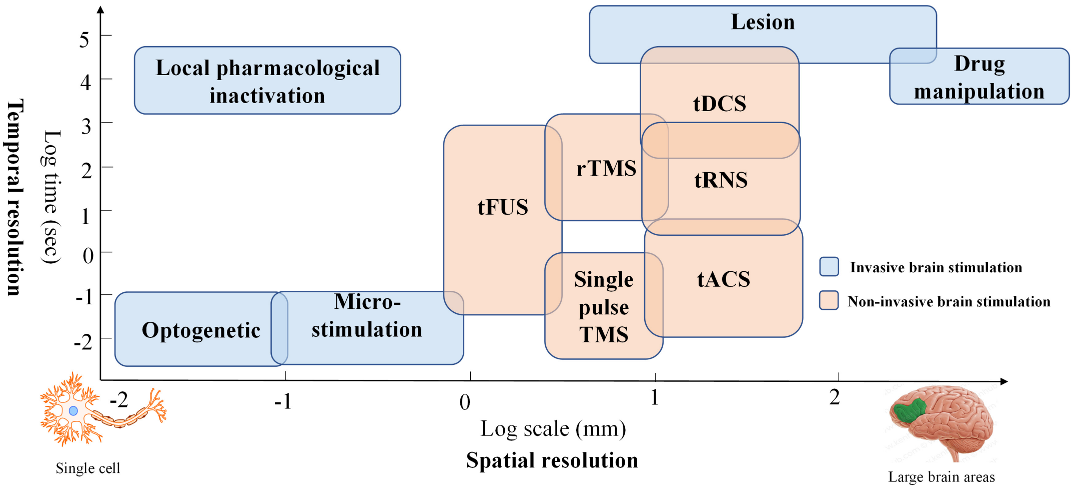

FIGURE 1 | Temporal and spatial resolution of various brain intervention methods: Blue boxes represent invasive brain stimulation techniques, and orange boxes denote non-invasive stimulation methods.

highly susceptible to motion artifacts, and have a low temporal resolution (compared with EEG and fNIRS).

As a noninvasive neuroimaging modality, EEG is one of the oldest techniques used to measure neural activation in the human brain for diagnosis or brain–computer interface (BCI) purposes (Naseer and Hong, 2013; Khan and Hong, 2017; Tanveer et al., 2019). Since they are portable and have the advantage of higher temporal resolution, EEG-based BCI applications have been widely designed for daily use (e.g., home automation control devices, EEG-based wheelchairs, brain disorder detection platforms) (Kim et al., 2019; Lee T. et al., 2020; Rashid et al., 2020; Yang et al., 2020b). EEG measurements are based on electrical potential differences between different electrodes on the scalp. A potential difference is caused by the propagation of the current flow induced by synchronized postsynaptic potentials in pyramidal neuron cell membranes. fNIRS is a promising noninvasive neuroimaging technique featuring the advantages of safety, low cost, mobility, excellent temporal resolution (compared with fMRI), moderate spatial resolution, and tolerance to motion artifacts (Nguyen et al., 2016; Ghafoor et al., 2019). The fNIRS principle is based on the absorption characteristics of oxygenated hemoglobin (HbO) and deoxygenated hemoglobin (HbR) in the spectrum ranging from 650 to 1,000 nm, for which brain tissues are more translucent than HbO or HbR (Aqil et al., 2012a,b). Changes in blood flow (i.e., increases or decreases) reflect a local brain region's hemodynamic activity resulting from neuronal firing. More specifically, activation of brain cortical neurons results in greater blood flow (detected by the surplus of oxyhemoglobin in veins) than in brain regions with inactive neurons (Berger et al., 2019; Hu et al., 2019; Shin, 2020). Types of tES, the hemodynamic response caused by neural activity, EEG and fNIRS principles, and examples of extracted features are depicted in **Figure 2**. EEG and fNIRS are widely applied in clinical brain state monitoring (Yang et al., 2019b, 2020a). The development of therapeutic strategies for neuropsychiatric disorders is based on the properties described above: minimal invasiveness, safety, ease of use, and repeatability (Dubreuil-Vall et al., 2019; Ermolova et al., 2019).

This study had two goals. The first aim was to review the current state of the application of tES, monitored by EEG and fNIRS, for treatment of nine common brain disorders: Alzheimer's disease (AD) and mild cognitive impairment (MCI), depression, autism spectrum disorder (ASD), attention-deficit hyperactivity disorder (ADHD), epilepsy, schizophrenia, Parkinson's disease (PD), stroke, and traumatic brain injury (TBI). Second, this study aimed to provide a general reference for future investigation of tES as a treatment for the nine diseases mentioned above: (i) how to conduct the stimulation (i.e., duration and intensity), (ii) where the electrodes should be placed, (iii) which types of EEG and fNIRS features can be used to evaluate the stimulation effect, and (iv) the behavioral and neurological effects following stimulation.

METHODS

In this study, a two-stage literature search was performed to identify relevant investigations. First, an online search was conducted using the PubMed and Web of Science databases, which included peer-reviewed articles from January 2000 to October 2020 with the following keywords: (functional near-infrared spectroscopy OR fNIRS OR EEG OR electroencephalography) ++ (transcranial electrical stimulation OR transcranial direct current stimulation OR transcranial alternating current stimulation OR transcranial random noise stimulation) + Alzheimer's disease OR AD OR depression OR autism spectrum disorder OR ASD OR attention-deficit hyperactivity disorder OR ADHD OR epilepsy OR schizophrenia OR Parkinson's disease OR PD OR stroke OR traumatic brain injury OR TBI). Second, an additional literature search was conducted through the reference lists in selected studies or the

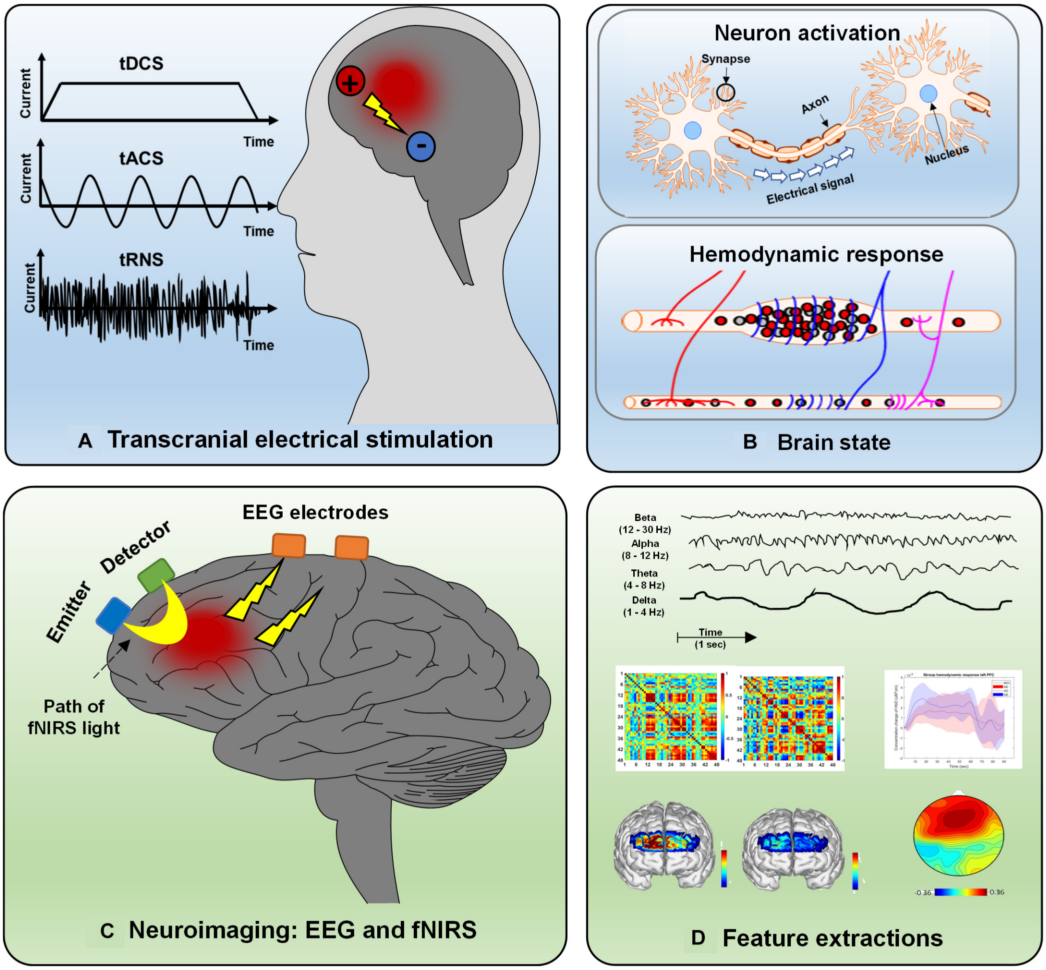

FIGURE 2 | Overview of electrical stimulation, EEG, fNIRS, and feature extraction: **(A)** Three types of electrical stimulation (tDCS, tACS, and tRNS), **(B)** hemodynamic response caused by neural activity, **(C)** principle of EEG and fNIRS, and **(D)** various features extracted from neurological signals.

related review paper. The aim of this two-stage literature search was to ensure that the studies included were as comprehensive as possible. As shown in **Figure 3**, the search identified 665 studies (i.e., 369 from PubMed and 296 from Web of Science). After removing 137 duplicates and 451 studies that did not relate to this review (i.e., review studies, animal model studies, meeting abstracts, investigations lacking stimulation or not involving brain disease, and those lacking EEG or fNIRS), 77 articles remained. Since several studies did not show the results (i.e., 10 trial studies), this systematized review consisted of 67 data sets (i.e., AD, 7; depression, 10; ASD, 2; ADHD, 4; epilepsy, 14; schizophrenia, 9; PD, 3; stroke, 14; and TBI, 4).

ALZHEIMER'S DISEASES AND MILD COGNITIVE IMPAIRMENT

Approximately 60–70% of dementia is caused by AD. AD is a progressive brain disorder in which memory and cognitive function cause increasing impairment until death (Vuksanović et al., 2019; Feng et al., 2020). To date, there is no pharmacological cure available, except for treatment to manage symptoms. MCI is considered to be the middle stage between healthy controls and patients with dementia. It has been reported that approximately 32–38% of patients with MCI develop dementia within five or more years (Alzheimer's Association, 2020). Brain stimulation is a promising therapeutic approach for improving memory and cognitive function in AD and preventing the progression from MCI to AD.

As shown in **Table 1**, six studies addressed AD (four studies) and MCI (three studies), and one was related to frontotemporal dementia. EEG neuroimaging techniques were conducted in all studies. The features extracted from EEG included the event-related potential, coherence, connectivity, and power spectra in different brain bands (e.g., alpha, beta, theta, gamma, etc.). The stimulation duration and intensity also differed for each study. One of the tACS studies (Naro et al., 2016) applied tACS to modulate gamma-band oscillations (GBOs) in AD, MCI, and HC groups. Anodal electrodes were positioned on the primary motor area (M1), premotor area (PMA), supplementary motor area

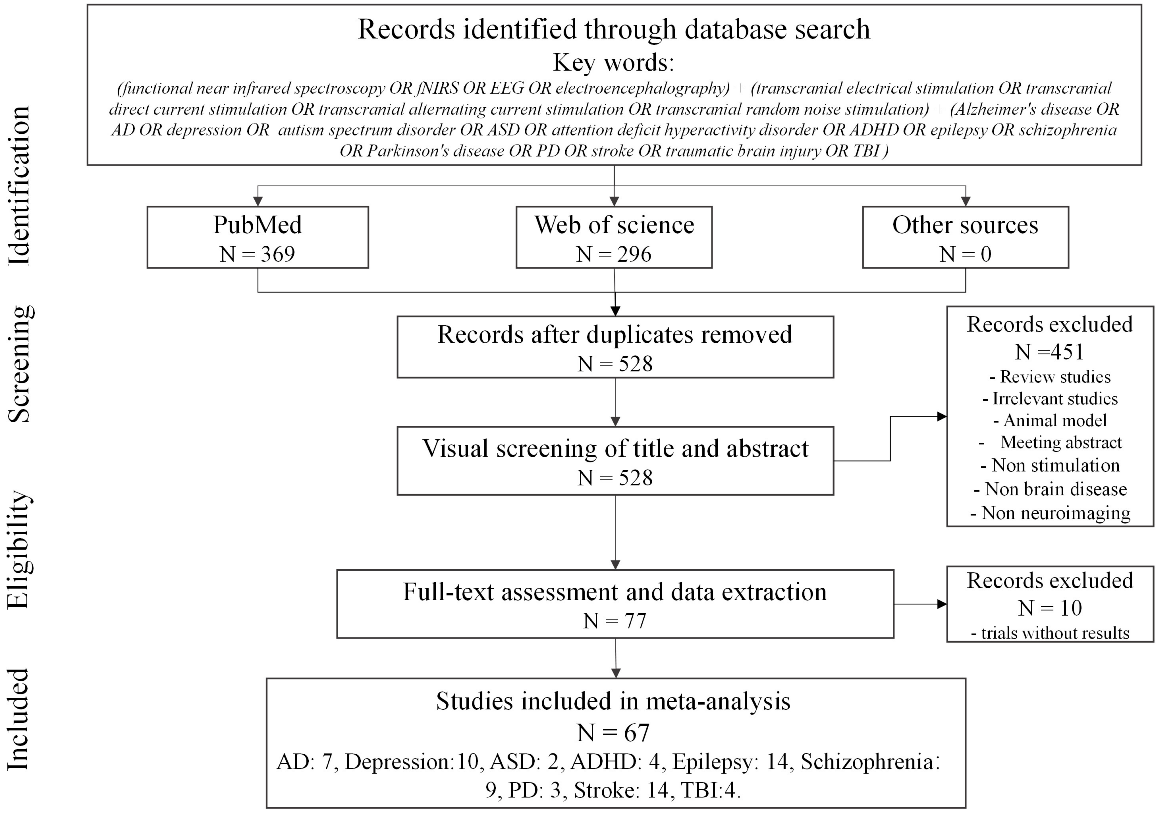

FIGURE 3 | Overview of literature search for review.

(SMA), dorsolateral prefrontal cortex (DLPFC), and dorsomedial prefrontal cortex (DMPFC). The reference electrode was placed on the right mastoid. The entire stimulation procedure lasted 10 min with a 40–120-Hz stimulation frequency and a 1-mA current intensity. The tACS (GBO and neuropsychological test) effect differed among the three groups (AD, MCI, and HC). In the HC group, GBO increased. Partial improvement of GBO was observed in the MCI group, whereas there was no significant effect for individuals with AD. Interestingly, after 2 years of follow-up, the individuals with MCI who failed to show a significant effect had progressed to AD. These results indicate the difficulty of employing tACS to modulate the neuroplasticity of patients with AD using the stimulation parameters mentioned above. In another slow-oscillation tDCS (so-tDCS) study (Ladenbauer et al., 2017), the authors used slow oscillatory stimulation at 0.75 Hz to modulate the brain activity pattern and memory consolidation during the daytime nap period in patients with MCI, with the anodes and cathodes placed on the frontal area (F3 and F4) and mastoid location, respectively. The slow cortical oscillation (0.5–1 Hz), spindle power, and declarative memory significantly improved after stimulation compared to the sham group. Similarly, the authors of one of the frontotemporal dementia studies (Ferrucci et al., 2018) stated that the effect of anodal tDCS (current, 2 mA; duration, 20 min; anode, frontotemporal cortex; cathode, right deltoid muscle) might be correlated with low-frequency band oscillation during the attentional processes. Two of the AD studies were quite similar. Both studies used tDCS with a 1.5-mA current to conduct the stimulation within a day visit. The most significant differences were in the duration and location of the simulation. The first study (Marceglia et al., 2016) delivered 15 min of stimulation from the bilateral temporoparietal area (left side, P3-T5; right side, P6-T4) with the reference on the right deltoid muscle. The results revealed that high-frequency power in the temporoparietal area and coherence at the temporal–parietal–occipital junction were increased in the AD group. Stimulation was applied in the second study (Cespón et al., 2019) over the left DLPFC, and the return electrode was placed on the right shoulder, with a stimulation duration of 13 min. The working memory, P200 amplitude, and theta band brain activity in the frontal area increased after cathodal tDCS. These two studies indicate that brain stimulation may rely significantly on the interaction among tDCS polarity, stimulation location, and brain state. One of the MCI studies (Emonson et al., 2019) applied an extended stimulation period (i.e., 20 min) to deliver the stimulation current (1 mA) from the left DLPFC (F3) to the contralateral supraorbital area (Fp2). Event-related potential (ERP) differed before and after stimulation for younger and older adult groups. However, this phenomenon was not observed in the MCI group. This finding is consistent with that of prior AD studies (Cespón et al., 2019). To compare the effects of short- and long-term tDCS, Gangemi et al. (2020) suggested that if brain stimulation (i.e., tDCS) can be effective with steady-state neurocognitive function over the short term, then this effect could be prolonged for 8 months. In addition, this study (current, 2 mA; duration, 20 min; visit, 10 days or 8 months; anode, left frontotemporal cortex; cathode, right frontal lobe) (Gangemi et al., 2020) demonstrated that anodal tDCS provides a technique to slow the progression of AD by influencing neurological patterns in the brain.

DEPRESSIVE DISORDER

Depression presents with sorrow, guilt, fatigue, low self-worth, irregular sleep/appetite, loss of interest, and low concentration (Xu J. et al., 2019; Olejarczyk et al., 2020). Commonly, these symptoms persist in the long term and recur easily. It substantially influences the patient's daily life. In the severe stage, depression may result in suicide. This disorder also occurs in children and adolescents (under 15 years old), but this age group's prevalence is lower than in adults. Researchers have found altered electrical activity in specific brain regions in patients with depression with neural science development. The cortex represents excitability, and other regions exhibit lower activities. tES, as an electrical stimulation therapy modality, has shown a promising advantage for improving the symptoms of depression.

Ten studies of depression were included in this review article, summarized in **Table 2**. Nine papers used EEG as the neuroimaging method to evaluate the neurological effect, and only one fNIRS study assessed therapeutic performance from a hemodynamic perspective. All EEG studies employed the alpha band power spectrum to compare the difference between the pre- and poststimulation. Some studies have considered an alpha band from 8 to 12 Hz, while others regard the ranges between 8 and 13 Hz or 7.5 and 12 Hz as the alpha band. The ERP power spectra in the delta, theta, beta, and gamma bands were also investigated as extracted EEG-based features. In addition to the standard features extracted from the alpha band, all anode stimulation locations for tACS and tDCS included the left DLPFC (F3). A possible explanation is that the left DLPFC is associated with right prefrontal hyperfunction and dysfunction of brain plasticity in depression.

In the fNIRS study (Li et al., 2019), 26 patients with poststroke depression received tDCS for 20 min with a 2-mA current on the left DLPFC and a return electrode at the right DLPFC. Each subject underwent five stimulation sessions weekly for 4 weeks. The results showed that working memory task performance and HbO concentration were improved after the treatment. Alexander et al. (2019) examined the feasibility and efficacy of modulating alpha oscillations by applying tACS at 10 and 40 Hz in the DLPFC (left DLPFC, F3; right DLPFC, F4) (Alexander et al., 2019). For 5 consecutive days, subjects received 40 min of either 10 Hz tACS, 40 Hz tACS, or sham trial. Reduced power in the alpha band was observed after 2 weeks of the intervention applying the 10-Hz tACS protocol.

Similarly, one tDCS study (Nikolin et al., 2020) also used a 2-mA stimulation current for 40 min. The current was delivered from the left DLPFC to the right shoulder, with patients receiving the therapy three times per week for 6 weeks. Although behavioral performance (e.g., mood and working memory) improved, neurophysiological measurements (e.g., power spectrum and ERP) did not significantly change following the intervention. One comparative study (Nishida et al., 2019) conducted tDCS at an intensity of 1 mA for 20 min from the left DLPFC and DMPFC. The return electrode at the left shoulder indicated that the effect of tDCS on anxiety reduction depends on the site of stimulation. The effect of tDCS stimulation at the left DLPFC on patients with depression was correlated with theta band activity acquired from the rostral anterior cingulate cortex. The effect of DMPFC stimulation on anxiety reduction was related to alpha-band activity in the left inferior parietal lobule. Three investigations were performed applying current from the left DLPFC to the right supraorbital area with a current intensity of 2 mA for 20 min. These studies differed in duration of stimulation periods: 1 day, 5 consecutive days, and 5 consecutive days each week for 3 weeks. In another study (Powell et al., 2014), a significant reduction in the N200 amplitude and theta band activity was observed over the memory task's frontal cortex substrate with one stimulation period. After five tDCS sessions, the depression score and the power spectrum (delta, theta, and low alpha band) were improved compared to the sham group, but this improvement was not sustained for 4 weeks (Liu et al., 2016). Long-term tDCS with 15 treatment periods has been found to affect mood and cognition in 50 and 60%, respectively, of individuals with depression (Al-Kaysi et al., 2017). Similarly, a lower-intensity (1 and 1.5 mA) tDCS protocol also resulted in reduced ERP (Shahsavar et al., 2018) and power spectra (e.g., delta, theta, and alpha frequency bands) (Palm et al., 2009; Khayyer et al., 2018) following stimulation. In particular, combined treatment with positive psychotherapy and tDCS can significantly affect depression. Effects are more pronounced following 3 months of follow-up than with the use of tDCS alone (Khayyer et al., 2018).

AUTISM SPECTRUM DISORDER

ASD refers to a developmental disorder characterized by (i) impaired communication, social behavior, language expression, and (ii) repetition of limited interests and activities. Typically, it begins in childhood and persists in adolescence and adulthood. Most individuals with ASD cannot live independently and require life-long care (Górriz et al., 2019). Several psychosocial interventions (behavioral treatment and skill training) have been applied to reduce communication difficulties and improve individuals' quality of life with ASD. However, the effect of psychosocial treatment depends on the individual's state. In addition to behavioral treatment, brain stimulation, as an alternative strategy, may improve symptoms from a neurological perspective by modulating deficient neural patterns.

The presence of abnormal gamma oscillations has been considered a biomarker and a target for therapeutic engagement; thus, tACS with a frequency-specific paradigm in the gamma band became the most suitable stimulation modality (Kayarian et al., 2020). Gamma band stimulation may also play a role in mediating the motor learning mechanism. Application of tACS

TABLE 1 | Studies and experimental characteristics of tES literature for AD and MCI.

Authors	**Subjects**	**Stimulation parameters**				**Neuroimaging**		**Conclusion**
		Type	**Current**	**Duration**	**Location**	**Type**	**Feature**	
Gangemi et al., 2020	26	tDCS	2 mA, 20 min	Daily for 10 sessions/ 80 sessions for 8 months	Anode: left frontotemporal (F7-T3), cathode: right frontal lobe (Fp2).	EEG	Alpha/ Beta/ Theta rhythm	The short- and long-term anodal-tDCS can be used as an effective treatment to slow the progression of dementia.
Emonson et al., 2019	49	tDCS	1 mA, 20 min	1 session	Anode: LDPFC (F3), cathode: contralateral supraorbital area (Fp2)	EEG	Event-related protentional	The manifestation and nature of tDCS induced neurobiological effects to differ based on age and the presence or absence of cognitive impairment.
Ferrucci et al., 2018	13	tDCS	2 mA, 20 min	Daily for 5 consecutive days	Anode: frontal-temporal lobes bilaterally(F7-F8), cathode: Right deltoid muscle	EEG	Power spectrum (2–7 Hz) and high (8–25 Hz) frequency	Anodal tDCS applied over the bilateral frontal-temporal cortex significantly improves cognitive ability.
Ladenbauer et al., 2017	16	So-tDCS	0.75 Hz, 0.522 mA/cm^2, 5 min	1 session (3–5 blocks)	Anode: prefrontal cortex (F3-F4), cathode: ipsilateral mastoid	EEG	Power spectrum (0.5–1 Hz) and fast spindles (12–15 Hz), phase-amplitude coupling	A well-tolerated therapeutic approach for disordered sleep physiology and memory deficits in patients with MCI and advances our understanding of offline memory consolidation.
Marceglia et al., 2016	7	tDCS	1.5 mA, 15 min	1 session	Anode: bilateral temporal-parietal area, cathode: right deltoid muscle.	EEG	Power spectral in low (2–7 Hz) and high (8–25 Hz) frequency, coherences	The modulation of cortical activity supports anodal tDCS benefits in patients with patients during working memory tasks.
Cespón et al., 2019	26	tDCS	1.5 mA, 13 min	1 session	Anode: left DLPFC (F3), cathode: right shoulder. Anode: M1 (C3), DLPFC	EEG	ERP, power spectrum in theta (4.1–7.9 Hz), alpha (8.1–13.9 Hz) and beta (15.1–24.6 Hz)	Functional neural modulations were promoted by anodal tDCS in healthy elderly and by cathodal tDCS in patients with AD
Naro et al., 2016	87	tACS	1 mA, 40–120 Hz, 10 min	31 session	(AF3-AF7), DMPFC (AF3-F1), PMA (FC3), or SMA (FCz) of the left hemisphere, cathode: right mastoid	EEG	Power spectrum in the gamma band	tACS can provide a novel way to diagnose MCI and AD, and it can identify patients with MCI at risk of developing dementia

TABLE 2 | Studies and experimental characteristics of the tES literature for depression.

Authors	Subjects	Type	Stimulation parameters			Neuroim aging		Conclusion
			Current	**Duration**	**Location**	**Type**	**Feature**	
Nikolin et al., 2020	20	tDCS	2 mA, 40 min	3 sessions per week for 6 weeks	Anode: left DLPFC (F3), cathode: right shoulder.	EEG	Power spectral in alpha (8–13 Hz) and theta (4–8 Hz), Event-related potential.	There is a significant improvement on the behavioral performance (i.e., mood, memory, cognitive).
Nishida et al., 2019	33	tDCS	1 mA, 20 min	1 session	Anode: left DLPFC (F5) or DMPFC (Afz), cathode: left shoulder.	EEG	Power spectral in alpha (8–12 Hz) and theta band (4–8 Hz), event-related potential.	tDCS could affect the brain activity on the stimulated brain area and influence the other related resting state neural network's cortical brain state.
Li et al., 2019	26	tDCS	2 mA, 20 min	5 sessions/ week for 4 weeks	Anode: left DLPFC (F3), cathode: right DLPFC (F4).	fNIR S	Concentration change in HbO	tDCS can improve depression symptoms in behavioral domains) and influence hemodynamic metabolism.
Alexander et al., 2019	32	tACS	1/2 mA, 10/40 Hz, 40 min	5 sessions in consecutive days	Anode: left/ right DLPFC (F3/ F4), cathode: Cz.	EEG	Power spectral in alpha (8–12 Hz).	10-Hz tACS could significantly reduce the alpha power over the left frontal cortex. tACS has potential for the treatment of depression.
Shahsavar et al., 2018	7	tDCS	1 mA, 20 min	5 session in consecutive days	Anode: left DLPFC (F3), cathode: right DLPFC (F4).	EEG	Event-related potential and the power spectrum in the different brain wave band	It was possible to estimate the change of depressed patients treated with tDCS with reasonable precision using the alpha band wavelet coefficients.
Al-Kaysi et al., 2017	10	tDCS	2 mA, 20 min	5 sessions per week for 3 weeks	Anode: left DLPFC (F3), cathode: F8	EEG	Power spectral in theta band (4–8 Hz), alpha (8–12 Hz), beta (13–30 Hz), and, gamma (30–100 Hz).	This study demonstrated the feasibility of predicting tDCS treatment outcomes by analyzing the EEG data recorded at baseline.
Liu et al., 2016	37	tDCS	2 mA, 20 min	5 session in consecutive days	Anode: left DLPFC (F3), cathode: right supraorbital area	EEG	Power spectral in alpha (8–13 Hz) and theta band (4–8 Hz).	tDCS could improve the depression symptom, but memory function was not immediately following or persisting after the stimulation
Powell et al., 2014	18	tDCS	2 mA, 20 min	1 session	Anode: left DLPFC (F3), cathode: F8	EEG	Power spectral in alpha (8–12 Hz) and theta band (4–8 Hz), event-related potential.	Anodal tDCS with a single session from the left DLPFC for the major depressive episode resulted in modulated brain activity of EEG.
Palm et al., 2009	1	tDCS	1 mA, 20 min	16 sessions in 27 days	Anode: F left DLPFC (F3), cathode: right supraorbital area	EEG	Power spectral in delta (1–3 Hz), theta band (4–7 Hz), alpha (8–12 Hz), and beta (13—5 Hz).	tDCS did not exert clinically meaningful antidepressant effects. The results for cognitive measures and EEG suggest that beneficial effects may occur in depressed subjects.
Khayyer et al., 2018	9	tDCS	1.5 mA, 15 min	3 sessions per week for 4 weeks	Anode: left or right DLPFC (F3 or F4), cathode: Cz.	EEG	Power spectrum in Delta (1–4 Hz), Theta (4.5–7 Hz), Alpha (7.5–12 Hz), Beta (12.5–24.5 Hz), High Beta (25–30 Hz)	The combined treatment of positive psychotherapy and tDCS showed the great performance to improve the neurological and clinical condition of major depressive disorder.

at 70 Hz increased motor learning capacity compared to sham treatment and tACS at 10 and 20 Hz (Sugata et al., 2018). For exploring multiple therapeutic strategies for patients with ASD, tDCS was used to modulate brain function in patients from different perspectives (abnormal synaptic maturation and connectivity). Two studies employed a 1-mA current intensity for 20 min to stimulate ASD models at the DLPFC region and evaluated EEG output effects. One study (Amatachaya et al., 2015) used one tDCS treatment period. The poststimulation results showed significant improvement in the autism treatment evaluation checklist in the social and behavioral domains compared to prestimulation scores. Besides, peak values of the alpha band also increased after stimulation. Similarly, Kang et al. (2018) conducted tDCS treatments every 2 days for 10 sessions. The maximum entropy ratio (an index of EEG signal complexity) was extracted to examine the tDCS effect and increase significantly following treatment. tDCS may be capable of rehabilitating children with ASD, as might tACS with frequency-specific characteristics. The related ASD studies are listed in **Table 3**.

ATTENTION-DEFICIT HYPERACTIVITY DISORDER

ADHD is also a developmental disorder characterized by two types of symptoms: (i) inattentiveness and (ii) hyperactivity/impulsiveness. Most cases are diagnosed at the ages of 6–12 years. Symptoms become particularly noticeable when circumstances change. Moreover, ADHD is commonly comorbid with other psychiatric disorders (e.g., depression and anxiety disorder), causing a substantial burden for patients and their families. Thus far, the medication-based intervention can achieve short-term effects, and the long-term effects of treatment for ADHD remain uncertain (Posner et al., 2020). It is essential to develop novel alternative strategies for treating ADHD.

There are four ADHD-related articles listed in **Table 4**, and all the studies used EEG for neuroimaging. Event-related potentials (P200 and P300) were employed in two of the papers and were used to evaluate the effects of tDCS (Breitling et al., 2020) and tACS (Dallmer-Zerbe et al., 2020), respectively. The remaining studies extracted functional brain connectivity (Cosmo et al., 2015b), power spectra (Dallmer-Zerbe et al., 2020), and statistical analysis (Cosmo et al., 2015a) as features for examining the neurological changes following tDCS. In all investigations, 20 min of tES therapy at low current intensity (1 mA) was applied. In the tACS study (Dallmer-Zerbe et al., 2020), the authors applied a stimulation with a mean frequency of 3 Hz, delivered from multiple electrodes (anodes: C3, C4, CP3, CP4, P3, and P4) and returned by cathodes at T7, T8, TP7, TP8, P7, and P8 (the distribution of electrodes following the international 10–20 EEG system). The neurological results following tACS demonstrated that the P300 amplitude significantly increased, accompanied by a decrease in omission errors compared to pre-tACS. Both tDCS studies share the same experimental paradigm (current intensity, duration, and stimulation location), but the results were reversed. The first study (Cosmo et al., 2015b) indicated

TABLE 3 | Studies and experimental characteristics of tES literature for ASD.

Authors	Subjects	Stimulation parameters				Neuroimaging		Conclusion
		Type	Current	Duration	Location	Type	Feature	
Kang et al., 2018	13	tDCS	1 mA, 20 min	10 sessions	Anode: DLPFC, cathode: right supraorbital	EEG	Complexity	The complexity of EEG significantly increased after tDCS. This study suggests that tDCS may be a helpful tool for the rehabilitation of children with ASD.
Amatachaya et al., 2015	24	tDCS	1 mA, 20 min	1 session	Anode: left DLPFC (F3), cathode: right shoulder	EEG	Peak alpha frequency	The clinical (autism treatment evaluation checklist) and neurological (peak alpha frequency) performance was improved after the treatment of active tDCS.

TABLE 4 | Studies and experimental characteristics of tES literature for ADHD.

Authors	Subjects	Stimulation parameters				Neuroimaging		Conclusion
		Type	Current	Duration	Location	Type	Feature	
Breitling et al., 2020	15	tDCS/ HD- tDCS	1 mA/0.5 mA, 20 min	1 session	Anode: right IFG (F8), cathode: contralateral supra-orbital	EEG	N-200 and P300	HD-tDCS could be equally suitable with typical tDCS for improving the working memory processing of patients with ADHD.
Dallmer-Zerbe et al., 2020	18	tACS	1 mA, 20 min, 3 Hz	1 session	Anode: motor-parietal cortex (C3, C4, CP3, Cp4, P3, P4); Cathode: temporal-parietal (T7, T8, TP7, TP8, P7, P8)	EEG	P300	A significant increase in P300 amplitude in the stimulation group, which was accompanied by a decrease in omission errors pre-to-post tACS.
Cosmo et al., 2015b	60	tDCS	1 mA, 20 min	1 session	Anode: left DLPFC (F3), Cathode: right DLPFC (F4).	EEG	Functional cortical network	Anodal tDCS increased the functional brain connectivity in individuals with ADHD compared to data recorded in the baseline resting state.
Cosmo et al., 2015a	60	tDCS	1 mA, 20 min	1 session	Anode: left DLPFC (F3), cathode: right DLPF)ˆp z(F4).	EEG	Statistical analysis	The statistical analysis indicated that anodal stimulation over the LDPFC could not improve inhibitory control in patients with ADHD.

that resting-state brain connectivity increased in individuals after DLPFC stimulation. The authors of the second study (Cosmo et al., 2015a) found no evidence supporting the capability of tDCS to improve inhibitory control by stimulating the left DLPFC in patients with ADHD performing the go/no–go task. A recent investigation (Breitling et al., 2020) compared the effectiveness of conventional (with one anodal electrode) and high-definition tDCS (with four anodal electrodes) for improving working memory performance, with the anode located near the right inferior frontal gyrus and the cathode placed over the contralateral supraorbital region. The results for working memory behavior were not generally influenced by conventional and high-definition tDCS (HD-tDCS). However, elevated P300 and N200 were observed after conventional and HD-tDCS since the current intensity differed between conventional tDCS (1 mA) and HD-tDCS (0.5 mA). The conclusion, which may be difficult to accept, is that HD-tDCS is equally suitable as conventional tDCS for improving the working memory performance of patients with ADHD. Therefore, comprehensive investigations are required to assess the effectiveness of tES for treating ADHD in the future.

EPILEPSY

Epilepsy is a chronic brain disease characterized by brief involuntary movement in part or the entire body with recurrent unprovoked seizures. Sometimes, seizures result in loss of consciousness and control of bladder function. Patients with epilepsy have three times the risk of premature death as the general population. Fortunately, approximately 70% of epilepsy cases can be controlled using proper antiseizure medication. It is suggested that in the remaining patients (approximately 30%) with drug-resistant epilepsy, seizure control should be achievable through surgery and neurostimulation therapies (Devinsky et al., 2018).

Abnormal EEG patterns are among the most consistent predictors of seizure recurrence (Scheffer et al., 2009). As shown in **Table 5**, EEG was employed in all 14 epilepsy studies as the neuroimaging method to assess the tES effect. The evaluated features included the power spectrum, connectivity, mean peak amplitude, mean number of spikers, and seizure frequency. Each study applied a different stimulation strategy to explore the optimal stimulation protocol. In the tACS study (San-Juan et al., 2016), patients received a sinusoidal fluctuating current (frequency, 3 Hz; intensity, 1 mA) from Fp1 to Fp2. The stimulated location was determined by visual inspection of EEG signals for the most active epileptiform cortex. Sessions of 60-min duration were conducted daily for 4 consecutive days. At the 2-month follow-up, patients were asked to report whether they had experienced one or more seizures in the previous 15 days. A lower oscillation (0.75 Hz) tACS was used to investigate the enhancement of memory consolidation during slow-wave sleep in patients with temporal lobe epilepsy (TLE) (Del Felice et al., 2015). The anode was placed over the frontotemporal lobe, and the cathode was placed on the ipsilateral mastoid. Visuospatial memory performance, slow spindles (10–12 Hz),

TABLE 5 | Studies and experimental characteristics of tES literature for epilepsy.

Authors	Subjects	Stimulation parameters				Neuroimaging		Conclusion
		Type	Current	Duration	Location	Type	Feature	
Meiron et al., 2019	1	HD-tDCS	1 mA, 20 min	5 sessions per week for 4 weeks	Anode: frontal-parietal cortex (AF8, F2, C2, PO4), cathode :C6	EEG	Power spectral in theta band (4–8 Hz), alpha (8–12 Hz), beta (13–30 Hz), spike frequency, duration, and amplitude.	tDCS reduces the interictal epileptic discharges and change in seizure-related delta activity.
Yang et al., 2019a	7	tDCS	1 or 2 mA, 40 min	14 sessions consecutive days	Anode: left or right supra-orbital area, cathode: P4 or P3	EEG	Seizure frequency and seizure reduction.	Repeated tDCS (cathode located in the bilateral parietal area) could safely reduce seizure frequency for epilepsy patients.
Lin et al., 2018	9	tDCS	2 mA, 20 min	6 sessions in one month	Anode: contralateral shoulder area, cathode: epileptogenic focus	EEG	Seizure frequency and phase lag index/	tDCS may be considered an alternative treatment option for patients with refractory epilepsy. Its effect might be cumulative after repeated stimulations and associated with a decrease in the phase lag index.
Tecchio et al, 2018	6	tDCS	1 mA, 20 min	1 session	Anode: opposite homologous, cathode: epileptogenic focus.	EEG	Functional connectivity and power spectrum.	The neurological alternation (functional connectivity) indicated that the cathode tDCS might contribute to epilepsy and provide a new therapy to modulate the epileptic people.
Meiron et al., 2018	1	HD-tDCS	0.1–1 mA, 20 min	5 sessions per week for 2 weeks	Anode: PO3, P6, AF3, F6, FC4, O1, CP3, C1, FC8, C6, FCz, FC3, O4, F2, CP4, PO4, O2, AF8, C2, cathode: C2, TP8, CP8, O3, TP8, T8	EEG	Mean number spikers, mean peak amplitude, mean absolute power.	HD-tDCS showed safety and feasibility of early-onset epileptic encephalopathy. It provides the first evidence of HD-tDCS effects on paroxysmal EEG features in electroclinical cases under the age of 36 months. Extending HD-tDCS treatment may enhance electrographic findings and clinical effects.
Karvigh et al., 2017	10	HD-tDCS	2 mA, 20 min	10 consecutive days	Anode: frontal-parietal-temporal cortex (F3/F4, P3/P4, Cz, T3/T4) Cathode: PF1/PF2, Fz, Tz/T8, C3/C4	EEG	Seizure frequency	The statistical analysis for the whole group does not show the effect of the tDCS since the change of epileptiform discharge was not significant. However, the clinical score (i.e., working memory performance) was improved.
San-Juan et al., 2016	1	tACS	1 mA, 3 Hz, 60 min	4 sessions consecutive days	Anode: frontal cortex (Fp1 and Fp2)	EEG	Spike-low wave at 3 Hz, polis piker-slow wave at 3–4 Hz, and slow rhythmic waves at 4 Hz	At the 1-month follow-up, the patients reported a 75% increase in seizure frequency. At the 2-month follow-up, the patient reported a 15-day seizure-free period.
Tekturk et al., 2016	12	tDCS	2 mA, 30 min	3 sessions consecutive days	Anode: temporal region (T3 and T4); cathode: contralateral supraorbital region	EEG	Seizure frequency	Our small series suggested that cathodal tDCS may be used as an additional treatment option in MTLE-HS. It may be tried in patients with TLE-HS waiting for or rejecting epilepsy surgery or even with ineffective surgical results.

(Continued)

TABLE 5 | Continued

Authors	Subjects	Stimulation parameters				Neuroimaging		Conclusion
		Type	Current	Duration	Location	Type	Feature	
Liu et al., 2016	37	tDCS	2 mA, 20 mins	5 sessions Consecutive days	Anode: DLPFC (F3, F4), cathode: right supraorbital area	EEG	Power spectral in delta (1–4 Hz), theta band (5–7 Hz), low alpha (8–10 Hz), high alpha (11–13 Hz), beta (14–32 Hz), low gamma (33–35 Hz).	tDCS improved the symptoms of depression for temporal lobe epilepsy. There were no changes in memory function immediately following or persisting after a stimulation course.
Del Felice et al., 2015	12	So-tDCS	0.75 Hz, 30 mins	1 session	Anode: frontal-temporal (F7-T3 or F8-T8), cathode: ipsilateral mastoid	EEG	Spindle frequency and Cortical sources	Anodal so-tDCS over the affected temporal lobe improves declarative and visuospatial memoryperformance by modulating slow sleep spindles cortical source generators.
Auvichayapat et al., 2013	36	tDCS	1 mA, 20 min	1 session	Anode: Contralateral shoulder area, cathode: epileptogenic focus	EEG	Spikes and sharp waves	A single session of cathodal tDCS improves epileptic EEG abnormalities for 48 h and is well tolerated in children.
Fregni et al., 2006	19	tDCS	1 mA, 20 min	1 session	Anode: silent area. cathode: epileptogenic focus	EEG	Seizure frequency	Cathodal tDCS polarization does not induce seizures and is well tolerated in patients with refractory epilepsy and MCDs. tDCS might have an antiepileptic effect based on clinical and electrophysiological criteria.
Faria et al., 2012	17	tDCS	1 mA, 30 min	3 sections for three weeks	Anode: central prefrontal area (FPz), cathode: CP6 Cp5.	EEG	The average number of epileptiform	Continuous monitoring of epileptic activity throughout tDCS improves safety and permits detailed evaluation of epileptic activity changes induced by tDCS in patients.
San-Juan et al., 2016	28	tDCS	2 mA, 30 min	3 or 5 sessions in consecutive days	Anode: silent area. cathode: most active interictal epileptiform discharges area	EEG	Seizure frequency	Cathodal tDCS (applied 3 and 5 sessions) reduced seizure frequency and interictal epileptiform discharges for patients with epilepsy and hippocampal sclerosis compared to placebo tDCS.

and fast spindles (12–14 Hz) were extracted as EEG features to assess the effect of stimulation. Both behavioral and neurological performance improved following stimulation. The results suggest that memory rehabilitation may be achieved by slow oscillatory stimulation in patients with TLE.

tDCS remains the primary intervention for epilepsy rehabilitation. Three of the studies applied HD-tDCS as the stimulation protocol with different stimulation parameters and locations. No adverse reactions were reported in any studies, but the reported results differed slightly. One of the studies (Meiron et al., 2019) stated that reduced interictal epileptic discharge and seizure-related delta activity changed. The stimulation intensity was set at 1 mA for 20 min in 20 interventions. Similarly, the interictal sharp wave amplitude after HD-tDCS (0.1–1 mA, 20 min, 10 sessions) was lower than the preintervention level. However, the seizure frequency was not significantly decreased (Meiron et al., 2018). On the other hand, Karvigh et al. (2017) reported that the mean seizure frequency decreased immediately after HD-tDCS (2 mA, 20 min, and 10 sessions). However, this reduction did not persist after 1 month of follow-up. Interestingly, the attention and working memory performance were improved in all patients even after 1 month. These discrepancies in results may have resulted from differences in stimulation protocol parameters (intensity, duration, and location). In five studies, cathodes were placed on the epileptogenic focus (i.e., focal disease-related area) to achieve adequate stimulation (Fregni et al., 2006; Auvichayapat et al., 2013; San-Juan et al., 2017; Lin et al., 2018; Tecchio et al, 2018). Although the stimulation parameters varied, a reduction in seizure frequency or a significant decrease in epileptic discharge was observed. Partial epileptic participants showed reduced seizure frequency when the anode–cathode pair was located between the temporoparietal and contralateral supraorbital regions (Tekturk et al., 2016; Yang et al., 2019a). In one of the studies (Faria et al., 2012), tDCS and EEG recordings were combined to investigate the feasibility of the simultaneous use of two modalities for continuous monitoring of epilepsy. The simultaneous recording signals were used to analyze the reduced interictal epileptiform EEG discharges. The feasibility of this technique may provide an approach for monitoring epileptic activity in real time during the intervention. However, the input current from the stimulation might also interfere with the recording of endogenous EEG signals. Therefore, future studies should consider the advantages and disadvantages of using these two tES modalities simultaneously.

SCHIZOPHRENIA

Schizophrenia is a type of psychosis that presents distortions in cognition, thinking, perception, feeling, emotions, and language. Patients experience hallucinations and delusions. For instance, patients may see/hear nonexistent voices/things and develop supernatural beliefs. Quality of life for schizophrenia patients is highly influenced by various risk factors, such as diabetes, cardiovascular disease, and suicide (Patel et al., 2014). The underlying mechanism remains poorly understood, and the gap between research and practical applications is considerable. Further investigation is required to arrive at a better diagnosis and effective therapeutic strategies.

Nine schizophrenia studies were included in this review (**Table 6**). All the studies employed EEG as the neuroimaging modality. The extracted EEG features consisted of the power spectrum (e.g., delta, theta, and gamma frequency bands), event-related potentials (e.g., P300, P170, etc.), and functional connectivity. The prefrontal cortex plays a crucial role in working memory, cognition, planning, decision making, emotional regulation, and social interaction (Ferguson and Gao, 2018). In over half of the examined studies (five of nine), electrodes were placed on the prefrontal cortex. Only one study (Rassovsky et al., 2018) reported no significant cognitive or neurological (i.e., event-related potentials) effects in patients with schizophrenia. The remaining four studies (Hoy et al., 2015; Dunn et al., 2016; Ahn et al., 2019; Boudewyn et al., 2020) demonstrated improvement following the intervention, either in the behavioral (working memory performance, steady-state auditory response, and proactive cognitive control) or the neurological domains (functional connectivity, gamma oscillation, alpha oscillation, and P300). A comparative study (tDCS, tACS, and sham) (Ahn et al., 2019) reported that 10-Hz tACS stimulation achieved better performance than tDCS in enhancing alpha oscillation modulation of functional connectivity in the alpha band. A similar study (Singh et al., 2019) found that theta oscillations were significantly elevated following theta frequency stimulation, but this phenomenon was not seen for delta frequency with tACS. An improved theta oscillation was also found following medial frontal tDCS in another study (Reinhart et al., 2015), in which tDCS modulated low-frequency oscillation in the absence of synchrony in the patient's brain. Some research teams have shifted the anodes' locations from the frontal cortex to the temporal or occipital lobes to probe the effects on the abnormal symptoms of schizophrenia (visual processing abnormalities, working memory deficits, and auditory hallucinations). Working memory performance and auditory deviance detection were increased by anodal frontal and temporal tDCS (Impey et al., 2017). The plasticity effect following occipital tDCS was not found during anodal and cathodal stimulation (Jahshan et al., 2020). Although significant positive effects were not observed in the investigations, a comparison of the results reveals the importance of parameter selection and emphasizes comprehensive research requirements for future studies.

PARKINSON'S DISEASE

PD is a neurodegenerative disorder that predominantly impacts the dopamine-producing neurons of the substantia nigra in the brain and further affects movement control. PD patients may experience outward symptoms such as tremors, bradykinesia, limb rigidity, and gait/balance problems. Treatment strategies are dependent on symptoms and may include medication therapy, surgical therapy, and lifestyle modification. Recently, deep brain stimulation (DBS) was approved by the Food and Drug Administration (FDA) to rehabilitate PD patients. However, the

TABLE 6 | Studies and experimental characteristics of tFS literature for schizonhrenia.

Authors	Subjects	Stimulation parameters				Neuroim aging		Conclusion
		Type	Current	Duration	Location	Type	Feature	
Boudewyn et al., 2020	37	tDCS	2 mA, 20 min	1 session	Anode: left dorsolateral PFC(F3), Cathode: right supraorbital site (FP2)	EEG	The power spectrum of the gamma band (30–80 Hz)	Gamma oscillations in proactive cognitive control and frontal tDCS may be a promising approach to enhancing proactive cognitive control in schizophrenia.
Jahshan et al., 2020	27	tDCS	2 mA, 20 min	3 sessions for one week	Anode: central occipital cortex, cathode: right shoulder.	EEG	Visual evoked potentials	It is no evidence of an input-specific plasticity effect and an inconsistent effect of tDCS delivered before visual stimulation on plasticity in people with schizophrenia.
Ahn et al., 2019	22	tACS and tDCS	1.5 or 2 mA, 10 Hz, 20 min	10 sessions	Anode: prefrontal cortex (F3, Fp1), cathode: T3, P3	EEG	Alpha oscillations, Power spectral density, functional connectivity.	tACS has potential as a network-level approach to modulate reduced neural oscillations in relation to clinical symptoms in patients with schizophrenia.
Rassovsky et al., 2018	38	tDCS	2 mA, 20 min	Twice daily for three visits	Anode: DLPFC, cathode: right supraorbital	EEG	P300 and N170	There was no significant improvement based on the results of the neurological and cognitive perspective after single-session tDCS.
Dunn et al., 2016	36	tDCS	1 mA, 20 min	1 session	Anode: bilateral DLPFC (FP1 and FP2), cathode:ˆ right upper arm	EEG	P300	tDCS can engage and modulate an EEG-based auditory processing measure in schizophrenia.
Hoy et al., 2015	16	tDCS	1 or 2 mA, 20 min	3 sessions			Gamma event-related synchronization and correlation.	tDCS may enhance working memory in schizophrenia by restoring normal gamma oscillatory function
					Anode: frontal cortex (F3), cathode: right supraorbital	EEG		
Smith et al., 2015	19	tDCS	1.5 mA, 20 min	1 session	Anode: medial frontal cortex	EEG	Interregional phase synchrony, event-related potential. Power spectrum	Behavioral performance improved. These results provide unique causal evidence for theories of executive control and cortical dysconnectivity in schizophrenia.
Singh et al., 2019	9	tACS	1 mA, 20 min	1 session	Anode: cerebellar vermis, cathode: right shoulder	EEG	Mean relative power at delta (1–4 Hz) and theta (4–8 Hz) frequency bands	Theta oscillations were obtained. Single-session theta frequency stimulation may modulate task-related oscillatory activity in the frontal cortex.
Impey et al., 2017	12	tDCS	2 mA, 20 min	2 sessions	Anode: left auditory or frontal cortex, cathode: contralateral forehead.	EEG	Event-related potential	Anodal frontal tDCS significantly increased working memory performance, which positively correlates with mismatch negativity-tDCS effects.

procedure for setting the DBS device requires a surgical step. Therefore, researchers have moved to the NIBS area, which seeks noninvasive therapy to avoid surgical pain.

Three PD studies (see **Table 7**) were included after screening by related keywords. Two of three studies applied EEG to describe the cortical activity, and one employed fNIRS as the neuroimaging modality. The extracted EEG/fNIRS-based features and applied stimulation protocols are varied. One of the studies (Schoellmann et al., 2019) used tDCS to deliver a current of 1 mA from the left sensorimotor cortex for 20 min and the return electrode to the right frontal lobe. After the intervention, the motor cortex's cortical activity and synchronization were altered, but it did not change the cortical oscillatory of PD patients. However, the reduced beta rhythm oscillation was obtained by the theta-tACS and tRNS, in which research was performed in a personalized stimulation setting (Del Felice et al., 2019). One fNIRS research (Beretta et al., 2020) examined the tDCS effect with different intensities (1 mA, 2 mA, and sham). Both tDCS intensities showed a reduced time response to recover the balance post perturbation. The 2-mA stimulation displayed a better performance than that of 1 mA.

STROKE

Stroke, known as cerebrovascular disease, is the second leading cause of death and the third leading cause of disability worldwide. The risk of death depends on the category of stroke (transient ischemic attack, blockage of an artery, carotid stenosis, and rupture of a cerebral blood vessel). Since brain cells die due to insufficient blood support, survivors typically experience paralysis, vision or speech loss, and confusion. Several behavioral rehabilitation approaches, such as physical therapy and speech training, are provided to recover impaired brain regions for these patients. NIBS is an emerging method for facilitating neural plasticity in the damaged brain from a neurological perspective, and its potential and capability have received much attention.

Most of the studies (12 of 14) used EEG to monitor the effects of stimulation, as shown in **Table 8**. Additionally, two studies investigated damaged neurovascular coupling in stroke survivors using a combination of EEG and fNIRS modalities. Both joint EEG-fNIRS studies (Dutta et al., 2015; Jindal et al., 2015) concluded that anodal tDCS could modulate impaired neurovascular coupling. In particular, the log-transformed EEG mean power within 0.5–11.25 Hz correlated with the hemodynamic response of HbO (initial dip). Moreover, functional connectivity (Nicolo et al., 2018), event-related potentials (D'Agata et al., 2016), event-related desynchronization (Kasashima et al., 2012; Ang et al., 2015; Kasashima-Shindo et al., 2015; Naros and Gharabaghi, 2017), and power spectra (theta, alpha, beta, and gamma EEG bands) (Hordacre et al., 2018; Bao et al., 2019; Mane et al., 2019) were also possible biomarkers for checking recovery after tDCS. In the EEG studies, three studies explored the feasibility of tDCS for treating apraxia (swallowing apraxia and aphasia) in stroke. Lower current intensities (1 and 1.2 mA) were used over long-term (10 and 15 sessions, respectively) interventions. Positive

TABLE 7 | Studies and experimental characteristics of tES literature for PD.

Authors	Subjects	Stimulation parameters				Neuroimaging		Conclusion
		Type	Current	Duration	Location	Type	Feature	
Del Felice et al., 2019	15	tACS++tRNS	4 or 30 Hz, 1 to 2 mA, 30 min	5 sessions per week for two weeks	Anode: The location of power spectral difference was detected, cathode: ipsilateral mastoid	EEG	Power spectral in delta (1–4 Hz), theta band (4.5–7.5 Hz), alpha1 (8–10 Hz), alpha2 (10.5–12.5 Hz), beta (13—0 Hz)	Individualized tACS in PD improves motor and cognitive performance. These changes are associated with a reduction of excessive fast EEG oscillations.
Beretta et al., 2020	24	tDCS	1 and 2 mA, 20 min	3 sessions 2 weeks apart	Anode: primary motor cortex, cathode: contralateral supraorbital region	fNIRS	The concentration changes of HbO	tDCS over M1 improved the postural response to external perturbation in PD, with better response observed for 2 mA compared with 1 mA, and was inefficient in modifying the habituation of perturbation
Schoellmann et al., 2019	21	tDCS	1 mA, 20 min	1 session	Anode: left sensorimotor (C3), cathode: right frontal area (FP2).	EEG	Frequency domain spectrum and coherence	tDCS improved PD motor symptoms.Neurophysiological features indicated amotor-task-specific modulation of activityand coherence from 22 to 27 Hz after 'verum'stimulation in PD.

TABLE 8 | Studies and experimental characteristics of tES literature for stroke.

Authors	Subjects	Stimulation parameters				Neuroim aging		Conclusion
		Type	Current	Duration	Location	Type	Feature	
Mane et al., 2019	19	tDCS	1 mA, 20 min	10 sessions	Anode: ipsilesional primary motor cortex, cathode: contralesionally primary motor cortex	EEG	Power spectral in delta (1–4 Hz), theta band (4–7.5 Hz), alpha (7.5–12.5Hz), beta (12.5–30 Hz), and correlation analysis.	QEEG features can act as prognostic and monitory biomarkers. tDCS-BCI can be pursued to predict a patient's expected response to an intervention uniquely.
Bao et al., 2019	30	HD-tDCS	1 mA, 10 min	4 sessions	Anode: ipsilesional motor cortex(C3), cathode: frontal-parietal cortex (F1, F5, P1, P5)	EEG	Cortico-muscular coherence and power spectral in alpha (8–13 Hz), beta (13–30 Hz), and low gamma (30–48 Hz).	Anode HD-tDCS induced significant CMC changes in stroke subjects. The largest neuromodulation effects were observed at 10 min immediately after anodal HD-tDCS.
Hordacre et al., 2018	10	tDCS	1 mA, 20 min	1 session	Anode: primary motor cortex, cathode: contralateral orbit	EEG	Connectivity in different frequency band delta (1–3 Hz), theta (4–7 Hz), alpha (8–13 Hz), low beta (14–19 Hz), high beta (20–0 Hz), and gamma (31–45 Hz).	Alpha band functional connectivity of an approximate ipsilesional sensorimotor and contralesionally motor-premotor network is a robust and specific biomarker of neuroplastic induction following anodal tDCS in chronic stroke survivors.
Nicolo et al., 2018	41	tDCS	1 mA, 25 min	3 sessions per week for 3 weeks	Anode: ipsilesional supraorbital region, cathode: contralesionally primary motor cortex	EEG	Effective connectivity and functional connectivity	The inhibition of the contralesionally primary motor cortex or the reduction of interhemispheric interactions was not clinically useful in aheterogeneous group of subacute stroke subjects. Enhancement of perilesional beta-band connectivity through tDCS might have more robust clinical gains if it started within the firstfour weeks after the onset of stroke.
Naros and Gharabaghi, 2017	20	tACS	1.1 mA, 20 Hz, 20 min	1 session 5 sessions per week for 3 weeks	Anode: ipsilesional sensorimotor cortex, cathode: contralesionally forehead.	EEG	Ipsilesional and contralesionally beta power in resting state and event related desynchronization	Intermittent β-tACS reduces the instantaneous variance of sensorimotor β oscillations and increases the specificity of brain self-regulation-based neurofeedback in patients with stroke patients.
Yuan et al., 2017	9	tDCS	1.2 mA, 20 min		Anode: primary sensorimotor cortex, cathode: contralateral shoulder	EEG	Approximate entropy	After tDCS, scores of swallowing apraxia assessments increased, and ApEn indices increased in both stimulated and non-stimulated areas.
D'Agata et al., 2016	34	tDCS	1.5 mA, 20 min	10 daily sessions for 2 weeks	Anode: damaged hemisphere corresponding to motor cortex (C3 or C4), cathode: opposite hemisphere	EEG	Event-related potential (P300, N200)	NIBS generally improved ERP, but transitorily. More than one NIBS cycle (2–4 weeks) should be used in rehabilitation to obtain clinically relevant results after a washout period only in responder patients.

(Continued)

TABLE 8 | Continued

Authors	Subjects	Stimulation parameters				Neuroim aging		Conclusion
		Type	Current	Duration	Location	Type	Feature	
Dutta et al., 2015	4	tDCS	0.526 A/m^2, 15 min	1 session	Anode: motor cortex (Cz), cathode left supraorbital notch	EEG and fNIRS	The concentration changes of HbO and HbR, power spectrum	The initial dip in HbO2 at the beginning of anodal tDCS corresponded with an increase in EEG's log-transformed mean power within the 0.5 Hz –11.25 Hz frequency band.
Kasashima-Shindo et al., 2015	18	tDCS	1 mA, 10 min	5 days per week for 2 weeks	Anode: primary sensorimotor cortex of the affected hemisphere, cathode: contralateral supraorbital area.	EEG	Event-related desynchronization	Event-related desynchronization was significantly increased in the tDCS-brain-computer interface group; anodal tDCS can be a conditioning tool for brain-computer interface training in patients with severe hemiparetic stroke.
Wu et al., 2015	12	tDCS	1.2 mA, 20 min	5 sessions per week for 4 weeks	Anode: left posterior peri-sylvian region, cathode: unaffected shoulder	EEG	Approximate entropy	A-tDCS over the left PPR coupled with speech-language therapy can improve picture naming and auditory comprehension in aphasic patients. Moreover, tDCS could modulate the related brain network, not only the stimulated brain areas.
Jindal et al., 2015	29	tDCS	0.526 A/m^2, 3 min	1 session	Anode: motor cortex (Cz), cathode: frontal cortex (F3 or F4)	EEG and fNIRS	The concentration changes of HbO and HbR, power spectrum	Anodal tDCS can perturb local neural and vascular activity, which can be used for assessing the functionality of regional cerebral microvessels where crematory clinical studies are required in small vessel diseases.
Dominguez et al., 2014	1	tDCS	1 mA, 20 min	5 sessions per week for 3 weeks	Anode: left frontal area. cathode: homologous right contra-lateral area	EEG	Coherence and power spectrum in the delta (0–4 Hz), theta (4–8 Hz), alpha (8–13 Hz), and beta (13–30 Hz) bands.	tDCS can be affected for behavioral performance and inhibit the irregular activity in the right hemisphere. A longer stimulus can produce greater recovery.
Kasashima et al., 2012	6	tDCS	1 mA, 10 min	1 session	Anode: primary motor cortex of the affected hemisphere, cathode: opposite side in thesupraorbital region	EEG	Event-related desynchronization	Anodal tDCS can increase mu ERD of the affected hemisphere in patients with severe hemiparetic stroke as well as in healthy persons.
Ang et al., 2015	19	tDCS	1 mA, 20 min	5 sessions per week for 2 weeks	Anode: silent area. cathode: most active interictal epileptiform discharges area	EEG	Seizure frequency and laterality coefficient.	tDCS improved the motor ability assessment score, and EEG laterality coefficients were improved after the intervention.

TABLE 9 | Studies and experimental characteristics of tES literature for TBI.

Authors	Subjects	Stimulation parameters				Neuroimaging		Conclusion
		Type	Current	Duration	Location	Type	Feature	
Zhang et al., 2020	10	tDCS	2 mA, 20 min	twice daily, 5 sessions per week for 4 weeks	Anode: Prefrontal area and left DLPFC, cathode: neck and F4.	EEG	Approximate entropy and cross-approximate entropy Relative power in	A-tDCS over the prefrontal area and left DLPFC improves psychomotor inhibition state. The recovery might be related to increased excitability in local and distant cortical networks connecting the sensorimotor area to the prefrontal area.
Straudi et al., 2019	10	tDCS	2 mA, 40 min	5 sessions per week for 2 weeks	Anode: bilaterally primary motor cortex, cathode: Nasion.	EEG	delta (1–3.5 Hz), theta (3.5–7.5 Hz), alpha1 (8–10 Hz), alpha2 (11–13 Hz), beta1 (13.5–18 Hz), beta2 (18.5–30 Hz)	This study tested and evaluated the preliminary effects of bilateral anodal transcranial direct current stimulation in patients with disorders of consciousness.
O'Neil-Pirozzi et al., 2017	8	tDCS	2 mA, 20 min	3 sessions (48 h apart)	Anode: left DLPFC, cathode: right supraorbital area.	EEG	Power spectrum in theta (4–8 Hz), alpha (8–13 Hz), and P300.	Individuals with memory impairments secondary to chronic TBI may benefit from LDLPFC anodal tDCS.
Ulam et al., 2015	26	tDCS	1 mA, 20 min	10 sessions consecutive day	Anode: left DLPFC (F3), cathode: right supraorbital area (Fp2).	EEG	Power spectrum in delta (1–4 Hz), theta (4–8 Hz), alpha (8–10 Hz), beta1 (12–25 Hz), beta2 (25–30 Hz)	Ten anodal tDCS sessions may beneficially modulate regulation of cortical excitability for patients with TBI.

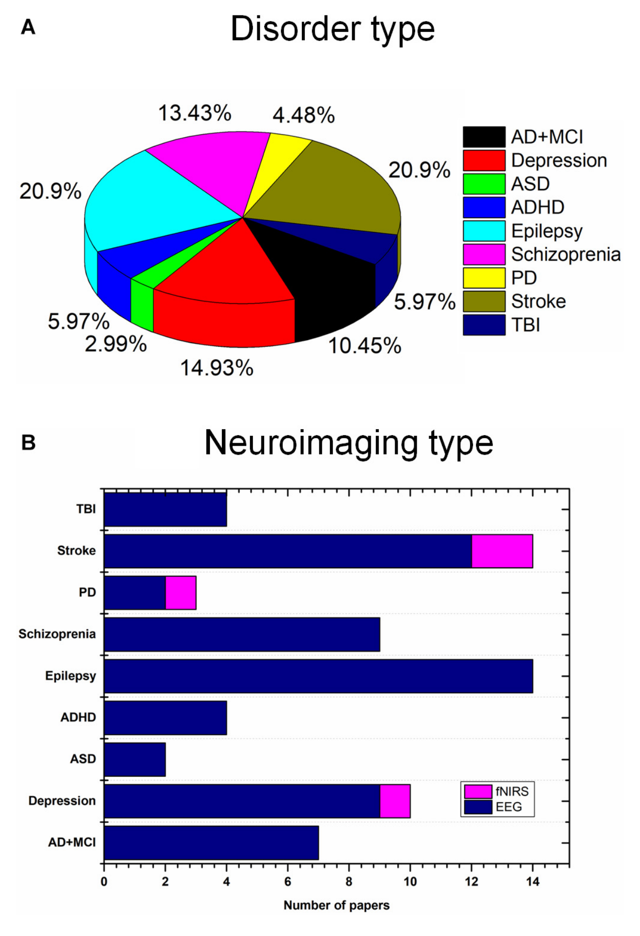

FIGURE 4 | Brain disorders and imaging techniques: **(A)** Nine brain disorders, **(B)** number of EEG/fNIRS papers per brain disorder.

behavioral and neurological results were obtained after tDCS for all three studies (Dominguez et al., 2014; Wu et al., 2015; Yuan et al., 2017). Anodal tDCS may offer a novel therapeutic means for the rehabilitation of aphasia and swallowing apraxia. Although all 14 stroke-related investigations applied different stimulation strategies, encouraging postintervention effects were achieved from either the neurological or cognitive perspective. These findings differ from the experimental results for other diseases (e.g., AD or schizophrenia), in which the various stimulation sites and parameters may lead to contrary results. Future studies should explore the underlying altered mechanism by monitoring prognostic neurological or hemodynamic biomarkers. Moreover, attention should be devoted to investigating HbO and neurovascular coupling concentration changes before and after the intervention, especially for small vessel diseases (such as stroke).

TRAUMATIC BRAIN INJURY

TBI is a disorder characterized by disrupted brain function that is generally caused by an external bump, violent blow, or jolt to the head. TBI may cause a wide range of symptoms due to various brain injury regions, including physical impairment, psychological changes, and sensory or cognitive alterations. Like the rehabilitation method for stroke, the most popular rehabilitation therapies for TBI include physical training, cognitive therapy, and psychological counseling. As reported in animal studies, tES can improve motor deficits by changing the neuroplasticity of TBI. NIBS may provide the potential to promote cognitive or motor recovery in TBI patients.

As shown in **Table 9**, there are four relevant types of research exploring the feasibility of tDCS for TBI treatment, in which EEG was used to examine neurological alterations. Although the studies employed various stimulation strategies, the outcomes, either in terms of behavioral measurement or neuroimaging, showed positive effects. For example, the positive effects included increased excitability of the sensorimotor brain area (Ulam et al., 2015), improvement of consciousness as measured by the revised JFK coma recovery scale (Straudi et al., 2019; Zhang et al., 2020), improved auditory memory function (O'Neil-Pirozzi et al., 2017), and reduced apathy level (Zhang et al., 2020). Most of these studies employed longer-term stimulation (i.e., 3, 10, and 40 sessions) with a higher current intensity (2 mA) and delivery of the current at the prefrontal cortex. Although some of the studies used different stimulation protocols, the stimulation effect was still achieved. The underlying mechanism needs to be investigated through a comprehensive evaluation to shine a light for future work. The extracted features included the approximate entropy, power spectra (delta, theta, alpha, and beta bands), and ERP (P300), selected as the characteristics for decoding brain signals to assess interventions' effects. Among those EEG features, delta band declines were significantly associated with neuropsychological test performance following tDCS. As the evidence indicates, the EEG pattern may be correlated with the severity of brain injury. Generally, the power in the slow frequency bands (delta and theta) increased, and the high-frequency band's power was reduced. Therefore, a possible explanation is that reduction in delta band power is a biomarker for recovery from brain injury in TBI and can be considered a reversed neurological symptom. Therefore, reversed features can be biomarkers for the initial diagnosis to monitor the effects of stimulation.

DISCUSSION

In this study, we investigated the current state of tES utilizing noninvasive neuroimaging techniques (EEG and fNIRS) to monitor altered neurological activity in brain disorders, including AD, MCI, depression, ASD, ADHD, epilepsy, schizophrenia, PD, stroke, and TBI. Moreover, this study presents general guidelines for selecting stimulation parameters for tES and examining the extracted EEG/fNIRS-based features, based on the results of 67 studies with a dataset of 1,385 patients. Epilepsy (20.9%), stroke (20.9%), and depression (14.93%) were most commonly considered. Most of the studies utilized EEG as the neuroimaging technique (**Figure 4**). This study is the first work to investigate the

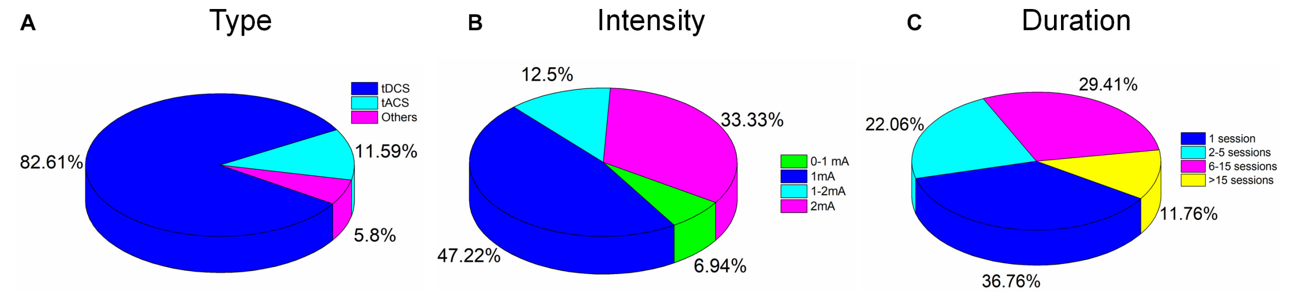

FIGURE 5 | Percentages of electrical stimulation parameters: **(A)** Type, **(B)** intensity, and **(C)** duration.

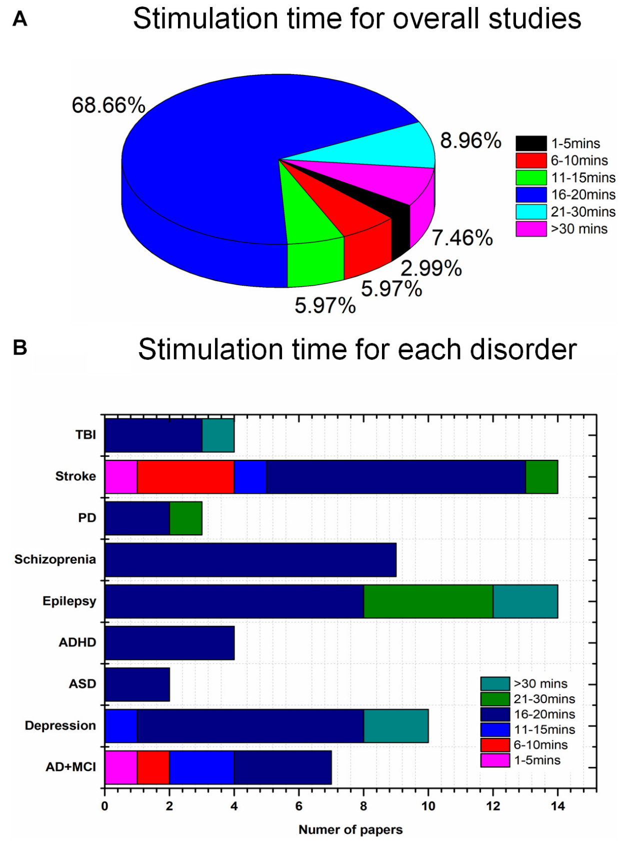

FIGURE 6 | Disease-wise stimulation time distribution (total 67 studies): **(A)** overall, **(B)** disease-wise.

integration of noninvasive neuroimaging and neuromodulation methods in nine brain disorders to the best of our knowledge.

Stimulation Modality of tES

tDCS is still a representative NIBS, and approximately 82.61% of the investigated studies employed tDCS as the stimulation modality. tACS and the other modalities accounted for 11.59 and 5.8%, respectively, as shown in **Figure 5A**. The other modalities included slow oscillation between tDCS and tRNS. There is no significant evidence to support the superiority of the treatment effect for each stimulation modality. However, some comparative studies have concluded that tACS or tRNS are the most effective NIBS methods for rehabilitating stroke (Inukai et al., 2016) or schizophrenia (Ahn et al., 2019). These claims still require validation by large sample sizes and multiple examination perspectives. Generally, tDCS cannot modulate the specific frequencies of oscillation but can induce excitability/inhibition, altering certain regions' cortical activity. Decreasing r-aminobutyric acid (GABA) and increasing glutamate/glutamine concentrations have been reported as the physiological mechanisms of tDCS (Reed and Cohen Kadosh, 2018). Declines in GABA have, in turn, been associated with the alteration of resting-state connectivity. It is consistent with studies that have demonstrated changes in functional connectivity following tDCS intervention. Unlike tDCS, tACS can entrain a large number of neuronal firing events with an exogenous frequency. Many studies have stated that tACS can selectively entrain brain oscillations. The entrainment of tACS is most effective when the endogenous oscillation is similar to the frequency of stimulation (Fröhlich and McCormick, 2010). This observation may explain the reported dependence of tACS on brain states. Similarly, altered GABA levels have been observed after tACS intervention (Nowak et al., 2017). Therefore, functional connectivity would be expected to change following stimulation. A future study could consider functional connectivity as an altered biomarker for monitoring the tES effect. The mechanism underlying tRNS, a novel tES modality for stimulating the human brain, is still not clearly understood. One research group (Inukai et al., 2016) concluded that tRNS is more effective than tDCS or tACS for inducing neural excitability. Since stimulation frequency in tRNS can vary, with normal distribution between 0.1 and 640 Hz, some researchers (Campana et al., 2016) have claimed that the opposite effect of cortical excitability would appear after low- and high-frequency stimulation. Two hypotheses have been proposed to explain physiological and pharmacological results. One states that tRNS induces random cortical activity and boosts the brain's sensitivity to further external input (Van Doren et al., 2014). Alternatively, the other hypothesis holds that repeated random stimulation prevents homeostasis in the brain and potentiates event-related neural activity (Fertonani et al., 2011). Much work remains to identify the mechanism underlying tRNS and obtain a reliable stimulation protocol.

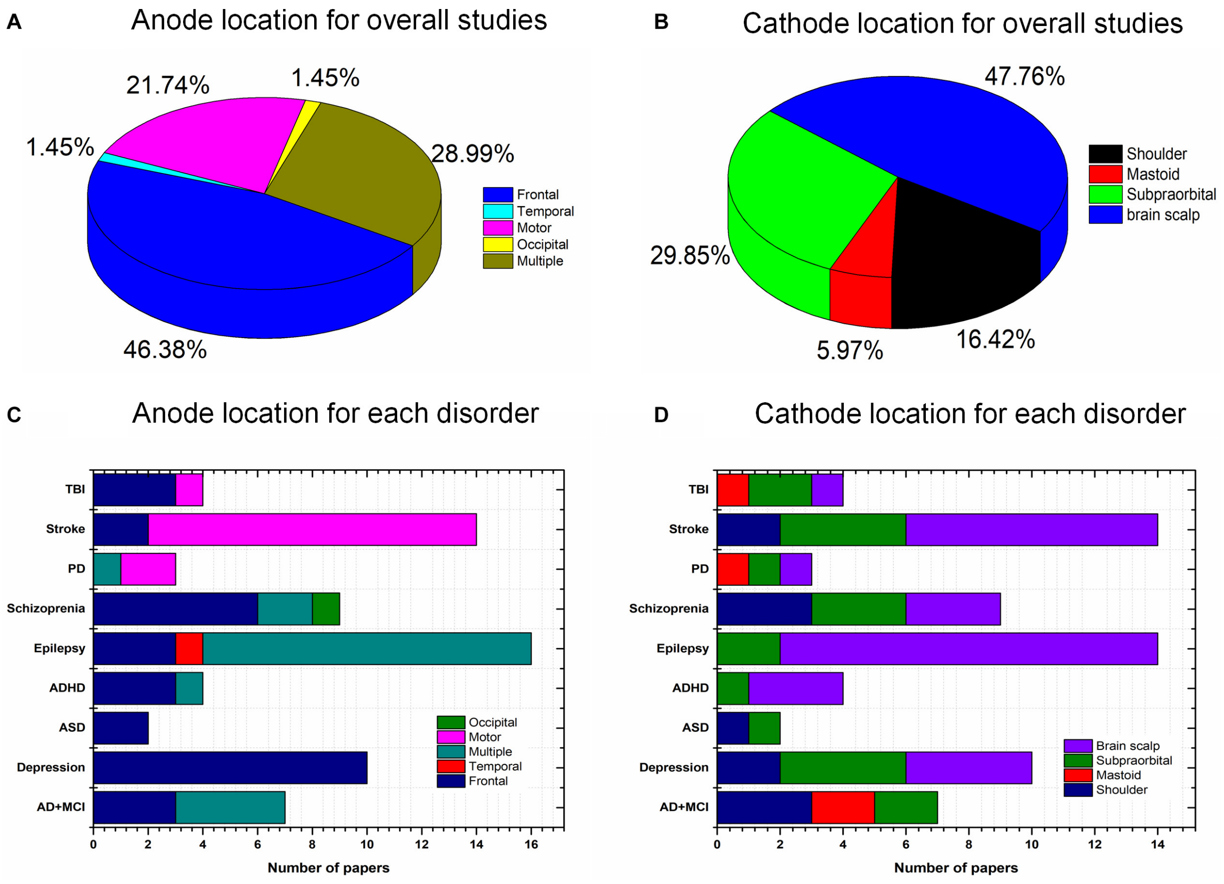

FIGURE 7 | Anode and cathode distributions: **(A)** Anode (overall), **(B)** cathode (overall), **(C)** anode locations for individual diseases, and **(D)** cathode locations for individual disorders.

Stimulation Intensity and Duration of tES

None of the 67 studies reported adverse effects. Conventionally, to avoid skin burns or irritation due to the increased temperature of the electrodes, care must be taken in the choice of stimulation parameters such as duration (<40 min) and intensity (<4 mA) (Bikson et al., 2016). Typically, for tACS and tRNS, patients experience a minimal perception of current relative to tDCS. Overall, differences in duration, intensity, location of stimulation, and combinations of these parameters and tasks performed can result in various postintervention outcomes. Stimulation intensities of 1 mA (47%) and 2 mA (33.3%) were commonly used to deliver the current in the reviewed studies, as shown in **Figure 5B**. For pediatric participants, the application of reduced current intensities (approximately 1 mA) was suggested. However, a review article with a dataset of 2,800 sessions across approximately 500 pediatric subjects reported that trials with 2 mA did not show severe adverse effects (Bikson et al., 2016). It is consistent with results for studies of children (e.g., ASD, ADHD) included in our review (**Tables 3**, **4**). There was no significant correlation between the stimulation effect and intervention duration. Most of the studies employed a 16–20-min (68.66%) or 21–30-min (8.96%) stimulation for each session, as shown in **Figure 6**. Although some of the studies applied the intervention in small time windows (<5 min), behavioral or neurological alterations could be observed. Few studies have explored and discussed the appropriate stimulation duration, either long term or short term. Most of the studies conducted tES in a single session (36.76%) or two to five sessions (22.06%), as illustrated in **Figure 5C**. One of the stroke studies (Dominguez et al., 2014) stated that more prolonged stimuli might lead to more remarkable recovery, which was not consistent with results comparing patients with AD between short- and long-term neurostimulation. In this comparative research, long-term intervention (8 months) slowed AD progression similar to the effect of the short-term intervention (10 days). It is essential to investigate whether it is necessary to apply a long-term neuromodulation session to treat each disorder. Perhaps, a closed-loop stimulation system could overcome this issue, in which the current (e.g., intensity, duration, etc.) is applied based on the real-time brain state.

Selection of Location for tES Stimulation

The placement of the anode and cathode is a crucial factor affecting the stimulation effect. Various intervention results have been achieved owing to the different stimulation locations. The frontal cortex (46.38%) has been widely used for the

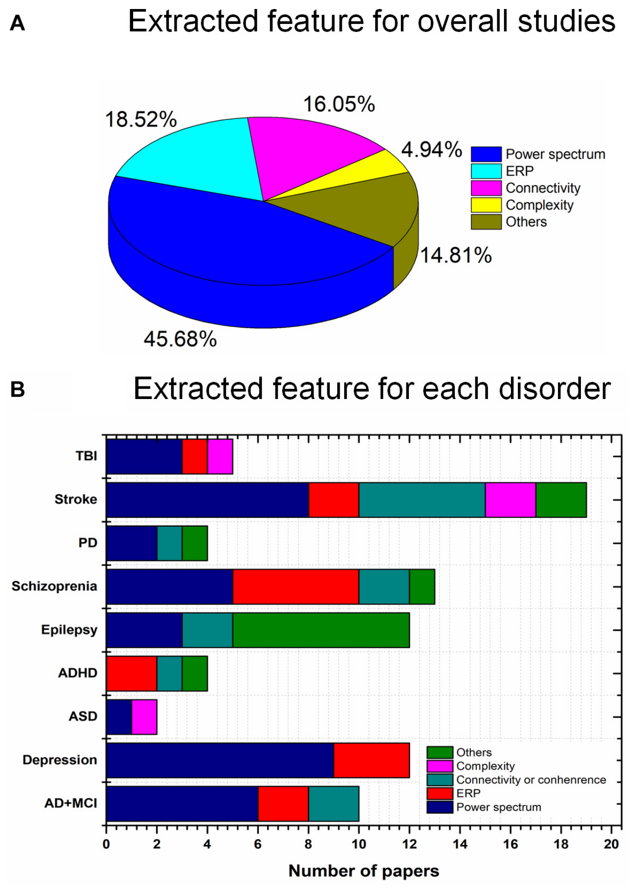

FIGURE 8 | Extracted features (total 67 studies): **(A)** overall and **(B)** individual disorders.

placement of the anode; in particular, over 80% of studies (**Figure 7**) of mental disorders (depression, ASD, ADHD, and schizophrenia) delivered current to the frontal brain region. This choice for anode location was mostly due to the specific cortical function and monitored deficits/changes in certain brain areas. For instance, the frontal cortex is used as the region of interest for mental disorders because of its importance in cognition, planning, emotional expression, decision making, and social behavior. Similarly, approximately 85% of stroke studies employed the motor cortex for stimulation due to the symptoms (i.e., trouble walking and loss of balance) in stroke patients. In studies of epilepsy, anodes are positioned in the epileptogenic focus area. Cathodes are usually placed on the supraorbital, mastoid, left/right shoulder, or brain scalp. To date, there is insufficient evidence to support the selection of cathodes to induce particular stimulation effects. Conceptually, the differences in the placement of the return electrode could result in various current trajectories. It would be interesting to investigate the proper placement of the anode and cathode for each brain disorder.

Neuroimaging in tES

Neuroimaging techniques enable monitoring brain states concerning localized neural activity and the cortical brain network, either offline or online. Neuroimaging is widely used as a monitoring/quantitative tool during or after neuromodulation to elucidate the mechanisms underlying altered symptoms (behavioral and cognitive domains) of brain disorders. It is employed to establish which stimulation protocols respond favorably in terms of symptoms and how the brain is affected from the functional and structural perspectives. Besides, the combination of neuromodulation and neuroimaging techniques enables a causal evaluation of the dynamic interactions among different brain regions (Shafi et al., 2012). As shown in **Figure 4B**, EEG was used in most tES studies as the neuroimaging method. A few studies utilized fNIRS to measure hemodynamic activity after the intervention. The extracted EEG/fNIRS-based features, such as power spectra, cortical oscillations, network complexity, and functional connectivity, could provide evidence for neuromodulatory effects. The power spectrum can describe an EEG signal's power distribution by frequency and time (Kim S. Y. et al., 2020). The commonly applied algorithm is a short-time Fourier transform and wavelet transform. Brain network complexity and connectivity reflect the information transmission status in a brain, determined by entropy analysis, Pearson correlation coefficients, spectral coherence, phase-locking values, and the phase lag index (Song et al., 2019; Fan et al., 2020). Nevertheless, EEG is limited in simultaneous use with the brain stimulation device because recorded signals affect the electric and magnetic fields. However, specific signal-processing algorithms can remove interference components, such as principal component analysis, independent component analysis, and adaptive filter

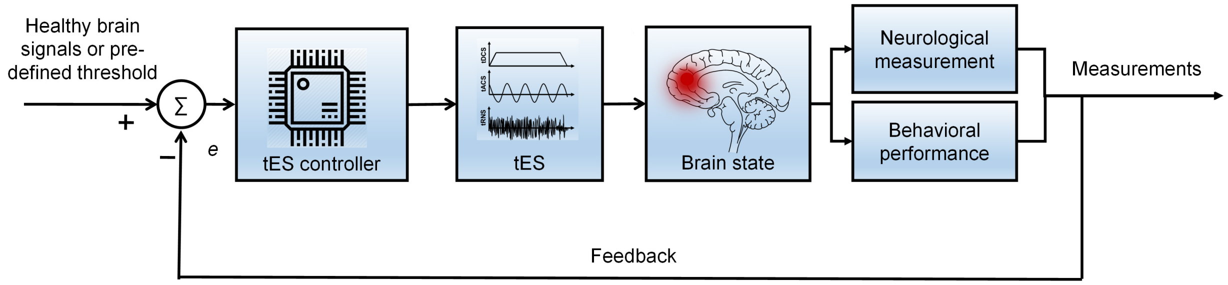

FIGURE 9 | Diagram of the proposed closed-loop tES strategy.

algorithms (Deng et al., 2019; Hong and Pham, 2019; Yoo, 2019; Park et al., 2020). Thus, a technique free of limitation, such as a noninvasive neuroimaging modality (i.e., fNIRS), as a promising method, should be considered the first choice. In addition, hybrid neuroimaging modalities have been suggested to evaluate the neuromodulation effect to seek reliable results (Kwon et al., 2020; Lee S. et al., 2020). For instance, hybrid neuroimaging modalities could improve detection accuracy and provide more compelling support from different perspectives (e.g., electrophysiological, electromagnetic, and hemodynamic) to examine cerebral reactions (Duan et al., 2019; Zhang et al., 2019; Tortora et al., 2020). Meanwhile, the neurovascular coupling can be further investigated as a biomarker for specific blood vascular diseases (e.g., stroke).

Various EEG- and fNIRS-based features were selected to quantify brain state alterations, including the power spectrum, ERP, brain connectivity, and complexity index. The power spectrum (45.68%) was widely used as the monitoring index to examine modulations' effects (**Figure 8**). Most of the studies did not explain feature selection or the mechanisms underlying altered features. Interestingly, one of the tACS studies (Del Felice et al., 2019) analyzed resting-state EEG signals in patients with PD to determine the neural oscillation deficit and brain location affected in each individual. The tACS delivered a sinusoidal fluctuating current with no frequency band to the detected location of the deficit. This investigation may offer a hint that the quantitative features for examining the effects of tES should be extracted based on diagnostic biomarkers in future studies. In other words, the diagnostic biomarker indicated abnormal features of patients relative to healthy controls. Similarly, therapy rehabilitation, in turn, should minimize this difference (diagnostic biomarkers).

Future Directions

As discussed above, brain states vary among individuals, and standard stimulation criteria are lacking. Therefore, a closed-loop brain stimulation strategy was proposed, providing a customized spatial, temporal, and parameter-specific stimulation protocol for participants based on integrating neuroimaging and neuromodulation techniques. In a strict sense, the closed-loop tES system interactively controls specific variables (current intensity, oscillation frequency, and stimulation duration) using an algorithm to adjust or minimize the error (Anna Paula et al., 2020). Error is generated between the feedback signals and the reference signals (healthy control signals and predefined thresholds) (Lv et al., 2021). Independent variable(s) can be established as any stimulation parameter(s) that need to be optimized (Xu H. et al., 2019). The overall diagram of the closed-loop stimulation is shown in **Figure 9**. Neurological information (power spectrum and hemodynamic response) and behavioral performance (working memory score and the response time for attention) could quantify the brain state as feedback signals to adjust the system. Future studies should develop a closed-loop tES system by combining different neuroimaging modalities to increase the therapy's precision and effectiveness. A meta-analysis of a specific disorder/neuroimaging modality/stimulation parameter is also recommended and could reference future studies in quantitative aspects.

CONCLUSION

This study investigated 67 studies with a total sample size of 1,385 patients to review the current state of brain disorder therapy applying tES intervention and monitored by noninvasive neuroimaging methods (EEG and fNIRS). Nine brain disorders were reviewed in this article, including AD, depression, ASD, ADHD, epilepsy, schizophrenia, PD, stroke, and TBI. This study presents a conclusive overview of the current development of tES as a neuromodulation modality for the disorders mentioned above. In addition, the summarized stimulation protocols from the 67 studies provide a reference for selecting stimulation parameters for future investigations. Moreover, a closed-loop stimulation strategy was suggested to be a customized tES therapy for patients with brain disease to achieve optimal efficacy and specificity.

AUTHOR CONTRIBUTIONS

DY conducted the literature review and wrote the first draft of the manuscript. Y-IS participated in revising the manuscript. K-SH conceived the idea, corrected the manuscript, and finalized the work. All authors have approved the final manuscript.

ACKNOWLEDGMENTS

This work was supported by the National Research Foundation (NRF) of Korea under the auspices of the Ministry of Science and ICT, Korea (Grant Nos. NRF-2017M3A9E9032772 and NRF-2020R1A2B5B03096000).

REFERENCES

Ahn, S., Mellin, J. M., Alagapan, S., Alexander, M. L., Gilmore, J. H., Jarskog, L. F., et al. (2019). Targeting reduced neural oscillations in patients with schizophrenia by transcranial alternating current stimulation. *Neuroimage* 186, 126–136. doi: 10.1016/j.neuroimage.2018.10.056

Alexander, M. L., Alagapan, S., Lugo, C. E., Mellin, J. M., Lustenberger, C., Rubinow, D. R., et al. (2019). Double-blind, randomized pilot clinical trial targeting alpha oscillations with transcranial alternating current stimulation (tACS) for the treatment of major depressive disorder (MDD). *Transl. Psychiatry* 9:106. doi: 10.1038/s41398-019-0439-0

Al-Kaysi, A. M., Al-Ani, A., Loo, C. K., Powell, T. Y., Martin, D. M., Breakspear, M., et al. (2017). Predicting tDCS treatment outcomes of patients with major depressive disorder using automated EEG classification. *J. Affect. Disord.* 208, 597–603. doi: 10.1016/j.jad.2016.10.021

Alzheimer's Association. (2020). 2020 Alzheimer's disease facts and figures. *Alzheimer's Dement.* 16, 391–460. doi: 10.1002/alz.12068

Amatachaya, A., Ensen, M. P., Patjanasoontorn, N., Auvichayapat, N., Suphakunpinyo, C., Janjarasjitt, S., et al. (2015). The short-term effects of transcranial direct current stimulation on electroencephalography in children with autism: a randomized crossover controlled trial. *Behav. Neurol.* 2015:928631.

Ang, K. K., Guan, C., Phua, K. S., Wang, C., Zhao, L., Teo, W. P., et al. (2015). Facilitating effects of transcranial direct current stimulation on motor imagery brain-computer interface with robotic feedback for stroke rehabilitation. *Arch. Phys. Med. Rehabil.* 96, S79–S87. doi: 10.1016/j.apmr.2014.08.008

Anna Paula, A. P. V., Acioli, G., and Barros, P. R. (2020). Evaluation and redesign of the inverted decoupler: open and closed-loop approaches. *Int. J. Control. Autom. Syst.* 18, 1435–1444. doi: 10.1007/s12555-019-0371-3

Aqil, M., Hong, K.-S., Jeong, M. Y., and Ge, S. S. (2012a). Cortical brain imaging by adaptive filtering of NIRS signals. *Neurosci. Lett.* 514, 35–41. doi: 10.1016/j.neulet.2012.02.048

Aqil, M., Hong, K.-S., Jeong, M. Y., and Ge, S. S. (2012b). Detection of event-related hemodynamic response to neuroactivation by dynamic modeling of brain activity. *Neuroimage* 63, 553–568. doi: 10.1016/j.neuroimage.2012.07.006

Auvichayapat, N., Rotenberg, A., Gersner, R., Ngodklang, S., Tiamkao, S., Tassaneeyakul, W., et al. (2013). Transcranial direct current stimulation for treatment of refractory childhood focal epilepsy. *Brain Stimul.* 6, 696–700. doi: 10.1016/j.brs.2013.01.009

Bao, S. C., Wong, W. W., Leung, T. W. H., and Tong, K. Y. (2019). Cortico-muscular coherence modulated by high-definition transcranial direct current stimulation in people with chronic stroke. *IEEE Trans. Neural Syst. Rehabil. Eng.* 27, 304–313. doi: 10.1109/TNSRE.2018.2890001

Beretta, V. S., Vitório, R., Nóbrega-Sousa, P., Conceição, N. R., Orcioli-Silva, D., Pereira, M. P., et al. (2020). Effect of different intensities of transcranial direct current stimulation on postural response to external perturbation in patients with parkinson's disease. *Neurorehabil. Neural Repair* 34, 1009–1019. doi: 10.1177/1545968320962513

Berger, A., Horst, F., Müller, S., Steinberg, F., and Doppelmayr, M. (2019). Current state and future prospects of EEG and fNIRS in robot-assisted gait rehabilitation: a brief review. *Front. Hum. Neurosci.* 13:172. doi: 10.3389/fnhum.2019.00172

Bikson, M., Esmaeilpour, Z., Adair, D., Kronberg, G., Tyler, W. J., Antal, A., et al. (2019). Transcranial electrical stimulation nomenclature. *Brain Stimul.* 12, 1349–1366. doi: 10.1016/j.brs.2019.07.010

Bikson, M., Grossman, P., Thomas, C., Zannou, A. L., Jiang, J., Adnan, T., et al. (2016). Safety of transcranial direct current stimulation: evidence based update 2016. *Brain Stimul.* 9, 641–661. doi: 10.1016/j.brs.2016.06.004

Boudewyn, M. A., Scangos, K., Ranganath, C., and Carter, C. S. (2020). Using prefrontal transcranial direct current stimulation (tDCS) to enhance proactive cognitive control in schizophrenia. *Neuropsychopharmacology* 45, 1877–1883. doi: 10.1038/s41386-020-0750-8

Breitling, C., Zaehle, T., Dannhauer, M., Tegelbeckers, J., Flechtner, H. H., and Krauel, K. (2020). Comparison between conventional and HD-tDCS of the right inferior frontal gyrus in children and adolescents with ADHD. *Clin. Neurophysiol.* 131, 1146–1154. doi: 10.1016/j.clinph.2019.12.412

Brunyé, T. T. (2018). Modulating spatial processes and navigation via transcranial electrical stimulation: a mini review. *Front. Hum. Neurosci.* 11:649. doi: 10.3389/fnhum.2017.00649

Brunyé, T. T., Hussey, E. K., Fontes, E. B., and Ward, N. (2019). Modulating applied task performance via transcranial electrical stimulation. *Front. Hum. Neurosci.* 13:140. doi: 10.3389/fnhum.2019.00140

Campana, G., Camilleri, R., Moret, B., Ghin, F., and Pavan, A. (2016). Opposite effects of high-and low-frequency transcranial random noise stimulation probed with visual motion adaptation. *Sci. Rep.* 6:38919. doi: 10.1038/srep38919

Cespón, J., Rodella, C., Miniussi, C., and Pellicciari, M. C. (2019). Behavioural and electrophysiological modulations induced by transcranial direct current stimulation in healthy elderly and Alzheimer's disease patients: a pilot study. *Clin. Neurophysiol.* 130, 2038–2052. doi: 10.1016/j.clinph.2019.08.016

Chou, I. H., and Chouard, T. (2008). Neuropsychiatric disease. *Nature* 455, 889–899. doi: 10.1038/455889a

Ciullo, V., Spalletta, G., Caltagirone, C., Banaj, N., Vecchio, D., Piras, F., et al. (2020). Transcranial direct current stimulation and cognition in neuropsychiatric disorders: systematic review of the evidence and future directions. *Neuroscientist* [Epub ahead of print] doi: 10.1177/1073858420936167

Cosmo, C., Baptista, A. F., De Araújo, A. N., Do Rosário, R. S., Miranda, J. G. V., Montoya, P., et al. (2015a). A randomized, double-blind, sham-controlled trial of transcranial direct current stimulation in attention-deficit/hyperactivity disorder. *PLoS One* 10:e0135371. doi: 10.1371/journal.pone.0135371

Cosmo, C., Ferreira, C., Miranda, J. G. V., do Rosário, R. S., do, Baptista, A. F., et al. (2015b). Spreading effect of tDCS in individuals with attention-deficit/hyperactivity disorder as shown by functional cortical networks: a randomized, double-blind, sham-controlled trial. *Front. Psychiatry* 6:111. doi: 10.3389/fpsyt.2015.00111

D'Agata, F., Peila, E., Cicerale, A., Caglio, M. M., Caroppo, P., Vighetti, S., et al. (2016). Cognitive and neurophysiological effects of non-invasive brain stimulation in stroke patients after motor rehabilitation. *Front. Behav. Neurosci.* 10:135. doi: 10.3389/fnbeh.2016.00135

Dallmer-Zerbe, I., Popp, F., Lam, A. P., Philipsen, A., and Herrmann, C. S. (2020). Transcranial alternating current stimulation (tacs) as a tool to modulate p300 amplitude in attention deficit hyperactivity disorder (ADHD): preliminary findings. *Brain Topogr.* 33, 191–207. doi: 10.1007/s10548-020-00752-x

Davis, S. E., and Smith, G. A. (2019). Transcranial direct current stimulation use in warfighting: benefits, risks, and future prospects. *Front. Hum. Neurosci.* 13:114. doi: 10.3389/fnhum.2019.00114

Del Felice, A., Castiglia, L., Formaggio, E., Cattelan, M., Scarpa, B., Manganotti, P., et al. (2019). Personalized transcranial alternating current stimulation (tACS) and physical therapy to treat motor and cognitive symptoms in Parkinson's disease: a randomized cross-over trial. *NeuroImage Clin.* 22:101768. doi: 10.1016/j.nicl.2019.101768

Del Felice, A., Magalini, A., and Masiero, S. (2015). Slow-oscillatory transcranial direct current stimulation modulates memory in temporal lobe epilepsy by altering sleep spindle generators: a possible rehabilitation tool. *Brain Stimul.* 8, 567–573. doi: 10.1016/j.brs.2015.01.410

Deng, F., Yang, H. L., and Wang, L. J. (2019). Adaptive unscented Kalman filter based estimation and filtering for dynamic positioning with model uncertainties. *Int. J. Control. Autom. Syst.* 17, 667–678. doi: 10.1007/s12555-018-9503-4

Devinsky, O., Vezzani, A., O'Brien, T. J., Jette, N., Scheffer, I. E., De Curtis, M., et al. (2018). Epilepsy. *Nat. Rev. Dis. Prim.* 4:18024. doi: 10.1038/nrdp.2018.24

Dominguez, A., Socas, R., Marrero, H., Leon, N., LLabres, J., and Enriquez, E. (2014). Transcranial direct current stimulation improves word production in conduction aphasia: electroencephalographic and behavioral evidences. *Int. J. Clin. Heal. Psychol.* 14, 240–245. doi: 10.1016/j.ijchp.2014.02.001

Duan, X., Xie, S., Xie, X., Meng, Y., and Xu, Z. (2019). Quadcopter flight control using a non-invasive multi-modal brain computer interface. *Front. Neurorobot.* 13:23. doi: 10.3389/fnbot.2019.00023

Dubreuil-Vall, L., Chau, P., Ruffini, G., Widge, A. S., and Camprodon, J. A. (2019). tDCS to the left DLPFC modulates cognitive and physiological correlates of executive function in a state-dependent manner. *Brain Stimul.* 12, 1456–1463. doi: 10.1016/j.brs.2019.06.006

Dunn, W., Rassovsky, Y., Wynn, J. K., Wu, A. D., Iacoboni, M., Hellemann, G., et al. (2016). Modulation of neurophysiological auditory processing measures by bilateral transcranial direct current stimulation in schizophrenia. *Schizophr. Res.* 174, 189–191. doi: 10.1016/j.schres.2016.04.021

Dutta, A., Jacob, A., Chowdhury, S. R., Das, A., and Nitsche, M. A. (2015). EEG-NIRS based assessment of neurovascular coupling during anodal transcranial direct current stimulation - a stroke case series. *J. Med. Syst.* 39:205. doi: 10.1007/s10916-015-0205-7

Emonson, M. R. L., Fitzgerald, P. B., Rogasch, N. C., and Hoy, K. E. (2019). Neurobiological effects of transcranial direct current stimulation in younger adults, older adults and mild cognitive impairment. *Neuropsychologia* 125, 51–61. doi: 10.1016/j.neuropsychologia.2019.01.003

Ermolova, M., Belyaeva, V., Novikov, N., Gutkin, B., Feurra, M., and Fedele, T. (2019). Changes in neuronal oscillations account for working memory dynamics: EEG-tACS study. *Brain Stimul.* 12:e168. doi: 10.1016/j.brs.2019.06.007

Fan, Y., Chen, J., Song, C., and Wang, Y. (2020). Event-triggered coordination control for multi-agent systems with connectivity preservation. *Int. J. Control. Autom. Syst.* 18, 966–979. doi: 10.1007/s12555-018-0700-y

Faria, P., Fregni, F., Sebastião, F., Dias, A. I., and Leal, A. (2012). Feasibility of focal transcranial DC polarization with simultaneous EEG recording: preliminary assessment in healthy subjects and human epilepsy. *Epilepsy Behav.* 25, 417–425. doi: 10.1016/j.yebeh.2012.06.027

Feigin, V. L., Nichols, E., Alam, T., Bannick, M. S., Beghi, E., Blake, N., et al. (2019). Global, regional, and national burden of neurological disorders, 1990–2016: a systematic analysis for the Global Burden of Disease Study 2016. *Lancet Neurol.* 18, 459–480. doi: 10.1016/S1474-4422(18)30499-X

Feigin, V. L., Vos, T., Nichols, E., Owolabi, M. O., Carroll, W. M., Dichgans, M., et al. (2020). The global burden of neurological disorders: translating evidence into policy. *Lancet Neurol.* 19, 255–265. doi: 10.1016/S1474-4422(19)30411-9

Feng, W., Halm-Lutterodt, N., Van, Tang, H., Mecum, A., Mesregah, M. K., et al. (2020). Automated RI-based deep learning model for detection of Alzheimer's disease process. *Int. J. Neural Syst.* 30:2050032. doi: 10.1142/S012906572050032X

Ferguson, B. R., and Gao, W. J. (2018). Pv interneurons: critical regulators of E/I balance for prefrontal cortex-dependent behavior and psychiatric disorders. *Front. Neural Circuits* 12:37. doi: 10.3389/fncir.2018.00037

Ferrucci, R., Mrakic-Sposta, S., Gardini, S., Ruggiero, F., Vergari, M., Mameli, F., et al. (2018). Behavioral and neurophysiological effects of transcranial direct current stimulation (tDCS) in fronto-temporal dementia. *Front. Behav. Neurosci.* 12:235. doi: 10.3389/fnbeh.2018.00235

Fertonani, A., Pirulli, C., and Miniussi, C. (2011). Random noise stimulation improves neuroplasticity in perceptual learning. *J. Neurosci.* 31, 15416–15423. doi: 10.1523/JNEUROSCI.2002-11.2011

Fregni, F., and Pascual-Leone, A. (2007). Technology insight: non-invasive brain stimulation in neurology - perspectives on the therapeutic potential of rTMS and tDCS. *Nat. Clin. Pract. Neurol.* 3, 383–393. doi: 10.1038/ncpneuro0530

Fregni, F., Thome-Souza, S., Nitsche, M. A., Freedman, S. D., Valente, K. D., and Pascual-Leone, A. (2006). A controlled clinical trial of cathodal DC polarization in patients with refractory epilepsy. *Epilepsia* 47, 335–342. doi: 10.1111/j.1528-1167.2006.00426.x

Fröhlich, F., and McCormick, D. A. (2010). Endogenous electric fields may guide neocortical network activity. *Neuron* 67, 129–143. doi: 10.1016/j.neuron.2010.06.005

Gangemi, A., Colombo, B., and Fabio, R. A. (2020). Effects of short- and long-term neurostimulation (tDCS) on Alzheimer's disease patients: two randomized studies. *Aging Clin. Exp. Res.* 33, 383–390. doi: 10.1007/s40520-020-01546-8

Ghafoor, U., Lee, J. H., Hong, K.-S., Park, S. S., Kim, J., and Yoo, H. R. (2019). Effects of acupuncture therapy on MCI patients using functional near-infrared spectroscopy. *Front. Aging Neurosci.* 11:237. doi: 10.3389/fnagi.2019.00237

Górriz, J. M., Ramírez, J., Segovia, F., Martínez, F. J., Lai, M. C., Lombardo, M. V., et al. (2019). A machine learning approach to reveal the neurophenotypes of autisms. *Int. J. Neural Syst.* 29:1850058. doi: 10.1142/S0129065718500582

Hong, K.-S., Ghafoor, U., and Khan, M. J. (2020). Brain–machine interfaces using functional near-infrared spectroscopy: a review. *Artif. Life Robot.* 25, 204–218. doi: 10.1007/s10015-020-00592-9

Hong, K.-S., and Khan, M. J. (2017). Hybrid brain-computer interface techniques for improved classification accuracy and increased number of commands: a review. *Front. Neurorobot.* 11:35. doi: 10.3389/fnbot.2017.00035

Hong, K.-S., and Pham, P. T. (2019). Control of axially moving systems: a review. *Int. J. Control. Autom. Syst.* 17, 2983–3008. doi: 10.1007/s12555-019-0592-5

Hong, K.-S., and Yaqub, M. A. (2019). Application of functional near-infrared spectroscopy in the healthcare industry: a review. *J. Innov. Opt. Health Sci.* 12:1930012. doi: 10.1142/S179354581930012X

Hordacre, B., Moezzi, B., and Ridding, M. C. (2018). Neuroplasticity and network connectivity of the motor cortex following stroke: a transcranial direct current stimulation study. *Hum. Brain Mapp.* 39, 3326–3339. doi: 10.1002/hbm.24079

Hoy, K. E., Bailey, N. W., Arnold, S. L., and Fitzgerald, P. B. (2015). The effect of transcranial direct current stimulation on gamma activity and working memory in schizophrenia. *Psychiatry Res.* 228, 191–196. doi: 10.1016/j.psychres.2015.04.032

Hu, X., Zhuang, C., Wang, F., Liu, Y. J., Im, C. H., and Zhang, D. (2019). FNIRS evidence for recognizably different positive emotions. *Front. Hum. Neurosci.* 13:120. doi: 10.3389/fnhum.2019.00120

Impey, D., Baddeley, A., Nelson, R., Labelle, A., and Knott, V. (2017). Effects of transcranial direct current stimulation on the auditory mismatch negativity response and working memory performance in schizophrenia: a pilot study. *J. Neural Transm.* 124, 1489–1501. doi: 10.1007/s00702-017-1783-y

Inukai, Y., Saito, K., Sasaki, R., Tsuiki, S., Miyaguchi, S., Kojima, S., et al. (2016). Comparison of three non-invasive transcranial electrical stimulation methods for increasing cortical excitability. *Front. Hum. Neurosci.* 10:668. doi: 10.3389/fnhum.2016.00668

Irani, F., Platek, S. M., Bunce, S., Ruocco, A. C., and Chute, D. (2007). Functional near infrared spectroscopy (fNIRS): an emerging neuroimaging technology with important applications for the study of brain disorders. *Clin. Neuropsychol.* 21, 9–37. doi: 10.1080/13854040600910018

Jahshan, C., Wynn, J. K., Roach, B. J., Mathalon, D. H., and Green, M. F. (2020). Effects of transcranial direct current stimulation on visual neuroplasticity in schizophrenia. *Clin. EEG Neurosci.* 51, 382–389. doi: 10.1177/1550059420925697

Jindal, U., Sood, M., Dutta, A., and Chowdhury, S. R. (2015). Development of point of care testing device for neurovascular coupling from simultaneous recording of EEG and NIRS during anodal transcranial direct current stimulation. *IEEE J. Transl. Eng. Heal. Med.* 3:2000112. doi: 10.1109/JTEHM.2015.2389230

Kang, J., Cai, E., Han, J., Tong, Z., Li, X., Sokhadze, E. M., et al. (2018). Transcranial direct current stimulation (tDCS) can modulate EEG complexity of children with autism spectrum disorder. *Front. Neurosci.* 12, AN:201. doi: 10.3389/fnins.2018.00201

Karvigh, S. A., Motamedi, M., Arzani, M., and Roshan, J. H. N. (2017). HD-tDCS in refractory lateral frontal lobe epilepsy patients. *Seizure* 47, 74–80. doi: 10.1016/j.seizure.2017.03.005

Kasashima, Y., Fujiwara, T., Matsushika, Y., Tsuji, T., Hase, K., Ushiyama, J., et al. (2012). Modulation of event-related desynchronization during motor imagery with transcranial direct current stimulation (tDCS) in patients with chronic hemiparetic stroke. *Exp. Brain Res.* 221, 263–268. doi: 10.1007/s00221-012-3166-9

Kasashima-Shindo, Y., Fujiwara, T., Ushiba, J., Matsushika, Y., Kamatani, D., Oto, M., et al. (2015). Brain-computer interface training combined with transcranial direct current stimulation in patients with chronic severe hemiparesis: proof of concept study. *J. Rehabil. Med.* 47, 318–324. doi: 10.2340/16501977-1925

Kayarian, F. B., Jannati, A., Rotenberg, A., and Santarnecchi, E. (2020). Targeting gamma−related pathophysiology in autism spectrum disorder using transcranial electrical stimulation: opportunities and challenges. *Autism Res.* 13, 1051–1071. doi: 10.1002/aur.2312

Khan, M. J., and Hong, K.-S. (2017). Hybrid EEG-FNIRS-based eight-command decoding for BCI: application to quadcopter control. *Front. Neurorobot.* 11:6. doi: 10.3389/fnbot.2017.00006

Khayyer, Z., Ngaosuvan, L., Sikström, S., and Ghaderi, A. H. (2018). Transcranial direct current stimulation based on quantitative electroencephalogram combining positive psychotherapy for major depression. *J. Integr. Neurosci.* 17, 141–155. doi: 10.3233/JIN-170045

Kim, E., Meinhold, W., Shinohara, M., and Ueda, J. (2020). Statistical inter-stimulus interval window estimation for transient neuromodulation via paired mechanical and brain stimulation. *Front. Neurorobot.* 14:1. doi: 10.3389/fnbot.2020.00001

Kim, M., Kim, M. K., Hwang, M., Kim, H. Y., Cho, J., and Kim, S. P. (2019). Online home appliance control using EEG-Based brain–computer interfaces. *Electronics* 8:1101. doi: 10.3390/electronics8101101

Kim, S. Y., Kang, C. H., and Park, C. G. (2020). Multiple frequency tracking and mitigation based on RSPWVD and adaptive multiple linear kalman notch filter. *Int. J. Control. Autom. Syst.* 18, 1139–1149. doi: 10.1002/navi.332

Kwon, J., Shin, J., and Im, C. H. (2020). Toward a compact hybrid brain-computer interface (BCI): performance evaluation of multi-class hybrid EEG-fNIRS BCIs with limited number of channels. *PLoS One* 15:e0230491. doi: 10.1371/journal.pone.0230491

Ladenbauer, J., Ladenbauer, J., Külzowä, N., De Boor, R., Avramova, E., Grittner, U., et al. (2017). Promoting sleep oscillations and their functional coupling by transcranial stimulation enhances memory consolidation in mild cognitive impairment. *J. Neurosci.* 37, 7111–7124. doi: 10.1523/JNEUROSCI.0260-17.2017

Lee, S., Lee, T., Yang, T., Yoon, C., and Kim, S. P. (2020). Detection of drivers' anxiety invoked by driving situations using multimodal biosignals. *Processes* 8:155. doi: 10.3390/pr8020155

Lee, T., Kim, M., and Kim, S. (2020). Improvement of P300-based brain–computer interfaces for home appliances control by data balancing techniques. *Sensors* 20:5576. doi: 10.3390/s20195576

Li, C. T., Chen, M. H., Juan, C. H., Liu, R. S., Lin, W. C., Bai, Y. M., et al. (2018). Effects of prefrontal theta-burst stimulation on brain function in treatment-resistant depression: a randomized sham-controlled neuroimaging study. *Brain Stimul.* 11, 1054–1062. doi: 10.1016/j.brs.2018.04.014

Li, H., Zhu, N., Klomparens, E. A., Xu, S., Wang, M., Wang, Q., et al. (2019). Application of functional near-infrared spectroscopy to explore the neural mechanism of transcranial direct current stimulation for post-stroke depression. *Neurol. Res.* 41, 714–721. doi: 10.1080/01616412.2019.1612539

Lin, L. C., Ouyang, C., Sen, Chiang, C. T., Yang, R. C., Wu, R. C., et al. (2018). Cumulative effect of transcranial direct current stimulation in patients with partial refractory epilepsy and its association with phase lag index-A preliminary study. *Epilepsy Behav.* 84, 142–147. doi: 10.1016/j.yebeh.2018.04.017

Liu, A., Bryant, A., Jefferson, A., Friedman, D., Minhas, P., Barnard, S., et al. (2016). Exploring the efficacy of a 5-day course of transcranial direct current stimulation (TDCS) on depression and memory function in patients with well-controlled temporal lobe epilepsy. *Epilepsy Behav.* 55, 11–20. doi: 10.1016/j.yebeh.2015.10.032

Lv, X., Fang, Y., Mao, Z., Jiang, B., and Qi, R. (2021). Fault detection for a class of closed-loop hypersonic vehicle system via hypothesis test method. *Int. J. Control. Autom. Syst.* 19, 350–362. doi: 10.1007/s12555-019-0906-7

Mane, R., Chew, E., Phua, K. S., Ang, K. K., Robinson, N., Vinod, A. P., et al. (2019). Prognostic and monitory EEG-biomarkers for BCI upper-limb stroke rehabilitation. *IEEE Trans. Neural Syst. Rehabil. Eng.* 27, 1654–1664. doi: 10.1109/TNSRE.2019.2924742

Marceglia, S., Mrakic-Sposta, S., Rosa, M., Ferrucci, R., Mameli, F., Vergari, M., et al. (2016). Transcranial direct current stimulation modulates cortical neuronal activity in Alzheimer's disease. *Front. Neurosci.* 10:134. doi: 10.3389/fnins.2016.00134

Meiron, O., Gale, R., Namestnic, J., Bennet-Back, O., David, J., Gebodh, N., et al. (2018). High-definition transcranial direct current stimulation in early onset epileptic encephalopathy: a case study. *Brain Inj.* 32, 135–143. doi: 10.1080/02699052.2017.1390254

Meiron, O., Gale, R., Namestnic, J., Bennet-Back, O., Gebodh, N., Esmaeilpour, Z., et al. (2019). Antiepileptic effects of a novel non-invasive neuromodulation treatment in a subject with early-onset epileptic encephalopathy: case report with 20 sessions of HDTDCS intervention. *Front. Neurosci.* 13:547. doi: 10.3389/fnins.2019.00547

Naro, A., Corallo, F., De Salvo, S., Marra, A., Di Lorenzo, G., Muscarà, N., et al. (2016). Promising role of neuromodulation in predicting the progression of mild cognitive impairment to dementia. *J. Alzheimer's Dis.* 53, 1375–1388. doi: 10.3233/JAD-160305

Naros, G., and Gharabaghi, A. (2017). Physiological and behavioral effects of β-tACS on brain self-regulation in chronic stroke. *Brain Stimul.* 10, 251–259. doi: 10.1016/j.brs.2016.11.003

Naseer, N., and Hong, K.-S. (2013). Classification of functional near-infrared spectroscopy signals corresponding to the right- and left-wrist motor imagery for development of a brain-computer interface. *Neurosci. Lett.* 553, 84–89. doi: 10.1016/j.neulet.2013.08.021

Naseer, N., and Hong, K.-S. (2015). fNIRS-based brain-computer interfaces: a review. *Front. Hum. Neurosci.* 9:3. doi: 10.3389/fnhum.2015.00003

Nguyen, H.-D., Hong, K.-S., and Shin, Y.-I. (2016). Bundled-optode method in functional near-infrared spectroscopy. *PLoS One* 11:e0165146. doi: 10.1371/journal.pone.0165146

Nicolo, P., Magnin, C., Pedrazzini, E., Plomp, G., Mottaz, A., Schnider, A., et al. (2018). Comparison of Neuroplastic responses to cathodal transcranial direct current stimulation and continuous theta burst stimulation in subacute stroke. *Arch. Phys. Med. Rehabil.* 99, 862.e1–872.e1. doi: 10.1016/j.apmr.2017.10.026

Nikolin, S., Martin, D., Loo, C. K., Iacoviello, B. M., and Boonstra, T. W. (2020). Assessing neurophysiological changes associated with combined transcranial direct current stimulation and cognitive-emotional training for treatment-resistant depression. *Eur. J. Neurosci.* 51, 2119–2133. doi: 10.1111/ejn.14656

Nishida, K., Koshikawa, Y., Morishima, Y., Yoshimura, M., Katsura, K., Ueda, S., et al. (2019). Pre-stimulus brain activity is associated with state-anxiety changes during single-session transcranial direct current stimulation. *Front. Hum. Neurosci.* 13:266. doi: 10.3389/fnhum.2019.00266

Nitsche, M. A., Cohen, L. G., Wassermann, E. M., Priori, A., Lang, N., Antal, A., et al. (2008). Transcranial direct current stimulation: state of the art 2008. *Brain Stimul.* 1, 206–223. doi: 10.1016/j.brs.2008.06.004

Nowak, M., Hinson, E., Van Ede, F., Pogosyan, A., Guerra, A., Quinn, A., et al. (2017). Driving human motor cortical oscillations leads to behaviorally relevant changes in local GABAA inhibition: a tACS-TMS study. *J. Neurosci.* 37, 4481–4492. doi: 10.1523/JNEUROSCI.0098-17.2017

Olejarczyk, E., Zuchowicz, U., Wozniak-Kwasniewska, A., Kaminski, M., Szekely, D., and David, O. (2020). The impact of repetitive transcranial magnetic stimulation on functional connectivity in major depressive disorder and bipolar disorder evaluated by directed transfer function and indices based on graph theory. *Int. J. Neural Syst.* 30:2050015. doi: 10.1142/S012906572050015X

O'Neil-Pirozzi, T. M., Doruk, D., Thomson, J. M., and Fregni, F. (2017). Immediate memory and electrophysiologic effects of prefrontal cortex transcranial direct current stimulation on neurotypical individuals and individuals with chronic traumatic brain injury: a pilot study. *Int. J. Neurosci.* 127, 592–600. doi: 10.1080/00207454.2016.1216415

Palm, U., Keeser, D., Schiller, C., Fintescu, Z., Reisinger, E., Baghai, T. C., et al. (2009). Transcranial direct current stimulation in a patient with therapy-resistant major depression. *World J. Biol. Psychiatry* 10, 632–635. doi: 10.1080/15622970802480905

Park, B. J., Pham, P. T., and Hong, K. S. (2020). Model reference robust adaptive control of control element drive mechanism in a nuclear power plant. *Int. J. Control. Autom. Syst.* 18, 1651–1661. doi: 10.1007/s12555-019-0987-3

Pasquinelli, C., Hanson, L. G., Siebner, H. R., Lee, H. J., and Thielscher, A. (2019). Safety of transcranial focused ultrasound stimulation: a systematic review of the state of knowledge from both human and animal studies. *Brain Stimul.* 12, 1367–1380. doi: 10.1016/j.brs.2019.07.024

Patel, K. R., Cherian, J., Gohil, K., and Atkinson, D. (2014). Schizophrenia: overview and treatment options. *P T* 39, 638–645.

Polanía, R., Nitsche, M. A., and Ruff, C. C. (2018). Studying and modifying brain function with non-invasive brain stimulation. *Nat. Neurosci.* 21, 174–187. doi: 10.1038/s41593-017-0054-4

Posner, J., Polanczyk, G. V., and Sonuga-Barke, E. (2020). Attention-deficit hyperactivity disorder. *Lancet* 395, 450–462. doi: 10.1016/S0140-6736(19)33004-1

Powell, T. Y., Boonstra, T. W., Martin, D. M., Loo, C. K., and Breakspear, M. (2014). Modulation of cortical activity by transcranial direct current stimulation in patients with affective disorder. *PLoS One* 9:0098503. doi: 10.1371/journal.pone.0098503

Rashid, M., Sulaiman, N., Abdul Majeed, A., Musa, R. M., Ahmad, A. F., Bari, B. S., et al. (2020). Current status, challenges, and possible solutions of EEG-based brain-computer interface: a comprehensive review. *Front. Neurorobot.* 14:25. doi: 10.3389/fnbot.2020.00025

Rassovsky, Y., Dunn, W., Wynn, J. K., Wu, A. D., Iacoboni, M., Hellemann, G., et al. (2018). Single transcranial direct current stimulation in schizophrenia: randomized, cross-over study of neurocognition, social cognition. ERPs, and side effects. *PLoS One* 13:e0197023. doi: 10.1371/journal.pone.0197023

Reed, T., and Cohen Kadosh, R. (2018). Transcranial electrical stimulation (tES) mechanisms and its effects on cortical excitability and connectivity. *J. Inherit. Metab. Dis.* 41, 1123–1130. doi: 10.1007/s10545-018-0181-4

Reinhart, R. M. G., Zhu, J., Park, S., and Woodman, G. F. (2015). Synchronizing theta oscillations with direct-current stimulation strengthens adaptive control in the human brain. *Proc. Natl. Acad. Sci. U.S.A.* 112, 9448–9453. doi: 10.1073/pnas.1504196112

San-Juan, D., Espinoza López, D. A., Vázquez Gregorio, R., Trenado, C., Fernández-González Aragón, M., Morales-Quezada, L., et al. (2017). Transcranial direct current stimulation in mesial temporal lobe epilepsy and hippocampal sclerosis. *Brain Stimul.* 10, 28–35. doi: 10.1016/j.brs.2016.08.013

San-Juan, D., Sarmiento, C. I., Hernandez-Ruiz, A., Elizondo-Zepeda, E., Santos-Vázquez, G., Reyes-Acevedo, G., et al. (2016). Transcranial alternating current stimulation: a potential risk for genetic generalized epilepsy patients (study case). *Front. Neurol.* 7:213. doi: 10.3389/fneur.2016.00213

Scheffer, M., Bascompte, J., Brock, W. A., Brovkin, V., Carpenter, S. R., Dakos, V., et al. (2009). Early-warning signals for critical transitions. *Nature* 461, 53–59. doi: 10.1038/nature08227

Schoellmann, A., Scholten, M., Wasserka, B., Govindan, R. B., Krüger, R., Gharabaghi, A., et al. (2019). Anodal tDCS modulates cortical activity and synchronization in Parkinson's disease depending on motor processing. *NeuroImage Clin.* 22:101689. doi: 10.1016/j.nicl.2019.101689

Schulz, R., Gerloff, C., and Hummel, F. C. (2013). Non-invasive brain stimulation in neurological diseases. *Neuropharmacology* 64, 579–587. doi: 10.1016/j.neuropharm.2012.05.016

Shafi, M. M., Westover, M. B., Fox, M. D., and Pascual-Leone, A. (2012). Exploration and modulation of brain network interactions with non-invasive brain stimulation in combination with neuroimaging. *Eur. J. Neurosci.* 35, 805–825. doi: 10.1111/j.1460-9568.2012.08035.x

Shahsavar, Y., Ghoshuni, M., and Talaei, A. (2018). Quantifying clinical improvements in patients with depression under the treatment of transcranial direct current stimulation using event related potentials. *Australas. Phys. Eng. Sci. Med.* 41, 973–983. doi: 10.1007/s13246-018-0696-x

Shin, J. (2020). Random subspace ensemble learning for functional near-infrared spectroscopy brain-computer interfaces. *Front. Hum. Neurosci.* 14:236. doi: 10.3389/fnhum.2020.00236

Smith, R. C., Boules, S., Mattiuz, S., Youssef, M., Tobe, R. H., Sershen, H., et al. (2015). Effects of transcranial direct current stimulation (tDCS) on cognition, symptoms, and smoking in schizophrenia: a randomized controlled study. *Schizophr. Res.* 168, 260–266. doi: 10.1016/j.schres.2015.06.011

Singh, A., Trapp, N. T., De Corte, B., Cao, S., Kingyon, J., Boes, A. D., et al. (2019). Cerebellar theta frequency transcranial pulsed stimulation increases frontal theta oscillations in patients with schizophrenia. *Cerebellum* 18, 489–499. doi: 10.1007/s12311-019-01013-9

Song, Y., Park, J., Lee, K. C., and Lee, S. (2019). Reducing the design complexity of automated vehicle electrical and electronic systems using a cyber-physical system concept. *Int. J. Control. Autom. Syst.* 17, 500–508. doi: 10.1007/s12555-018-0246-z

Straudi, S., Bonsangue, V., Mele, S., Craighero, L., Montis, A., Fregni, F., et al. (2019). Bilateral M1 anodal transcranial direct current stimulation in post traumatic chronic minimally conscious state: a pilot EEG-tDCS study. *Brain Inj.* 33, 490–495. doi: 10.1080/02699052.2019.1565894

Sugata, H., Yagi, K., Yazawa, S., Nagase, Y., Tsuruta, K., Ikeda, T., et al. (2018). Modulation of motor learning capacity by transcranial alternating current stimulation. *Neuroscience* 391, 131–139. doi: 10.1016/j.neuroscience.2018.09.013

Tanveer, M. A., Khan, M. J., Qureshi, M. J., Naseer, N., and Hong, K. S. (2019). Enhanced drowsiness detection using deep learning: an fNIRS Study. *IEEE Access.* 7, 137920–137929. doi: 10.1109/ACCESS.2019.2942838

Tecchio, F., Cottone, C., Porcaro, C., Cancelli, A., Lazzaro, V., Di, et al. (2018). Brain functional connectivity changes after transcranial direct current stimulation in epileptic patients. *Front. Neural Circuits* 12:044. doi: 10.3389/fncir.2018.00044

Tekturk, P., Erdogan, E. T., Kurt, A., Vanli-yavuz, E. N., Ekizoglu, E., Kocagoncu, E., et al. (2016). The effect of transcranial direct current stimulation on seizure frequency of patients with mesial temporal lobe epilepsy with hippocampal sclerosis. *Clin. Neurol. Neurosurg.* 149, 27–32. doi: 10.1016/j.clineuro.2016.07.014

Tortora, S., Tonin, L., Chisari, C., Micera, S., Menegatti, E., and Artoni, F. (2020). Hybrid human-machine interface for gait decoding through Bayesian fusion of EEG and EMG classifiers. *Front. Neurorobot.* 14:582728. doi: 10.3389/fnbot.2020.582728

Ulam, F., Shelton, C., Richards, L., Davis, L., Hunter, B., Fregni, F., et al. (2015). Cumulative effects of transcranial direct current stimulation on EEG oscillations and attention/working memory during subacute neurorehabilitation of traumatic brain injury. *Clin. Neurophysiol.* 126, 486–496. doi: 10.1016/j.clinph.2014.05.015

Van Doren, J., Langguth, B., and Schecklmann, M. (2014). Electroencephalographic effects of transcranial random noise stimulation in the auditory cortex. *Brain Stimul.* 7, 807–812. doi: 10.1016/j.brs.2014.08.007

Vosskuhl, J., Strüber, D., and Herrmann, C. S. (2018). Non-invasive brain stimulation: a paradigm shift in understanding brain oscillations. *Front. Hum. Neurosci.* 12:211. doi: 10.3389/fnhum.2018.00211

Vuksanović, V., Staff, R. T., Ahearn, T., Murray, A. D., and Wischik, C. M. (2019). Cortical thickness and surface area networks in healthy aging, Alzheimer's disease and behavioral variant fronto-temporal dementia. *Int. J. Neural Syst.* 29:1850055. doi: 10.1142/S0129065718500557

World Health Organization (2018). *Mental Health Atlas 2017*. Geneva: World Health Organization.

Wu, D., Wang, J., and Yuan, Y. (2015). Effects of transcranial direct current stimulation on naming and cortical excitability in stroke patients with aphasia. *Neurosci. Lett.* 589, 115–120. doi: 10.1016/j.neulet.2015.01.045

Xu, H., Ding, F., Alsaedi, A., and Hayat, T. (2019). Recursive identification algorithms for a class of linear closed-loop systems. *Int. J. Control Autom. Syst.* 17, 3194–3204. doi: 10.1007/s12555-018-0640-6

Xu, J., Wang, J., Bai, T., Zhang, X., Li, T., Hu, Q., et al. (2019). Electroconvulsive therapy induces cortical morphological alterations in major depressive disorder revealed with surface-based morphometry analysis. *Int. J. Neural Syst.* 29:1950005. doi: 10.1142/S0129065719500059

Yang, D., Du, Q., Huang, Z., Li, L., Zhang, Z., Zhang, L., et al. (2019a). Transcranial direct current stimulation for patients with pharmacoresistant epileptic spasms: a pilot study. *Front. Neurol.* 10:50. doi: 10.3389/fneur.2019.00050

Yang, D., Hong, K.-S., Yoo, S.-H., and Kim, C.-S. (2019b). Evaluation of neural degeneration biomarkers in the prefrontal cortex for early identification of patients with mild cognitive impairment: an fNIRS study. *Front. Hum. Neurosci.* 13:317. doi: 10.3389/FNHUM.2019.00317

Yang, D., Huang, R., Yoo, S. H., Shin, M. J., Yoon, J. A., Shin, Y. II, et al. (2020a). Detection of mild cognitive impairment using convolutional neural network: temporal-feature maps of functional near-infrared spectroscopy. *Front. Aging Neurosci.* 12:141. doi: 10.3389/fnagi.2020.00141

Yang, D., Nguyen, T.-H., and Chung, W. (2020b). A bipolar-channel hybrid brain-computer interface system for home automation control utilizing steady-state visually evoked potential and eye-blink signals. *Sensors* 20:5474. doi: 10.3390/s20195474

Yaqub, M. A., Woo, S., and Hong, K. (2018). Effects of HD-tDCS on resting-state functional connectivity in the prefrontal cortex?: an fNIRS study. *Complexity* 2018:1613402.

Yin, Z., Luo, Y., Jin, Y., Yu, Y., Zheng, S., Duan, J., et al. (2019). Is awake physiological confirmation necessary for DBS treatment of Parkinson's disease today? A comparison of intraoperative imaging, physiology, and physiology imaging-guided DBS in the past decade. *Brain Stimul.* 12, 893–900. doi: 10.1016/j.brs.2019.03.006

Yoo, W. K., Vernet, M., Hoon Kim, J., Brem, A. K., Bashir, S., Ifert-Miller, F., et al. (2020). Interhemispheric and intrahemispheric connectivity from the left pars opercularis within the language network is modulated by transcranial stimulation in healthy subjects. *Front. Hum. Neurosci.* 14:63. doi: 10.3389/fnhum.2020.00063

Yoo, Y. J. (2019). Fault detection method using multi-mode principal component analysis based on gaussian mixture model for sewage source heat pump system. *Int. J. Control Autom. Syst.* 17, 2125–2134. doi: 10.1007/s12555-018-0758-6

Yuan, Y., Wang, J., Wu, D., Huang, X., and Song, W. (2017). Effect of transcranial direct current stimulation on swallowing apraxia and cortical excitability in stroke patients. *Top. Stroke Rehabil.* 24, 503–509. doi: 10.1080/10749357.2017.1322250

Zhang, J., Wang, B., Zhang, C., Xiao, Y., and Wang, M. Y. (2019). An EEG/EMG/EOG-based multimodal human-machine interface to real-time control of a soft robot hand. *Front. Neurorobot.* 13:7. doi: 10.3389/fnbot.2019.00007

Zhang, X., Liu, B., Li, N., Li, Y., Hou, J., Duan, G., et al. (2020). Transcranial direct current stimulation over prefrontal areas improves psychomotor inhibition state in patients with traumatic brain injury: a pilot study. *Front. Neurosci.* 14:386. doi: 10.3389/fnins.2020.00386

Conflict of Interest: The authors declare that the research was conducted in the absence of any commercial or financial relationships that could be construed as a potential conflict of interest.

frontiers
in Neuroscience

REVIEW
published: 29 June 2021
doi: 10.3389/fnins.2021.636424

When Is Simultaneous Recording Necessary? A Guide for Researchers Considering Combined EEG-fMRI

*Catriona L. Scrivener**

MRC Cognition and Brain Sciences Unit, University of Cambridge, Cambridge, United Kingdom

Edited by:
Camillo Porcaro,
Italian National Research Council, Italy

Reviewed by:
Marco Marino,
KU Leuven, Belgium
Xu Lei,
Southwest University, China

***Correspondence:**
Catriona L. Scrivener
catriona.scrivener@mrc-cbu.cam.ac.uk
orcid.org/0000-0002-9507-5587

Specialty section:
This article was submitted to Brain Imaging Methods, a section of the journal Frontiers in Neuroscience

Received: *01 December 2020*
Accepted: *01 June 2021*
Published: *29 June 2021*

Citation:
Scrivener CL (2021) When Is Simultaneous Recording Necessary? A Guide for Researchers Considering Combined EEG-fMRI. Front. Neurosci. 15:636424. doi: 10.3389/fnins.2021.636424

Electroencephalography (EEG) and functional magnetic resonance imaging (fMRI) provide non-invasive measures of brain activity at varying spatial and temporal scales, offering different views on brain function for both clinical and experimental applications. Simultaneous recording of these measures attempts to maximize the respective strengths of each method, while compensating for their weaknesses. However, combined recording is not necessary to address all research questions of interest, and experiments may have greater statistical power to detect effects by maximizing the signal-to-noise ratio in separate recording sessions. While several existing papers discuss the reasons for or against combined recording, this article aims to synthesize these arguments into a flow chart of questions that researchers can consider when deciding whether to record EEG and fMRI separately or simultaneously. Given the potential advantages of simultaneous EEG-fMRI, the aim is to provide an initial overview of the most important concepts and to direct readers to relevant literature that will aid them in this decision.

Keywords: simultaneous EEG and fMRI, multimodal neuroimaging, EEG-informed fMRI, fMRI-informed EEG, combined recording

INTRODUCTION

The ideal neuroimaging tool would provide a minimum of millimeter spatial resolution at millisecond temporal resolution, enabling researchers to obtain a detailed map of neural function in a living brain. Currently, this method does not exist, and we rely on the synthesis of information from a mixture of methods, each with their own strengths and weaknesses. Among the most common methods available are electroencephalography (EEG), and functional magnetic resonance imaging (fMRI), providing non-invasive measures of brain activity at different spatial and temporal scales. This article focuses on the increasingly common method of combining EEG and fMRI signals by recording them simultaneously.

The concurrent acquisition of EEG and fMRI has the ambitious aim of improving the spatial and temporal limitations of respective measures, promising increased understanding of brain function. Some of the first applications of simultaneous EEG-fMRI aimed to improve localization of epileptic seizures in epilepsy patients, where increased spiking in the EEG can be correlated with activation in contributing brain areas (Ives et al., 1993). In addition, epileptic spikes recorded in the EEG can be used to indicate the onset of epileptic events and inform the time course of fMRI analysis (Bénar et al., 2003, 2006; Vulliemoz et al., 2009; Gotman and Pittau, 2011). In a similar application, EEG signals can be used to indicate sleep phases and facilitate partitioning of simultaneously recorded fMRI signal (Portas et al., 2000; Horovitz et al., 2008).

The primary advantage of simultaneous EEG-fMRI recording is that it allows one to obtain two complementary data sets capturing identical brain activity. There are many circumstances in which separate recordings of EEG and fMRI would be unlikely to contain the same information, for example in resting state or decision-making paradigms (Mayhew et al., 2013; Pisauro et al., 2017). During combined recording, the same neural activity contributes to the EEG and fMRI data at each trial. This assumption is necessary for many existing EEG-fMRI analysis methods, such as EEG-informed fMRI or resting state network analysis (Eichele et al., 2005; Mantini et al., 2007; Wirsich et al., 2021) and provides a rich data set for cognitive and clinical investigation. Other differences between separate EEG and fMRI experiments are also avoided by a single recording session, such as variance in sensory stimulation, stimuli habituation, subject position, and preparation time; all of which may have subtle but important impacts on the recorded data (Herrmann and Debener, 2008).

The primary disadvantage of simultaneous EEG-fMRI recording is that each data set is negatively impacted by the presence of the other. EEG data recorded inside the MRI environment contains gradient (Mandelkow et al., 2006), ballistocardiogram (BCG; Debener et al., 2008; Marino et al., 2018a), pump (Rothlübbers et al., 2015), and ventilator related artifacts (Nierhaus et al., 2013). The EEG data quality is therefore reduced compared to a separate recording session in a shielded environment, which affords greater flexibility regarding the type of EEG cap used (for a comparison see Mathewson et al., 2017). For example, auditory event-related potentials (ERPs) can be influence by the increased noise inside the MRI scanner (Mulert et al., 2004), and there is some evidence of changes to cognitive ERPs and steady-state visually evoked potentials (Novitski et al., 2001, 2003; Sammer et al., 2005) when they are recorded during EEG-fMRI. However, other studies report comparable ERP results inside and outside the MRI environment, and this may depend on factors such as the ERP of interest and the signal-to-noise ratio of the recorded data (Becker et al., 2005; Comi et al., 2005; Bregadze and Lavric, 2006; Mayhew et al., 2010). The MRI signal can also be impacted by combined recording, as the EEG electrodes increase inhomogeneity in the magnetic field and reduce MRI signal (Mullinger et al., 2008c). However, the continued development of novel methods to remove artifacts and improve data quality in simultaneously recorded data provides optimism for the future of EEG-fMRI (Marino et al., 2018b; Bullock et al., 2021) and continues to reduce the weight of this disadvantage.

Simultaneous EEG-fMRI is increasingly used to investigate brain activation in healthy subjects and a range of methods have been proposed for data integration (for other more detailed conceptual and methodological reviews, see Ritter and Villringer, 2006; Huster et al., 2012; Laufs, 2012; Jorge et al., 2014). However, combined EEG-fMRI is not necessarily better than separate sessions, and researchers should consider their research question and experimental design before recording EEG and fMRI simultaneously. This article highlights the challenges faced when recording simultaneous EEG-fMRI, including the nature of the signals that we record and when we can expect them to overlap. Presented here is a flow chart to help researchers decide whether simultaneous EEG-fMRI is necessary, or whether separate EEG and fMRI experiments would be more appropriate (see **Figure 1**). The flow chart begins with the assumption that researchers would like to acquire both fMRI data and EEG data, but are deciding whether these need to be recorded during the same experimental session, or separately (the decision whether to

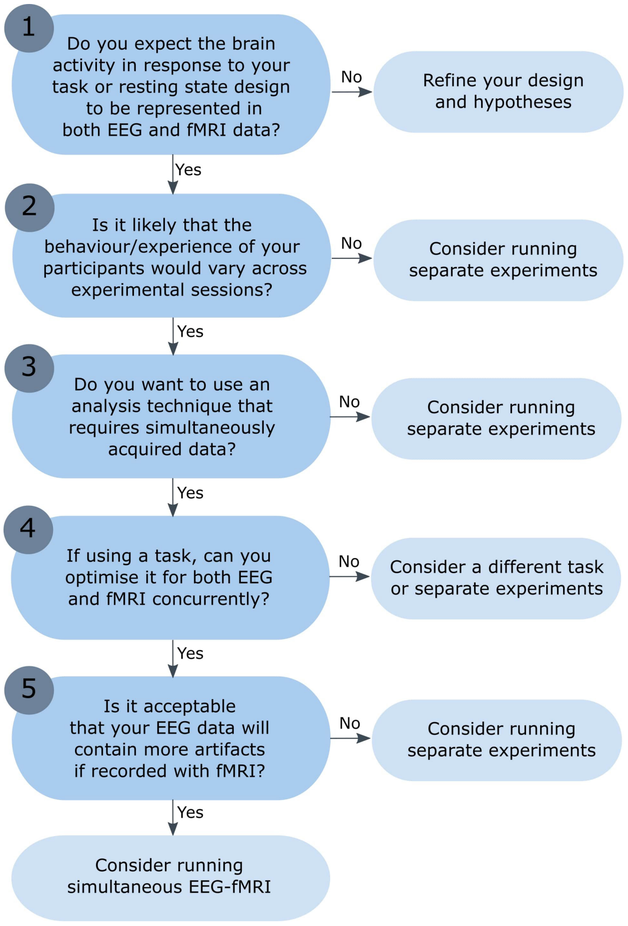

FIGURE 1 | Flow chart: is simultaneous EEG-fMRI necessary? The numbered questions correspond to numbered sections of the text, which describe each question and the possible outcomes in more detail. While the experimental process will not necessarily take the linear progression presented here, the aim is to offer a set of key questions to answer before undertaking simultaneous EEG-fMRI recording. The reader is directed to the critical literature referenced throughout each section to aid them in their response to each question.

record just EEG *or* just fMRI data would require an additional set of statements). Although this list of questions is not exhaustive, and the experimental process will not always take the linear progression presented here, this article points to useful resources and aims to provide a good starting point for any researcher considering combined EEG-fMRI recording.

1. DO YOU EXPECT THE BRAIN ACTIVITY IN RESPONSE TO YOUR TASK OR RESTING STATE DESIGN TO BE REPRESENTED IN BOTH EEG AND fMRI DATA?

The first question is perhaps the most important, but also the most difficult to answer. A pre-requisite for combined EEG-fMRI is that you expect both modalities to capture and reflect the activation that you hypothesize to find. If you do not expect this, then there is little to gain from recording both data sets, either simultaneously or not. If this is the case, you should refine your experimental design and hypotheses before coming back to this question. An ideal combined EEG-fMRI recording would provide a data set with an integrated view of the underlying neural activity, such that the EEG, fMRI, and behavioral measures have some degree of overlap. You could consider this using a Venn diagram with three overlapping circles, where the center portion captures information from all three measures (Jorge et al., 2014). However, there are multiple reasons why this may not always be the case, and it is possible for correlations to occur between behavior and each modality separately, without any overlap between the EEG and fMRI signals themselves. [For an in-depth discussion on the neural sources of both modalities, see the chapters on the physiological basis of EEG and blood oxygen level dependent (BOLD) signals in Ullsperger and Debener, 2010, and the review on EEG-fMRI integration from Rosa et al., 2010].

As EEG and fMRI are sensitive to activity at different spatial and temporal scales, it is plausible to find a decoupling between electrophysiological and hemodynamic signals (Nunez and Silberstein, 2000; Rosa et al., 2010; Jorge et al., 2014). For example, fMRI BOLD can be recorded in the absence of EEG if the neural activity is not detectable at the scalp. This can occur if the electrophysiological activity is non-synchronized, forms a closed source, or is present in deep sources that are subject to volume conduction and signal decay (Henze et al., 2000; but see Seeber et al., 2019). It is also possible for areas with high metabolic load to contribute to BOLD but not to EEG (Ritter and Villringer, 2006).

Similarly, it is possible to detect EEG in the absence of BOLD if the sources of EEG signals do not consume enough energy to facilitate the hemodynamic changes detectable in fMRI (Mulert and Lemieux, 2009). Dynamics with high temporal resolution may also be missed or smoothed by the sampling rate of fMRI BOLD. Further, reduced inhibitory cell activity can decrease metabolic load but increase pyramidal activity (Nunez and Silberstein, 2000), resulting in divergent effects in EEG and fMRI.

Given these possibilities, it is beneficial to use a task/experiment that has already been run separately for EEG and fMRI with replicable results. If previous research has found measurable signals in both data sets using a similar paradigm, then you may not need to run these experiments again. However, if you have designed a new paradigm, or plan to use a new analysis method, it may be beneficial to check that your expected signal can be found in both EEG and fMRI before running combined recording. A further point to emphasize here is that researchers should have some idea of what they expect to find in both modalities using their analysis technique(s). When confronted with a large data set from simultaneous recording, it is important to have some idea of the analysis pipelines that will be run and what results it is reasonable to expect. The flexibility and extent of possible analysis pipelines can result in different conclusions, even from the same data set, in the hands of different researchers (Botvinik-Nezer et al., 2020). With more data comes an increased chance of spurious results, and without a clear direction for analysis it is possible to find *something*, even if not meaningful. Registered reports and pre-registered analysis pipelines go some way to ensure the reproducibility of neuroscience research, by illuminating planned versus *post hoc* hypotheses and analysis (Gorgolewski and Poldrack, 2016).

In summary, researchers should be confident that their signal of interest is detectable with both EEG and fMRI, from previous research or knowledge of the neural source. If this is not the case, then simultaneous EEG-fMRI may not provide any additional information, and relationships between the EEG and fMRI signals may not be detectable.

2. IS IT LIKELY THAT THE BEHAVIOR/EXPERIENCE OF YOUR PARTICIPANTS WOULD VARY ACROSS EXPERIMENTAL SESSIONS?

Question 2 asks the researcher if it is likely that the behavior/experience of their participants would vary across experimental sessions, for example in a learning or emotional task. If this is the case, then even if identical paradigms were recorded using the same participants across separate EEG and fMRI experiments, it would be difficult to ensure that the brain activity at each individual trial was the same. Another example is the application of simultaneous EEG-fMRI recording to investigate resting state networks, given that spontaneous activation across sessions cannot be matched (Mantini et al., 2007; Scheeringa et al., 2008; Britz et al., 2010; Marino et al., 2019; Wirsich et al., 2021). If it is likely that the behavior/experience of your participants would vary across experimental sessions, then simultaneous recording is beneficial. Other differences between separate EEG and fMRI experiments are avoided by implementing a single recording session, such as variance in sensory stimulation, stimuli habituation, subject position, and preparation time; all of which may have subtle but important impacts on the recorded data (Herrmann and Debener, 2008).

However, if stability across sessions is likely, then separate recordings may be sufficient.

3. DO YOU WANT TO USE AN ANALYSIS TECHNIQUE THAT REQUIRES SIMULTANEOUSLY ACQUIRED DATA?

Question 3 asks the researcher if their analysis requires data recorded during the same session. The answer to this question is dependent on several factors, including the answer to question 2 above, and the chosen method of analysis. If you are certain that the brain activation in response to two separate sessions will be relatively stable, and you can classify each trial type predictably (for example, in some well controlled visual stimulation experiments), then you may be able to run your analysis on separately recorded data. However, if you predict that the activity at each trial will vary across experimental sessions, then simultaneous recording may be necessary for most analysis techniques (for example, if the response of the participant determines the trial type/condition).

The existing analysis methods for combined EEG-fMRI can be broadly grouped into two categories; symmetrical and asymmetrical analysis (for more detailed reviews, see Huster et al., 2012; Jorge et al., 2014). In asymmetric analysis, one modality is used as a predictor for the other. EEG-informed fMRI uses values extracted from single-trial EEG as predictors in a standard fMRI GLM analysis (general linear model). This identifies voxels with activation that co-varies with fluctuations in the EEG signal over time. Example EEG features include ERPs and frequency-band power fluctuations, the choice of which will determine the conclusions that can be drawn from the results (Laufs et al., 2003; Novitskiy et al., 2011).

An ongoing challenge for the application of EEG-informed fMRI is to maximize the signal-to-noise ratio in single trial estimates of EEG activity. Methods to improve the efficiency of data pre-processing before integration are therefore highly important to the field of EEG-fMRI and continue to be developed. Key examples include linear classifiers (Goldman et al., 2009; Walz et al., 2015), autoregressive models (Nguyen et al., 2014), spatial Laplacian filters (Liu et al., 2016), and functional source separation (Porcaro et al., 2010). Unless it can be assumed that single-trial values will be stable across two experimental sessions, and not negatively influenced by habituation or learning effects, ERP-informed fMRI method will generally require simultaneously recorded data (Debener et al., 2006; Bagshaw and Warbrick, 2007). Another important consideration for single trial EEG analysis is that it relies on EEG effects that are present at the within-subject level. Not all ERPs are stable across participants if analyzed at a single-subject level (e.g., Petit et al., 2020), which may negatively impact single trial ERP-informed fMRI analysis. Therefore, it may be beneficial to check the variance across subjects and sessions of an EEG measure before using in combined EEG-fMRI analysis.

In the opposite direction, fMRI-informed EEG uses fMRI GLM results to guide and/or constrain EEG source reconstruction, which benefits from the additional spatial information provided by fMRI. The strength of the assumed overlap between EEG sources and fMRI BOLD will determine the source reconstruction constraints (see the discussion in Chapter 3.7 of Ullsperger and Debener, 2010, for a mathematical overview). Arguably, this could also be achieved using separately recorded data, but this decision will be influenced by the same considerations mentioned above for EEG-informed fMRI.

In symmetrical analysis, researchers avoid giving preference to one modality by modeling relationships between the data or calculating joint independent components (Daunizeau et al., 2007; Moosmann et al., 2008). Current symmetrical analysis can be divided into data-driven and model-based methods. Independent component analysis (ICA; Calhoun et al., 2006; Lei et al., 2011) and methods based on information theory (Ostwald et al., 2011) are data-driven, as they do not require modeling of hemodynamics or neurovascular coupling. In contrast, dynamic causal modeling (Friston et al., 2003; Nguyen et al., 2014) and other model-based methods attempt to determine the underlying neural components of EEG and fMRI using individual forward models (Rosa et al., 2010).

There are several ICA based methods for EEG-fMRI analysis, including parallel ICA and joint ICA. In the parallel application, temporal ICA is typically run on the EEG data, whereas spatial ICA is run on the fMRI data (Liu and Calhoun, 2007; Eichele et al., 2008). Components are then matched, for example, by correlating the component time series. As the temporal sequence of events is preserved, this method also assumes consistent activation across modalities in single trials, and may require simultaneous recording. In joint ICA, EEG and fMRI data is included in the same ICA decomposition, such that the mixing matrix contains information from both modalities (Moosmann et al., 2008; Calhoun et al., 2009). It is possible to conduct joint ICA with averaged ERPs and fMRI contrast maps, or with single trial data, of which the former can feasibly be run on separately recorded data (Calhoun et al., 2006).

Although many of the analysis methods mentioned above ideally require simultaneous recording, methods designed for combining magnetoencephalography (MEG) and fMRI could also be applied to separately recorded EEG and fMRI data. M/EEG fMRI fusion methods based on representation similarity analysis (RSA) search for shared information across data sets condition-by-condition, rather than trial-by-trial, and therefore do not require simultaneous recording (Cichy and Oliva, 2020). These multivariate methods have additional advantages; they identify differences in the patterns of activation across regions or time points, rather than the overall activation as identified in univariate analysis. Additionally, all M/EEG channels are typically entered into the analysis, which may be more informative than the few channels that are usually selected for EEG-informed fMRI analysis as a larger proportion of the available data is used.

In summary, if you plan to run traditional EEG and fMRI analyses separately, using averages over trials or representations of shared information, then separate recording may be sufficient. However, if you plan to run combined EEG-fMRI analysis with the assumption that the same behavior and neurological activity is represented in both modalities at each trial, then concurrent recording is beneficial.

4. IF USING A TASK, CAN YOU OPTIMIZE IT FOR BOTH EEG AND FMRI CONCURRENTLY?

Question 4 is important for the design of a combined EEG-fMRI experiment, and asks if the task can be optimized for both EEG and fMRI. Traditional EEG experiments are often fast with short trial durations, given that researchers are usually interested in activity within the first 600 ms after stimulus onset. The BOLD response measured using fMRI is much slower, and therefore fast paradigms must be designed with caution. Researchers may consider adding larger inter-trial intervals and jitter between image presentations to ensure that the BOLD in response to separate trials can be separated (Amaro and Barker, 2006). Furthermore, not all fMRI safe EEG equipment can be used in conjunction with all fMRI acquisition techniques such as multiband sequences, therefore constraining the fMRI sequence design (Chen et al., 2020). An advantage of separate recording sessions is that the task and recording setup can be individually optimized for each modality, and therefore the signal-to-noise maximized in both data sets.

5. IS IT ACCEPTABLE THAT YOUR EEG DATA WILL CONTAIN MORE ARTIFACTS HAVE A REDUCED SIGNAL-TO-NOISE RATIO WHEN RECORDED INSIDE THE MRI SCANNER?

The final question asks researchers if they are happy to accept that their EEG data will contain more artifacts and have a reduced signal-to-noise ratio when recorded inside the MRI scanner. Unfortunately, it is not possible for anyone to accurately quantify the loss of signal that will occur for a given paradigm or EEG feature. However, the EEG data recorded in the MRI environment will have additional artifacts that need to be removed (Ritter and Villringer, 2006; Marino et al., 2019; Bullock et al., 2021). Strategies for the removal of these artifacts have variable success, and it is possible that additional data sets will need to be excluded due to pre-processing failures (e.g., Scrivener et al., 2020).

When EEG is recorded during MRI acquisition, several additional EEG artifacts are incurred. The first is caused by the gradient pulse, and therefore known as the gradient artifact. As this is related to the sequence of the MRI scanner, which is known, and is stable over time, the gradient artifact can be removed by subtracting a template of its form (see Allen et al., 2000). This is facilitated by synchronizing the EEG and fMRI clocks, which improves removal of the gradient artifact (Mandelkow et al., 2006; Mullinger et al., 2008a).

The second artifact is the BCG, which is considerably harder to remove, and a reliable solution to this is yet to be achieved. The BCG artifact is related to the heartbeat of the participant lying down in the scanner. More specifically, expansion and contraction of arteries in the scalp cause movements in the electrodes and wires in the EEG cap (Goldman et al., 2000; Debener et al., 2008). This movement of blood also influences the static magnetic field and can result in artifacts with larger power than the EEG signal of interest (Ritter and Villringer, 2006). With similarities to the removal of the gradient artifact, one method used to remove the BCG is to construct a template of the heartbeat artifact, identify its occurrence across the recording, and subtract it from the EEG signal (Allen et al., 1998).

However, there are several factors that reduce the success of this method. Unlike the gradient artifact, the heartbeat of the participant is not stable over time, which can make its removal more of a challenge. Several other methods for removing the BCG artifact have been suggested, for example, ICA (Srivastava et al., 2005), adaptive filtering based on a time varying finite impulse response (Bonmassar et al., 2001), and adaptive optimal basis set methods (Marino et al., 2018b). However, no method claims to successfully remove all BCG artifacts for all participants, and they are not consistently applied across studies (for a review of existing methods, see Abreu et al., 2018 and Bullock et al., 2021).

The third artifact present in EEG recorded inside the MRI environment is caused by the helium pump, which results in widespread peaks across the frequency spectrum, far above the amplitude range of normal EEG (Mullinger et al., 2008b). Given the spread across frequencies, and the difficulty in distinguishing true neural signal from helium pump noise, this can be difficult to remove (but see Rothlübbers et al., 2015). A further complication is the large between-site differences in helium artifact, driven by factors such as the scanner manufacturer and physical set up (Neuner et al., 2014). One way to avoid this artifact is to switch off the helium pump before running the experiment (Laufs et al., 2008). However, as the helium pump is essential for the continued functioning of the MRI scanner, this cannot be left switched off for long time periods.

The MRI signal can also be affected by combined recording, with greater impact reported at higher field strengths (Mullinger et al., 2008c; Jorge et al., 2015). The EEG electrodes increase inhomogeneity in the magnetic field and reduce MRI signal (Mullinger et al., 2008c; Abreu et al., 2018), as well as producing artifacts at the location of EEG electrodes (de Munck et al., 2012; Scrivener and Reader, 2021). However, as the distortion and signal drop-out caused by electrodes is located at the scalp, the signal within the brain is not significantly affected (Mullinger et al., 2008c). Further, several studies have reported comparable BOLD sensitivity with and without the presence of an EEG cap (Luo and Glover, 2012; Klein et al., 2015).

Some researchers have also reported spurious correlations between EEG and fMRI signals that are related to motion artifacts, rather than a common neural source. For example, EEG power in the frequency domain was found to be significantly higher during trials with high motion, compared to low motion, especially in low frequency bands (Fellner et al., 2016). The presence of additional EEG artifacts may also influence ICA based analysis, as a larger proportion of the ICA components will relate to artifacts than in a standard EEG experiment. Given that the number of identified ICA components is restricted to the maximum number of recording channels, this may reduce the ability to separate meaningful EEG components (Ullsperger and Debener, 2010).

FUTURE DIRECTIONS

Recent technological and methodological developments continue to expand and improve the application of combined EEG-fMRI. For example, real-time pre-processing and feedback of sensorimotor EEG activation has been implemented during EEG-fMRI recording, enhancing task related activity during motor imagery (Zich et al., 2015). It is therefore possible to conduct online EEG analysis and use the outcome measure to influence participant behavior and subsequent neural activation. The complex concurrent application of TMS-EEG-fMRI has also been implemented, suggesting that strong pre-stimulus alpha power is associated with a reduced TMS-induced BOLD response in the motor execution network (Peters et al., 2020). An interesting extension of this work would be to use online EEG measures, such as alpha peak or trough onsets, to inform the timing of TMS pulses delivered to the brain (Thut et al., 2011a,b), enabling a comparison of the TMS-induced changes to BOLD and behavior.

While most combined EEG-fMRI recordings are done at magnetic field strengths of 3T, several groups are developing methods to combine EEG with ultra-high field MRI imaging at 7T (Meyer et al., 2020; Philiastides et al., 2021). Despite the increased number of artifacts associated with combined EEG-fMRI recording over 3T (Mullinger et al., 2008c; Neuner et al., 2013; Jorge et al., 2015), ultra-high field MRI measures provide increased spatial resolution at the mesoscopic level (Balchandani and Naidich, 2015). Combining this with EEG can therefore facilitate precise mapping between EEG signals and BOLD activation across individual layers of the cortex (e.g., Scheeringa et al., 2016), with greater detail than can be achieved at lower field strengths.

SUMMARY

The aim of this article is to provide a resource for researchers considering whether to record EEG and fMRI separately or simultaneously. Presented here are a series of questions for the researcher to consider in reaching a decision. In summary, separate recordings are sufficient if; (a) you plan to run traditional EEG and fMRI analyses separately, using averages over trials, rather than combined analysis and single-trial data; (b) you assume that participant behavior and neurological responses would be relatively stable across experimental sessions; and (c) if you cannot find a suitable paradigm that can be optimized for EEG and fMRI concurrently. If you do not know what to expect in the individual modalities or how you would analyze your data, it may be beneficial to run pilot studies in each modality first before coming back to the question of simultaneous EEG-fMRI. There are several advantages to separate recording, including the ability to optimize the recording parameters for each modality separately, without requiring specialized fMRI safe EEG equipment that may constrain the available fMRI sequences. The data quality of separate data sets will also be greater, and the likelihood that subjects need to be excluded from analysis is reduced by the smaller number of possible artifacts.

However, simultaneous EEG-fMRI may be justified if; (a) you can reasonably expect your signal of interest to be detected in both EEG and fMRI signals; (b) you know what to expect from each modality individually and are therefore interested in running combined analysis to extract simultaneous temporal and spatial information; (c) you plan to run combined EEG-fMRI analysis with the assumption that the same behavior and neurological activity is represented in both modalities at each trial; and (d) you expect that this behavior and neurological activity would vary across experimental sessions or you are measuring spontaneous activity during resting state. An advantage of simultaneous recording is the mitigation of potential confounds associated with multiple testing sessions, such as habituation, learning, or differences in set up and participant experience.

Overall, the aim of this article is to equip new researchers with the resources needed to make an informed decision regarding the necessity of simultaneous EEG-fMRI. As multi-modal neuroimaging requires additional time, equipment, and financial resources, it is important to thoroughly consider the recording options available. Ongoing technological and methodological developments continue to facilitate the successful application of combined EEG-fMRI to ask questions about the brain and behavior with increasing precision, and it will no doubt continue to be a powerful tool in cognitive neuroscience.

AUTHOR CONTRIBUTIONS

The author confirms being the sole contributor of this work and has approved it for publication.

ACKNOWLEDGMENTS

Thank you to Arran Reader and David Scrivener for their comments on this manuscript. Thank you also to the EBRlab at the University of Reading for the interesting discussions on the subject; Asad Malik, Ivano Ras, Michael Lindner, and Etienne Roesch.

REFERENCES

Abreu, R., Leal, A., and Figueiredo, P. (2018). EEG-Informed fMRI: A Review of Data Analysis Methods. *Front. Hum. Neurosci.* 12:00029. doi: 10.3389/fnhum.2018.00029

Allen, P. J., Josephs, O., and Turner, R. (2000). A Method for Removing Imaging Artifact from Continuous EEG Recorded during Functional MRI. *NeuroImage* 12, 230–239. doi: 10.1006/nimg.2000.0599

Allen, P. J., Polizzi, G., Krakow, K., Fish, D. R., and Lemieux, L. (1998). Identification of EEG Events in the MR Scanner: The Problem of Pulse Artifact and a Method for Its Subtraction. *NeuroImage* 8, 229–239. doi: 10.1006/nimg.1998.0361

Amaro, E., and Barker, G. J. (2006). Study design in fMRI: Basic principles. *Brain Cognit.* 60, 220–232. doi: 10.1016/j.bandc.2005.11.009

Bagshaw, A. P., and Warbrick, T. (2007). Single trial variability of EEG and fMRI responses to visual stimuli. *NeuroImage* 38, 280–292. doi: 10.1016/j.neuroimage.2007.07.042

Balchandani, P., and Naidich, T. P. (2015). Ultra-High-Field MR Neuroimaging. *Am. J. Neuroradiol.* 36, 1204–1215. doi: 10.3174/ajnr.A4180

Becker, R., Ritter, P., Moosmann, M., and Villringer, A. (2005). Visual evoked potentials recovered from fMRI scan periods. *Hum. Brain Mapp.* 26, 221–230. doi: 10.1002/hbm.20152

Bénar, C.-G., Aghakhani, Y., Wang, Y., Izenberg, A., Al-Asmi, A., Dubeau, F., et al. (2003). Quality of EEG in simultaneous EEG-fMRI for epilepsy. *Clin. Neurophysiol.*114, 569–580. doi: 10.1016/S1388-2457(02)00383-8

Bénar, C.-G., Grova, C., Kobayashi, E., Bagshaw, A. P., Aghakhani, Y., Dubeau, F., et al. (2006). EEG–fMRI of epileptic spikes: Concordance with EEG source localization and intracranial EEG. *NeuroImage* 30, 1161–1170. doi: 10.1016/j.neuroimage.2005.11.008

Bonmassar, G., Schwartz, D. P., Liu, A. K., Kwong, K. K., Dale, A. M., and Belliveau, J. W. (2001). Spatiotemporal Brain Imaging of Visual-Evoked Activity Using Interleaved EEG and fMRI Recordings. *NeuroImage* 13, 1035–1043. doi: 10.1006/nimg.2001.0754

Botvinik-Nezer, R., Holzmeister, F., Camerer, C. F., Dreber, A., Huber, J., Johannesson, M., et al. (2020). Variability in the analysis of a single neuroimaging dataset by many teams. *Nature* 582, 84–88. doi: 10.1038/s41586-020-2314-9

Bregadze, N., and Lavric, A. (2006). ERP differences with vs. Without concurrent fMRI. *Int. J. Psychophysiol.* 62, 54–59. doi: 10.1016/j.ijpsycho.2006.01.010

Britz, J., Van De Ville, D., and Michel, C. M. (2010). BOLD correlates of EEG topography reveal rapid resting-state network dynamics. *NeuroImage* 52, 1162–1170. doi: 10.1016/j.neuroimage.2010.02.052

Bullock, M., Jackson, G. D., and Abbott, D. F. (2021). Artifact Reduction in Simultaneous EEG-fMRI: A Systematic Review of Methods and Contemporary Usage. *Front. Neurol.* 12:622719. doi: 10.3389/fneur.2021.622719

Calhoun, V. D., Adali, T., Pearlson, G. D., and Kiehl, K. A. (2006). Neuronal chronometry of target detection: Fusion of hemodynamic and event-related potential data. *NeuroImage* 30, 544–553. doi: 10.1016/j.neuroimage.2005.08.060

Calhoun, Vince, D., Liu, J., and Adalı, T. (2009). A review of group ICA for fMRI data and ICA for joint inference of imaging, genetic, and ERP data. *NeuroImage* 45, S163–S172. doi: 10.1016/j.neuroimage.2008.10.057

Chen, J. C. C., Forsyth, A., Dubowitz, D. J., and Muthukumaraswamy, S. D. (2020). On the Quality, Statistical Efficiency, and Safety of Simultaneously Recorded Multiband fMRI/EEG. *Brain Topogr.* 33, 303–316. doi: 10.1007/s10548-020-00761-w

Cichy, R. M., and Oliva, A. (2020). A M/EEG-fMRI Fusion Primer: Resolving Human Brain Responses in Space and Time. *Neuron* 107, 772–781. doi: 10.1016/j.neuron.2020.07.001

Comi, E., Annovazzi, P., Silva, A. M., Cursi, M., Blasi, V., Cadioli, M., et al. (2005). Visual evoked potentials may be recorded simultaneously with fMRI scanning: A validation study. *Hum. Brain Mapp.* 24, 291–298. doi: 10.1002/hbm.20087

Daunizeau, J., Grova, C., Marrelec, G., Mattout, J., Jbabdi, S., Pélégrini-Issac, M., et al. (2007). Symmetrical event-related EEG/fMRI information fusion in a variational Bayesian framework. *NeuroImage* 36, 69–87. doi: 10.1016/j.neuroimage.2007.01.044

de Munck, J. C., van Houdt, P. J., Verdaasdonk, R. M., and Ossenblok, P. P. W. (2012). A semi-automatic method to determine electrode positions and labels from gel artifacts in EEG/fMRI-studies. *NeuroImage* 59, 399–403. doi: 10.1016/j.neuroimage.2011.07.021

Debener, S., Mullinger, K. J., Niazy, R. K., and Bowtell, R. W. (2008). Properties of the ballistocardiogram artefact as revealed by EEG recordings at 1.5, 3 and 7 T static magnetic field strength. *Int. J. Psychophysiol.* 67, 189–199. doi: 10.1016/j.ijpsycho.2007.05.015

Debener, S., Ullsperger, M., Siegel, M., and Engel, A. K. (2006). Single-trial EEG–fMRI reveals the dynamics of cognitive function. *Trends Cognit. Sci.* 10, 558–563. doi: 10.1016/j.tics.2006.09.010

Eichele, T., Specht, K., Moosmann, M., Jongsma, M. L. A., Quiroga, R. Q., Nordby, H., et al. (2005). Assessing the spatiotemporal evolution of neuronal activation with single-trial event-related potentials and functional MRI. *Proc. Natl. Acad. Sci.* 102, 17798–17803. doi: 10.1073/pnas.0505508102

Eichele, T., Calhoun, V. D., Moosmann, M., Specht, K., Jongsma, M. L. A., et al. (2008). Unmixing concurrent EEG-fMRI with parallel independent component analysis. *Int. J. Psychophysiol.* 67, 222–234. doi: 10.1016/j.ijpsycho.2007.04.010

Fellner, M.-C., Volberg, G., Mullinger, K. J., Goldhacker, M., Wimber, M., Greenlee, M. W., et al. (2016). Spurious correlations in simultaneous EEG-fMRI driven by in-scanner movement. *NeuroImage* 133, 354–366. doi: 10.1016/j.neuroimage.2016.03.031

Friston, K. J., Harrison, L., and Penny, W. (2003). Dynamic causal modelling. *NeuroImage* 19, 1273–1302. doi: 10.1016/S1053-8119(03)00202-7

Goldman, R. I., Stern, J. M., Engel, J., and Cohen, M. S. (2000). Acquiring simultaneous EEG and functional MRI. *Clin. Neurophysiol.* 111, 1974–1980. doi: 10.1016/S1388-2457(00)00456-9

Goldman, R. I., Wei, C.-Y., Philiastides, M. G., Gerson, A. D., Friedman, D., Brown, T. R., et al. (2009). Single-trial discrimination for integrating simultaneous EEG and fMRI: Identifying cortical areas contributing to trial-to-trial variability in the auditory oddball task. *NeuroImage* 47, 136–147. doi: 10.1016/j.neuroimage.2009.03.062

Gorgolewski, K. J., and Poldrack, R. A. (2016). A Practical Guide for Improving Transparency and Reproducibility in Neuroimaging Research. *PLoS Biol.* 14:e1002506. doi: 10.1371/journal.pbio.1002506

Gotman, J., and Pittau, F. (2011). Combining EEG and fMRI in the study of epileptic discharges. *Epilepsia* 52, 38–42. doi: 10.1111/j.1528-1167.2011.03151.x

Henze, D. A., Borhegyi, Z., Csicsvari, J., Mamiya, A., Harris, K. D., and Buzsáki, G. (2000). Intracellular Features Predicted by Extracellular Recordings in the Hippocampus *In Vivo*. *J. Neurophysiol.* 84, 390–400. doi: 10.1152/jn.2000.84.1.390

Herrmann, C. S., and Debener, S. (2008). Simultaneous recording of EEG and BOLD responses: A historical perspective. *Int. J. Psychophysiol.* 67, 161–168. doi: 10.1016/j.ijpsycho.2007.06.006

Horovitz, S. G., Fukunaga, M., Zwart, J. A., de, Gelderen, P., van, et al. (2008). Low frequency BOLD fluctuations during resting wakefulness and light sleep: A simultaneous EEG-fMRI study. *Hum. Brain Mapp.* 29, 671–682. doi: 10.1002/hbm.20428

Huster, R. J., Debener, S., Eichele, T., and Herrmann, C. S. (2012). Methods for Simultaneous EEG-fMRI: An Introductory Review. *J. Neurosci.* 32, 6053–6060. doi: 10.1523/JNEUROSCI.0447-12.2012

Ives, J. R., Warach, S., Schmitt, F., Edelman, R. R., and Schomer, D. L. (1993). Monitoring the patient's EEG during echo planar MRI. *Electroencephalogr. Clin. Neurophysiol.* 87, 417–420. doi: 10.1016/0013-4694(93)90156-P

Jorge, J., Grouiller, F., Ipek, Ö., Stoermer, R., Michel, C. M., Figueiredo, P., et al. (2015). Simultaneous EEG–fMRI at ultra-high field: Artifact prevention and safety assessment. *NeuroImage* 105, 132–144. doi: 10.1016/j.neuroimage.2014.10.055

Jorge, J., van der Zwaag, W., and Figueiredo, P. (2014). EEG–fMRI integration for the study of human brain function. *NeuroImage* 102, 24–34. doi: 10.1016/j.neuroimage.2013.05.114

Klein, C., Hänggi, J., Luechinger, R., and Jäncke, L. (2015). MRI with and without a high-density EEG cap—What makes the difference? *NeuroImage* 106, 189–197. doi: 10.1016/j.neuroimage.2014.11.053

Laufs, H (2012). A personalized history of EEG–fMRI integration. *NeuroImage* 62, 1056–1067. doi: 10.1016/j.neuroimage.2012.01.039

Laufs, H., Daunizeau, J., Carmichael, D. W., and Kleinschmidt, A. (2008). Recent advances in recording electrophysiological data simultaneously with magnetic resonance imaging. *NeuroImage* 40, 515–528. doi: 10.1016/j.neuroimage.2007.11.039

Laufs, H., Kleinschmidt, A., Beyerle, A., Eger, E., Salek-Haddadi, A., Preibisch, C., et al. (2003). EEG-correlated fMRI of human alpha activity. *NeuroImage* 19, 1463–1476. doi: 10.1016/S1053-8119(03)00286-6

Lei, X., Ostwald, D., Hu, J., Qiu, C., Porcaro, C., Bagshaw, A. P., et al. (2011). Multimodal Functional Network Connectivity: An EEG-fMRI Fusion in Network Space. *PLoS One* 6:e24642. doi: 10.1371/journal.pone.0024642

Liu, J., and Calhoun, V. (2007). "PARALLEL INDEPENDENT COMPONENT ANALYSIS FOR MULTIMODAL ANALYSIS: APPLICATION TO FMRI AND EEG DATA," in *2007 4th IEEE International Symposium on Biomedical Imaging: From Nano to Macro* (Washington, DC: IEEE), 1028–1031. doi: 10.1109/ISBI.2007.357030

Liu, Y., Bengson, J., Huang, H., Mangun, G. R., and Ding, M. (2016). Top-down Modulation of Neural Activity in Anticipatory Visual Attention: Control Mechanisms Revealed by Simultaneous EEG-fMRI. *Cereb. Cortex* 26, 517–529. doi: 10.1093/cercor/bhu204

Luo, Q., and Glover, G. H. (2012). Influence of dense-array EEG cap on fMRI signal. *Magnetic Resonance Med.* 68, 807–815. doi: 10.1002/mrm.23299

Mandelkow, H., Halder, P., Boesiger, P., and Brandeis, D. (2006). Synchronization facilitates removal of MRI artefacts from concurrent EEG recordings and increases usable bandwidth. *NeuroImage* 32, 1120–1126. doi: 10.1016/j.neuroimage.2006.04.231

Mantini, D., Perrucci, M. G., Gratta, C. D., Romani, G. L., and Corbetta, M. (2007). Electrophysiological signatures of resting state networks in the human brain. *Proc. Natl. Acad. Sci.* 104, 13170–13175. doi: 10.1073/pnas.0700668104

Marino, M., Arcara, G., Porcaro, C., and Mantini, D. (2019). Hemodynamic Correlates of Electrophysiological Activity in the Default Mode Network. *Front. Neurosci.* 13:01060. doi: 10.3389/fnins.2019.01060

Marino, M., Liu, Q., Del Castello, M., Corsi, C., Wenderoth, N., and Mantini, D. (2018a). Heart–Brain Interactions in the MR Environment: Characterization of the Ballistocardiogram in EEG Signals Collected During Simultaneous fMRI. *Brain Topogr.* 31, 337–345. doi: 10.1007/s10548-018-0631-1

Marino, M., Liu, Q., Koudelka, V., Porcaro, C., Hlinka, J., Wenderoth, N., et al. (2018b). Adaptive optimal basis set for BCG artifact removal in simultaneous EEG-fMRI. *Sci. Rep.* 8:8902. doi: 10.1038/s41598-018-27187-6

Mathewson, K. E., Harrison, T. J. L., and Kizuk, S. A. D. (2017). High and dry? Comparing active dry EEG electrodes to active and passive wet electrodes. *Psychophysiology* 54, 74–82. doi: 10.1111/psyp.12536

Mayhew, S. D., Dirckx, S. G., Niazy, R. K., Iannetti, G. D., and Wise, R. G. (2010). EEG signatures of auditory activity correlate with simultaneously recorded fMRI responses in humans. *NeuroImage* 49, 849–864. doi: 10.1016/j.neuroimage.2009.06.080

Mayhew, S. D., Ostwald, D., Porcaro, C., and Bagshaw, A. P. (2013). Spontaneous EEG alpha oscillation interacts with positive and negative BOLD responses in the visual–auditory cortices and default-mode network. *NeuroImage* 76, 362–372. doi: 10.1016/j.neuroimage.2013.02.070

Meyer, M. C., Scheeringa, R., Webb, A. G., Petridou, N., Kraff, O., and Norris, D. G. (2020). Adapted cabling of an EEG cap improves simultaneous measurement of EEG and fMRI at 7T. *J. Neurosci. Methods* 331:108518. doi: 10.1016/j.jneumeth.2019.108518

Moosmann, M., Eichele, T., Nordby, H., Hugdahl, K., and Calhoun, V. D. (2008). Joint independent component analysis for simultaneous EEG–fMRI: Principle and simulation. *Int. J. Psychophysiol.* 67, 212–221. doi: 10.1016/j.ijpsycho.2007.05.016

Mulert, C., and Lemieux, L. (2009). *EEG - fMRI: Physiological Basis, Technique, and Applications*. Berlin: Springer Science & Business Media.

Mulert, C., Jäger, L., Schmitt, R., Bussfeld, P., Pogarell, O., Möller, H.-J., et al. (2004). Integration of fMRI and simultaneous EEG: Towards a comprehensive understanding of localization and time-course of brain activity in target detection. *NeuroImage* 22, 83–94. doi: 10.1016/j.neuroimage.2003.10.051

Mullinger, K. J., Morgan, P. S., and Bowtell, R. W. (2008a). Improved artifact correction for combined electroencephalography/functional MRI by means of synchronization and use of vectorcardiogram recordings. *J. Magnetic Resonance Imaging* 27, 607–616. doi: 10.1002/jmri.21277

Mullinger, K., Brookes, M., Stevenson, C., Morgan, P., and Bowtell, R. (2008b). Exploring the feasibility of simultaneous electroencephalography/functional magnetic resonance imaging at 7 T. *Magnetic Resonan. Imaging* 26, 968–977. doi: 10.1016/j.mri.2008.02.014

Mullinger, K., Debener, S., Coxon, R., and Bowtell, R. (2008c). Effects of simultaneous EEG recording on MRI data quality at 1.5, 3 and 7 tesla. *Int. J. Psychophysiol.* 67, 178–188. doi: 10.1016/j.ijpsycho.2007.06.008

Neuner, I., Arrubla, J., Felder, J., and Shah, N. J. (2014). Simultaneous EEG–fMRI acquisition at low, high and ultra-high magnetic fields up to 9.4T: Perspectives and challenges. *NeuroImage* 102, 71–79. doi: 10.1016/j.neuroimage.2013.06.048

Neuner, I., Warbrick, T., Arrubla, J., Felder, J., Celik, A., Reske, M., et al. (2013). EEG acquisition in ultra-high static magnetic fields up to 9.4T. *NeuroImage* 68, 214–220. doi: 10.1016/j.neuroimage.2012.11.064

Nguyen, V. T., Breakspear, M., and Cunnington, R. (2014). Fusing concurrent EEGŰfMRI with dynamic causal modeling: Application to effective connectivity during face perception. *NeuroImage*, 102, 60–70. doi: 10.1016/j.neuroimage.2013.06.083

Nierhaus, T., Gundlach, C., Goltz, D., Thiel, S. D., Pleger, B., and Villringer, A. (2013). Internal ventilation system of MR scanners induces specific EEG artifact during simultaneous EEG-fMRI. *NeuroImage* 74, 70–76. doi: 10.1016/j.neuroimage.2013.02.016

Novitski, N., Alho, K., Korzyukov, O., Carlson, S., Martinkauppi, S., Escera, C., et al. (2001). Effects of Acoustic Gradient Noise from Functional Magnetic Resonance Imaging on Auditory Processing as Reflected by Event-Related Brain Potentials. *NeuroImage* 14, 244–251. doi: 10.1006/nimg.2001.0797

Novitski, Nikolai, Anourova, I., Martinkauppi, S., Aronen, H. J., Näätänen, R., et al. (2003). Effects of noise from functional magnetic resonance imaging on auditory event-related potentials in working memory task. *NeuroImage* 20, 1320–1328. doi: 10.1016/S1053-8119(03)00390-2

Novitskiy, N., Ramautar, J. R., Vanderperren, K., De Vos, M., Mennes, M., Mijovic, B., et al. (2011). The BOLD correlates of the visual P1 and N1 in single-trial analysis of simultaneous EEG-fMRI recordings during a spatial detection task. *NeuroImage* 54, 824–835. doi: 10.1016/j.neuroimage.2010.09.041

Nunez, P. L., and Silberstein, R. B. (2000). On the Relationship of Synaptic Activity to Macroscopic Measurements: Does Co-Registration of EEG with fMRI Make Sense? *Brain Topogr.* 13, 79–96. doi: 10.1023/A:1026683200895

Ostwald, D., Porcaro, C., and Bagshaw, A. P. (2011). Voxel-wise information theoretic EEG-fMRI feature integration. *NeuroImage* 55, 1270–1286. doi: 10.1016/j.neuroimage.2010.12.029

Peters, J. C., Reithler, J., Graaf, T. A., de, Schuhmann, T., Goebel, R., et al. (2020). Concurrent human TMS-EEG-fMRI enables monitoring of oscillatory brain state-dependent gating of cortico-subcortical network activity. *Communicat. Biol.* 3, 1–11. doi: 10.1038/s42003-020-0764-0

Petit, S., Badcock, N. A., Grootswagers, T., Rich, A. N., Brock, J., Nickels, L., et al. (2020). Toward an Individualized Neural Assessment of Receptive Language in Children. *J. Speech Language Hearing Res.* 63, 2361–2385. doi: 10.1044/2020_JSLHR-19-00313

Philiastides, M. G., Tu, T., and Sajda, P. (2021). Inferring Macroscale Brain Dynamics via Fusion of Simultaneous EEG-fMRI. *Annu. Rev. Neurosci.* 44:093239. doi: 10.1146/annurev-neuro-100220-093239

Pisauro, M. A., Fouragnan, E., Retzler, C., and Philiastides, M. G. (2017). Neural correlates of evidence accumulation during value-based decisions revealed via simultaneous EEG-fMRI. *Nat. Communicat.* 8:15808. doi: 10.1038/ncomms15808

Porcaro, C., Ostwald, D., and Bagshaw, A. P. (2010). Functional source separation improves the quality of single trial visual evoked potentials recorded during concurrent EEG-fMRI. *NeuroImage* 50, 112–123. doi: 10.1016/j.neuroimage.2009.12.002

Portas, C. M., Krakow, K., Allen, P., Josephs, O., Armony, J. L., and Frith, C. D. (2000). Auditory processing across the sleep-wake cycle: Simultaneous EEG and fMRI monitoring in humans. *Neuron*, 28, 991–999. doi: 10.1016/S0896-6273(00)00169-0

Ritter, P., and Villringer, A. (2006). Simultaneous EEG–fMRI. *Neurosci. Biobehav. Rev.* 30, 823–838. doi: 10.1016/j.neubiorev.2006.06.008

Rosa, M. J., Daunizeau, J., and Friston, K. J. (2010). EEG-fMRI integration: A critical review of biophysical modelling and data analysis approaches. *J. Integrat. Neurosci.* 09, 453–476. doi: 10.1142/S0219635210002512

Rothlübbers, S., Relvas, V., Leal, A., Murta, T., Lemieux, L., and Figueiredo, P. (2015). Characterisation and Reduction of the EEG Artefact Caused by the Helium Cooling Pump in the MR Environment: Validation in Epilepsy Patient Data. *Brain Topogr.* 28, 208–220. doi: 10.1007/s10548-014-0408-0

Sammer, G., Blecker, C., Gebhardt, H., Kirsch, P., Stark, R., and Vaitl, D. (2005). Acquisition of typical EEG waveforms during fMRI: SSVEP, LRP, and frontal theta. *NeuroImage* 24, 1012–1024. doi: 10.1016/j.neuroimage.2004.10.026

Scheeringa, R., Bastiaansen, M. C. M., Petersson, K. M., Oostenveld, R., Norris, D. G., and Hagoort, P. (2008). Frontal theta EEG activity correlates negatively with the default mode network in resting state. *Int. J. Psychophysiol.* 67, 242–251. doi: 10.1016/j.ijpsycho.2007.05.017

Scheeringa, R., Koopmans, P. J., Mourik, T., van, Jensen, O., and Norris, D. G. (2016). The relationship between oscillatory EEG activity and the laminar-specific BOLD signal. *Proc. Natl. Acad. Sci.* 113, 6761–6766. doi: 10.1073/pnas.1522577113

Scrivener, C. L., and Reader, A. T. (2021). Variability of EEG electrode positions and their underlying brain regions: Visualising gel artifacts from a simultaneous EEG-fMRI dataset. *BioRxiv* 2021:434424. doi: 10.1101/2021.03.08.434424

Scrivener, C. L., Malik, A., Lindner, M., and Roesch, E. B. (2020). Sensing and seeing associated with overlapping occipitoparietal activation in simultaneous EEG-fMRI. *BioRxiv* 2020:193326. doi: 10.1101/2020.07.08.193326

Seeber, M., Cantonas, L.-M., Hoevels, M., Sesia, T., Visser-Vandewalle, V., and Michel, C. M. (2019). Subcortical electrophysiological activity is detectable with high-density EEG source imaging. *Nat. Commun.* 10:753. doi: 10.1038/s41467-019-08725-w

Srivastava, G., Crottaz-Herbette, S., Lau, K. M., Glover, G. H., and Menon, V. (2005). ICA-based procedures for removing ballistocardiogram artifacts from EEG data acquired in the MRI scanner. *NeuroImage* 24, 50–60. doi: 10.1016/j.neuroimage.2004.09.041

Thut, G., Schyns, P., and Gross, J. (2011a). Entrainment of Perceptually Relevant Brain Oscillations by Non-Invasive Rhythmic Stimulation of the Human Brain. *Front. Psychol.* 2:00170. doi: 10.3389/fpsyg.2011.00170

Thut, G., Veniero, D., Romei, V., Miniussi, C., Schyns, P., and Gross, J. (2011b). Rhythmic TMS Causes Local Entrainment of Natural Oscillatory Signatures. *Curr. Biol.* 21, 1176–1185. doi: 10.1016/j.cub.2011.05.049

Ullsperger, M., and Debener, S. (2010). *Simultaneous EEG and fMRI: Recording, Analysis, and Application*. Oxford: Oxford University Press.

Vulliemoz, S., Thornton, R., Rodionov, R., Carmichael, D. W., Guye, M., Lhatoo, S., et al. (2009). The spatio-temporal mapping of epileptic networks: Combination of EEG–fMRI and EEG source imaging. *NeuroImage* 46, 834–843. doi: 10.1016/j.neuroimage.2009.01.070

Walz, J. M., Goldman, R. I., Carapezza, M., Muraskin, J., Brown, T. R., and Sajda, P. (2015). Prestimulus EEG alpha oscillations modulate task-related fMRI BOLD responses to auditory stimuli. *NeuroImage* 113, 153–163. doi: 10.1016/j.neuroimage.2015.03.028

Wirsich, J., Jorge, J., Iannotti, G. R., Shamshiri, E. A., Grouiller, F., Abreu, R., et al. (2021). The relationship between EEG and fMRI connectomes is reproducible across simultaneous EEG-fMRI studies from 1.5T to 7T. *NeuroImage* 231:117864. doi: 10.1016/j.neuroimage.2021.117864

Zich, C., Debener, S., Kranczioch, C., Bleichner, M. G., Gutberlet, I., and De Vos, M. (2015). Real-time EEG feedback during simultaneous EEG–fMRI identifies the cortical signature of motor imagery. *NeuroImage* 114, 438–447. doi: 10.1016/j.neuroimage.2015.04.020

Conflict of Interest: The author declares that the research was conducted in the absence of any commercial or financial relationships that could be construed as a potential conflict of interest.

frontiers | Frontiers in Neuroscience

ORIGINAL RESEARCH
published: 11 May 2022
doi: 10.3389/fnins.2022.848737

EEG Microstate-Specific Functional Connectivity and Stroke-Related Alterations in Brain Dynamics

Zexuan Hao[1], Xiaoxue Zhai[2], Dandan Cheng[2], Yu Pan[2]*† and Weibei Dou[1]*†

[1] Department of Electronic Engineering, Beijing National Research Center for Information Science and Technology (BNRist), Tsinghua University, Beijing, China, [2] Department of Rehabilitation Medicine, School of Clinical Medicine, Beijing Tsinghua Changgung Hospital, Tsinghua University, Beijing, China

The brain, as a complex dynamically distributed information processing system, involves the coordination of large-scale brain networks such as neural synchronization and fast brain state transitions, even at rest. However, the neural mechanisms underlying brain states and the impact of dysfunction following brain injury on brain dynamics remain poorly understood. To this end, we proposed a microstate-based method to explore the functional connectivity pattern associated with each microstate class. We capitalized on microstate features from eyes-closed resting-state EEG data to investigate whether microstate dynamics differ between subacute stroke patients ($N = 31$) and healthy populations ($N = 23$) and further examined the correlations between microstate features and behaviors. An important finding in this study was that each microstate class was associated with a distinct functional connectivity pattern, and it was highly consistent across different groups (including an independent dataset). Although the connectivity patterns were diminished in stroke patients, the skeleton of the patterns was retained to some extent. Nevertheless, stroke patients showed significant differences in most parameters of microstates A, B, and C compared to healthy controls. Notably, microstate C exhibited an opposite pattern of differences to microstates A and B. On the other hand, there were no significant differences in all microstate parameters for patients with left-sided vs. right-sided stroke, as well as patients before vs. after lower limb training. Moreover, support vector machine (SVM) models were developed using only microstate features and achieved moderate discrimination between patients and controls. Furthermore, significant negative correlations were observed between the microstate-wise functional connectivity and lower limb motor scores. Overall, these results suggest that the changes in microstate dynamics for stroke patients appear to be state-selective, compensatory, and related to brain dysfunction after stroke and subsequent functional reconfiguration. These findings offer new insights into understanding the neural mechanisms of microstates, uncovering stroke-related alterations in brain dynamics, and exploring new treatments for stroke patients.

Keywords: EEG, microstates, brain dynamics, functional connectivity, stroke, machine learning, lower extremity motor function

Edited by:
Oscar Arias-Carrion,
Hospital General Dr. Manuel Gea González, Mexico

Reviewed by:
Marc Sebastián-Romagosa,
g.tec Medical Engineering GmbH, Austria
Anthony Zanesco,
University of Miami, United States

Correspondence:
Yu Pan
panyu@btch.edu.cn
Weibei Dou
douwb@tsinghua.edu.cn

†These authors have contributed equally to this work

Specialty section:
This article was submitted to Brain Imaging Methods, a section of the journal Frontiers in Neuroscience

Received: *05 January 2022*
Accepted: *08 April 2022*
Published: *11 May 2022*

Citation:
Hao Z, Zhai X, Cheng D, Pan Y and Dou W (2022) EEG Microstate-Specific Functional Connectivity and Stroke-Related Alterations in Brain Dynamics. Front. Neurosci. 16:848737. doi: 10.3389/fnins.2022.848737

INTRODUCTION

It is now a consensus that the brain at rest is not truly "at rest", and the spontaneous brain activity exhibits complex dynamic spatiotemporal configurations (Raichle et al., 2001; Fox and Greicius, 2010; Pirondini et al., 2017). Of note, spontaneous brain activity can predict behavioral performance, and intrinsic activity plays a basic and functional role in brain function (Spisak et al., 2020). On the other hand, brain injury (e.g., stroke) causes behavioral deficits as well as widespread structural and functional network dysfunction (Salvalaggio et al., 2020). Motor and sensory impairments are the two most common deficits after stroke, affecting approximately 85 and 50% of stroke patients, respectively (Wu et al., 2015; Ramsey et al., 2017). To date, using neurophysiological techniques, a tremendous number of studies based on spectral analysis, functional connectivity, and graph theory analysis have been reported in the field of brain injury mechanisms and stroke rehabilitation (Wu et al., 2015; Stinear, 2017; Trujillo et al., 2017; Mane et al., 2019; Chiarelli et al., 2020; Ros et al., 2022). These studies laid an important foundation for our understanding of stroke-related neurological alterations and neuroplasticity and for finding neural markers that can indicate prognosis and outcomes. However, given the intrinsic non-stationary nature of brain neural signals, static features are not time-resolved and lose the information about the time dimension. Dynamic analysis methods may better reflect the full profile of brain activity and capture critical features of the spatiotemporal dimensions in health and disease (Kabbara et al., 2017; Chang et al., 2018; O'Neill et al., 2018; Bonkhoff et al., 2020; Wang et al., 2020). Dynamic functional connectivity is the most commonly used method in functional magnetic resonance imaging (fMRI) studies to investigate the connectivity dynamics in stroke patients. It has shown that stroke alters the brain's preference for distinct connectivity states (Bonkhoff et al., 2020; Wang et al., 2020). However, the sliding-window approach, which is typically utilized in dynamic functional connectivity, has the limitation of requiring a *prior* unknown window width (O'Neill et al., 2018). Windows that are too short or too long will not capture the true temporal dynamics of the brain. Several alternative approaches have been applied to electrophysiological data to describe the brain dynamics, including hidden Markov models (HMMs) (Vidaurre et al., 2018; Bai et al., 2021a) and microstate analysis (Pascual-Marqui et al., 1995; van de Ville et al., 2010; Zanesco et al., 2020). Spatially distinct patterns of oscillatory power and coherence at the source level have been observed in health and disorders of consciousness by HMMs (Vidaurre et al., 2018; Bai et al., 2021a). Nonetheless, it remains unclear whether the assumptions underlying HMMs are met in resting-state EEG (Gschwind et al., 2015; von Wegner et al., 2016). In addition, little is known about the electromagnetic properties of the brain injury regions, and techniques for constructing accurate head models of patients with brain injuries (e.g., stroke) have not yet been well developed. Microstates reflect short periods (~100 ms) of quasi-stable brain states that evolve in time, resulting from the synchronous and coordinated activity of brain networks (Pascual-Marqui et al., 1995; Koenig et al., 2002; Zanesco et al., 2020). Importantly, microstate analysis is traditionally at the sensor level and needs minimal assumptions regarding the properties of the neural signals.

Numerous studies based on EEG have demonstrated that resting-state functional connectivity and microstate analyses are successful and valuable methods for studying neurological and psychiatric diseases (Khanna et al., 2015; Zappasodi et al., 2017; Zuchowicz et al., 2018; Eldeeb et al., 2019; Musaeus et al., 2019a; Riahi et al., 2020; Tait et al., 2020). Additionally, there are associations between EEG microstates and fMRI resting-state networks (RSNs) (Britz et al., 2010; van de Ville et al., 2010; Custo et al., 2017). Furthermore, motor scores are related to EEG features (e.g., functional connectivity) of spontaneous brain activity (Riahi et al., 2020; Hoshino et al., 2021). Given the tight link between microstates and brain networks of spontaneous brain activity, we speculated that microstate dynamics could reflect the motor capacity (e.g., lower/upper limb function) to some extent (Pirondini et al., 2017; Spisak et al., 2020; Zhang et al., 2021). However, the current microstate studies have mainly focused on the cognitive functions of the brain in health (Brechet et al., 2019; Pirondini et al., 2020; Zanesco et al., 2020) and diseases like schizophrenia (da Cruz et al., 2020) and Alzheimer (Musaeus et al., 2019b; Tait et al., 2020). Only a limited number of studies focused on patients with brain injuries, such as stroke (Zappasodi et al., 2017) and consciousness of disorders (Gui et al., 2020; Bai et al., 2021b). To date, only one study (to our knowledge) with the complete microstate analysis (Zappasodi et al., 2017) focused on stroke (at the acute stage). This research suggested that microstate B duration explained the 11% of the effective recovery of the National Institute of Health Stroke Scale (NIHSS), and there was a significant difference between patients with left-sided and right-sided stroke in parameters of microstate C and D. Further in-depth research is needed to verify and explore the stroke-related alterations in microstate dynamics.

There are still three critical questions that need to be deeply investigated. First, is each microstate class associated with a specific functional connectivity pattern? Several studies have explored state-wise functional connectivity in different scenarios (Comsa et al., 2019; Duc and Lee, 2019), but the connectivity pattern corresponding to each microstate class in the resting state is still unclear. In addition, according to previous studies, each microstate template has distinct topographic distribution and bright characteristics (Michel and Koenig, 2018; Li et al., 2021; Zanesco et al., 2021). Therefore, we assumed that each microstate class corresponds to a unique pattern of functional connectivity. It is instructive for addressing this question to extend our understanding of the mechanisms underlying microstates and help us explain microstate dynamics. Second, how do the microstate parameters evolve in time after stroke, and how are they perturbed or altered by stroke? Third, do microstate parameters encode information that reflects the motor capacity of the lower limbs? Lower limb motor function is an important basis for restoring walking function and activities of daily living after stroke. However, currently few studies have assessed lower limb function by neural features derived from EEG (Sebastian-Romagosa et al., 2020; Hoshino et al., 2021). The answers to the latter two questions will help us to explore the crucial characteristics of stroke patients, the possible patterns of brain functional reorganization, and the possibility of using microstate dynamics for functional assessment.

In the current study, we proposed a microstate-based approach and leveraged the EEG datasets of patients at two-time points (i.e., before and after the rehabilitation therapy) and healthy controls to explore the three aforementioned questions. The Lower-extremity part of Fugl-Meyer Assessment (FMAL) was used to evaluate the lower limb functional status of stroke patients at the two-time points (Fugl-Meyer et al., 1975). Previous research has suggested that intra-cortical alpha oscillations primarily account for the emergence of microstate classes (Milz et al., 2017), and most microstate studies are based on larger bandwidths such as 2–20 or 1–40 Hz (Khanna et al., 2015). Here, we used the EEG signal in the 1–20 Hz frequency band for microstate analysis. Phase-locked synchronization of neural signals in the brain may be the key mechanism for brain information integration (Michel and Koenig, 2018). Therefore, in this study, functional connectivity in the alpha band was constructed by the phase-locking value (PLV) method (Lachaux et al., 1999; Duc and Lee, 2019; Yao et al., 2021). Microstate-specific connectivity was computed by connected instantaneous phase signals belonging to a particular microstate class. We compared one microstate-specific functional connectivity with the others to examine whether there were differences among microstate-wise connectivity. The results were also validated in an independent EEG dataset (Babayan et al., 2019). In addition, due to the functional and structural deficits after stroke, we predicted that some microstate parameters would be significantly different in stroke patients compared to those in healthy controls. We also tested how microstate features changed after rehabilitation training, and whether there were significant differences in microstate features between patients with left-sided and right-sided stroke. Moreover, we utilized support vector machine (SVM) models to investigate their ability to distinguish stroke patients from healthy controls by only microstate features. Finally, we explored the cross-sectional correlations between the microstate features and FMAL scores. This may allow us to identify potential neural markers that provide insight into lower limb function recovery after stroke.

In sum, we explored the functional connectivity patterns underlying microstates and investigated how microstate dynamics are altered in stroke patients at two-time points compared to healthy individuals and the associations between microstate features and FMAL scores. No such study exists for microstates.

MATERIALS AND METHODS

Participants

Patients

Fifty-nine patients were recruited, and 31 patients (mean age 56.7 years with range 31.7–77.4; *SD* = 12.1; 29 right-handed; 24 males; 19 with left-sided stroke) satisfied the post-enrollment inclusion criteria. No statistical methods were used to predetermine the sample sizes in this study, but our sample sizes were similar to those reported in previous research (Pirondini et al., 2020; Wang et al., 2021).

Inclusion Criteria of Patients

(1) Aged 30–80. (2) First-ever unilateral brain lesion. (3) Subacute stroke (2 weeks to 6 months poststroke). (4) Sufficient cognition (Mini-Mental State Examination, MMSE score > 21). (5) Moderate-to-severe paralysis (Brunnstrom score $\leq$ IV). (6) No other diagnosis substantially affecting the lower limbs. (7) No other neurological or psychiatric disorders. (8) Medically stable.

Healthy Controls

Twenty-three healthy controls (mean age 58.9 years with range 31.5–73.2; *SD* = 12.0; 21 right-handed; 13 males) were recruited for this study. In addition, an external site EEG dataset of healthy subjects (*N* = 32; age range 30–80; 29 right-handed; 21 males) selected from the "Mind-Brian-Body dataset" (Babayan et al., 2019) was used to validate the stability of the results of microstate-specific functional connectivity (**Supplementary Table 1**). To distinguish the external site EEG dataset from the healthy controls in this study, "LEMON" was used to refer to the external site dataset.

The study was conducted according to the tenets of the Declaration of Helsinki, the guidelines for Good Clinical Practice, and the Consolidated Standards of Reporting Trials (CONSORT), approved by the Ethics Committee of Beijing Tsinghua Changgung Hospital (18172-0-01). All subjects provided written informed consent before participating in the study.

Treatment Protocol and Clinical Evaluation

All patients received 10-session ankle stretching training using the robot-aided stretching (five times a week over 2 weeks, 20 min/session). An ankle rehabilitation robot (Beijing LTK Science and Technology Co., Ltd., Beijing, China) was used for intervention. The ankle rehabilitation robot was driven by a servomotor controlled by a digital signal processor. The stretching protocol has been described in detail in our previous research (Zhai et al., 2021). During the 2 weeks, all patients received standard medical care and rehabilitation, which consisted of routine physiotherapy (PT) and occupational therapy (OT). Patients completed a 1-h PT session and 1-h OT per day, 5 days per week, for a total of 10 sessions. PT included continued movement exercises for hemiplegia, muscle strength training, and balance and walking function exercises. OT focused on rehabilitation of arm and hand movements used in daily activities. Subjects were evaluated before and after the interventions by a designated physiotherapist. FMAL (0–34 points) was used to evaluate the lower limb motor function of stroke patients and was conducted at two-time points: before the therapy (T0, baseline) and immediately after 10 training sessions (T1) (Fugl-Meyer et al., 1975; Gladstone et al., 2002; See et al., 2013). In addition, EEG data were also collected for each

TABLE 1 | Sample demographics and clinical information.

	Patients (*N* = 31)	Controls (*N* = 23)	*p*	Effect size
Age (M ± *SD*, range)	56.7 ± 12.1, 31.7–77.4	58.9 ± 12.0, 31.5–73.2	0.52	–0.18
Gender (female/male)	7/24	10/13	0.10	0.22
Handedness (left/right)	2/29	2/21	0.76	0.04
Lesion side (left/right)	19/12			
Stroke type (hemorrhagic/ischemic)	6/25			
Days poststroke at T0 (M ± *SD*, range)	65.9 ± 39.7, 15–154			

M ± SD: mean ± standard deviation. The two-sample t-test for age and Pearson's chi-squared tests for gender and handedness were performed between patients and controls. The effect size was estimated using Cohen's d for age and Cramer's V for gender and handedness.

patient at two-time points (**Supplementary Figure 1A**). Group characteristics and clinical information are presented in **Table 1**.

EEG Data Acquisition and Preprocessing

Eyes-closed resting-state EEG data were acquired from a 64-channel electrode cap (NeuSen W64, Neuracle, China), with 59 scalp electrodes (Ag/AgCl) placed according to the 10-10 international system. The data file of the channel locations is provided in **Supplementary Material**. EEG data were recorded using a Neuracle amplifier with 24-bit resolution and a sampling rate of 1,000 Hz, and lowpass filtered with the cutoff frequency (−3 dB) at 250 Hz for between approximately 3–5 min. The reference electrode was located at CPz, and the ground electrode was located at AFz. During the recording, the impedance was kept below 20 kΩ for all scalp electrodes. EEG data were recorded in a specific, dimly lit, sound-attenuated, but not electrically shielded room. An investigator focused on the status of the participants, and they were requested to minimize their movements and remain awake.

EEG data were preprocessed offline in MATLAB (R2020b, Mathworks, Natick, MA, United States) using the EEGLAB toolbox (version 2019.0, Swartz Center for Computational Neuroscience, San Diego, CA, United States) and its extensions in combination with some custom MATLAB scripts. All preprocessing steps consistently maintained double-precision computations. FIR filters were used in this study and designed using the function *pop_firws()* with a Hamming window. First, EEG data were lowpass filtered (order: 660, transition width: 5.0 Hz, −6 dB cutoff frequency: 45 Hz) to remove the line noise and then resampled to 250 Hz. In addition, low-frequency noise was attenuated using a high-pass filter (order: 826, transition width: 1 Hz, −6 dB cutoff frequency: 0.5 Hz). Then, bad channels and EEG segments containing large, non-stereotype artifacts were discarded semi-automatically. The signal of the bad channels was interpolated through spherical interpolation and then EEG data were re-referenced to the common average and the signal of the original reference CPz channel was restored. Next, EEG data were decomposed by independent component analysis (ICA) using the default *binica* method in the EEGLAB toolbox. Artifactual components (e.g., eye blinks, movement, channel noise, muscle activity, and heart) were discarded *via* visual inspection with the help of plugin extensions in EEGLAB (i.e., ICLabel, DIPIT, and ADJUST). There were no significant differences in the number of bad channels or artifactual components between stroke patients and healthy controls. See **Supplementary Table 2** for more details. EEG data acquisition and preprocessing of the LEMON dataset were extensively described in the previous studies (Babayan et al., 2019; Férat et al., 2020; Zanesco et al., 2020).

Microstate-Based Analysis of Brain Dynamics

Microstate analyses were performed in MATLAB. Some steps were based on the Microstate toolbox (MST, version 1.0) (Poulsen et al., 2018) and Microstate[1] (version 1.2). The complete analysis pipeline used in this study is shown in **Figure 1**. EEG data were first lowpass filtered (order: 208, transition width: 4.0 Hz, −6 dB cutoff frequency: 22 Hz) and then re-referenced to the common average before microstate analysis. Local maximal values (peaks) of the global field power (GFP) were extracted from each EEG recording. GFP was calculated as the standard deviation of the amplitude across all channels at each time point. EEG maps at GFP peaks are reliable representations of the topographic maps because of their high signal-to-noise ratio (Koenig et al., 2002). Considering the high uncertainty in the assignment of states for maps with low GFP, we discarded the bottom 15% of GFP peaks (Mishra et al., 2020). GFP peaks that were greater than three times the standard deviation were also excluded. EEG maps at the remaining GFP peaks (also called original maps) were used for further analysis.

Identifying Recording-Specific Microstate Templates

For each recording, a modified k-means clustering algorithm (ignoring the polarity) was used to find 2–10 (k = [2:10]) templates using the original maps (Murray et al., 2008; Poulsen et al., 2018). For each k, the clustering procedure was repeated 100 times and returned the templates of the run with the largest global explained variance (GEV). Meanwhile, the GEV and the value of the Krzanowski–Lai (KL) criterion (Krzanowski and Lai, 1988; Murray et al., 2008) were determined for each k.

Identifying Group-Specific Microstate Templates

To have equal contributions of microstates per participant in the group, each participant provided the same number of templates to the second modified k-means clustering (van de Ville et al., 2010; Nishida et al., 2013). For each group, the optimal number of

---

[1] https://www.thomaskoenig.ch/index.php/software/microstates-in-eeglab/getting-started

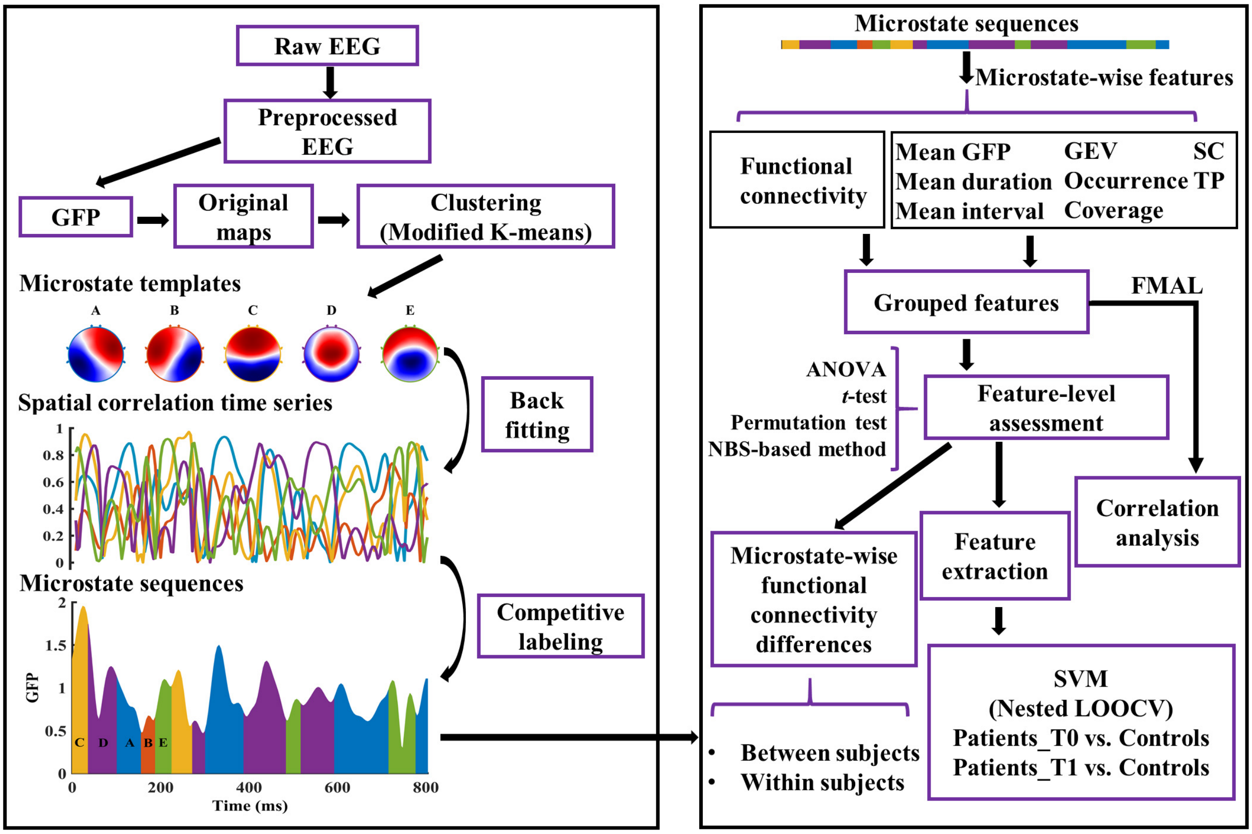

FIGURE 1 | Graphical representation of the analysis method in the study. The microstate templates used in this study are common templates of patients and healthy controls. See "Materials and Methods" section for details. GFP, Global Field Power; GEV, Global Explained Variance; SC, Spatial Correlation metric; TP, Transition Probability; FMAL, Lower-extremity part of Fugl-Meyer Assessment; SVM, Support Vector Machine; LOOCV, Leave-One-Out Cross-Validation.

templates at the group level (k^*) was determined by the number of clusters corresponding to the maximum value of the mean of the normalized KL across all recordings in the group. The k^* templates from each participant of the group were concatenated, and then k^* clusters were determined by the modified k-means algorithm. The centroids of the k^* clusters were the group-specific microstate templates.

Identifying Common Microstate Templates

In this study, the optimal number was five in both the stroke patients and healthy controls. To avoid systematic variances derived from the differences of group-specific microstate templates between patients and healthy controls, the common microstate templates were used. To get the common templates, the modified K-means method was utilized for the group-specific microstate templates of patients and controls. The common templates were labeled A–E according to their similarities to the templates in the previous research (Férat et al., 2020; Shi et al., 2020; Zanesco et al., 2020).

Back-Fitting of the Microstate Templates

The common templates were fitted back to all the EEG maps (not just the maps at the GFP peaks) of each preprocessed EEG recording. EEG map at each time point was assigned a label according to the map with which the template demonstrated the highest absolute spatial correlation. Thereafter, EEG maps were converted into microstate sequences. Temporal smoothing was then employed in the microstate sequence by changing the labels of small segments (<30 ms) to the next most likely microstate class until no microstate segment was smaller than 30 ms (Poulsen et al., 2018; Liu et al., 2020). Note that the first and last microstates in each EEG segment (caused by the removal of artifacts) were potentially truncated. Thus, these microstates were not taken into consideration when calculating the parameters of each microstate class.

Microstate-Wise Functional Connectivity

In this study, the functional connectivity of each microstate class was computed by a phase-based method (i.e., PLV) across all channel pairs for the alpha band (8–12 Hz). EEG data were first applied with surface Laplacian transform using the CSD toolbox (Kayser and Tenke, 2006) to overcome the volume conduction problem. The phase signal was then extracted by applying the Hilbert transform to the band-filtered EEG data, and 10% phase angles of each side were discarded due to the edge effects. The segments of the phase angles belonging to a particular microstate class were picked up and concatenated together. Thereafter, the microstate-wise functional connectivity over time across all channel pairs was calculated. For instance, PLV of microstate class *m* between two channels *i* and *j* is calculated by the formula:

$$PLV_{i,j}^{m} = \left| \frac{1}{N} \sum_{n=1}^{N} e^{-\mathrm{i}(\varphi_{jn} - \varphi_{in})} \right|,$$

where N is the number of time points belonging to microstate m, and φ_i, φ_j are phase angles from channels *i* and *j*.

Microstate Parameters

For each EEG recording, the microstate sequence and microstate spatial correlation time series (dimension: # microstate classes × # time points) were computed (see **Figure 1**). Subsequently, dynamic parameters per microstate class were estimated. *GEV*, which measures the percentage of variance explained for the EEG maps across all time points by each specific microstate template. *Mean duration*, defined as the average of the continuous length of time during which the EEG time series is determined to be a certain microstate class. *Occurrence*, the average number of occurrences per second of each microstate class. *Coverage*, defined as the percentage of total analysis time occupied by each microstate class. *Mean interval*, the average across all the lengths of time from the end of a particular microstate class to the start of the next same microstate class. *Mean GFP*, the average amplitude of GFP during each microstate class dominance. *Spatial correlation metric* (SC), the mean absolute correlation values of each microstate template with maps of a given microstate class. For example, SC_{AB} is the average absolute correlation coefficients between the template of microstate A and all the maps belonging to microstate B. *Transition probability* (TP), defined as the probability (observed transition probability minus expected transition probability) from each microstate class to another (Nishida et al., 2013). See Murray et al. (2008), Nishida et al. (2013), Khanna et al. (2015), and Michel and Koenig (2018) for the details of the interpretation of microstate parameters.

Statistical Analysis

In the study, the significance level is 0.05. All statistical tests are two-sided tests. All the reported *p*-values were based on the non-parametric permutation method (Knijnenburg et al., 2009; Zalesky et al., 2010). For multiple comparisons, we reported the *p*-values corrected by the Bonferroni-Holm method, unless specified otherwise.

For Microstate-Wise Functional Connectivity

A method based on the network-based statistic (NBS) was constructed to control the family-wise error rate as massive univariate tests were performed in connection comparisons (Zalesky et al., 2010). Briefly, the NBS-based algorithm utilized in this study comprises the following steps. (1) Compute both *p*-value and test-statistic (e.g., *t*-value or correlation coefficient) maps resulting from the statistical test of all connections. (2) A threshold (p_{thr}) was applied to the *p*-value map. Elements below the threshold were set to 1, and the others were set to 0. The resulting mask was applied to the test-statistic map. The sparse test-statistic map was divided into two parts according to the signs of the elements. MATLAB function *conncomp* was used to determine the connection components for each part. The connected components and the size (e.g., the sum of *t*-values or correlation coefficient) of each component were determined for each part. (3) Perform permutation tests (2,000 permutations). For each iteration, the labels were randomly shuffled. More specifically, for between-subjects designs, condition labels were randomly shuffled; for within-subjects designs, the signs of the differences of a feature for each subject between two conditions were randomly assigned; for Pearson correlations, the orders of the FMAL scores were randomly shuffled. Repeat steps (1) and (2). Then, calculate the sizes of the largest positive and negative components and store them in a matrix, respectively. Note that the observed connected components and their sizes were computed and stored before the permutation procedure. (4) After all iterations, two null distributions were obtained, namely the sizes of the largest positive and negative components. For each observed connected component, the *p*-value was computed as the following formula:

$$p = 2 \times \frac{sum\left(abs\left(\boldsymbol{S_{null}}\right) > abs\left(s_{obs}\right)\right) + 1}{N + 1},$$

where N is the number of permutations, s_{obs} is the size of the observed connected component, and $\boldsymbol{S_{null}}$ is one null distribution chosen based on the sign of the observed connected component's size. For difference or correlation analysis, computing the mean of the functional connectivity strength within the connected component (mean FCSCC) is one way to reduce the feature dimension.

For Microstate Parameters

For patients at T0/T1 vs. healthy controls, for each microstate parameter, we conducted a two-way mixed ANOVA, with Group, Microstate Class/Spatial correlation Pair/Transition Pair as factors. Accordingly, for patients at T0 vs. patients at T1, for each microstate parameter, we conducted a two-way repeated ANOVA. If the interaction effect was significant, *post hoc* permutation tests were used for pairwise group comparisons for each level of the Microstate Class/Spatial correlation Pair/Transition Pair factor.

For ANOVAs above, the sphericity, normality, and homogeneity of variance were assessed by the Mauchly's test, Kolmogorov-Smirnov test, and Levene's test, respectively. If the assumption of sphericity was violated, the degrees of freedom were corrected using Greenhouse-Geisser correction if $\varepsilon < 0.75$, otherwise, using Huynh-Feldt correction. If the assumption of normality or homogeneity of variance was violated, pairwise group comparisons were directly performed using permutation tests. Permutation tests for two samples and paired samples were computed with 100,000 replications using the *t*-value as a measure of group difference. We also performed correlation analysis between microstate parameters and FMAL scores. *p*-values were calculated by permutation test with 100,000 replications using Pearson correlation coefficient as the test statistic. The 95% confidence interval (CI) was generated by the bootstrap method (10,000 bootstrap data samples; CI = bias corrected and accelerated).

Classification

We employed SVM models to assess whether microstate-wise features could provide reliable signatures of stroke. Due to the massive number of features, the microstate parameters, including mean FCSCC, which were significantly different between stroke and health at both T0 and T1 were retained for further analysis. SVM models were conducted with the Python package *scikit-learn*. We constructed the SVM classifiers using linear and radial basis function (RBF) kernels, respectively. To avoid an optimistically biased evaluation of the model performance, the nested leave-one-out cross-validation (nested LOOCV) was utilized to evaluate the tuned SVM models. Moreover, the *scikit-learn pipeline* of the preprocessing steps was employed to prevent data leakage in the cross-validation and hyper-parameter tuning procedures. For each iteration of the outer LOOCV loop, one sample was split as the test dataset and the rest as the training dataset. We first scaled the features to have mean 0 and variance 1 and then used principal component analysis (PCA) for feature reduction (retaining 95% variance) before training each model. Then, in the inner LOOCV loop, select the best hyperparameters based on grid search hyperparameter optimization and refit a model with the entire training dataset with the parameters. This model then was used to predict the test dataset of the outer LOOCV loop. After all iterations of the outer loop, the prediction results of all samples were collected, and then the model performance was evaluated by the receiver operating characteristic (ROC) curve and the area under the curve (AUC) of the ROC.

Statistical and Visualization Tools

All ANOVAs were carried out in IBM SPSS Statistics 26 (SPSS IBM, Armonk, New York, United States). The other statistical analysis was conducted with custom MATLAB scripts. Schemaball plots were made with some modifications to the schemaball project.[2] Networks with EEG electrodes as nodes (Koessler et al., 2009) were created by BrainNet Viewer software (Xia et al., 2013). Violin plots were generated by OriginPro 2022 Beta2 (OriginLab Corporation, Northampton, MA, United States). Other figures were created using custom MATLAB scripts.

RESULTS

Patients Findings

The sample demographics and clinical information are summarized in **Table 1**. After 10 sessions of training, patients ($N = 31$) showed significantly increased FMAL scores ($p = 1.000\text{e-}5$) compared to the baseline (**Supplementary Figure 1B**). Moreover, patients with right-sided stroke ($N = 12$) presented higher FMAL scores than those with left-sided stroke, but the differences were not significant at both T0 ($p = 0.131$) and T1 ($p = 0.161$). On average, the time poststroke at T0 was 65.9 days ($SD = 39.7$ days) and patients with left-sided stroke showed a slightly shorter time than patients with right-sided stroke ($p = 0.419$). In this study, only six patients had a hemorrhagic stroke and seven patients were female. Considering the reliability of the results, no further statistical analysis was conducted to compare the differences between stroke-type subgroups or between gender subgroups.

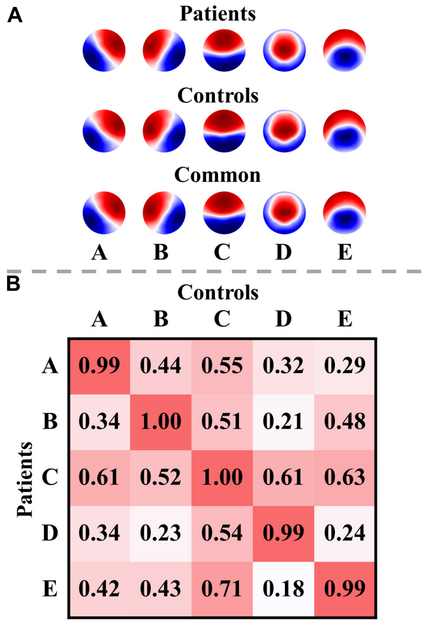

	A	B	C	D	E
A	0.99	0.44	0.55	0.32	0.29
B	0.34	1.00	0.51	0.21	0.48
C	0.61	0.52	1.00	0.61	0.63
D	0.34	0.23	0.54	0.99	0.24
E	0.42	0.43	0.71	0.18	0.99

FIGURE 2 | Microstate templates and spatial correlations. **(A)** Microstate templates. **(B)** Spatial correlations between the microstate templates of patients and controls. Polarity was ignored when computing the correlations. The templates of the patients were calculated from all their EEG data at T0 and T1.

Microstate Templates

The optimal number of microstate classes was five for both the patients and controls. The five microstate templates of the patients and controls were provided in **Figure 2A**. Interestingly, the microstate templates of patients and controls were highly similar (all $rs > 0.99$), as shown in **Figure 2B**. Nevertheless, to reduce the potential systematic variances caused by the template differences between patients and controls, the common microstate templates were utilized in further analysis. The five common microstate templates were labeled A–E according to their similarities to the templates reported in the previous large sample size study (Zanesco et al., 2020). On average, the templates explained 80.52, 80.82, and 79.86% of the GEV (fitting to maps at GFP local maxima) for patients at T0, patients at T1, and healthy controls, respectively.

Microstate-Wise Functional Connectivity

The functional connectivity associated with each microstate class is displayed in **Supplementary Figure 2**. Intuitively, the functional connectivity of microstate C appeared to be stronger compared to the other microstate classes. The microstate-wise connectivity seemed similar to each other due to the masking of strong short-range connections. However, the

---

[2] https://github.com/okomarov/schemaball

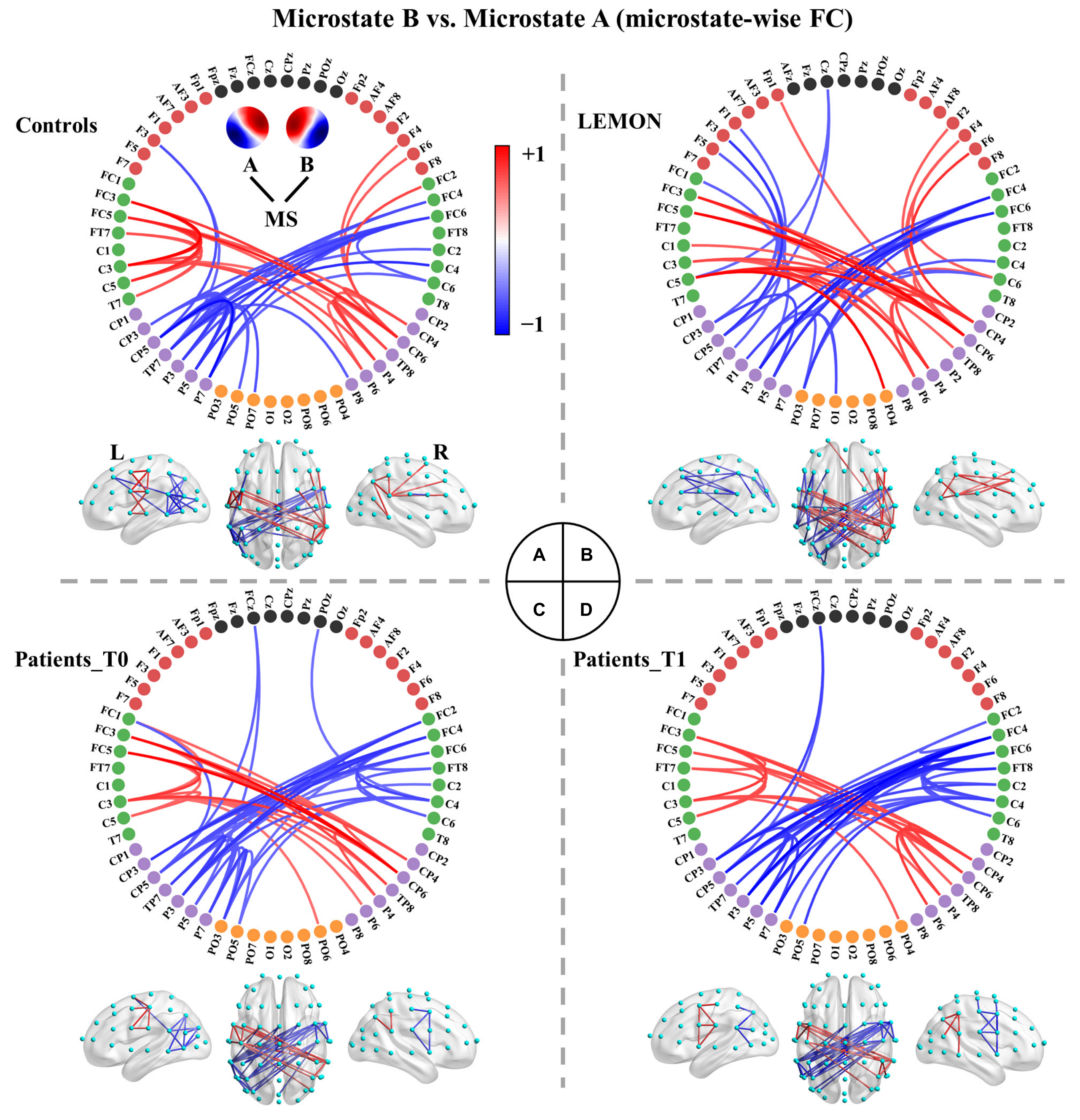

FIGURE 3 | Comparisons between functional connectivity of microstates A and B for the four groups. **(A)** Healthy controls. **(B)** LEMON. **(C)** Patients at T0. **(D)** Patients at T1. For visual clarity, only the top 50 connections (according to absolute *t*-values) in the connected components with significant differences ($p < 0.05$, NBS-based method corrected) are displayed in the figure. The red color indicates greater connectivity for microstate B vs. microstate A, while the blue color indicates greater connectivity for microstate A vs. microstate B. Color depth represents the size of the connection difference (*t*-value). The complete connected components are provided in the first column of **Supplementary Figure 3**.

comparison results ($p_{thr} = 0.001$) demonstrated significant differences between functional connectivity of microstate classes (**Supplementary Table 3**). For convenience, FC_X refers to the functional connectivity of microstate X. To further evaluate the stability and robustness of the results, an independent EEG dataset of healthy subjects, LEMON, was introduced in the present study. Briefly, after NBS-based correction, all but two of the comparison pairs of microstate-wise functional connectivity were significant ($ps < 0.05$) for all four groups (the smallest p-value of $FC_C < FC_A$ of controls $p = 0.096$ and $FC_C < FC_B$ of patients at T1 $p = 0.099$). Strikingly, the patterns of differences between microstate-wise functional connectivity

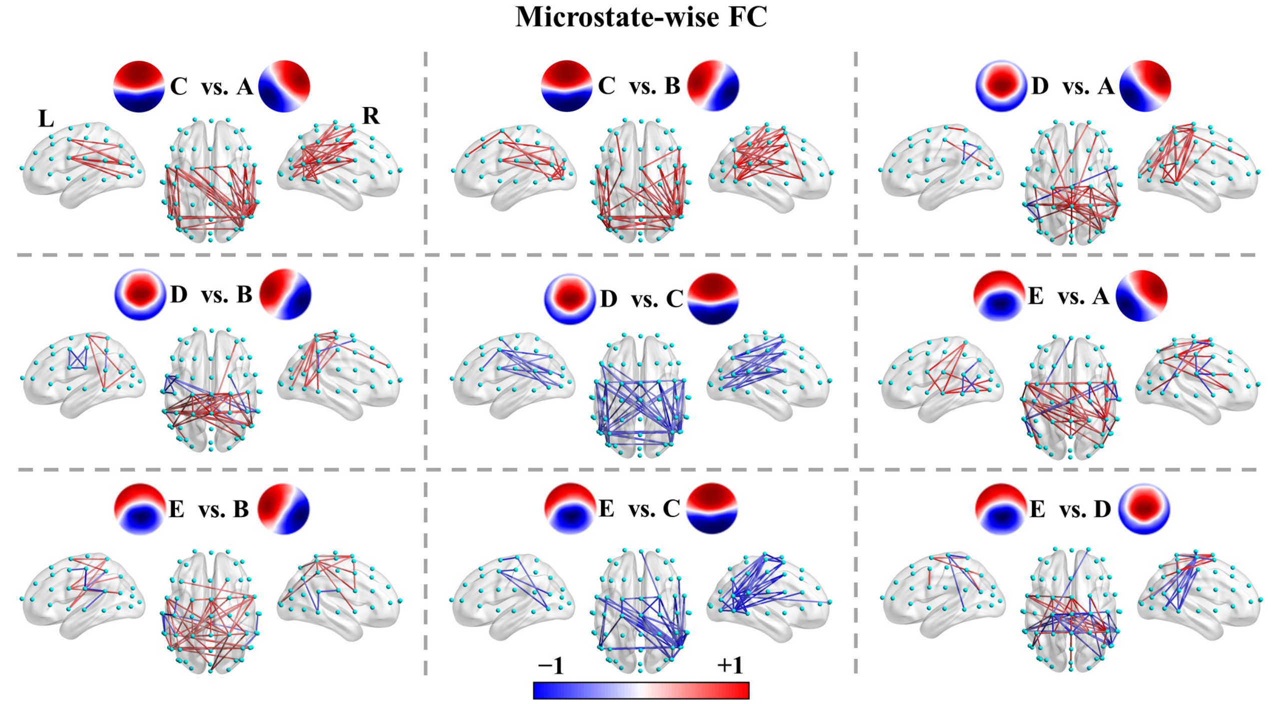

FIGURE 4 | Microstate-wise functional connectivity comparisons in healthy controls. For X vs. Y, the red color indicates greater connectivity for microstate X vs. microstate Y, while the blue color indicates greater connectivity for microstate Y vs. microstate X. Color depth represents the size of the connection difference (*t*-value). For visual clarity, only the top 50 connections (according to absolute *t*-values) of the connected components with significant differences ($p < 0.05$, NBS-based method corrected) are displayed in the figure. The complete significant connected components of the four groups are shown in the first column of **Supplementary Figures 4–12**.

were highly consistent and stable for all groups, as provided in **Figure 3** and **Supplementary Figures 3–12**. For instance, as illustrated in **Figure 3** and **Supplementary Figure 3**, for the comparison between FC_A and FC_B of each group, there was a significant connected component for $FC_A > FC_B$ ($p = 0.001$) and $FC_A < FC_B$ ($p = 0.001$) respectively. FC_A showed a stronger strength of PLV mainly involving interhemispheric connections between the left parietal and right frontocentral-central areas, and intrahemispheric connections between the left parietal and left frontal areas and connections within the left parietal/right frontocentral areas compared to FC_B. However, for $FC_A < FC_B$, there was a symmetrical pattern about the anterior-posterior axis relative to $FC_A > FC_B$. Microstate templates A and B exhibited a left-posterior right-frontal orientation and right-posterior left-frontal orientation, respectively (see **Figure 3A**). Interestingly, the patterns of the differences between FC_A and FC_B also revealed the corresponding symmetry and harmony.

We recapitulated the unique connectivity pattern of each microstate class based on the patterns of differences between the functional connectivity of one microstate class and the other microstate classes (**Figure 4**). See **Supplementary Figures 3–12** for more details. FC_A showed stronger connections mainly between the left parietal (e.g., CP3, CP5, P1, P3, P5, P7) and right frontocentral-central (e.g., FC2, FC4, FC6, FT8, C4, C6) areas and within the left parietal/right frontocentral areas. Accordingly, FC_B displayed greater connections mainly between the right parietal (CP4, CP6, P2, P4, P6, P8) and left frontocentral-central (e.g., FC1, FC3, FC5, FT7, C3, C5) areas and within the right parietal/left frontocentral areas. FC_C exhibited a stronger strength of PLV mainly involving bilateral frontocentral-parietal (e.g., FC1, FC3, FC5, P3, P5, P7; FC2, FC4, FC6, P4, P6, P8) connections and interhemispheric parietal (e.g., P5, P6, P7, P8) connections. The pattern of FC_C displayed a U shape and was symmetrical about the anterior-posterior axis like template C. Moreover, FC_D presented greater connections mainly within the central areas (e.g., Cz, C1, C2, CPz, CP1, CP2). Furthermore, FC_E showed stronger connections mainly between the left frontocentral (e.g., FCz, FC5, FT7)/left parietal (e.g., CPz, CP1, P3) and right frontocentral (e.g., FC6, FT8) areas/right parietal areas (e.g., CP2, P4) and between middle line channels (e.g., FCz, Cz, CPz, Pz). In sum, these results suggest each microstate class has a distinct connectivity preference and corresponds to a unique functional connectivity pattern. Intriguingly, the connectivity pattern of a microstate class appeared to reflect its template.

For patients with left- or right-sided stroke, the connectivity patterns were weakened to varying degrees, but the main skeleton of the patterns seemed to be preserved (see **Supplementary Figures 13–16**). Next, we examined the difference in microstate-specific connectivity between the patients at T0 and patients at T1 ($p_{thr} = 0.01$). Patients at T1 showed weaker connections mainly in the anterior regions in FC_A ($p = 0.176$) and stronger long-range connections (e.g., frontal-parietal connections) in FC_D ($p = 0.075$), but none connected components survived the NBS-based correction (see **Supplementary Figure 17**). We then examined the differences between patients at T0/T1 and controls ($p_{thr} = 0.01$). Once again, none of the connected components survived the correction.

Microstate Parameters

Two-Way ANOVAs

For patients at T0 vs. patients at T0, two-way repeated-measures ANOVAs showed non-significant Time × Microstate Class interaction effects for all microstate features. The main effects of Time were also non-significant. Therefore, *post hoc* comparisons were not further performed.

For patients at T0 vs. healthy controls, two-way mixed ANOVAs showed significant Microstate Class × Group interaction effects for occurrence [$F(3.721, 193.488) = 5.728$, $p = 3.268\text{e-}4$, $\eta_p^2 = 0.099$], coverage [$F(2.370, 123.251) = 9.228$, $p = 7.073\text{e-}5$, $\eta_p^2 = 0.151$], and mean GFP [$F(2.965, 154.176) = 7.741$, $p = 8.092\text{e-}5$, $\eta_p^2 = 0.130$]. The analysis also revealed significant Spatial Correlation pairs × Group interaction for SC [$F(4.515, 234.781) = 6.090$, $p = 5.149\text{e-}5$, $\eta_p^2 = 0.105$], and Transition pairs × Group interaction for TP [$F(6.715, 241.758) = 3.591$, $p = 0.001$, $\eta_p^2 = 0.091$]. For patients at T1 vs. healthy controls, two-way mixed ANOVAs demonstrated significant Microstate Class × Group interaction effects for occurrence [$F(3.533, 183.693) = 3.042$, $p = 0.025$, $\eta_p^2 = 0.055$], coverage [$F(2.148, 111.693) = 5.446$, $p = 0.004$, $\eta_p^2 = 0.095$], and mean GFP [$F(2.712, 141.039) = 5.059$, $p = 0.003$, $\eta_p^2 = 0.089$]. There was also significant Spatial Correlation Items × Group interaction for SC [$F(4.418, 229.711) = 4.957$, $p = 4.710\text{e-}4$, $\eta_p^2 = 0.087$], and Transition pairs × Group interaction for TP [$F(5.834, 204.174) = 2.795$, $p = 0.013$, $\eta_p^2 = 0.074$]. The two-way mixed ANOVAs for GEV, duration and interval at both T0 and T1 had one combination of two factors severely violating the homogeneity of variances hypothesis. For these three microstate parameters, pairwise comparisons for each microstate class between patients and controls were performed by permutation test directly.

Post hoc Comparisons

Global Explained Variance (GEV)

On average, the GEV for each microstate class ranged from 4.84 to 20.05% in patients at T0, from 5.22 to 21.31% in patients at T1, and from 5.06 to 27.74% in healthy controls. Group average statistics (± *SD*) for microstate parameters are provided in **Supplementary Table 4**. It is worth noting that microstate template C explained more variance relative to other templates (all $ps < 0.05$), and was the only template that explained more than 15% variance for each group (**Figure 5**). Furthermore, microstate C showed a significantly higher GEV in healthy controls compared to patients at T0 ($p = 0.002$) and T1 ($p = 0.027$), whereas microstates A and B showed significantly lower GEV in healthy controls compared to patients at T0 ($p = 1.000\text{e-}4$, $p = 0.001$) and T1 ($p = 0.006$, $p = 0.010$). For microstates D and E, there was no significant difference between the patients and controls. The detailed statistical results are summarized in **Supplementary Tables 5**, **6**.

Mean Duration

On average, the mean duration for each microstate class lasted between 51.42 and 68.63 ms in patients at T0, between 52.04 and 71.04 ms in patients at T1, and between 52.81 and 82.24 ms in healthy controls. The mean duration of microstate C was predominant and significantly longer than that of the other microstate classes (all $ps < 0.001$) in healthy controls. However, the predominant pattern of microstate C was considerably weakened in patients. No significant differences between microstates A and C were observed in patients at either T0 ($p = 0.898$) and T1 ($p = 0.300$). Microstate C showed a significantly longer duration in healthy controls compared to patients at T0 ($p = 0.003$) and T1 ($p = 0.040$). In contrast, The mean duration of microstate A was significantly longer in patients at T0 ($p = 0.003$) and T1 ($p = 0.045$) relative to healthy controls.

Occurrence

In healthy controls, on average, microstate C occurred 4.09 times (*SD* = 0.46) per second, and microstates A, B, D, and E occurred 3.24 (*SD* = 0.65), 3.07 (*SD* = 0.56), 2.51 (*SD* = 0.61), and 2.80 (*SD* = 0.66) times per second, respectively. As shown in **Figure 5**, in patients at T0 and T1, the occurrences of microstates A, B, and C were all about 4 times per second on average. More specifically, microstates A and B occurred more frequently in patients at T0 ($p = 0.001$, $p = 0.015$) and T1 ($p = 0.037$, $p = 0.191$) compared to healthy controls, and the predominant pattern of microstate C in controls disappeared in patients.

Coverage

There were significant differences between patients at T0 and controls in microstates A ($p = 1.800\text{e-}4$), B ($p = 0.012$), and C ($p = 0.005$), and between patients at T1 and controls in microstates A ($p = 0.023$) and C ($p = 0.043$). The dominant pattern of microstate C also existed in the coverage, especially in healthy controls.

Mean Interval

For each group, the mean interval of microstate C was the shortest among all microstate classes (all $ps < 0.001$). For patients at T0 vs. healthy controls, the mean interval was significantly shorter in microstates A ($p = 0.001$) and B ($p = 0.018$). In contrast, the opposite pattern was observed in microstate C ($p = 0.021$). At T1, only the mean interval of microstate A ($p = 0.031$) was still significant between patients and controls.

Mean Global Field Power (GFP)

Microstate C exhibited a significantly stronger GFP compared to the other microstate classes (all $ps < 0.001$) in healthy controls, but for patients, this pattern was weakened. Microstate C presented significantly stronger GFP in healthy controls relative to patients at both T0 ($p = 0.001$) and T1 ($p = 0.015$), but microstates A ($p = 0.001$, $p = 0.116$) and B ($p = 0.003$, $p = 0.049$)

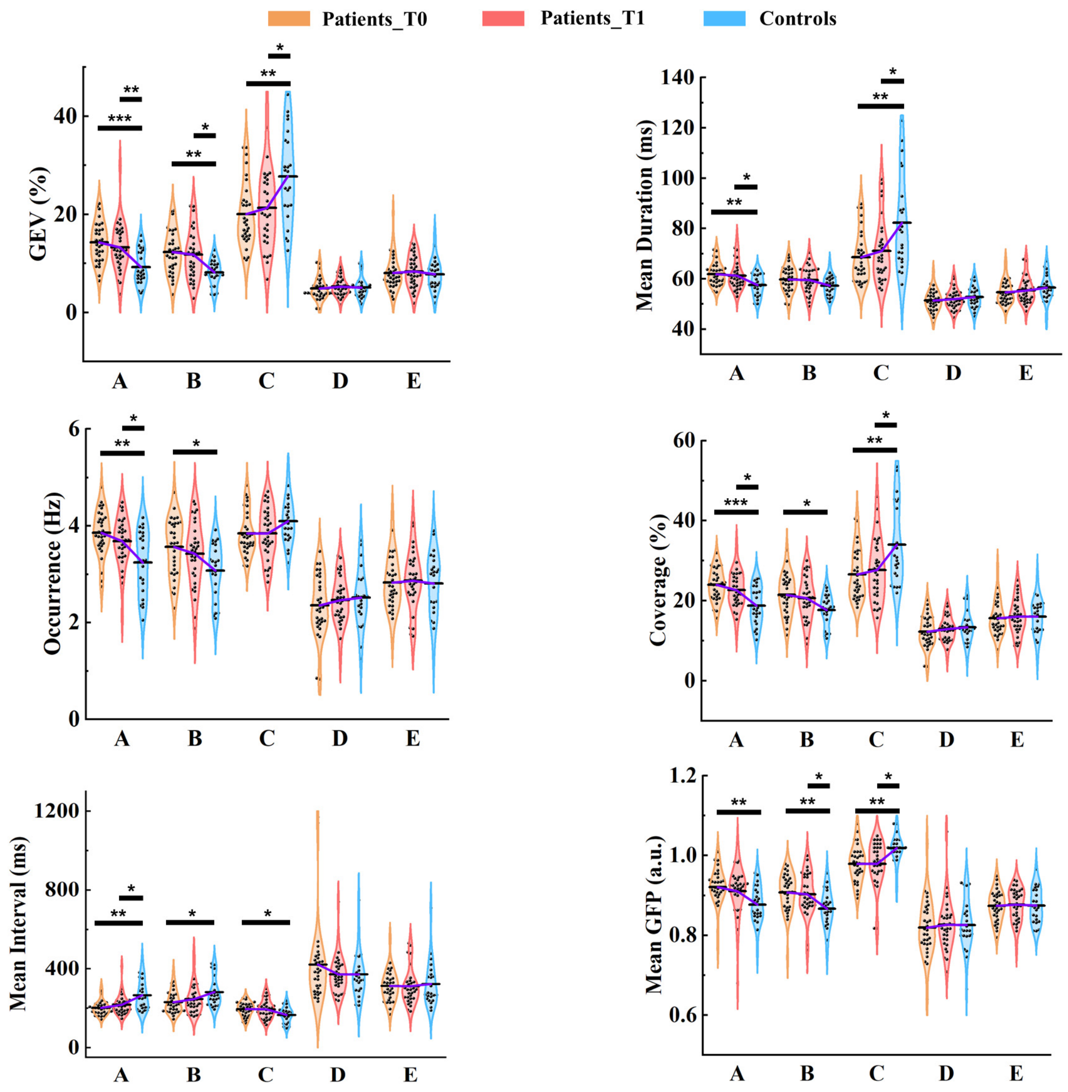

FIGURE 5 | Results of microstate parameter analysis for patients and controls. *Post hoc* pairwise comparisons (patients at T0 vs. controls; patients at T1 vs. controls) were performed for GEV, mean duration, occurrence, coverage, mean interval, and mean GFP. The means of the three groups for each microstate class are linked by the solid purple line. $^*p < 0.05$; $^{**}p < 0.01$; $^{***}p < 0.001$.

showed greater GFP in patients at T0 and T1 compared to healthy controls.

Of Note, there were no differences in the summed/average microstate parameters across the five microstate classes between patients at T0/T1 and healthy controls. Moreover, although the differences between the patients at T0 and T1 were not significant, we observed that microstate parameters at T1 of patients were closer to those of healthy controls compared to T0 at the group level.

Spatial Correlation Metric (SC)

As demonstrated in **Supplementary Figure 18**, intuitively, all three groups followed a similar pattern in SC. However, patients presented higher spatial correlations in SC_{AA}, SC_{AB}, SC_{BA}, SC_{BB}, SC_{CC}, SC_{DD}, and SC_{EE} at both T0 and T1 compared to healthy controls (see also **Supplementary Table 7**). SC_{AB}, SC_{BA}, and SC_{BB} were still signifificantly higher for patients at both T0 and T1 relative to healthy controls after correction for 25 times comparisons.

Transition Probability (TP)

We observed that TP_{BC}, TP_{DC}, and TP_{EC} significantly decreased, and TP_{BA} and TP_{EA} significantly increased in patients at T0 compared to controls, but none survived Bonferroni-Holm correction for 20 times comparisons. At T1, similar patterns were also observed, but to a lesser degree (**Supplementary Figure 19**).

We conducted further analysis to examine whether the microstate parameters differed between patients with left- and right-sided stroke. No significant differences were observed in any of the microstate parameters at either T0 or T1. The results of

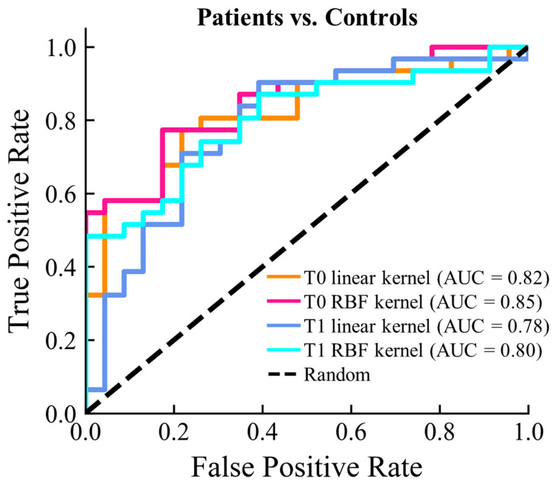

FIGURE 6 | Classifications results between patients and controls. The ROC curve and the corresponding AUC for each classification model are displayed.

mean duration and occurrence are presented in **Supplementary Figure 20**.

Classification

To evaluate the ability to discriminate between patients and healthy controls using only the microstate features, we constructed SVM models with different kernel types. It is worth noting that we only sought to assess whether there was a basic discriminating ability of the microstate parameters instead to find the best-performing model through complex feature selection and parameter tuning procedures. For feature selection, we first selected microstate features that were both significantly different between patients and controls at T0 and T1. PCA was utilized to further reduce the dimensions of the features and retained only the 95% variance. To avoid the optimistically biased evaluation of the model performance, the nested LOOCV was used, and the *scikit-learn pipeline* was adopted to prevent data leakage in the cross-validation and hyper-parameter tuning procedures. As shown in **Figure 6**, AUCs were larger than 0.80 for patients at T0 vs. controls with both the linear and RBF kernels. AUCs were slightly lower (linear: 0.78; RBF: 0.80) for patients at T1 vs. controls. In addition, the AUC of the SVM model with RBF kernel was slightly higher at both T0 and T1. These results demonstrate that moderate discrimination between patients and healthy controls can be achieved using only the microstate features.

Correlation Analysis

We finally examined the correlations between the microstate features and the FMAL scores. We also used the NBS-based method for multiple comparison correction for correlations between microstate-specific connectivity and FMAL score ($p_{thr} = 0.005$). Broadly speaking, there was a significant connected component with negative correlations at T0 and T1 for most microstate classes (see **Supplementary Figure 21**). At T0, the significant connected components mainly involved the right hemisphere. More connections involving the left hemisphere and middle line channels were included in the significant connected components at T1. For instance, the distribution of the connected component of microstate C mainly affected the connections between the right central (e.g., C2, C4, C6, T8) and right posterior/frontal areas at T0 and between the left central (C1, C3, C5, CP3)/right frontal-central (AF8, FC2, FC4, C2, C4) and middle line (FCz, Cz)/right posterior areas at T1 (**Figure 7A**).

Moreover, we identified significant correlations between the mean FCSCC of microstate C and FMAL score at both T0 ($r = -0.697$, $p = 5.000\text{e-}5$, 95% CI [-0.830, -0.452]) and T1 ($r = -0.779$, $p = 1.000\text{e-}5$, 95% CI [-0.895, -0.546]). FMAL score was moderately correlated with microstate parameters (e.g., occurrence, coverage) mainly in microstates C and D at T1 and similar relationships were observed at T0, but to a lesser degree (see **Supplementary Table 8**). Intriguingly, the parameters in microstates C and D showed opposite correlation patterns with the FMAL score. For instance, at T1, the mean interval was positively correlated with the FMAL score in microstate C ($r = 0.394$, $p_0 = 0.027$, $p = 0.110$, 95% CI [0.046, 0.645]) but negatively correlated with the FMAL score in microstate D ($r = -0.512$, $p_0 = 0.003$, $p = 0.015$, 95% CI [-0.755, -0.045]) (see **Figure 7B**). p_0 is the uncorrected p-value. On the other hand, there were moderate correlations between the FMAL score and SC at T0 (e.g., SC_{AA}, SC_{AB}, SC_{AD}, SC_{AD}, SC_{AE}). For example, SC_{AA} at T0 was negatively correlated with the FMAL score ($r = -0.420$, $p_0 = 0.020$, $p = 0.498$, 95% CI [-0.650, -0.087]), but none of them was significant after the Bonferroni-Holm correction for multiple comparisons (see **Supplementary Table 9**).

DISCUSSION

The brain is a complex dynamically distributed information processing system with stable structural connections that support time-varying information transfer between brain regions (Park et al., 2021). Yet, after the stroke, it remains unclear how the dynamic neural signals of the brain are altered due to damage to the neural tissue of the brain, together with changes in receptor distribution. Understanding the mechanisms underlying brain dynamics and the alterations in brain dynamics after brain injury is a cutting-edge question in neuroscience and neurological rehabilitation (Comsa et al., 2019; Bonkhoff et al., 2020; Zanesco et al., 2020; Bai et al., 2021a; Ploner and Tiemann, 2021). We explored the phase-coupling pattern of each microstate class and the spatiotemporal dynamics of the brain in stroke patients and healthy controls using microstate-based analysis. Our results demonstrate that each microstate class corresponds to a distinct pattern of functional connectivity, and the results of different datasets are highly similar from a macroscopic point of view. On the other hand, stroke patients showed significant changes in almost all types of microstate parameters compared to the healthy population. In addition, some microstate-related features were significantly associated with lower limb motor function. Together, our work demonstrates the close association between

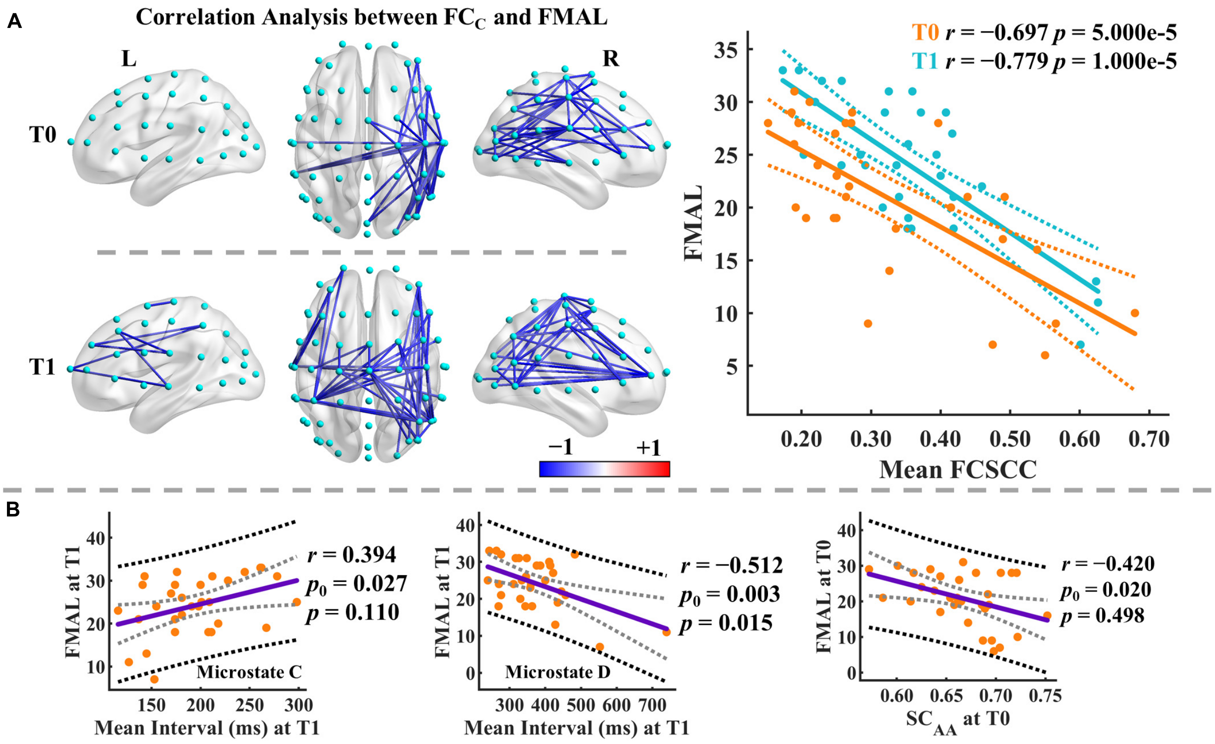

FIGURE 7 | Results of correlation analysis. **(A)** Correlation analysis between the functional connectivity of microstate C and FMAL score. Only the significant connected components are displayed. Mean FCSCC refers to the mean of the functional connectivity strength within the significant connected component. The blue color indicates negative correlations between the connectivity of microstate C and the FMAL score. Color depth represents the size of the correlation coefficient. Dashed lines imply the 95% confidence intervals for the regression estimates. Pearson correlation coefficient (*r*) and the corresponding permutation-based *p*-value are given. **(B)** Correlation analysis between microstate parameters and FMAL score. The black and gray dashed lines indicate the 95% prediction and 95% confidence intervals, respectively. Pearson correlation coefficient (*r*) and the corresponding permutation-based *p*-value are given. p_0 is the uncorrected *p*-value.

microstates and functional connectivity, and the importance of studying altered neural features of the brain after stroke from a dynamic perspective.

We found that the optimal number of microstate classes was five in both healthy controls and stroke patients, and the microstate topographies were highly similar between the groups. There is no consensus on how to determine the optimal number of microstate classes (Custo et al., 2017; Michel and Koenig, 2018; Gui et al., 2020). The number of microstate classes was determined or set to four in many previous experimental and clinical studies (Michel and Koenig, 2018). Although the optimal number is associated with the dataset used and the selection of the determination criterion, a low number of microstate classes may leave a large amount of data variance unexplained (for all maps, not only those at GFP peaks), as well as the risk of merging different classes (Custo et al., 2017). Here, the microstate templates were highly similar to those reported in previous studies (Shi et al., 2020; Zanesco et al., 2020, 2021). Yet, only one previous study, to our knowledge, used the complete microstate analysis in stroke patients (Zappasodi et al., 2017). In the study by Zappasodi and colleagues, the optimal number determined using the KL criteria and cross-validation (CV) criteria was four, and the microstate templates of healthy controls differed from those of stroke patients (patients with the lesion in the left/right hemisphere). Compared to our results, one possible reason for the discrepancy is that they used a different method for determining the optimal number of microstate classes and utilized 19-channel EEG data from acute stroke patients, whereas our study used 60-channel EEG data from subacute stroke patients.

Having computed the common microstate templates, we investigated the microstate-specific functional connectivity in the sensor space. Many studies have explored the source localization of microstates, and the association between the microstates and RSNs (Britz et al., 2010; Yuan et al., 2012; Custo et al., 2017; Milz et al., 2017; Michel and Koenig, 2018). Currently, only limited studies have sought to uncover the relationship between resting EEG microstates and their corresponding functional connectivity (Comsa et al., 2019). The functional connectivity patterns underlying each microstate class remain unclear. Moreover, a popular approach for studying brain dynamics in EEG and fMRI is dynamic functional connectivity (Hutchison et al., 2013; Allen et al., 2014; Hansen et al., 2015; Kabbara et al., 2017; O'Neill et al., 2018; Ploner and Tiemann, 2021). The major limitation of the dynamic functional connectivity analysis based on the sliding window approach is the need to manually select a fixed window length. This means that the signals under this window length may not belong to the same brain state. Microstate-specific functional connectivity analysis is similar in nature to dynamic functional connectivity, but in this study, the connectivity template for each microstate class is computed by the data belonging to this microstate class. More specifically, microstate analysis provides prior knowledge for computing the state-specific connectivity templates. Our analysis highlighted that each microstate class is associated with a unique phase synchronized pattern, and the functional connectivity pattern seems to reflect the character of the corresponding microstate template. These findings were highly consistent across patients and healthy controls groups and were replicated in an independent dataset. The connectivity patterns were weakened to varying degrees in patients with left- or right-sided stroke, but the main skeleton of the patterns seemed to be preserved. Moreover, there were no significant differences between patients and controls in microstate-wise functional connectivity. These results indicate that the similarity of connectivity patterns between groups may explain the similarity of the microstate templates. Note that the similarity of connectivity patterns was not a sufficient and necessary condition for no significant differences between healthy controls and patients. Due to the large heterogeneity of the patients, the effect size may be reduced at the channel-level connection. Importantly, these findings appear to prove that flipping the data in some studies to unify the lesions to one side may have an unpredictable effect on the results. For example, microstates A and B appear to be exchanged after the data are flipped. Our study extends and refines our understanding of microstates. Microstate analysis has the potential to study dynamic functional connectivity from a new perspective.

Due to the brain damage introduced by stroke, the cognition and behavior of the patients were impaired. We found significant changes in microstate parameters between patients and controls. The most striking results were in the parameters of microstates A, B, and C. In patients, microstate C explained less variance, was of lower mean GFP, had a shorter duration, longer mean interval, occupied less time and occurred less frequently compared to healthy controls. In contrast, microstates A and B exhibited the opposite pattern relative to microstate C. Importantly, no difference was observed in the summed parameters across five microstates between the patients and healthy controls. On the other hand, functional connectivity of microstate C showed stronger connectivity in a large connected component compared to other microstate classes. Partially in line with the findings of dynamic functional connectivity (Bonkhoff et al., 2020; Wang et al., 2020), stroke patients prefer to spend more time in states with low levels of connectivity. After brain injury, the alpha power is generally considerably decreased (Edlow et al., 2021). Herein stroke patients showed a decreased mean duration of microstate C. This may be partly explained by the positive association between the duration of microstate C and alpha power (Croce et al., 2020). Moreover, our study did not find significant differences between patients with left-sided and right-sided stroke in all microstate parameters, whereas the duration, occurrence, and coverage in microstates C and D significantly differed between patients with left-sided and right-sided stroke in a previous study (Zappasodi et al., 2017). A possible explanation is that the microstate templates between the two groups were different in the prior study and the poststroke time of the patients was different from that of our study. Further studies are needed to investigate this issue. In addition, stroke patients showed clearer patterns of changes in spatial correlation metrics relative to healthy controls. Briefly, the mean absolute correlation coefficients between the maps belonging to each microstate class and the corresponding template increased. The previous study has demonstrated that there were gradual map changes from one microstate to another (Mishra et al., 2020). These results suggest that after stroke the signal variability over time is diminished, and the microstate segregation seems to increase. One potential explanation is that the disruption of structural and functional connections after the stroke affects brain information integration and transmission, and limits the ability to dynamically configure the brain network. Moreover, the stroke-related alterations were also reflected in transition probability. TP_{BC}, TP_{DC}, and TP_{EC} occurred less frequently, while TP_{BA} and TP_{EA} were more likely to occur compared to controls. Overall, the results of this study suggest that the original dynamic balance between microstates is broken and seems to reflect the compensation and reconfiguration of network dynamics after stroke and that the reconfiguration of temporal dynamics is state-selective.

Previous studies have investigated the association between microstates and RSNs (Britz et al., 2010; Custo et al., 2017; Milz et al., 2017; Brechet et al., 2019; Zoubi et al., 2020). However, no complete consensus has yet been reached. Prior study (Britz et al., 2010) suggested that microstate classes and the corresponding most relevant RSNs were: the auditory network (microstate A), visual network (microstate B), saliency network (microstate C), and attention network (microstate D). However, other studies suggested that microstate C reflects a portion of the default mode network (Seitzman et al., 2017), and microstates A and B considerably overlap with the somatomotor network (Zoubi et al., 2020). An increase in the coverage and occurrence of microstate B was observed in certain cognitive tasks with direct visual input (Zappasodi et al., 2019), and an increased presence in microstate C and decreased presence in microstate D was observed in schizophrenia (da Cruz et al., 2020). Moreover, One microstate study demonstrated that spontaneous brain activity could encode detailed information about motor control (Pirondini et al., 2017). Given the complex relationships of microstate, cognition, and behavior, it is arbitrary to reduce microstates to specific functions with current knowledge.

Despite the high heterogeneity of stroke patients, we demonstrated the ability to achieve a moderate level of discrimination between stroke patients and healthy controls using only microstate features. Although stroke patients did not show differences in microstate parameters between T0 and T1, microstate parameters at the group level were closer to those of controls after the 2-week rehabilitation therapy. Finally, we evaluated the associations between microstate parameters and the clinical score of lower limb motor function. For each microstate class, the connectivity in a large connected component was negatively correlated with the FMAL score at both T0 and T1. These connected components mainly involved connections between sensorimotor areas and frontal/posterior regions and connections within sensorimotor areas. The negative correlation between static functional connectivity and FMAL was also observed in a recent study (Hoshino et al., 2021). In addition, the microstate dynamics may reflect the selective inhibition of specific intra-cortical regions (Milz et al., 2017). Patients with eyes closed were in an internally focused state, under the functional competition between different networks, weaker phase synchronization may reflect a greater potential for movement. Moreover, some spatial correlation metrics (e.g., SC_{AA}) were negatively correlated with the FMAL score at T0. At T1, the correlations between the FMAL score and other parameters (e.g., occurrence, coverage, mean interval) of microstates C and D increased. Brain dynamics may be modulated by rehabilitation therapy, and resting-state brain dynamics can encode information reflecting motor ability. Furthermore, microstates C and D exhibited opposite patterns of association with the FMAL score in occurrence, coverage, mean interval, duration, etc. This may be due to the different functional connection patterns underlying microstates C and D. Together, these findings provide the first evidence that the microstate-related features are associated with the lower limb function status. Further studies are needed to validate these results and elucidate these correlations.

Several considerations should be taken into account. First, for patients in this study, we only focused on the stroke patients in the subacute phase. Given the sample size of the study, the analysis in more specific groups (e.g., grouping according to gender, stroke type, or age) was not performed. In addition, because of the large heterogeneity of stroke patients (e.g., age, lesion location, poststroke time, stroke type, and treatment), the results in this study are not sufficient to be applicable across the entire spectrum of stroke patients and need to be interpreted with caution. In addition, information on age- and gender-related changes of microstate dynamics is sparse, and there are huge discrepancies in the results of different studies, especially on gender (Tomescu et al., 2018; Zanesco et al., 2020). Second, although the differences in the microstate templates between patients and controls were small, we used the common templates to minimize the systematic errors. Due to the possible differences in the number of microstate classes or microstate templates, comparisons between studies need to be made with caution. Third, for microstate-wise functional connectivity, we only investigated the results in the alpha band. This is because the study of phase synchronization using the Hilbert transform approach requires the use of narrowband signals (Lachaux et al., 1999), and microstates are predominantly generated by intracortical sources in the alpha band (Milz et al., 2017). In addition, functional connectivity is based on the phase synchronization method, and phase- and amplitude-coupling patterns may reflect partly distinct neuronal mechanisms (Siems and Siegel, 2020). Fourth, a large number of dependent measures and multiple comparisons were conducted in this study. After strict *p*-value correction, there is a risk that the true effects will not be identified as statistically significant. The original *p*-values of the results are provided in **Supplementary Material**. To sum up, given the limitations of this study and the unsolved problems in this field, more meticulous and large sample size studies are needed in the future to validate and expand this research in the hope of gaining a deeper and more comprehensive understanding of brain dynamics.

CONCLUSION

In a nutshell, our results provide a novel perspective on one of the major issues in neuroscience and neurological rehabilitation: the connectivity patterns underlying different functional states and how the neural dynamics are altered in brain injury patients (e.g., stroke) (O'Neill et al., 2018; Bai et al., 2021a; Bian et al., 2021). Centered on this issue, we proposed and implemented a microstate-based method to investigate the phase synchronization pattern underlying each microstate class and the alterations of microstate dynamics on the order of milliseconds in stroke patients. The results suggested that each microstate class was associated with a specific functional connectivity pattern, and the findings were highly consistent across different datasets. On the other hand, most microstate parameters (e.g., mean duration, occurrence, coverage, mean interval) in patients significantly differed from healthy controls in microstates A, B, and C. Importantly, the change patterns in stroke patients in microstate C relative to healthy controls were opposite to those in microstates A and B. Microstate integration and transmission were disrupted to some degree after stroke. These findings indicated the compensation and reorganization of neural dynamics after the disruption of neural function due to stroke. Moreover, we found that certain dynamic parameters were associated with lower limb function and spontaneous microstate dynamics seemed to encode information about motor ability. Overall, we extend our understanding of the brain dynamics, uncover the connectivity patterns underlying microstates, and provide new insights not obtained in studies using static features. Since the microstate dynamics can be modulated by neurofeedback and external stimulation (Michel and Koenig, 2018; Gui et al., 2020), our results open avenues for understanding the network reorganization and the development of new treatments for stroke patients.

DATA AVAILABILITY STATEMENT

The data supporting the findings of the present study (e.g., EEG features, microstate templates) are provided in **Supplementary Material**. In addition, preprocessed EEG recordings of the LEMON dataset are available for use at http://fcon_1000.projects.nitrc.org/indi/retro/MPI_LEMON.html.

ETHICS STATEMENT

The studies involving human participants were reviewed and approved by the Ethics Committee of Beijing Tsinghua

Changgung Hospital. The patients/participants provided their written informed consent to participate in this study.

AUTHOR CONTRIBUTIONS

ZH: conceptualization, data curation, methodology, software, formal analysis, validation, visualization, writing—original draft, and writing—review and editing. XZ and DC: data curation and writing—review and editing. YP: funding acquisition, project administration, and writing—review and editing. WD: funding acquisition, project administration, conceptualization, supervision, and writing—review and editing. All authors contributed to the article and approved the submitted version.

FUNDING

This study was supported by the National Natural Science Foundation of China (Nos. 61171002 and 60372023), the Tsinghua University Precision Medicine Research Program (No. 12020B7049), the Tsinghua University Initiative Scientific Research Program (No. 20131089382), Beijing Area Key Lab of Opto-Mechatronic Equipment Technology (BIPT-OMET-2020-02), and the Capital's Funds for Health Improvement and Research (No.12021B2005-A). No additional external funding was received for this study. The funders had no role in study design, data collection, analysis, decision to publish, or preparation of the manuscript.

ACKNOWLEDGMENTS

We thank Yanlin Zhang from the Department of Rehabilitation Medicine, Beijing Tsinghua Changgung Hospital for his assistance in EEG data acquisition. We are grateful to all the patients and their families and the healthy individuals for their participation in this study. We also thank Yunxiang Ge, Ziliang Zhang, and Zhimin Shao from the Department of Electronic Engineering, Beijing National Research Center for Information Science and Technology (BNRist), Tsinghua University for helpful discussions.

SUPPLEMENTARY MATERIAL

The Supplementary Material for this article can be found online at: https://www.frontiersin.org/articles/10.3389/fnins.2022.848737/full#supplementary-material

REFERENCES

Allen, E. A., Damaraju, E., Plis, S. M., Erhardt, E. B., Eichele, T., and Calhoun, V. D. (2014). Tracking whole-brain connectivity dynamics in the resting state. *Cereb. Cortex* 24, 663–676. doi: 10.1093/cercor/bhs352

Babayan, A., Erbey, M., Kumral, D., Reinelt, J. D., Reiter, A. M. F., Robbig, J., et al. (2019). A mind-brain-body dataset of MRI, EEG, cognition, emotion, and peripheral physiology in young and old adults. *Sci. Data* 6:180308. doi: 10.1038/sdata.2018.308

Bai, Y., He, J., Xia, X., Wang, Y., Yang, Y., Di, H., et al. (2021a). Spontaneous transient brain states in EEG source space in disorders of consciousness. *NeuroImage* 240:118407. doi: 10.1016/j.neuroimage.2021.118407

Bai, Y., Lin, Y., and Ziemann, U. (2021b). Managing disorders of consciousness: the role of electroencephalography. *J. Neurol.* 268, 4033–4065. doi: 10.1007/s00415-020-10095-z

Bian, L., Cui, T., Thomas Yeo, B. T., Fornito, A., Razi, A., and Keith, J. (2021). Identification of community structure-based brain states and transitions using functional MRI. *NeuroImage* 244:118635. doi: 10.1016/j.neuroimage.2021.118635

Bonkhoff, A. K., Espinoza, F. A., Gazula, H., Vergara, V. M., Hensel, L., Michely, J., et al. (2020). Acute ischaemic stroke alters the brain's preference for distinct dynamic connectivity states. *Brain* 143, 1525–1540. doi: 10.1093/brain/awaa101

Brechet, L., Brunet, D., Birot, G., Gruetter, R., Michel, C. M., and Jorge, J. (2019). Capturing the spatiotemporal dynamics of self-generated, task-initiated thoughts with EEG and fMRI. *NeuroImage* 194, 82–92. doi: 10.1016/j.neuroimage.2019.03.029

Britz, J., Van De Ville, D., and Michel, C. M. (2010). BOLD correlates of EEG topography reveal rapid resting-state network dynamics. *NeuroImage* 52, 1162–1170. doi: 10.1016/j.neuroimage.2010.02.052

Chang, C., Keilholz, S., Miller, R., and Woolrich, M. (2018). Mapping and interpreting the dynamic connectivity of the brain. *NeuroImage* 180, 335–336. doi: 10.1016/j.neuroimage.2018.07.018

Chiarelli, A. M., Croce, P., Assenza, G., Merla, A., Granata, G., Giannantoni, N. M., et al. (2020). Electroencephalography-Derived prognosis of functional recovery in acute stroke through machine learning approaches. *Int. J. Neural Syst.* 30:2050067. doi: 10.1142/S0129065720500677

Comsa, I. M., Bekinschtein, T. A., and Chennu, S. (2019). Transient topographical dynamics of the electroencephalogram predict brain connectivity and behavioural responsiveness during drowsiness. *Brain Topogr.* 32, 315–331. doi: 10.1007/s10548-018-0689-9

Croce, P., Quercia, A., Costa, S., and Zappasodi, F. (2020). EEG microstates associated with intra- and inter-subject alpha variability. *Sci. Rep.* 10:2469. doi: 10.1038/s41598-020-58787-w

Custo, A., Van De Ville, D., Wells, W. M., Tomescu, M. I., Brunet, D., and Michel, C. M. (2017). Electroencephalographic resting-state networks: source localization of microstates. *Brain Connect.* 7, 671–682. doi: 10.1089/brain.2016.0476

da Cruz, J. R., Favrod, O., Roinishvili, M., Chkonia, E., Brand, A., Mohr, C., et al. (2020). EEG microstates are a candidate endophenotype for schizophrenia. *Nat. Commun.* 11:3089. doi: 10.1038/s41467-020-16914-1

Duc, N. T., and Lee, B. (2019). Microstate functional connectivity in EEG cognitive tasks revealed by a multivariate Gaussian hidden Markov model with phase locking value. *J. Neural Eng.* 16:026033. doi: 10.1088/1741-2552/ab0169

Edlow, B. L., Claassen, J., Schiff, N. D., and Greer, D. M. (2021). Recovery from disorders of consciousness: mechanisms, prognosis and emerging therapies. *Nat. Rev. Neurol.* 17, 135–156. doi: 10.1038/s41582-020-00428-x

Eldeeb, S., Akcakaya, M., Sybeldon, M., Foldes, S., Santarnecchi, E., Pascual-Leone, A., et al. (2019). EEG-based functional connectivity to analyze motor recovery after stroke: a pilot study. *Biomed. Signal Process. Control* 49, 419–426. doi: 10.1016/j.bspc.2018.12.022

Férat, V., Seeber, M., Michel, C. M., and Ros, T. (2020). Beyond broadband: towards a spectral decomposition of EEG microstates. *bioRxiv [preprint]* doi: 10.1101/2020.10.16.342378

Fox, M. D., and Greicius, M. (2010). Clinical applications of resting state functional connectivity. *Front. Syst. Neurosci.* 4:19. doi: 10.3389/fnsys.2010.00019

Fugl-Meyer, A. R., Jaasko, L., Leyman, I., Olsson, S., and Steglind, S. (1975). The post-stroke hemiplegic patient. 1. a method for evaluation of physical performance. *Scand. J. Rehabil. Med.* 7, 13–31.

Gladstone, D. J., Danells, C. J., and Black, S. E. (2002). The fugl-meyer assessment of motor recovery after stroke: a critical review of its measurement properties. *Neurorehabil. Neural Repair* 16, 232–240. doi: 10.1177/154596802401105171

Gschwind, M., Michel, C. M., and Van De Ville, D. (2015). Long-range dependencies make the difference-Comment on "A stochastic model for EEG microstate sequence analysis". *NeuroImage* 117, 449–455. doi: 10.1016/j.neuroimage.2015.05.062

Gui, P., Jiang, Y., Zang, D., Qi, Z., Tan, J., Tanigawa, H., et al. (2020). Assessing the depth of language processing in patients with disorders of consciousness. *Nat. Neurosci.* 23, 761–770. doi: 10.1038/s41593-020-0639-1

Hansen, E. C., Battaglia, D., Spiegler, A., Deco, G., and Jirsa, V. K. (2015). Functional connectivity dynamics: modeling the switching behavior of the resting state. *NeuroImage* 105, 525–535. doi: 10.1016/j.neuroimage.2014.11.001

Hoshino, T., Oguchi, K., Inoue, K., Hoshino, A., and Hoshiyama, M. (2021). Relationship between lower limb function and functional connectivity assessed by EEG among motor-related areas after stroke. *Top. Stroke Rehabil.* 28, 614–623. doi: 10.1080/10749357.2020.1864986

Hutchison, R. M., Womelsdorf, T., Allen, E. A., Bandettini, P. A., Calhoun, V. D., Corbetta, M., et al. (2013). Dynamic functional connectivity: promise, issues, and interpretations. *NeuroImage* 80, 360–378. doi: 10.1016/j.neuroimage.2013.05.079

Kabbara, A., El Falou, W., Khalil, M., Wendling, F., and Hassan, M. (2017). The dynamic functional core network of the human brain at rest. *Sci. Rep.* 7:2936. doi: 10.1038/s41598-017-03420-6

Kayser, J., and Tenke, C. E. (2006). Principal components analysis of *Laplacian waveforms* as a generic method for identifying ERP generator patterns: I. evaluation with auditory oddball tasks. *Clin. Neurophysiol.* 117, 348–368. doi: 10.1016/j.clinph.2005.08.034

Khanna, A., Pascual-Leone, A., Michel, C. M., and Farzan, F. (2015). Microstates in resting-state EEG: current status and future directions. *Neurosci. Biobehav. Rev.* 49, 105–113. doi: 10.1016/j.neubiorev.2014.12.010

Knijnenburg, T. A., Wessels, L. F., Reinders, M. J., and Shmulevich, I. (2009). Fewer permutations, more accurate P-values. *Bioinformatics* 25, i161–i168. doi: 10.1093/bioinformatics/btp211

Koenig, T., Prichep, L., Lehmann, D., Sosa, P. V., Braeker, E., Kleinlogel, H., et al. (2002). Millisecond by millisecond, year by year: normative EEG microstates and developmental stages. *NeuroImage* 16, 41–48. doi: 10.1006/nimg.2002.1070

Koessler, L., Maillard, L., Benhadid, A., Vignal, J. P., Felblinger, J., Vespignani, H., et al. (2009). Automated cortical projection of EEG sensors: anatomical correlation via the international 10-10 system. *NeuroImage* 46, 64–72. doi: 10.1016/j.neuroimage.2009.02.006

Krzanowski, W. J., and Lai, Y. T. (1988). A criterion for determining the number of groups in a data set using sum-of-squares clustering. *Biometrics* 44, 23–34. doi: 10.2307/2531893

Lachaux, J. P., Rodriguez, E., Martinerie, J., and Varela, F. J. (1999). Measuring phase synchrony in brain signals. *Hum. Brain Mapp.* 8, 194–208. doi: 10.1002/(SICI)1097-0193(1999)8:4<194::AID-HBM4>3.0.CO;2-C

Li, Z., Ren, G., Liu, C., Wang, Q., Liang, K., Han, C., et al. (2021). Dysfunctional brain dynamics of Parkinson's disease and the effect of acute deep brain stimulation. *Front. Neurosci.* 15:697909. doi: 10.3389/fnins.2021.697909

Liu, J., Xu, J., Zou, G., He, Y., Zou, Q., and Gao, J. H. (2020). Reliability and individual specificity of EEG microstate characteristics. *Brain Topogr.* 33, 438–449. doi: 10.1007/s10548-020-00777-2

Mane, R., Chew, E., Phua, K. S., Ang, K. K., Robinson, N., Vinod, A. P., et al. (2019). Prognostic and monitory EEG-biomarkers for BCI upper-limb stroke rehabilitation. *IEEE Trans. Neural Syst. Rehabil. Eng.* 27, 1654–1664. doi: 10.1109/TNSRE.2019.2924742

Michel, C. M., and Koenig, T. (2018). EEG microstates as a tool for studying the temporal dynamics of whole-brain neuronal networks: a review. *NeuroImage* 180, 577–593. doi: 10.1016/j.neuroimage.2017.11.062

Milz, P., Pascual-Marqui, R. D., Achermann, P., Kochi, K., and Faber, P. L. (2017). The EEG microstate topography is predominantly determined by intracortical sources in the alpha band. *NeuroImage* 162, 353–361. doi: 10.1016/j.neuroimage.2017.08.058

Mishra, A., Englitz, B., and Cohen, M. X. (2020). EEG microstates as a continuous phenomenon. *NeuroImage* 208:116454. doi: 10.1016/j.neuroimage.2019.116454

Murray, M. M., Brunet, D., and Michel, C. M. (2008). Topographic ERP analyses: a step-by-step tutorial review. *Brain Topogr.* 20, 249–264. doi: 10.1007/s10548-008-0054-5

Musaeus, C. S., Nielsen, M. S., and Hogh, P. (2019a). Microstates as disease and progression markers in patients with mild cognitive impairment. *Front. Neurosci.* 13:563. doi: 10.3389/fnins.2019.00563

Musaeus, C. S., Salem, L. C., Kjaer, T. W., and Waldemar, G. (2019b). Microstate changes associated with Alzheimer's disease in persons with down syndrome. *Front. Neurosci.* 13:1251. doi: 10.3389/fnins.2019.01251

Nishida, K., Morishima, Y., Yoshimura, M., Isotani, T., Irisawa, S., Jann, K., et al. (2013). EEG microstates associated with salience and frontoparietal networks in frontotemporal dementia, schizophrenia and Alzheimer's disease. *Clin. Neurophysiol.* 124, 1106–1114. doi: 10.1016/j.clinph.2013.01.005

O'Neill, G. C., Tewarie, P., Vidaurre, D., Liuzzi, L., Woolrich, M. W., and Brookes, M. J. (2018). Dynamics of large-scale electrophysiological networks: a technical review. *NeuroImage* 180, 559–576. doi: 10.1016/j.neuroimage.2017.10.003

Park, B. Y., Vos, De Wael, R., Paquola, C., Lariviere, S., Benkarim, O., et al. (2021). Signal diffusion along connectome gradients and inter-hub routing differentially contribute to dynamic human brain function. *NeuroImage* 224:117429. doi: 10.1016/j.neuroimage.2020.117429

Pascual-Marqui, R. D., Michel, C. M., and Lehmann, D. (1995). Segmentation of brain electrical activity into microstates: model estimation and validation. *IEEE Trans. Biomed. Eng.* 42, 658–665. doi: 10.1109/10.391164

Pirondini, E., Coscia, M., Minguillon, J., Millan, J. D. R., Van De Ville, D., and Micera, S. (2017). EEG topographies provide subject-specific correlates of motor control. *Sci. Rep.* 7:13229. doi: 10.1038/s41598-017-13482-1

Pirondini, E., Goldshuv-Ezra, N., Zinger, N., Britz, J., Soroker, N., Deouell, L. Y., et al. (2020). Resting-state EEG topographies: reliable and sensitive signatures of unilateral spatial neglect. *NeuroImage: Clin.* 26:102237. doi: 10.1016/j.nicl.2020.102237

Ploner, M., and Tiemann, L. (2021). Exploring dynamic connectivity biomarkers of neuropsychiatric disorders. *Trends Cogn. Sci.* 25, 336–338. doi: 10.1016/j.tics.2021.03.005

Poulsen, A. T., Pedroni, A., Langer, N., and Hansen, L. K. (2018). Microstate EEGlab toolbox: an introductory guide. *bioRxiv [preprint]* doi: 10.1101/289850

Raichle, M. E., Macleod, A. M., Snyder, A. Z., Powers, W. J., Gusnard, D. A., and Shulman, G. L. (2001). A default mode of brain function. *Proc. Natl. Acad. Sci. U S A.* 98, 676–682. doi: 10.1073/pnas.98.2.676

Ramsey, L. E., Siegel, J. S., Lang, C. E., Strube, M., Shulman, G. L., and Corbetta, M. (2017). Behavioural clusters and predictors of performance during recovery from stroke. *Nat. Hum. Behav.* 1:0038. doi: 10.1038/s41562-016-0038

Riahi, N., Vakorin, V. A., and Menon, C. (2020). Estimating Fugl-Meyer upper extremity motor score from functional-connectivity measures. *IEEE Trans. Neural Syst. Rehabil. Eng.* 28, 860–868. doi: 10.1109/TNSRE.2020.2978381

Ros, T., Michela, A., Mayer, A., Bellmann, A., Vuadens, P., Zermatten, V., et al. (2022). Disruption of large-scale electrophysiological networks in stroke patients with visuospatial neglect. *Netw. Neurosci.* 6, 69–89. doi: 10.1162/netn_a_00210

Salvalaggio, A., De Filippo, De Grazia, M., Zorzi, M., Thiebaut, De Schotten, M., et al. (2020). Post-stroke deficit prediction from lesion and indirect structural and functional disconnection. *Brain* 143, 2173–2188. doi: 10.1093/brain/awaa156

Sebastian-Romagosa, M., Udina, E., Ortner, R., Dinares-Ferran, J., Cho, W., Murovec, N., et al. (2020). EEG biomarkers related with the functional state of stroke patients. *Front. Neurosci.* 14:582. doi: 10.3389/fnins.2020.00582

See, J., Dodakian, L., Chou, C., Chan, V., Mckenzie, A., Reinkensmeyer, D. J., et al. (2013). A standardized approach to the Fugl-Meyer assessment and its implications for clinical trials. *Neurorehabil. Neural Repair* 27, 732–741. doi: 10.1177/1545968313491000

Seitzman, B. A., Abell, M., Bartley, S. C., Erickson, M. A., Bolbecker, A. R., and Hetrick, W. P. (2017). Cognitive manipulation of brain electric microstates. *NeuroImage* 146, 533–543. doi: 10.1016/j.neuroimage.2016.10.002

Shi, W., Li, Y., Liu, Z., Li, J., Wang, Q., Yan, X., et al. (2020). Non-Canonical microstate becomes salient in high density EEG during propofol-induced altered states of consciousness. *Int. J. Neural Syst.* 30:2050005. doi: 10.1142/S0129065720500057

Siems, M., and Siegel, M. (2020). Dissociated neuronal phase- and amplitude-coupling patterns in the human brain. *NeuroImage* 209:116538. doi: 10.1016/j.neuroimage.2020.116538

Spisak, T., Kincses, B., Schlitt, F., Zunhammer, M., Schmidt-Wilcke, T., Kincses, Z. T., et al. (2020). Pain-free resting-state functional brain connectivity predicts individual pain sensitivity. *Nat. Commun.* 11:187. doi: 10.1038/s41467-019-13785-z

Stinear, C. M. (2017). Prediction of motor recovery after stroke: advances in biomarkers. *Lancet Neurol.* 16, 826–836. doi: 10.1016/S1474-4422(17)30283-1

Tait, L., Tamagnini, F., Stothart, G., Barvas, E., Monaldini, C., Frusciante, R., et al. (2020). EEG microstate complexity for aiding early diagnosis of Alzheimer's disease. *Sci. Rep.* 10:17627. doi: 10.1038/s41598-020-74790-7

Tomescu, M. I., Rihs, T. A., Rochas, V., Hardmeier, M., Britz, J., Allali, G., et al. (2018). From swing to cane: sex differences of EEG resting-state temporal patterns during maturation and aging. *Dev. Cogn. Neurosci.* 31, 58–66. doi: 10.1016/j.dcn.2018.04.011

Trujillo, P., Mastropietro, A., Scano, A., Chiavenna, A., Mrakic-Sposta, S., Caimmi, M., et al. (2017). Quantitative EEG for predicting upper limb motor recovery in chronic stroke robot-assisted rehabilitation. *IEEE Trans. Neural Syst. Rehabil. Eng.* 25, 1058–1067. doi: 10.1109/TNSRE.2017.2678161

van de Ville, D., Britz, J., and Michel, C. M. (2010). EEG microstate sequences in healthy humans at rest reveal scale-free dynamics. *Proc. Natl. Acad. Sci. U S A.* 107, 18179–18184. doi: 10.1073/pnas.1007841107

Vidaurre, D., Hunt, L. T., Quinn, A. J., Hunt, B. A. E., Brookes, M. J., Nobre, A. C., et al. (2018). Spontaneous cortical activity transiently organises into frequency specific phase-coupling networks. *Nat. Commun.* 9:2987. doi: 10.1038/s41467-018-05316-z

von Wegner, F., Tagliazucchi, E., Brodbeck, V., and Laufs, H. (2016). Analytical and empirical fluctuation functions of the EEG microstate random walk - Short-range vs. long-range correlations. *NeuroImage* 141, 442–451. doi: 10.1016/j.neuroimage.2016.07.050

Wang, H. D., Wang, Y. B., Zhang, Y., Dong, Z., Yan, F., Song, D. W., et al. (2021). Differentiating propofol-induced altered states of consciousness using features of EEG microstates. *Biomed. Signal Process. Control* 64:102316. doi: 10.1016/j.bspc.2020.102316

Wang, Y., Wang, C., Miao, P., Liu, J., Wei, Y., Wu, L., et al. (2020). An imbalance between functional segregation and integration in patients with pontine stroke: a dynamic functional network connectivity study. *NeuroImage: Clin.* 28:102507. doi: 10.1016/j.nicl.2020.102507

Wu, J., Quinlan, E. B., Dodakian, L., Mckenzie, A., Kathuria, N., Zhou, R. J., et al. (2015). Connectivity measures are robust biomarkers of cortical function and plasticity after stroke. *Brain* 138, 2359–2369. doi: 10.1093/brain/awv156

Xia, M., Wang, J., and He, Y. (2013). BrainNet viewer: a network visualization tool for human brain connectomics. *PLoS One* 8:e68910. doi: 10.1371/journal.pone.0068910

Yao, R., Xue, J., Yang, P., Wang, Q., Gao, P., Yang, X., et al. (2021). Dynamic changes of brain networks during working memory tasks in schizophrenia. *Neuroscience* 453, 187–205. doi: 10.1016/j.neuroscience.2020.11.007

Yuan, H., Zotev, V., Phillips, R., Drevets, W. C., and Bodurka, J. (2012). Spatiotemporal dynamics of the brain at rest–exploring EEG microstates as electrophysiological signatures of BOLD resting state networks. *NeuroImage* 60, 2062–2072. doi: 10.1016/j.neuroimage.2012.02.031

Zalesky, A., Fornito, A., and Bullmore, E. T. (2010). Network-based statistic: identifying differences in brain networks. *NeuroImage* 53, 1197–1207. doi: 10.1016/j.neuroimage.2010.06.041

Zanesco, A. P., Denkova, E., and Jha, A. P. (2021). Self-reported mind wandering and response time variability differentiate prestimulus electroencephalogram microstate dynamics during a sustained attention task. *J. Cogn. Neurosci.* 33, 28–45. doi: 10.1162/jocn_a_01636

Zanesco, A. P., King, B. G., Skwara, A. C., and Saron, C. D. (2020). Within and between-person correlates of the temporal dynamics of resting EEG microstates. *NeuroImage* 211:116631. doi: 10.1016/j.neuroimage.2020.116631

Zappasodi, F., Croce, P., Giordani, A., Assenza, G., Giannantoni, N. M., Profice, P., et al. (2017). Prognostic value of EEG microstates in acute stroke. *Brain Topogr.* 30, 698–710. doi: 10.1007/s10548-017-0572-0

Zappasodi, F., Perrucci, M. G., Saggino, A., Croce, P., Mercuri, P., Romanelli, R., et al. (2019). EEG microstates distinguish between cognitive components of fluid reasoning. *NeuroImage* 189, 560–573. doi: 10.1016/j.neuroimage.2019.01.067

Zhai, X., Wu, Q., Li, X., Xu, Q., Zhang, Y., Fan, S., et al. (2021). Effects of robot-aided rehabilitation on the ankle joint properties and balance function in stroke survivors: a randomized controlled trial. *Front. Neurol.* 12:719305. doi: 10.3389/fneur.2021.719305

Zhang, Y. S., Takahashi, D. Y., Hady, A. E., Liao, D. A., and Ghazanfar, A. A. (2021). Active neural coordination of motor behaviors with internal states. *bioRxiv [preprint]* doi: 10.1101/2021.12.10.472142

Zoubi, O. A., Misaki, M., Tsuchiyagaito, A., Mayeli, A., Zotev, V., Refai, H., et al. (2020). Canonical EEG microstate dynamic properties and their associations with fMRI signals at resting brain. *bioRxiv [preprint]* doi: 10.1101/2020.08.14.251066

Zuchowicz, U., Wozniak-Kwasniewska, A., Szekely, D., Olejarczyk, E., and David, O. (2018). EEG phase synchronization in persons with depression subjected to transcranial magnetic stimulation. *Front. Neurosci.* 12:1037. doi: 10.3389/fnins.2018.01037

Conflict of Interest: The authors declare that the research was conducted in the absence of any commercial or financial relationships that could be construed as a potential conflict of interest.

frontiers | Frontiers in Neuroscience

ORIGINAL RESEARCH
published: 03 June 2022
doi: 10.3389/fnins.2022.912075

Assessing Neurokinematic and Neuromuscular Connectivity During Walking Using Mobile Brain-Body Imaging

Mingqi Zhao[1], Gaia Bonassi[2], Jessica Samogin[1], Gaia Amaranta Taberna[1], Camillo Porcaro[3,4,5], Elisa Pelosin[6,7], Laura Avanzino[7,8] and Dante Mantini[1]*

[1] Movement Control and Neuroplasticity Research Group, KU Leuven, Leuven, Belgium, [2] S.C. Medicina Fisica e Riabilitazione Ospedaliera, Azienda Sanitaria Locale Chiavarese, Genoa, Italy, [3] Department of Neuroscience and Padova Neuroscience Center, University of Padua, Padua, Italy, [4] Institute of Cognitive Sciences and Technologies—National Research Council, Rome, Italy, [5] Centre for Human Brain Health and School of Psychology, University of Birmingham, Birmingham, United Kingdom, [6] Department of Neuroscience, Rehabilitation, Ophthalmology, Genetics and Maternal Child Health, University of Genoa, Genoa, Italy, [7] IRCCS Ospedale Policlinico San Martino, Genoa, Italy, [8] Department of Experimental Medicine, Section of Human Physiology, University of Genoa, Genoa, Italy

Edited by:
Laura Marzetti,
University of Studies G. d'Annunzio
Chieti and Pescara, Italy

Reviewed by:
Qunxi Dong,
Beijing Institute of Technology, China
Andrea Turolla,
University of Bologna, Italy

***Correspondence:**
Dante Mantini
dante.mantini@kuleuven.be

Specialty section:
This article was submitted to
Brain Imaging Methods,
a section of the journal
Frontiers in Neuroscience

Received: *03 April 2022*
Accepted: *16 May 2022*
Published: *03 June 2022*

Citation:
Zhao M, Bonassi G, Samogin J, Taberna GA, Porcaro C, Pelosin E, Avanzino L and Mantini D (2022) Assessing Neurokinematic and Neuromuscular Connectivity During Walking Using Mobile Brain-Body Imaging. Front. Neurosci. 16:912075. doi: 10.3389/fnins.2022.912075

Gait is a common but rather complex activity that supports mobility in daily life. It requires indeed sophisticated coordination of lower and upper limbs, controlled by the nervous system. The relationship between limb kinematics and muscular activity with neural activity, referred to as neurokinematic and neuromuscular connectivity (NKC/NMC) respectively, still needs to be elucidated. Recently developed analysis techniques for mobile high-density electroencephalography (hdEEG) recordings have enabled investigations of gait-related neural modulations at the brain level. To shed light on gait-related neurokinematic and neuromuscular connectivity patterns in the brain, we performed a mobile brain/body imaging (MoBI) study in young healthy participants. In each participant, we collected hdEEG signals and limb velocity/electromyography signals during treadmill walking. We reconstructed neural signals in the alpha (8–13 Hz), beta (13–30 Hz), and gamma (30–50 Hz) frequency bands, and assessed the co-modulations of their power envelopes with myogenic/velocity envelopes. Our results showed that the myogenic signals have larger discriminative power in evaluating gait-related brain-body connectivity with respect to kinematic signals. A detailed analysis of neuromuscular connectivity patterns in the brain revealed robust responses in the alpha and beta bands over the lower limb representation in the primary sensorimotor cortex. There responses were largely contralateral with respect to the body sensor used for the analysis. By using a voxel-wise analysis of variance on the NMC images, we revealed clear modulations across body sensors; the variability across frequency bands was relatively lower, and below significance. Overall, our study demonstrates that a MoBI platform based on hdEEG can be used for the investigation of gait-related brain-body connectivity. Future studies might involve more complex walking conditions to gain a better understanding of fundamental neural processes associated with gait control, or might be conducted in individuals with neuromotor disorders to identify neural markers of abnormal gait.

Keywords: electroencephalography (EEG), electromyography (EMG), mobile brain-body imaging (MoBI), gait analysis, brain oscillations, motor control

INTRODUCTION

Gait is a common but rather complex activity that supports mobility in daily life. The successful performance of normal gait relies on rhythmic steps of left and right lower limbs in alternation, with arms and trunk providing stability and balance (Vaughan, 2003). This is mediated by the musculoskeletal system and requires sophisticated coordination of the nervous system (Alamdari and Krovi, 2017). The involvement of cortical and subcortical regions to support gait control has been documented by studies using neuroimaging techniques such as functional magnetic resonance imaging (fMRI), positron emission tomography (PET), and single photon emission computer tomography (SPECT) (Bakker et al., 2007a,b; Takakusaki, 2013, 2017; Hamacher et al., 2015). Electroencephalography (EEG), which measures changes in scalp potentials associated with neuronal electrical activity, can be used to directly examine neural dynamics during gait. Specifically, wireless EEG systems can be used in combination with kinematic and/or electromyography (EMG) sensors placed over the limbs for mobile brain/body imaging (MoBI) experiments (Jungnickel et al., 2019). EEG-based MoBI platforms record body signals and neural signals simultaneously, and can be useful for the study of gait-related brain dynamics.

The analysis of gait usually requires precise information on limb kinematics (Jasiewicz et al., 2006; Kotiadis et al., 2010). Normal gait consists of recurrent cycles that contain consecutive stance and swing phases for each lower limb (Vaughan, 2003; Schmeltzpfenning and Brauner, 2013; Alamdari and Krovi, 2017; Price et al., 2021). A stance phase starts with the corresponding foot striking on the ground (i.e., heel strike event) and ends with the toe of that foot detaching the ground (i.e., toe off event). The subsequent swing phase starts with the toe off event and ends with the heel strike event, which moves the body forward. Since the lower limbs move in alternation, the stance is further subdivided into a single support period where only one foot is in contact with the ground, and two double support periods, before and after the single support period, where two feet are supporting the weight of the body. These gait phases rely on coordinated contractions of lower limb muscles, which can be captured by surface EMG sensors (Cappellini et al., 2006; Agostini et al., 2010; Bonnefoy-Mazure and Armand, 2015). For instance, the vastus, the biceps femoris and the tibialis anterior of a heel-striking leg show stronger EMG activity during the double support phase to maintain the equilibrium while allowing forward progression. The vastus contracts during the initial part of the single support phase whereas the gastrocnemius is active during the whole single support phase. Also, the EMG signals of the tibialis anterior and the biceps femoris are strong throughout and at the end of the swing phase, respectively.

Gait-related EEG signals typically contain, in addition to neural signals, relatively large ocular/movement/myogenic artifacts. These artifacts can be effectively attenuated (Zhao et al., 2021) or corrupted data segments can be excluded (Gwin et al., 2011; Seeber et al., 2014, 2015; Nathan and Contreras-Vidal, 2016; Wagner et al., 2016; Oliveira et al., 2017) to ensure a reliable analysis of gait-related neural oscillations. These neural oscillations are typically distinguished in delta (1–4 Hz), theta (4–8 Hz), alpha (8–13 Hz), beta (13–30 Hz), and gamma (>30 Hz) oscillations. Several studies used EEG recordings to evaluate modulations of specific neural oscillations with respect to kinematic events and phases of the gait cycle. For example, modulations of neural oscillations across the gait cycle were found in EEG data collected using treadmill walking (Gwin et al., 2011). Further EEG studies on gait also differentiated the functional roles of neural modulations in beta, low gamma and high gamma bands (Seeber et al., 2014, 2015). Other studies reported distinct beta band oscillatory networks in subserving gait adaptation (Bulea et al., 2015), and suggested that the prefrontal, posterior parietal, and sensorimotor network activity underlies speed control during walking (Wagner et al., 2016). More recent studies observed correlates of power reduction in alpha and beta oscillations with increase of gait speed (Nordin et al., 2020), as well as gait-phase-independent neural activity during voluntary gait modifications (Yokoyama et al., 2021).

It should be considered that EEG-based MoBI platforms permit not only the study of brain activity during movement, but also of its relationships with body signals. Associations between brain and body signals are typically referred to as brain-body connectivity. Coherence analysis (Shaw, 1984) has been the first technique proposed to assess the link between movement and EEG dynamics, or neurokinematic connectivity (NKC) (Bourguignon et al., 2011, 2015; Piitulainen et al., 2013), and between EMG and EEG dynamics, or neuromuscular connectivity (NMC) (Bayraktaroglu et al., 2011; Gwin and Ferris, 2012). The first NKC and NMC experiments were conducted in controlled settings and mainly involved the contraction of limb muscles, but subsequent studies also extended such analysis to treadmill and free walking conditions (Petersen et al., 2012; Roeder et al., 2018). Mobile EEG measures are characterized by a larger contribution of movement-related artifacts, thereby reducing the sensitivity of coherence analyses for NKC and NMC assessment (Bourguignon et al., 2011, 2015; Bayraktaroglu et al., 2013). To address this problem, other brain-body connectivity measures were proposed, which rely on the analysis of temporal correlations between neural oscillations and peripheral signal envelopes (Bayraktaroglu et al., 2013; Dähne et al., 2014; Tanaka and Saga, 2019; Watanabe et al., 2020). It should also be noted that all the studies conducted so far quantified the relationships of body signals with EEG signals at the scalp level.

Notably, recent developments in the field of EEG data acquisition and analysis have permitted to perform a reliable source localization, i.e., the estimate of neural activity in the brain (Michel and Murray, 2012). Particularly, it has been shown that the application of high-density EEG (hdEEG) montages with more than hundred electrodes yields a fine spatial sampling of scalp potentials (Liu et al., 2015; Song et al., 2015; Seeck et al., 2017); furthermore, the implementation of advanced artifact attenuation approaches (Zhao et al., 2021) and head modeling solutions (Taberna et al., 2019a,b, 2021) permits a more accurate characterization of neural oscillations in the source space from hdEEG recordings. In a recent study, we have demonstrated that the application of these advanced solutions on hdEEG data collected in walking participants can support a finer characterization of neural oscillations in different phases of the gait cycle (Zhao et al., 2022). Yet, it remains to be evaluated if the increased spatial specificity brought by hdEEG in neuronal signal reconstruction can support the reliable assessment of gait-related NKC and NMC in the source space, and if this approach provides additional information as compared to previous studies that quantified NKC and NMC at the sensor level (Petersen et al., 2012; Roeder et al., 2018). To address these questions, we conducted an experiment in young healthy participants using a hdEEG-based MoBI platform and assessed gait-related brain-body connectivity in the source space. More specifically, we aimed to test whether brain-body connectivity is characterized by specific spatial patterns depending on the specific body sensors and the neural oscillations of interest, and to evaluate if the brain regions showing robust brain-body connectivity are those typically related to motor execution, or also to motor planning and coordination.

MATERIALS AND METHODS

In this study, we designed and used a MoBI platform to collect myogenic and kinematic body signals, as well as hdEEG recordings in a group of healthy participants during treadmill walking. With the resulting MoBI data, we evaluated the discriminative power of the myogenic and kinematic signals by analyzing temporal correlations of the signal envelopes across body sensors. We also assessed the frequency-wise NKC and NMC in selected regions of interest (ROIs) across body sensors by calculating correlations of the envelopes of body signals with the power of the neural signals in each frequency, and evaluated the connectivity levels separately for alpha (8–13 Hz), beta (13–30 Hz), and gamma (30–50 Hz) frequency bands. We finally extended the analysis to the whole brain and examined the connectivity images in the source space across body sensors.

Experiment and Participants

The experiment included 24 young, healthy participants (14 females and 10 males, age 22–31 years), who were not affected by any brain-related injury/disease or any other medical condition. The experimental procedures were approved by the Ethics Committee of the Liguria Region, Italy (reference: 238/2019) and were conducted in accordance with the 1964 Helsinki declaration and its later amendments. An informed consent was obtained from each participant. The participant was equipped with the MoBI platform described below, and was asked to walk with normal and constant speed during the experiment (Gwin et al., 2011; Wagner et al., 2016) on a Forcelink treadmill (Motek Medical B.V., Houten, Netherlands). Data collection started after familiarization with the treadmill walking. The task design consisted of three blocks of walk, each lasting 2 min, with 1-min rest in between.

Mobile Brain-Body Imaging Platform

The MoBI platform consisted of three main parts: *the backpack*; *the wireless body sensors*; and *the base station* (**Figure 1A**). *(1) The backpack* weighted about 1.7 kg and contained an ActiCHamp EEG amplifier (Brain Products GmbH, Gilching, Germany) with 128 channels, a Surface Go tablet (Microsoft Corporation, Redmond, WA, United States) and a light-weighted battery. The amplifier, powered by the battery, was connected to the tablet for reliable data storage. The EEG sensors, which were integrated in a cap with standard 10/20 montage, were connected to the subject's scalp using a conductive gel. *(2) The wireless body sensors* were attached on the skin of the participant and permitted to collect simultaneous 3-axis acceleration and EMG signals. *(3) The base station* contained a 16-channel Trigno base (Delsys Inc., Natick, MA, United States) and a laptop. The Trigno base was used to receive acceleration/EMG data from the wireless sensors and to transfer them to the laptop through a USB cable connection. The laptop also controlled the Trigno base and the EEG data acquisition tablet for experimental flow management. A pulse signal (**Figure 1B**) was sent from the tablet to one of the auxiliary channels of the hdEEG amplifier and to one of the wireless sensors for an offline synchronization of the two systems. The temporal difference between the two was quantified using cross correlation (**Supplementary Figure 1a**). The temporal jitters after synchronization were below 5 ms (**Supplementary Figure 1b**).

Data Collection

During the experiment, we collected 128-channel hdEEG signals at 1 kHz sampling rate, using the FCz electrode as physical reference. In addition, we collected 3-axis acceleration signals and EMG signals, respectively at 148 Hz and 2 kHz sampling rate, using wireless body sensors over the following bilateral muscles: vastus medialis, biceps femoris, tibialis anterior, gastrocnemius; using the same system, we also measured 3-axis acceleration signals from body sensors placed over the left and right ankles (**Supplementary Figure 2**). These anatomical locations were specifically chosen as they were reported to be related to walking movements (Winter and Yack, 1987; Liu et al., 2008; Bonnefoy-Mazure and Armand, 2015). The sensor positioning was performed in compliance with published guidelines (Hermens et al., 2000). Immediately after the experiment, we acquired a 3D scan of the participant's head using an iPad (Apple Inc., Cupertino, CA, United States) equipped with a Structure Sensor camera (Occipital Inc., Boulder, CO, United States), to extract the locations of the hdEEG electrodes (Taberna et al., 2019a,b).

In a separate session, the structural MR image of each participant's head was collected with a 3T Philips Achieva MR scanner (Philips Medical Systems, Best, Netherlands) using a T1-weighted magnetization-prepared rapid-acquisition gradient-echo (MP-RAGE) sequence. The scanning parameters were: repetition time (TR) = 9.6 ms, echo time

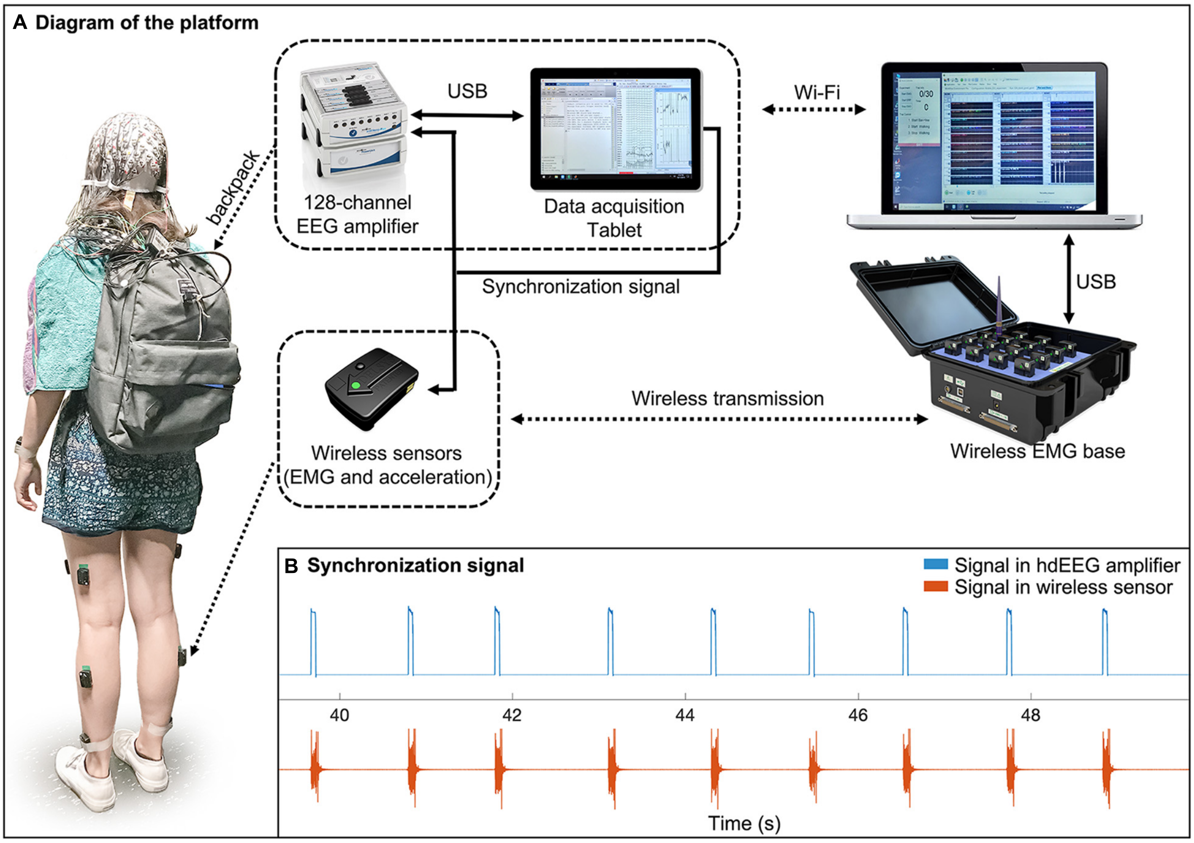

FIGURE 1 | Diagram of the mobile brain-body imaging platform. **(A)** The platform consists of three parts: a backpack, a set of wireless body sensors, and a base station. The backpack contains a high-density EEG (hdEEG) amplifier, an EEG data acquisition tablet, and a light-weighted battery for powering the amplifier. During the experiment, a participant wears a hdEEG cap that is connected to the EEG amplifier in the backpack. The amplifier is connected to a tablet in the backpack for reliable EEG data recording. The EEG recording software on the tablet is remotely controlled by a laptop *via* Wi-Fi connection. The laptop is also connected to a wireless sensor base that receives EMG and acceleration data from sensors attached on the participant. The EEG system and wireless sensor system are synchronized by receiving a synchronization signal from the tablet through an auxiliary channel and one of the wireless sensors, respectively. **(B)** An example of synchronization signals recorded from the two systems.

(TE) = 4.6 ms, 160 coronal slices, 250×250 matrix, voxel size = 0.98 × 0.98 × 1.2 mm^3.

Analysis of Kinematic and Electromyographic Data

For each participant, we estimated the velocities using the integrals of left and right ankle total acceleration (**Supplementary Figure 3**). Total ankle acceleration signal segments with stable velocity were isolated and extracted to detect gait events and gait cycles in line with previous kinematic studies (Jasiewicz et al., 2006; Kotiadis et al., 2010). Accordingly, we detected the following gait events: left heel strike (LHS), right heel strike (RHS), left toe off (LTO), and right toe off (RTO) (Gwin et al., 2011; Seeber et al., 2014; Wagner et al., 2016). A full gait cycle was defined as the period between two adjacent left heel strikes (Zhao et al., 2022).

We then extracted trial-averaged velocity envelopes and EMG envelopes according to the acceleration signals and the EMG signals from the sensors on the limbs. Specifically, for each body sensor, the velocity was estimated from the integral of the total acceleration signal; the EMG signals were digitally filtered in the band [1–500] Hz and rectified (Türker, 1993; Rainoldi et al., 2004; Halliday and Farmer, 2010). The velocity envelopes and the EMG envelopes, as derived separately from the Hilbert transformation of the velocity and processed EMG signals, were resampled to 200 Hz, epoched based on the gait cycles, standardized to gait cycle percentage according to the corresponding RHS, LTO, and RTO events, and finally averaged for each participant.

The two types of trial-averaged envelopes were plotted for each body sensor as range curves (minimum to maximum range, intra-quartile range, and median curve) to examine the movements and the muscular activations of the limbs across the gait cycle. The inter-dependence of the envelopes was quantified using correlations across body sensors. The resulting correlation values were transformed to z-values using the Fisher transform, and then subject to one-sample *t*-tests to assess their statistical significance. The z-values were also averaged across participants; the resulting z-values were back-transformed to correlation

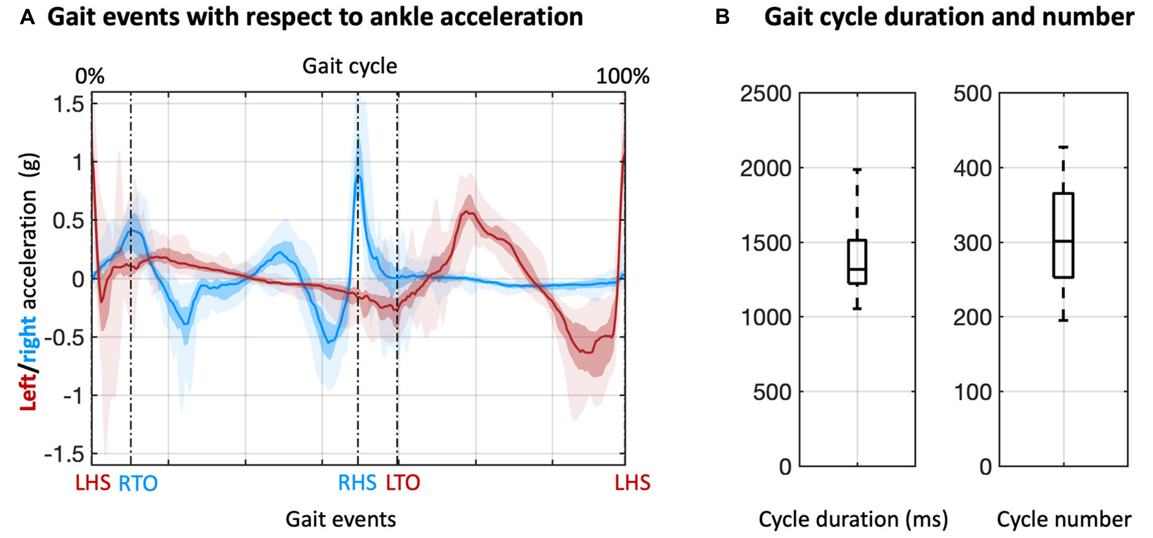

FIGURE 2 | Detection and analysis of gait cycles. **(A)** Gait cycles were defined based on two adjacent left heel strike (LHS) events, detected from the acceleration of the left and right ankles. The acceleration data were also used to define right toe off (RTO), right heel strike (RHS), and left toe off (LTO) events. The lines denote the median across participants; the colored areas denote the intra-quartile range; the areas with semi-transparent color denote the full-range (from minimum to maximum) across participants. **(B)** Duration and number of gait cycles across participants.

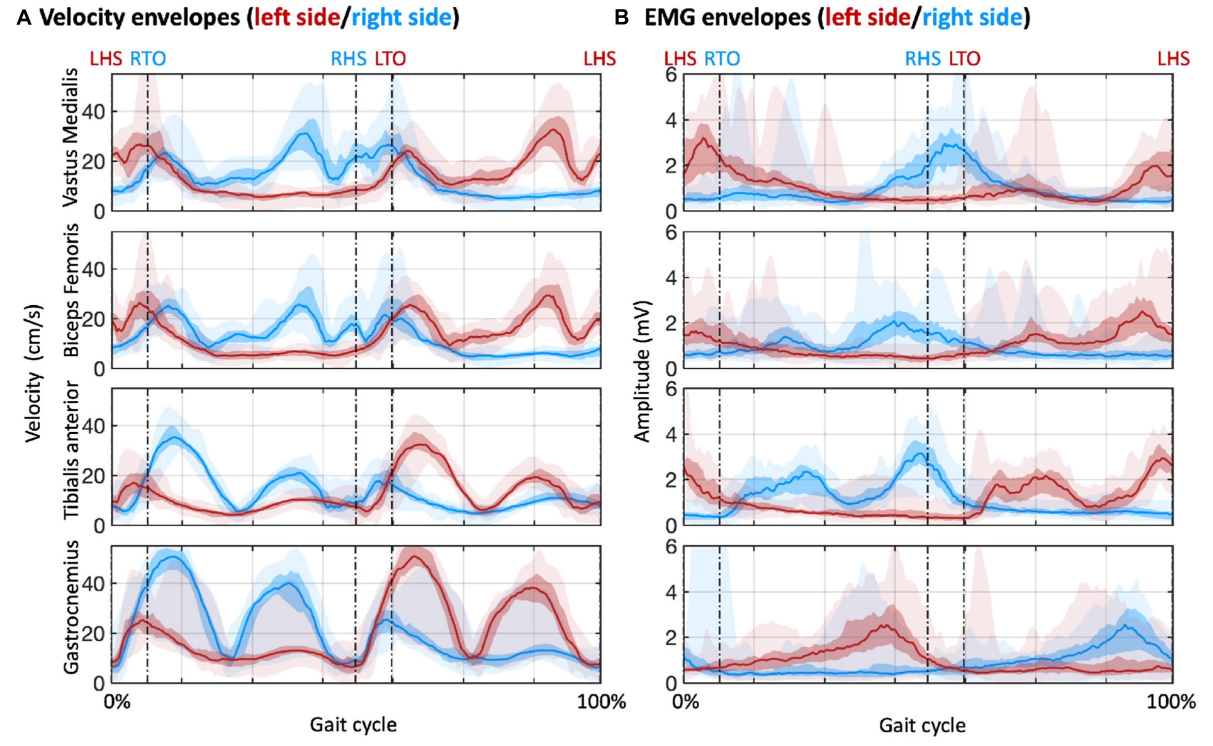

FIGURE 3 | Velocity and EMG envelopes for sensors placed over selected muscles of the lower limbs. The muscles are the vastus medialis, biceps femoris, tibialis anterior, and gastrocnemius. **(A)** Velocity envelopes in the gait cycles across participants. **(B)** EMG envelopes in the gait cycles across participants. The lines denote the median across participants; the colored areas denote the intra-quartile range; the areas with semi-transparent color denote the full range (from minimum to maximum) across participants. Red and blue colors are used to indicate results for the muscles in the left and right sides of the body, respectively. LHS, left heel strike; RHS, right heel strike; LTO, left toe off; RTO, right toe off.

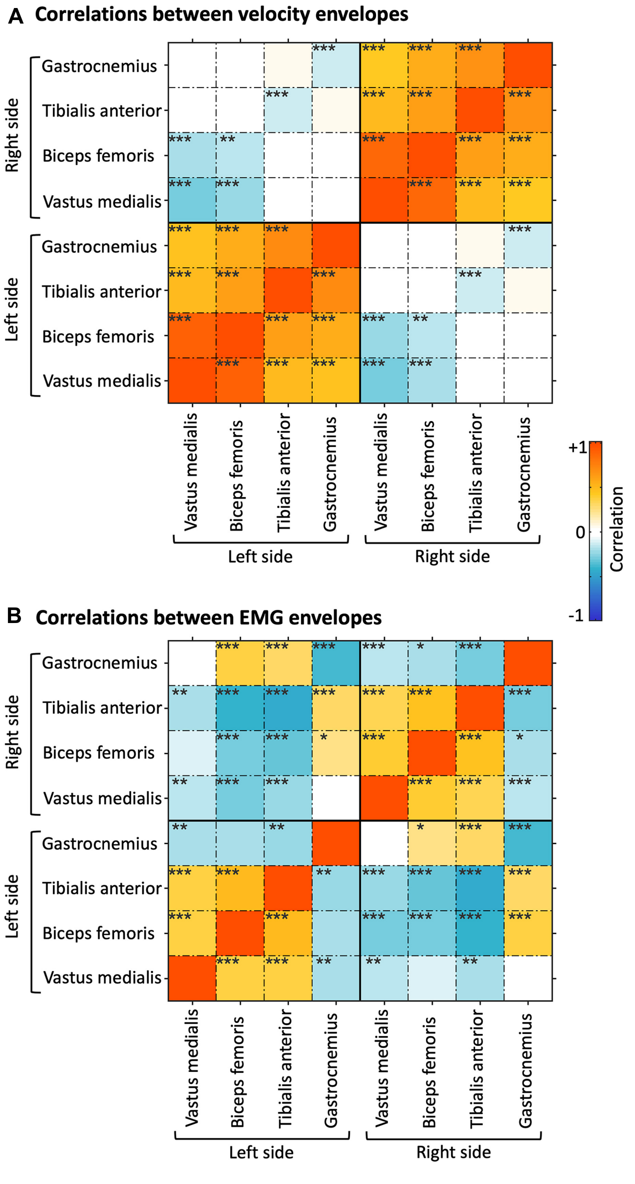

FIGURE 4 | Correlation analysis of velocity and EMG envelopes. **(A)** Correlations of velocity envelopes across body sensors. **(B)** Correlations of EMG envelopes across body sensors. The results presented refer to the average across participants. $^{*}p_{FDR} < 0.05$; $^{**}p_{FDR} < 0.01$; $^{***}p_{FDR} < 0.001$.

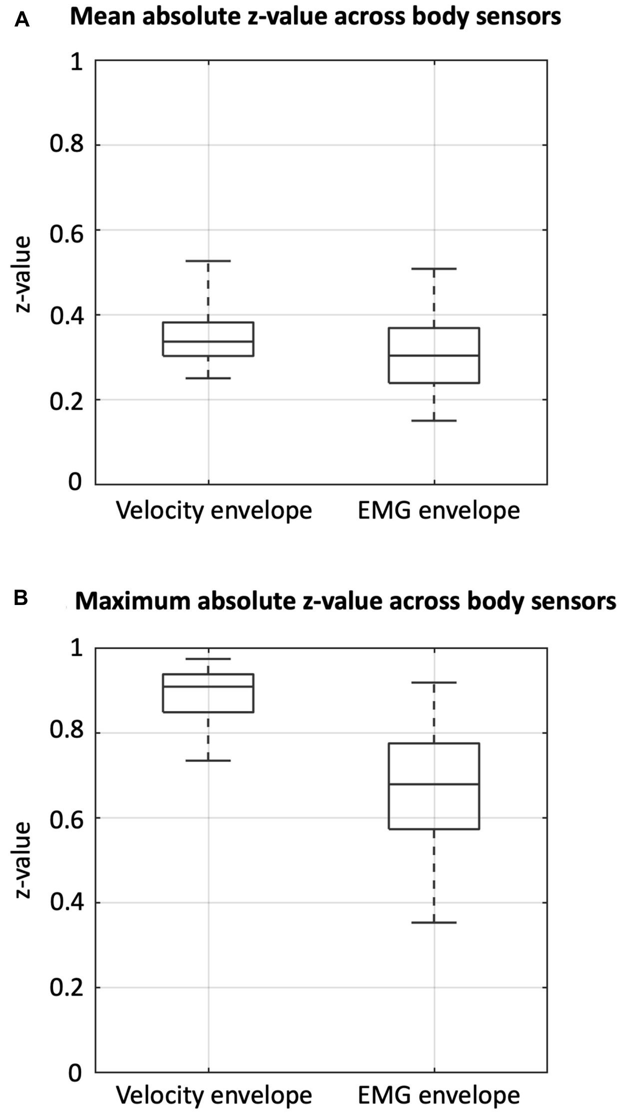

FIGURE 5 | Inter-dependence of velocity and EMG envelopes across body sensors. Box plots indicating **(A)** the mean absolute z-value and **(B)** the maximum absolute z-value, for velocity and EMG envelopes, respectively.

values using the inverse Fisher transformation. These group-level correlation values were used for visualization purposes. Furthermore, the mean z-value and the maximum absolute z-value across body sensors were calculated for each subject, and the resulting values were visualized using box plots, separately for each signal type (velocity/EMG envelopes).

Analysis of Neural Data

The hdEEG data analysis involved three main steps: EEG data preprocessing, head model creation, neural signal reconstruction. These steps will be described in the following sections.

Electroencephalography Data Preprocessing

We first corrected the bad channels in the hdEEG data (Guarnieri et al., 2018), digitally filtered them in the frequency band between 1 and 80 Hz and downsampled them to 200 Hz. Then, we applied a multi-step blind source separation approach to minimize the impact of ocular, movement and myogenic artifacts in the mobile hdEEG data (Zhao et al., 2021). Specifically, we attenuated the ocular artifacts by decomposing the hdEEG data with deflation-FastICA (Hyvarinen, 1999) and removing the components with maximum kurtosis over 5-s windows above 12; then, we attenuated the movement artifacts by decomposing the data with symmetric-FastICA (Hyvarinen, 1999) and removing the resulting components with mean sample entropy over 20-s windows below 0.8; finally, we attenuated the myogenic artifacts by decomposing the data with independent vector analysis (Anderson et al., 2011) and removing the components with power in the [30–80 Hz] band larger than the power in the [1–30 Hz] band. After artifact attenuation, we re-referenced the hdEEG signals using the average reference approach (Liu et al., 2015).

Head Model Creation

For each participant, a 12-layer realistic head volume conduction model was created for the neural activity reconstruction step. Specifically, three steps were followed: *electrodes position detection and coregistration*; *head tissue segmentation*; and *lead-field matrix calculation* (Taberna et al., 2021). *(1) Electrodes position detection and coregistration*. We detected the precise locations of the EEG electrodes using the SPOT3D toolbox, and coregistered them to the scalp of the individual MR image (Taberna et al., 2019a,b). *(2) Head tissue segmentation*. Using the MR-TIM software (Taberna et al., 2021), we segmented the individual MR image to 12 tissue layers: skin, eyes, muscle, fat, spongy bone, compact bone, cortical/subcortical gray matter, cerebellar gray matter, cortical/subcortical white matter, cerebellar white matter, cerebrospinal fluid, and brain stem. The conductivity value of each tissue layer was defined according to relevant studies (Haueisen et al., 1997; Holdefer et al., 2006). *(3) Lead-field matrix calculation*. The individual lead-field matrix projects the neural activity from the source space to scalp electric potentials. The matrix was calculated using the Simbio finite element method (Vorwerk et al., 2018), by meshing the tissue layers to 6-mm hexahedrons and placing source dipoles in the hexahedrons located inside the gray matter.

Neural Activity Reconstruction

We reconstructed the neural activity in the source space for each participant using the exact low-resolution brain electromagnetic tomography (eLORETA) algorithm (Pascual-Marqui et al., 2011), as in our previous hdEEG studies (Liu et al., 2017; Samogin et al., 2019; Zhao et al., 2019, 2021). This choice is corroborated by a comparative analysis performed on different source localization methods, which showed eLORETA to be particularly suitable for neural source signal reconstruction from hdEEG data (Liu et al., 2018). The preprocessed hdEEG data and the individual head model were fed to the eLORETA algorithm, resulting in an estimation of the oscillation strength and orientation of the dipole in each voxel of the gray matter, at each temporal moment. The estimated three-dimensional current density signal of each voxel was projected to a representative signal by taking the first principal components obtained from a principal component analysis (PCA).

Brain-Body Connectivity Analyses

The reconstructed neural signals were analyzed in combination with kinematic and EMG data to assess frequency-dependent NKC and NMC, respectively. We initially assessed the NKC and NMC in a region of interest (ROI) located in the right primary motor cortex (M1) (**Supplementary Table 1**). For each participant, we first transformed the MNI coordinates into individual coordinates, and extracted the signals from the voxels within a 6-mm sphere centered on the coordinates in individual space. Then, a representative ROI signal was calculated as the first principal component of the signals in the different ROI

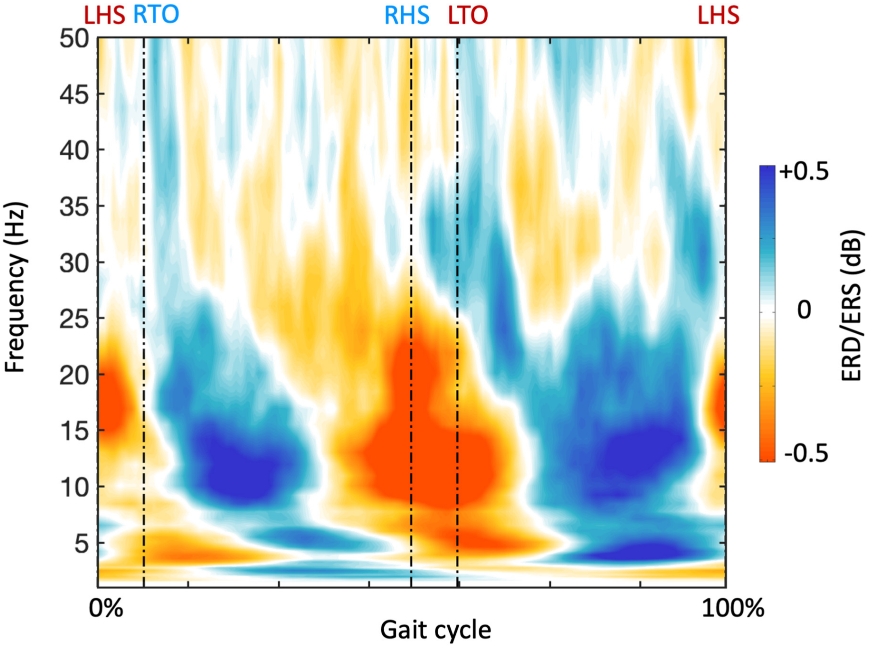

FIGURE 6 | Gait-related time-frequency analysis for a representative region of interest. The plot shows the average frequency-dependent modulations of neural signals in the gait cycle across participants, calculated from the neural signal of the right primary motor cortex (M1). The timing of gait events is indicated using dashed vertical lines. LHS, left heel strike; RHS, right heel strike; LTO, left toe off; RTO, right toe off.

voxels. We calculated a spectrogram in the frequency range [1–50 Hz] by using a continuous wavelet transformation (number of octaves = 6, voices per octave = 8). The frequency-specific power modulations of the spectrogram were epoched, standardized and averaged according to the same procedure used for the velocity/EMG envelopes. This approach permitted the estimate of frequency-dependent neural power dynamics during gait. After, the correlation between neural power dynamics at each frequency and velocity/EMG envelopes in the gait cycle was calculated to quantify frequency-dependent NKC/NMC. Such analysis was conducted for the M1 region in both hemispheres. Specifically, brain-body connectivity was assessed for ROIs that were either ipsilateral or contralateral to the body sensor, in alpha (8–13 Hz), beta (13–30 Hz), and gamma (30–50 Hz) bands, respectively. The connectivity values were also analyzed statistically. Specifically, we tested for differences across body sensors, ROIs, frequency bands and body signal types, using a four-way analysis of variance (ANOVA). To test whether gait-related brain-body connectivity was not only present in brain regions associated in motor execution, but also motor planning and coordination, we extended the ROI analysis to bilateral regions in thalamus (THAL), premotor cortex (PMC), posterior parietal cortex (PPC), and cerebellum (CER) (**Supplementary Table 1**). For each ROI, we used a two-way ANOVA on the connectivity values, with body sensor and frequency band as factors; we also conducted additional statistical analyses using one-sample *t*-tests. Probabilities were corrected for multiple comparisons using the false discovery rate (FDR) method.

We finally conducted a brain-body connectivity analysis across brain voxels, by creating volumetric images for each participant. The individual connectivity images were warped to MNI space by applying a non-rigid deformation calculated from the head MR image of each participant (Zhao et al., 2019). The group-level connectivity patterns were obtained by averaging

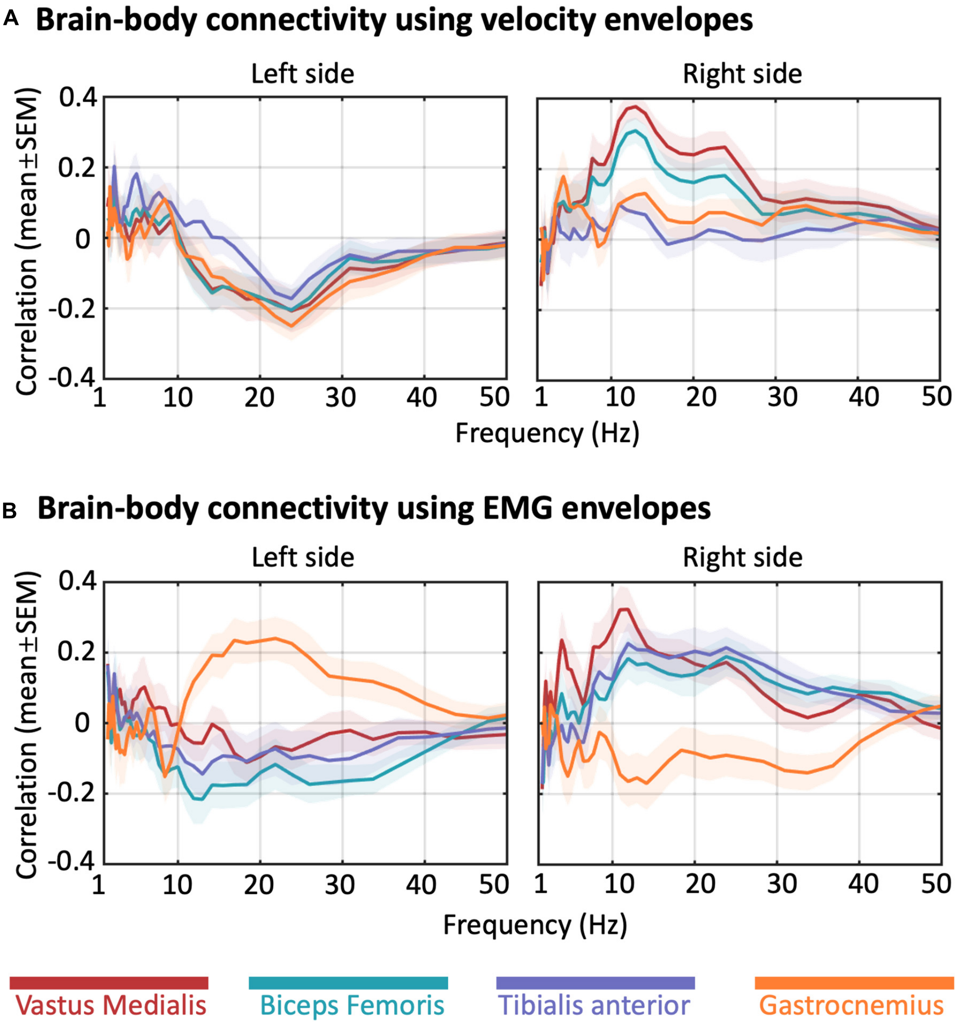

FIGURE 7 | Frequency-dependent brain-body connectivity for a representative region of interest. The plots show the brain-body connectivity calculated from the neural signal of the right primary motor cortex (M1), using **(A)** velocity envelopes and **(B)** EMG envelopes, respectively. Colored lines denote the mean across participants, and colored areas denote the standard error of the mean.

the images across participants for each frequency band, body sensor and signal type. To further examine the main effects and interaction of frequency band and body sensor, we applied a voxel-wise two-way ANOVA on the same connectivity images. The resulting statistical parametric images were thresholded at $p < 0.001$ with multiple comparison correction using FDR.

RESULTS

Gait-Related Kinematic and Electromyographic Profiles

Our analysis started from the detection of the gait events and gait cycles (**Figure 2**). Clear gait-related modulations of left and right ankle acceleration signals were observed, with a consistent pattern across participants (**Figure 2A**). Based on the LHS events of the continuous steps, we detected about 200 to more than 400 gait cycles for each participant, with average cycle duration ranging from 1000 to 2000 ms (**Figure 2B**). With these gait events, we examined myogenic and kinematic signals of the body sensors across the gait cycle. Clear and consistent modulations both in velocity envelopes (**Figure 3A**) and EMG envelopes (**Figure 3B**) were observed across participants. The analysis of EMG envelopes evidenced contractions of ipsilateral leg muscles in different phases of the gait cycle. The vastus medialis contracted during a short period before and after the heel strike event. The biceps femoris and tibialis anterior activated mainly during the swing

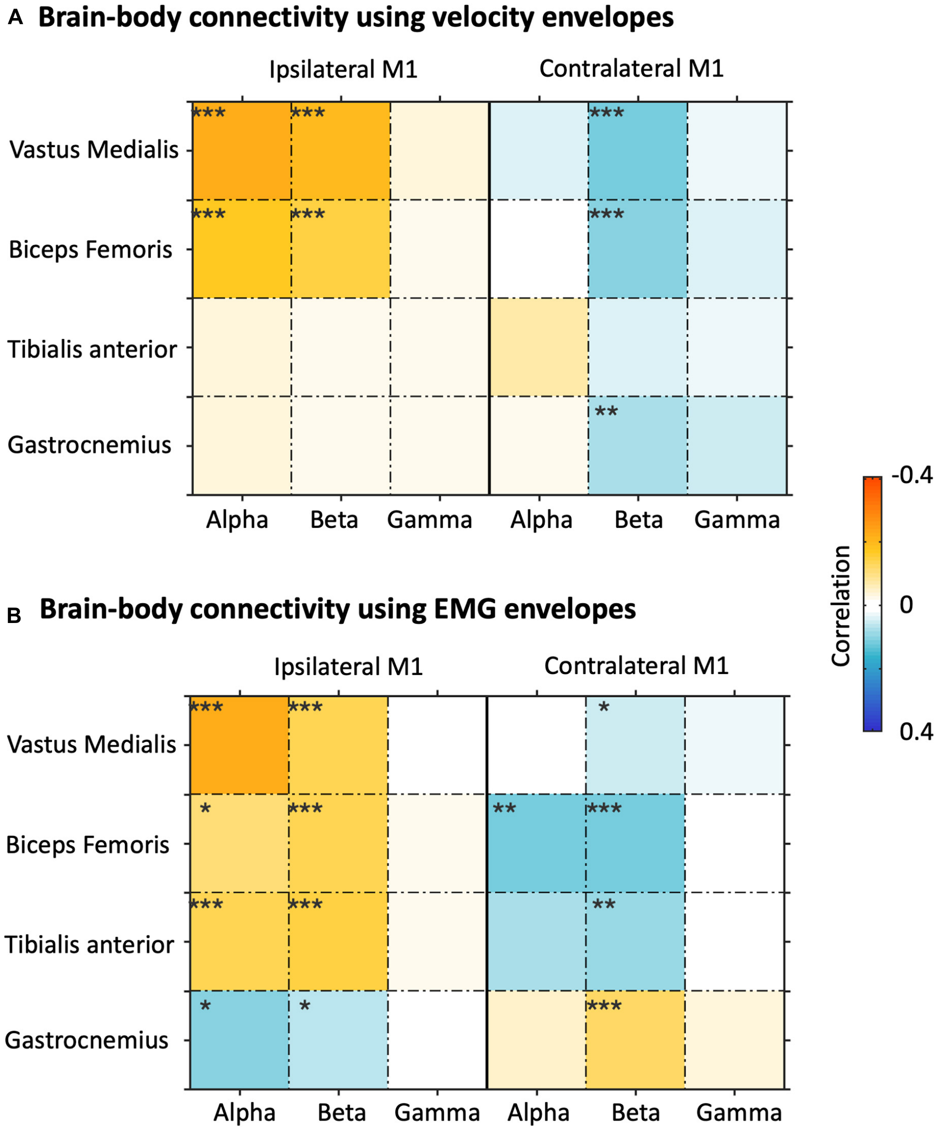

FIGURE 8 | Analysis of brain-body connectivity for ipsilateral and contralateral primary motor cortex (M1), in alpha, beta, and gamma frequency bands. **(A)** Brain-body connectivity assessed using envelopes of reconstructed neural signals and velocity envelopes. **(B)** Brain-body connectivity assessed using envelopes of reconstructed neural signals and EMG envelopes. $^{*}p_{FDR} < 0.05$; $^{**}p_{FDR} < 0.01$; $^{***}p_{FDR} < 0.001$.

phase and around the heel strike event. The gastrocnemius contracted mainly in the stance phase. On the contrary, the velocity envelopes did not show substantial differences across ipsilateral sensors: the velocity fluctuated during swinging and kept flat during stance.

To examine the cross-sensor inter-dependence of the velocity and the EMG envelopes, we calculated correlations across sensors, separately for the two signal types (**Figure 4**) and between them (**Supplementary Figure 4**). The velocity envelopes showed significant positive correlations in all the ipsilateral sensors, and a significant negative correlation between contralateral sensors for the thigh (i.e., vastus medialis and biceps femoris) (**Figure 4A**). The EMG envelopes of vastus medialis, biceps femoris, and tibialis anterior had significant positive correlation for the ipsilateral lower limb, and significant negative correlation for the contralateral lower limb (**Figure 4B**). Conversely, a reversed correlation pattern was found in the EMG envelopes of gastrocnemius (**Figure 4B**). We further analyzed the average level of inter-dependence of each of the two signal types (**Figure 5A**). This analysis revealed a higher inter-dependence between velocity envelopes ($\bar{r}_{abs\_mean} = 0.35$) than EMG envelopes ($\bar{r}_{abs\_mean} = 0.31$). The difference between signal types was more prominent when the maximum level of inter-dependence was considered ($\bar{r}_{abs\_max} = 0.89$ and 0.68, respectively) (**Figure 5B**).

Brain-Body Connectivity in Regions Related to Motor Planning, Execution, and Coordination

In order to examine NKC and NMC, we reconstructed band-limited power envelopes of the neural signal for the right M1 region (**Figure 6**). The power in alpha and beta bands decreased during leg swings and rebounded after the swings, whereas a reverse modulation emerged for the gamma band. By calculating the correlation of the power signals in each frequency with each type of body signals, we generally revealed visible and stable NKC and NMC in the alpha and beta bands for the right M1 (**Figure 7**). The NKC were negative for all the left limb sensors (**Figure 7A**, left panel), and were positive for all the right limb sensors (**Figure 7A**, right panel). The NMC was negative for the vastus medialis, biceps femoris, and tibialis anterior located in the left lower limb, whereas it was positive for the gastrocnemius on the same limb (**Figure 7B**, left panel). A completely reversed connectivity pattern was observed for the sensors of the right leg (**Figure 7B**, right panel).

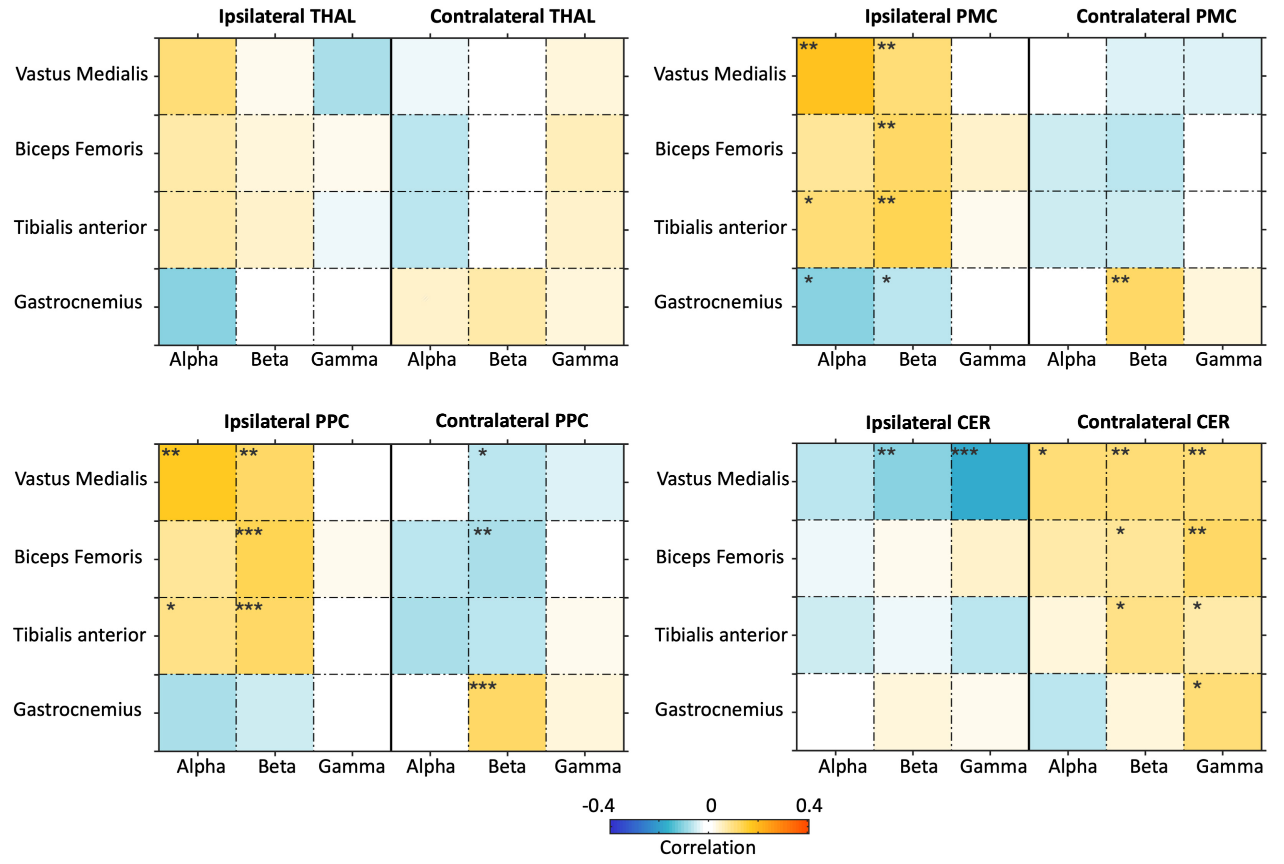

FIGURE 9 | Analysis of brain-body connectivity for ipsilateral and contralateral thalamus (THAL), premotor cortex (PMC), posterior parietal cortex (PPC), and cerebellum (CER), in alpha, beta, and gamma frequency bands. The brain-body connectivity is assessed using envelopes of reconstructed neural signals and EMG envelopes. $^{*}p_{FDR} < 0.05$; $^{**}p_{FDR} < 0.01$; $^{***}p_{FDR} < 0.001$.

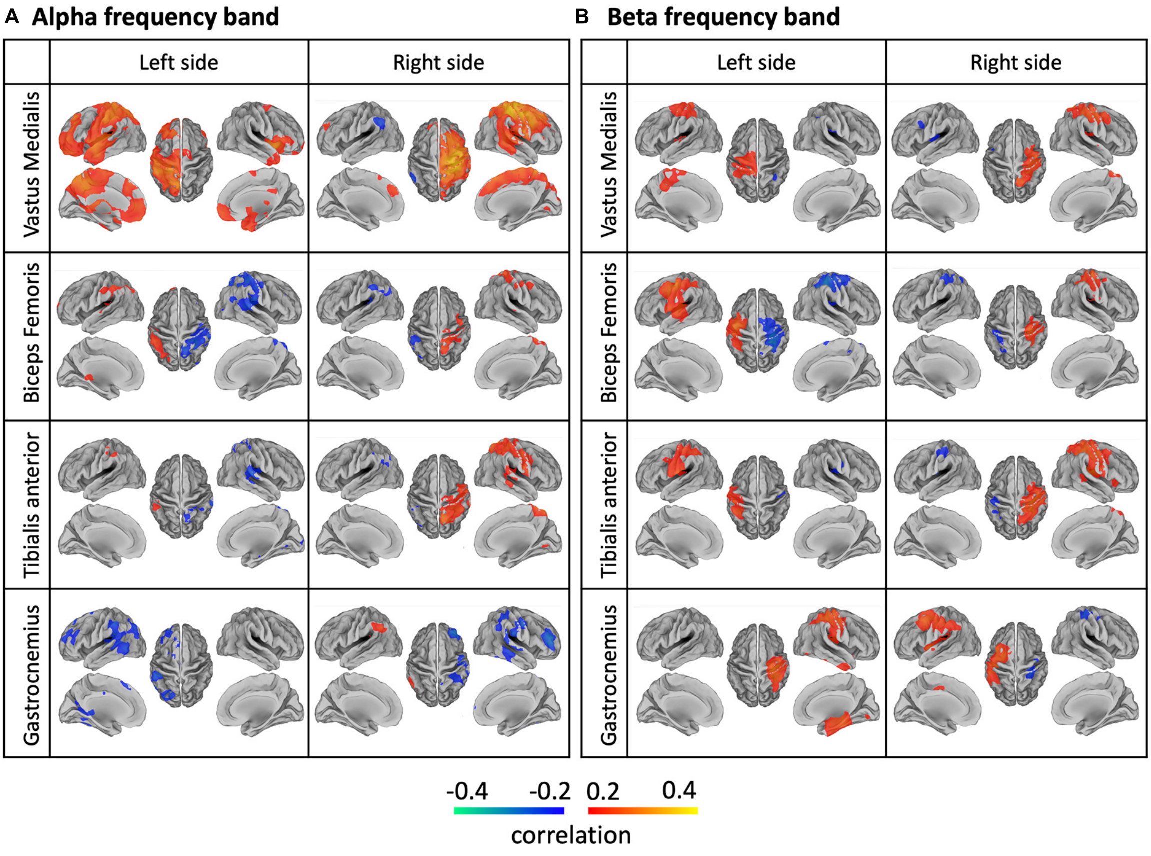

FIGURE 10 | Brain-body connectivity maps for **(A)** alpha and **(B)** beta frequency bands, obtained using EMG envelopes. We considered the EMG envelopes for each of the eight body sensors: left/right vastus medialis, biceps femoris, tibialis anterior, gastrocnemius. We used the threshold $r > 0.2$ for visualization purposes.

We then extended the NKC and NMC analysis also to the left M1 ROIs, and examined the connectivity matrices in alpha, beta, and gamma band for bilateral M1 ROIs (**Figure 8**). In general, strong and significant brain-body connectivity was present in the alpha and beta bands, whereas less reliable connectivity was found in the gamma band. The NKC of all the sensors was positive in the ipsilateral M1 and was negative in the contralateral M1, with relatively fewer sensors showing significant values as compared to the NMC (**Figure 8A**). For the vastus medialis, biceps femoris, and tibialis anterior, the NMC was positive in the ipsilateral M1 and was negative in the contralateral M1 (**Figure 8B**). Conversely for the gastrocnemius, the ipsilateral M1 showed negative connectivity and the contralateral M1 showed positive connectivity. To test the relative contribution of body sensor, ROI, frequency band, and body signal type on the connectivity values, we run a four-way ANOVA (**Supplementary Table 2**). The results revealed significant differences in connectivity across body sensors, ROIs and frequency bands ($p < 0.001$ for each of the three factors). Conversely, we found no significant differences between body signal types ($p = 0.806$).

Considering that the two NKC and NMC metrics were dependent to each other, and the muscular signals showed relatively lower inter-dependence, we focused on NMC only from this point on. By extending the ROI analysis to THAL, PMC, PPC, and CER, we specifically investigated whether brain-body connectivity involves not only M1, a brain region supporting motor execution, but also other regions typically associated with motor planning and coordination (**Figure 9**). Overall, we found robust NMC in M1, PMC, PPC, and CER regions, whereas much weaker effects were observed in THAL. The ANOVA results showed the NMC values were strongly modulated ($p_{FDR} < 0.001$) on the body sensor in bilateral M1, bilateral PMC, ipsilateral PPC, and ipsilateral CER, and by the frequency band in the ipsilateral M1 only (**Supplementary Table 3**).

Whole-Brain Analysis of Brain-Body Connectivity

A whole-brain analysis was conducted to assess the spatial specificity of the NMC patterns. In general, we observed lateralized NMC patterns for each sensor both in the alpha and beta bands over or close to the primary sensorimotor cortex (**Figure 10**). For the vastus medialis, the biceps femoris and the tibialis anterior, alpha-band and beta-band NMC had positive values over the ipsilateral hemisphere, and peaked at different locations of the primary sensorimotor cortex; furthermore, the positive alpha-band NMC was more widespread, and therefore

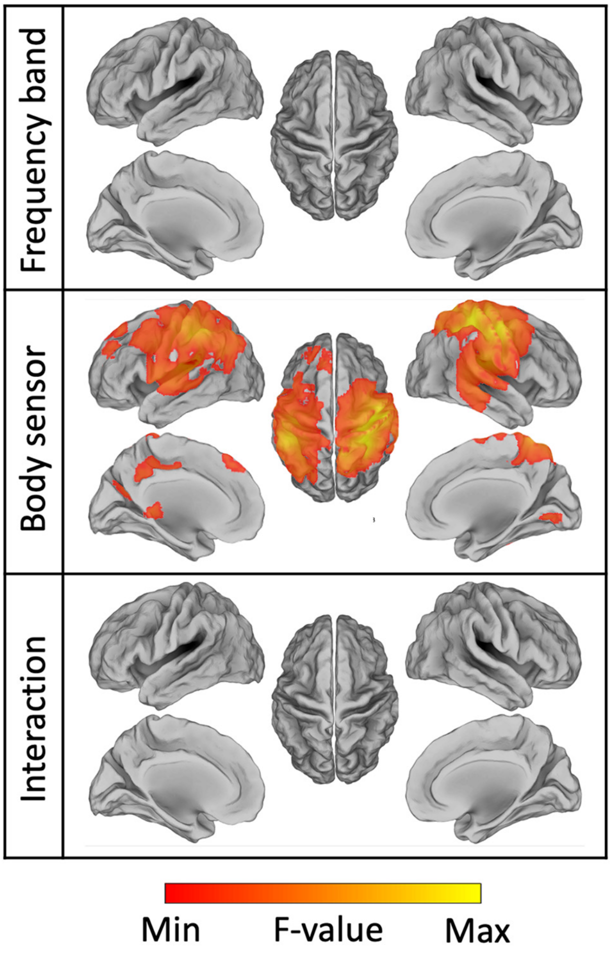

FIGURE 11 | Results of the ANOVA conducted on the source images of brain-body connectivity. We specifically performed a two-way ANOVA, using the frequency band and the body sensors as factors, respectively. The resulting maps for the main effects of frequency band, body sensor, and their interaction are thresholded at $p_{FDR} < 0.001$.

less spatially specific, than the beta-band NMC, whereas beta-band NMC was more focal over the ipsilateral sensorimotor cortex. Negative alpha- and beta-band NMC values were primarily found in the contralateral hemisphere, and had less consistent spatial distribution across body sensors than positive NMC values. The alpha- and beta-band NMC for the gastrocnemius appeared to have reversed polarity with respect to that of the other sensors. The NMC maps for the gamma band had lower intensity than for the alpha and beta bands, and were less reliable across body sensors (**Supplementary Figure 5**).

To further test the effect of frequency band, body sensor and their interaction, we applied a voxel-wise full factorial ANOVA on the connectivity images (**Figure 11**). The analysis revealed significant differences ($p_{FDR} < 0.001$) in NMC across the body sensors mainly over the bilateral primary sensorimotor cortex, but did not result in any regions with either significant differences across frequency bands ($p_{FDR} > 0.99$) or significant interaction between body sensor and frequency band ($p_{FDR} > 0.98$). Overall, the ANOVA map obtained for the body sensor as factor spanned not only M1 regions, but included also other regions in the premotor and posterior parietal cortex. These results were largely consistent with what already observed thorough the ROI analyses (**Figures 8B**, **9** and **Supplementary Table 3**).

DISCUSSION

In this study, we investigated brain-body connectivity during gait using a hdEEG-based mobile brain-body imaging platform. Considering that brain-body connectivity can be quantified either using muscular (NMC) or kinematic (NKC) signals, we also evaluated which of the two measures may yield the largest discriminative power. Next, we tested whether gait-related brain-body connectivity is characterized by specific spatial patterns depending on the specific body sensor and the neural oscillations of interest, and we evaluated if the brain regions showing robust gait-related brain-body connectivity are those typically related to motor execution, or also to motor planning and coordination. To the best of our knowledge, this was the first study that addressed these specific questions by examining source-reconstructed EEG signals, rather than EEG recordings. Our results showed that myogenic body signals have more discriminative power than kinematic signals in evaluating gait-related brain-body connectivity, and that brain-body connectivity measures map on brain regions related to motor execution, but also motor planning and coordination. In addition, the gait-related brain-body connectivity showed to be dependent on the body sensor used to extract kinematic/EMG dynamics, and only to a much lesser extent to the frequency of the neural oscillations measured using EEG. We will more extensively discuss these findings in the following sections.

Kinematic and Myogenic Signals for Brain-Body Connectivity Analysis

We started our investigations by analyzing the kinematic and myogenic signals, respectively. We generally observed significant correlations across body sensors, not only within but also between signal types. This was expected, as the contractions of skeletal muscles are the main drivers of the lower limb velocities and accelerations (van Leeuwen et al., 2003). Several EMG studies provided a detailed characterization of lower-limb muscular activity profiles during normal gait (Winter and Yack, 1987; Liu et al., 2008; Allen et al., 2013; Bonnefoy-Mazure and Armand, 2015). Specifically, it was observed that the leg muscles are activated in a coordinated sequential pattern across the gait cycle, supporting balance and movement control (Bonnefoy-Mazure and Armand, 2015). The EMG envelopes in our study were largely in line with previous findings. For example, the vastus medialis of a heel-striking lower limb was activated from the initial double support phase to the beginning of the stance. The biceps femoris activated from the terminal part of the swing phase until the double support phase, which occurs just after the heel strike. The activity of the tibialis anterior spanned the swing and the subsequent double support phases. The gastrocnemius mainly activated during stance, in opposition to the above-mentioned muscles. Overall, the leg movements can be modeled as two double-pendulums, and accelerations/velocities of the same bone should share a similar pattern (Kubo et al., 2004; Sartori et al., 2014). It is therefore not surprising that we found relatively higher inter-dependence in kinematic signals than in myogenic signals. We therefore concluded that the myogenic signals had more discriminative power, and were more suited to assess brain-body connectivity.

Characterization of Brain-Body Connectivity Images

We characterized gait-related brain-body connectivity in the whole brain by generating source images of NMC for each frequency band across body sensors. Reliable connectivity images were generally obtained with neural oscillations in the alpha and beta bands. This is consistent with several studies that reported modulations of alpha and beta oscillations during movement performance, both in seated conditions (Pfurtscheller et al., 1996; Tan et al., 2016; Porcaro et al., 2018, 2021; Zhao et al., 2019) and walking conditions (Wagner et al., 2016; Zhao et al., 2022). Strongest brain-body connectivity values were located over or close to the bilateral M1, the portion of cortex that is primarily associated with movement execution (Todorov, 2000; Lemon, 2008). Brain regions that are typically associated with motor planning and coordination, as for instance PMC, PPC, and CER (Battaglia-Mayer and Caminiti, 2019; Zhao et al., 2022), showed less strong but still significant NMC values. Furthermore, the voxel-wise ANOVA that we conducted in our study revealed significant differences in brain-body connectivity across body sensors over the bilateral primary sensorimotor cortex. This indicates that the leg muscles connect with the brain in a somatotopic manner (Artoni et al., 2017), and that the activity of the brain regions involved may be temporally modulated to support sophisticated muscular actions of gait performance (Neptune et al., 2004; Liu et al., 2008; Bonnefoy-Mazure and Armand, 2015). The ANOVA on NMC maps revealed no significant difference across frequency bands, and no interaction between frequency bands and sensors. Accordingly, alpha and beta neural oscillations, and to some extent also gamma neuronal oscillations, support the coordinated muscular actions of gait performance (Zhao et al., 2022), but no clear functional dissociation between them could be detected in terms of brain-body connectivity at the whole-brain level.

Gait-Related Brain-Body Connectivity in Motor-Related Regions

In this study, we also conducted analyses on frequency-dependent brain-body connectivity for several motor-related ROIs, among which M1, THAL, PMC, PPC, and CER. These analyses provided largely coherent results as compared to the whole-bran analyses, showing that myogenic activity is not only related to neural activity in M1, but also PMC, PPC, and CER. The results that we obtained for THAL were much less clear than the other regions. For the bilateral M1, NMC, and NKC values were rather weak for the gamma band, probably because that gamma oscillations are more associated with motor planning (Brovelli et al., 2005; Thürer et al., 2016) and coordination (Santarnecchi et al., 2017; Li et al., 2020) than motor execution. The vastus medialis, biceps femoris, and tibialis anterior showed negative alpha- and beta-band NMC for the contralateral M1. Notably, this finding is in line with one of our previous hdEEG studies, in which the contraction of tibialis anterior yielded a power decrease of alpha- and beta-band neural oscillations in the contralateral hemisphere of the primary sensorimotor cortex (Zhao et al., 2019), which is indicative of an increased excitability of local neurons supporting motor performance (Pfurtscheller and Lopes da Silva, 1999; Neuper et al., 2006). It should be noted that, unlike the other muscles, the gastrocnemius activation during gait correlated with alpha- and beta-band neural power increases in the contralateral M1. Furthermore, leg velocity correlated with decreases in alpha- and beta-band neural power for the contralateral M1. Taking these observations together, we can further infer that the gait-related desynchronization of alpha and beta oscillations may primarily relate to the leg movements, rather than the leg muscle contractions. This may be the case that the fluctuations in the level of recruitment of local neurons in contralateral M1 during walking mainly reflect the changes in uncertainty estimations between sensory predictions and actual sensory inputs of the lower limb movements, rather than being exclusively related to muscle control (Tan et al., 2016).

Limitations

We should acknowledge that our study has a number of limitations. First, we only included a treadmill walking task. Future investigation of brain-body connectivity in overground free walking conditions are warranted, as they may reveal further information regarding the neural processes of gait control. Second, our analysis of NKC only included velocity signals acquired from the lower limbs. The use a three-dimensional infrared camera system (Pfister et al., 2014) and force measuring treadmill (De Witt and Ploutz-Snyder, 2014) may provide additional data, for instance joint angles and ground reaction forces, that would enable more extensive investigations on NKC; likewise, collecting EMG signals from additional lower limb muscles, as compared to those we included in this study, may be beneficial for future investigations on NMC (Bonnefoy-Mazure and Armand, 2015). Third, the synchronization between EMG and EEG in the MoBI platform was performed offline. It should be considered, however, that real-time synchronization may be desirable for applications out of the research field (King and Parada, 2021). Lastly, we evaluated the NMC and NKC using a trial-averaged approach to increase the signal to noise ratio. The use of trial-level modeling methods (Kamiński et al., 2001; Chen et al., 2021) is warranted in future studies to examine temporal delays between brain and body signals (Artoni et al., 2017; Xu et al., 2017).

CONCLUSION

Overall, our study contributed to a finer characterization of brain-body connectivity during gait in healthy individuals, revealing robust relationships between muscular, kinematic, and neural signals. Notably, we performed a characterization of muscular signals considering one EMG sensor at the time. An interesting avenue for future research is extraction of gait-related muscle synergies from multi-channel EMG data (Chia Bejarano et al., 2017), and the analysis of their relationship with neural signals. Future studies may also be directed toward the investigation of different walking conditions, such as passive walking with exoskeleton support (Alqahtani et al., 2021) or gravity-reduced walking (Richter et al., 2021). Furthermore, we believe it would be interesting to use the MoBI approach to simultaneously collect kinematic, EMG and EEG data in individuals with neuromotor disorders such as Parkinson's disease, to identify neural correlates of abnormal gait (Cao et al., 2021; Tosserams et al., 2022).

DATA AVAILABILITY STATEMENT

The original contributions presented in the study are included in the article/**Supplementary Material**, further inquiries can be directed to the corresponding author.

ETHICS STATEMENT

The studies involving human participants were reviewed and approved by Ethics Committee of the Liguria Region, Italy (reference: 238/2019). The patients/participants provided their written informed consent to participate in this study.

AUTHOR CONTRIBUTIONS

MZ: experimental design, methodology, data acquisition, data analysis, visualization, and writing. GB: data acquisition and writing. JS and GT: methodology and writing. CP: conceptualization and writing. EP and LA: conceptualization, data acquisition, and writing. DM: conceptualization, experimental design, methodology, visualization, and writing. All authors contributed to the article and approved the submitted version.

FUNDING

The work was supported by the KU Leuven Special Research Fund (grant C16/15/070) and the Research Foundation Flanders (FWO) (grants G0F76.16N, G0936.16N, and EOS.30446199). MZ, GB, and CP were supported by the Chinese Scholarship Council (scholarship 201708620182), the Italian Ministry of Health (fellowship SG-2018-12368232), and the Italian Ministry of Education, University and Research ("Department of Excellence 2018–2022" initiative for the Department of Neuroscience of Padua University), respectively.

SUPPLEMENTARY MATERIAL

The Supplementary Material for this article can be found online at: https://www.frontiersin.org/articles/10.3389/fnins.2022.912075/full#supplementary-material

REFERENCES

Agostini, V., Nascimbeni, A., Gaffuri, A., Imazio, P., Benedetti, M. G., and Knaflitz, M. (2010). Normative EMG activation patterns of school-age children during gait. *Gait Posture* 32, 285–289. doi: 10.1016/j.gaitpost.2010.06.024

Alamdari, A., and Krovi, V. N. (2017). "Chapter Two - A Review of Computational Musculoskeletal Analysis of Human Lower Extremities," in *Human Modelling for Bio-Inspired Robotics*, Eds J. Ueda and Y. Kurita (Cambridge: Academic Press), 37–73.

Allen, J. L., Kautz, S. A., and Neptune, R. R. (2013). The influence of merged muscle excitation modules on post-stroke hemiparetic walking performance. *Clin. Biomechanics* 28, 697–704. doi: 10.1016/j.clinbiomech.2013.06.003

Alqahtani, M. S., Cooper, G., Diver, C., and Bártolo, P. J. (2021). "Exoskeletons for Lower Limb Applications: a Review," in *Bio-Materials and Prototyping Applications in Medicine*, eds P. J. Bártolo and B. Bidanda (New York : Springer), 139–164.

Anderson, M., Adali, T., and Li, X.-L. (2011). Joint blind source separation with multivariate Gaussian model: algorithms and performance analysis. *IEEE Trans. Signal Process* 60, 1672–1683.

Artoni, F., Fanciullacci, C., Bertolucci, F., Panarese, A., Makeig, S., Micera, S., et al. (2017). Unidirectional brain to muscle connectivity reveals motor cortex control of leg muscles during stereotyped walking. *NeuroImage* 159, 403–416. doi: 10.1016/j.neuroimage.2017.07.013

Bakker, M., de Lange, F. P., Stevens, J. A., Toni, I., and Bloem, B. R. (2007a). Motor imagery of gait: a quantitative approach. *Exp. Brain Res.* 179, 497–504. doi: 10.1007/s00221-006-0807-x

Bakker, M., Verstappen, C. C. P., Bloem, B. R., and Toni, I. (2007b). Recent advances in functional neuroimaging of gait. *J. Neural Trans.* 114, 1323–1331. doi: 10.1007/s00702-007-0783-8

Battaglia-Mayer, A., and Caminiti, R. (2019). Corticocortical Systems Underlying High-Order Motor Control. *J. Neurosci.* 39, 4404–4421. doi: 10.1523/JNEUROSCI.2094-18.2019

Bayraktaroglu, Z., von Carlowitz-Ghori, K., Curio, G., and Nikulin, V. V. (2013). It is not all about phase: amplitude dynamics in corticomuscular interactions. *NeuroImage* 64, 496–504. doi: 10.1016/j.neuroimage.2012.08.069

Bayraktaroglu, Z., von Carlowitz-Ghori, K., Losch, F., Nolte, G., Curio, G., and Nikulin, V. V. (2011). Optimal imaging of cortico-muscular coherence through a novel regression technique based on multi-channel EEG and un-rectified EMG. *NeuroImage* 57, 1059–1067. doi: 10.1016/j.neuroimage.2011.04.071

Bonnefoy-Mazure, A., and Armand, S. (2015). *Normal Gait. Orthopedic Management of Children With Cerebral Palsy: a Comprehensive Approach*. Hauppauge, NY: Nova Science Publishers Inc.

Bourguignon, M., De Tiège, X., de Beeck, M. O., Pirotte, B., Van Bogaert, P., Goldman, S., et al. (2011). Functional motor-cortex mapping using corticokinematic coherence. *NeuroImage* 55, 1475–1479. doi: 10.1016/j.neuroimage.2011.01.031

Bourguignon, M., Piitulainen, H., De Tiège, X., Jousmäki, V., and Hari, R. (2015). Corticokinematic coherence mainly reflects movement-induced proprioceptive feedback. *NeuroImage* 106, 382–390. doi: 10.1016/j.neuroimage.2014.11.026

Brovelli, A., Lachaux, J.-P., Kahane, P., and Boussaoud, D. (2005). High gamma frequency oscillatory activity dissociates attention from intention in the human premotor cortex. *NeuroImage* 28, 154–164. doi: 10.1016/j.neuroimage.2005.05.045

Bulea, T. C., Kim, J., Damiano, D. L., Stanley, C. J., and Park, H.-S. (2015). Prefrontal, posterior parietal and sensorimotor network activity underlying speed control during walking. *Front. Hum. Neurosci.* 9:247. doi: 10.3389/fnhum.2015.00247

Cao, Z., John, A. R., Chen, H. T., Martens, K. E., Georgiades, M., Gilat, M., et al. (2021). Identification of EEG Dynamics During Freezing of Gait and

Voluntary Stopping in Patients With Parkinson's Disease. *IEEE Trans. Neural Syst. Rehabilitation Eng.* 29, 1774–1783. doi: 10.1109/TNSRE.2021.3107106

Cappellini, G., Ivanenko, Y. P., Poppele, R. E., and Lacquaniti, F. (2006). Motor Patterns in Human Walking and Running. *J. Neurophysiol.* 95, 3426–3437. doi: 10.1152/jn.00081.2006

Chen, X., Ma, Y., Liu, X., Kong, W., and Xi, X. (2021). Analysis of corticomuscular connectivity during walking using vine copula. *Math. Biosci. Eng.* 18, 4341–4357. doi: 10.3934/mbe.2021218

Chia Bejarano, N., Pedrocchi, A., Nardone, A., Schieppati, M., Baccinelli, W., Monticone, M., et al. (2017). Tuning of Muscle Synergies During Walking Along Rectilinear and Curvilinear Trajectories in Humans. *Ann. Biomed. Eng.* 45, 1204–1218. doi: 10.1007/s10439-017-1802-z

Dähne, S., Meinecke, F. C., Haufe, S., Höhne, J., Tangermann, M., Müller, K.-R., et al. (2014). SPoC: a novel framework for relating the amplitude of neuronal oscillations to behaviorally relevant parameters. *NeuroImage* 86, 111–122. doi: 10.1016/j.neuroimage.2013.07.079

De Witt, J. K., and Ploutz-Snyder, L. L. (2014). Ground reaction forces during treadmill running in microgravity. *J. Biomechanics* 47, 2339–2347. doi: 10.1016/j.jbiomech.2014.04.034

Guarnieri, R., Marino, M., Barban, F., Ganzetti, M., and Mantini, D. (2018). Online EEG artifact removal for BCI applications by adaptive spatial filtering. *J. Neural Eng.* 15:056009. doi: 10.1088/1741-2552/aacfdf

Gwin, J., and Ferris, D. (2012). Beta- and gamma-range human lower limb corticomuscular coherence. *Front. Hum. Neurosci.* 6:258. doi: 10.3389/fnhum.2012.00258

Gwin, J. T., Gramann, K., Makeig, S., and Ferris, D. P. (2011). Electrocortical activity is coupled to gait cycle phase during treadmill walking. *NeuroImage* 54, 1289–1296. doi: 10.1016/j.neuroimage.2010.08.066

Halliday, D. M., and Farmer, S. F. (2010). On the Need for Rectification of Surface EMG. *J. Neurophysiol.* 103, 3547–3547. doi: 10.1152/jn.00222.2010

Hamacher, D., Herold, F., Wiegel, P., Hamacher, D., and Schega, L. (2015). Brain activity during walking: a systematic review. *Neurosci. Biobehav. Rev.* 57, 310–327.

Haueisen, J., Ramon, C., Eiselt, M., Brauer, H., and Nowak, H. (1997). Influence of tissue resistivities on neuromagnetic fields and electric potentials studied with a finite element model of the head. *IEEE Trans. Biomed. Eng.* 44, 727–735. doi: 10.1109/10.605429

Hermens, H. J., Freriks, B., Disselhorst-Klug, C., and Rau, G. (2000). Development of recommendations for SEMG sensors and sensor placement procedures. *J. Electromyogr. Kinesiol.* 10, 361–374. doi: 10.1016/s1050-6411(00)00027-4

Holdefer, R., Sadleir, R., and Russell, M. (2006). Predicted current densities in the brain during transcranial electrical stimulation. *Clin. Neurophysiol.* 117, 1388–1397. doi: 10.1016/j.clinph.2006.02.020

Hyvarinen, A. (1999). Fast and robust fixed-point algorithms for independent component analysis. *IEEE Trans. Neural Netw.* 10, 626–634. doi: 10.1109/72.761722

Jasiewicz, J. M., Allum, J. H. J., Middleton, J. W., Barriskill, A., Condie, P., Purcell, B., et al. (2006). Gait event detection using linear accelerometers or angular velocity transducers in able-bodied and spinal-cord injured individuals. *Gait Posture* 24, 502–509. doi: 10.1016/j.gaitpost.2005.12.017

Jungnickel, E., Gehrke, L., Klug, M., and Gramann, K. (2019). *MoBI—Mobile Brain/Body Imaging. Neuroergonomics The brain at Work and in Everyday*. Amsterdam: Elsevier, 59–63.

Kamiński, M., Ding, M., Truccolo, W. A., and Bressler, S. L. (2001). Evaluating causal relations in neural systems: granger causality, directed transfer function and statistical assessment of significance. *Biol. Cybern.* 85, 145–157. doi: 10.1007/s004220000235

King, J. L., and Parada, F. J. (2021). Using mobile brain/body imaging to advance research in arts, health, and related therapeutics. *Euro. J. Neurosci.* 54, 8364–8380. doi: 10.1111/ejn.15313

Kotiadis, D., Hermens, H. J., and Veltink, P. H. (2010). Inertial Gait Phase Detection for control of a drop foot stimulator: inertial sensing for gait phase detection. *Med. Eng. Physics.* 32, 287–297. doi: 10.1016/j.medengphy.2009.10.014

Kubo, M., Wagenaar, R. C., Saltzman, E., and Holt, K. G. (2004). Biomechanical mechanism for transitions in phase and frequency of arm and leg swing during walking. *Biol. Cybern.* 91, 91–98. doi: 10.1007/s00422-004-0503-5

Lemon, R. N. (2008). Descending Pathways in Motor Control. *Annu. Rev. Neurosci.*31, 195–218.

Li, X., Mota, B., Kondo, T., Nasuto, S., and Hayashi, Y. (2020). EEG dynamical network analysis method reveals the neural signature of visual-motor coordination. *PLoS One* 15:e0231767. doi: 10.1371/journal.pone.0231767

Liu, M. Q., Anderson, F. C., Schwartz, M. H., and Delp, S. L. (2008). Muscle contributions to support and progression over a range of walking speeds. *J. Biomechanics* 41, 3243–3252. doi: 10.1016/j.jbiomech.2008.07.031

Liu, Q., Balsters, J. H., Baechinger, M., van der Groen, O., Wenderoth, N., and Mantini, D. (2015). Estimating a neutral reference for electroencephalographic recordings: the importance of using a high-density montage and a realistic head model. *J. Neural Eng.* 12:056012. doi: 10.1088/1741-2560/12/5/056012

Liu, Q., Farahibozorg, S., Porcaro, C., Wenderoth, N., and Mantini, D. (2017). Detecting large-scale networks in the human brain using high-density electroencephalography. *Hum. Brain Map.* 38, 4631–4643. doi: 10.1002/hbm.23688

Liu, Q., Ganzetti, M., Wenderoth, N., and Mantini, D. (2018). Detecting large-scale brain networks using EEG: impact of electrode density, head modeling and source localization. *Front. Neuroinformatics* 12:4. doi: 10.3389/fninf.2018.00004

Michel, C. M., and Murray, M. M. (2012). Towards the utilization of EEG as a brain imaging tool. *NeuroImage* 61, 371–385. doi: 10.1016/j.neuroimage.2011.12.039

Nathan, K., and Contreras-Vidal, J. L. (2016). Negligible motion artifacts in scalp electroencephalography (EEG) during treadmill walking. *Front. Hum. Neurosci.* 9:708. doi: 10.3389/fnhum.2015.00708

Neptune, R. R., Zajac, F. E., and Kautz, S. A. (2004). Muscle force redistributes segmental power for body progression during walking. *Gait Posture* 19, 194–205. doi: 10.1016/S0966-6362(03)00062-6

Neuper, C., Wörtz, M., and Pfurtscheller, G. (2006). "ERD/ERS patterns reflecting sensorimotor activation and deactivation," in *Progress in Brain Research*, eds C. Neuper and W. Klimesch (Amsterdam: Elsevier), 211–222. doi: 10.1016/S0079-6123(06)59014-4

Nordin, A. D., Hairston, W. D., and Ferris, D. P. (2020). Faster Gait Speeds Reduce Alpha and Beta EEG Spectral Power From Human Sensorimotor Cortex. *IEEE Trans. Biomed. Eng.* 67, 842–853. doi: 10.1109/TBME.2019.2921766

Oliveira, A. S., Schlink, B. R., Hairston, W. D., König, P., and Ferris, D. P. (2017). Restricted vision increases sensorimotor cortex involvement in human walking. *J. Neurophysiol.* 118, 1943–1951. doi: 10.1152/jn.00926.2016

Pascual-Marqui, R. D., Lehmann, D., Koukkou, M., Kochi, K., Anderer, P., Saletu, B., et al. (2011). Assessing interactions in the brain with exact low-resolution electromagnetic tomography. Philosophical Transactions of the Royal Society A: mathematical. *Physical. Eng. Sci.* 369, 3768–3784. doi: 10.1098/rsta.2011.0081

Petersen, T. H., Willerslev-Olsen, M., Conway, B. A., and Nielsen, J. B. (2012). The motor cortex drives the muscles during walking in human subjects. *J. Physiol.* 590, 2443–2452. doi: 10.1113/jphysiol.2012.227397

Pfister, A., West, A. M., Bronner, S., and Noah, J. A. (2014). Comparative abilities of Microsoft Kinect and Vicon 3D motion capture for gait analysis. *J. Med. Eng. Technol.* 38, 274–280. doi: 10.3109/03091902.2014.909540

Pfurtscheller, G., and Lopes da Silva, F. H. (1999). Event-related EEG/MEG synchronization and desynchronization: basic principles. *Clin. Neurophysiol.* 110, 1842–1857. doi: 10.1016/s1388-2457(99)00141-8

Pfurtscheller, G., Stancák, A., and Neuper, C. (1996). Post-movement beta synchronization. A correlate of an idling motor area? *Electroencephalogr. Clin. Neurophysiol.* 98, 281–293. doi: 10.1016/0013-4694(95)00258-8

Piitulainen, H., Bourguignon, M., De Tiège, X., Hari, R., and Jousmäki, V. (2013). Corticokinematic coherence during active and passive finger movements. *Neuroscience* 238, 361–370. doi: 10.1016/j.neuroscience.2013.02.002

Porcaro, C., Cottone, C., Cancelli, A., Salustri, C., and Tecchio, F. (2018). Functional Semi-Blind Source Separation Identifies Primary Motor Area Without Active Motor Execution. *Int. J. Neural. Syst.* 28:1750047. doi: 10.1142/S0129065717500472

Porcaro, C., Mayhew, S. D., and Bagshaw, A. P. (2021). Role of the Ipsilateral Primary Motor Cortex in the Visuo-Motor Network During Fine Contractions and Accurate Performance. *Int. J. Neural. Syst.* 31:2150011. doi: 10.1142/S0129065721500118

Price, C., Schmeltzpfenning, T., Nester, C. J., and Brauner, T. (2021). "Foot and footwear biomechanics and gait," in *Handbook of Footwear Design* *and Manufacture (Second Edition)*, ed. A. Luximon (Sawston: Woodhead Publishing), 79–103.

Rainoldi, A., Melchiorri, G., and Caruso, I. (2004). A method for positioning electrodes during surface EMG recordings in lower limb muscles. *J. Neurosci. Met.* 134, 37–43. doi: 10.1016/j.jneumeth.2003.10.014

Richter, C., Braunstein, B., Staeudle, B., Attias, J., Suess, A., Weber, T., et al. (2021). Gastrocnemius medialis contractile behavior during running differs between simulated Lunar and Martian gravities. *Sci. Rep.* 11:22555. doi: 10.1038/s41598-021-00527-9

Roeder, L., Boonstra, T. W., Smith, S. S., and Kerr, G. K. (2018). Dynamics of corticospinal motor control during overground and treadmill walking in humans. *J. Neurophysiol.* 120, 1017–1031. doi: 10.1152/jn.00613.2017

Samogin, J., Liu, Q., Marino, M., Wenderoth, N., and Mantini, D. (2019). Shared and connection-specific intrinsic interactions in the default mode network. *NeuroImage* 200, 474–481. doi: 10.1016/j.neuroimage.2019.07.007

Santarnecchi, E., Biasella, A., Tatti, E., Rossi, A., Prattichizzo, D., and Rossi, S. (2017). High-gamma oscillations in the motor cortex during visuo-motor coordination: a tACS interferential study. *Brain Res. Bull.* 131, 47–54. doi: 10.1016/j.brainresbull.2017.03.006

Sartori, M., Farina, D., and Lloyd, D. G. (2014). Hybrid neuromusculoskeletal modeling to best track joint moments using a balance between muscle excitations derived from electromyograms and optimization. *J. Biomechanics* 47, 3613–3621. doi: 10.1016/j.jbiomech.2014.10.009

Schmeltzpfenning, T., and Brauner, T. (2013). "Foot biomechanics and gait," in *Handbook of Footwear Design and Manufacture*, ed. A. Luximon (Sawston: Woodhead Publishing), 27–48.

Seeber, M., Scherer, R., Wagner, J., Solis-Escalante, T., and Müller-Putz, G. R. (2014). EEG beta suppression and low gamma modulation are different elements of human upright walking. *Front. Hum. Neurosci.* 8:485. doi: 10.3389/fnhum.2014.00485

Seeber, M., Scherer, R., Wagner, J., Solis-Escalante, T., and Müller-Putz, G. R. (2015). High and low gamma EEG oscillations in central sensorimotor areas are conversely modulated during the human gait cycle. *NeuroImage* 112, 318–326. doi: 10.1016/j.neuroimage.2015.03.045

Seeck, M., Koessler, L., Bast, T., Leijten, F., Michel, C., Baumgartner, C., et al. (2017). The standardized EEG electrode array of the IFCN. *Clin. Neurophysiol.*128, 2070–2077. doi: 10.1016/j.clinph.2017.06.254

Shaw, J. C. (1984). Correlation and coherence analysis of the EEG: a selective tutorial review. *Int. J. Psychophysiol.* 1, 255–266. doi: 10.1016/0167-8760(84)90045-x

Song, J., Davey, C., Poulsen, C., Luu, P., Turovets, S., Anderson, E., et al. (2015). EEG source localization: sensor density and head surface coverage. *J. Neurosci. Met.* 256, 9–21. doi: 10.1016/j.jneumeth.2015.08.015

Taberna, G. A., Guarnieri, R., and Mantini, D. (2019a). SPOT3D: spatial positioning toolbox for head markers using 3D scans. *Sci. Rep.* 9:12813. doi: 10.1038/s41598-019-49256-0

Taberna, G. A., Marino, M., Ganzetti, M., and Mantini, D. (2019b). Spatial localization of EEG electrodes using 3D scanning. *J. Neural Eng.* 16:026020. doi: 10.1088/1741-2552/aafdd1

Taberna, G. A., Samogin, J., and Mantini, D. (2021). Automated Head Tissue Modelling Based on Structural Magnetic Resonance Images for Electroencephalographic Source Reconstruction. *Neuroinformatics* 19, 585–596. doi: 10.1007/s12021-020-09504-5

Takakusaki, K. (2013). Neurophysiology of gait: from the spinal cord to the frontal lobe. *Mov. Disord.* 28, 1483–1491. doi: 10.1002/mds.25669

Takakusaki, K. (2017). Functional Neuroanatomy for Posture and Gait Control. *J. Mov. Disord.* 10, 1–17. doi: 10.14802/jmd.16062

Tan, H., Wade, C., and Brown, P. (2016). Post-Movement Beta Activity in Sensorimotor Cortex Indexes Confidence in the Estimations from Internal Models. *J. Neurosci.* 36, 1516–1528. doi: 10.1523/JNEUROSCI.3204-15.2016

Tanaka, Y., and Saga, N. (2019). Frequency-Dependent EEG Corresponding to EMG under Voluntary Movement. *IEEJ Trans. Electrical Electronic Eng.* 14, 501–502.

Thürer, B., Stockinger, C., Focke, A., Putze, F., Schultz, T., and Stein, T. (2016). Increased gamma band power during movement planning coincides with motor memory retrieval. *NeuroImage* 125, 172–181. doi: 10.1016/j.neuroimage.2015.10.008

Todorov, E. (2000). Direct cortical control of muscle activation in voluntary arm movements: a model. *Nat. Neurosci.* 3, 391–398. doi: 10.1038/73964

Tosserams, A., Weerdesteyn, V., Bal, T., Bloem, B. R., Solis-Escalante, T., and Nonnekes, J. (2022). Cortical Correlates of Gait Compensation Strategies in Parkinson Disease. *Ann. Neurol.* 91, 329–341. doi: 10.1002/ana.26306

Türker, K. S. (1993). Electromyography: some Methodological Problems and Issues. *Physical. Therapy* 73, 698–710. doi: 10.1093/ptj/73.10.698

van Leeuwen, J., Aerts, P., and Pandy, M. G. (2003). Simple and complex models for studying muscle function in walking. Philosophical Transactions of the Royal Society of London. *Biol. Sci.* 358, 1501–1509.

Vaughan, C. L. (2003). Theories of bipedal walking: an odyssey. *J. Biomechanics* 36, 513–523. doi: 10.1016/s0021-9290(02)00419-0

Vorwerk, J., Oostenveld, R., Piastra, M. C., Magyari, L., and Wolters, C. H. (2018). The FieldTrip-SimBio pipeline for EEG forward solutions. *BioMed. Eng. OnLine* 17:37. doi: 10.1186/s12938-018-0463-y

Wagner, J., Makeig, S., Gola, M., Neuper, C., and Müller-Putz, G. (2016). Distinct β band oscillatory networks subserving motor and cognitive control during gait adaptation. *J. Neurosci.* 36, 2212–2226. doi: 10.1523/JNEUROSCI.3543-15.2016

Watanabe, H., Tanaka, H., Sakti, S., and Nakamura, S. (2020). Synchronization between overt speech envelope and EEG oscillations during imagined speech. *Neurosci. Res.* 153, 48–55. doi: 10.1016/j.neures.2019.04.004

Winter, D. A., and Yack, H. J. (1987). EMG profiles during normal human walking: stride-to-stride and inter-subject variability. *Electroencephalogr. Clin. Neurophysiol.* 67, 402–411. doi: 10.1016/0013-4694(87)90003-4

Xu, Y., McClelland, V. M., Cvetkoviæ, Z., and Mills, K. R. (2017). Corticomuscular Coherence With Time Lag With Application to Delay Estimation. *IEEE Trans. Biomed. Eng.* 64, 588–600. doi: 10.1109/TBME.2016.2569492

Yokoyama, H., Kaneko, N., Masugi, Y., Ogawa, T., Watanabe, K., and Nakazawa, K. (2021). Gait-phase-dependent and gait-phase-independent cortical activity across multiple regions involved in voluntary gait modifications in humans. *Eur. J. Neurosci.* 54, 8092–8105. doi: 10.1111/ejn.14867

Zhao, M., Bonassi, G., Guarnieri, R., Pelosin, E., Nieuwboer, A., Avanzino, L., et al. (2021). A multi-step blind source separation approach for the attenuation of artifacts in mobile high-density electroencephalography data. *J. Neural Eng.* 18:066041. doi: 10.1088/1741-2552/ac4084

Zhao, M., Bonassi, G., Samogin, J., Taberna, G. A., Pelosin, E., Nieuwboer, A., et al. (2022). Frequency-dependent modulation of neural oscillations across the gait cycle. *Hum. Brain Map.* [Epub ahead of print]. doi: 10.1002/hbm.25856

Zhao, M., Marino, M., Samogin, J., Swinnen, S. P., and Mantini, D. (2019). Hand, foot and lip representations in primary sensorimotor cortex: a high-density electroencephalography study. *Sci. Rep.* 9:19464. doi: 10.1038/s41598-019-55369-3

Conflict of Interest: The authors declare that the research was conducted in the absence of any commercial or financial relationships that could be construed as a potential conflict of interest.

frontiers | Frontiers in Neuroscience

TYPE Original Research
PUBLISHED 29 July 2022
DOI 10.3389/fnins.2022.911034

OPEN ACCESS

EDITED BY
Thomas T. Liu,
University of California, San Diego,
United States

REVIEWED BY
Mingxiong Huang,
University of California, San Diego,
United States
Thomas R. Knösche,
Max Planck Institute for Human
Cognitive and Brain Sciences,
Germany

*CORRESPONDENCE
Morten Mørup
mmor@dtu.dk

†These authors have contributed
equally to this work and share first
authorship

SPECIALTY SECTION
This article was submitted to
Brain Imaging Methods,
a section of the journal
Frontiers in Neuroscience

RECEIVED 01 April 2022
ACCEPTED 11 July 2022
PUBLISHED 29 July 2022

CITATION
Olsen AS, Høegh RMT, Hinrich JL,
Madsen KH and Mørup M (2022)
Combining electro- and
magnetoencephalography data using
directional archetypal analysis.
Front. Neurosci. 16:911034.
doi: 10.3389/fnins.2022.911034

Combining electro- and magnetoencephalography data using directional archetypal analysis

Anders S. Olsen[1†], Rasmus M. T. Høegh[1,2†], Jesper L. Hinrich[1], Kristoffer H. Madsen[1,3] and Morten Mørup[1]*

[1]Department of Applied Mathematics and Computer Science, Technical University of Denmark, Lyngby, Denmark, [2]WS Audiology, Lynge, Denmark, [3]Danish Research Centre for Magnetic Resonance, Centre for Functional and Diagnostic Imaging and Research, Copenhagen University Hospital Amager and Hvidovre, Hvidovre, Denmark

Metastable microstates in electro- and magnetoencephalographic (EEG and MEG) measurements are usually determined using modified k-means accounting for polarity invariant states. However, hard state assignment approaches assume that the brain traverses microstates in a discrete rather than continuous fashion. We present multimodal, multisubject directional archetypal analysis as a scale and polarity invariant extension to archetypal analysis using a loss function based on the Watson distribution. With this method, EEG/MEG microstates are modeled using subject- and modality-specific *archetypes* that are representative, distinct topographic maps between which the brain continuously traverses. Archetypes are specified as convex combinations of unit norm input data based on a shared generator matrix, thus assuming that the timing of neural responses to stimuli is consistent across subjects and modalities. The input data is reconstructed as convex combinations of archetypes using a subject- and modality-specific continuous archetypal mixing matrix. We showcase the model on synthetic data and an openly available face perception event-related potential data set with concurrently recorded EEG and MEG. In synthetic and unimodal experiments, we compare our model to conventional Euclidean multisubject archetypal analysis. We also contrast our model to a directional clustering model with discrete state assignments to highlight the advantages of modeling state trajectories rather than hard assignments. We find that our approach successfully models scale and polarity invariant data, such as microstates, accounting for intersubject and intermodal variability. The model is readily extendable to other modalities ensuring component correspondence while elucidating spatiotemporal signal variability.

KEYWORDS

archetypal analysis, microstates, electroencephalography, magnetoencephalography, multimodal integration, spatiotemporal variability, directional statistics, Watson distribution

1. Introduction

Brain function may be understood in terms of metastable states of activity involving anatomically distinct brain areas working in synchrony. Metastability refers to the brain lingering in a state before switching to another state. In functional magnetic resonance imaging (fMRI) literature, dynamic functional connectivity has revealed brain connectivity states using unsupervised machine learning methods (Cabral et al., 2017; Preti et al., 2017), and elucidated how the activity of these states varies following perturbations to the resting state, e.g., sleep (Stevner et al., 2019) or the administration of psychedelic drugs (Lord et al., 2019; Olsen et al., 2021). However, the frequency content in blood-oxygen-level-dependent (BOLD) fMRI is limited to very slow oscillations (<0.1 Hz) and thus does not allow for investigation of "real-time" brain state transitions and complicates, for instance, the analysis of evoked responses.

In electro- and magnetoencephalography (EEG and MEG), metastable states of sub-second activity span, denoted microstates, have been a research topic for many years (Lehmann, 1971; Lehmann et al., 1987)—see Khanna et al. (2015) and Michel and Koenig (2018) for reviews. Rather than involving specific brain regions, microstates are defined by whole-brain dipolar topographic maps. Microstates may be defined in a multitude of ways, including characterizations by principal and independent component analysis (Skrandies, 1989; Makeig et al., 1999), modified *k*-means (Pascual-Marqui et al., 1995), hidden Markov modeling of MEG power envelopes (Quinn et al., 2018; Coquelet et al., 2022) or agglomerative hierarchical clustering methods (Murray et al., 2008; Khanna et al., 2014). Of particular interest is the polarity invariance of the topographic maps; as M/EEG signals are naturally oscillating, the same microstate may be active although the sign of the input data changes (i.e., maxima become minima and vice versa) (Poulsen et al., 2018). In addition, the global scaling of the topographic maps is usually also irrelevant—it is, rather, the electrode activity relative to other electrodes that is important (Van De Ville et al., 2010). The current gold standard microstate analysis involves modified *k*-means clustering of instantaneous activity maps assessed using, e.g., global field power (Skrandies, 1990). Prototypes are constrained to unit norm, and the angle from data points to the prototypes is squared to account for polarity invariance. Other interesting models include Leading Eigenvector Dynamics Analysis (Cabral et al., 2017), which, although previously unused in EEG modeling, models interregional coherence by assessing the eigenvector of instantaneous coherence maps. Eigenvectors are axially symmetric unit vectors (scale-free) and may be modeled using diametrical clustering (Dhillon et al., 2003) to account for polarity invariance (Olsen et al., 2021).

The notion of meta-stability of EEG microstates has recently been challenged by Mishra et al. (2020) and Dekker et al. (2021) arguing that the brain traverses microstates in a continuous rather than discrete fashion. Thus, models that assign data to prototypes in an all-or-nothing fashion, such as *k*-means, may be too simple. As such, there is a need for methods that model data as traversing through continuous trajectories between states. A solution to this problem would be to define state topographies by extreme data points and describe brain activity as continuous navigation in the convex hull spanned by these states. Such a model has yet to be established for EEG and MEG microstates.

Another topic of interest in the analysis of brain function is multimodal integration. While EEG and MEG measure the same sources in the brain, i.e., synchronized postsynaptic currents in the dendrites of cortical pyramidal neurons, the electric potential and the normal component of the magnetic field of a tangential current source are rotated 90° relative to each other (Lopes da Silva, 2013). Furthermore, EEG and MEG complement each other regarding radially oriented sources, sensitivity to source depth, and tissue-specific signal attenuation. The combination of EEG and MEG is known to improve source localization accuracy (Sharon et al., 2007). Several approaches to M/EEG fusion have been suggested, including the use of Kalman filtering (Hamid et al., 2013), modeling modality dissimilarity correlations (Cichy et al., 2016), modality-specific error weighting using Bayesian optimization (Henson et al., 2009), and maximum entropy on the mean framework (Chowdhury et al., 2015). Although M/EEG integration is well-described in the literature, multimodal microstate analysis has not previously been explored.

Here we introduce directional archetypal analysis (DAA) and apply it for the joint integration of simultaneously recorded event-related potential (ERP) EEG and MEG data. Archetypal analysis (AA) is an unsupervised learning method for finding interpretable patterns in high-dimensional data. AA determines extreme points, denoted archetypes, that reside on the convex hull of the data cloud and determines how to express the data as convex combinations of such archetypes optimally. The determined archetypes can be considered distinct characteristics, forming prominent corners of the data (Cutler and Breiman, 1994). Thus, AA deviates from *k*-means that determine prototypical points or centers of the data cloud. Similarly, Hidden Markov Models, which model continuous transitions between states, also estimate prototypes rather than archetypes (Vidaurre et al., 2017). AA has been applied successfully in a variety of fields, including astronomy (Chan et al., 2003), survey and performance data (Seth and Eugster, 2016), chemistry and collaborative filtering (Mørup and Hansen, 2012), bio-informatics (Thøgersen et al., 2013; Hart et al., 2015), and neuroimaging (Mørup and Hansen, 2012; Hinrich et al., 2016; Cona et al., 2019; Krohne et al., 2019), including for the analysis of single-trial electroencephalography (EEG) brain response variability (Tsanousa et al., 2015).

While conventional AA determines archetypes based on a least-squares loss function of the reconstruction, we here reformulate the method to account for axially symmetric spherical data using a distance measure derived from the Watson distribution (Watson, 1965; Sra and Karp, 2013). By projecting every measured data point onto a $(D-1)$-dimensional sphere (D being the number of electrodes or magnetometers), we ensure that the decomposition is not driven by the scale of the input data. Similarly, by employing a statistical distribution that models diametrically opposite points as equal, we also directly model the polarity invariance of the input data. We demonstrate the utility of the developed method for the joint modeling of EEG and MEG ERPs, ensuring component correspondence while accounting for the shared modality-wide complementary information regarding how the extracted sources are spatiotemporally elicited in the two modalities. We use a similar approach to Hinrich et al. (2016) for the modeling of multisubject data utilizing a shared archetype-generating mechanism across subjects while allowing for subject-specific archetypes and mixing matrices. Specifically, we conduct multimodal integration by identifying shared archetypal temporal profiles used to generate the archetypes while determining the modality- and subject-specific expression of these shared temporal profiles.

In summary, we propose the DAA model accounting for scale- and sign-invariant modeling of EEG and MEG data as well as their joint integration, assuming the timing of the neural responses to stimuli are consistent across EEG and MEG. Based on the developed DAA we demonstrate:

(i) The merits of DAA as opposed to conventional AA when data resides on the unit (hyper-)sphere.
(ii) The merits of DAA as opposed to a DAA-clustering model with hard assignments.
(iii) How DAA can be used to model microstates in evoked response EEG and MEG data.
(iv) How DAA can be used for the joint integration of EEG and MEG data.

The novelty of this work lies both in the development of a new AA framework for directional statistics (DAA) as well as a novel approach for multimodal integration of EEG and MEG accounting for spatiotemporal variability while ensuring component correspondence across modalities as defined by an assumed shared timing of the responses to stimuli.

2. Methods

2.1. Data

Analysis was carried out on the openly available multimodal face perception data set introduced by Wakeman and Henson (2015) with concurrent EEG and MEG recordings in 19 subjects (8 females), whom all provided written informed consent. The study was originally approved by the Cambridge University Psychological Ethics Committee, and the data is openly accessible through OpenNeuro (accession number: ds000117, version 1.0.4[1]). Each participant completed six sessions where they were presented with approximately 150 images of famous, unfamiliar, or scrambled (head shape preserved but face unrecognizable) faces. Each functional trial started with the appearance of a fixation cross for a random duration (400–600 ms) and then a stimulus (face or scrambled face, 800–1,000 ms). Between stimuli, a white circle was shown for 1,700 ms. Across the experiment, participants were told to focus on a fixation cross at the center of the screen and refrain from blinking during stimulus presentation. All faces were shown twice, either immediately after or following 5–15 other stimuli (50/50 of each).

MEG and EEG data were recorded simultaneously using an Elekta Neuromag Vectorview 306 system (Helsinki, FI) with 102 magnetometers and a 70-channel Easycap EEG cap with the reference electrode on the nose. The common ground electrode was placed at the left collar bone. Electrooculograms, both vertical and horizontal, were measured using two sets of bipolar electrodes, and similarly for electrocardiogram with electrodes at the left lower rib and right collarbone.

2.2. Preprocessing

Data from 16 subjects (the data set authors excluded three subjects due to poor data quality) were provided in a maxfiltered version and were subsequently preprocessed in Fieldtrip (Oostenveld et al., 2011) using modified processing scripts provided by Robert Oostenveld[2]. Our pipeline consisted of (1) epoching the data according to trials and conditions, (2) rejecting epochs with EEG, MEG, or electrooculography artifacts, (3) bandpass filtering the data between 0.5 and 40 Hz, (4) modality-wise principal component analysis retaining the first 50 components and subsequently subtracting the channel-wise mean, and (5) downsampling the data from 1,100 Hz to 200 Hz. Finally, trials were averaged within-subject over multiple presentations of the three stimuli: familiar, unfamiliar, and scrambled.

2.3. Archetypal analysis

In the classic archetypal analysis, we seek a decomposition $\mathbf{X} \approx \mathbf{AS}$ of a data matrix $\mathbf{X} \in \mathbb{R}^{D \times N}$, where $N \in \mathbb{N}$ corresponds to the number of observations and $D \in \mathbb{N}$ corresponds to the

---

[1] https://openneuro.org/datasets/ds000117/versions/1.0.4

[2] https://github.com/robertoostenveld/Wakeman-and-Henson-2015

dimensionality (e.g., number of channels) (Cutler and Breiman, 1994). The decomposition determines a set of archetypes $\mathbf{A} = \tilde{\mathbf{X}}\mathbf{C}$, which are weighted combinations of the matrix $\tilde{\mathbf{X}}$ that, as introduced in Hinrich et al. (2016), may differ from the input matrix $\mathbf{X}$, e.g., through some transformation, and a mixing matrix $\mathbf{S}$. The two matrices $\mathbf{C} \in \mathbb{R}^{N\times K}$ and $\mathbf{S} \in \mathbb{R}^{K\times N}$ (where $K \in \mathbb{N}$ corresponds to the number of archetypes to be extracted) are used to reconstruct the data matrix, and we denote the reconstruction $\hat{\mathbf{X}} = \tilde{\mathbf{X}}\mathbf{C}\mathbf{S} \in \mathbb{R}^{D\times N}$. In this formulation, the archetypes are found by convex combination (weights sum to one) of the existing data points in $\tilde{\mathbf{X}}$ by matrix multiplication with $\mathbf{C}$, such that the archetypes are defined by the columns of the matrix $\tilde{\mathbf{X}}\mathbf{C}$. Each observation in the reconstruction $\hat{\mathbf{X}}$ is then defined in terms of a convex combination of these archetypes given by the columns of $\mathbf{S}$.

For some measure of distance between the data and reconstructions, $D(\circ|\circ)$, the problem of identifying $\mathbf{C}$ and $\mathbf{S}$ can be formulated as:

$$\begin{aligned} &\underset{\mathbf{C},\mathbf{S}}{\arg\min} \left(D(\mathbf{X}|\hat{\mathbf{X}})\right) \\ &s.t. \quad |\mathbf{c}_{\cdot,k}|_1 = 1, \quad |\mathbf{s}_{\cdot,n}|_1 = 1, \\ &\qquad \mathbf{C} \geq \mathbf{0}, \quad \mathbf{S} \geq \mathbf{0}, \end{aligned} \tag{1}$$

where $\mathbf{c}_{\cdot,k}$ corresponds to column k in $\mathbf{C}$ (the k'th archetype generator), $\mathbf{s}_{\cdot,n}$ corresponds to column n in $\mathbf{S}$ (the n'th observation), $|\cdot|_1$ is the ℓ_1-norm which is constrained to one (i.e., sum of absolute values constrained to 1), and $\mathbf{C}, \mathbf{S} \geq 0$ enforces non-negativity in the elements of $\mathbf{C}$ and $\mathbf{S}$. Together, the constraints ensure the archetypes and reconstructions are related through convex combinations (non-negative and sum to one). The problem is solved by alternately updating $\mathbf{C}$ and $\mathbf{S}$ (i.e., alternately finding optimal archetypes for a given expression $\mathbf{S}$ of the archetypes, and finding optimal expression of the archetypes given the definition of archetypes by $\mathbf{C}$). The classic Euclidean distance measure amounts to a least squares loss, $\mathcal{L}_{ls}$, and can be expressed using the Frobenius norm as: $D(\mathbf{X}|\hat{\mathbf{X}}) = ||\mathbf{X} - \tilde{\mathbf{X}}\mathbf{C}\mathbf{S}||_F^2$.

Whereas the Euclidean AA implicitly assumes normally distributed noise, the AA has been advanced to other types of data sets, including binary (Bernoulli likelihood) and integer variables (Poisson likelihood) (Seth and Eugster, 2016) as well as ordinal responses (Fernández et al., 2021). However, no generalization of AA in the context of directional statistics currently exists.

2.4. Directional archetypal analysis

In the current treatment of directional archetypal analysis (DAA), we focus on axially symmetric data as characterized by the Watson distribution with the probability density function:

$$W(\mathbf{x}|\boldsymbol{\mu}, \kappa) = c_D(\kappa)\exp(\kappa\left(\boldsymbol{\mu}^T\mathbf{x}\right)^2), \tag{2}$$

where $\mathbf{x} \in \mathbb{S}^{D-1}$ (the $(D-1)$-dimensional unit hypersphere), $\boldsymbol{\mu}$ defines a mean direction, κ defines a concentration around that mean direction, and $c_D(\kappa)$ is a normalization constant (see Watson, 1965). Specifically, we consider data where a direction, $\mathbf{x}$, and its negative are equivalent (invariance to sign flip), which corresponds to $\mathbf{x} \in \mathbb{P}^{D-1}$, where $\mathbb{P}^{D-1}$ is the $(D-1)$-projective hyperplane (Sra and Karp, 2013).

Instead of a Euclidean distance (least squares) loss, the Watson distribution measures the squared difference in the angle between the reconstruction and the corresponding data point. Contrary to classic archetypal analysis, we will investigate angular properties between observations that lie on the surface of the unit hypersphere, i.e., if the n'th observation in the data matrix $\mathbf{X}$ is denoted $\mathbf{x}_n$, then we can reparameterize any observation as $\mathbf{x}_n = \sqrt{\kappa_n}\tilde{\mathbf{x}}_n$ such that $\tilde{\mathbf{x}}_n \in \mathbb{S}^{D-1}$ with precision $\kappa_n = ||\mathbf{x}_n||_2^2$. Notably, the precision κ_n can thereby be absorbed in $\mathbf{x}_n$ by scaling $\tilde{\mathbf{x}}_n$ by $\sqrt{\kappa_n}$. Thereby κ_n can be interpreted as the amount of precision assigned to the spherically distributed observations according to the Watson distribution given in (2). By optimizing with respect to the original data $\mathbf{x}_n$ (1), emphasis will be given to the reconstruction $\tilde{\mathbf{x}}_n$ with high precision κ_n while ensuring that the archetypes themselves are not influenced by scale-difference in data. We further assume that diametrically opposed $\tilde{\mathbf{x}}_n$ are equivalent, and thus that $\tilde{\mathbf{x}}_n \in \mathbb{P}^{D-1}$. For each observation, the angle (in D-dimensional space) can be measured as the inner product of the reconstruction (normalized to have unit l_2-norm) and the data points. We define the (unnormalized) reconstruction of $\mathbf{x}_n$ according to the AA model as $\hat{\mathbf{x}}_n = \tilde{\mathbf{X}}\mathbf{C}\mathbf{s}_n$. The loss $\mathcal{L}_W$, over N points is then:

$$\mathcal{L}_W = -\sum_{n=1}^{N}\left(\mathbf{x}_n^\top\hat{\mathbf{x}}_n/||\hat{\mathbf{x}}_n||_2\right)^2 \tag{3}$$

Note that this loss function, while inspired by the Watson distribution, is not a density, and we do not, e.g., determine the normalization constant. To derive update rules for the DAA algorithm, we seek the derivative of the loss with respect to the model parameters $\mathbf{S}$ and $\mathbf{C}$. We define two vectors of inner products $\mathbf{z}$ and $\mathbf{q}$ with elements $z_n = \mathbf{x}_n^\top\hat{\mathbf{x}}_n$ and $q_n = \hat{\mathbf{x}}_n^\top\hat{\mathbf{x}}_n$ and denote the matrices with the elements of $\mathbf{z}$ and $\mathbf{q}$ in their diagonal as $\mathbf{D}_z = \mathrm{diag}\,(\mathbf{z})$ and $\mathbf{D}_q = \mathrm{diag}\,(\mathbf{q})$, respectively. Summing over all the squared angles between data and reconstruction can be written as the following loss (defining $\mathbf{V} = \mathbf{D}_z\mathbf{D}_q{}^{-1/2}$):

$$\mathcal{L}_W = \mathbf{V} : \mathbf{V}, \tag{4}$$

where the colon operator "$\circ : \circ$" designates the inner product such that for matrices $\mathbf{A}$ and $\mathbf{B}$ we have that $\mathbf{A} : \mathbf{B} = \mathrm{Tr}(\mathbf{A}^\top\mathbf{B})$. We will approach determining the scalar by matrix derivatives by initially working in the (total) differential form and then converting to canonical form[3]. Thus, to obtain the gradient of a scalar $\mathcal{F}(\mathbf{A})$ w.r.t a matrix $\mathbf{A}$, i.e., $\nabla_{\mathbf{A}}\mathcal{F}(\mathbf{A})$, we need to determine a matrix $\mathbf{B}$ such that $\delta\mathcal{F}(\mathbf{A}) = \mathrm{Tr}\left(\mathbf{B}^\top \delta\mathbf{A}\right) = \mathbf{B} : \delta\mathbf{A}$, because then $\nabla_{\mathbf{A}}\mathcal{F}(\mathbf{A}) = \mathbf{B}$. The differential of $\mathcal{L}_W$ is then:

$$\begin{aligned}\delta\mathcal{L}_W &= 2\mathbf{V} : \delta\mathbf{V} = 2\mathbf{V} : \delta\left(\mathbf{D}_z\mathbf{D}_q{}^{-1/2}\right)\\ &= 2\mathbf{V} : \delta\mathbf{D}_z\mathbf{D}_q{}^{-1/2} + 2\mathbf{V} : \mathbf{D}_z\delta\mathbf{D}_q{}^{-1/2} \qquad (5)\end{aligned}$$

The gradients of $\mathcal{L}_W$ w.r.t. $\mathbf{S}$ and $\mathbf{C}$ can then be found to be:

$$\begin{aligned}\delta\mathcal{L}_W(\mathbf{C}) &= 2\mathbf{TV} : \tilde{\mathbf{X}}\mathbf{C}\delta\mathbf{S} = 2\mathbf{C}^\top\tilde{\mathbf{X}}^\top\mathbf{TV} : \delta\mathbf{S}\\ &\Rightarrow \nabla_{\mathbf{S}}\mathcal{L}_W = 2\mathbf{C}^\top\tilde{\mathbf{X}}^\top\mathbf{TV} \qquad (6)\\ \delta\mathcal{L}_W(\mathbf{S}) &= 2\mathbf{TV} : \tilde{\mathbf{X}}\delta\mathbf{C}\mathbf{S} = 2\tilde{\mathbf{X}}^\top\mathbf{TVS}^\top : \delta\mathbf{C}\\ &\Rightarrow \nabla_{\mathbf{C}}\mathcal{L}_W = 2\tilde{\mathbf{X}}^\top\mathbf{TVS}^\top, \qquad (7)\end{aligned}$$

where we defined $\mathbf{T} = \mathbf{X}\mathbf{D}_q{}^{-1/2} - \hat{\mathbf{X}}\mathbf{D}_q{}^{-3/2}\mathbf{D}_z$.

For this application, we constrain $\tilde{\mathbf{X}}$ to the hypersphere, i.e., we normalize every time-point for each modality, subject, and condition across channels. We introduce an additional constraint on $\tilde{\mathbf{X}}\mathbf{C}$ to ensure that the archetypes lie on the same hyper-hemisphere. We can ensure this by only allowing the archetypes to be constructed using a flipped version, $\tilde{\mathbf{X}}_f$ of $\tilde{\mathbf{X}}$ which is projected onto a chosen hyper-hemisphere. We determine the dominant hyper-hemisphere in the data by the first principal component. We then negate ("flip") each data point if its projection onto this dominant direction is negative and obtain the archetypes as $\tilde{\mathbf{X}}_f\mathbf{C}$. We also scale the data matrix $\mathbf{X}$ by its Frobenius norm (across all data points) for each subject and modality to ensure each subject and modality has a similar influence on the loss when considering the multisubject and multimodal modeling described next.

2.5. Multimodal multisubject directional archetypal analysis

Similar to how Hinrich et al. (2016) extended archetypal analysis to multisubject data, we extend DAA to parameterize multisubject and multimodal data sets. For modalities $m = 1, \ldots, M$ and subjects $b = 1, \ldots, B$, we approximate our observed data matrices $\mathbf{X}^{(m,b)}$ as $\mathbf{X}^{(m,b)} \approx \tilde{\mathbf{X}}^{(m,b)}\mathbf{C}\mathbf{S}^{(m,b)}$. As such, our model contains a global archetype generator matrix $\mathbf{C}$ and modality- and subject-specific mixing matrices $\mathbf{S}^{(m,b)}$ as well as archetypes $\tilde{\mathbf{X}}^{(m,b)}\mathbf{C}$, while the archetypes are generated from the same convex combination of features. The loss function in (3) is thereby extended to multiple subjects and modalities by:

$$\mathcal{L}_{MW} = -\sum_{m=1}^{M}\sum_{b=1}^{B}\sum_{n=1}^{N}\left(\mathbf{x}_n^{(m,b)\top}\hat{\mathbf{x}}_n^{(m,b)}/||\hat{\mathbf{x}}_n^{(m,b)}||_2\right)^2, \qquad (8)$$

where $\hat{\mathbf{x}}_n^{(m,b)} = \tilde{\mathbf{X}}^{(m,b)}\mathbf{C}\mathbf{s}_n^{(m,b)}$ and Equations (6) and (7) revised accordingly. We ensure the unit-norm of the columns of $\mathbf{C}$ and $\mathbf{S}$ by recasting the problem in l_1-normalization invariant variables, as introduced in Mørup and Hansen (2012). For instance, for an element in $\mathbf{S}^{(m,b)}$, $s_{k,n}^{(m,b)}$, the recast parameter is $\tilde{s}_{k,n}^{(m,b)} = s_{k,n}^{(m,b)} / \sum_{k'} s_{k',n}^{(m,b)}$. We will omit the tilde for simplicity. We ensure non-negativity using a projected gradient method, which simplified amounts to a parameter update based on some step size μ and some gradient w.r.t. the distance defined above, $g_{k,n}^{(m,b)}$, as: $s_{k,n}^{(m,b)} \leftarrow \max\left(s_{k,n}^{(m,b)} - \mu g_{k,n}^{(m,b)}, 0\right)$. For details regarding the projected gradient procedure, we refer to Mørup and Hansen (2012, Section 2.3).

In practice, we determine the gradient for $\mathbf{C}$ for every subject and modality and subsequently sum the gradients across these. We then update $\mathbf{C}$ and the step size μ_c. That is, we decrease the step size with a factor $\frac{1}{2}$ if the new summed loss is worse than the previous one. If the new loss is improved, we slightly increase the step size (by a factor 1.1) and end the update. For $\mathbf{S}^{(m,b)}$, the gradient is once again determined for every subject and modality, though this time without summation across these. The loss for every time point, modality, and subject is computed, and corresponding elements of $\mathbf{S}^{(m,b)}$ are only updated if the new loss is lower than the previous one. Likewise, step sizes, which are specific to sample, subject, and modality, are increased/decreased (by the same factors as above) if the new loss is improved/worsened compared to the previous one.

In our implementation, we compute, for every update of the archetype generator matrix $\mathbf{C}$, the matrices $(\tilde{\mathbf{X}}^{(m,b)}\mathbf{C})^\top\tilde{\mathbf{X}}^{(m,b)}\mathbf{C}$ and $\mathbf{X}^{(m,b)\top}\tilde{\mathbf{X}}^{(m,b)}\mathbf{C}$ for fast computation of $\mathbf{D}_z^{(m,b)}$ and $\mathbf{D}_q^{(m,b)}$. This reduces the overall time complexity updating $\mathbf{S}^{(m,b)}$ substantially to be $\mathcal{O}(MBNK)$, whereas the overall time-complexity updating $\mathbf{C}$ is $\mathcal{O}(MBDNK)$.

2.6. Multimodal multisubject directional clustering

In order to contrast the performance of the developed DAA to conventional clustering based on directional statistics as used in the modified k-means procedure of Pascual-Marqui et al. (1995) we further develop a hard clustering multimodal, multisubject clustering procedure inspired by the DAA. In conventional clustering, either modalities and subjects need to be modeled separately, or data merged, to ensure consistent centroids across subjects. By defining the cluster centroids in terms of a latent generator as in the DAA, it is possible to define a multimodal, multisubject hard assigned clustering procedure

---

[3] See e.g., https://tminka.github.io/papers/matrix/minka-matrix.pdf.

by endowing the DAA model with hard assigned clusters, i.e., by replacing the AA model formulation in (1) with ℓ_0 constraints on $\mathbf{S}$ as opposed to ℓ_1 constraints. Thereby the optimization of $\mathbf{S}$ changes to a k-means type assignment of observation to centroids according to the maximally squared inner product, i.e.,

$$k^* = \arg\min_k \left[- \left(\mathbf{x}_n^{(m,b)\top} \hat{\mathbf{X}}^{(m,b)} \mathbf{c}_k / ||\hat{\mathbf{X}}^{(m,b)} \mathbf{c}_k||_2 \right)^2 \right] \quad (9)$$

such that $s_{k,n}^{(m,b)} = 1$ for $k = k^*$ and 0 otherwise.

2.7. Model comparison and consistency

We evaluated DAA and our clustering approach using the Watson loss and conventional AA solutions across runs with sum of squared errors (SSE). While the Watson loss is given in (8), we assessed the least squares reconstruction error of the Euclidean AA model as

$$\mathrm{SSE} = \sum_m \sum_b ||\mathbf{X}^{(m,b)} - \tilde{\mathbf{X}}^{(m,b)} \mathbf{C}\mathbf{S}^{(m,b)}||_F^2. \quad (10)$$

To evaluate the consistency of the archetypal mixing, we employed normalized mutual information (NMI) similarly to Hinrich et al. (2016), since each column of $\mathbf{S}^{(m,b)}$ may be considered a probability distribution over components. For $k = 1, \ldots, K$ archetypes and two runs r and r', NMI is here given by:

$$\mathrm{NMI}(\mathbf{S}^r, \mathbf{S}^{r'}) = \frac{2\mathrm{MI}(\mathbf{S}^r, \mathbf{S}^{r'})}{\mathrm{MI}(\mathbf{S}^r, \mathbf{S}^r) + \mathrm{MI}(\mathbf{S}^{r'}, \mathbf{S}^{r'})} \quad (11)$$

$$\mathrm{MI}(\mathbf{S}^r, \mathbf{S}^{r'}) = \sum_{k,k'} p(k,k') \log \frac{p(k,k')}{p(k)p(k')} \quad (12)$$

$$p(k,k') = \frac{1}{N} \sum_k s_{kn}^r s_{k'n}^{r'}. \quad (13)$$

NMI gives a score between 0 and 1 and is invariant to permutations of components. Here we compared losses and NMI between 5 runs of each model, where each model was compared to the preceding model. That is, comparisons were made between models $1-2, 2-3, \ldots, 5-1$ to avoid correcting for dependent comparisons if evaluating all model combinations. Presented NMI values are averages across subjects, modalities, and conditions. To minimize the effect of local minima, each run is the best of 100 randomly initialized models, where both $\mathbf{C}$ and $\mathbf{S}$ were initialized as rate 1 exponential random variables exp(1) normalized to the simplex.

3. Results

3.1. Three-dimensional illustration

To illustrate DAA, we applied it to four synthetic three-dimensional data sets, two of which were defined on $\mathbb{S}^2$, and contrasted the results obtained to the classic Euclidean AA approach and DAA modified to hard assignment, hereafter denoted directional clustering (see Figure 1). All three models were run in five sets of 100 random initializations of the matrices $\mathbf{C}$ and $\mathbf{S}$, where the best model, in terms of loss, for each of the five runs was selected. In total, this leads to 500 model fits for each model and each number of estimated archetypes K.

The first synthetic dataset occupies one octant of the unit sphere with three natural corners constituting the archetypes. While DAA determines archetypes very close to the true archetypes and produces a convex hull on the surface of the sphere octant, the Euclidean solution produces archetypes further from the truth and a simplex-shaped principal convex hull encompassing the interior of the sphere (see Figure 1A). Directional clustering is even less flexible and locates centroids further away from the true archetypes. Due to the binary representation of the assignment matrix $\mathbf{S}$, this solution corresponds to clustering, i.e., defining prototypes as opposed to archetypes. The loss curves indicate a deflection at $K = 3$ components (highlighted) for all three models. Whereas DAA converges to the true solution at $K = 3$, Euclidean AA and the directional clustering model show a less trivial loss curve gradually improving by including more components (i.e., clusters). The same models also have very high consistency for all component numbers. When $K > 3$, extra DAA components become ambiguous and thus, model consistency decreases for this model, indicating that high model consistency is not necessarily equivalent to a well-performing model reconstruction.

In the second example, data were generated occupying two opposing octants of the unit sphere using the same true archetypes and their diametrical opposites, reflecting polarity invariant data (Figure 1B). The three models visualized using three components show vastly different results—while DAA remains able to produce a spherical principal convex hull close to the original solution defining a polarity invariant spherical convex hull, Euclidean AA is not able to produce a principal convex hull that encapsulates the data, identifying two archetypes along one direction and one archetype in the opposite hemisphere. Upon inspecting the loss curves, the Euclidean AA deflects at $K = 6$ components, i.e., double the number of true archetypes, whereas DAA and directional clustering bend at the expected $K = 3$ components. As such, Euclidean AA requires more components to explain polarity-invariant data. Similar to the former example, directional clustering with hard-assignment of states provides polarity-invariant centroids rather than data extremes defined by clusters at the interior of the

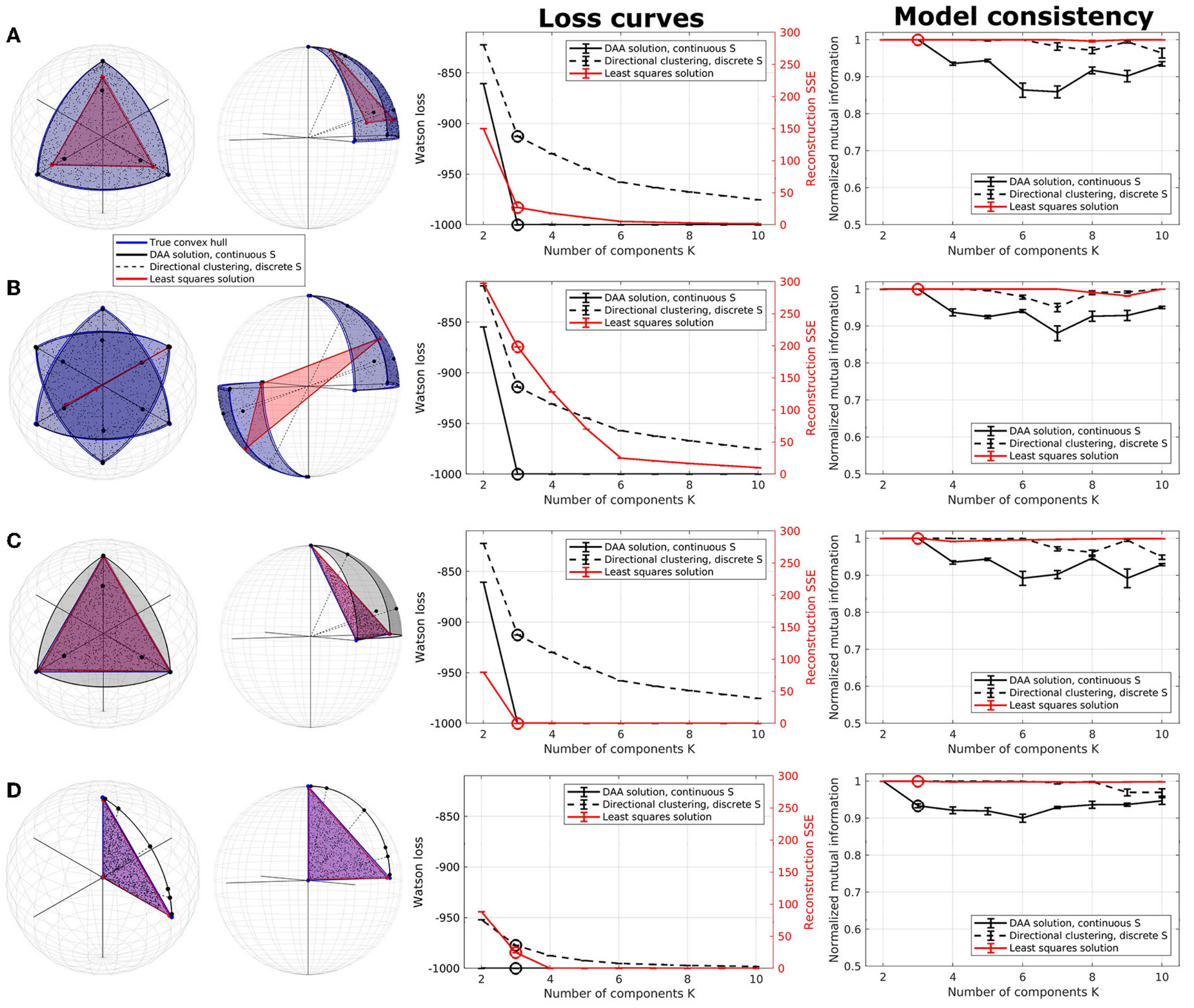

FIGURE 1
Illustration of directional archetypal analysis (DAA) vs. its Euclidean counterpart and a directional clustering model in three dimensions, including loss curves and normalized mutual information (NMI), which are evaluated on 5 models each being the best of 100 simulations. **(A)** Spherical data simulated using three true archetypes situating on the axis corners. The solutions obtained using conventional Euclidean archetypal analysis and directional archetypal analysis with $K = 3$ components and the convex hull spanned by the archetypes, as well as centroids determined using directional clustering, are also shown. **(B)** Spherical data simulated with three true archetypes situating on the axis corners as well as their diametrical opposite, i.e., polarity-invariant archetypes. **(C)** Non-spherical data simulated using the same three true archetypes as in **(A)**. **(D)** Data simulated with three true archetypes, of which one is the origin. Error bars represent standard error of the mean. Note that the loss functions for the models (Watson loss and sum of squared errors, respectively) are not directly comparable but are shown on the same graph to highlight corners in the loss indicating a potential optimal model.

spherical convex hull. Thus, for polarity invariant spherical data, DAA successfully provides a solution that determines archetypes defining a spherical convex hull that, through their convex combinations defined by the matrix **S**, optimally span the synthetic data points.

The third data set is simulated on the simplex spanned by the same three archetypes as in the first example, although without normalizing data to the sphere (Figure 1C). Both DAA, which projects data to the sphere before modeling, and Euclidean AA determine archetypes close to the true solution. Their loss curves also show similar deflection at $K = 3$, showcasing that when the data points are simulated on a non-spherical simplex, the two solutions produce similar archetypes although the simplex spanned by the DAA archetypes is spherical.

DAA and directional clustering project data points to the sphere surface prior to modeling, which may be problematic if the archetypes are far from the sphere surface. Especially if, in the extreme case, one of the archetypes is the origin. This case is exemplified in Figure 1D, where neither DAA nor directional clustering is able to extract sensible archetypes. To summarize,

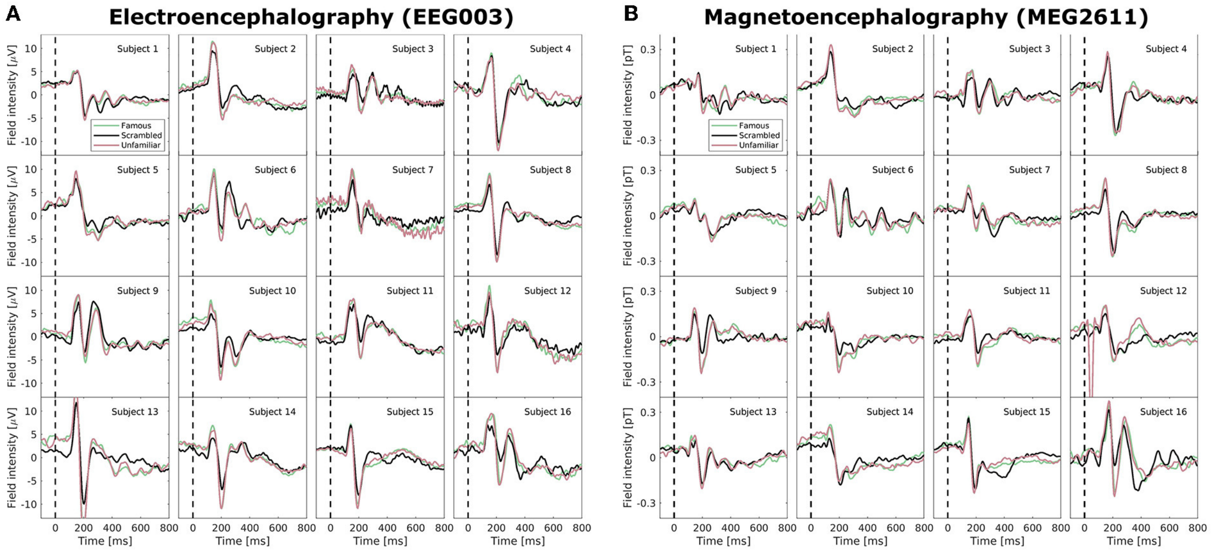

FIGURE 2
Average mean-subtracted time-locked subject event related potentials (ERPs) after preprocessing but without normalization for the three face perception conditions (familiar, unfamiliar, scrambled). **(A)** A selected electroencephalographic electrode (EEG003) located near the right occipital lobe. **(B)** A selected magnetoencephalographic magnetometer (MEG2611) located near the right temporal lobe.

DAA and directional clustering may be used to model scale- and polarity-invariant data but suffer if the underlying convex hull is spanned by the origin.

3.2. Examination of event-related potential subject variability

Neuroimaging data, including EEG and MEG recordings of ERPs, carry large intra- and inter-subject variability. In Figure 2, we examined the Wakeman and Henson (2015) data set after pre-processing but before normalization; specifically, we highlight the EEG electrode with the largest amplitude (EEG003, located to the right of the occipital pole) and similarly for MEG (MEG2611, located near the right temporal lobe). The ERPs, which are averages of many time-locked trials within-subject, deviate vastly between subjects. While a positive deflection at approximately 100 ms and a stronger negative component at approximately 170 ms are generally visible for all subjects (as also reported in Wakeman and Henson, 2015), both scale and morphology of the ERP tend to vary. High variability is also visible in the post-170 ms positive deflections, and, for example, subjects 3, 6, 9, and 16 show sufficiently high positive deflections that they may even be considered a third ERP component. We observe very little consistent deviation between the three conditions (familiar, scrambled, unfamiliar). With the added difficulty of combining two modalities that display highly different topographies, a model that can account for inter-subject and inter-modal variability in microstate analyses is needed.

3.3. ERP data, unimodal

To illustrate the effects of multimodal fusion, we first applied our algorithms to unimodal data (i.e., data coming from a single modality) with a multisubject model. That is, we produced separate models for only EEG data and only MEG data. We compared our results to the multisubject AA model by Hinrich et al. (2016) with a least-squares loss function. To minimize the effect of local minima, we ran our models 100 times with randomly (exponentially) sampled **C** and **S** and selected the model with the lowest loss. Figure 3 shows average loss curves and NMI for five such runs, with error bars representing standard error of the mean. The results show that, for both EEG (Figure 3A) and MEG (Figure 3C), the loss curves for all three models decrease steadily with an increasing number of components. DAA consistently shows improved loss compared to directional clustering with discrete state assignment. Figures 3B,D highlights the topographical maps for the determined archetypes for the models with the lowest loss for $K = 5$ and $K = 10$ for the directional and Euclidean models, respectively. The archetypes, which are averages across subjects and conditions, are ordered according to their percentage total occupation of the averaged archetypal mixing matrix **S**. Given the shared use of sign- and scale-invariance, the archetypes

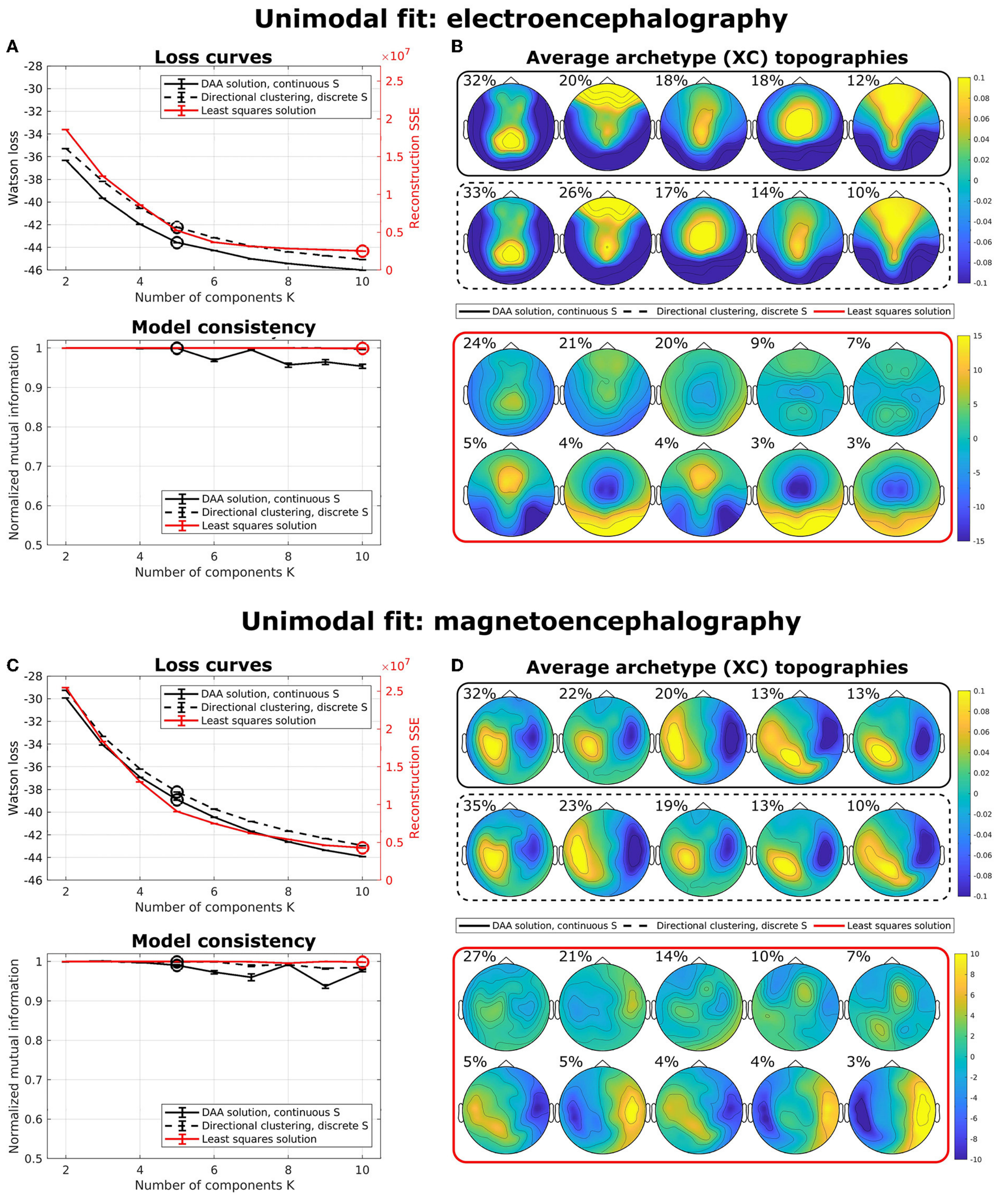

FIGURE 3

Unimodal multisubject archetypal analysis fits using DAA, conventional Euclidean archetypal analysis, and a directional clustering model derived from DAA using hard class assignment. **(A,C)** Loss curves and model consistency evaluated using NMI evaluated on 5 models, where each is the best of 100 model fits. Error bars represent standard error of the mean. **(B,D)** Archetype topographical maps for the best model fits with $K = 5$ and $K = 10$ for the directional models and the Euclidean model for EEG and MEG data, respectively. Archetypes are averaged across subjects and are ordered according to the total occupation of the archetypal mixing matrix $\mathbf{S}$.

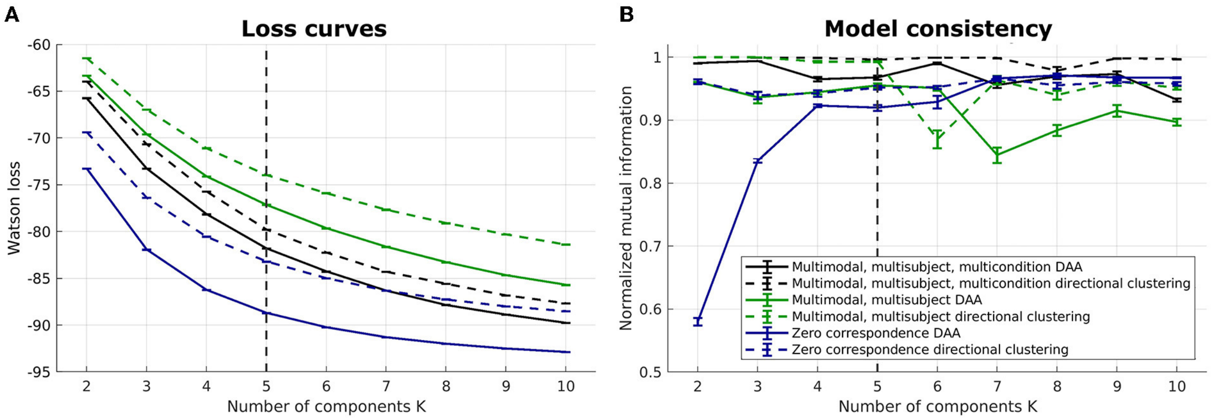

FIGURE 4
Loss curves and NMI for multimodal, multisubject DAA and directional clustering models. **(A)** loss curves for the six models, including multimodal, multisubject, multicondition DAA, a model where the three conditions are concatenated in time to enforce equal archetypes, and a model modeling all subjects separately with no correspondence between subjects. Error bars represent standard error of the mean. **(B)** NMI to inform on model consistency. Both loss curves and NMI are evaluated on 5 model fits for each model, each being the best of 100 fits.

for DAA and the clustering equivalent are similar, with only a minor change in archetype proportion and ordering. The same results for Euclidean AA show some archetype duplications (e.g., archetypes 6 and 8). The AA archetypes vary more in scale, since this model explicitly models the scale of the data.

For both unimodal models, the NMI for the Euclidean implementation is very high, which indicates that this model is very stable upon selecting the best of 100 models to avoid local minima. However, model consistency is generally high for all three models.

3.4. ERP data, multimodal

We illustrate the multimodal, multisubject DAA results in Figures 4–7. Once again, we performed runs with an inner loop of 100 initializations to avoid local minima and an outer loop of 5 to estimate run-to-run variability between best-performing solutions. We do not include the Euclidean equivalent as the existing code (Hinrich et al., 2016) does not support fusion of multiple modalities.

Six models were evaluated: (1) a multimodal, multisubject, multicondition DAA where the three conditions (familiar, unfamiliar, scrambled) are modeled similarly to modalities and subject, i.e., with a shared archetype-generating matrix $\mathbf{C}$ but modality-, subject-, and conditions-specific archetypes $\tilde{\mathbf{X}}^{(m,b,c)}\mathbf{C}$ and mixing matrices $\mathbf{S}^{(m,b,c)}$, where $c = \{1, 2, 3\}$ is conditions, (2) a multimodal, multisubject DAA where the three conditions were concatenated in time for each subject to enforce equal archetypes $\left[\tilde{\mathbf{X}}^{(m,b,1)}, \tilde{\mathbf{X}}^{(m,b,2)}, \tilde{\mathbf{X}}^{(m,b,3)}\right]\mathbf{C}$ across conditions but retain separate mixing matrices $\mathbf{S}^{(m,b,c)}$, and (3) a model where there is no correspondence, i.e., each subject, modality, and condition is modeled separately with their own archetype-generating matrix $\mathbf{C}^{(m,b,c)}$. For all three mentioned models, the corresponding model using directional clustering was evaluated.

On Figure 4, we once again observe a steadily decreasing loss with an increasing number of components, and it is difficult to identify a model that constitutes a sound balance between low loss and few components. Generally, we observe lower loss the more flexible the model is. As such, the models where all subjects are modeled separately have a lower loss, while the models where conditions are concatenated in time display the highest loss. Model consistency is generally lower for the zero-correspondence models, and as expected from our synthetic and unimodal analysis, directional clustering consistently performs worse in terms of loss than DAA, with model consistency slightly improved compared to DAA.

In Figure 5A, the archetype generator ($\mathbf{C}$) is shown for the best multimodal, multisubject, multicondition DAA model with $K = 5$ archetypes. Since AA constrains $\mathbf{C}$ to be non-negative, the result is a sparse representation of the post-stimulus time points. As expected, almost none of the archetypes are generated by time points prior to the earliest ERP deflection at about 100 ms. Subsequently, each archetype is generated by a closely located selection of time points, each responsible for a section of the ERP. Interestingly, the late reaction ($>$ 600 ms) is covered by a separate archetype, indicating that the late response contains structure beyond the pre-100 ms time points.

Figure 5B shows the archetypal mixing matrix ($\mathbf{S}$) averaged across subjects, i.e., the soft assignments of each time-point in the ERP to archetypes. The archetypes have been ordered according to their activation pattern. Archetypal mixing generally follows the pattern in the archetypal generator with little deviation between conditions and modalities. As expected, the prestimulus period until around 100 ms shows no

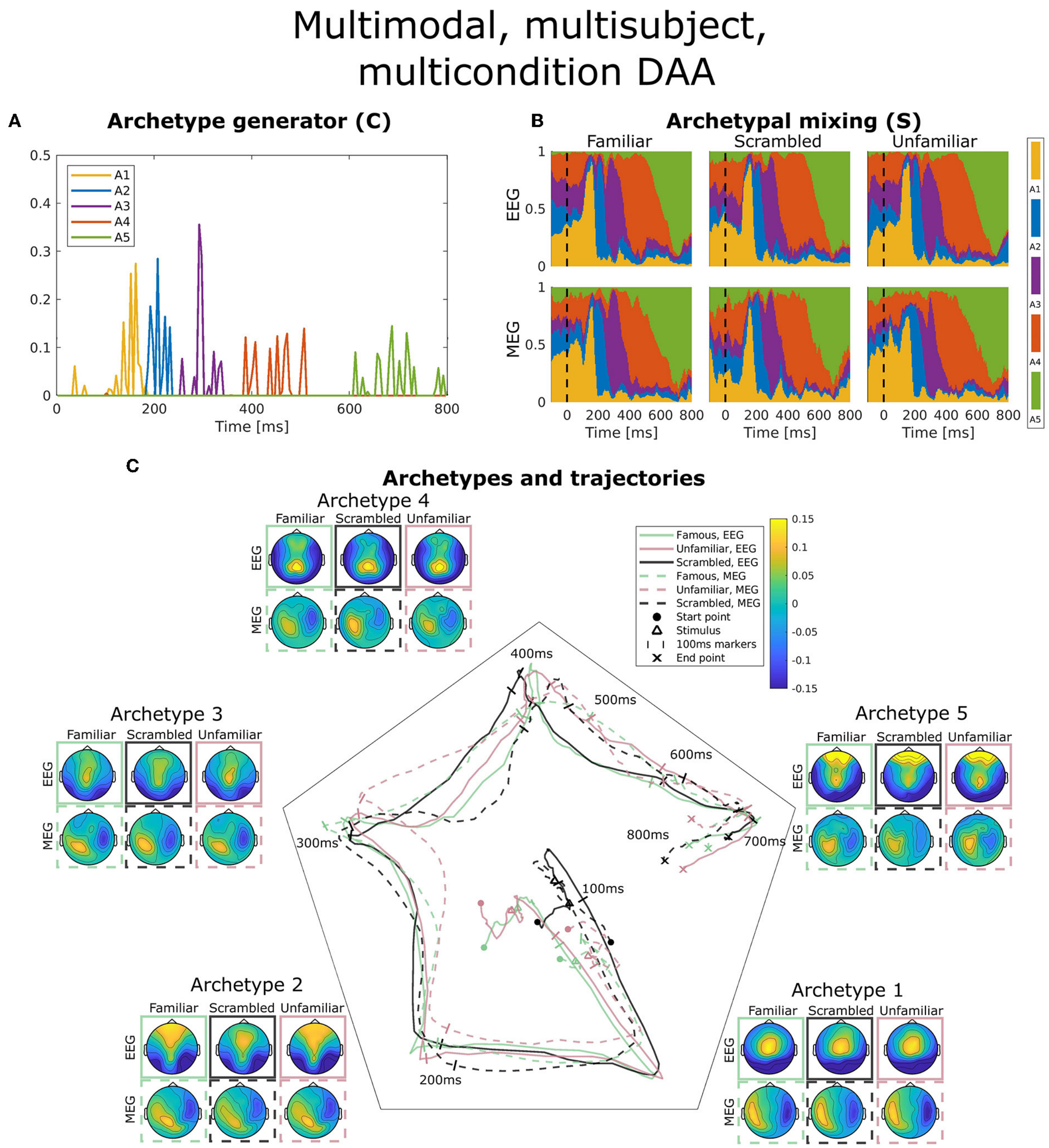

FIGURE 5
Visualization of the best obtained fit for multimodal, multisubject, multicondition DAA with $K = 5$ components. **(A)** The subject-, modality-, and condition-shared archetype generator matrix $\mathbf{C}$ with information on the specific samples from which archetypes are generated. **(B)** The archetypal mixing matrix $\mathbf{S}$ averaged across subjects showing how samples are probabilistically allocated to archetypes. The mixing matrix has been smoothed with a rectangular window of size 3 samples. **(C)** Archetype trajectory averaged across subjects based on the mixing matrix $\mathbf{S}$ smoothed with a rectangular window of 10 samples as well as average archetype topographical maps.

discernible structure. To further investigate archetypal mixing, we show the average ERP trajectory between archetypes in Figure 5C. By arranging the K archetypes with equal angle spacing on the unit circle in the plane, we can visualize the trajectory using the mixing coefficients ($\mathbf{S}$) for each archetype as coordinates in this plane. Equal expression of all archetypes will be in the middle of the plane, and if one archetype is expressed more than others, the trajectory is dragged toward the corresponding archetype's edge. The trajectory similarly shows fast activation of archetypes 1, 2, and 3 and slower recruitment of archetypes 4 and 5. The path from one archetype to the next involves a general shift in the archetypal activation probability of all other archetypes, i.e., the trajectory curves toward the center of the trajectory space. Generally, we observe indistinguishable trajectories between the two modalities. This was expected since a deviation would indicate that EEG and MEG observed different evoked responses to the same stimuli. For the multimodal, multisubject, and multicondition model, we observe almost no difference in archetypal trajectory between conditions (famous, unfamiliar, scrambled).

Figure 5C also shows the archetype topographical maps averaged across subjects. Upon visual activation, archetype 1 is activated around 100 ms post-stimulus. Archetype 1 is represented by an expected occipital/central dipolarity for EEG corresponding to V1 activation and a strong left/right MEG component. The negative ERP deflection at 170 ms is seen here as a shift from archetype 1 to 2 represented by lateral occipital vs. frontal EEG topography. Wakeman and Henson (2015) commented on a significantly larger ERP component at 170 ms for familiar and unfamiliar faces vs. scrambled faces. Spatially, the authors reported that this difference was significant for frontal electrodes (more positive for familiar and unfamiliar faces compared to scrambled) and lateral occipital electrodes (more negative). Our results show that this difference manifests itself in a stronger lateral occipital vs. frontal activation in EEG topography for familiar and unfamiliar conditions as opposed to scrambled, i.e., very similar results to Wakeman and Henson (2015). This result also falls in line with the general notion that the N170 component corresponds to fusiform gyrus activation for face recognition (Gao et al., 2019). While the corresponding topographic maps for MEG show a larger frontal/occipital polarity, the distinction between conditions is less clear. Archetype 3, which is active at around 300 ms, is a less strong (polarity-wise) version of archetype 2, which does not differ between conditions. Archetype 4 is longer-lasting, dominated by parietal EEG topography. Finally, archetype 5 once again displays strong occipital vs. frontal activation in all three conditions. This corresponds well with the late activation of frontal areas reported in Wakeman and Henson (2015). Generally, we observe similar archetype topographies as observed in the unimodal analysis (Figure 3) with frontal/central/occipital variation in EEG maps and left/right variation in MEG maps.

Figure 6 displays the same visualizations for the model in which conditions have been concatenated in time to enforce equal archetypes between conditions. The result is a **C**-matrix three times the length, which in Figure 6A has been split and stacked to compare condition effects on our model. Interestingly, archetype 4 (red) is purely generated by the scrambled condition (middle), and the late archetype 5 (green) is predominantly generated by the familiar and unfamiliar condition. Archetypal mixing, visible in the mixing matrix visualization on Figure 6B and trajectories on Figure 6C, shows that while the initial part of the ERP displays similar archetypal trajectory between conditions, archetype 4 is almost exclusively visited by the scrambled condition, whereas the familiar and unfamiliar condition visit archetypes 3 and 5. Following fusiform face area activation (archetypes 2 and 3), these results indicate that the familiar and unfamiliar conditions are followed by a late, 400 ms frontal and parietal activation. In contrast, the scrambled condition does not show the frontal component. Smaller differences are present between the familiar and unfamiliar condition seen late, at about 550–600 ms, evident by the unfamiliar condition being dominated by archetype 5 to a greater extent than the familiar condition, especially for the EEG modality.

As previously mentioned, subject variability is high in this data set (Figure 2). The present model accounts for both intermodal and intersubject variability, and accordingly, we can further explore subject variability in the trajectory plots and archetypes of the multimodal, multisubject, multicondition model (see Figure 7). Evidently, subject variability is higher in archetypal mixing than in the archetypes. This makes sense since the archetypes are directly computed from the same convex combinations of the input data. As such, the variability in input data is propagated to the archetypes.

Most of the subjects follow an archetypal trajectory pattern that starts centrally and, approximately 100 ms after stimulus, travels to archetype 1, and then quickly onto archetype 2-5 in a circular pattern. However, some conditions for some subjects fall outside this pattern (see, once again, subjects 3, 6, and 9). The scrambled condition does not appear to be the cause of these deviations. Likewise, there is little visible difference between trajectories for EEG and MEG.

4. Discussion

We have presented the directional archetypal analysis (DAA) for scale- and polarity-invariant modeling of brain microstates and demonstrated its utility in modeling both unimodal and multimodal M/EEG ERP data from a visual perception task. We validated our models on synthetic data, compared results to the conventional Euclidean AA model, and showed that DAA, unlike Euclidean AA, can efficiently characterize antipodally symmetric, spherical data. Our unimodal analyses showed that DAA loss as a function of the number of components (K) saturated earlier when compared to its Euclidean counterpart, although loss functions are not directly comparable. Notably, Euclidean AA potentially computes archetypes corresponding to the dipole counterpart of other archetypes. We further observed that the Euclidean AA was more affected by the scale of the input data. The scale of the learned archetypes were inherently equal for DAA but the Euclidean AA produces archetypes with highly varying scales. However, if the underlying convex hull generating the data are obscured

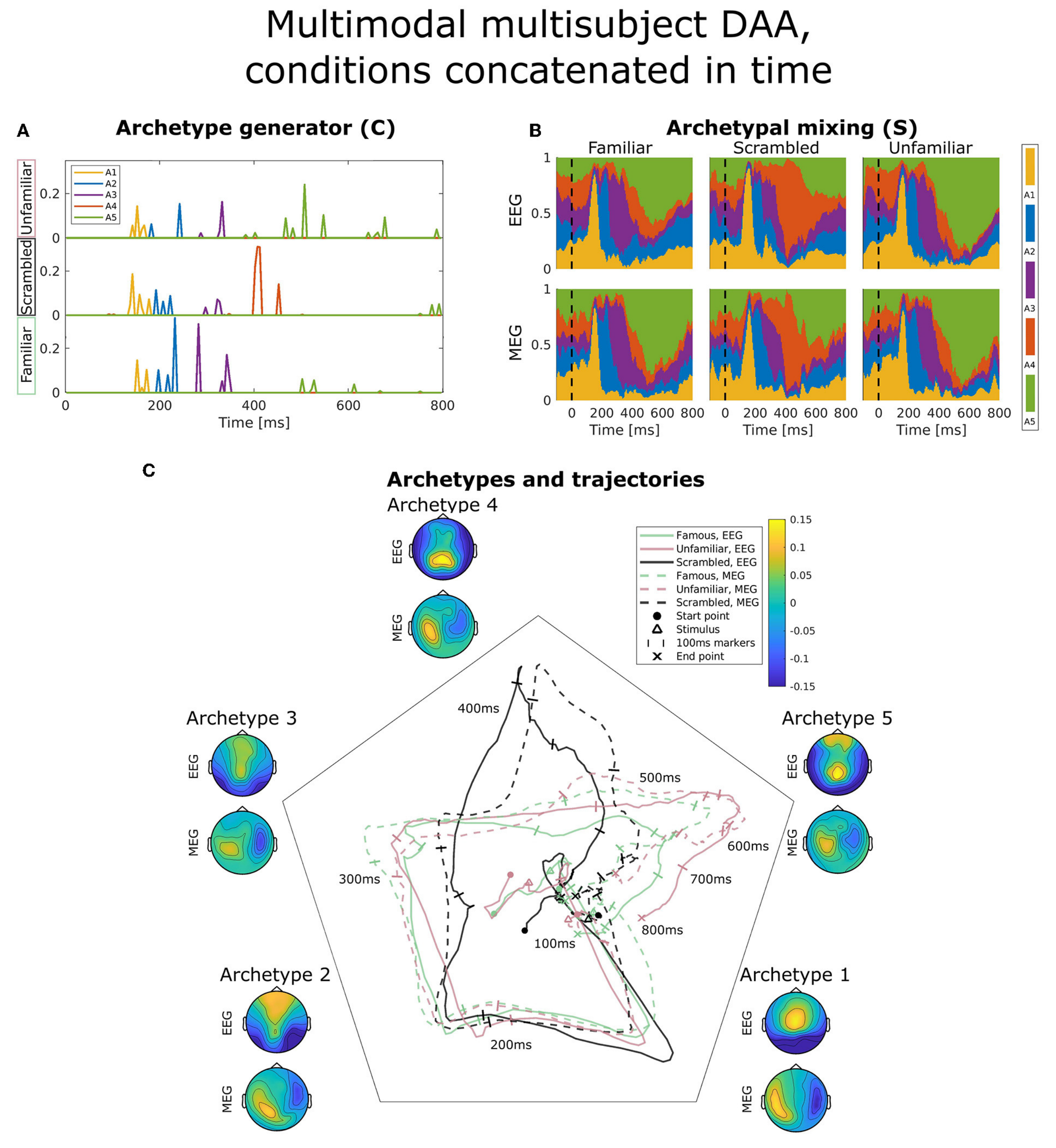

FIGURE 6
Visualization of the best obtained fit for multimodal, multisubject DAA with $K = 5$ components, where the three conditions have been concatenated in time for all subjects and modalities prior to modeling to enforce equal archetypes. **(A)** The subject- and modality-shared archetype generator matrix **C** with information on the specific samples from which archetypes are generated. The matrix has been split into three parts corresponding to the three conditions and subsequently stacked for visualization purposes. **(B)** The archetypal mixing matrix **S** averaged across subjects showing how samples are probabilistically allocated to archetypes. The mixing matrix has been smoothed with a rectangular window of size 3 samples. **(C)** Archetype trajectory averaged across subjects based on the mixing matrix **S** smoothed with a rectangular window of 10 samples as well as average archetype topographical maps.

by the projection onto the sphere, i.e., by including the origin as an archetype, the directional models cannot viably model the data.

We contrasted DAA to a clustering model that constrain the archetypal mixing matrix **S** to hard assignment, corresponding to a multimodal and multisubject extension of the modified

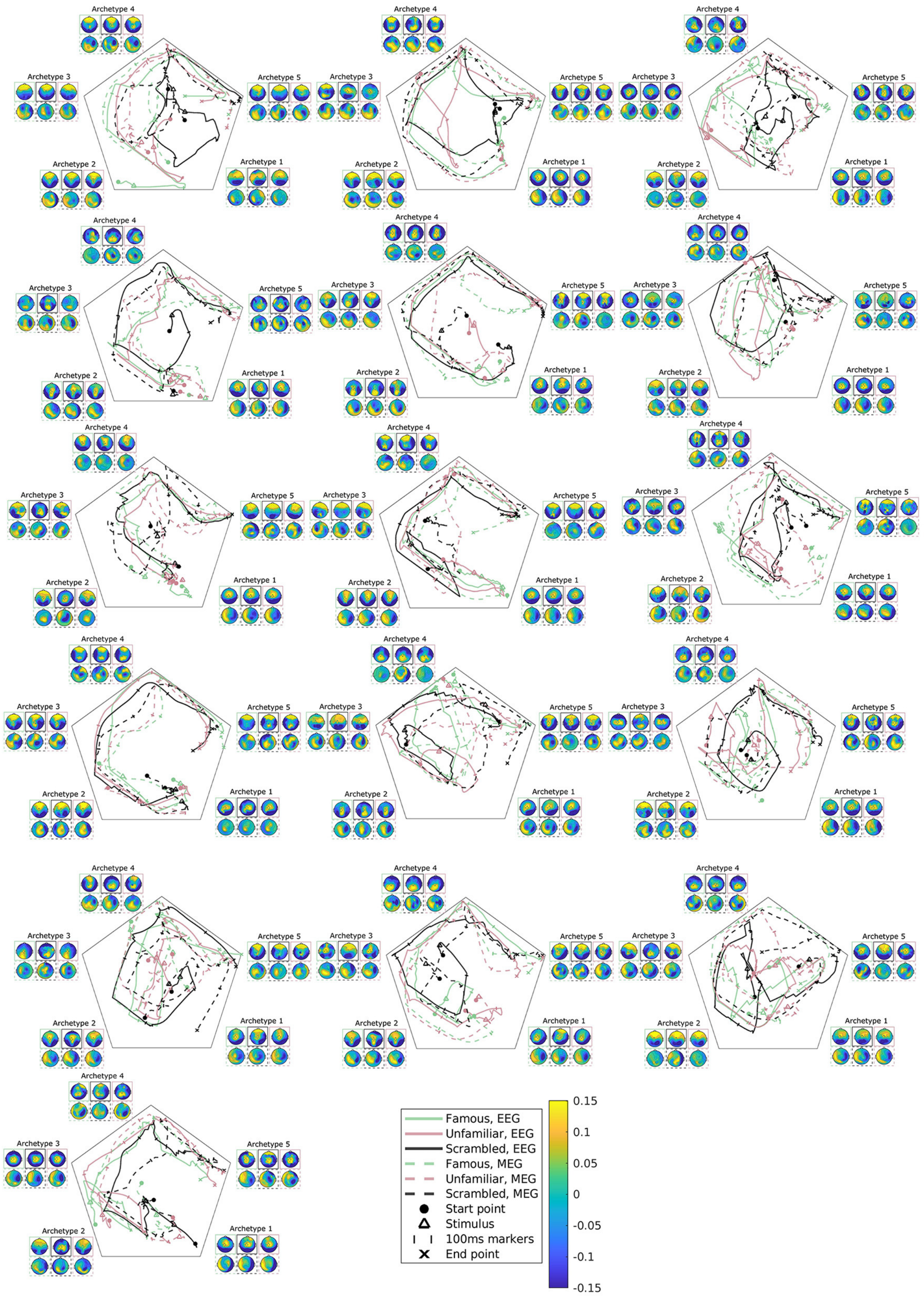

FIGURE 7

Subject, modality, and condition-specific archetypal trajectories and archetypes for the best multimodal, multisubject DAA model in terms of loss with $K = 5$ components. The matrix $\mathbf{S}$ has been smoothed with a rectangular window of size 30 samples for visualization purposes. The figures are ordered by subjects, arranged from left to right.

k-means procedure (Pascual-Marqui et al., 1995). Our synthetic example showed that a clustering model might be suitable for polarity invariant data, although it determines prototypes, or centroids, defining *typical* points. In contrast, DAA identifies archetypes constituting representative, extremal points of the data set. This clustering model is akin to conventional brain microstate analyses, which employ a polarity-invariant *k*-means approach allowing component correspondence while accounting for spatiotemporal variability. While such a model is useful, it also heavily simplifies the notion of brain states to be a one-at-a-time phenomenon. This approach has recently been challenged by Mishra et al. (2020) who suggested that the brain traverses microstates in a continuous rather than discrete pattern. Our proposed DAA approach is a potential solution to this problem by determining microstates based on archetypes rather than prototypes and estimating a (continuous) mixing matrix based on the archetypes. With the added flexibility, we also observed that our model leads to improved loss compared to the corresponding clustering formulation highlighting how the model representation provides more detailed characterizations of the data.

DAA is readily extended to both multisubject and multimodal modeling. Here, we approached the problem by estimating a shared archetype generator matrix $\mathbf{C}$ and subject and modality-specific archetype mixing matrix $\mathbf{S}^{(m,b)}$. Importantly, the archetypes $\tilde{\mathbf{X}}^{(m,b)}\mathbf{C}$ themselves are subject and modality-specific since they are constructed through convex combinations of the input data. In our analyses of ERP data from several conditions (familiar, scrambled, unfamiliar), we extended this approach to also account for conditions. As such, each condition was treated as a new subject to get subject, modality, and condition-specific archetypes and mixing matrices. Our model (Figure 5) showed some variation between conditions observed in an archetype active at approximately 200 ms with stronger bilateral occipital vs. frontal polarity for familiar and unfamiliar compared to scrambled faces. These results were in line with a previous study on the same data set (Wakeman and Henson, 2015) and are also consistent with the general N170 ERP peak representing fusiform gyrus activation specific for face recognition (Gao et al., 2019). Another solution to having multiple conditions is to concatenate these over time and thus allow the archetype generator ($\mathbf{C}$) to be driven by specific condition(s) and not necessarily the same time points across conditions. This approach showed a clear distinction between scrambled and the two face conditions. Specifically, one of the five archetypes was purely generated and visited by the scrambled condition, while two others were mostly generated and visited by the familiar and unfamiliar conditions. Larger frontal activation in face conditions has been observed previously on the same data set (Wakeman and Henson, 2015; Quinn et al., 2018).

By having a shared archetype-generator matrix $\mathbf{C}$ across subjects, modalities, and conditions, we implicitly assume that the *timing* of the neural response to stimuli is the same. This assumption is valid across modalities since these were acquired simultaneously and thus measured the same underlying response. Similarly, it would be expected that the timing is similar for multiple stimuli for the same subject; however, the assumption of zero latency might not be valid across subjects. One solution to this problem is to employ an even more flexible model that does not assume any correspondence between subjects, modalities, or conditions. As highlighted in Figure 4, such a model would lead to improved loss. However, it is much more difficult to establish component correspondence and infer population-level archetypes and archetypal trajectory behavior. We expect that future work may look into developing latency-invariant models inspired by shift-invariant decompositions (Mørup et al., 2008). The zero-latency assumption currently limits the extension of our framework to continuous data, such as resting-state. Similarly, multimodal fusion with vastly different modalities, such as fMRI, which usually measures slow blood-oxygen response to stimuli, and EEG or MEG would violate the assumption of equal timing of the neural response.

A multisubject AA framework, first presented in Hinrich et al. (2016), allows us to account for subject variability, which we know is present in the data set under consideration (see Figure 2). Figure 7 displays the estimated subject-specific archetypes and trajectories and shows that generally, the subject variability manifests itself in archetypal trajectories. Archetype topographies generally also vary across subjects, however, not to the same degree. This highlights the importance of accounting for spatiotemporal variability.

In our analyses on real data, we did not observe a corner point, or clear bend, in the loss curves that would otherwise indicate a potential optimal number of archetypes for any of the evaluated models. Future work may consider cross-validation for model selection. Specifically, we believe that a split-half setup, in which trials are randomly split into two groups prior to preprocessing, where one group is used for training the model and the other for evaluating model loss, is favorable. When the number of trials is high, split-half ensures all subjects and conditions are represented in both groups and high SNR in the corresponding averages while avoiding the excessive computational demands of, e.g., K-fold cross-validation.

Archetypal analysis is generally prone to local minima, a characteristic we also observed in our analyses. All presented loss curves were averages of 5 runs, each the best of 100 different initializations. This higher number of initializations also affected the presented Euclidean AA results (i.e., Figures 1, 3). Generally, we observed that model consistency for DAA was slightly improved by increasing the number of models in the inner loop from 20 to 100, while for conventional AA, model consistency was generally lower than DAA for 20 models in the inner loop and very high for 100 models. While we did not present these results, we argue that all AA models, whether directional or not, benefit from evaluating multiple initializations. For 100 runs in the inner loop, especially for the synthetic data set, Euclidean AA showed higher NMI than DAA, which shows that the robustness of DAA may be somewhat challenged. While it has been shown that the optimization of $\mathbf{C}$ and $\mathbf{S}$ individually is convex for a least-squares loss function, this property breaks down for the proposed Watson equivalent due to the normalization term projecting the reconstruction to the sphere. As a result, we hypothesize that the reduced DAA robustness compared to least-squares for 100 runs could be a consequence of the optimization landscape being more prone to local minima issues.

Here we initialized our models by random sampling from an exponential distribution. Previous studies have shown that initializing $\mathbf{C}$ as carefully selected samples through the *FurthestFirst* (Cutler and Breiman, 1994) or the improved *FurthestSum* (Mørup and Hansen, 2012), may lead to improved convergence speed. However, over multiple initializations, random initialization has been shown to lead to lower losses (Krohne et al., 2019). Further studies could evaluate the effect of initialization to potentially decrease the number of estimated models needed to ensure robustness of the obtained results.

Directional archetypal analysis and clustering assume that data resides on a (unit) hypersphere. In our case, the dimensionality of the hypersphere corresponds to the number of electrodes and magnetometers, respectively. AA, including DAA, allows for the archetypes $\tilde{\mathbf{X}}\mathbf{C}$ to be constructed from a data matrix $\tilde{\mathbf{X}}$ potentially different from the original data matrix $\mathbf{X}$. Here, we constrained each sample of the input data $\tilde{\mathbf{X}}^{(m,b)}$ to unit l_2-norm, while $\mathbf{X}$ was normalized by the Frobenius norm of all samples across all subjects, conditions, and modalities, to ensure that these were given similar influence on the model. Normalization of $\tilde{\mathbf{X}}$ by the l_2-norm was our approach to scale and polarity invariant modeling of microstates. Optimization of $\mathbf{C}$ and $\mathbf{S}$ occurred with a loss function of the reconstruction (using $\tilde{\mathbf{x}}_n$) to the original, unnormalized data $\mathbf{x}_n$. In this way, the squared magnitude of the data, interpreted as the precision parameter κ absorbed by $\mathbf{x}_n$, enabled DAA to emphasize regions with high SNR when defining the archetypes. This is similar to how conventional microstate analysis procedures typically restrict the analysis to regions of high global field power (Poulsen et al., 2018).

In conclusion, we have introduced directional archetypal analysis for (1) modeling of scale and polarity invariant data, (2) fusion of multiple modalities, and (3) incorporating subject variability in archetypes and archetypal mixing. Our model represents an approach to modeling brain microstates without assuming hard assignment of states to samples that accounts for spatiotemporal variability of the brain's response to stimuli while preserving component correspondence.

Data availability statement

Publicly available datasets were analyzed in this study. The code for DAA as well as the hard assignment multimodal multisubject clustering procedure and further information regarding the experiments are available at https://github.com/anders-s-olsen/DirectionalArchetypalAnalysis. The data may be freely downloaded at https://openneuro.org/datasets/ds000117/versions/1.0.4.

Ethics statement

The studies involving human participants were reviewed and approved by Cambridge University Psychological Ethics Committee. The patients/participants provided their written informed consent to participate in this study.

Author contributions

AO and RH: methodology, software, validation, formal analysis, data curation, visualization, writing—original draft, and writing—review and editing JH: conceptualization, methodology, supervision, and writing—review and editing. KM: methodology, supervision, and writing—review and editing. MM: conceptualization, formal analysis, methodology, project administration, software, supervision, writing—original draft, and writing—review and editing. All authors contributed to the article and approved the submitted version.

Funding

Through RH, this work was partly funded by the Innovation Fund Denmark (IFD, grant number: 9065-00077B). MM was supported by Ingeborg and Leo Dannins scholarship for scientific research.

Conflict of interest

Author RH is employed by WS Audiology.

The remaining authors declare that the research was conducted in the absence of any commercial or financial relationships that could be construed as a potential conflict of interest.

Publisher's note

References

Cabral, J., Vidaurre, D., Marques, P., Magalhães, R., Silva Moreira, P., Miguel Soares, J., et al. (2017). Cognitive performance in healthy older adults relates to spontaneous switching between states of functional connectivity during rest. *Sci. Rep.* 7. 1–13. doi: 10.1038/s41598-017-05425-7

Chan, B. H., Mitchell, D. A., and Cram, L. E. (2003). Archetypal analysis of galaxy spectra. *Monthly Notices R. Astron. Soc.* 338, 790–795. doi: 10.1046/j.1365-8711.2003.06099.x

Chowdhury, R. A., Zerouali, Y., Hedrich, T., Heers, M., Kobayashi, E., Lina, J. M., et al. (2015). MEG-EEG information fusion and electromagnetic source imaging: from theory to clinical application in epilepsy. *Brain Topogr.* 28, 785–812. doi: 10.1007/s10548-015-0437-3

Cichy, R. M., Pantazis, D., and Oliva, A. (2016). Similarity-based fusion of MEG and fMRI reveals spatio-temporal dynamics in human cortex during visual object recognition. *Cereb. Cortex* 26, 3563–3579. doi: 10.1093/cercor/bhw135

Cona, G., Kocillari, L., Palombit, A., Bertoldo, A., Maritan, A., and Corbetta, M. (2019). Archetypes of human cognition defined by time preference for reward and their brain correlates: an evolutionary trade-off approach. *Neuroimage* 185, 322–334. doi: 10.1016/j.neuroimage.2018.10.050

Coquelet, N., De Tiége, X., Roshchupkina, L., Peigneux, P., Goldman, S., Woolrich, M., et al. (2022). Microstates and power envelope hidden Markov modeling probe bursting brain activity at different timescales. *Neuroimage* 247, 118850. doi: 10.1016/j.neuroimage.2021.118850

Cutler, A., and Breiman, L. (1994). Archetypal analysis. *Technometrics* 36, 338. doi: 10.1080/00401706.1994.10485840

Dekker, M. M., Franca, A. S., Panja, D., and Cohen, M. X. (2021). Characterizing neural phase-space trajectories via principal louvain clustering. *J. Neurosci. Methods* 362, 109313. doi: 10.1016/j.jneumeth.2021.109313

Dhillon, I. S., Marcotte, E. M., and Roshan, U. (2003). Diametrical clustering for identifying anti-correlated gene clusters. *Bioinformatics* 19, 1612–1619. doi: 10.1093/bioinformatics/btg209

Fernández, D., Epifanio, I., and McMillan, L. F. (2021). Archetypal analysis for ordinal data. *Inform. Sci.* 579, 281–292. doi: 10.1016/j.ins.2021.07.095

Gao, C., Conte, S., Richards, J. E., Xie, W., and Hanayik, T. (2019). The neural sources of N170: understanding timing of activation in face-selective areas. *Psychophysiology* 56, e13336. doi: 10.1111/psyp.13336

Hamid, L., Aydin, U., Wolters, C., Stephani, U., Siniatchkin, M., and Galka, A. (2013). "MEG-EEG fusion by Kalman filtering within a source analysis framework," in *Proceedings of the Annual International Conference of the IEEE Engineering in Medicine and Biology Society, EMBS* (Osaka). doi: 10.1109/EMBC.2013.6610626

Hart, Y., Sheftel, H., Hausser, J., Szekely, P., Ben-Moshe, N. B., Korem, Y., et al. (2015). Inferring biological tasks using Pareto analysis of high-dimensional data. *Nat. Methods* 12, 233–235. doi: 10.1038/nmeth.3254

Henson, R. N., Mouchlianitis, E., and Friston, K. J. (2009). MEG and EEG data fusion: Simultaneous localisation of face-evoked responses. *Neuroimage* 47, 581–589. doi: 10.1016/j.neuroimage.2009.04.063

Hinrich, J. L., Bardenfleth, S. E., Roge, R. E., Churchill, N. W., Madsen, K. H., and Morup, M. (2016). Archetypal analysis for modeling multisubject fMRI data. *IEEE J. Select. Top. Signal Process.* 10, 1160–1171. doi: 10.1109/JSTSP.2016.2595103

Khanna, A., Pascual-Leone, A., Michel, C. M., and Farzan, F. (2015). Microstates in resting-state EEG: current status and future directions. *Neurosci. Biobehav. Rev.* 49, e114163. doi: 10.1016/j.neubiorev.2014.12.010

Khanna, A., Pascual-Leone, A., and Farzan, F. (2014). Reliability of resting-state microstate features in electroencephalography. *PLoS ONE* 9, e0114163. doi: 10.1371/journal.pone.0114163

Krohne, L. G., Wang, Y., Hinrich, J. L., Moerup, M., Chan, R. C., and Madsen, K. H. (2019). Classification of social anhedonia using temporal and spatial network features from a social cognition fMRI task. *Hum. Brain Mapp.* 40, 4965–4981. doi: 10.1002/hbm.24751

Lehmann, D. (1971). Multichannel topography of human alpha EEG fields. *Electroencephalogr. Clin. Neurophysiol.* 31, 439–449. doi: 10.1016/0013-4694(71)90165-9

Lehmann, D., Ozaki, H., and Pal, I. (1987). EEG alpha map series: brain micro-states by space-oriented adaptive segmentation. *Electroencephalogr. Clin. Neurophysiol.* 67, 271–288. doi: 10.1016/0013-4694(87)90025-3

Lopes da Silva, F. (2013). EEG and MEG: relevance to neuroscience. *Neuron* 80, 1112–1128. doi: 10.1016/j.neuron.2013.10.017

Lord, L. D., Expert, P., Atasoy, S., Roseman, L., Rapuano, K., Lambiotte, R., et al. (2019). Dynamical exploration of the repertoire of brain networks at rest is modulated by psilocybin. *Neuroimage* 199, 127–142. doi: 10.1016/j.neuroimage.2019.05.060

Makeig, S., Westerfield, M., Jung, T. P., Covington, J., Townsend, J., Sejnowski, T. J., et al. (1999). Functionally independent components of the late positive event-related potential during visual spatial attention. *J. Neurosci.* 19, 2665–2680. doi: 10.1523/JNEUROSCI.19-07-02665.1999

Michel, C. M., and Koenig, T. (2018). EEG microstates as a tool for studying the temporal dynamics of whole-brain neuronal networks: a review. *Neuroimage* 180, 577–593. doi: 10.1016/j.neuroimage.2017.11.062

Mishra, A., Englitz, B., and Cohen, M. X. (2020). EEG microstates as a continuous phenomenon. *Neuroimage* 208, 116454. doi: 10.1016/j.neuroimage.2019.116454

Mørup, M., and Hansen, L. K. (2012). Archetypal analysis for machine learning and data mining. *Neurocomputing* 80, 54–63. doi: 10.1016/j.neucom.2011.06.033

Mørup, M., Hansen, L. K., Arnfred, S. M., Lim, L.-H., and Madsen, K. H. (2008). Shift-invariant multilinear decomposition of neuroimaging data. *Neuroimage* 42, 1439–1450. doi: 10.1016/j.neuroimage.2008.05.062

Murray, M. M., Brunet, D., and Michel, C. M. (2008). Topographic ERP analyses: a step-by-step tutorial review. *Brain Topogr.* 20, 249–264. doi: 10.1007/s10548-008-0054-5

Olsen, A. S., Lykkebo-Valløe, A., Ozenne, B., Madsen, M. K., Stenbæk, D. S., Armand, S., et al. (2021). Psilocybin modulation of dynamic functional connectivity is associated with plasma psilocin and subjective effects. *medRxiv [Preprint]*. doi: 10.1101/2021.12.17.21267992

Oostenveld, R., Fries, P., Maris, E., and Schoffelen, J. M. (2011). FieldTrip: Open source software for advanced analysis of MEG, EEG, and invasive electrophysiological data. *Comput. Intell. Neurosci.* 2011, 156869. doi: 10.1155/2011/156869

Pascual-Marqui, R. D., Michel, C. M., and Lehmann, D. (1995). Segmentation of brain electrical activity into microstates; model estimation and validation. *IEEE Trans. Biomed. Eng.* 42, 658–665. doi: 10.1109/10.391164

Poulsen, A. T., Pedroni, A., Langer, N., and Hansen, L. K. (2018). Microstate eeglab toolbox: an introductory guide. *bioRxiv [Preprint]*. doi: 10.1101/289850

Preti, M. G., Bolton, T. A., and Van De Ville, D. (2017). The dynamic functional connectome: state-of-the-art and perspectives. *Neuroimage* 160, 41–54. doi: 10.1016/j.neuroimage.2016.12.061

Quinn, A. J., Vidaurre, D., Abeysuriya, R., Becker, R., Nobre, A. C., and Woolrich, M. W. (2018). Task-evoked dynamic network analysis through Hidden Markov Modeling. *Front. Neurosci.* 12, 603. doi: 10.3389/fnins.2018.00603

Seth, S., and Eugster, M. J. (2016). Probabilistic archetypal analysis. *Mach. Learn.* 102, 85–113. doi: 10.1007/s10994-015-5498-8

Sharon, D., Hämäläinen, M. S., Tootell, R. B., Halgren, E., and Belliveau, J. W. (2007). The advantage of combining MEG and EEG: comparison to fMRI in focally stimulated visual cortex. *Neuroimage* 36, 1225–1235. doi: 10.1016/j.neuroimage.2007.03.066

Skrandies, W. (1990). Global field power and topographic similarity. *Brain Topography*, 3(1). doi: 10.1007/BF01128870

Skrandies, W. (1989). Data reduction of multichannel fields: global field power and principal component analysis. *Brain Topogr*. 2, 73x96-80. doi: 10.1007/BF01128845

Sra, S., and Karp, D. (2013). The multivariate watson distribution: maximum-likelihood estimation and other aspects. *J. Multivariate Anal*. 114, 256–269. doi: 10.1016/j.jmva.2012.08.010

Stevner, A. B., Vidaurre, D., Cabral, J., Rapuano, K., Nielsen, S. F., Tagliazucchi, E., et al. (2019). Discovery of key whole-brain transitions and dynamics during human wakefulness and non-REM sleep. *Nat. Commun*. 10, 1035. doi: 10.1038/s41467-019-08934-3

Thøgersen, J. C., Mørup, M., Damkiær, S., Molin, S., and Jelsbak, L. (2013). Archetypal analysis of diverse *Pseudomonas aeruginosa* transcriptomes reveals adaptation in cystic fibrosis airways. *BMC Bioinformatics* 14, 279. doi: 10.1186/1471-2105-14-279

Tsanousa, A., Laskaris, N., and Angelis, L. (2015). A novel single-trial methodology for studying brain response variability based on archetypal analysis. *Expert Syst. Appl. Int. J*. 42, 8454–8462. doi: 10.1016/j.eswa.2015.06.058

Van De Ville, D., Britz, J., and Michel, C. M. (2010). EEG microstate sequences in healthy humans at rest reveal scale-free dynamics. *Proc. Natl. Acad. Sci. U.S.A*. 107, 18179–18184. doi: 10.1073/pnas.1007841107

Vidaurre, D., Smith, S. M., and Woolrich, M. W. (2017). Brain network dynamics are hierarchically organized in time. *Proc. Natl. Acad. Sci. U.S.A*. 114, 12827–12832. doi: 10.1073/pnas.1705120114

Wakeman, D. G., and Henson, R. N. (2015). A multi-subject, multi-modal human neuroimaging dataset. *Sci. Data* 2, 1–10. doi: 10.1038/sdata.2015.1

Watson, G. S. (1965). Equatorial distributions on a sphere. *Biometrika* 52, 193. doi: 10.2307/2333824

frontiers | Frontiers in Neuroscience

TYPE Original Research
PUBLISHED 09 August 2022
DOI 10.3389/fnins.2022.936975

Remote ischemic preconditioning improves cognitive control in healthy adults: Evidence from an event-related potential study

Yaling Li[1,2,3], Pei Huang[1,2,3], Jun Huang[4], Zhifeng Zhong[1,2,3], Simin Zhou[1,2,3], Huaping Dong[1,2,3], Jiaxin Xie[1,2,3], Yu Wu[1,2,3]* and Peng Li[1,2,3]*

[1]Department of High Altitude Operational Medicine, College of High Altitude Military Medicine, Army Medical University, Chongqing, China, [2]Key Laboratory of Extreme Environmental Medicine, Ministry of Education of China, Army Medical University, Chongqing, China, [3]Key Laboratory of High Altitude Medicine, Army Medical University, Chongqing, China, [4]Chongqing Key Laboratory of Psychological Diagnosis and Education Technology for Children With Special Needs, College of Education Science, Chongqing Normal University, Chongqing, China

OPEN ACCESS

EDITED BY
Camillo Porcaro,
Università degli Studi di Padova, Italy

REVIEWED BY
Miriam Gade,
Medical School Berlin, Germany
Mohamed Aly,
Assiut University, Egypt
Heming Gao,
Liaoning Normal University, China

*CORRESPONDENCE
Yu Wu
wuyu1261@foxmail.com
Peng Li
lipeng@tmmu.edu.cn

SPECIALTY SECTION
This article was submitted to Brain Imaging Methods, a section of the journal Frontiers in Neuroscience

RECEIVED 05 May 2022
ACCEPTED 19 July 2022
PUBLISHED 09 August 2022

CITATION
Li Y, Huang P, Huang J, Zhong Z, Zhou S, Dong H, Xie J, Wu Y and Li P (2022) Remote ischemic preconditioning improves cognitive control in healthy adults: Evidence from an event-related potential study. *Front. Neurosci.* 16:936975.
doi: 10.3389/fnins.2022.936975

It is suggested that remote ischemic preconditioning (RIPC) may be a promising treatment for improving healthy adults' cognitive control. However, direct empirical evidence was absent. Therefore, this study aims to provide evidence for the impact of RIPC on cognitive control. Sixty healthy young male volunteers were recruited, and 30 of them received 1-week RIPC treatment (RIPC group), while the rest did not receive RIPC (control group). Their cognitive control before and after RIPC treatment was evaluated using the classic Stroop task, and the scalp electricity activity was recorded by event-related potentials (ERPs). The behavioral results showed a conventional Stroop interference effect of both reaction times (RTs) and the accuracy rate (ACC), but the Stroop interference effect of RTs significantly decreased in the posttest compared to the pretest. Furthermore, at the electrophysiological level, ERP data showed that N450 and SP for incongruent trials were larger than that for congruent trials. Importantly, the SP differential amplitude increased after RIPC treatment, whereas there was no significant change in the control group. These results implied that RIPC treatment could improve cognitive control, especially conflict resolving in the Stroop task.

KEYWORDS

remote ischemic preconditioning, cognitive control, classic Stroop task, ERPs, N450, SP

Introduction

One prominent advantage humans have over animals is that our action is intentional and not entirely driven by the environmental stimulus. The process underlying such adaptability was cognitive control (also called executive function) (Botvinick et al., 2001), which was defined as the ability to coordinate thought and behavior in accord with internally represented intentions and plans (Miller and Cohen, 2001). Substantial studies suggested that the prefrontal cortex (PFC) played a crucial role in this cognitive function (Miller and Cohen, 2001; Koechlin et al., 2003). Many neuroimaging studies confirmed that when participants accomplish tasks requiring cognitive control, their PFC was significantly activated (Braver et al., 2003; Koechlin et al., 2003; Braver, 2012). Meanwhile, results from lesion studies showed that individuals with PFC focal damage had a poor performance in tasks involving cognitive control (Miller, 2000; Gläscher et al., 2012).

Cognitive control subserves higher cognition processes, such as attention, thinking, planning, and reasoning in our daily life (Koechlin et al., 2003). Indeed, individuals with mood or behavior disorders have been proved to be deficient in cognitive control. For example, individuals with anxiety and depression disorders were more likely to be interfered with by unrelated threatening stimuli compared to non-threatening ones (Pishyar et al., 2004; Hofmann, 2007; Staugaard, 2010), which was associated with impaired cognitive control (Hallion et al., 2017). Additionally, Stewart et al. (2017) proposed that the increase in suicide behaviors among adolescents might also be related to general deficits in cognitive control, which generally did not have enough time to get mature (Luna, 2009). Therefore, a variety of psychology and clinical research was pursued to improve individuals' cognitive control. Currently, there are a variety of effective methods. For example, well-designed video game training could contribute to cognitive control in older adults (Anguera et al., 2013), and non-invasive current stimulation was also reported (Hsu et al., 2011; Jacobson et al., 2012). Interestingly, the musical experience also could enhance cognitive control (Slevc et al., 2016; Sharma et al., 2019), probably because inhibitory control and attention shift play crucial roles in playing music (Slevc et al., 2016). However, these methods might also have some deficiencies. For example, video game training might lead to addiction, especially for adolescents with immature cognitive control, and the current stimulation might not be accepted by some populations owing to its unsafety (Antal et al., 2017). Musical training is demanding, and musical instrument playing is highly professional, thus it might take a long time for individuals to get benefit from this method.

Interestingly, Sugimoto et al. (2021) recently reported that the blood flow restriction, similar to ischemic preconditioning (IPC), could improve healthy adults' cognitive control when combined with a walking train, thus proposing that the clinical IPC may be a potential treatment for improving cognitive control of healthy adults without exercise. IPC is a systemic strategy characterized by a brief episode of ischemia that renders the target organs more resistant to subsequent longer ischemic events (Murry et al., 1986). Its direct stress on target organs, such as the brain itself, however, would be more challenging and less practical than to other organs, and also lead to mechanical trauma to major vascular structures, which has limited its clinical application (Tapuria et al., 2008). As the derivative of IPC, remote ischemic preconditioning (RIPC) did not stress to target tissue directly but protected it through several transient and non-lethal limb ischemia of distant organs (Jensen et al., 2011; Moskowitz and Waeber, 2011; Zhao et al., 2017). In comparison to IPC, RIPC is inexpensive, safe, and non-invasive (Moskowitz and Waeber, 2011), which has been widely used in clinical brain injury treatment and cognitive function improvement. RIPC could protect the brain against injury caused by various diseases (Jensen et al., 2011; Zhao et al., 2018), for instance, Zhao et al. (2018) reported that RIPC could improve cerebral circulation in patients with symptomatic intracranial arterial stenosis. Additionally, RIPC also plays a critical role in protecting cognitive function after brain injury (Hudetz et al., 2015; He et al., 2017; Wang et al., 2017), for example, Wang et al. (2017) showed that RIPC alleviated cognitive function impairment in patients with the cerebral small-vessel disease.

However, to data, there is no direct evidence of the improvement of healthy adults' cognitive control through RIPC treatment, because in these existing studies, RIPC was applied to improve the cognitive control of these individuals who undergoing surgery or in special circumstances. Furthermore, these studies are very scant and their results are inconsistent (Meybohm et al., 2013, 2018; Hudetz et al., 2015; Li et al., 2020; Sugimoto et al., 2021). For instance, in the investigations by Meybohm et al. (2013, 2018), the patients who underwent a wide range of cardiac surgery accomplished a Stroop test (a test demanding cognitive control) before and after receiving the RIPC intervention (induced by four cycles of upper-limb ischemia, 5 min), aim to examine the effect of RIPC on reducing postoperative neurocognitive dysfunction, as a result, they failed to demonstrate the efficacy of a RIPC protocol on cognitive control. Hudetz et al. (2015) reported that the cognitive control tested by the Stroop task before and after surgery were not changed in individuals who both accepted and rejected the RIPC treatment (four cycles of brief upper extremity ischemia, 5 min) but found that the RIPC treatment can prevent deterioration of other short-term cognitive abilities, such as non-verbal and verbal memory. Li et al. (2020) found that the alertness but not the executive function of attention in the attentional network test (ANT) was changed by RIPC (5 min bilateral upper limbs ischemia and 5 min reperfusion for five cycles, twice a day, for 7 days) in adults unacclimatized to high altitude. In summary, except for the study by Sugimoto et al. (2021), the above four research did not observe the protective effect of RIPC on cognitive control. One of the most possible reasons was that any slight effect of RIPC was masked by the negative impact of the surgery or hypoxia itself in these studies (Meybohm et al., 2018).

The present study aimed to demonstrate the possible impact of RIPC on cognitive control, if any, which may provide an alternative treatment for improving cognitive control. To prevent the effect of RIPC that was canceled out by surgery or other factors, healthy adults were recruited and their cognitive control was measured in a normal environment. Furthermore, previous research did not find a positive effect of RIPC on cognitive control at the behavioral level (e.g., Meybohm et al., 2013, 2018; Li et al., 2020). One possible reason was that behavioral indicator, such as reaction times (RTs) and the accuracy rate (ACC) only a gross reflection of the cognitive process, which is insensitive to minor distinctions. Hence, in our study, besides behavioral data, the participants' scalps' electrical activity was also recorded via event-related potentials (ERPs). ERP reflected electrical activity locked to a specific task event or response and offered a real-time temporal resolution of neural processes for the task performance, which could be used to investigate the time course of cognitive processing (Hillyard and Anllo-Vento, 1998). Undoubtedly, ERP was a more sensitive indicator for the subtle distinction in the cognitive process than RTs and ACC.

The RIPC treatment scheme was based on previous schemes and combined with the reality of this study: four cycles of RIPC therapy were performed daily for 7 days with 5 min of bilateral upper limb ischemia (180 mm Hg) and 5 min of reperfusion (Li et al., 2020). This study adopted the classic Stroop task (Stroop, 1935) to assess participants' cognitive control before and after receiving RIPC. In the Stroop task, participants were required to name the color of the word and ignore its meaning. Under the congruent condition, words have the same color and meanings (e.g., the "red" word printed with red ink). Under the incongruent condition, the word color and meanings were different (e.g., the "red" word printed with green ink), compared with the congruent conditions, the participant's RTs would take longer and ACC would decrease to name the ink color under the incongruent conditions, known as the Stroop interference effect (MacLeod, 1991). The mechanism of the Stroop interference effect was proposed to reflect the competition between the control brain system and the automatic processing brain system (Cohen et al., 1990). Accessing the meaning of words was automatic while naming the color was controlled. Therefore, the meaning of the word was acquired preferentially than its color, leading to the conflict between the stimulus and response under the incongruent condition, so the conflict must be resolved at the cost of slowing their response (Cohen et al., 1990).

Two ERP components, N450 and sustained potential (SP) were reported in the Stroop task, which are the two markers of conflict processing (Liotti et al., 2000; West et al., 2005; Larson et al., 2009, 2014). N450 was a negative wave peaking at about 450 ms after the stimuli presentation over fronto-central electrodes (West et al., 2005). A wealth of studies showed that N450 elicited by incongruent trials was greater than that of congruent trials, reflecting the process of conflict detection (Szûcs and Soltész, 2010; Tillman and Wiens, 2011; Larson et al., 2014). ERPs source localization analysis implied that the N450 was mainly derived from the anterior cingulate cortex (ACC) (Van Veen and Carter, 2002; Hanslmayr et al., 2008). The SP was identified in the incongruent vs. congruent difference wave succeeding the N450 (Liotti et al., 2000; West and Alain, 2000; West, 2003; Lansbergen et al., 2007). SP is more positive for incongruent trials than for congruent trials or errors counterparts in the Stroop task, leading to the suggestion that the conflict SP reflects the process of conflict resolution (Liotti et al., 2000; West and Alain, 2000; West et al., 2005; Larson et al., 2009). SP was presumably generated from the dorsal lateral prefrontal cortex (dlPFC) (Lansbergen et al., 2007). In summary, these ERP findings indicated that conflict processing in the Stroop task includes conflict monitoring and resolution, represented by N450 and SP, respectively.

We hypothesize that participants' cognitive control will be enhanced after 1 week of RIPC treatment (performed once a day for 7 consecutive days, 5 min ischemia with 180 mm Hg cuff pressure, followed by 5 min reperfusion). The greater the difference between incongruent and congruent conditions of N450 and SP, the better would be conflict monitoring and resolution ability (Badzakova-Trajkov et al., 2009; Larson et al., 2014). Therefore, we predict that the enhanced cognitive control would be reflected by a larger N450 or SP differential amplitude.

Materials and methods

Participants

We used the G*power software to calculate the number of subjects needed in this study before the sample size was determined. The calculated parameters are as follows: effect size f: 0.25, α err prob: 0.05, power (1-β err prob): 0.8, number of groups: 2, and number of measurements: 4. The total sample size was calculated to be 24. Thus, a total of 60 healthy Chinese male participants were enrolled in this study. All participants were right-handed, as well as had normal or corrected vision. Additional inclusion criteria included no history of neurological or psychiatric disorders, no color weakness or color blindness, and could well tolerate RIPC. The participants were randomly divided into two groups: the RIPC group (n = 30) receiving RIPC and the control group (n = 30) without RIPC treatment. The schematic diagram of the whole procedure is shown in **Figure 1A**. Twelve participants were excluded due to excessive Electroencephalogram (EEG) artifacts or technical problems during EEG data preprocessing, leading to more than half of the ERP epochs being discarded. Finally, 20 (control group) and 28 (RIPC group) participants' behavioral and electrophysiological data were further analyzed. There was no significant difference in the age (p = 0.41),

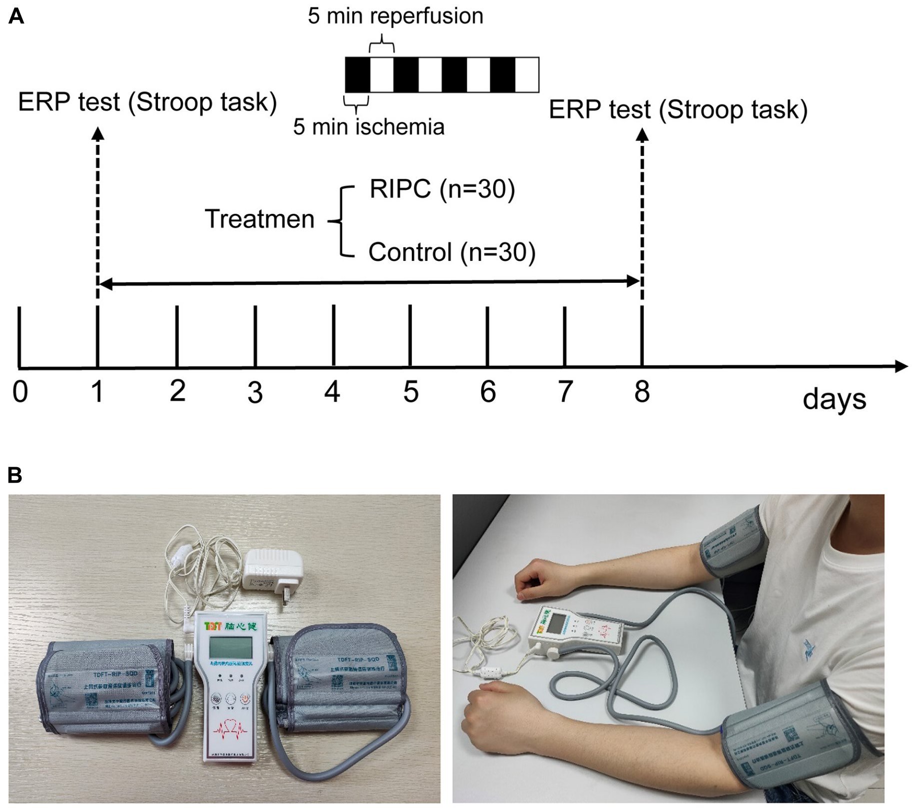

FIGURE 1
The schematic diagram of the whole procedure, RIPC device, and the usage diagram. **(A)** The Stroop task and event-related potentials (ERPs) were adopted to evaluate cognitive control ability before and after RIPC treatment. The RIPC group (*n* = 30) was assigned to accept 40 min per day for a total of 7 days of RIPC treatment, four cycles of 5 min ischemia (180 mmHg) and 5 min reperfusion were performed on the bilateral upper limb, and the control group (*n* = 30) were not accepted RIPC. **(B)** The RIPC device (left image) and how it is used (right image), the consent statement about the human image has been approved.

weight (*p* = 0.13), height (*p* = 0.24), and Body Mass Index (BMI) between the RIPC [mean age = 20.50 years, standard deviation (SD) = 1.35; mean weight = 65.48 kg, SD = 9.33; mean height = 171.35 cm, SD = 6.49; mean BMI = 22.27 kg/m^2, SD = 2.66] and control group (mean age = 20.85 years, SD = 1.53; mean weight = 62.35 kg, SD = 4.61; mean height = 169.55 cm, SD = 3.97; mean BMI = 21.71 kg/m^2, SD = 1.75). The study was approved by the Medical Ethics Committee of Army Medical University. All ethical principles were stringently followed during the entire course of the study. Moreover, all participants signed a consent form before starting the experiment.

Intervention

The RIPC treatment consisted of four cycles of bilateral upper limb ischemia for 5 min followed by reperfusion for 5 min, performed once a day for 1 week. The treatment was carried out using an automatic electric control device; the device and its usage are shown in **Figure 1B**. Limb ischemia was induced by inflating blood pressure cuffs to 180 mmHg. The Stroop task was performed before and after the RIPC treatment. In the event of discomfort or lack of tolerance, the participants could abort the RIPC process at any time. The control group underwent the same process, except without the RIPC treatment.

Stimulus and procedure

The experiment was conducted with the software E-Prime3.0. Participants were presented with the Chinese color words “红” (red), “绿” (green), and “黄” (yellow) printed in different colors on the center of the computer screen. The stimulus under the congruent condition was color words printed in the congruent ink color [e.g., “红” (red) printed in red color], and the stimulus under the incongruent condition is the same Chinese character but printed with incongruent colors [i.e., “红” (red) printed in yellow or green color], two examples of the Stroop task as shown in **Figure 2A**. The three colors (red, yellow, and green) were randomly mapped to three keys on the computer keyboard (j, k, and l). The participants were

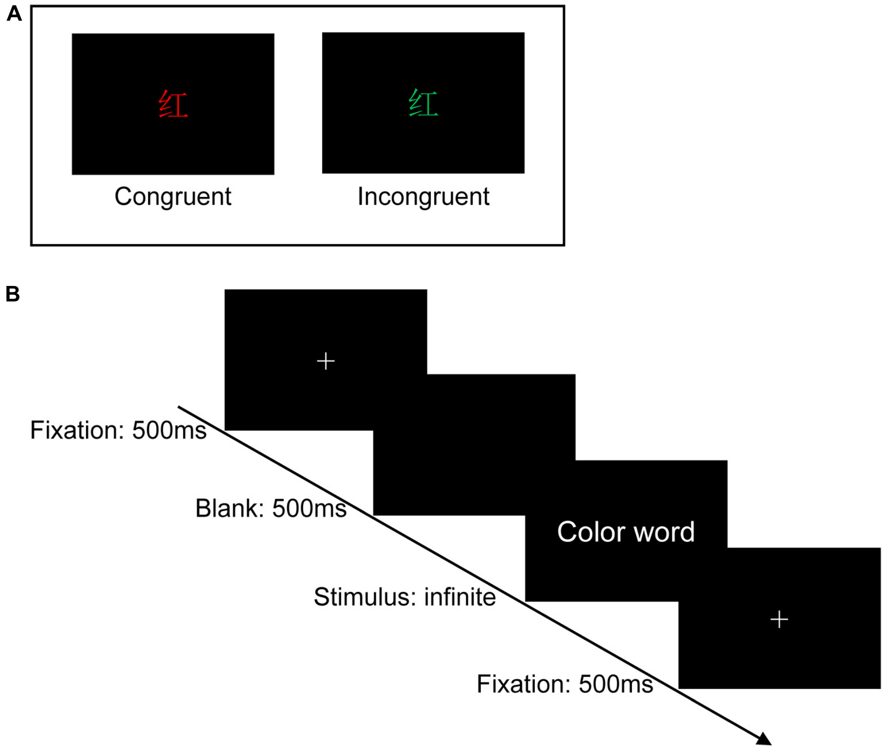

FIGURE 2
Experimental design. **(A)** Two examples of the Stroop task (Chinese character "红" means red). **(B)** Single-trial settings. During each trial, a white cross was first shown on the center of the black background for 500 ms, followed by a blank screen (500 ms), and then the color words appeared on the center of the black background, which was remained on the screen until participants pressed the specific key.

instructed to respond to the ink colors of the word and ignore its meaning by pressing one of three keys, and the responding keys were balanced between the participants.

In a dimly lit and sound-attenuated room with only the participant seated in, stimuli were presented on a 14-inch Lenovo laptop at a resolution of 1,920 × 1,080 pixels, with a refresh rate of 60 Hz. The distance between the participants and the computer monitor was 70 cm approximately. Before the formal experiment, the experimenter explained the overall process and details to the participants and required them to practice 20 trials to ensure they had fully understood the operation of the Stroop task. There are 180 trials in total in the formal Stroop task, 90 trials for the congruent condition (three kinds of stimulus, each was repeated 30 times) and 90 trials for the incongruent condition (six kinds of stimulus, each was repeated 15 times). The 180 trails were divided into three blocks and each contained 60 trials. Half of the trials were congruent and the other half were incongruent. The trials were mixed and presented in random order. During each trial, a white cross was first shown on the center of the black background for 500 ms, followed by a blank screen (500 ms), and then the color words appeared on the center of the black background, which remained on the screen until participants pressed the specific key. After accomplishing one block, each subject would have a short rest. The experiment procedure is shown in **Figure 2B**.

EEG acquisition and preprocessing

The data were recorded using a BioSemi ActiveTwo system with a 64 Ag-AgCl Active-electrode array (BioSemi B.V., Amsterdam, Netherlands; for exact position coordinates).[1] These coordinates were converted into the extended international 10–20 system, and electrode offsets were kept below 50 mV during recording, with a sampling frequency of 1,024 Hz.

EEG data analyses were performed in MATLAB (R2019b, The MathWorks, Inc., Natick, United States) with custom-made scripts supported by EEGLAB (Delorme and Makeig, 2004). Continuous EEG data were down-sampled to 500 Hz, re-referenced offline to the average of the activity recorded at the whole brain, and were then digitally band-pass filtered at 0.1–40 Hz, then the data were segmented to epochs from −1,000 to 2,000 ms around the target onset. The average value in the 200-ms time window preceding stimulus onset was used for

---

[1] http://www.biosemi.com/headcap.htm

baseline correction. First, all errors and extreme epochs (RTs exceeding ± 3 SD of mean) were excluded. Next, independent component analysis (ICA) was computed to isolate artifacts in the EEG signal using the logistic infomax ICA algorithm in the runica function of EEGLAB. Independent components representing eye blinks and movements, muscle artifacts, or other types of noise automatically identified by IClabel plugins in EEGLAB were removed from the data (Pion-Tonachini et al., 2019). Finally, the preprocessed EEG data were re-examined visually to ensure that significant artifacts were removed and at least 60 trials were available for each subject. The mean number of trials in each condition after excluding all artifacts as follows: congruent condition in pretest (Control vs. RIPC = 68 vs. 77), incongruent condition in pretest (Control vs. RIPC = 69 vs. 79), congruent condition in posttest (Control vs. RIPC = 69 vs. 80), and incongruent condition in posttest (Control vs. RIPC = 71 vs. 78).

Data analysis

For the behavioral data, these trials of errors and RTs exceeding ± 3 SD of mean were first excluded. Next, a three-way repeated measure ANOVA was done for ACC and RTs, using the group (Control/RIPC) as a between-subject variable, time (Pretest/Posttest), and condition (Congruent/Incongruent) as the within-subjects variable. Then, we calculated the Stroop interference effect of ACC and RTs for each participant, which was defined as the difference between congruent and incongruent conditions separately (MacLeod, 1991). Subsequently, a 2 (group: Control/RIPC) × 2 (time: Pretest/Posttest) repeated measures ANOVA was done for the Stroop interference effect of ACC and RTs, using the group as a between-subject variable and time as a within-subjects variable.

For the ERP data, we combined our grand average ERP waveforms and topographical map with previous studies to select the measure time window and region of interest (ROI) for calculating the amplitude of each component. The ROI of the N450 component was selected as fronto-central including FCz, FC1, FC2, and Cz electrodes (Tillman and Wiens, 2011), and the mean amplitude of N450 between 400 and 600 ms was calculated by averaging these electrodes. For the SP component, the ROI was selected as the parietal region, where was reported record the maximal conflict SP amplitudes (Larson et al., 2009), including Pz, P1, P2, P3, and P4 electrodes, and SP were computed as mean amplitude in the time window of 600–1,000 ms after these electrodes were averaged. We performed a 2 (group: Control/RIPC) × 2 (time: Pretest/Posttest) × 2 (condition: Congruent/Incongruent) repeated measures ANOVA for each component, using the group as a between-subject variable and time and condition as the within-subjects variable.

All statistical analyses were performed using the SPSS, 28.0 version. A two-tailed significance level of 0.05 was used for all statistical tests and p-values were corrected for sphericity assumption violations using the Greenhouse-Geisser correction, and partial eta-squared (η_p^2) was calculated to describe effect sizes.

Results

Behavioral results

The raw data of ACC and RTs in each condition/group are presented in **Table 1**.

For a three-way repeated measure ANOVA of ACC, only the main effect of congruency reached significance, $F(1,46) = 13.96$, $p < 0.001$, $\eta_p^2 = 0.23$, showing that participants' ACC was higher for congruent trials than for incongruent trials. The main effect of time, $F(1,46) = 0.38$, $p = 0.54$, $\eta_p^2 < 0.01$, the two-way interactions of time by group [$F(1,46) = 0.11$, $p = 0.74$, $\eta_p^2 < 0.01$], condition by group [$F(1,46) = 1.51$, $p = 0.23$, $\eta_p^2 = 0.03$] and time by condition [$F(1,46) = 0.02$, $p = 0.90$, $\eta_p^2 < 0.001$], and the three-way interaction of group by time by condition [$F(1,46) < 0.01$, $p = 0.96$, $\eta_p^2 < 0.001$] were not significant. For the Stroop interference effect of ACC, the main effects of time [$F(1,46) = 0.02$, $p = 0.90$, $\eta_p^2 < 0.001$] and group [$F(1,46) = 1.51$, $p = 0.23$, $\eta_p^2 = 0.03$], the two-way interaction of time by group [$F(1,46) < 0.01$, $p = 0.95$, $\eta_p^2 < 0.001$] was not significant, as shown in **Figure 3A**.

For a three-way repeated measures ANOVA of RTs, main effects of both time [$F(1,46) = 19.60$, $p < 0.001$, $\eta_p^2 = 0.30$] and condition [$F(1,46) = 102.59$, $p < 0.001$, $\eta_p^2 = 0.69$] were discovered. For the time effect, participants responded faster to the ink color of words in the posttest (710.36 ms) than to the pretest (789.77 ms). Furthermore, for the condition effect, participants' RTs for incongruent trials (813.91 ms) were longer than that for congruent trials (686.22 ms). There was also a two-way interaction of time and condition, $F(1,46) = 15.11$, $p < 0.001$, $\eta_p^2 = 0.25$, and further simple effects analysis showed participants responded more slowly to incongruent trials (pretest: 715.73 ms, posttest: 656.71 ms) than to congruent trials (pretest: 863.81 ms, posttest: 764.01 ms), but this difference was smaller in the posttest (107.30 ms) than that in the pretest (148.08 ms). The two-way interactions of time by group [$F(1,46) = 0.79$, $p = 0.38$, $\eta_p^2 = 0.02$], condition by group [$F(1,46) = 2.07$, $p = 0.16$, $\eta_p^2 = 0.04$], and the three-way interaction of group by time by condition [$F(1,46) = 1.41$, $p = 0.24$, $\eta_p^2 = 0.03$] were not significant.

For the Stroop interference effect of RTs, the main effect of time was significant, $F(1,46) = 19.60$, $p < 0.001$, $\eta_p^2 = 0.30$, indicating that the interference effect of RTs decreased in the posttest (107.30 ms) compared to the pretest (148.08 ms). The main effect of the group [$F(1,46) = 2.07$, $p = 0.16$, $\eta_p^2 = 0.04$] and interaction of time by group [$F(1,46) = 1.41$, $p = 0.24$, $\eta_p^2 = 0.03$] were not significant (**Figure 3B**).

TABLE 1 The raw behavioral data in pretest and posttest of control and RIPC group.

Behavioral data	Group	Pretest (M ± SD)		Posttest (M ± SD)	
		Congruent	Incongruent	Congruent	Incongruent
ACC (%)	Control (n = 20)	97.17 ± 2.92	96.11 ± 3.41	97.61 ± 2.82	96.67 ± 3.28
	RIPC (n = 28)	97.90 ± 2.04	95.48 ± 4.18	98.02 ± 1.82	95.56 ± 4.11
RTs (ms)	Control (n = 20)	714.05 ± 154.05	839.11 ± 169.41	629.98 ± 97.97	727.22 ± 102.32
	RIPC (n = 28)	717.41 ± 164.12	888.51 ± 268.26	683.44 ± 142.93	800.80 ± 207.71

Values are presented as mean ± SD; n, number of participants; ACC, the accuracy rate; RTs, reaction times; Pretest, before treatment; Posttest, immediately after treatment.

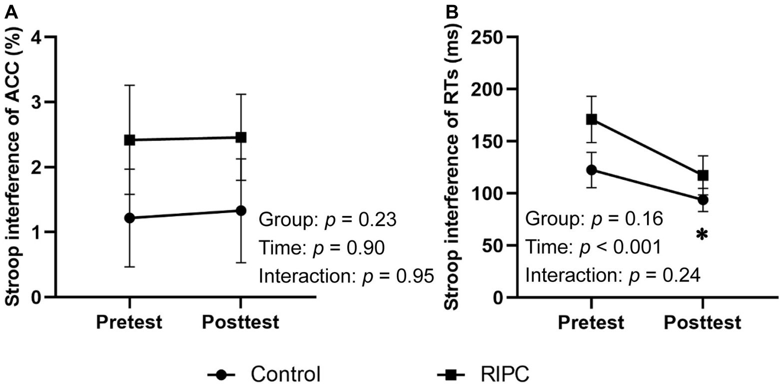

FIGURE 3

Behavioral results of two groups. **(A)** Stroop interference effect of ACC. **(B)** Stroop interference effect of RTs. Error bar represents the stand error; ACC, the accuracy rate; RTs, reaction times; Pretest, before treatment; Posttest, immediately after treatment. *Significant difference ($P < 0.001$) between time points.

Event-related potential results

N450

For the N450, there was only a main effect of condition, $F(1,46) = 4.17$, $p < 0.05$, $\eta_p^2 = 0.08$, indicating that N450 induced by incongruent trials (–0.68 μV) was greater than that by congruent trials (−0.44 μV), as shown in Figure 4A. Figure 4B shows other main effects and interactions were not significant, demonstrating that the N450 difference wave (incongruent minus congruent) was comparable between pretest and posttest in the control (–0.29 vs. –0.15 μV) and the RIPC (–0.17 vs. –0.34 μV) group. The main effect of time, $F(1,46) = 0.64$, $p = 0.43$, $\eta_p^2 = 0.01$; the two-way interactions of time by group [$F(1,46) = 0.03$, $p = 0.86$, $\eta_p^2 = 0.001$], condition by group [$F(1,46) = 0.04$, $p = 0.85$, $\eta_p^2 = 0.001$] and time by condition [$F(1,46) = 0.02$, $p = 0.90$, $\eta_p^2 < 0.001$], and the two-way interaction of group by time by condition [$F(1,46) = 1.08$, $p = 0.30$, $\eta_p^2 = 0.02$] were not significant.

Sustained potential

For the SP, the main effect of the condition was found, $F(1,46) = 52.18$, $p < 0.001$, $\eta_p^2 = 0.53$, SP produced by incongruent trials (1.49 μV) was larger than congruent trials (0.67 μV), as shown in Figure 5A. Importantly, the three-way interaction of the group, time and the condition was significant, $F(1,46) = 4.86$, $p = 0.03$, $\eta_p^2 = 0.10$. Further simple effects analysis showed that, for the control group, the SP amplitude was larger for incongruent trials than for congruent trials in both pretest (1.93 vs. 0.97 μV, $p < 0.001$) and posttest (1.66 vs. 0.98 μV, $p < 0.01$). The amplitude of SP differential wave (incongruent minus congruent) was comparable between the pretest (0.96 μV) and posttest (0.68 μV). The RIPC group was the same as the control group, and the SP for incongruent trials was larger than that for congruent trials at both pretest (1.32 vs. 0.76 μV, $p = 0.001$) and posttest (1.03 vs. −0.04 μV, $p < 0.001$). However, the amplitude of the SP differential wave was enlarged at the posttest (1.06 μV) compared to the pretest (0.57 μV, $p = 0.03$), as shown in Figure 5B. The main effect of time, $F(1,46) = 1.69$, $p = 0.20$, $\eta_p^2 = 0.04$; the two-way interactions of time by group [$F(1,46) = 0.66$, $p = 0.42$, $\eta_p^2 = 0.01$], condition by group [$F(1,46) = 0.001$, $p = 0.98$, $\eta_p^2 < 0.001$] and time by condition [$F(1,46) = 0.40$, $p = 0.53$, $\eta_p^2 < 0.01$] were not significant.

Correlation analysis

We further compute the Pearson relation between the interference effects of RTs and ACC and SP differential

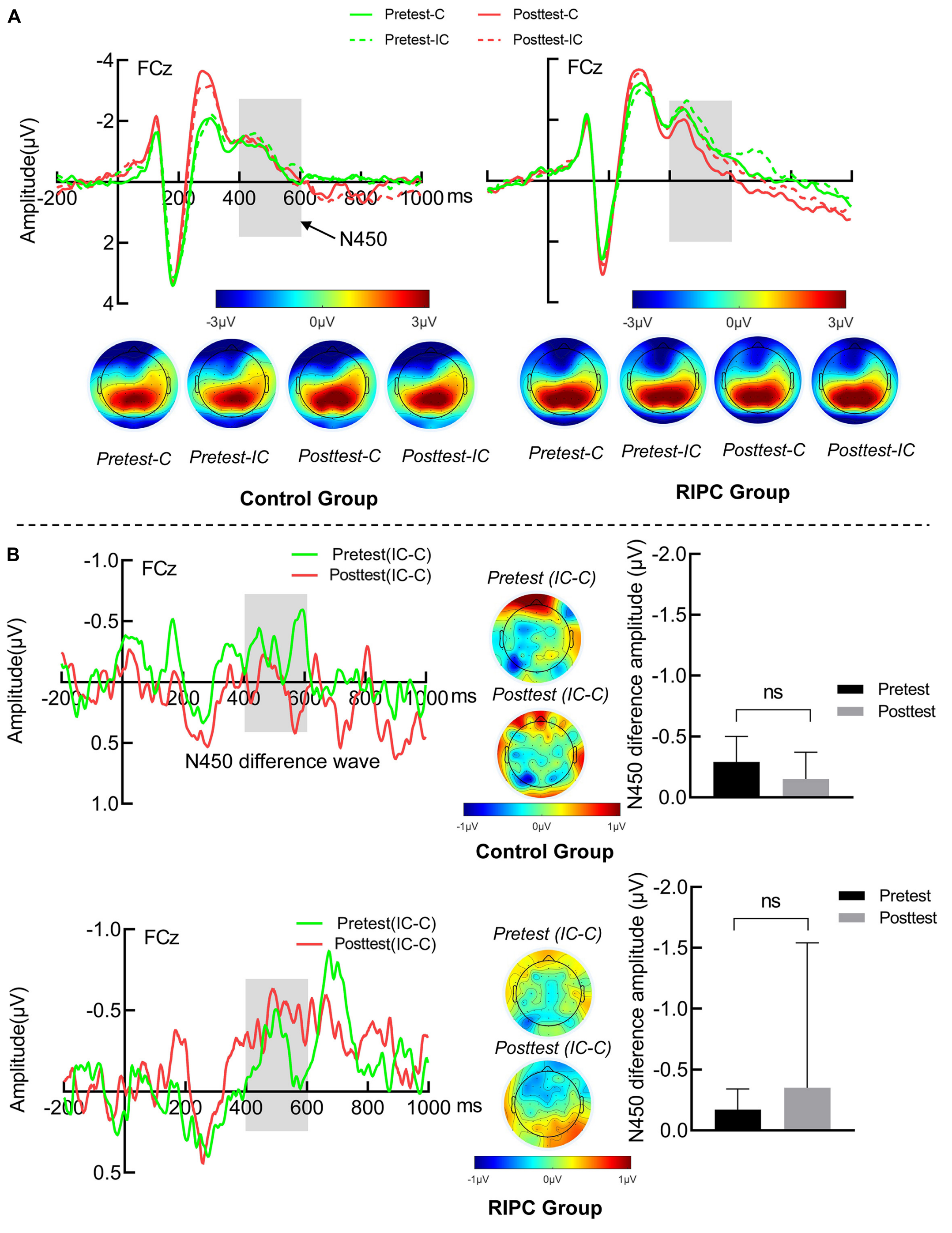

FIGURE 4
(A) The N450 grand average waveform (FCz) and topographical map of two groups. **(B)** The averaged difference wave and topographical map of N450 in two groups. The dark gray rectangles represent the measure time window of N450. Error bar represents the stand error; Pretest: before treatment, Posttest: immediately after treatment. C: Congruent, IC: Incongruent, IC-C: Incongruent minus Congruent. ns, no significance between the average difference wave of pretest and posttest.

amplitude (incongruent minus congruent), respectively, for the RIPC group. The results showed that in the pretest, the interference effects of ACC were negatively related to SP differential amplitude, r (28) = –0.46, p = 0.01, that is, the larger the differential SP amplitude, the smaller the interference effects of ACC (see Figure 6). Other relationships were not significant. In the pretest, RTs: r (28) = 0.19, p = 0.33; in the posttest, RTs: r (28) = –0.34, p = 0.08, ACC: r (28) = –0.27, p = 0.17.

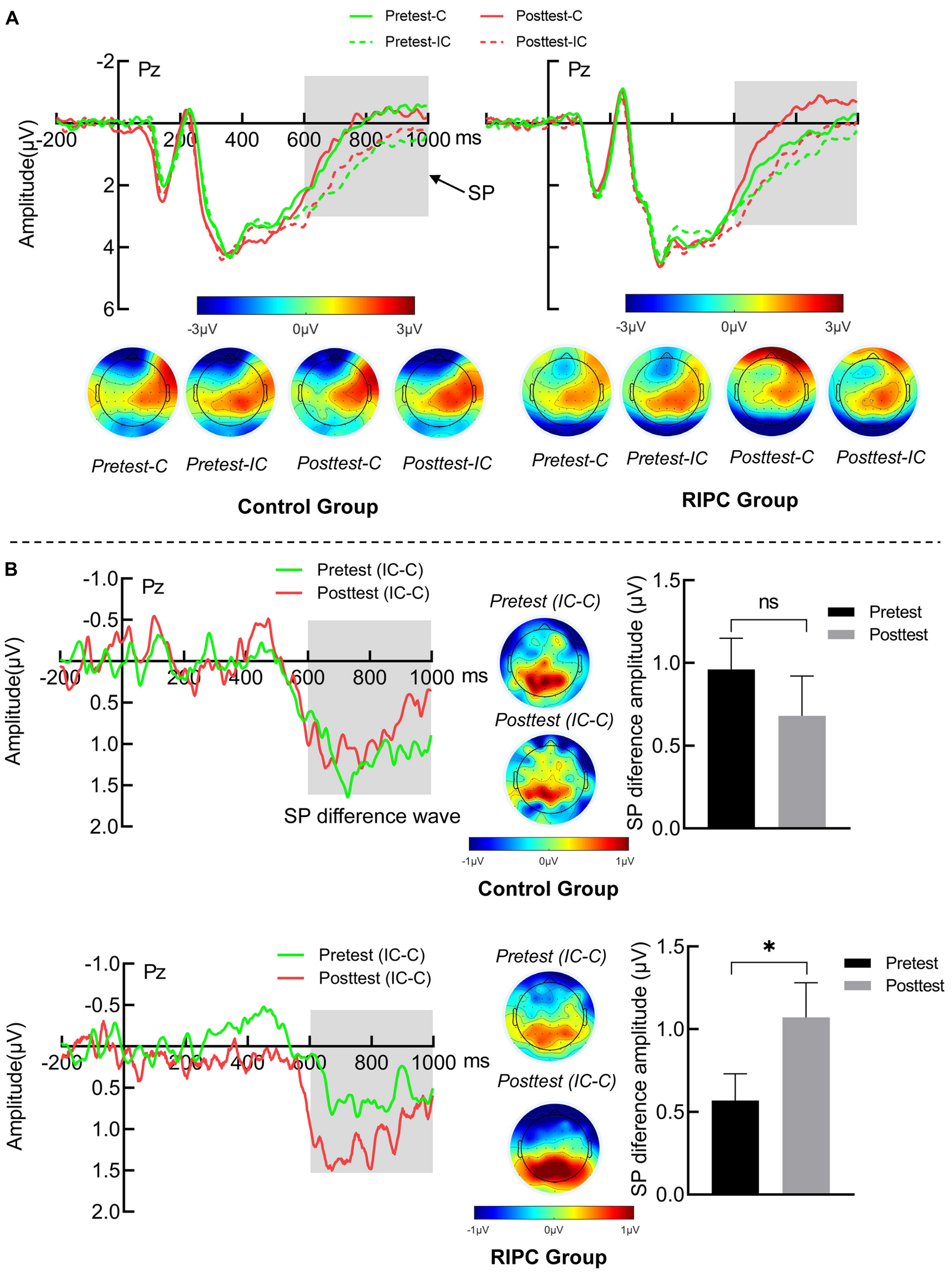

FIGURE 5
(A) The SP grand average waveform (Pz) and topographical map of two groups. **(B)** The averaged difference wave and topographical map of SP in two groups. The dark gray rectangles represent the measure time window of SP. Error bar represents the stand error; Pretest: before treatment, Posttest: immediately after treatment. C: Congruent, IC: Incongruent, IC-C: Incongruent minus Congruent. ns, no significance between the average difference wave of pretest and posttest. *Significant difference ($P < 0.05$) between the average difference wave of pretest and posttest.

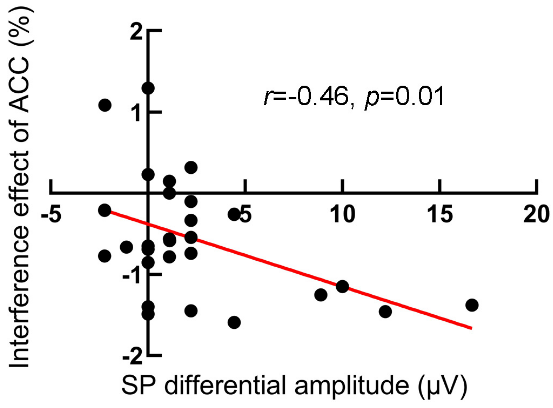

FIGURE 6
The scatter plot of the relationship between the interference effect of ACC and SP differential amplitude in the pretest for the RIPC group. The larger the differential SP amplitude, the smaller the interference effects of ACC.

Discussion

Few studies suggested nearly no effect of RIPC on cognitive control of clinical patients or individuals in a special environment (e.g., Meybohm et al., 2013, 2018; Li et al., 2020). However, it remains uncertain whether healthy adults' cognitive control could benefit from this treatment, although Sugimoto et al. (2021) proposed that the RIPC may be a potential treatment for improvement of this cognitive ability. Therefore, in the research, we seek empirical evidence of RIPC improving the cognitive control of healthy adults through the classic Stroop task and the ERP technique. To the best of our knowledge, this is the first research to evaluate the effect of the RIPC treatment on healthy individuals' cognitive control using the ERP marker (perform 40 min per day for 7 days, 5 min 180 mm Hg ischemia, and 5 min reperfusion on a bilateral upper limb for four cycles). Behaviorally, participants' RTs were longer and ACC was lower under the incongruent condition than under the congruent condition, indicating the phenomenon of the Stroop interference effect. In addition, compared with the pretest, the Stroop interference effect of RTs was reduced in the posttest. At the electrophysiological level, we mainly focused on the N450 and SP components, which indexed the conflict detection and resolution in the Stroop task respectively. Our ERP data showed that both N450 and SP elicited by incongruent trials were larger than those by congruent trials. Importantly, the SP differential amplitude between incongruent and congruent trials increased after participants received RIPC treatment compared with before RIPC, but this effect was not found in the control group.

The current behavioral data were consistent with previous studies of the Stroop effect (MacLeod, 1991; Hershman and Henik, 2019). When the ink color and meanings of words were incongruent, participants had to withhold accessing the meaning of words to overcome the conflict at the cost of slower response and reduced accuracy if they failed. Additionally, the response time was shortened and the interference effect from incongruent trials was reduced in the posttest compared with the pretest, which might be related to the extensive practice. Indeed, many previous Stroop studies also showed a reduction in the Stroop interference effect after participants extensively practice (MacLeod, 1991; Dulaney and Rogers, 1994; Davidson et al., 2003). However, we also should consider the effect of RIPC treatment on the interference effect reduction in the RIPC group. In this study, we included a control group that kept the same as the RIPC group in all aspects possible except for not receiving RIPC treatment. Thus, although it was difficult to solely distinguish the effect of practice and RIPC treatment on the Stroop interference reduction for the RIPC group. The difference in reduced interference effects between the two groups should be accounted for by the RIPC treatment because the practice effect actually would exist in the two groups in the meanwhile. This inference was indirectly supported by the results that, the magnitude of the reduced interference effect of RTs in the RIPC group (53.74 ms) was larger than that in the control group (27.81 ms), though this difference was not statistically significant.

Event-related potential data provide a window to observe the time course of the conflict processing in the Stroop task. Our electrophysiological data showed that the N450 amplitude of incongruent trials was larger than that of congruent trials, consistent with the previous work (West, 2003, 2004; Tillman and Wiens, 2011; Szűcs and Soltész, 2012). N450 was thought to be involved in the stimulus or response conflict monitoring processes (Lansbergen et al., 2007), so our N450 results suggested that participants perceived the conflict between the color and the meaning in incongruent trials. For the SP component, in line with the previous study (Liotti et al., 2000; Lansbergen et al., 2007), incongruent trials produced larger SP than congruent trials in the present study, representing the subsequent conflict solution stage or attentional control after conflict detection (West et al., 2005; Larson et al., 2009, 2014). More importantly, RIPC modulated the SP difference between congruent and incongruent trials, that is, the SP differential amplitude increased after RIPC treatment. But it is important to note that this result could not be interpreted by practice effects, as the same change did not occur in the control group. The enhanced SP difference has been associated with stronger conflict-resolving ability. For instance, individuals with schizophrenia had weaker cognitive control compared with healthy participants, which resulted in a smaller SP difference wave (McNeely et al., 2003). This viewpoint was also supported by the present study showing that increased SP differential amplitude between incongruent and congruent trials was associated with decreased interference effect of ACC in the pretest, indicating that the better conflict resolution, the less probability of responsive incorrect. In the posttest, although there was also a tendency for the interference effect of RTs and ACC to be negatively related to SP differential amplitude, but did not reach a significant level. This could be due to several factors, including the possibility that behavioral data reflect intermediate processes not necessarily reflected in the short-latency ERP component (Cacioppo and Tassinary, 1990). Taken together, combining the SP with the N450 results, we concluded that RIPC treatment might improve healthy adults' ability to resolve but not monitor the conflict in the Stroop task.

Our data were also compatible with previous studies showing that RIPC treatment did not improve cognitive control at the behavioral level (Meybohm et al., 2013, 2018; Hudetz et al., 2015; Li et al., 2020; Sugimoto et al., 2021). For example, the executive function of attention in unacclimatized healthy adults both exposed to high altitudes and in the plain was not improved after accepted RIPC (Li et al., 2020). The behavioral performance of surgical patients treated with and without RIPC was comparable in the Stroop task (e.g., Hudetz et al., 2015; Meybohm et al., 2018). However, in our study, the positive effect of RIPC on cognitive control was confirmed by the electrophysiological marker (SP), suggesting that RIPC improved individuals' conflict resolution ability. Therefore, the zero effect of RIPC on cognitive control in the present and previous studies might be due to behavioral indicators could not effectively capture the time course of conflict processing. The findings indicated that electrophysiological recordings were more sensitive to probing the subtle difference in the cognitive process than behavioral indicators.

Remote ischemic preconditioning is an inexpensive and non-invasive technique to alleviate brain and cognitive function impairment, operation of which is safe and simple, thus having good clinical application prospects (Moskowitz and Waeber, 2011). In addition to cognitive training methods such as game interventions, current stimulation, and music training, we offered PIRC as a potentially more promising option for individuals who required strong cognitive control or needed cognitive protection. Especially, some populations with emotional or behavioral disorders, such as cohorts with depression tendency and adolescents or elderly people who possess low cognitive control could use RIPC to improve cognitive control. Nonetheless, the physiological mechanism by which RIPC protects cognitive function had not been extensively recognized. For example, some authors hypothesized that biological factors such as bradykinin, adenosine, nitric oxide/calcitonin gene-related peptide, opioids, or endocannabinoids released by remote tissues can be carried via circulation to the target organ (Moskowitz and Waeber, 2011). Some authors also proposed that suppression of proinflammatory genes might be a candidate mechanism for the protective effect of RIPC on brain function (Konstantinov et al., 2004; He et al., 2017). Li et al. (2020) interpreted the effect of RIPC on alerting function of attention as improved brain microcirculation. The neural generator of SP was located in the frontal cortex (West, 2003; Lansbergen et al., 2007); thus, we speculated that the mechanism of facilitating the conflict resolution in the Stroop task may be the improved frontal microcirculation by RIPC treatment. Actually, this inference got supported to some extent by previous findings, for example, Ma et al. (2016) reported that RIPC treatment could protect ketamine-induced neuroapoptosis in the frontal cerebral cortex. A recent study by Oh et al. (2017) revealed that RIPC could increase cerebral oxygenation of the frontal lobe. However, the mechanism of this cognitive promotion should be further defined accurately in the future, by collecting and analyzing more physiological indicators such as blood and neurotransmitter before and after RIPC treatment.

Other limitations of this study should also be addressed. First, at the behavioral level, the effects of practice and RIPC treatment on the Stroop interference effect of RTs were mixed, which made it difficult to quantify the real effect of RIPC treatment on cognitive control. In the future, this problem can be avoided to some extent by using different tasks but involving in the same cognitive process of conflict processing, such as the Stroop and flanker task in pretest and posttest respectively (Eriksen and Eriksen, 1974; Tillman and Wiens, 2011), or decrease the presentation probability of incongruent trials to weak the practice effects. Second, the sample size was small, and all participants were non-clinical individuals. It remained unclear whether the results could be used to guide the clinic therapy. Thus, it was necessary to recruit clinical populations with impaired cognitive control such as individuals with attention deficit hyperactivity disorder (ADHD) and autism to extend our conclusion. Third, the participants were all young men, so the effects of gender and age should be considered. Finally, further study was necessary to explore a possibly better RIPC treatment program to protect cognitive control, given the effect of RIPC was not reflected in behavioral performance.

Conclusion

To sum up, in this study, we examined the effect of RIPC treatment on healthy adults' cognitive control. We conclude that healthy adults' cognitive control especially the conflict resolving in the Stroop task could be improved by RIPC treatment, which is reflected in the increase of SP component at the electrophysiological level. In the future, the RIPC could be an alternative treatment for improving healthy adults' cognitive control, meanwhile, the researcher also should further investigate the exact physiological mechanism of RIPC's protective effect on cognitive control, and other populations, such as individuals with ADHD and autism, should be included.

Data availability statement

The raw data supporting the conclusions of this article will be made available by the authors, without undue reservation.

Ethics statement

The studies involving human participants were reviewed and approved by the Medical Ethics Committee of Army Medical University. The patients/participants provided their written informed consent to participate in this study.

Author contributions

PL and YW conceived the idea for the study, supervised the RIPC treatment, and approved the version to be published. YL designed the experiment and wrote the manuscript. JH, PH, and ZZ revised the manuscript. YL, YW, JH, PH, SZ, HD, ZZ, and JX performed and obtained the data. YL and JH analyzed the data and drew the figures. All authors have approved its submission and publication.

Funding

This work was supported by the National Natural Science Foundation of China (Grant numbers: 41977403 and 82001992).

Conflict of interest

The authors declare that the research was conducted in the absence of any commercial or financial relationships that could be construed as a potential conflict of interest.

Publisher's note

References

Anguera, J. A., Boccanfuso, J., Rintoul, J. L., Al-Hashimi, O., Faraji, F., Janowich, J., et al. (2013). Video game training enhances cognitive control in older adults. *Nature* 501, 97–101. doi: 10.1038/nature12486

Antal, A., Alekseichuk, I., Bikson, M., Brockmöller, J., Brunoni, A. R., Chen, R., et al. (2017). Low intensity transcranial electric stimulation: Safety, ethical, legal regulatory and application guidelines. *Clin. Neurophysiol.* 128, 1774–1809. doi: 10.1016/j.clinph.2017.06.001

Badzakova-Trajkov, G., Barnett, K. J., Waldie, K. E., and Kirk, I. J. (2009). An ERP investigation of the Stroop task: The role of the cingulate in attentional allocation and conflict resolution. *Brain Res.* 1253, 139–148. doi: 10.1016/j.brainres.2008.11.069

Botvinick, M. M., Braver, T. S., Barch, D. M., Carter, C. S., and Cohen, J. D. (2001). Conflict monitoring and cognitive control. *Psychol. Rev.* 108:624. doi: 10.1037/0033-295X.108.3.624

Braver, T. S. (2012). The variable nature of cognitive control: A dual mechanisms framework. *Trends Cogn. Sci.* 16, 106–113. doi: 10.1016/j.tics.2011.12.010

Braver, T. S., Reynolds, J. R., and Donaldson, D. I. (2003). Neural mechanisms of transient and sustained cognitive control during task switching. *Neuron* 39, 713–726. doi: 10.1016/S0896-6273(03)00466-5

Cacioppo, J. T., and Tassinary, L. G. (1990). Inferring psychological significance from physiological signals. *Am. Psychol.* 45:16. doi: 10.1037/0003-066X.45.1.16

Cohen, J. D., Dunbar, K., and McClelland, J. L. (1990). On the control of automatic processes: A parallel distributed processing account of the Stroop effect. *Psychol. Rev.* 97:332. doi: 10.1037/0033-295X.97.3.332

Davidson, D. J., Zacks, R. T., and Williams, C. C. (2003). Stroop interference, practice, and aging. *Aging Neuropsychol. Cogn.* 10, 85–98. doi: 10.1076/anec.10.2.85.14463

Delorme, A., and Makeig, S. (2004). EEGLAB: An open source toolbox for analysis of single-trial EEG dynamics including independent component analysis. *J. Neurosci. Methods* 134, 9–21. doi: 10.1016/j.jneumeth.2003.10.009

Dulaney, C. L., and Rogers, W. A. (1994). Mechanisms underlying reduction in Stroop interference with practice for young and old adults. *J. Exp. Psychol.* 20:470. doi: 10.1037/0278-7393.20.2.470

Eriksen, B. A., and Eriksen, C. W. (1974). Effects of noise letters upon the identification of a target letter in a nonsearch task. *Percept. Psychophys.* 16, 143–149. doi: 10.3758/BF03203267

Gläscher, J., Adolphs, R., Damasio, H., Bechara, A., Rudrauf, D., Calamia, M., et al. (2012). Lesion mapping of cognitive control and value-based decision making in the prefrontal cortex. *Proc. Natl. Acad. Sci. U.S.A.* 109, 14681–14686. doi: 10.1073/pnas.1206608109

Hallion, L. S., Tolin, D. F., Assaf, M., Goethe, J., and Diefenbach, G. J. (2017). Cognitive control in generalized anxiety disorder: Relation of inhibition impairments to worry and anxiety severity. *Cogn. Ther. Res.* 41, 610–618. doi: 10.1007/s10608-017-9832-2

Hanslmayr, S., Pastötter, B., Bäuml, K.-H., Gruber, S., Wimber, M., and Klimesch, W. (2008). The electrophysiological dynamics of interference during the Stroop task. *J. Cogn. Neurosci.* 20, 215–225. doi: 10.1162/jocn.2008.20020

He, Z., Xu, N., and Qi, S. (2017). Remote ischemic preconditioning improves the cognitive function of elderly patients following colon surgery: A randomized clinical trial. *Medicine* 96:e6719. doi: 10.1097/MD.0000000000006719

Hershman, R., and Henik, A. (2019). Dissociation between reaction time and pupil dilation in the Stroop task. *J. Exp. Psychol.* 45:1899. doi: 10.1037/xlm0000690

Hillyard, S. A., and Anllo-Vento, L. (1998). Event-related brain potentials in the study of visual selective attention. *Proc. Natl. Acad. Sci. U.S.A.* 95, 781–787. doi: 10.1073/pnas.95.3.781

Hofmann, S. G. (2007). Cognitive factors that maintain social anxiety disorder: A comprehensive model and its treatment implications. *Cogn. Behav. Ther.* 36, 193–209. doi: 10.1080/16506070701421313

Hsu, T.-Y., Tseng, L.-Y., Yu, J.-X., Kuo, W.-J., Hung, D. L., Tzeng, O. J., et al. (2011). Modulating inhibitory control with direct current stimulation of the superior medial frontal cortex. *Neuroimage* 56, 2249–2257. doi: 10.1016/j.neuroimage.2011.03.059

Hudetz, J. A., Patterson, K. M., Iqbal, Z., Gandhi, S. D., and Pagel, P. S. (2015). Remote ischemic preconditioning prevents deterioration of short-term postoperative cognitive function after cardiac surgery using cardiopulmonary bypass: Results of a pilot investigation. *J. Cardiothoracic Vasc. Anesth.* 29, 382–388. doi: 10.1053/j.jvca.2014.07.012

Jacobson, L., Ezra, A., Berger, U., and Lavidor, M. (2012). Modulating oscillatory brain activity correlates of behavioral inhibition using transcranial direct current stimulation. *Clin. Neurophysiol.* 123, 979–984. doi: 10.1016/j.clinph.2011.09.016

Jensen, H. A., Loukogeorgakis, S., Yannopoulos, F., Rimpiläinen, E., Petzold, A., Tuominen, H., et al. (2011). Remote ischemic preconditioning protects the brain against injury after hypothermic circulatory arrest. *Circulation* 123, 714–721. doi: 10.1161/CIRCULATIONAHA.110.986497

Koechlin, E., Ody, C., and Kouneiher, F. (2003). The architecture of cognitive control in the human prefrontal cortex. *Science* 302, 1181–1185. doi: 10.1126/science.1088545

Konstantinov, I. E., Arab, S., Kharbanda, R. K., Li, J., Cheung, M. M., Cherepanov, V., et al. (2004). The remote ischemic preconditioning stimulus modifies inflammatory gene expression in humans. *Physiol. Genomics* 19, 143–150. doi: 10.1152/physiolgenomics.00046.2004

Lansbergen, M. M., van Hell, E., and Kenemans, J. L. (2007). Impulsivity and conflict in the Stroop task: An ERP study. *J. Psychophysiol.* 21, 33–50. doi: 10.1027/0269-8803.21.1.33

Larson, M. J., Clayson, P. E., and Clawson, A. (2014). Making sense of all the conflict: A theoretical review and critique of conflict-related ERPs. *Int. J. Psychophysiol.* 93, 283–297. doi: 10.1016/j.ijpsycho.2014.06.007

Larson, M. J., Kaufman, D. A., and Perlstein, W. M. (2009). Neural time course of conflict adaptation effects on the Stroop task. *Neuropsychologia* 47, 663–670. doi: 10.1016/j.neuropsychologia.2008.11.013

Li, S., Han, C., Asmaro, K., Quan, S., Li, M., Ren, C., et al. (2020). Remote ischemic conditioning improves attention network function and blood oxygen levels in unacclimatized adults exposed to high altitude. *Aging Disease* 11:820. doi: 10.14336/AD.2019.0605

Liotti, M., Woldorff, M. G., Perez, R. III, and Mayberg, H. S. (2000). An ERP study of the temporal course of the Stroop color-word interference effect. *Neuropsychologia* 38, 701–711. doi: 10.1016/S0028-3932(99)00106-2

Luna, B. (2009). Developmental changes in cognitive control through adolescence. *Adv. Child Dev. Behav.* 37, 233–278. doi: 10.1016/S0065-2407(09)03706-9

Ma, W., Cao, Y. Y., Qu, S., Ma, S. S., Wang, J. Z., Deng, L. Q., et al. (2016). Remote ischemic preconditioning provides neuroprotection: Impact on ketamine-induced neuroapoptosis in the developing rat brain. *Eur. Rev. Med. Pharmacol. Sci.* 20, 4972–4979.

MacLeod, C. M. (1991). Half a century of research on the Stroop effect: An integrative review. *Psychol. Bull.* 109:163. doi: 10.1037/0033-2909.109.2.163

McNeely, H. E., West, R., Christensen, B. K., and Alain, C. (2003). Neurophysiological evidence for disturbances of conflict processing in patients with schizophrenia. *J. Abnorm. Psychol.* 112:679. doi: 10.1037/0021-843X.112.4.679

Meybohm, P., Kohlhaas, M., Stoppe, C., Gruenewald, M., Renner, J., Bein, B., et al. (2018). RIPHeart (Remote Ischemic Preconditioning for Heart Surgery) Study: Myocardial Dysfunction, Postoperative Neurocognitive Dysfunction, and 1 Year Follow-Up. *J. Am. Heart Assoc.* 7:e008077. doi: 10.1161/JAHA.117.008077

Meybohm, P., Renner, J., Broch, O., Caliebe, D., Albrecht, M., Cremer, J., et al. (2013). Postoperative neurocognitive dysfunction in patients undergoing cardiac surgery after remote ischemic preconditioning: A double-blind randomized controlled pilot study. *PLoS One* 8:e64743. doi: 10.1371/journal.pone.0064743

Miller, E. K. (2000). The prefontral cortex and cognitive control. *Nat. Rev. Neurosci.* 1, 59–65. doi: 10.1038/35036228

Miller, E. K., and Cohen, J. D. (2001). An integrative theory of prefrontal cortex function. *Annu. Rev. Neurosci.* 24, 167–202. doi: 10.1146/annurev.neuro.24.1.167

Moskowitz, M. A., and Waeber, C. (2011). Remote ischemic preconditioning: Making the brain more tolerant, safely and inexpensively. *Circulation* 123, 709–711. doi: 10.1161/CIRCULATIONAHA.110.009688

Murry, C. E., Jennings, R. B., and Reimer, K. A. (1986). Preconditioning with ischemia: A delay of lethal cell injury in ischemic myocardium. *Circulation* 74, 1124–1136. doi: 10.1161/01.CIR.74.5.1124

Oh, C. S., Kim, S. H., Lee, J., and Rhee, K. Y. (2017). Impact of remote ischaemic preconditioning on cerebral oxygenation during total knee arthroplasty. *Int. J. Med. Sci.* 14:115. doi: 10.7150/ijms.17227

Pion-Tonachini, L., Kreutz-Delgado, K., and Makeig, S. (2019). ICLabel: An automated electroencephalographic independent component classifier, dataset, and website. *NeuroImage* 198, 181–197. doi: 10.1016/j.neuroimage.2019.05.026

Pishyar, R., Harris, L. M., and Menzies, R. G. (2004). Attentional bias for words and faces in social anxiety. *Anxiety Stress Coping* 17, 23–36. doi: 10.1080/10615800310001601458

Sharma, V. V., Thaut, M., Russo, F., and Alain, C. (2019). Absolute pitch and musical expertise modulate neuro-electric and behavioral responses in an auditory Stroop paradigm. *Front. Neurosci.* 13:932. doi: 10.3389/fnins.2019.00932

Slevc, L. R., Davey, N. S., Buschkuehl, M., and Jaeggi, S. M. (2016). Tuning the mind: Exploring the connections between musical ability and executive functions. *Cognition* 152, 199–211. doi: 10.1016/j.cognition.2016.03.017

Staugaard, S. R. (2010). Threatening faces and social anxiety: A literature review. *Clin. Psychol. Rev.* 30, 669–690. doi: 10.1016/j.cpr.2010.05.001

Stewart, J. G., Glenn, C. R., Esposito, E. C., Cha, C. B., Nock, M. K., and Auerbach, R. P. (2017). Cognitive control deficits differentiate adolescent suicide ideators from attempters. *J. Clin. Psychiatry* 78:3157. doi: 10.4088/JCP.16m10647

Stroop, J. R. (1935). Studies of interference in serial verbal reactions. *J. Exp. Psychol.* 18:643. doi: 10.1037/h0054651

Sugimoto, T., Suga, T., Tomoo, K., Dora, K., Mok, E., Tsukamoto, H., et al. (2021). Blood flow restriction improves executive function after walking. *Med. Sci. Sports Exerc.* 53, 131–138. doi: 10.1249/MSS.0000000000002446

Szûcs, D., and Soltész, F. (2010). Stimulus and response conflict in the color–word Stroop task: A combined electro-myography and event-related potential study. *Brain Res.* 1325, 63–76. doi: 10.1016/j.brainres.2010.02.011

Szûcs, D., and Soltész, F. (2012). Functional definition of the N450 event-related brain potential marker of conflict processing: A numerical Stroop study. *BMC Neuroscience* 13:35. doi: 10.1186/1471-2202-13-35

Tapuria, N., Kumar, Y., Habib, M. M., Amara, M. A., Seifalian, A. M., and Davidson, B. R. (2008). Remote ischemic preconditioning: A novel protective method from ischemia reperfusion injury—a review. *J. Surg. Res.* 150, 304–330. doi: 10.1016/j.jss.2007.12.747

Tillman, C. M., and Wiens, S. (2011). Behavioral and ERP indices of response conflict in Stroop and flanker tasks. *Psychophysiology* 48, 1405–1411. doi: 10.1111/j.1469-8986.2011.01203.x

Van Veen, V., and Carter, C. S. (2002). The anterior cingulate as a conflict monitor: fMRI and ERP studies. *Physiol. Behav.* 77, 477–482. doi: 10.1016/S0031-9384(02)00930-7

Wang, Y., Meng, R., Song, H., Liu, G., Hua, Y., Cui, D., et al. (2017). Remote ischemic conditioning may improve outcomes of patients with cerebral small-vessel disease. *Stroke* 48, 3064–3072. doi: 10.1161/STROKEAHA.117.017691

West, R. (2003). Neural correlates of cognitive control and conflict detection in the Stroop and digit-location tasks. *Neuropsychologia* 41, 1122–1135. doi: 10.1016/S0028-3932(02)00297-X

West, R. (2004). The effects of aging on controlled attention and conflict processing in the Stroop task. *J. Cogn. Neurosci.* 16, 103–113. doi: 10.1162/089892904322755593

West, R., and Alain, C. (2000). Effects of task context and fluctuations of attention on neural activity supporting performance of the Stroop task. *Brain Res.* 873, 102–111. doi: 10.1016/S0006-8993(00)02530-0

West, R., Jakubek, K., Wymbs, N., Perry, M., and Moore, K. (2005). Neural correlates of conflict processing. *Exp. Brain Res.* 167, 38–48. doi: 10.1007/s00221-005-2366-y

Zhao, W., Meng, R., Ma, C., Hou, B., Jiao, L., Zhu, F., et al. (2017). Safety and efficacy of remote ischemic preconditioning in patients with severe carotid artery stenosis before carotid artery stenting: A proof-of-concept, randomized controlled trial. *Circulation* 135, 1325–1335. doi: 10.1161/CIRCULATIONAHA.116.024807

Zhao, W., Zhang, J., Sadowsky, M. G., Meng, R., Ding, Y., and Ji, X. (2018). Remote ischaemic conditioning for preventing and treating ischaemic stroke. *Cochrane Database System. Rev.* 7:CD012503. doi: 10.1002/14651858.CD012503.pub2

frontiers | Frontiers in Neuroscience

TYPE Methods
PUBLISHED 10 October 2022
DOI 10.3389/fnins.2022.938518

OPEN ACCESS

EDITED BY
Camillo Porcaro,
Università degli Studi di Padova, Italy

REVIEWED BY
Marc Cavazza,
National Institute of Informatics, Japan
Hendrik Santosa,
University of Pittsburgh, United States
Yalda Shahriari,
University of Rhode Island,
United States

*CORRESPONDENCE
Feng Gao
gaofeng@tju.edu.cn

SPECIALTY SECTION
This article was submitted to
Brain Imaging Methods,
a section of the journal
Frontiers in Neuroscience

RECEIVED 07 May 2022
ACCEPTED 12 September 2022
PUBLISHED 10 October 2022

CITATION
Zhang Y, Liu D, Zhang P, Li T, Li Z and Gao F (2022) Combining robust level extraction and unsupervised adaptive classification for high-accuracy fNIRS-BCI: An evidence on single-trial differentiation between mentally arithmetic- and singing-tasks.
Front. Neurosci. 16:938518.
doi: 10.3389/fnins.2022.938518

Combining robust level extraction and unsupervised adaptive classification for high-accuracy fNIRS-BCI: An evidence on single-trial differentiation between mentally arithmetic- and singing-tasks

Yao Zhang[1], Dongyuan Liu[1], Pengrui Zhang[1], Tieni Li[1], Zhiyong Li[1] and Feng Gao[1,2]*

[1]College of Precision Instrument and Optoelectronics Engineering, Tianjin University, Tianjin, China, [2]Tianjin Key Laboratory of Biomedical Detecting Techniques and Instruments, Tianjin University, Tianjin, China

Functional near-infrared spectroscopy (fNIRS) is a safe and non-invasive optical imaging technique that is being increasingly used in brain-computer interfaces (BCIs) to recognize mental tasks. Unlike electroencephalography (EEG) which directly measures neural activation, fNIRS signals reflect neurovascular-coupling inducing hemodynamic response that can be slow in time and varying in the pattern. The established classifiers extend the EEG-ones by mostly employing the feature based supervised models such as the support vector machine (SVM) and linear discriminant analysis (LDA), and fail to timely characterize the level-sensitive hemodynamic pattern. A dedicated classifier is desired for intentional activity recognition of fNIRS-BCI, including the adaptive acquisition of response relevant features and accurate discrimination of implied ideas. To this end, we herein propose a specifically-designed joint adaptive classification method that combines a Kalman filtering (KF) for robust level extraction and an adaptive Gaussian mixture model (a-GMM) for enhanced pattern recognition. The simulative investigations and paradigm experiments have shown that the proposed KF/a-GMM classification method can effectively track the random variations of task-evoked brain activation patterns, and improve the accuracy of single-trial classification task of mental arithmetic vs. mental singing, as compared to the conventional methods, e.g., those that employ combinations of the band-pass filtering (BPF) based feature extractors (mean, slope, and variance, etc.) and the classical recognizers (GMM, SVM, and LDA). The proposed approach paves a promising way for developing the real-time fNIRS-BCI technique.

KEYWORDS

activation level, adaptive Gaussian mixture model, brain-computer interface, classification accuracy, fNIRS, feature extraction, general linear model, Kalman filtering

Introduction

Functional near-infrared spectroscopy (fNIRS) is a non-invasive, safe, more portable, low-motion artifact, and low-cost optical neural imaging technique that measures the cerebral hemodynamic changes associated with functional brain activity in multiple channels while people performing a wide range of mental tasks (Ferrari and Quaresima, 2012; Alzahab et al., 2021). The regional cerebral blood flow variation is caused by the concentration variation of oxygenated hemoglobin (HbO) and deoxygenated hemoglobin (HbR), which are primary absorbing chromophores in the capillaries of the brain (Boas et al., 2004). These days, many brain imaging modalities have been investigated for use in brain-computer interface (BCI). Nevertheless, fNIRS has received an enormous amount of attention due to its superior environmental robustness to EEG (Hong et al., 2020), and is silent and more tolerant to subtle movement artifacts than functional magnetic resonance imaging (fMRI) (Glover, 1999). Another notable advantage of fNIRS-BCI is its suitability for repeated measurements within short intervals and long-term continuous measurements for future clinical use (Li et al., 2017).

To measure the fNIRS signal, the optodes require direct contact with the scalp, as hair (especially dark hair) leads to attenuation of the fNIRS signal (Herff et al., 2013). However, hair-covered regions of interest (ROI) such as the motor and visual cortex regions have difficulty meeting this condition, as a long preparation time may be required to remove the hair from under the optodes before the experiment to ensure that there is the minimum amount of hair is under the optode. Nevertheless, the hair-free prefrontal cortex (PFC) region is an ideal ROI for fNIRS measurements because it does not cause attenuation of light intensity and allows for a fast set-up of optode layout. In studies where the ROI is the PFC region, fNIRS signal classification is essential to the development of the fNIRS-BCI system. The classification of fNIRS signals acquired in the PFC has applications in many fields, including volitional control such as motor imagery (MI) (Ma et al., 2021), the identification of different emotions (Nguyen et al., 2021), the classification of mental workload levels (Lim et al., 2020), and the discrimination of intentional activity of the brain such as different mental tasks (Power et al., 2012; Chen et al., 2020). Most studies of fNIRS-BCI have focused on MI, affective responses, and mental workload, and less on mental task recognition. In this paper, to investigate the suitability of different mental tasks for BCI control and to improve their discrimination accuracy, we conducted experiments on two mental tasks, namely mental arithmetic (MA) and mental singing (MS). This is because MA and MS are common and robust mental tasks in fNIRS-BCI (Power et al., 2010). Among the studies on the classification of mental tasks, Power et al. (2010) investigated a Hidden Markov Model (HMM) classifier based on light intensity data to classify MA and MS mental tasks. The results of the study showed an average accuracy of 77.2% in 10 able-bodied participants. The results suggest the potential of a two-choice fNIRS-BCI based on mental tasks. In another study, Power et al. (2012) investigated LDA classifiers constructed from feature sets of slope and amplitude to classify the MA vs. MS vs. no-control state of seven able-bodied adults, and the results indicated an overall accuracy of 56.2%. Excluding the ineffective MS task, the accuracy of the three untrained subjects was approaching 70%, which is generally considered effective for binary BCI communication. When users use and practice the fNIRS-BCI system to operate external devices through mental tasks for prolonged periods of time, factors such as learning effects and cognitive fatigue across BCI trials may lead to slow variations in activation patterns over time, which is leading to a reduction in accuracy. The goal of the currently study was to overcome these dilemmas and achieve accurately capturing changes in activation patterns and improving the accuracy of mental tasks. Feature extraction techniques and classification models are essential for improving accuracy. For fNIRS signals, immediate characterization of level-sensitive hemodynamic patterns is critical to improve identification accuracy. Currently, fNIRS-BCI researchers have mostly used various classification models based on statistical features to enhance the classification accuracy of fNIRS signal from ROI.

For using different feature extraction methods to improve accuracy, the most used feature extraction techniques rely on the use of BPF reconstructed hemodynamic response function (HRF) to extract the statistical characteristics of the task-related time-domain fNIRS signals, such as mean, slope, variance, skewness, and kurtosis, and so on (Hwang et al., 2016; Noori et al., 2017; Aydin, 2020). Hwang et al. used the Fisher score method to select the best individual statistical feature for each participant to construct the LDA classifier. The results showed that the average accuracy of "yes" and "no" intentions for the eight healthy participants was ∼75% when using the best individual features (Hwang et al., 2016). However, these statistical features cannot well characterize the hemodynamic response in fNIRS-BCI that is fully depicted by the time-varying activation levels. However, the highest accuracy may depend on the participant-specific BPF-statistical features set and the size of the selected time window. One limitation of fNIRS-BCI is that it is time-consuming to process the fNIRS signal to determine the optimal subset of features. Therefore, more suitable adaptive feature extraction techniques are required to overcome the limitations of BPF-statistical features that cannot well characterize the HRF and the time-consuming optimization of a subset of BPF-statistical features. For using different classifiers to improve accuracy, many researchers have tried to apply many machine learning-based classifiers in fNIRS-BCI, such as LDA, SVM, HMM, *k*-nearest neighbor, Gaussian mixture model (GMM), and artificial neural networks (Power et al., 2010; Li et al., 2017; Zhang et al., 2018; Aydin, 2020; Hong et al., 2020), and also tried to apply convolutional neural networks, recurrent neural networks, and other deep learning (DL) algorithms (Trakoolwilaiwan et al., 2018; Asgher et al., 2020; Wickramaratne and Mahmud, 2021), but limited studies are available so far. Yoo et al. developed a long short-term memory network (LSTM) classifier to classify three categories of mental tasks (MA, mental counting, and puzzle solving) (Yoo et al., 2018). The results indicated that the maximum accuracy of the LSTM was 83.30%, which was higher than that of the LDA (37.50%) and SVM (37.96%) classifiers. Although DL methods can automatically extract features and provide improvements in classification performance, a non-negligible problem is that DL usually requires a large amount of data to allow the model to be adequately trained to prevent overfitting. However, it is unrealistic, or even impossible, to obtain substantial-scale labeled fNIRS signals. Therefore, the classifiers currently used in fNIRS-BCI mostly employ the BPF-statistical features based supervised classical models such as SVM and LDA. These EEG-extending methods fail to characterize the HRF and trace changes in activation patterns. For long-term measurements of fNIRS signals, the fNIRS-BCI desires the design of a dedicated adaptive classification method that includes adaptive extraction of the activation level feature and accurate discrimination of the intentional activities, which can capture the changes in the neural activation pattern of users when they use and practice a BCI system.

To this end, we herein propose a novel joint adaptive classification approach called KF/a-GMM that combines the KF method for robust level extraction and the unsupervised a-GMM classification method for accuracy-enhanced pattern recognition. The KF robustly extracts the activation level based on the general linear observational model and the Gaussian-Markov dynamic model, while the a-GMM adaptively classifies the mental tasks through pattern changes-based parameter adjustment. The general linear model (GLM) has been established as a standard method for fMRI data analysis and has also been applied to fNIRS studies using task-based and event-related experimental designs (Schroeter et al., 2004; Abdelnour and Huppert, 2009; Hu et al., 2010). In our model, the KF is used to adaptively estimate the weight coefficients in GLM from all channels of fNIRS data in parallel (Welch and Bishop, 1995; Hu et al., 2010). The HRF-related coefficient estimated at the last time step of a given channel is the extracted activation level feature. The a-GMM has been successfully applied to signal processing in neuroscience and has achieved excellent classification results (Li et al., 2017; Cao et al., 2021). A recent study made by Li et al. showed that an a-GMM classifier could track activation pattern changes without requiring the true labels of the input data (Li et al., 2017). In this paper, we utilize an unsupervised adaptive GMM method, abbreviated as a-GMM, with a transition model that has managed hyper-parameters to adaptively classify different mental tasks. However, the study by Li et al. may be inadequate in simulations, as they only performed single-pattern variation studies and only extracted mean features for pattern recognition (Li et al., 2017). Glover et al. investigated the temporal characteristics of BOLD responses in the sensorimotor and auditory cortex during finger tapping while subjects performed listening to the metronome pacing tones (Glover, 1999). Slow changes and shifts in the size and center of activation regions over time were observed in the dynamic brain activation map of motor and auditory cortical regions, respectively. A similar phenomenon was observed in the dynamic brain activation maps of pairing and transphrasing stimuli in Lin et al.'s study of fNIRS-based Chinese-English simultaneous interpretation (Lin et al., 2018). These changes in neural activation patterns were also studied in simulations by Li et al. (2017). Furthermore, considering that learning effects and cross-trial cognitive fatigue may lead to changes in hemodynamic patterns, it is reasonable to generalize to a possible stochastic form of real-world changes in hemodynamic patterns induced by prolonged mental task stimuli. Therefore, in the present study, more complex randomly varying activation patterns were simulated rather than single-pattern changes. In addition, related *in-vivo* paradigm experiments were performed to validate the classification performance of the proposed method in recognizing different mental tasks.

To demonstrate the efficiency and superiority of the proposed KF/a-GMM approach for high-accuracy classification in mental tasks for fNIRS-BCI, simulation experiments and paradigm experiments are performed to compare mostly employ the BPF-statistical features based classical methods such as GMM, SVM, and LDA. A total of six simulations with randomly varying activation patterns over time are simulated to mimic the possible random variations more realistically in the spatial patterns of neural activation evoked by the two different tasks (i.e., MA vs. MS). These simulations incorporate random walks in the center of the activation region, random variations in the size of the activation region, and random variations in the amplitude of the hemodynamic response. The *in-vivo* paradigm experiments are performed in single-trial classification between the MA vs. MS mental tasks from the prefrontal activity in eight healthy participants.

Methods

General linear model

In fNIRS-based studies, changes in the concentrations of HbO and HbR (i.e., $\Delta[\mathrm{HbO}]$ and $\Delta[\mathrm{HbR}]$) can reflect changes in regional cerebral blood flow (rCBF). Since more pronounced amplitude changes of $\Delta[\mathrm{HbO}]$ can more sensitively reflect the changes of rCBF. Therefore, only $\Delta[\mathrm{HbO}]$ was considered in subsequent studies. For a given measurement channel, using GLM to analyze the time series of $\Delta[\mathrm{HbO}]$ signal (Abdelnour and Huppert, 2009). The least-squares method (LSM) is generally used to solve the coefficient β in the

GLM. The β constructed by the LSM method is shown below (Hu et al., 2010):

$$\beta_{LSM} = (\mathbf{X}^{\mathrm{T}}\mathbf{X})^{-1}\mathbf{X}^{\mathrm{T}}\Delta\mathbf{c} \tag{1}$$

where $\Delta\mathbf{c} \in \mathbb{R}^{T\times 1}$ is the T-point time series of observed raw Δ[HbO] signal (i.e., unfiltered Δ[HbO] signal), $\mathbf{X} \in \mathbb{R}^{T\times L}$ is the design matrix in GLM with five explanatory variables, including HRF, heartbeat signal, Mayer wave signal, respiration signal, and constant (baseline drift). The frequencies of the heartbeat, respiration, and Mayer wave are selected based on the spectral analysis of the raw light intensity, as described in Section Feature extraction. L is the total number of explanatory variables ($L = 5$). $\beta_{LSM} \in \mathbb{R}^{L\times 1}$ is an unbiased estimate of β with the minimum variance according to the Gaussian-Markov theorem (Abdelnour and Huppert, 2009). However, this method requires complete measurement data to calculate β but fails the real-time estimation (Wang et al., 2018). In this study, we use KF to recursively estimate the state value β at each time step.

Kalman filtering

The KF method is an adaptive tracking scheme that performs an optimal estimation of the state of a process using a recursively regularized linear inversion routine (Kalman, 1960). In the present study, the KF is used to robustly and parallelly estimate activation level features from all channels of unfiltered single-trial fNIRS data (Abdelnour and Huppert, 2009). For a given measurement channel, the transition equation and observation equation can be described as:

$$\begin{cases} \beta_k = \mathbf{A}\beta_{k-1} + \mathbf{w}_k \\ \Delta c_k = \mathbf{X}_k\beta_k + v_k \end{cases} \tag{2}$$

where $\beta = [\beta_k^1, \beta_k^2, \ldots, \beta_k^L]^T (k = 1, 2, \ldots, T)$ is the state vector representing the magnitude of each explanatory variable in the GLM estimated at time step k, Δc_k is the measured raw Δ[HbO] signal at time step k. Since the magnitude of each explanatory variable is slowly varying with time, it can be assumed that the state β_k is a random walk with zero drift in the transition equation over time. Therefore, the state transition matrix $\mathbf{A}$ equals the identity matrix (Hu et al., 2010). As the random walk process is a non-stationary process, the state vector can be updated iteratively using KF. The distribution of process noise and observation noise are $w_k \sim \mathcal{N}(\mathbf{0}, \mathbf{Q})$ and $v_k \sim \mathcal{N}(\mathbf{0}, \mathbf{R})$, respectively. The *priori* estimates of the process noise covariance $\mathbf{Q}$ and the observation noise covariance $\mathbf{R}$ are set to $\mathbf{Q} = (1\%)^2\mathbf{I}$ and $\mathbf{R} = (1.5)^2\mathbf{I}$ (Abdelnour and Huppert, 2009), where $\mathbf{I}$ is the identity matrix. The iterative process for updating the estimate of state β_k can be found in Hu et al. (2010). The state vector β_k is initialized to zero.

After processing the observed single-trial Δ[HbO] data through the iterative process, the β_T estimated at the last time step T is the final reconstructed β. The first element β_T^1 in the final estimated vector β_T is the estimated activation level, which represents the amplitude of the HRF. The $\beta=[(\beta_T^1)^1, (\beta_T^1)^2, \cdots, (\beta_T^1)^D]$ is a feature sample of the observed single-trial data, which consists of the estimated level features for all channels. $(\beta_T^1)^d (d = 1, 2, \cdots, D)$ denotes the level feature extracted from the d-th channel, and D is the total number of measurement channels.

Adaptive Gaussian mixture model

The a-GMM is a well-known model for data clustering and classification. The uncertainty of the a-GMM parameters can be described by a probability distribution to form a hierarchical probability model. When a new sample arrives, variational Bayesian inference is used to update a-GMM parameters, using the previous parameter distributions as *priors*. Then, the a-GMM gives clustering labels to the new sample data points, and the clustering parameters are updated by a small amount of data because the *priors* are strong. The detailed derivation process of the unsupervised a-GMM approach can be found in the literature (Li et al., 2017), and here, we only give a brief description.

Probability model

For robustly extract level features by KF, the level feature sample $\hat{\beta} \in \mathbb{R}^{1\times D}$ extracted from single-trial fNIRS data for all channels from class k are modeled as having a multivariate normal distribution:

$$\hat{\beta} \sim \pi_k\mathcal{N}(\mu_k, \Lambda_k^{-1}) \tag{3}$$

where $\pi_k (k = 1, 2, \cdots, K)$ is the probability of the k-th category of fNIRS data in the a-GMM, k indicates the category of fNIRS data, and K is the total number of categories of fNIRS data. K is set to 2 in this study, but it has no limitations in a-GMM. μ_k is the d-dimensional mean vector, Λ_k^{-1} is the $d \times d$ covariance matrix, and Λ_k is the precision matrix. To solve the parameters π_k, μ_k, and Λ_k in the Gaussian mixture distribution, first, the non-informative *prior* distribution needs to be selected. These *prior* distributions are generally determined by the conjugate distribution method, Jeffery principle, and principle of maximum entropy (Li et al., 2017). The non-informative *priors* are shown as follows:

$$\begin{cases} \pi_{k=1,\ldots,K} \sim SymDir(j, \alpha_0) \\ \Lambda_{k=1,\ldots,K} \sim \mathcal{W}(\mathbf{W}_0, v_0) \\ \mu_{k=1,\ldots,K} \sim \mathcal{N}[m_0, (\beta_0\Lambda_k)^{-1}] \\ \mathbf{z}_{n=1,..,N} \sim Mult(1, \pi) \end{cases} \tag{4}$$

where N is the total number of trials $SymDir(\cdot)$, is the j-dimensional symmetrical Dirichlet distribution, $\mathcal{W}(\cdot)$ is the normal-Wishart distribution, $Mult(\cdot)$ is the multinomial distribution, and the $\mathbf{z}_n$ is the latent variable. For each observed feature sample $\hat{\beta}_n$, we have a corresponding latent variable $\mathbf{z}_n = \{z_{n1}, \cdots, z_{nK}\}$ comprising a 1-of-K binary vector with elements z_{nk} for $k = 1, \ldots, K$. The $\mathbf{z}_n$ is used to indicate the category to which the corresponding observed feature sample belongs to the fNIRS data. In order to distinguish the parameters of the joint probability distribution, the above-mentioned *prior* distribution parameters such as K, α_0, β_0, $\mathbf{W}_0$, v_0, and m_0 are known as hyper-parameters. During the parameter fitting, these hyper-parameters are fitted to the training data. An independent Gaussian-Wishart prior defined using known hyper-parameters can govern the random variable of μ_k and Λ_k of each Gaussian component, given by:

$$p(\mu_k, \Lambda_k) = \prod_{k=1}^{k} \mathcal{N}[\mu_k | m_0, (\beta_0 \Lambda_k)^{-1}] \mathcal{W}(\Lambda_k | \mathbf{W}_0, v_0), \quad (5)$$

where m_0, β_0, $\mathbf{W}_0$, and v_0 are hyper-parameters in the *prior* distribution.

Variational Bayesian inference

The variational Bayesian method is used to classify new sample data and to update the hyper-parameters of the a-GMM approximately. Then, the Bayesian *posterior* of the parameters is calculated using the previous parameter distributions regarding *priors*. However, the form of the *posterior* probability is usually extremely complicated, and then we use the mean-field theory to find another simple model (inferred *posterior* distribution) to approximate instead of the true *posterior* distribution (Bishop, 2006). The difference between the *posterior* distribution and inferred *posterior* distribution is measured using the Kullback-Leibler (*KL*) divergence (Li et al., 2017).

The variational inference is to find the settings of the hyper-parameters which minimizes the *KL* divergence. This is equivalent to maximizing the variational lower bound. The process is performed in an iterative manner, assigning probabilistic labels to new sample data, and sequentially updating a-GMM hyper-parameters until the lower bound converges. The detailed iteration formula derivation can be found in (Bishop, 2006) and (Li et al., 2017). For the class labels, we define responsibility r_{nk} as the probability that the observed sample data $\hat{\beta}_n$ belongs to class k. We set r_{nk} as follows:

$$r_{nk} \propto \pi_k |\Lambda_k|^{1/2} \exp[-0.5(\hat{\beta}_n - \mu_k)^T \Lambda_k (\hat{\beta}_n - \mu_k)] \quad (6)$$

The normalized r_{nk} satisfies the condition $\sum_{k=1}^{K} r_{nk} = 1$. In the present study, convergence in the iterative algorithm is regarded as the change of the lower bound of <0.1%. Besides, we also set a hard limit of 200 iterations. After the iterative algorithm ends, the class label for each new sample data n belongs to class k with the highest responsibility r_{nk}. This is the maximum a *posteriori* estimation. After that, when more sample data are reached, these updated hyper-parameter values are used for the next run of the algorithm.

Transition model

The difference between the a-GMM approach and the GMM approach is the addition of a transition model, which is used to manage the hyper-parameters and, thus, change the parameters of the a-GMM (Li et al., 2017). Since we hope that the a-GMM classifier can adaptively track the changes of task-evoked brain activation patterns over time. This requires that the parameters of the a-GMM are updated with newly arrived sample data rather than becoming increasingly deterministic based on the cumulative statistics of the previous sample data (i.e., the parameter updates from newly arrived data will be smaller and smaller). To this end, we need to model the change in the parameters of the a-GMM classifier over time in order to handle the change process of the activation pattern adaptively.

The transition model governing the hyper-parameters of the *prior* distribution is presented in Equation (7). The transition model can effectively force a certain degree of forgetting of the old information so that the newly arrived data can still update the a-GMM parameters. It makes the center of the distribution of the a-GMM classifier parameters constant while the distribution becomes wider, i.e., reduces the certainty of the parameters. The parameters of the transition model are used to directly reflect the rate of change of the hyper-parameters, instead of simply using statistical variables to update. This allows the classifier can classify tasks adaptively over time. The hyper-parameters for the k-th category of fNIRS data are directly updated as follows:

$$\begin{cases} \tilde{\beta}_0^k = \beta_0^k / (1 + c_1 \beta_0^k) \\ \tilde{v}_0^k = v_0^k c_2 \\ \tilde{\mathbf{W}}_0^k = \mathbf{W}_0^k / c_2 \end{cases} \quad (7)$$

where $0 \leq c_1$ and $0 < c_1 \leq 1$ are constants indicating the rate of change of parameters. The right side of the equation is the posterior hyper-parameter value from the previous algorithm run, while the left side with the tilde sign is a *prior* hyper-parameter value for the next run. Variational inference is performed on one or a batch of new sample data by running the algorithm to converge.

Experiments

Simulation experiments

Simulation of fNIRS signal

A series of simulation experiments of random variations in the spatial patterns of brain activation over time is performed.

TABLE 1 Detailed settings for generating simulated fNIRS signal.

	hrf	**bp**	**br**	**bl**	**rn**
Generation/parameters	cHRF*boxcar	Heartbeat (1.0 Hz) Mayer wave (0.1 Hz) Initial amplitude = 10	Respiration (0.2 Hz) Initial amplitude = 10	$bl = 10$	$SNR = 10$ dB
Spatial filter	Dynamic variation	Randomly generated and static	Randomly generated and static	-	-

*Denotes the convolution operator.

First, we simulated task-related brain fNIRS signals (i.e., Δ[HbO]), then simulated task-evoked random variations in activation patterns of the prefrontal region over time, and finally performed adaptive decoding for two different tasks (i.e., MA vs. MS). The simulated fNIRS signal of one channel is modeled as a linear combination of five components (Duan et al., 2018):

$$\mathbf{s}_{\mathrm{fNIRS}} = \mathbf{hrf} + \mathbf{bp} + \mathbf{br} + \mathbf{bl} + \mathbf{rn} \tag{8}$$

where **hrf** is the hemodynamic response of the task-evoked prefrontal regions, **bp** and **br** are changes in fNIRS signal induced by blood pressure and respiration, respectively, **bl** is the baseline drift, and **rn** is the random noise (systemic noise), i.e., additional background white noise during the measurement period of the instrument, and $\mathbf{s}_{\mathrm{fNIRS}}$ is the final simulated fNIRS signal.

The detailed settings for generating the simulated fNIRS signal are shown in Table 1. An example of the simulated **hrf**, **rn**, and the final combined fNIRS signal is illustrated in Figure 1. The time series of the **hrf** component is generated by convolving the canonical HRF (cHRF) evoked by a single stimulus with a boxcar function for task activation time series, representing the task and rest states alternation. The cHRF is modeled as a linear combination of two different gamma-variant time-dependent functions (Glover, 1999). The simulated **hrf**s evoked by the two different tasks (i.e., MA vs. MS) are normalized to ensure equal levels of activation. The time series of **hrf** components of all channels are then multiplied by a spatial filter that varies with time and obeys a two-dimensional (2D) Gaussian distribution to simulate dynamic changes in brain activation patterns. The time series of the physiological interference components are generated based on realistic a priori physiological parameters, and then multiplied by a spatial filter whose values for each channel are randomly generated from the standard normal distribution and are statically invariant, i.e., do not change over time (Li et al., 2017). The **bp** signal is composed of two sinusoids representing heartbeat (1.0 Hz) and Mayer wave (0.1 Hz). The **br** signal is a 0.2 Hz respiration signal (Scarpa et al., 2013; Hoang-Dung et al., 2018). The initial amplitudes of **bp** and **br** are set to 10, at which point the average *SNR* (**hrf** for signal and all noise components for noise) across all channels is −31.35 dB, i.e., the noise level is 35. This higher noise level is a more realistic simulation of the realistic measurement scenario. Each sinusoid has a random phase and amplitude distortions. The baseline amplitude is set to $bl = 10$.

To more realistically mimic the measurement process, we also add Gaussian white noise (i.e., **rn**) with a signal-to-noise ratio (*SNR*) of 10 dB to the baseline for each channel. The difference in *SNR* between the $\overline{\mathbf{hrf}}$ ($\overline{\mathbf{hrf}} = \mathbf{hrf} + \mathbf{bl}$) and the baseline (**bl**) at time step k is proportional to the square root of the absolute values of the difference between the amplitude of the hemodynamic response $\overline{\mathbf{hrf}}$ and the baseline (i.e., $\Delta SNR_k \propto \sqrt{\left|\overline{\mathbf{hrf}}_k - bl\right|}$; Wang et al., 2020). $\overline{\mathbf{hrf}}$ signal indicates **hrf** signal with baseline drift.

Simulation of randomly varying activation patterns

We simulated an 18-channel montage (3×6) of fNIRS measurements in the PFC region with a sampling rate of 10 Hz, as shown in Figure 2A, where the black numbers indicate the position of the channels. One trial of the simulated fNIRS data lasts 40 s, in which the first 20 s are the rest periods and the last 20 s contain the task-related activation. A total of 500 trials were simulated in one simulation, with alternating trials for task 1 and task 2. The simulated activation pattern varies randomly once every 50 trials and in total it varies randomly 10 times in one simulation. To the best of our knowledge, the randomly varying activation pattern has not been previously simulated in any fNIRS-BCI study. To mimic the possible changes more realistically in the spatial pattern of brain activation, a total of six simulations are implemented for randomly varying activation patterns as shown in Figure 2, which illustrates the optical topographies (OT) of random variations in activation patterns over the first 100 trials. Figures 2A–F correspond to simulation experiments 1–6, respectively.

For a random walk in the center of the activation region (Figure 2A), the center of the activation region moves linearly during the two different activation pattern changes as shown by the white arrow in Figure 2, but the change of the center of the activation region from the initial point to the end point is a random walking process. In simulation 1, the HRF spatial filter obeys a 2D Gaussian distribution with a covariance matrix of 0.2**I** (**I** denote the identity matrix) and remains constant,

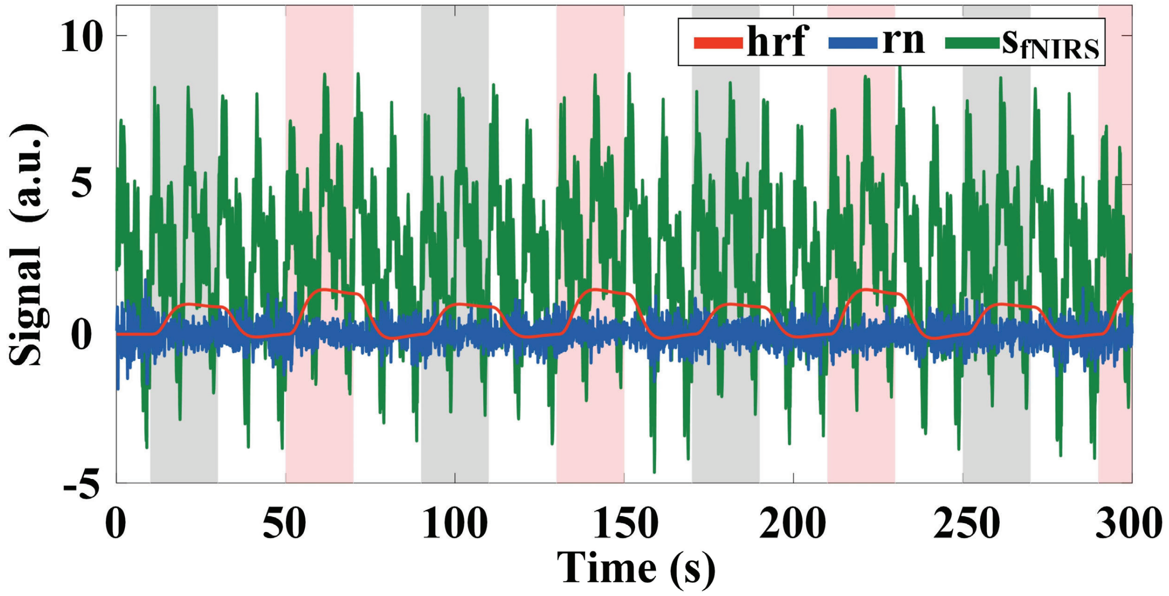

FIGURE 1
Example of simulated fNIRS signal with the amplitude of the baseline set to 2, the initial amplitude of the physiological interference set to 2, and a Gaussian white noise with $SNR = 10$ dB. The gray and pink highlighted rectangles indicate stimulation periods for task 1 and task 2, respectively.

changing only its center. Two spatial filters are randomly generated from 2D Gaussian distributions with three different covariance matrixes (0.2**I**, 1.0**I**, and 5.0**I**, respectively) as the initial and final patterns of random variation and multiplied with the HRF of all channels to achieve random variation in the size of the activation region (Figure 2B). The change in the HRF spatial filter from the initial pattern to the final pattern is a linear and slow morphing in time, whose specific setup can be found in the literature (Li et al., 2017). The pattern variation in Figure 2C is a superimposed hybrid pattern of Figures 2A,B, i.e., both the center and the size of the activation region change randomly with time. When the size of the activation region evoked by task 2 in the simulations of Figures 2A,C no longer remains stationary also varies randomly, corresponding to the simulations of Figures 2D,E. The amplitude and waveform of the HRF are the same for all channels between the two tasks in simulations 1–5, and the amplitudes are normalized to 1 indicating the same level of activation for both tasks. Additionally, we also simulated differences in the amplitude of the hemodynamic responses evoked by two tasks, as shown in Figure 2F. The difference in the HRF amplitude for the two tasks was set to be small in the stochastic dynamic variation of the activation pattern. The HRF magnitude for task 2 is normalized to 1, whereas that for task 1 is randomly generated from a uniform distribution of 1.1–1.2 at each pattern change. The centers of the activation regions for both tasks are randomly walking rather than stationary, and the size of the activation regions remains constant during the random variation.

Since the feature extraction and classification methods for simulated experimental data and paradigm experimental data are the same, a detailed description of the feature extraction, feature data normalization and data classification for simulated experimental data can be found in Subsections Feature extraction and Classification of the "Paradigm experiments" section. To better evaluate the classification accuracy of the classifier for all simulated experiments, 10 runs of 10-fold cross-validation were performed.

Paradigm experiments

Participants

Eight healthy right-handed participants (mean age: 23.5 ± 2.1 years, three men and five women) were recruited from the students at Tianjin University to conduct the experiments. None of the participants had reported a previous history of any psychiatric, neurological, or brain disorder. The study was conducted with informed consent and received ethical approval from Tianjin University.

Data acquisition

We have implemented a continuous wave fNIRS diffuse optical tomography (DOT) system that adopts a lock-in photon-counting technology to enable multi-channel parallel measurements, as exhibited in Figure 3A (Liu et al., 2019).

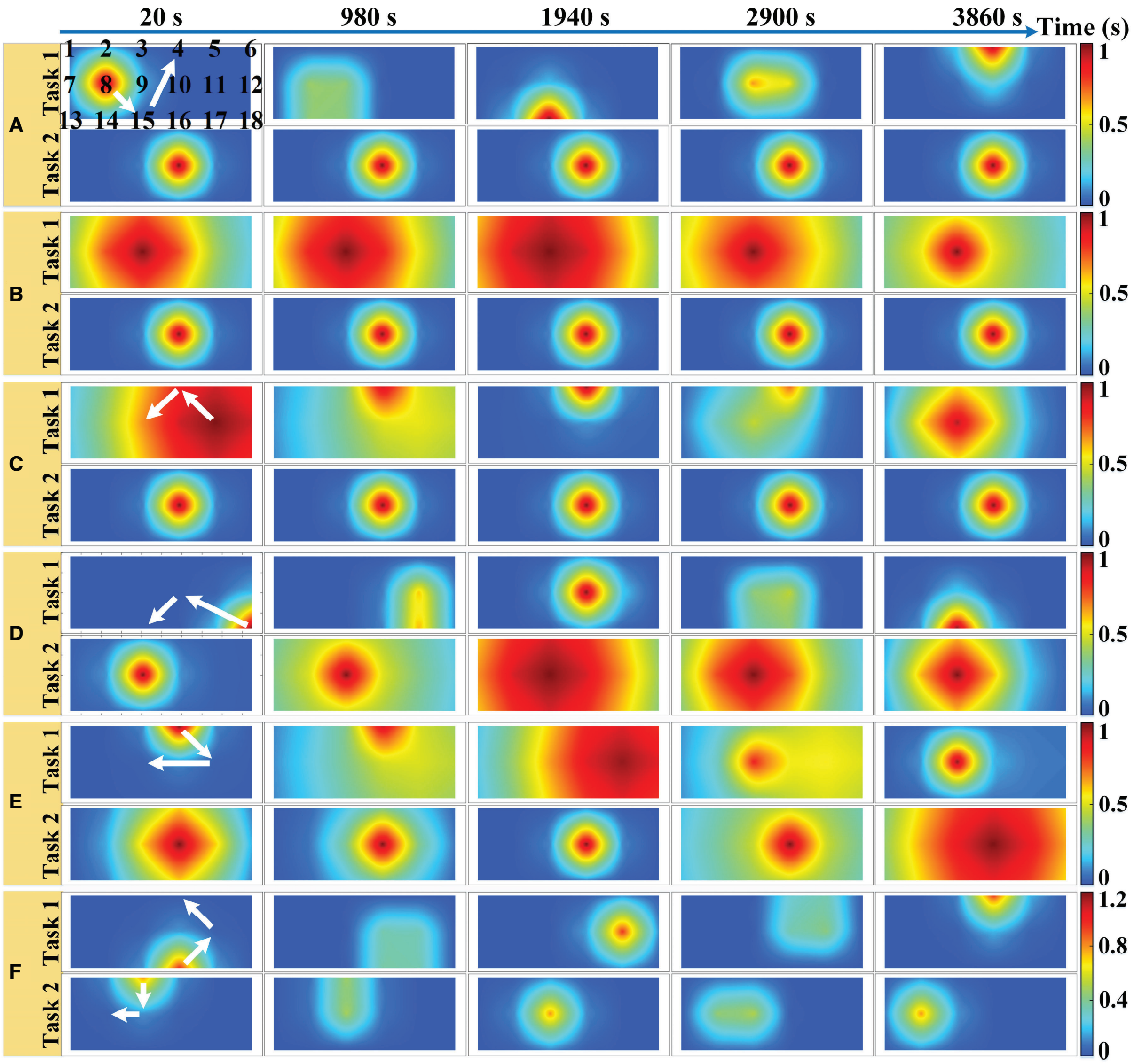

FIGURE 2
Six simulations with random varying spatial patterns of brain activation in prefrontal regions: **(A)** The center of the activation region is the random walk but its size remains constant. **(B)** The size of the activation region varies randomly but its center remains the same. **(C)** Both the center and the size of the activation region change randomly with time. **(D)** The center of the task 1 evoked activation region randomly walks while the size of task 2 evoked activation region varies randomly. **(E)** Both the center and the size of the task 1 evoked activation region change randomly with time while the size of task 2 evoked activation region varies randomly. **(F)** The center of the activation region is random walk for both tasks, but the amplitude of the HRF for task 1 is randomly varying, while that of task 2 remains constant. The white arrows indicate the direction of linear movement of the center of the activation region. The black numbers indicate the location of the sampling channels.

We use a total of four source-pairs, each containing both 785 nm and 830 nm laser diode sources and four photomultiplier (PMT) detectors form a single-lattice arrangement scheme (Figure 3B), resulting in 20 measurement channels for collecting fNIRS signals, are secured against the PFC region of the participant. The system sampling rate for data acquisition is 4 Hz, which is lower than the setting of the simulation experiment. However, it is a moderate temporal resolution for our measurement system, which can improve the *SNR* of the measured data and meet the requirements of real-time data processing.

According to the international 10–20 system, the source-pair and detector are arranged to cover the optode positioning points FP1 and FP2 of the PFC region, as shown in Figure 3B. In the given configuration, we only considered signals arising from the source-detector distance of 30 mm (Power et al., 2010).

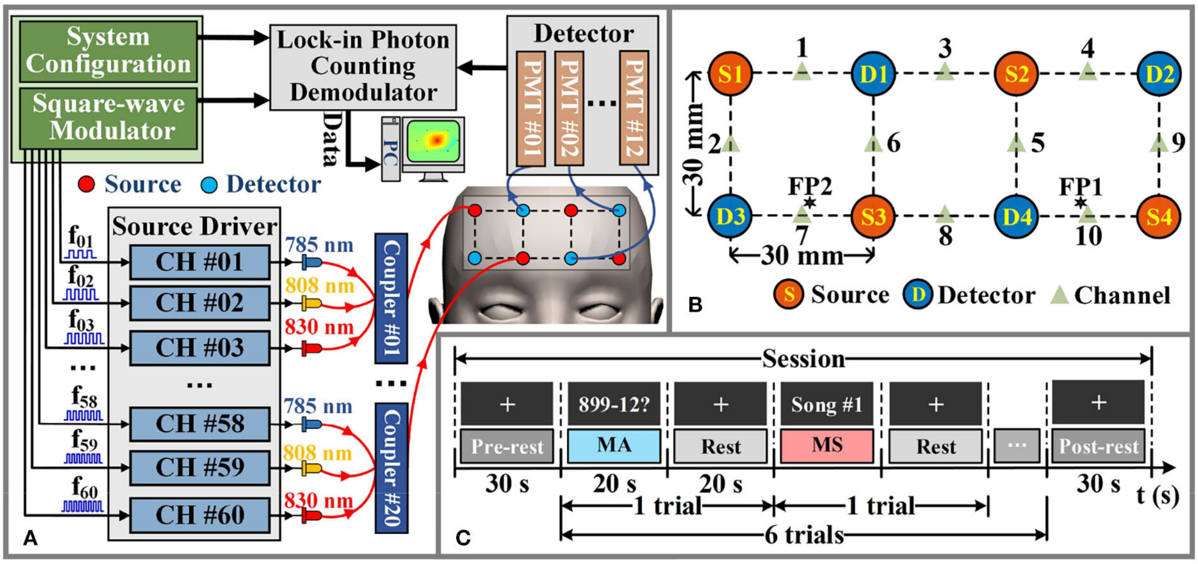

FIGURE 3
Hardware instruments and experimental paradigms for *in-vivo* experimental data acquisition. **(A)** The schematic diagram of the fNIRS-DOT instrument. **(B)** Experimental source and detector configuration. **(C)** Experimental paradigm of MA and MS.

Experimental protocol

In the paradigm experiment, all participants performed the MA and MS mental tasks. The MA is one of the most widely used and robust mental tasks in fNIRS-BCI research (Power et al., 2012). The mental workload level of the MA task was the same because participants were asked to repeatedly subtract a small number (between 9 and 15) from a randomly generated three-digit number. For the MS mental task (Hwang et al., 2016), participants silently rehearsed self-selected Chinese song fragments that they felt would provoke a strong and positive emotional response within them. This means that the MS task utilizes the emotional component of the music. The self-selected Chinese songs were different in each trial for each participant. The self-selected song presented in each trial was randomly generated from the participant's self-constructed song library.

The schematic diagram of the *in-vivo* experimental paradigm is shown in Figure 3C. Each participant was required to perform 20 data collection sessions on the same day. Figure 3C illustrates a data collection session consisting of a 30 s pre-rest period (i.e., baseline period), 6 trials, where each trial consisted of a 20 s of MA or MS mental task followed by 20 s of rest, and a 30 s post-rest period in the end. During each data collection session, each participant performed 6 trials in which MA trials and MS trials were alternated. The fNIRS optodes were not removed from the participants during all data collection sessions. Data collection for all participants was completed over a period of 5 days. The total number of trials collected for each category of the mental task for each participant is 60. Therefore, the total number of trials collected for each participant is 120.

Signal pre-processing

The 5th order zero-phase Butterworth digital low-pass filter with a cut-off frequency of 0.5 Hz is used to eliminate the heartbeat noise and high-frequency instrument noise for the raw light intensity data. Then, the coefficient of variation (CV) of the low-pass filtered raw light intensity signal is calculated to evaluate the quality of data (i.e., the effect of motion artifacts on the measured data) for each measurement channel. The CV can be defined as:

$$CV = (\sigma[\mathbf{I}]/E[\mathbf{I}]) \times 100 \tag{9}$$

where $\mathbf{I}$ denote the raw light intensity for a data collection session. $E[\cdot]$ and $\sigma[\cdot]$ denote the mean and standard deviation, respectively. When the measured raw light intensity data meets the condition of $CV > 10$ (Piper et al., 2014), the channels are rejected and not used in the subsequent further data analysis. Furthermore, we used the modified Beer-Lambert law (MBLL) to convert the raw light intensity signal into Δ[HbO] and Δ[HbR] (Weyand et al., 2015). The unfiltered Δ[HbO] signal, which has not been subjected to BPF or other filtering methods to remove baseline drift and global physiological interferences, was used in the GLM-KF for adaptive extraction of level features. The GLM considers baseline drift and physiological interferences when modeling the fNIRS signal. However, when applying the GLM-KF method to real fNIRS data, it is required to consider pre-task calibration. In long-term measurements of real fNIRS data, excessive cognitive load can cause rapid fatigue of the subject, causing changes in baseline across data collection sessions for the same subject. In addition, due to individual differences, the baselines between subjects were also different. Therefore, the pre-task calibration for each session of each subject used the fNIRS data for the baseline period under that session. The parameter settings of the BPF for the extraction of statistical-features are described in detail in Section Hemodynamic changes. A zero-phase digital high-pass filter (0.018 Hz cutoff) in the BPF effectively removes the baseline drift when extracting statistical-features (Bejm et al., 2019).

Feature extraction

In the previous fNIRS-BCI study, the most widely used features including mean, variance, slope, skewness, and kurtosis, which these BPF-statistical features are not designed to better characterize hemodynamic responses (Weyand et al., 2015; Hong et al., 2020). The fNIRS-BCI desires adaptive extraction of dedicated level features of single-trial fNIRS data. In this study, KF was used to extract the activation level recursively by solving the GLM.

The frequency selection for each physiological interference of the design matrix in GLM is based on the fast Fourier transform of the raw light intensity measured by each participant for spectrum analysis. Figure 4A shows the frequency spectra for participant 1, where the normalized power amplitude of the stimulation frequency (0.0233 Hz) is relatively higher, and it is slightly less than the theoretical value (1/40 = 0.0250 Hz) of the frequency of neural activation. This is due to the hemodynamic response being delayed by 2–3 s after the neural activity (Tomita et al., 2014).

Classification

The assessment metric used to quantitatively assess the classifier's ability to accurately discriminate the task is accuracy, defined as shown below (Wickramaratne and Mahmud, 2021).

$$Accuracy = \frac{TP + TN}{TP + FP + TN + FN} \tag{10}$$

where TP is the number of true positives, FP is the number of false positives, TN is the number of true negatives, and FN is the number of false negatives. The accuracy results, in this paper, are all obtained from the test set data. The classification process is performed in an offline mode. To better assess the classification performance of the classifier for the MA and MS mental tasks, 10 runs of 10-fold cross-validation were also performed as in the simulations.

We compared the classification performance of the proposed KF/a-GMM approach with the BPF-statistical features based classical methods such as the GMM classifier, which uses GMM to fit parameters on the same training data in the same way, but does not update the parameters when it classifies the testing data, SVM classifier with radial basis kernel function and regularization parameter of 20, and LDA classifier. The flow chart of activation level-based fNIRS signals decoding is shown in Figure 4B. Feature samples are normalized by calculating z-scores. For these normalized values, we use the principal component analysis (PCA) method with the smallest principal component number whose cumulative contribution rate exceeds 95% to reduce the dimensionality of feature sample data (Li et al., 2020). The final dimensionality reduction data is used to construct a classifier.

Statistical analysis

In the real-time classification of mental tasks, we are also more interested in whether the channel is significantly activated at each time step k. First, we proposed the null hypothesis ($H_0 : \mathbf{c}^T \beta_k = 0$) that the channel is not activated at time step k, where $\mathbf{c}$ is a vector of contrast used to select the coefficients of interest. This hypothesis is tested by calculating the relevant t-values from the estimated GLM coefficient vectors at all time steps and then performing a t-test with significance criteria of 0.05 (Hu et al., 2010). Finally, we used paired-samples t-tests of SPSS 22.0 software (IBM SPSS Inc., Chicago, IL, USA) with significance criteria of 0.05 for statistical analysis of classification accuracy.

Results

Simulative investigations

Extraction of activation level feature

Both the KF and LSM can extract the activation level features for each channel of the measurement data. We construct the same a-GMM classifier based on these two methods to extract activation level features, respectively. Then, the effect of both level extraction methods on accuracy in all simulations is shown in Figure 5. Figure 5A shows the average accuracy of 10 runs of the 10-fold cross-validation for each simulation experiment. The average accuracy based on the two different level extraction methods across all simulations is illustrated in Figure 5B.

As observed from the results that the accuracy of the KF-based levels was higher than that of the LSM-based levels in each of the simulations (Figure 5A). The average accuracy obtained based on KF-level was 97.89% higher than that based on LSM-level at 91.31% across all simulations (Figure 5B). The paired samples t-test yielded statistically significant differences in the two methods of level extraction. Since both KF and LSM invisibly encompass the filtering process when solving the GLM,

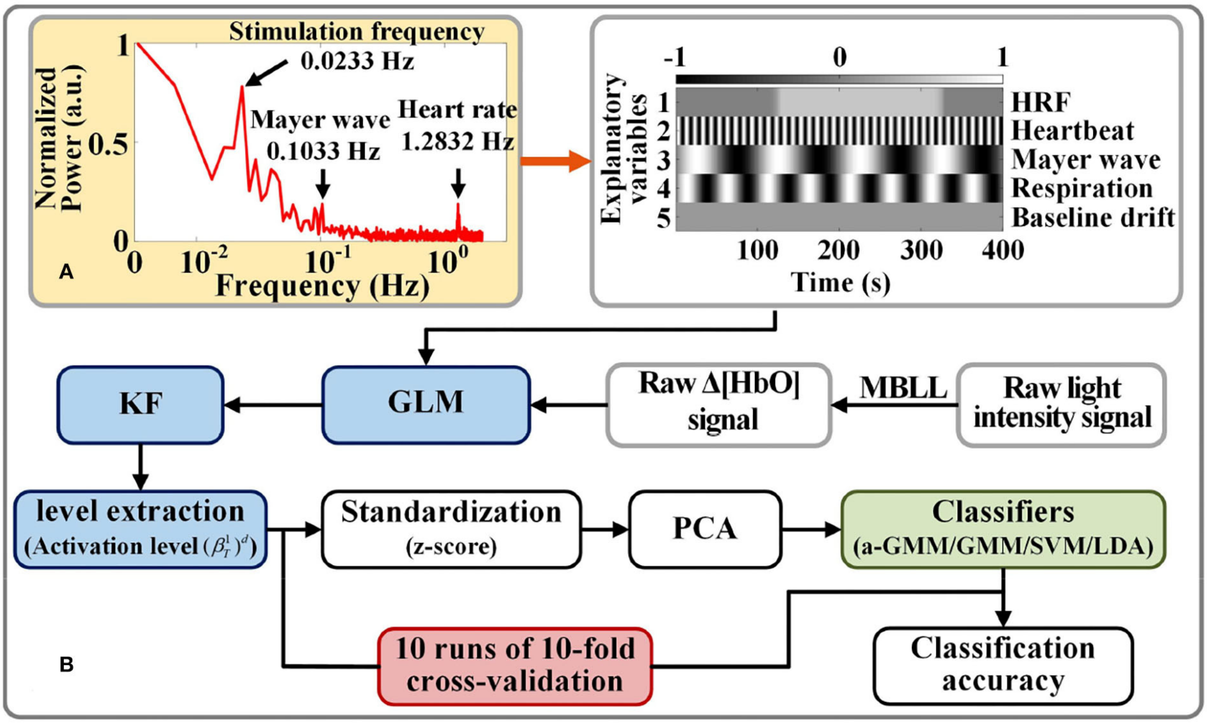

FIGURE 4
Activation level feature extraction and classification strategy for fNIRS signals: **(A)** Example of a spectrogram of participant 1 for frequency selection of physiological interferences in the design matrix. **(B)** Flow chart of fNIRS signal classification based on level features.

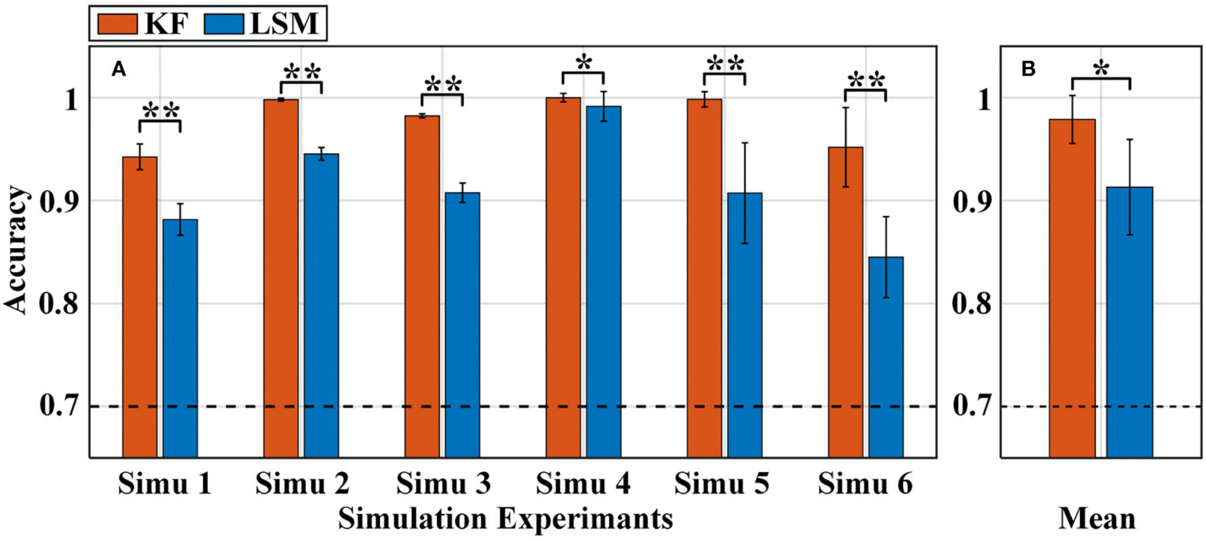

FIGURE 5
Classification accuracy of the a-GMM classifier in all simulations was based on the level feature extracted by KF and LSM methods. **(A)** Average accuracy of each simulated experiment, **(B)** average accuracy across all simulated experiments. The black dashed line indicates 70% accuracy of effective binary BCI communication. Error bars indicate the standard deviations, *Represents the significant difference, *$p < 0.01$ and **$p < 0.001$.

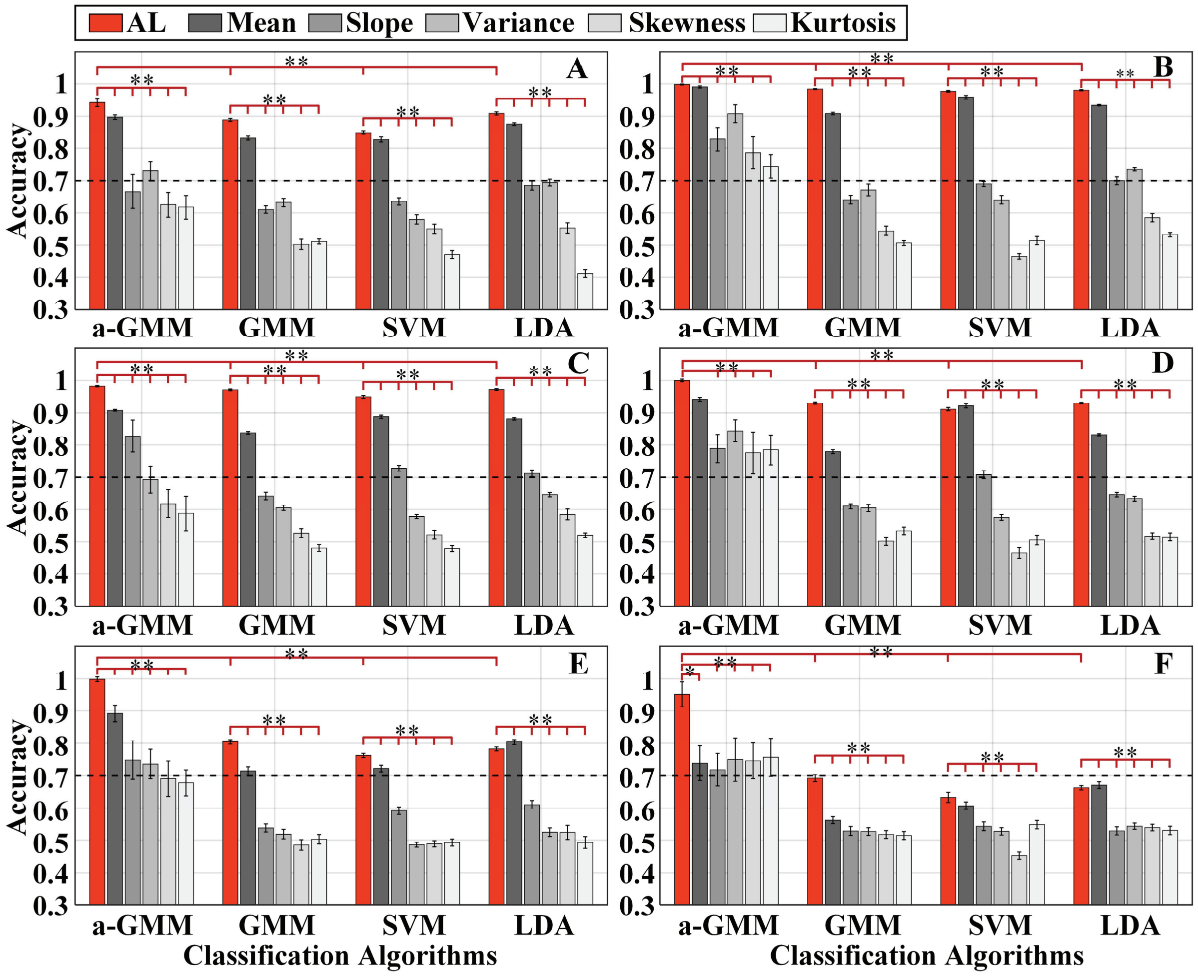

FIGURE 6
The single-trial average accuracy of six simulations with randomly varying activation patterns of the brain under Gaussian white noise with *SNR* = 10 dB added at the baseline: **(A–F)** Are the accuracy results of simulations 1–6, respectively. AL is an abbreviated form of activation level. The red bars indicate accuracy based on the activation level features, while the gray bars with different saturation levels indicate the accuracy based on five BPF-statistical features, namely mean, slope, variance, skewness, and kurtosis. Error bars indicate the standard deviations, *Represents the significant difference, empty: $p > 0.05$, $^*p < 0.01$, and $^{**}p < 0.001$.

the filtering effect of KF is better than that of LSM, resulting in a more accurate estimation of activation levels. Therefore, KF was used for the level feature extraction method in the subsequent sections.

Recognition of randomly varying activation patterns

The single-trial average accuracy of six simulations with randomly varying activation patterns under Gaussian white noise with $SNR = 10$ dB added at the baseline is illustrated in Figure 6. Figures 6A–F shows the results of the average accuracy of simulations 1–6, respectively. The results exhibit the accuracies obtained by the four classifiers based on activation level features and BPF-statistical features. For the same classifier, we only compared the accuracy based on the proposed level features with that based on the individual BPF-statistical features. This is because it would be fairer to compare the proposed level features with individual BPF-statistical features (for a one-to-one comparison) than with a set of BPF-statistical features (for a one-to-many comparison).

As observed from the accuracy results, the decoding accuracy based on level features was mostly higher than that based on BPF-statistical features in each classifier for each simulation. The accuracy of the level-based SVM classifier for simulation 4 was slightly lower than that of the mean-based one, and the accuracy of the LDA classifier for simulation 5 and simulation 6 performs in the same way. In addition, the paired-samples *t*-tests yielded significant differences in the level features and each BPF-statistical feature of each classifier in each simulation, except for the level feature vs. the mean feature for the a-GMM classifier in simulation 4. Moreover, the classification performance based on the mean feature was the best among the five BPF-statistical features. Moreover, the accuracy of a-GMM was mostly higher than that of GMM, SVM, and LDA in six simulations, whether based on BPF-statistical features or level features. Paired-samples *t*-tests yielded significant differences between a-GMM classifiers based on level features and other classifiers based on level features in all simulations.

As observed from the results, the KF/a-GMM approach can indeed accurately capture the random walk of the center of the activation region (Figure 6A), the random variation in the size of the activation region (Figure 6B), and their superimposed hybrid pattern (Figure 6C), with corresponding accuracies of 94.25, 99.81, and 98.25%, respectively. When the activation pattern evoked by task 2 changes from a stationary invariant state to a random variation as well, the accuracies of the control methods (relative to the KF/a-GMM) mostly decrease as illustrated in Figures 6D,E. It is also observed from the classification results that the accuracies of the control methods in simulation 5 were lower than that in simulation 4. However, the KF/a-GMM approach in simulations 4 and 5 still maintains a significantly higher accuracy of 99.98 and 99.85%, respectively. The accuracy of random varies magnitude of the HRF under a random walk in the center of the activation region was presented in Figure 6F. The accuracies of GMM, SVM, and LDA classifiers were all below 70%, while accuracies of a-GMM were all above 70%, whereas those based on BPF-statistical features are slightly above 70% and those based on level features have a significant advantage of up to 95.18%.

Noise sensitivity

To investigate the sensitivity of the KF/a-GMM method to noise, we added different levels of Gaussian white noise with *SNRs* of 1, 5, 10, 15, 20, 30, and 40 dB to the baseline for all channels of the simulated data. In the pre-processing of the fNIRS data, since the classical BPF method can effectively suppress most of the physiological interferences, the white noise in the passband of the filter cannot be eliminated. Therefore, the effect of different levels of Gaussian white noise on the classification results is investigated in all simulations with a fixed level of physiological interference.

First, the effect of different levels of Gaussian white noise on the accuracies of the four classifiers based on the same level features was analyzed. As expected, the accuracy of all classifiers increases with *SNR* in the six simulations, as illustrated in Figure 7. However, the accuracy of a-GMM at each *SNR* was higher than the other three classifiers. Moreover, at lower *SNR* ($SNR \leq 10$ dB), the a-GMM has a prominent decoding advantage in simulations 4–6. Even at the lowest $SNR = 1$ dB, the accuracy of a-GMM for all simulations was higher than 70%, which demonstrates superior noise robustness. In simulation 6 with random variation in magnitude of the HRF, the accuracy obtained by a-GMM demonstrated an overwhelming advantage compared to control classifiers.

In addition, we also analyze the effect of different levels of Gaussian white noise on the accuracy of the same a-GMM classifier based on level feature and BPF-statistical features as shown in Figure 8. As observed from the results, the accuracy of a-GMM based on activation level, mean, and slope features increases with *SNR* in all simulations, but the variance, skewness, and kurtosis features do not reveal any regularity. The accuracy of the skewness and kurtosis features fluctuated irregularly with the *SNR*, but both have lower accuracy at each *SNR* compared to the level feature. Also, an attractive phenomenon found in the accuracy results is that there is an abnormal fluctuation in the accuracy based on the variance feature in the lower *SNR* region, especially in simulation 2 where the fluctuation of $SNR = 5$ dB reaches a maximum peak of 96.25%. A reasonable reason for this occurrence may be that the white noise in the passband of the Butterworth BPF is not entirely suppressed, and the spurious activation caused by the white noise at this level has the strongest effect on the statistical characteristic-based variance feature, which happens to magnify the difference between the activation patterns of the two-class tasks and finally leads to abnormally high accuracy. However, the accuracy of the a-GMM based on the level feature was the highest among all simulations, except for the variance-based feature of simulation 2. In addition, the classification performance of the mean-based feature was the best among all BPF-statistical features when the *SNR* was >10 dB.

In-vivo paradigm experiments

Hemodynamic changes

The primitive Δ[HbO] and Δ[HbR] data are band-pass filtered with the 5th order zero-phase Butterworth filter with cutoffs of 0.018 and 0.3 Hz to eliminate global physiological interference. The hemodynamic signals obtained across the six repeated trials of the MA and MS mental tasks during the two data collection sessions were averaged, respectively. To evaluate whether the channels are activated at each time step, the estimated GLM coefficients are converted into the corresponding *t*-statistics value. At time step *k*, a larger *t*-value for a channel indicates a more significant activation of that channel. The *t*-values for all channels of participant 1 after 15 s from the onset of the MA and MS tasks stimulation are presented in Table 2. As observed from the results in Table 2, the most significantly activated channels were channel #5 of the MA and channel #6 of the MS. The corresponding hemodynamic changes of the two channels were shown in Figure 9. As expected, an

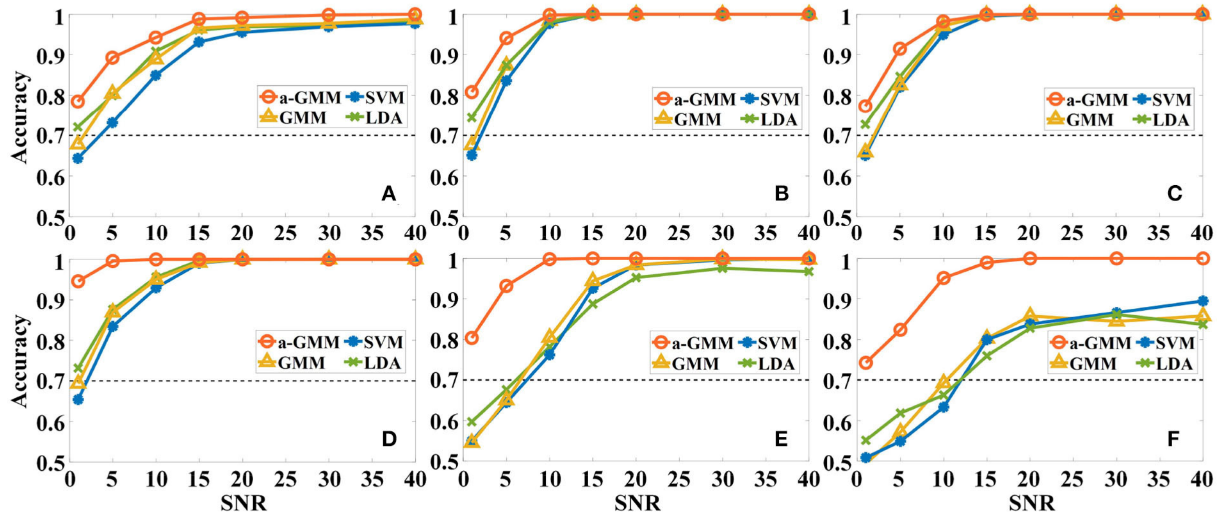

FIGURE 7
The effect of different levels of Gaussian white noise on the classification accuracies of the four classifiers based on the level feature. **(A–F)** Correspond to the accuracy results of simulations 1–6.

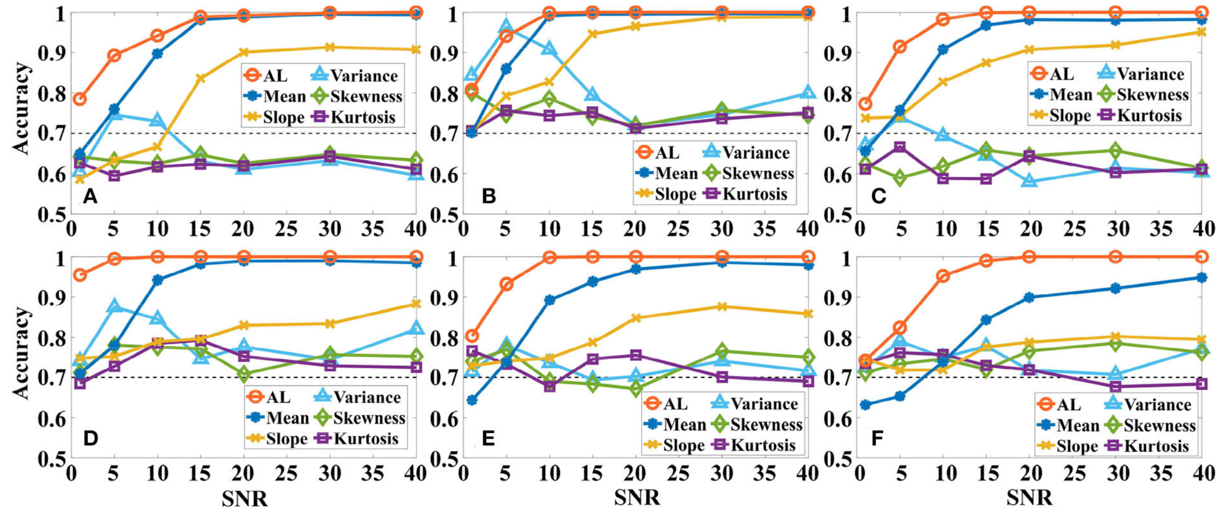

FIGURE 8
The effect of different levels of Gaussian white noise on the classification accuracy of the same a-GMM classifier based on level feature and BPF-statistical features. **(A–F)** Correspond to the accuracy results of simulations 1–6. AL is an abbreviated form of activation level.

TABLE 2 The *t*-values for all channels of participant 1 after 15 s from the onset of the MA and MS tasks stimulation.

	t-values									
Mental task	**CH #1**	**CH #2**	**CH #3**	**CH #4**	**CH #5**	**CH #6**	**CH #7**	**CH #8**	**CH #9**	**CH #10**
MA	2.63	−8.05	−4.15	1.95	10.16	2.59	4.72	3.53	−14.15	−15.54
MS	−0.18	−1.27	−1.74	−1.00	−0.31	1.44	0.70	−0.07	−1.33	1.38

CH, channel.

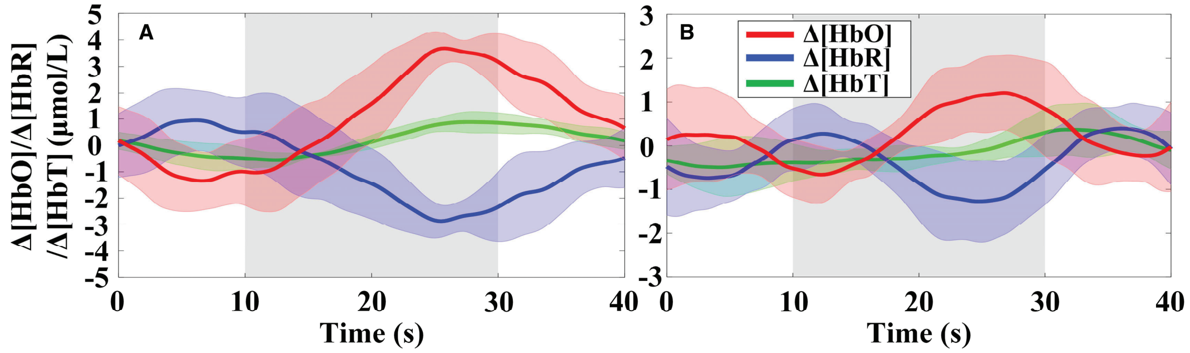

FIGURE 9
Trial-averaged hemoglobin concentration changes for participant 1 in the most significantly activated channels: **(A)** Channel #5 in the MA and **(B)** channel #6 in the MS were significantly activated. The gray highlighted rectangles indicate the stimulation periods. Δ[HbT] indicates the change in total hemoglobin concentration. The shades of the same color around the curves represent the standard deviation.

increase in Δ[HbO] and a decrease in Δ[HbR] were observed during the MA and the MS stimulation period as shown in the gray shaded area in Figures 9A,B.

The OT of trial-averaged Δ[HbO] signal across 6 repetitions of MA and MS tasks during two data collection sessions for participant 1, after 15 s from the task onset, are shown in Figures 10A,B, respectively. The magnitude of the MA-evoked Δ[HbO] is significantly higher than that of the MS for participant 1. Furthermore, channels #5 and #6 were significantly activated under the MA and MS stimulation task, respectively.

Classification accuracy

Primarily, we used the same a-GMM classifier to classify MA and MS tasks, comparing the single-trial accuracy between the level feature and the BPF-statistical features. The individual and average accuracy of MA vs. MS is illustrated in Figure 11. The red dashed line indicates 70% accuracy of effective binary BCI communication (Vidaurre and Blankertz, 2010). The paired-sample t-test yielded significant differences between activation level features and BPF-statistical features at average accuracy for all participants. As observed from the results, the individual and average accuracy obtained by the KF/a-GMM method are significantly higher than those BPF-statistical features. In addition, the average accuracy of only the activation level and mean feature reached above 70%, which has been regarded as a threshold for practical binary communication.

Then, different classifiers are performed to classify MA vs. MS based on the same level features. The individual and average accuracy of MA vs. MS is illustrated in Figure 12. The paired-samples t-test yielded significant differences between the a-GMM classifier and other classifiers in accuracy for all participants. As observed from the results, the average accuracy obtained by the a-GMM classifier was the highest among all classifiers, with an average accuracy of 87.01 ± 4.11%. However, only the LDA classifier obtained an average accuracy below 70% among all classifiers. For the a-GMM classifier, participant 1 and participant 2 achieved excellent classification accuracies of 91.50 and 93.09%, while participant 3 and participant 6 are also very close to 90%.

Discussions

For *in-vivo* paradigm experiments, we initially compared the accuracy of the same a-GMM classifier based on different features, and the average accuracy of the KF/a-GMM approach reached 87.01 ± 4.11% for all participants, as shown in Figure 11. Compared with the skewness feature (61.50 ± 3.41%, $p = 8.8975 \times 10^{-7}$), the classification performance based on the level feature has a maximum improvement of up to 41.48%, and the minimum improvement is 11.31% compared with the mean feature (78.17 ± 5.22%, $p = 0.0051$). Then the classification performance of different classifiers based on the same level feature is compared. As observed in the results of Figure 12, up to 6.20, 15.72, and 26.50% improvement in average accuracy was achieved by a-GMM compared with GMM (81.93 ± 5.54%, $p = 0.0012$), SVM (75.19 ± 4.69%, $p = 3.9656\times10^{-5}$), and LDA (68.78 ± 7.26%, $p = 0.0020$) classifier for all participants, respectively. In classifying MA vs. MS, the classification accuracy of our proposed KF/a-GMM method was 12.71% improved over that of the light intensity based HMM classifier used by Power et al. (2010). Therefore, the KF/a-GMM approach can indeed enhance the accuracy of binary classification for MA and MS mental tasks.

The effect of the c_1 and c_2 parameters of the transition model in the a-GMM classifier on the 10-fold cross-validated accuracy of MA and MS for all participants is shown in Figure 13. The

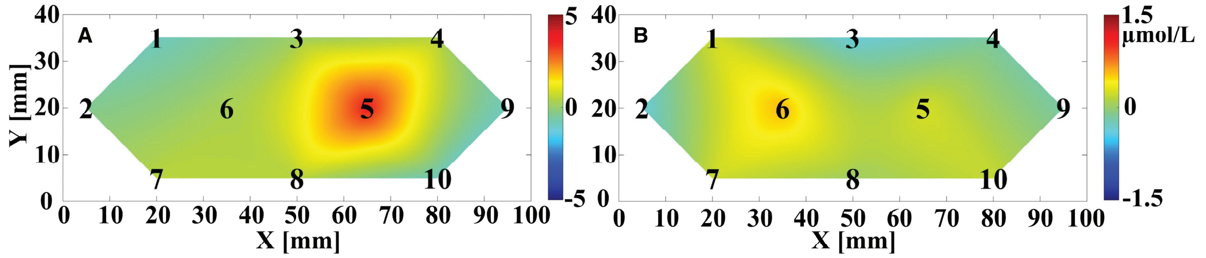

FIGURE 10
The OT of averaged Δ[HbO] across the six repeated trials for participant 1 evoked by **(A)** MA and **(B)** MS after 15 s from the onset of the task. The black numbers denote the position of the sampling channels. The vertical color bar indicates the range in μmol/L.

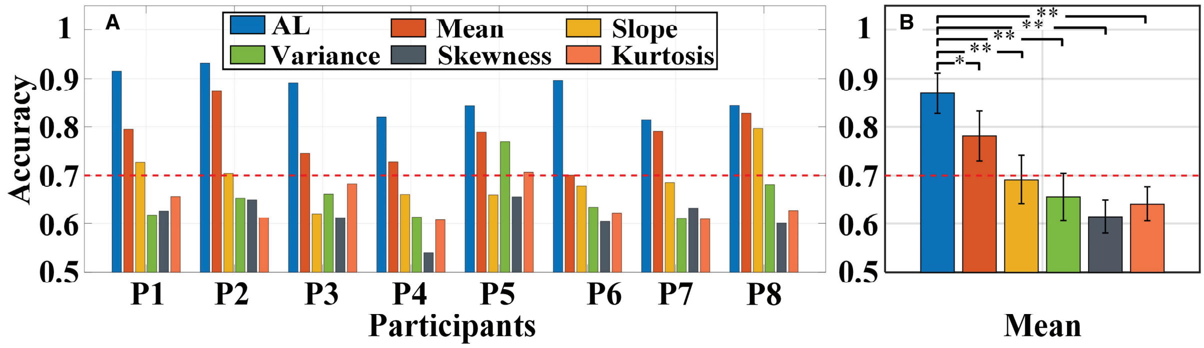

FIGURE 11
Classification accuracy of MA vs. MS obtained using the same a-GMM classifier based on different features extracted from single-trial data of all participants: **(A)** Individual accuracy and **(B)** average accuracy. Error bars indicate the standard deviations, *Represents the significant difference, *$p < 0.01$ and **$p < 0.001$. The red dashed line indicates 70% classification accuracy of effective binary BCI communication.

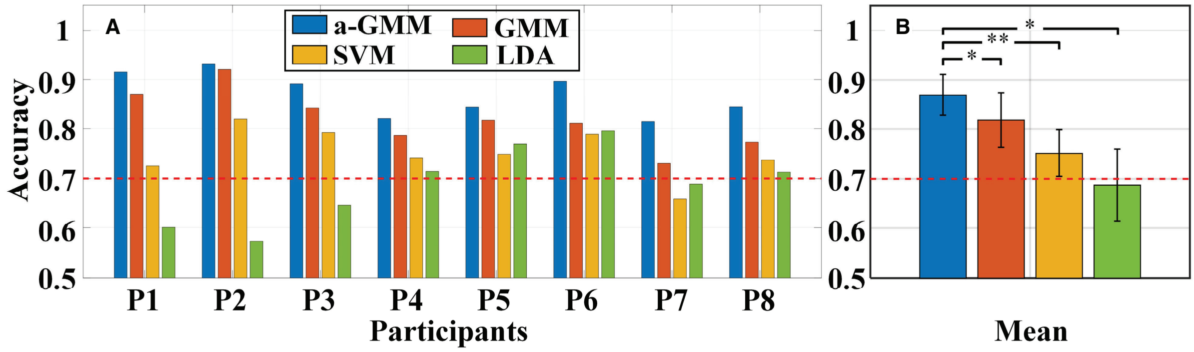

FIGURE 12
Classification accuracy of MA vs. MS for different classifiers constructed by extracting the same level features: **(A)** Individual accuracy and **(B)** average accuracy. Error bars indicate the standard deviations, *Represents the significant difference, *$p < 0.01$ and **$p < 0.001$. The red dashed line indicates 70% classification accuracy of effective binary BCI communication.

accuracy of a-GMM was the highest at $c_1 = 0.01$ and $c_2 = 1$. The c_1 parameter adjusts the rate of change of the activation mean, slightly >0 will achieve higher accuracy. The c_2 parameter is related to the rate of change of the activations covariance, and accuracy is probably better when it is close to 1. Further study on parameter selection can be adaptively iterated over a range of a priori parameters to obtain the optimal combination rather than relying on empirical selections.

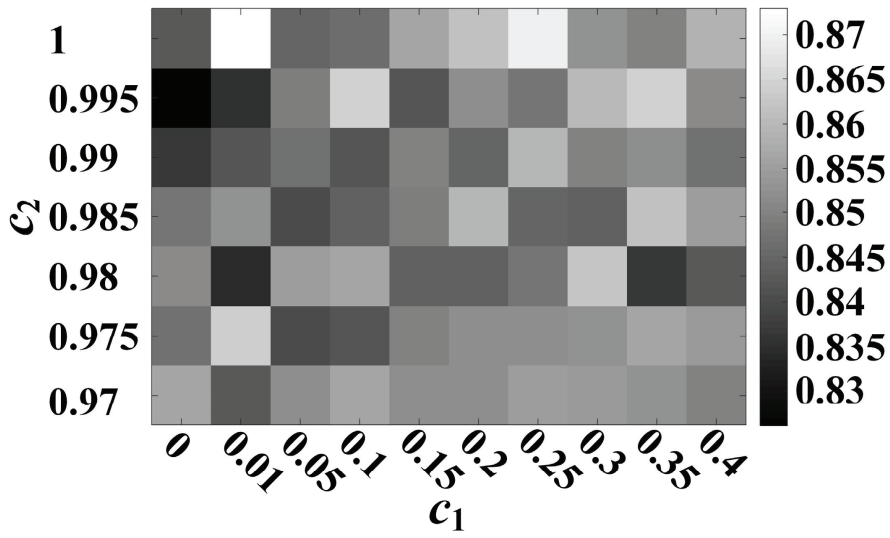

FIGURE 13
Effect of c_1 and c_2 parameters of the transition model on the 10-fold cross-validated accuracy of MA vs. MS for all participants.

Our proposed KF/a-GMM classification method has achieved considerable success in subject-level decoding. However, achieving the goal of across-subject fNIRS decoding is still quite challenging as the large individual differences make it more difficult to find population-level regularities that hold between individuals. Across-subject decoding in fNIRS-BCI classification is an important future direction (Raizada and Connolly, 2012; Jin and Kim, 2020). The drawback of k-fold cross-validation used to evaluate the classification model is that fNIRS data from the same subject are present in both the training and test datasets. Hence, classification models with parameters and hyper-parameters learned from the same subject's data may struggle to generalize to new subjects. Thus, the leave-one-subject-out cross-validation was used to evaluate and compare the performance of the classification model (Gholamiangonabadi et al., 2020). In each cross-validation iteration, one subject's data is used for testing and the remaining subjects' data for training to conduct the subject-independent evaluation. In the across-subject fNIRS decoding MA vs. MS, the decoding accuracy of the a-GMM classifier based on the same level features was 78.44%, higher than that of the GMM (52.81%), SVM (49.69%), and LDA (51.46%) classifiers. The preliminary research results showed that our proposed KF/a-GMM method can learn population-level regularities under the same mental task and has potential advantages in across-subject decoding. The across-subject fNIRS decoding mental task is more complex and needs further study in the future.

The levels estimated by the KF algorithm at each time point k can also be used as real-time features, which can subsequently be used for the real-time classification of the classifier. The potential advantage of KF lies in the real-time and parallel estimation of level features for all channels. The KF algorithm takes an average time of 0.0040 ± 0.0017 s (about 250 Hz) to estimate the simulated fNIRS signal with 18-channel at each time step in parallel on a computer configured with an Intel(R) Core (TM) i7-4790 CPU @ 3.60 GHz and 16.0G RAM. In addition, the average time required by the a-GMM algorithm to decode each test data is 0.0035 ± 0.0023 s (about 286 Hz). Hence, both the KF and a-GMM have low computational costs when they deal with fNIRS data acquired at sampling rates of a few Hz to tens of Hz, and their fast computational speed greatly meets the requirements for real-time classification. It also incorporates the fact that a-GMM can be used for multi-class task classification (without the need to convert a multi-class classification problem into multiple binary classification problems), so that the KF/a-GMM approach can handle the real-time classification of multi-class tasks and be applied to long-term neurofeedback training (NFT) (Luhrs and Goebel, 2017) and rehabilitation training (Matarasso et al., 2021). The threshold for the a-GMM in the practical real-time BCI decoding is typically set to 50% (Abdelnour and Huppert, 2009). The KF/a-GMM method is used to calculate the estimation of the mental task at each time point after stimulus onset. If more than half of the time points within the stimulus period during a single-trial epoch are correctly classified, we obtain an overall correct classification label.

This study has some limitations that will be addressed in the future study. First, the baseline component added to the simulated fNIRS signal is a constant. It might be more realistic to give the baseline a Gaussian pattern. Second, since we use the HRF with fixed parameters in the design matrix, but the HRF of each participant is different, we should accurately estimate the

HRF for each participant. Third, the physiological interference components of the design matrix can be acquired in real-time by auxiliary measurements, replacing manual selection based on spectral analysis. Fourth, as motion artifacts and probe registration have a large impact on single-trial level analysis, it is also worthwhile to investigate how to ensure the robustness of the single-trial GLM model. Measurement equipment for more accurate and rapid positioning of optodes and advanced algorithms for removing motion artifacts are also important directions for future study. Fifth, the initial values of the **Q** and **R** in the KF have a significant influence on the estimated results (Hu et al., 2010). However, the selection of **Q** and **R** based on prior knowledge at the beginning of the experiment also depends on the rich user experience to give an appropriate tracking of the evoked signals. Sixth, the combination of the proposed level features and BPF-statistical features to form a feature set is interesting and valuable and may be helpful in further improving the recognition accuracy of our proposed approach for single-trial mental tasks. Seventh, the comparison of classification methods in this paper is incomplete, comparing only the commonly used LDA classifiers and not the regularized LDA classifier (Bauernfeind et al., 2014) and the adaptive LDA classifier (Li et al., 2017). Eighth, considering the low sample size, preliminary conclusions have been drawn for now. Future studies will increase the sample size to corroborate again. Ninth, channel selection plays a critical role in classifying mental tasks for fNIRS-BCI by reducing data dimensionality, saving model training time, and improving model classification performance (Gulraiz et al., 2022). Besides the commonly used Fisher score method for channel selection (Hwang et al., 2016), the least absolute shrinkage and selection operator homotopy-based sparse representation method proposed by Gulraiz et al. for channel selection can improve the accuracy of walking and resting states (Gulraiz et al., 2022). This method has aroused our great interest and may improve the accuracy of our proposed KF/a-GMM. Tenth, the ongoing activation patterns may vary during the NFT session due to learning effects, and this process may affect the performance of brain state classifiers trained using data obtained before the session (Bagarinao et al., 2020). However, the biggest advantage of our proposed KF/a-GMM is that it is good at tracking changes in activation patterns, which can improve the accuracy of real-time brain states in NFT. On the other hand, the findings of Wang et al. demonstrated that visual-haptic NFT based on EEG-BCI improved cortical activation and the accuracy of MI (Wang et al., 2019). Thus, both our proposed KF/a-GMM and NFT can improve the classification performance of the BCI system, and jointly they can be used to improve cognitive function and enhance the quality of life of patients suffering from brain cognitive disorders. Finally, this approach currently only uses offline mode for data processing and analysis, and we will develop an online version.

Conclusion

A joint adaptive classification approach KF/a-GMM that combines the KF and the unsupervised a-GMM classifier is proposed for accuracy-enhanced pattern recognition for mental tasks. Its effectiveness and advantages are validated by performing both simulation experiments and *in-vivo* paradigm experiments. The results show that this approach is an effective strategy for tracking random variations in brain activation patterns with time evoked by two-class mental tasks and considerably ameliorates the single-trial accuracy of unfiltered and unlabeled fNIRS data from MA and MS mental tasks. The average accuracy of the KF/a-GMM method for all participants in the MA and MS mental tasks was 87.01%, higher than the BPF-statistical features based GMM, SVM, and LDA classifiers. Overall, these results are encouraging and demonstrate the potential of the KF/a-GMM method to improve classification accuracy on mental tasks and provide a new perspective for real-time multi-class mental task classification.

Data availability statement

The original contributions presented in the study are included in the article/supplementary material, further inquiries can be directed to the corresponding author/s.

Ethics statement

The studies involving human participants were reviewed and approved by Tianjin University. The patients/participants provided their written informed consent to participate in this study.

Author contributions

YZ: study design and article writing. PZ, TL, and ZL: data acquisition. PZ, DL, and FG: technical guidance. YZ and FG: data analysis and interpretation. FG: manuscript review—editing and supervision. All authors contributed to the article and approved the submitted version.

Funding

This study was supported by grants from the National Natural Science Foundation of China (Nos. 81871393, 81971656, 62075156, and 61575140).

Conflict of interest

The authors declare that the research was conducted in the absence of any commercial or financial relationships that could be construed as a potential conflict of interest.

Publisher's note

References

Abdelnour, A. F., and Huppert, T. (2009). Real-time imaging of human brain function by near-infrared spectroscopy using an adaptive general linear model. *Neuroimage* 46, 133–143. doi: 10.1016/j.neuroimage.2009.01.033

Alzahab, N. A., Apollonio, L., Di Iorio, A., Alshalak, M., Iarlori, S., Ferracuti, F., et al. (2021). Hybrid Deep Learning (hDL)-Based Brain-Computer Interface (BCI) systems: a systematic review. *Brain Sci.* 11, 75. doi: 10.3390/brainsci11010075

Asgher, U., Khalil, K., Khan, M. J., Ahmad, R., Butt, S. I., Ayaz, Y., et al. (2020). Enhanced accuracy for multiclass mental workload detection using long short-term memory for brain-computer interface. *Front. Neurosci.* 14, 584. doi: 10.3389/fnins.2020.00584

Aydin, E. A. (2020). Subject-specific feature selection for near infrared spectroscopy based brain-computer interfaces. *Comput. Methods Progr. Biomed.* 195, 105535. doi: 10.1016/j.cmpb.2020.105535

Bagarinao, E., Yoshida, A., Terabe, K., Kato, S., and Nakai, T. (2020). Improving real-time brain state classification of motor imagery tasks during neurofeedback training. *Front. Neurosci.* 14, 623. doi: 10.3389/fnins.2020.00623

Bauernfeind, G., Steyrl, D., Brunner, C., and Mueller-Putz, G. R. (2014). Single trial classification of fNIRS-based brain-computer interface mental arithmetic data: a comparison between different classifiers. *Annu. Int. Conf. IEEE Eng. Med. Biol. Soc.* 2014, 2004–2007. doi: 10.1109/EMBC.2014.6944008

Bejm, K., Wojtkiewicz, S., Sawosz, P., Perdziak, M., Pastuszak, Z., Sudakou, A., et al. (2019). Influence of contrast-reversing frequency on the amplitude and spatial distribution of visual cortex hemodynamic responses. *Biomed. Opt. Expr.* 10, 6296–6312. doi: 10.1364/BOE.10.006296

Bishop, C. M. (2006). "Approximate inference," in *Pattern Recognition and Machine Learning (Information Science and Statistics)* (New York, NY: Springer-Verlag), 461–513.

Boas, D. A., Chen, K., Grebert, D., and Franceschini, M. A. (2004). Improving the diffuse optical imaging spatial resolution of the cerebral hemodynamic response to brain activation in humans. *Opt. Lett.* 29, 1506–1508. doi: 10.1364/OL.29.001506

Cao, J. W., Chen, L., Hu, D. H., Dong, F., Jiang, T. J., Gao, W. D., et al. (2021). Unsupervised eye blink artifact detection from EEG with Gaussian mixture model. *IEEE J. Biomed. Health Informat.* 25, 2895–2905. doi: 10.1109/JBHI.2021.3057891

Chen, C., Wen, Y. Z., Cui, S. Y., Qi, X. G., Liu, Z. H., Zhou, L. F., et al. (2020). A multichannel fNIRS system for prefrontal mental task classification with dual-level excitation and deep forest algorithm. *J. Sens.* 2020, 1567567. doi: 10.1155/2020/1567567

Duan, L., Zhao, Z. P., Lin, Y. L., Wu, X. Y., Luo, Y. J., and Xu, P. F. (2018). Wavelet-based method for removing global physiological noise in functional near-infrared spectroscopy. *Biomed. Opt. Expr.* 9, 3805–3820. doi: 10.1364/BOE.9.003805

Ferrari, M., and Quaresima, V. (2012). A brief review on the history of human functional near-infrared spectroscopy (fNIRS) development and fields of application. *Neuroimage* 63, 921–935. doi: 10.1016/j.neuroimage.2012.03.049

Gholamiangonabadi, D., Kiselov, N., and Grolinger, K. (2020). Deep neural networks for human activity recognition with wearable sensors: leave-one-subject-out cross-validation for model selection. *IEEE Access* 8, 133982–133994. doi: 10.1109/ACCESS.2020.3010715

Glover, G. H. (1999). Deconvolution of impulse response in event-related BOLD fMRI. *Neuroimage* 9, 416–429. doi: 10.1006/nimg.1998.0419

Gulraiz, A., Naseer, N., Nazeer, H., Khan, M. J., Khan, R. A., and Khan, U. S. (2022). LASSO homotopy-based sparse representation classification for fNIRS-BCI. *Sensors* 22, 2575. doi: 10.3390/s22072575

Herff, C., Heger, D., Putze, F., Hennrich, J., and Schultz, T. (2013). "Classification of mental tasks in the prefrontal cortex using fNIRS," in *Annual International Conference of the IEEE Engineering in Medicine and Biology Society*. Osaka, 2160–2163. doi: 10.1109/EMBC.2013.6609962

Hoang-Dung, N., Yoo, S.-H., Bhutta, M. R., and Hong, K.-S. (2018). Adaptive filtering of physiological noises in fNIRS data. *Biomed. Eng. Onl.* 17, 180. doi: 10.1186/s12938-018-0613-2

Hong, K.-S., Ghafoor, U., and Khan, M. J. (2020). Brain-machine interfaces using functional near-infrared spectroscopy: a review. *Artif. Life Robot.* 25, 204–218. doi: 10.1007/s10015-020-00592-9

Hu, X.-S., Hong, K.-S., Ge, S. S., and Jeong, M.-Y. (2010). Kalman estimator- and general linear model-based on-line brain activation mapping by near-infrared spectroscopy. *Biomed. Eng. Onl.* 9, 82. doi: 10.1186/1475-925X-9-82

Hwang, H.-J., Choi, H., Kim, J.-Y., Chang, W.-D., Kim, D.-W., Kim, K., et al. (2016). Toward more intuitive brain-computer interfacing: classification of binary covert intentions using functional near-infrared spectroscopy. *J. Biomed. Opt.* 21, 091303. doi: 10.1117/1.JBO.21.9.091303

Jin, L. B., and Kim, E. Y. (2020). Interpretable cross-subject EEG-based emotion recognition using channel-wise features (dagger). *Sensors* 20, 6719. doi: 10.3390/s20236719

Kalman, R. E. (1960). A new approach to linear filtering and prediction problems. *J. Basic Eng.* 82, 35–45. doi: 10.1115/1.3662552

Li, L. M., Zhao, J., Wang, C. R., and Yan, C. J. (2020). Comprehensive evaluation of robotic global performance based on modified principal component analysis. *Int. J. Adv. Robot. Syst.* 17, 1729881419896881. doi: 10.1177/1729881419896881

Li, Z., Jiang, Y. H., Duan, L., and Zhu, C. Z. (2017). A Gaussian mixture model based adaptive classifier for fNIRS brain-computer interfaces and its testing *via* simulation. *J. Neural Eng.* 14, 46014. doi: 10.1088/1741-2552/aa71c0

Lim, L. G., Ung, W. C., Chan, Y. L., Lu, C. K., Sutoko, S., Funane, T., et al. (2020). A unified analytical framework with multiple fNIRS features for mental workload assessment in the prefrontal cortex. *IEEE Trans. Neural Syst. Rehabil. Eng.* 28, 2367–2376. doi: 10.1109/TNSRE.2020.3026991

Lin, X. H., Lei, V. L. C., Li, D. F., and Yuan, Z. (2018). Which is more costly in Chinese to English simultaneous interpreting, "pairing" or "transphrasing?" Evidence from an fNIRS neuroimaging study. *Neurophotonics* 5, 25010. doi: 10.1117/1.NPh.5.2.025010

Liu, D., Wang, B., Pan, T., Li, J., and Gao, F. (2019). Towards quantitative near infrared brain functional imaging: lock-in photon counting instrumentation combined with tomographic reconstruction. *IEEE Access* 7, 8629–8642. doi: 10.1109/ACCESS.2019.2924710

Luhrs, M., and Goebel, R. (2017). Turbo-Satori: a neurofeedback and brain-computer interface toolbox for real-time functional near-infrared spectroscopy. *Neurophotonics* 4, 41504. doi: 10.1117/1.NPh.4.4.041504

Ma, T., Wang, S., Xia, Y., Zhu, X., Evans, J., Sun, Y., et al. (2021). CNN-based classification of fNIRS signals in motor imagery BCI system. *J. Neural Eng.* 18, 56019. doi: 10.1088/1741-2552/abf187

Matarasso, A. K., Rieke, J. D., White, K., Yusufali, M. M., and Daly, J. J. (2021). Combined real-time fMRI and real time fNIRS brain computer interface (BCI): training of volitional wrist extension after stroke, a case series pilot study. *PLoS ONE* 16, e0250431. doi: 10.1371/journal.pone.0250431

Nguyen, T., Condy, E. E., Park, S., Friedman, B. H., and Gandjbakhche, A. (2021). Comparison of functional connectivity in the prefrontal cortex during a simple and an emotional go/no-go task in female versus male groups: an fNIRS study. *Brain Sci.* 11, 909. doi: 10.3390/brainsci11070909

Noori, F. M., Naseer, N., Qureshi, N. K., Nazeer, H., and Khan, R. A. (2017). Optimal feature selection from fNIRS signals using genetic algorithms for BCI. *Neurosci. Lett.* 647, 61–66. doi: 10.1016/j.neulet.2017.03.013

Piper, S. K., Krueger, A., Koch, S. P., Mehnert, J., Habermehl, C., Steinbrink, J., et al. (2014). A wearable multi-channel fNIRS system for brain imaging in freely moving subjects. *Neuroimage* 85, 64–71. doi: 10.1016/j.neuroimage.2013.06.062

Power, S. D., Falk, T. H., and Chau, T. (2010). Classification of prefrontal activity due to mental arithmetic and music imagery using hidden Markov models and frequency domain near-infrared spectroscopy. *J. Neural Eng.* 7, 26002. doi: 10.1088/1741-2560/7/2/026002

Power, S. D., Kushki, A., and Chau, T. (2012). Automatic single-trial discrimination of mental arithmetic, mental singing and the no-control state from prefrontal activity: toward a three-state NIRS-BCI. *BMC Res. Not.* 5, 1–10. doi: 10.1186/1756-0500-5-141

Raizada, R. D. S., and Connolly, A. C. (2012). What makes different people's representations alike: neural similarity space solves the problem of across-subject fMRI decoding. *J. Cogn. Neurosci.* 24, 868–877. doi: 10.1162/jocn_a_00189

Scarpa, F., Brigadoi, S., Cutini, S., Scatturin, P., Zorzi, M., Dell'Acqua, R., et al. (2013). A reference-channel based methodology to improve estimation of event-related hemodynamic response from fNIRS measurements. *Neuroimage* 72, 106–119. doi: 10.1016/j.neuroimage.2013.01.021

Schroeter, M. L., Bucheler, M. M., Muller, K., Uludag, K., Obrig, H., Lohmann, G., et al. (2004). Towards a standard analysis for functional near-infrared imaging. *Neuroimage* 21, 283–290. doi: 10.1016/j.neuroimage.2003.09.054

Tomita, Y., Vialatte, F.-B., Dreyfus, G., Mitsukura, Y., Bakardjian, H., and Cichocki, A. (2014). Bimodal BCI using simultaneously NIRS and EEG. *IEEE Trans. Biomed. Eng.* 61, 1274–1284. doi: 10.1109/TBME.2014.2300492

Trakoolwilaiwan, T., Behboodi, B., Lee, J., Kim, K., and Choi, J.-W. (2018). Convolutional neural network for high-accuracy functional near-infrared spectroscopy in a brain-computer interface: three-class classification of rest, right-, and left-hand motor execution. *Neurophotonics* 5, 11008. doi: 10.1117/1.NPh.5.1.011008

Vidaurre, C., and Blankertz, B. (2010). Towards a cure for BCI illiteracy. *Brain Topogr.* 23, 194–198. doi: 10.1007/s10548-009-0121-6

Wang, B., Zhang, Y., Liu, D., Pan, T., Liu, Y., Bai, L., et al. (2020). Joint direct estimation of hemodynamic response function and activation level in brain functional high density diffuse optical tomography. *Biomed. Opt. Expr.* 11, 3025–3042. doi: 10.1364/BOE.386567

Wang, B. Y., Zhang, Y., Liu, D. Y., Ding, X. M., Dan, M., Pan, T. T., et al. (2018). Towards real-time diffuse optical tomography for imaging brain functions cooperated with Kalman estimator. *Clin. Transl. Neurophoton.* 10480, 1–8. doi: 10.1117/12.2291732

Wang, Z. P., Zhou, Y. J., Chen, L., Gu, B., Liu, S., Xu, M. P., et al. (2019). A BCI based visual-haptic neurofeedback training improves cortical activations and classification performance during motor imagery. *J. Neural Eng.* 16, 66012. doi: 10.1088/1741-2552/ab377d

Welch, G., and Bishop, G. (1995). *An Introduction to the Kalman Filter. Technical Report*. Chapel Hill, NC: University of North Carolina at Chapel Hill.

Weyand, S., Schudlo, L., Takehara-Nishiuchi, K., and Chau, T. (2015). Usability and performance-informed selection of personalized mental tasks for an online near-infrared spectroscopy brain-computer interface. *Neurophotonics* 2, 25001. doi: 10.1117/1.NPh.2.2.025001

Wickramaratne, S. D., and Mahmud, M. S. (2021). Conditional-GAN based data augmentation for deep learning task classifier improvement using fNIRS data. *Front. Big Data* 4, 659146. doi: 10.3389/fdata.2021.659146

Yoo, S.-H., Woo, S.-W., and Amad, Z. (2018). "Classification of three categories from prefrontal cortex using LSTM networks: fNIRS study," in *18th International Conference on Control, Automation and Systems (ICCAS).* PyeongChang, 1141–1146.

Zhang, Y., Wang, B., and Gao, F. (2018). "Real-time decoding for fNIRS-based Brain Computer Interface using adaptive Gaussian mixture model classifier and Kalman estimator," in *Asia Communications and Photonics Conference (ACP).* Hangzhou. doi: 10.1109/ACP.2018.8596271

frontiers | Frontiers in Neuroscience

TYPE Original Research
PUBLISHED 03 November 2022
DOI 10.3389/fnins.2022.1033379

OPEN ACCESS

EDITED BY
Camillo Porcaro,
Università degli Studi di Padova, Italy

REVIEWED BY
Yanlu Wang,
Karolinska Institutet (KI), Sweden
Pedro Miguel Rodrigues,
Universidade Católica Portuguesa,
Portugal
Francesco Mattioli,
Institute of Cognitive Sciences
and Technologies (ISTC-CNR), Italy

*CORRESPONDENCE
Seung Wan Kang
seungwkang@imedisync.com;
drdemian@snu.ac.kr

SPECIALTY SECTION
This article was submitted to
Brain Imaging Methods,
a section of the journal
Frontiers in Neuroscience

RECEIVED 31 August 2022
ACCEPTED 14 October 2022
PUBLISHED 03 November 2022

CITATION
Jeong T, Park U and Kang SW (2022)
Novel quantitative
electroencephalogram feature image
adapted for deep learning:
Verification through classification
of Alzheimer's disease dementia.
Front. Neurosci. 16:1033379.
doi: 10.3389/fnins.2022.1033379

Novel quantitative electroencephalogram feature image adapted for deep learning: Verification through classification of Alzheimer's disease dementia

Taegyun Jeong[1], Ukeob Park[1] and Seung Wan Kang[1,2]*

[1]iMediSync, Inc., Seoul, South Korea, [2]National Standard Reference Data Center for Korean EEG, College of Nursing, Seoul National University, Seoul, South Korea

Quantitative electroencephalography (QEEG) analysis is commonly adopted for the investigation of various neurological disorders, revealing electroencephalogram (EEG) features associated with specific dysfunctions. Conventionally, topographies are widely utilized for spatial representation of EEG characteristics at specific frequencies or frequency bands. However, multiple topographies at various frequency bands are required for a complete description of brain activity. In consequence, use of topographies for the training of deep learning algorithms is often challenging. The present study describes the development and application of a novel QEEG feature image that integrates all required spatial and spectral information within a single image, overcoming conventional obstacles. EEG powers recorded at 19 channels defined by the international 10–20 system were pre-processed using the EEG auto-analysis system iSyncBrain®, removing the artifact components selected through independent component analysis (ICA) and rejecting bad epochs. Hereafter, spectral powers computed through fast Fourier transform (FFT) were standardized into Z-scores through iMediSync, Inc.'s age- and sex-specific normative database. The standardized spectral powers for each channel were subsequently rearranged and concatenated into a rectangular feature matrix, in accordance with their spatial location on the scalp surface. Application of various feature engineering techniques on the established feature matrix yielded multiple types of feature images. Such feature images were utilized in the deep learning classification of Alzheimer's disease dementia (ADD) and non-Alzheimer's disease dementia (NADD) data, in order to validate the use of our novel feature images. The resulting classification accuracy was 97.4%. The Classification criteria were further inferred through an explainable artificial intelligence (XAI) algorithm, which complied with the conventionally known EEG characteristics of AD. Such outstanding classification performance bolsters the potential of our novel QEEG feature images in broadening QEEG utility.

KEYWORDS

electroencephalogram, EEG, QEEG, deep learning, Alzheimer's disease, XAI

Introduction

Electroencephalogram (EEG) is an electrical pattern measured at multiple channel locations on the scalp, reflecting cortical activities of the underlying brain regions. Quantitative electroencephalography (QEEG) enables mapping of specific brain functions with the features extracted from digitized EEG through various techniques, such as spectral analysis (Nuwer, 1988).

Raw EEG signals can be decomposed into various waveforms defined by oscillation frequencies through Fourier transform, typically consisting of five frequency bands, designated delta, theta, alpha, beta, and gamma. Delta and theta waves are dominant during the sleeping state, whereas alpha waves (resting state rhythm) are dominant in eyes-closed resting state. Beta waves become dominant when put under stress or during concentration and gamma waves are found when highly alert. However, gamma waves are easily contaminated with a signal artifact that arise from muscle movements (Malik and Amin, 2017; Moini and Piran, 2020).

Quantitative electroencephalography has been employed in the diagnosis of several neurological disorders (Livint Popa et al., 2020), in view of the fact that atypical spectral properties during a certain state correspond to clinically relevant abnormalities. Furthermore, employment of a age- and sex-differentiated normative database can aid in the standardization of the spectral powers, which eliminates variations that arise due to differences in age and sex.

Visualization of EEG spectral powers is crucial for the inspection and diagnosis of abnormalities. Several studies adopt topographic representation, which maps the EEG powers measured at pre-defined channels onto their respective locations over the surface of the scalp. The process can be performed at various frequencies or bands of frequencies, and at different power scales (Yuvaraj et al., 2014).

Although spectral topographies are useful for the visualization of brain activity, it is often difficult to interpret brain functionality as a whole from a single topography which represents spectral power distribution at a specific frequency band. Thus, several topographies at various ranges of frequencies are required to provide a more complete description of brain functionality. Due to this, the use of topographies as feature images for the training of deep learning algorithms becomes problematic seeing as how multiple topographies are required to fully describe a single class label. Therefore, the present study developed a novel QEEG-derived feature image which is capable of overcoming the disadvantages of prior QEEG-based feature sets. The novel feature image sufficiently holds both spatial and temporal information with high resolution and is fully adapted for the training of deep learning algorithms.

Alzheimer's disease (AD), which the present study focuses on for the verification of the novel feature image, is an irreversible neurodegenerative disorder which is associated with the formation of beta amyloid plaques or neurofibrillary tangles resulting from the dysfunction of microtubule-associated protein tau. The plaques form inside or outside of neurons in the brain, progressively destroying neurons and shrinking the brain, resulting in a gradual decline in cognitive function (Iqbal et al., 2005; Murphy and LeVine, 2010). Patients are usually diagnosed as having AD dementia (ADD) if they are incapable of independent daily living and exhibit imaging β-amyloid plaques and/or tauopathy above a certain threshold, which is most evident in positron emission tomography (PET) scans (Haller et al., 2020). However, PET scans are highly costly, and many nations lack sufficient access to PET scanners. Hence, there have been previous attempts to screen for ADD through QEEG-based features, which are easier to access. For example, Meghdadi et al. (2021) claims that there are resting state EEG biomarkers that can sufficiently indicate characteristics of ADD and mild cognitive impairment (MCI), with strong emphasis on the spectral band theta and alpha. Porcaro et al. (2022) also attempted discrimination of ADD from MCI and an elderly control group using P300 response which is an event-related potential (ERP) component. However, their studies did not employ deep learning algorithms.

Instead, we performed deep learning classification of clinically labeled ADD and non-ADD (NADD) data in the present study, using the novel feature image dataset. Provided that the deep learning model developed in the present study yields a promising classification performance, our novel feature images bear great potential for application in deep learning classification of several other neurological diseases, ultimately resulting in the expansion of QEEG utility.

Materials and methods

Electroencephalogram recording and processing

All EEG data employed in the present study were recorded using wet sensor-based Mitsar-EEG systems (Mitsar Co. Ltd., St. Petersburg, Russia) in the eyes-closed resting state, at the 19 channel locations defined by the international 10–20 system (Fp1, Fp2, F7, F8, F3, F4, Fz, T3, T4, C3, C4, Cz, T5, T6, P3, P4, Pz, O1, O2) with linked-ear reference. Electrical impedance was kept at 10 kΩ or below for all channel electrodes. All data were digitized in continuous recording mode for approximately 2–3 min, with sampling rate of 250 Hz which prevents aliasing effects. The ground electrode was located between the AFz and Fz electrodes. All recorded data were re-referenced to a common average reference post-data collection for standardization of the data.

The re-referenced data were further processed using an AI-driven auto-analysis system iSyncBrain® (Ver. 3.0, iMediSync, Inc., Seoul, South Korea) which performs bandpass filtering of signals outside the frequency band of interest (1–45.5 Hz), bad epoch rejection, and independent component analysis (ICA). Electrical patterns detected at multiple channels on the scalp represent a complex weighted sum of several electrical signals, comprised of components originating from electrical sources in the brain, non-stationary noises such as drowsiness or poor contact between electrodes and the scalp, and stationary noises such as eye movement (electrooculography), muscle movement (electromyography), and heartbeats (electrocardiography). Bad epoch rejection aids in elimination of non-stationary noises, while ICA can separate stationary noises as well as help identify their origins (Jutten and Herault, 1991). The ICA components for all data were carefully inspected to assure robust data quality through the removal of artifact components.

Feature engineering

Standardization of the electroencephalogram data

Brain functionalities are known to vary with gender and clearly degenerate with age. To account for this, our study utilized iMediSync, Inc's normative database ISB-NormDB which holds EEG data of 1,289 healthy control subjects (553 males, 736 females) aged 4.5–81 years old (Ko et al., 2021). The database provides standardized age- and sex-specific features referred to as Z-scores, which are common and statistically robust measures of variation from norms and capture standard deviation. Use of such features can also help reduce a strong dominance of alpha waves, commonly observed in the resting state EEGs of healthy adults measured in the eyes closed condition (Halgren et al., 2019).

The present study utilized sensor level relative power values ranging from 1 to 45 Hz, with a resolution of 0.25 Hz. Z-scores were then calculated *via* reference to ISB-NormDB, which returned 176 Z-score values at 19 electrode locations. We also grouped the spectral powers into eight different frequency bands, namely, delta (1–4 Hz), theta (4–8 Hz), alpha1 (8–10 Hz), alpha2 (10–12 Hz), beta1 (12–15 Hz), beta2 (15–20 Hz), beta3 (20–30 Hz), and gamma (30–45 Hz). Alpha band was subdivided into slower and faster alpha bands (alpha1 and alpha2) since resting state alpha waves are highly related to the cognition status (Ramsay et al., 2021). Beta bands were also subdivided into low, mid, and high beta bands (beta1, beta2, and beta3) in order to dissociate the characteristics of the sensorimotor rhythm (Arroyo et al., 1993).

Feature matrix

Channel locations specified by the international 10–20 system were split into left and right regions, where the central electrodes were taken to belong in both regions. Through rearrangement of the locations into a rectangular format (**Figure 1**), a single feature matrix was created with the x-axis representing the frequency, and the y-axis representing the channels. Each side of the rearranged matrix consists of 176 frequency bins with a 0.25 Hz resolution, hence the x-axis holds 352 bins in total when both sides are summed. The 19 channels were also rearranged with foremost channels at the top of the matrix and central channels included in both sides. As a result, we acquired a matrix with a shape of 352 by 11.

Feature image

Topographies visualize spatial representation of EEG data, at a given frequency band (Arab et al., 2010) while power spectral density presents the amplitude of EEG power per frequency bins describing frequency characteristics (Shim and Shin, 2020). Rearrangement of channels and spectral powers into the above rectangular orientation adopts both the spatial and spectral benefits of topographies and power spectral density. **Figure 2** represents the feature matrix visualized as an image with the range of color scale set as -1.96 to 1.96 Z-score, and topographies, yielded from the same EEG data using iSyncBrain®.

Multiple feature engineering approaches were applied to the matrix, yielding four types of feature images. The established datasets were used to train and test neural network models. Thereafter, the effects of varying feature images on the classification performance were analyzed.

The first method applied nearest interpolation to the feature matrix, which simply stretches the matrix in the y-direction to match the sizes of the x-axis and y-axis. This yields a square image with a shape of 352 by 352 pixels, with clear edges between consecutive rows and columns (**Figures 2**, **3A**).

In order to smoothen out the edges, bicubic interpolation was applied instead to the feature matrix as the second method.

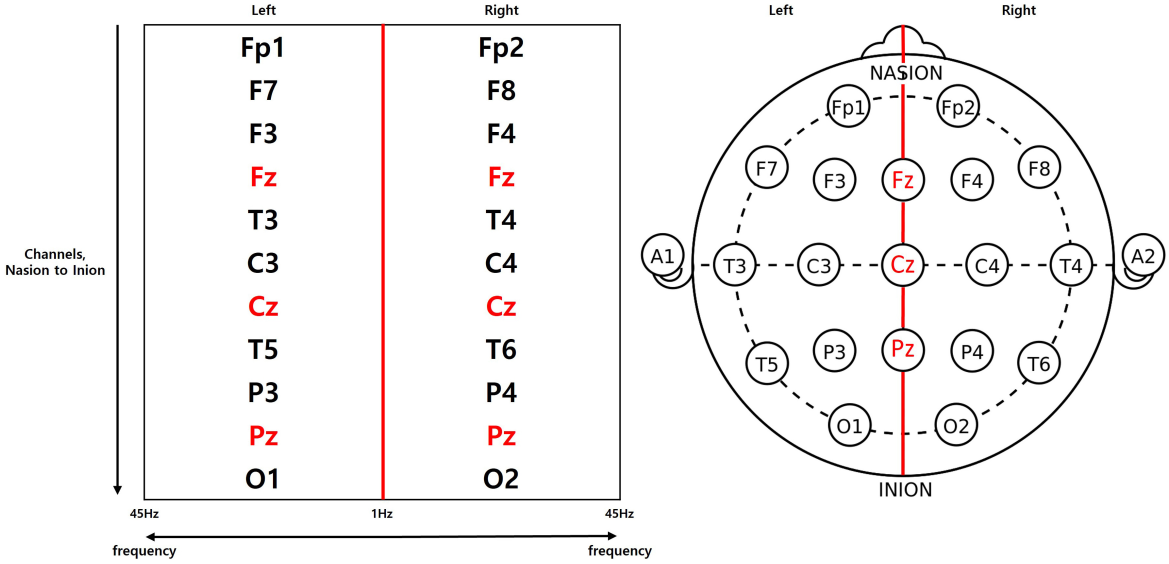

FIGURE 1
Feature matrix which redistributes the channels into a rectangular arrangement.

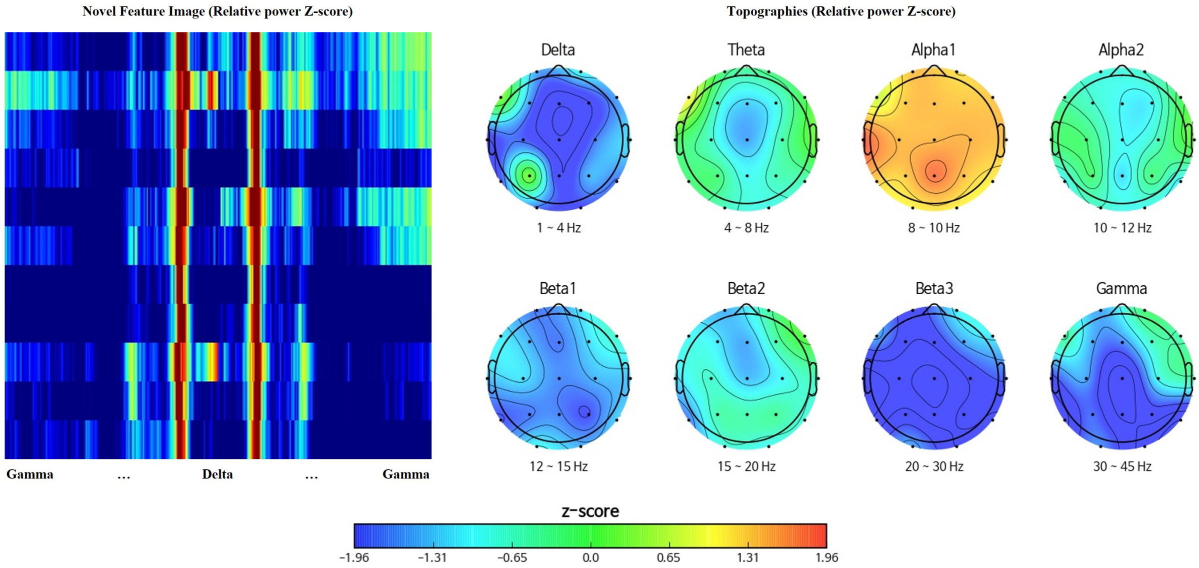

FIGURE 2
Comparison between the novel feature image and traditional topographies showing clear spatiotemporal resemblance.

Bicubic interpolation adopts a third degree polynomial to resample data points in both the x- and y- directions, resulting in smoother color transitions (**Figure 3B**). Equation 1 represents the third degree polynomial used to compute data points through bicubic interpolation. Given that we want to estimate the value of the interpolation surface within the four points (x, x), (x, y), (y, x), and (y, y), spatial derivatives from the 16 neighboring points to the point (x, x) are expressed in terms of 16 coefficients a $(a_{00}{-}a_{33})$ using Eq. 1. The interpolation surface $p\,(x, y)$ can be calculated through the determined values of a (Gao and Gruev, 2011).

$$p\left(x, y\right) = \sum_{i=0}^{3}\sum_{j=0}^{3} a_{ij}x^{i}y^{j} \tag{1}$$

All EEG data were measured in a calm resting state with the subjects' eyes closed. It is commonly accepted that alpha waves are dominant in such a state, whereas very high frequency waves

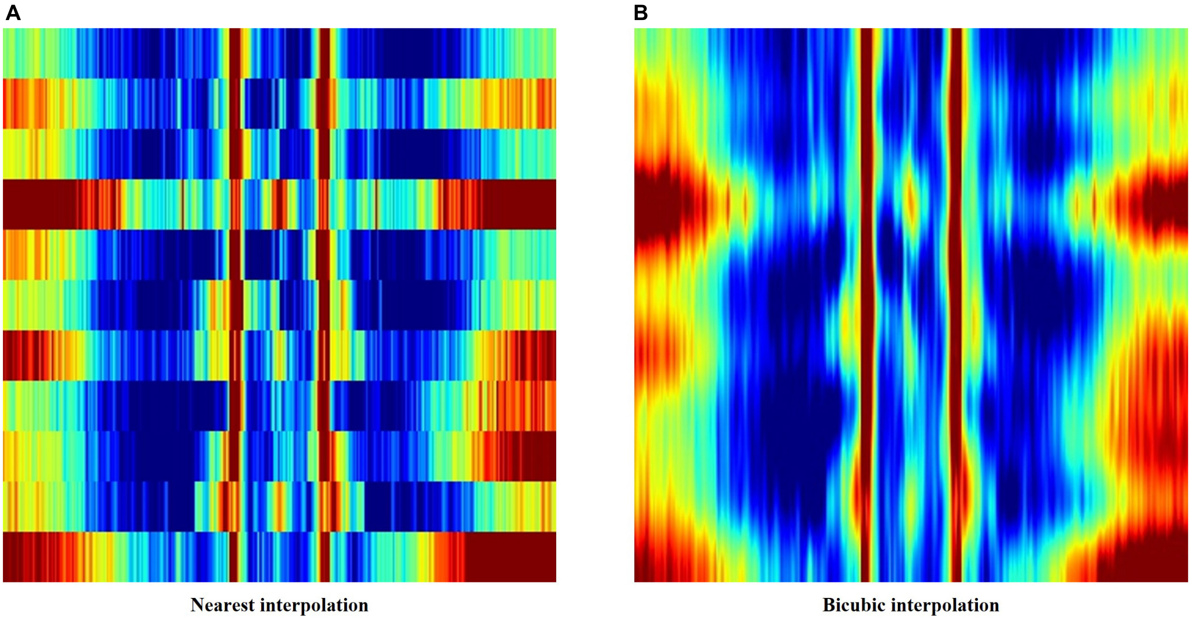

FIGURE 3
(A) Feature image created using nearest interpolation. **(B)** Feature image created using bicubic interpolation from the same electroencephalography (EEG) data.

are easily contaminated by electromyography or external noise. Hence, we created a weight map which zero pads the image regions representing beta3 and gamma frequency bands. In doing so, zero padded pixels appear black when mapped into RGB values (Figure 4), losing their significance as distinguishing features.

Lastly, we rescaled the proportions of frequency bands within the feature image. High frequency regions (beta3–gamma) were first deleted from the feature matrix. A rectangular image with size of 152 by 152 pixels was created by adopting bicubic interpolation, which includes six frequency bands ranging from 1 to 20 Hz (delta–beta2). Each frequency band has a resolution of 0.25 Hz, resulting in a different number of bins. Hence, their proportions are different when visualized as an image, which could influence the effect of a specific frequency band on classification. In order to avoid this, we rescaled each region into matching widths and recreated the feature image (Figure 5 and Table 1).

Four different image datasets were created using the feature engineering techniques described above and were subsequently used in the deep learning-based classification of ADD and NADD data.

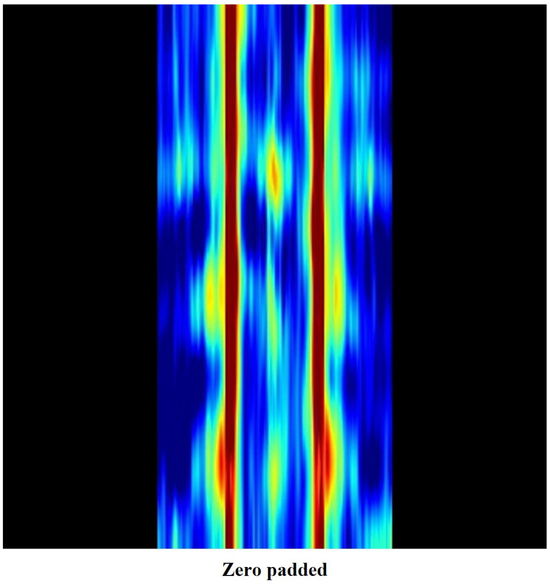

FIGURE 4
Weight map image where frequencies over 20 Hz are zero padded.

Classification data

Diagnostic criteria

The present study utilized community-based subjective cognitive decline (SCD), MCI, and ADD data received from multiple clinical institutions in South Korea: Chung-Ang University (CAU) hospital; Hanyang university hospital; Inha university hospital; Seoul National University Boramae Medical Center (SNUBMC); Yonsei Severance hospital. Clinical

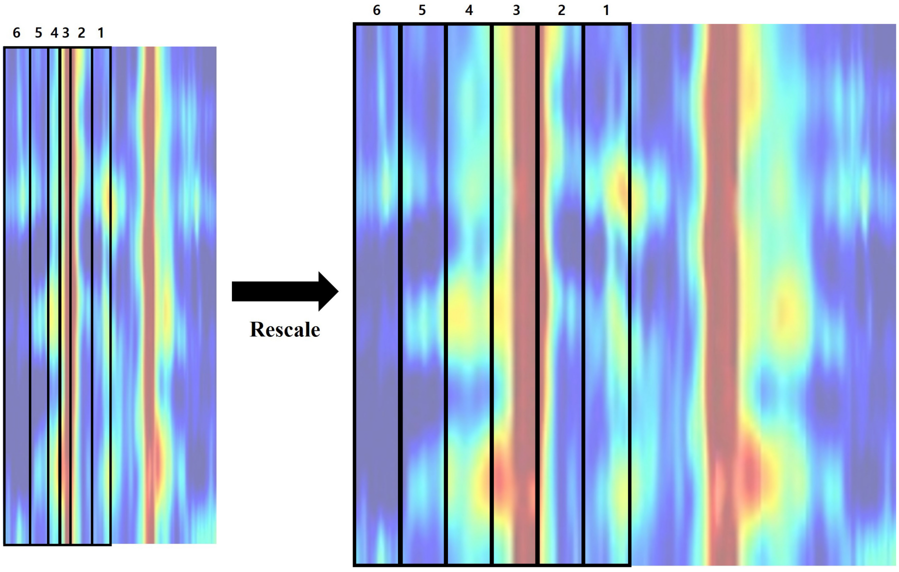

FIGURE 5
Rescaling the proportions of frequency bands composing the feature image.

TABLE 1 Size of each frequency band region before and after the rescaling process.

Region	Frequency band	Initial size (x by y)	Rescaled size (x by y)
1	Delta (1–4 Hz)	12 by 152	20 by 240
2	Theta (4–8 Hz)	16 by 152	20 by 240
3	Alpha1 (8–10 Hz)	8 by 152	20 by 240
4	Alpha2 (10–12 Hz)	8 by 152	20 by 240
5	Beta1 (12–15 Hz)	12 by 152	20 by 240
6	Beta2 (15–20 Hz)	20 by 152	20 by 240

Dementia Rating (CDR) was the main diagnostic criterion along with several other factors, including the clinicians' independent judgements based on their experiences. CDR is a globally employed method for clinical judgment of the individual's cognition status through the assessment of six cognitive and behavioral categories (Kim et al., 2017). SCD data is comprised of individuals that met the following criteria commonly used by the Korean AD society (Ho and Yang, 2020): CDR = 0; 60 years old or older; persistent subjective complaints of cognitive decline; completed 6 years of primary school or more; memory test and cognitive test scores below the normative mean within 0–1.5 standard deviations.

Mild cognitive impairment data is comprised of individuals that met the following criteria: CDR = 0 or 0.5; 60 years old or older; persistent subjective complaints of cognitive decline; completed 6 years of primary school or more; memory test and cognitive test scores below the normative mean by more than 1.5 standard deviations; normal performance in activities of daily living (ADL). In addition, clinicians further examined and diagnosed the patients through more comprehensive tests.

Alzheimer's disease dementia data is comprised of individuals that met the following criteria: CDR $\geq$ 1; 60 years or older; completed 6 years of primary school or more; memory test and cognitive test scores severely below the normative mean; poor performance in ADL.

Quantitative electroencephalography-based comparisons between the ADD group and NADD group can help identify distinguishing characteristics of ADD and begin to reveal the nature of progression from MCI to ADD. One obvious application for such research includes improving early detection by extending diagnostic signs beyond the current imprecise measure of ADL (Mlinac and Feng, 2016).

Dataset establishment

The dataset was segregated into two groups, ADD and NADD. The NADD group consisted of subjective cognitive decline (SCD) and mild cognitive impairment (MCI) data, along

TABLE 2 Table describing the dataset used in classification.

		NADD			
	ADD	Normal		MCI	Total
		NormDB	SCD		
Clinical institutions	137	0	262	142	541
iMediSync, Inc.	0	224	0	0	224
Total	137	224	262	142	765

with iMediSync, Inc.'s EEG data of healthy individuals from ISB-NormDB (Ko et al., 2021). The inclusion of MCI data in the NADD group was crucial for the identification of significant ADD-specific characteristics that are not observed in the pre-clinical stage of ADD. The final dataset (N = 765; 137 ADD, 628 NADD) was established, in which 10% of the data (N = 77; 14 ADD, 63 NADD) were randomly selected and excluded as test data for later verification of the developed classification model.

Data imbalance is often inevitable when the classification task involves community-based clinical data collected from clinical institutions. The dataset provided for the present study consisted of significantly less ADD data. Hence, a 9 to 1 train to test ratio was selected, since deep neural networks often require significantly more information for a sufficient training of the network due to its more complex structure in comparison to machine learning algorithms. Although this may raise concerns in chances of overfitting, the significant differences in ADD and NADD QEEG characteristics aid in prevention of overfitting. Thorough verification has also been carried out *via* an explainable artificial intelligence (XAI) algorithm to make certain that the models are not overfitted.

Table 2 describes the established dataset. Age and sex information were not included since age-and sex-standardized Z-scores were employed in the study.

Classification model

Transfer learning is a commonly employed method in computer vision research. Building a neural network structure from scratch is time consuming, since various structures must be trained and tested in order to find a structure that outputs a sufficient classification performance. Hence, structures of various pre-established image networks that are known to result in an outstanding image classification performance can be imported and used to train custom datasets (Best et al., 2020). Various image classification tasks, namely, in the detection of objects within images, adopt convolutional neural network (CNN) based image network structures that have already been

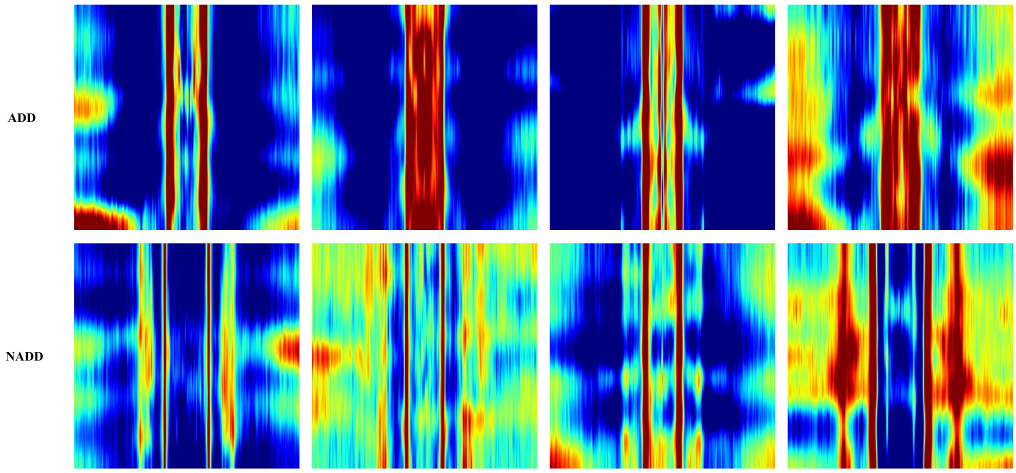

FIGURE 6
Typical feature images representing the classes Alzheimer's disease dementia (ADD) and non-Alzheimer's disease dementia (NADD).

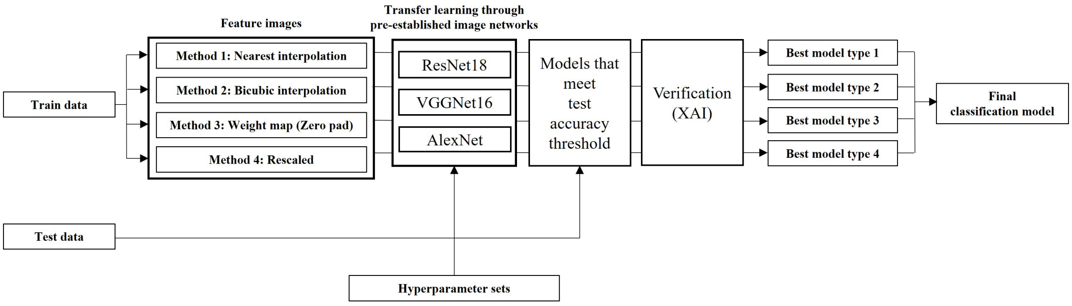

FIGURE 7
Modeling pipeline which summarizes model yielding and verification processes.

pre-trained with large-scale data, due to difficulties in the collection of sufficient data needed to train the network from scratch. However, the use of such pre-trained networks is only applicable when classifying similar types of images, in which the network has been pre-trained with. The image datasets established in the present study significantly differ from the dataset that were employed in the pre-training of such image networks. Hence, we adopted only the network structures, training them from scratch.

The objective of the present study is the verification of novel feature images as features for deep learning training, not the development of a state-of-the-art classifier. Hence, complex fine tuning of the image networks had not been performed. Instead, various user-provided sets of hyperparameters were

TABLE 3 Confusion matrices for selected best models trained with different types of image networks and images constructed through varying feature engineering techniques.

<table>
<tr><th colspan="6">18-layer ResNet</th></tr>
<tr><th colspan="3">1. Nearest</th><th colspan="3">2. Bicubic</th></tr>
<tr><th></th><th>True ADD</th><th>True NADD</th><th></th><th>True ADD</th><th>True NADD</th></tr>
<tr><td>Pred ADD</td><td>12</td><td>5</td><td>Pred ADD</td><td>13</td><td>4</td></tr>
<tr><td>Pred NADD</td><td>2</td><td>58</td><td>Pred NADD</td><td>1</td><td>59</td></tr>
<tr><th colspan="3">3. Weight map</th><th colspan="3">4. Rescaled</th></tr>
<tr><th></th><th>True ADD</th><th>True NADD</th><th></th><th>True ADD</th><th>True NADD</th></tr>
<tr><td>Pred ADD</td><td>14</td><td>2</td><td>Pred ADD</td><td>13</td><td>5</td></tr>
<tr><td>Pred NADD</td><td>0</td><td>61</td><td>Pred NADD</td><td>1</td><td>58</td></tr>
<tr><th colspan="6">16-layer VGGNet</th></tr>
<tr><th colspan="3">1. Nearest</th><th colspan="3">2. Bicubic</th></tr>
<tr><th></th><th>True ADD</th><th>True NADD</th><th></th><th>True ADD</th><th>True NADD</th></tr>
<tr><td>Pred ADD</td><td>12</td><td>5</td><td>Pred ADD</td><td>13</td><td>5</td></tr>
<tr><td>Pred NADD</td><td>2</td><td>58</td><td>Pred NADD</td><td>1</td><td>58</td></tr>
<tr><th colspan="3">3. Weight map</th><th colspan="3">4. Rescaled</th></tr>
<tr><th></th><th>True ADD</th><th>True NADD</th><th></th><th>True ADD</th><th>True NADD</th></tr>
<tr><td>Pred ADD</td><td>13</td><td>2</td><td>Pred ADD</td><td>13</td><td>5</td></tr>
<tr><td>Pred NADD</td><td>1</td><td>61</td><td>Pred NADD</td><td>1</td><td>58</td></tr>
<tr><th colspan="6">AlexNet</th></tr>
<tr><th colspan="3">1. Nearest</th><th colspan="3">2. Bicubic</th></tr>
<tr><th></th><th>True ADD</th><th>True NADD</th><th></th><th>True ADD</th><th>True NADD</th></tr>
<tr><td>Pred ADD</td><td>12</td><td>5</td><td>Pred ADD</td><td>13</td><td>4</td></tr>
<tr><td>Pred NADD</td><td>2</td><td>58</td><td>Pred NADD</td><td>1</td><td>59</td></tr>
<tr><th colspan="3">3. Weight map</th><th colspan="3">4. Rescaled</th></tr>
<tr><th></th><th>True ADD</th><th>True NADD</th><th></th><th>True ADD</th><th>True NADD</th></tr>
<tr><td>Pred ADD</td><td>13</td><td>3</td><td>Pred ADD</td><td>12</td><td>5</td></tr>
<tr><td>Pred NADD</td><td>1</td><td>60</td><td>Pred NADD</td><td>2</td><td>58</td></tr>
</table>

used to train the following pre-established image networks: Alex Network (AlexNet); 16-layer visual geometry group network (VGGNet); 18-layer ResNet. High-performance models that met the set threshold of classification accuracy for each type of image networks were selected and saved. They were then further compared and verified using XAI techniques.

Image network structures

Alex network

AlexNet structure consists of five convolutional layers with selective max pooling layers, and three fully connected layers with 1,000-way softmax at the end. AlexNet employs rectified linear unit (ReLU) activation function instead of the tanh function, which was the standard before the introduction of AlexNet. Dropout regularization method was also applied for the prevention of overfitting (Krizhevsky et al., 2017). Although it showed outstanding classification performance at the time, the network employs large convolution kernels, which results in rapid decline of the feature map size and resolution. Hence, the structure is prone to loss of local features (Xiao et al., 2017; Li et al., 2021).

TABLE 4 Accuracy, sensitivity, and specificity of the established best models trained with different types of image networks and images constructed through varying feature engineering techniques.

18-layer ResNet

Models	Accuracy	Sensitivity	Specificity
1. Nearest	90.9%	85.7%	92.1%
2. Bicubic	93.5%	92.9%	93.7%
3. Weight map	97.4%	100.0%	96.8%
4. Rescaled	92.2%	92.9%	92.1%

16-layer VGGNet

Models	Accuracy	Sensitivity	Specificity
1. Nearest	90.9%	85.7%	92.1%
2. Bicubic	92.2%	92.9%	92.1%
3. Weight map	96.1%	92.9%	96.8%
4. Rescaled	92.2%	92.9%	92.1%

AlexNet

Models	Accuracy	Sensitivity	Specificity
1. Nearest	90.9%	85.7%	92.1%
2. Bicubic	93.5%	92.9%	93.7%
3. Weight map	94.8%	92.9%	95.2%
4. Rescaled	90.9%	85.7%	92.1%

Visual geometry group network

The structure VGGNet was established through the investigation of the effect of network depth on the classification performance. As opposed to large convolutional filters adopted by the AlexNet, VGGNet adopts 3 × 3 convolutional kernels, which enables building of deeper network structure, since there is a slower decline of feature map size and resolution (Simonyan and Zisserman, 2015).

Residual network

Residual network (ResNet) structure resolved vanishing gradient problem and overfitting, which are downsides of conventional neural network structures, through the use of residual blocks. A residual block passes the input x through the first convolutional layer, followed by ReLU activation and second convolutional layer. The output of the second convolution which is referred to as $f(x)$ is added to the original input x. The added value $f(x) + x$ is then passed onto ReLU activation function (He et al., 2016). Although a deeper network with more residual blocks may result in improved classification performance, it is computationally expensive due to the large number of parameters (Okinda et al., 2020).

Inference of classification criteria: Explainable artificial intelligence

Neural networks are commonly referred to as "black boxes," since we cannot directly observe or determine the means by which the model classifies unseen data. However, the use of algorithms such as Local Interpretable Model-Agnostic Explanations (LIME) allows us to infer which features the model used for classification. The LIME algorithm creates locally perturbed samples at the borders of a model's decision function. Each sample carries weights in accordance with the distance between the sample and the initial instance. LIME then learns a local linear predictive model, which is repeated for the multiple borders that exist, but which we cannot discern. Equation 2 represents how the explanations about classification are produced by LIME. $\mathcal{L}$ represents local fidelity functions, which is a measure of how unfaithful the prediction model g is in approximation of the classification probability f in the locally defined space π_x. Ω represents the complexity measures of the prediction model (Ribeiro et al., 2016; Gramegna and Giudici, 2021).

$$\xi(x) = \underset{g \in G}{\operatorname{argmin}} \mathcal{L}(f, g, \pi_x) + \Omega(g) \tag{2}$$

In short, LIME explanations are computed through the minimization of $\mathcal{L}$ while keeping Ω low enough for sufficient interpretability of the prediction model. Hereafter, regions that affect the local predictive function are highlighted in order to aid in the understanding of the model's prediction.

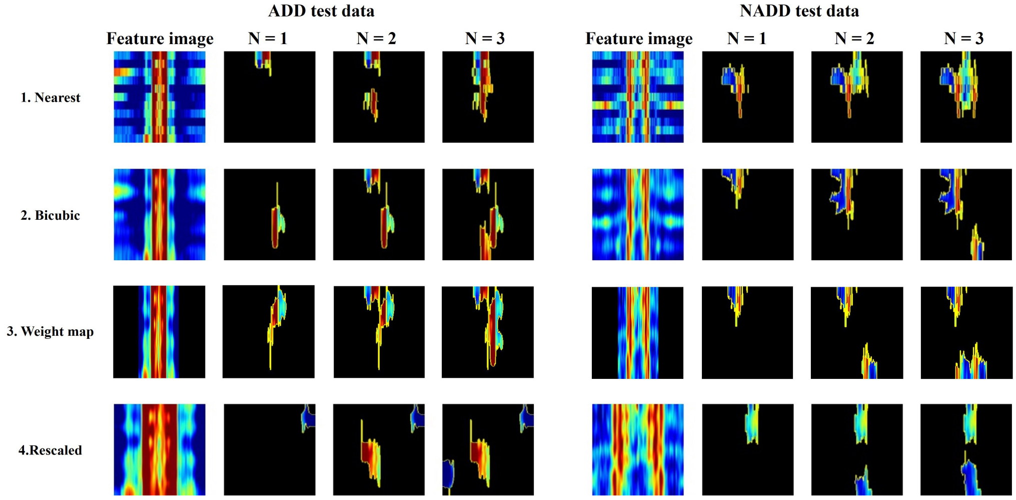

FIGURE 8
Local Interpretable Model-Agnostic Explanations (LIME) algorithm highlighting summed area of top N regions of importance in classification for a randomly selected Alzheimer's disease dementia (ADD) and non-Alzheimer's disease dementia (NADD) test data.

Figure 6 presents typical feature images representing the classes ADD and NADD. The images clearly represent differences in QEEG characteristics between the groups, but we would not be able to identify what exactly the model interprets. In the present study, LIME was employed for clarification of the distinguishable characteristics between groups. The regions which LIME interpreted as top distinguishing features for classification were then used to verify the model's credibility, in which we take account of clinically known facts in relation to ADD. We further examine the consistency of the selected regions.

Final model selection

Due to limited computation power, relatively shallower 16-layer VGGNet and 18-layer ResNet were employed in the present study along with the AlexNet. Classification models that showed sufficient accuracy were selected for all types of networks, and images constructed through varying feature engineering methodologies. Each model was inspected through LIME in order to select the best models for each type of image. We then selected the final model which showcased the best classification accuracy. Figure 7 summarizes model yielding and verification processes.

Results

The same training and test datasets were applied to assess and compare the results of the best classification models, trained using varying types feature images drawn from the aforementioned feature engineering techniques. The 18-layer ResNet image network structure yielded the best classification performance for all four types of images in comparison with other image networks. Table 3 presents the achieved confusion matrices of the best models selected for each network and technique, and Table 4 lists each network's accuracy, sensitivity, and specificity.

All classification models showed adequate performance, which suggests that the difference in QEEG characteristics between the ADD and NADD groups was significant, and that it was well-represented in our novel feature image. However, the performance of the bicubic model was superior to that of the nearest model, indicating that the block edges among image pixels may negatively affect the classification performance of image networks. The best performance was achieved from

TABLE 5 Final model (18-layer ResNet)'s presumed classification criteria from the regions of importance selected by Local Interpretable Model-Agnostic Explanations (LIME).

Models	ADD classification criteria	Non-ADD classification criteria
1. Nearest	High power of slower waves (delta-theta).	High power of alpha waves and low power of slower waves (delta-theta).
2. Bicubic	High power of slower waves (delta-theta).	High power of alpha waves.
3. Weight map	High power of slower waves (delta-theta).	High power of alpha waves and low power of slower waves (delta-theta).
4. Rescaled	Low power of faster waves (beta 2) and high power of slower waves (delta-theta).	Low power of slower waves (delta-theta).

the weight map model. This may be because waveforms at faster frequencies are comparatively less important features for classification of ADD. The present assumptions were further verified using LIME, which allowed for comparison among the extracted regions of high importance in classification. A random data index from each group was drawn for comparison among the models (**Figure 8**). N represents the number of regions that has been added (i.e., $N = 1$ image represents the region of highest importance, and $N = 3$ image represents the sum of the top 3 regions of importance that affected the classification result).

From the regions of importance selected by LIME represented in **Figure 8**, the classification criteria of the 18-layer ResNet model have been presumed as shown in **Table 5**.

Discussion

Through the analysis of 18-layer ResNet classification models *via* LIME, we can infer that the first three models' classification criteria for ADD involve high power of slower waves, while the rescaled model's classification criteria involve low power of faster waves. In addition, the rescaled model's classification criteria for NADD only involved low power of slower waves. Moreover, the bicubic model's classification criteria for NADD were highly specific to the power of alpha waves. After careful verification with the full test dataset, we deduced that the weight map model yields the best classification performance with foremost robustness.

The objective of the present study was in the establishment and verification of our novel feature image's capability to contain all useful spatiotemporal information from the EEG data. Since conventional features used for visualization of EEG, namely, topographies are difficult to employ for the training of deep learning models (neural networks), we developed novel feature images from EEG data acquired in a clinical environment and yielded an outstanding deep learning based ADD classification model. The main advantage in use of our feature image is in the visualization of classification criteria through XAI algorithms, which enables more comprehensible analysis on the established classification models.

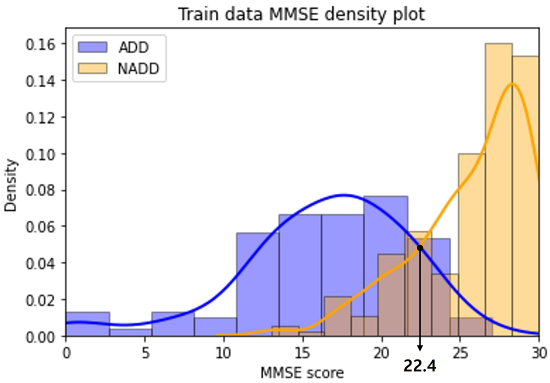

FIGURE 9
Alzheimer's disease dementia (ADD) and non-Alzheimer's disease dementia (NADD) train dataset mini-mental state examination (MMSE) density plot.

For further validation, several trials were made to extract regions of importance from test images through LIME. Slight differences were observed for each trial due to the random image sampling algorithm used by LIME. However, each trial showed adequate consistency, hence the classification criteria did not vary. Our findings verified that the power of the slow waves (delta and theta) and that of alpha waves (resting state waves) were crucial factors in differentiating the groups, based on the classification criteria inferred through LIME. The result corresponds to the conventionally known EEG characteristics of ADD, an increment in delta and theta power and a parallel decrement in alpha and beta power in comparison with normal subjects (Jeong, 2004). Moreover, the classification results indicate no signs of overfitting. If the model is overfitted due to an imbalance in the dataset, the model tends to classify data toward the class with larger amount of data. However, the classification model established in the present study resulted in balanced sensitivity and specificity.

In addition, we have made a further comparison between the novel feature image-based classification model established in the present study, with a mini-mental state examination (MMSE) score based method. MMSE is a cognitive mental status examination which are widely in use to aid the diagnosis of several neurological disorders. It consists of short and practical cognitive-specific tests which requires approximately 10 min to complete. The result is scored within the range of 0 which suggests critical deterioration of cognitive functions, to 30 which reflects healthy cognition (Folstein et al., 1975; Perneczky et al., 2006).

The distribution of MMSE scores of the ADD and NADD classes in the train dataset were visualized as a density plot (**Figure 9**), smoothed off by kernel density estimation.

The classification standard was determined as a cutoff value in accordance with the intersection point of the two density plots: ADD ($\text{MMSE} \leq 22$); NADD ($\text{MMSE} > 22$). As a result, 1 ADD data and 5 NADD data were misclassified, which is inferior to the classification result of the final model established in the present study.

In addition, we can observe a significant overlap of ADD and NADD MMSE scores, in which signifying that MMSE based classification is less robust. Chapman et al. (2016) also claim that the use of MMSE score cutoffs for the diagnosis of ADD resulted in limited accuracy and were insufficient in the discrimination of MCI from ADD. As opposed to this, the inferred classification criteria for our classification model *via* LIME is based on clear QEEG characteristics that are visually distinguishable.

The novel feature images used here only utilized z-scores of relative powers, which conveniently describe the ratio among

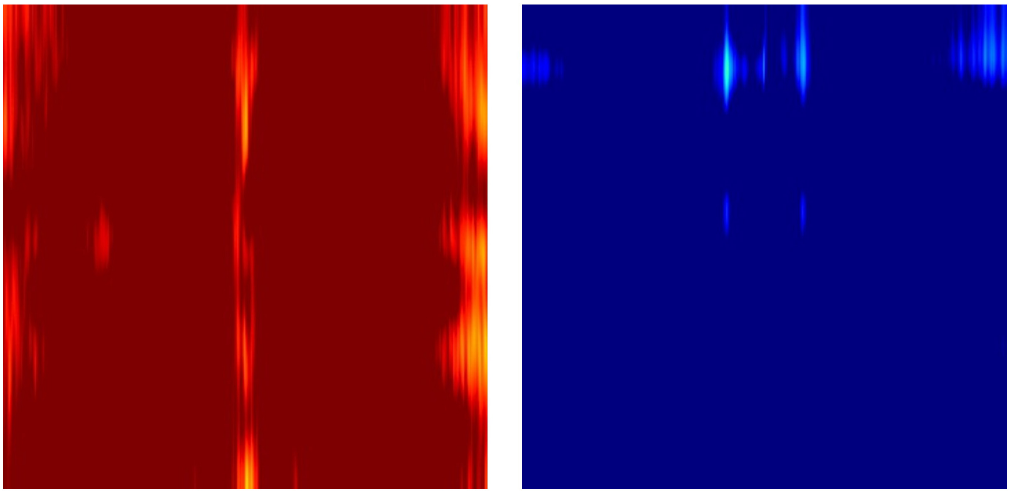

FIGURE 10
Example outlier images that represent absolute Z-scores of electroencephalography (EEG) power magnitude.

the powers of waveforms at different frequencies, but not the absolute powers in comparison to the age- and sex- specific normative database. This was due to the fact that individuals have various overall magnitudes of EEG power, which is dependent on thickness of the skull (Hagemann et al., 2008). Therefore, the outliers with excessively strong or weak EEG magnitudes result in almost completely red or blue images when mapped to a -1.96 to 1.96 Z-score color scale (**Figure 10**).

The downside of the feature matrix extraction method proposed in this study is in the averaging of the time dynamics. In order to account for this, multiple feature matrices can be extracted using a time epoch window that slides over the data and can be concatenated into a 3 dimensional feature matrix. Epoch length used to create each image frame and overlap between consecutive time windows can be altered to yield various resolutions of the time dynamics.

Moreover, the presented feature matrix extraction method is adapted for the spatial representation of 19-channel EEG data since the y-axis of the matrix is essentially a stack of the channels from frontal to rear side regions. Therefore, the presented method might insufficiently represent the spatial information for other commonly used 34- or 64-channel EEG data with several lateral channels. For such cases, the electrodes may be grouped into appropriate regions instead and rearranged accordingly.

The classification model's outstanding performance and coherence with clinical facts suggest a high potential of the usage of novel feature image as a clinical tool for the diagnosis of several other neurological diseases. Not only limited to this, it can also be utilized for brain-computer interface (BCI) applications, provided that the third of the investigated cases of BCI studies utilized spatiotemporal features (Alzahab et al., 2021). The continual refinement in usage of novel feature images will enhance the ensemble of tools available to more comprehensively leverage the power of QEEG.

Data availability statement

Inquiries regarding the data used in this present study can be directed to the corresponding author.

Ethics statement

Ethical review and approval was not required for the study on human participants in accordance with the local legislation and institutional requirements. The patients/participants provided their written informed consent to participate in this study.

Author contributions

TJ conducted the research and wrote the manuscript. UP supervised the research. SK provided guidance throughout the course of research. All authors approved the submitted version of the manuscript.

Funding

This research was supported by the Korea Health Technology R&D Project through the Korea Health Industry Development Institute (KHIDI) and

Korea Dementia Research Center (KDRC), funded by the Ministry of Health and Welfare and Ministry of Science and ICT, Republic of Korea (grant number: HU20C0511000020).

Conflict of interest

The authors were employed by the company iMediSync, Inc.

Publisher's note

References

Alzahab, N. A., Apollonio, L., Di Iorio, A., Alshalak, M., Iarlori, S., Ferracuti, F., et al. (2021). Hybrid deep learning (hDL)-based brain-computer interface (BCI) systems: A systematic review. *Brain Sci.* 11:75. doi: 10.3390/brainsci11010075 ?

Arab, M. R., Suratgar, A. A., and Ashtiani, A. R. (2010). Electroencephalogram signals processing for topographic brain mapping and epilepsies classification. *Comput. Biol. Med.* 40, 733–739. doi: 10.1016/j.compbiomed.2010.06.001

Arroyo, S., Lesser, R. P., Gordon, B., Uematsu, S., Jackson, D., and Webber, R. (1993). Functional significance of the mu rhythm of human cortex: An electrophysiologic study with subdural electrodes. *Electroencephalogr. Clin. Neurophysiol.* 87, 76–87. doi: 10.1016/0013-4694(93)90114-B

Best, N., Ott, J., and Linstead, E. J. (2020). Exploring the efficacy of transfer learning in mining image-based software artifacts. *J. Big Data* 7:59. doi: 10.1186/s40537-020-00335-4

Chapman, K. R., Bing-Canar, H., Alosco, M. L., Steinberg, E. G., Martin, B., Chaisson, C., et al. (2016). Mini mental state examination and logical memory scores for entry into Alzheimer's disease trials. *Alzheimers Res. Ther.* 8:9. doi: 10.1186/s13195-016-0176-z

Folstein, M. F., Folstein, S. E., and McHugh, P. R. (1975). "Mini-mental state". A practical method for grading the cognitive state of patients for the clinician. *J. Psychiatr. Res.* 12, 189–198. doi: 10.1016/0022-3956(75)90026-6

Gao, S., and Gruev, V. (2011). Bilinear and bicubic interpolation methods for division of focal plane polarimeters. *Opt. Express* 19, 26161–26173. doi: 10.1364/OE.19.026161

Gramegna, A., and Giudici, P. (2021). SHAP and LIME: An evaluation of discriminative power in credit risk. *Front. Artif. Intell.* 4:752558. doi: 10.3389/frai.2021.752558

Hagemann, D., Hewig, J., Walter, C., and Naumann, E. (2008). Skull thickness and magnitude of EEG alpha activity. *Clin. Neurophysiol.* 119, 1271–1280. doi: 10.1016/j.clinph.2008.02.010

Halgren, M., Ulbert, I., Bastuji, H., Fabó, D., Erőss, L., Rey, M., et al. (2019). The generation and propagation of the human alpha rhythm. *Proc. Natl. Acad. Sci. U.S.A.* 116, 23772–23782. doi: 10.1073/pnas.1913092116

Haller, S., Montandon, M. L., Lilja, J., Rodriguez, C., Garibotto, V., Herrmann, F. R., et al. (2020). PET amyloid in normal aging: Direct comparison of visual and automatic processing methods. *Sci. Rep.* 10:16665. doi: 10.1038/s41598-020-73673-1

He, K., Zhang, X., Ren, S., and Sun, J. (2016). "Deep residual learning for image recognition," in *Proceedings of the IEEE conference on computer vision and pattern recognition* (Las Vegas, NV: IEEE), 770–778.

Ho, S. H., and Yang, D.-W. (2020). Risk factors predicting amyloid PET positivity in patients with mild cognitive impairment and apolipoprotein E 3∈/3∈ genotypes. *J. Alzheimers Dis.* 77, 1017–1024. doi: 10.3233/JAD-200439

Iqbal, K., Alonso Adel, C., Chen, S., Chohan, M. O., El-Akkad, E., Gong, C. X., et al. (2005). Tau pathology in Alzheimer disease and other tauopathies. *Biochim. Biophys. Acta* 1739, 198–210. doi: 10.1016/j.bbadis.2004.09.008

Jeong, J. (2004). EEG dynamics in patients with Alzheimer's disease. *Clin. Neurophysiol.* 115, 1490–1505. doi: 10.1016/j.clinph.2004.01.001

Jutten, C., and Herault, J. (1991). Blind separation of sources, part I: An adaptive algorithm based on neuromimetic architecture. *Signal Process.* 24, 1–10. doi: 10.1016/0165-1684(91)90079-X

Kim, J. W., Byun, M. S., Sohn, B. K., Yi, D., Seo, E. H., Choe, Y. M., et al. (2017). Clinical dementia rating orientation score as an excellent predictor of the progression to Alzheimer's disease in mild cognitive impairment. *Psychiatry Investig.* 14, 420–426. doi: 10.4306/pi.2017.14.4.420

Ko, J., Park, U., Kim, D., and Kang, S. W. (2021). Quantitative electroencephalogram standardization: A sex- and age-differentiated normative database. *Front. Neurosci.* 15:766781. doi: 10.3389/fnins.2021.766781

Krizhevsky, A., Sutskever, I., and Hinton, G. E. (2017). ImageNet classification with deep convolutional neural networks. *Commun. ACM* 60, 84–90. doi: 10.1145/3065386

Li, S., Wang, L., Li, J., and Yao, Y. (2021). Image classification algorithm based on improved AlexNet. *J. Phys. Conf. Ser.* 1813:012051. doi: 10.1088/1742-6596/1813/1/012051

Livint Popa, L., Dragos, H., Pantelemon, C., Verisezan, Rosu O, and Strilciuc, S. (2020). The role of quantitative EEG in the diagnosis of neuropsychiatric disorders. *J. Med. Life* 13, 8–15. doi: 10.25122/jml-2019-0085

Malik, A. S., and Amin, H. U. (2017). "Chapter 1 – designing an EEG experiment," in *Designing EEG experiments for studying the brain*, eds A. S. Malik and H. U. Amin (Cambridge, MA: Academic Press), 1–30. doi: 10.1016/B978-0-12-811140-6.00001-1

Meghdadi, A. H., Stevanoviæ Kariæ, M., McConnell, M., Rupp, G., Richard, C., Hamilton, J., et al. (2021). Resting state EEG biomarkers of cognitive decline associated with Alzheimer's disease and mild cognitive impairment. *PLoS One* 16:e0244180. doi: 10.1371/journal.pone.0244180

Mlinac, M. E., and Feng, M. C. (2016). Assessment of activities of daily living, self-care, and independence. *Arch. Clin. Neuropsychol.* 31, 506–516. doi: 10.1093/arclin/acw049

Moini, J., and Piran, P. (2020). "Chapter 6 – cerebral cortex," in *Functional and clinical neuroanatomy*, eds J. Moini and P. Piran (Cambridge, MA: Academic Press), 177–240. doi: 10.1016/B978-0-12-817424-1.00006-9

Murphy, M. P., and LeVine, H. (2010). Alzheimer's disease and the β-amyloid peptide. *J. Alzheimers Dis.* 19, 311–323. doi: 10.3233/JAD-2010-1221

Nuwer, M. R. (1988). Quantitative EEG: I. Techniques and problems of frequency analysis and topographic mapping. *J. Clin. Neurophysiol.* 5, 1–44.

Okinda, C., Nyalala, I., Korohou, T., Okinda, C., Wang, J., Achieng, T., et al. (2020). A review on computer vision systems in monitoring of poultry: A welfare perspective. *Artif. Intell. Agric.* 4, 184–208. doi: 10.1016/j.aiia.2020.09.002

Perneczky, R., Wagenpfeil, S., Komossa, K., Grimmer, T., Diehl, J., and Kurz, A. (2006). Mapping scores onto stages: Mini-mental state examination and clinical dementia rating. *Am. J. Geriatr. Psychiatry* 14, 139–144. doi: 10.1097/01.JGP.0000192478.82189.a8

Porcaro, C., Vecchio, F., Miraglia, F., Zito, G., and Rossini, P. M. (2022). Dynamics of the "cognitive" brain wave P3b at rest for Alzheimer dementia prediction in mild cognitive impairment. *Int. J. Neural Syst.* 32:2250022. doi: 10.1142/S0129065722500228

Ramsay, I. S., Lynn, P., Schermitzler, B., and Sponheim, S. (2021). Individual alpha peak frequency is slower in schizophrenia and related to deficits in visual perception and cognition. *Sci. Rep.* 11:17852. doi: 10.1038/s41598-021-97303-6

Ribeiro, M. T., Singh, S., and Guestrin, C. (2016). "Why should I trust you?": Explaining the predictions of any classifier," in *Proceedings of the 22nd ACM SIGKDD international conference on knowledge discovery and data mining*

(New York, NY: Association for Computing Machinery), 1135–1144. doi: 10.1145/2939672.2939778

Shim, Y. S., and Shin, H.-E. (2020). Analysis of neuropsychiatric symptoms in patients with Alzheimer's disease using quantitative EEG and sLORETA. *Neurodegener. Dis.* 20, 12–19. doi: 10.1159/000508130

Simonyan, K., and Zisserman, A. (2015). Very deep convolutional networks for large-scale image recognition. *arXiv* [Priprint]. arxiv 1409.1556

Xiao, L., Yan, Q., and Deng, S. (2017). "Scene classification with improved AlexNet model," in *Proceedings of the 2017 12th international conference on intelligent systems and knowledge engineering (ISKE)* (Nanjing: IEEE), 1–6. doi: 10.1109/ISKE.2017.8258820

Yuvaraj, R., Murugappan, M., Omar, M. I., Ibrahim, N. M., Sundaraj, K., Mohamad, K., et al. (2014). Emotion processing in Parkinson's disease: An EEG spectral power study. *Int. J. Neurosci.* 124, 491–502. doi: 10.3109/00207454.2013.860527

frontiers | Frontiers in Neuroscience

TYPE Original Research
PUBLISHED 10 November 2022
DOI 10.3389/fnins.2022.933391

OPEN ACCESS

EDITED BY
Morten Mørup,
Technical University of Denmark,
Denmark

REVIEWED BY
Lior Shamir,
Kansas State University, United States
Marco Marino,
KU Leuven, Belgium

*CORRESPONDENCE
Franca Tecchio
franca.tecchio@cnr.it

†These authors have contributed equally to this work

SPECIALTY SECTION
This article was submitted to
Brain Imaging Methods,
a section of the journal
Frontiers in Neuroscience

RECEIVED 30 April 2022
ACCEPTED 19 October 2022
PUBLISHED 10 November 2022

CITATION
Pascarella A, Gianni E, Abbondanza M, Armonaite K, Pitolli F, Bertoli M, L'Abbate T, Grifoni J, Vitulano D, Bruni V, Conti L, Paulon L and Tecchio F (2022) Normalized compression distance to measure cortico-muscular synchronization. *Front. Neurosci.* 16:933391.
doi: 10.3389/fnins.2022.933391

Normalized compression distance to measure cortico-muscular synchronization

Annalisa Pascarella[1†], Eugenia Gianni[2,3†], Matteo Abbondanza[4†], Karolina Armonaite[2,5], Francesca Pitolli[4], Massimo Bertoli[2,6], Teresa L'Abbate[2,5,6], Joy Grifoni[2,5], Domenico Vitulano[1,4], Vittoria Bruni[1,4], Livio Conti[7,8], Luca Paulon[2,9] and Franca Tecchio[2*]

[1]Institute for the Applications of Calculus "M. Picone", National Research Council, Rome, Italy, [2]Laboratory of Electrophysiology for Translational NeuroScience, Institute of Cognitive Sciences and Technologies, Consiglio Nazionale delle Ricerche, Rome, Italy, [3]Unit of Neurology, Neurophysiology, Neurobiology, Department of Medicine, University Campus Bio-Medico of Rome, Rome, Italy, [4]Department of Basic and Applied Sciences for Engineering (SBAI), University of Rome "La Sapienza", Rome, Italy, [5]Faculty of Psychology, Uninettuno University, Rome, Italy, [6]Department of Neuroscience, Imaging and Clinical Sciences, University "Gabriele D'Annunzio" of Chieti-Pescara, Chieti, Italy, [7]Faculty of Engineering, Uninettuno University, Rome, Italy, [8]Istituto Nazionale di Fisica Nucleare, Sezione Roma Tor Vergata, Rome, Italy, [9]Independent Researcher, Rome, Italy

The neuronal functional connectivity is a complex and non-stationary phenomenon creating dynamic networks synchronization determining the brain states and needed to produce tasks. Here, as a measure that quantifies the synchronization between the neuronal electrical activity of two brain regions, we used the normalized compression distance (NCD), which is the length of the compressed file constituted by the concatenated two signals, normalized by the length of the two compressed files including each single signal. To test the NCD sensitivity to physiological properties, we used NCD to measure the cortico-muscular synchronization, a well-known mechanism to control movements, in 15 healthy volunteers during a weak handgrip. Independently of NCD compressor (Huffman or Lempel Ziv), we found out that the resulting measure is sensitive to the dominant-non dominant asymmetry when novelty management is required (p = 0.011; p = 0.007, respectively) and depends on the level of novelty when moving the non-dominant hand (p = 0.012; p = 0.024). Showing lower synchronization levels for less dexterous networks, NCD seems to be a measure able to enrich the estimate of functional two-node connectivity within the neuronal networks that control the body.

KEYWORDS

normalized compression distance (NCD), electrophysiology, handedness, neuronal synchronization, feedback

Introduction

The neurons of the various brain areas communicate with each other through fluctuating signals in dynamic synchrony (Varela et al., 2001) both during rest and while performing tasks (Deco et al., 2011). By sustaining communication among networks (Fries, 2005), synchronization of neural activity mediates information processing in the brain (Singer, 1993; Borisyuk et al., 1998; Fries, 2009). In other words, the correlated neurons' behaviors, even though they are generated by spatially discrete and/or distant areas (Gray et al., 1989), emerge from the integration of their signals that allow for sensory (Gray, 1994), attentional (Womelsdorf and Fries, 2007), or motor processing as well as for memory (Axmacher et al., 2006), and for other fundamental cognitive processes (Daffertshofer and Pietras, 2020). As a classical example, in visual areas, phase-locked oscillations of spatially segregated neuronal pools mediate binding of diverse visual features like motion, shape, and color into a coherent perception (Singer and Gray, 1995). Consistently, the multimodal neuroscience community converges in viewing the brain as a neuronal network where the nodes of the network represent either distinct cortical/subcortical areas, neuronal pools, or even single neurons and the edges represent their connections, that is their functional connectivity (FC) (Bullmore and Sporns, 2012; Wang et al., 2014). FC across distinct nodes is assessed as a statistical dependence among their signal times series measured through one of multiple methodologies from electro-encephalography (EEG) to magneto-encephalography (MEG) to functional-magnetic resonance imagining (fMRI) (Hutchison et al., 2013; Wang et al., 2014).

Functional connectivity among and within brain networks even in resting state clearly emerging by diverse technologies like fMRI (Damoiseaux et al., 2006) and EEG (Samogin et al., 2020) are characterized by specific frequency and spatial domains. In the case of motor behavior, FC emerges within and among several areas of the central nervous system—such as the motor, frontal, parietal, premotor cortices, subcortical, and cerebellar areas, as well as the spinal cord—finally expressing in the muscles' contractions (van Wijk et al., 2012). Fine motor commands resulting from central processing (Lemon, 2008; Moreno-López et al., 2016) parallel the synchronization features of the electrical activity recorded on the surface of the muscles with those of primary sensorimotor cortex (Wolpert et al., 2011).

Linear measures (coherence and correlation) have been traditionally used to assess the degree of functional connectivity among different nodes (Gross et al., 2001; Broyd et al., 2009; Jensen and Mazaheri, 2010). Notably, some authors noticed that the absence of a linear statistical link between two nodes does not mean absence of FC (Fingelkurts et al., 2005). This is one of the reasons why non-linear measures of FC, such as mutual information, are attracting more and more attention (Hlinka et al., 2011; Wang et al., 2016).

In the case of cortico-muscular synchronization, a classically used electrophysiological measure is the cortico-muscular coherence (CMC) (Mima and Hallett, 1999; Liu et al., 2019). This is the spectral coherence between the EEG or MEG signal from the contralateral cortex and electro-myographic (EMG) signal recorded by involved muscles while executing a motor task. CMC showed how neurons synchronize their firing patterns at different frequencies according to diverse behavioral states (Mima and Hallett, 1999) as for example as a function of different force levels of contraction (Brown et al., 1998; Mima et al., 1999; Brown, 2000), initiating movement (Ramayya et al., 2021), exerting either a static force (Kristeva et al., 2007) or dynamic ones (Omlor et al., 2007).

Though CMC is considered a well-established index of cortex-muscle information flow both in healthy and pathological conditions (Mima and Hallett, 1999; Liu et al., 2019), clear limitations emerged (Yang et al., 2018). Recently, we measured CMC sensitivity to visual feedback information and handedness, while participants were performing a weak handgrip task with the right or the left hand with or without undirect visual feedback (L'Abbate et al., 2022). Tough we observed sensitivity of CMC to visual feedback, no significant variation of CMC related to handedness emerged, nor was it present in previous literature (Tecchio et al., 2006). Therefore, given the central role of asymmetries in the functioning of our body-brain system and the importance of handedness in our everyday lives, we hypothesized that limit in assessing such crucial feature originates from the CMC measure itself.

We propose here that measures sensitive to the complex nature of the exchanged signals can be sensitive to the differences in the organization of cortical areas controlling the two hands. Accordingly, other authors pointed out the limitations of linear electrophysiological measurements in view of the known features of the sensorimotor system (Yang et al., 2016, 2018; Tan et al., 2022). For example they observed that, while the synchronization in the sensorimotor system originates from ascending somatosensory feedback and descending motor commands (Kilner et al., 2004; Witham et al., 2011), CMC cannot separate this bidirectional contribution in cortico-muscular interaction. Moreover, they observed that, from the last studies the sensorimotor system appears to be non-linear, showing cross-frequency coupling (Chen et al., 2010; Yang et al., 2018), paving the way to non-linear measures able to complement linear ones (Palva et al., 2005; Yang et al., 2016; Siebenhühner et al., 2020).

Here we propose to study FC using a novel non-linear measure, the normalized compression distance (NCD). It is a parameter-free measure that estimates the information shared by two signals by comparing the compression length of a file obtained concatenating one signal with the other. NCD seems suitable for biological systems, as it yields excellent results in comparing genomes, clustering languages or music (Li and Vitányi, 1990). Notably, NCD is robust in the sense that its performance appears somewhat independent of the type of compressor used for coding the data. NCD does not require any features or background knowledge about the data. We selected this synchronization measure because it estimates the information shared by the two signals without requiring any representation of the individual signal in harmonics and does not require the signal to be stationary. In fact, the hypotheses of stationary signal and the representation with sinusoid functions condemn the estimates to be insensitive to relevant parts of the interior dynamics of the neuronal pool activity (Buzsáki, 2009; Buzsáki et al., 2013; Cottone et al., 2017; Armonaite et al., 2021).

Study aim

The design of our study is to test the NCD sensitivity to fundamental physiological features.

Aware of the lack of a gold standard for the FC quantification we propose here a heuristic approach to find a solution that better reflects the state of the art of the interrelation among networks. In other words, we search for a FC measure sensitive to the networks' ability, which is well known to depend on its FC levels. In fact, it is an established notion that neural networks in their resting state express characteristics relating to their ability to perform the functions in which they are involved (Deco and Corbetta, 2011; Kim and Kang, 2018; Bansal et al., 2021; Doucet et al., 2022). On this basis, we expect that there will be functional measures that differ between cortical representation of the dominant and non-dominant hand even when tested via a simple task. Accordingly, in our experience with the primary somatosensory area, the activation properties of networks with different levels of ability, particularly the thumb and little finger representation networks, differed when tested while responding to elemental galvanic stimulation (Tecchio et al., 2007). Based on this reasoning, we expect that even tested by a simple handgrip—performed with the same quality by the left hand and the right hand (L'Abbate et al., 2022)—we can perceive the differential organization of the representation networks of the two hands by NCD.

As paradigmatic example we studied with the NCD the synchronization between cortex and muscle (CMncd) while executing a simple movement typical of everyday activity. Higher CMncd corresponds to lower synchronization. Especially we pose the working hypothesis that CMncd will show dependence on hand executing the task and the level of visual feedback. That is, we expect that: (i) left non-dominant hand control will express higher CMncd than right dominant hand control and (ii) providing undirect visual feedback CMncd will increase, as suggested by the behavior of cortico-muscular coherence (L'Abbate et al., 2022). To test the two working hypotheses, we collected EEG and EMG simultaneously when subjects were performing a weak isometric handgrip task, with either the right or left hand, with or without undirect visual feedback of their exerted pressure.

Materials and methods

Study design

The study was approved by the Ethical Committee of S. Giovanni Calibita Hospital, Rome, Italy (**Figure 3C**). It was a cross-over investigation study with two interacting conditions (moved hand and visual feedback). Since our goal was to test CMncd sensitivity to diverse levels of network ability, in the present work we considered the representations of the dominant and non-dominant hand while executing a mono-lateral weak handgrip in presence or absence of undirect visual feedback.

Participants

Fifteen healthy volunteers (10 females and 5 males, age range from 22 to 48 years with mean 29 ± 6 years) participated in the study after signing a written informed consent. All subjects were right-handed (as tested by Edinburgh Handedness Questionnaire Oldfield, 1971), and had normal or corrected-to normal vision.

Experimental procedure

Behavioral scoring

The fine hand-motor control was evaluated with the 9-hole peg test (Wang et al., 2015) executed by the right and left hands.

Electro-encephalography, electro-myographic, electrooculography, and electrocardiogram data recordings

The individual EEG (Brain Products GmbH, Munich, Germany) was recorded using a 64-channel acti-CHamp System with montage according to the 10-10 EEG International System and referenced to the Fz electrode. Electrode impedances were maintained below 5 kΩ. Surface EMG—recorded by using Ag–AgCl cup electrodes—of the right and left opponents pollicis muscle (EMG_{OPr} and EMG_{OPl}) were recorded with a belly tendon montage. EEG and EMG were sampled at 5 kHz (pre-sampling analogical band pass filtering 0.1–2,000 Hz) and stored for off-line processing.

Visuo-motor task

Each subject sat on a chair in front of a monitor at about 1 m (**Figure 1A**). As detailed in **Figure 1** legend, the

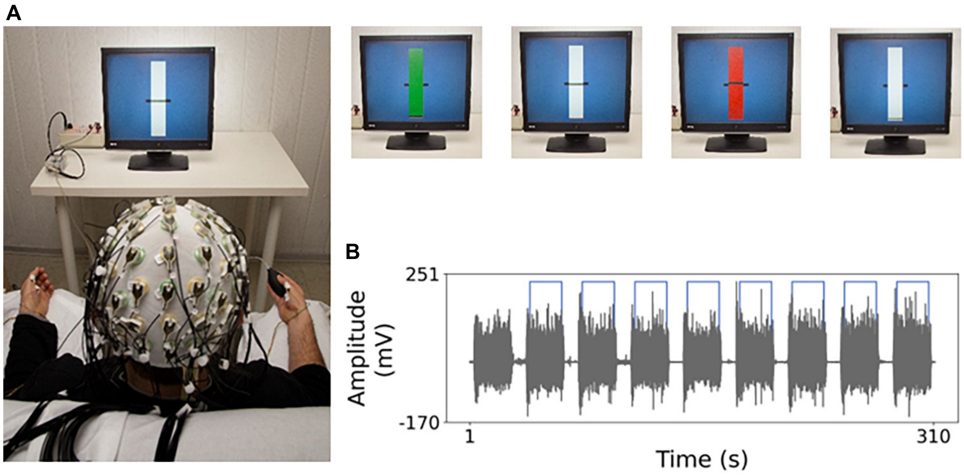

FIGURE 1
Experimental setting. **(A)** Electro-encephalography (EEG) recordings and task. The general set-up to record the EEG during the weak handgrip executed in sequences of 20 s starting with a go signal (green rectangle) and ending with a stop signal (red rectangle) intermingled by 10 s at rest. In the visual feedback "yes" ("no") condition, a horizontal segment indicates the level of exerted pressure on the bulb by vertical oscillations (blocked). After determining handgrip maximum voluntary contraction (MVC), a rest period of at least 2 min was provided. Then, the weak isometric handgrip and rest sequences lasted about 5 min. The target level was set to 5% MVC, to minimize weariness related to the task.
(B) Example of electro-myographic (EMG) acquisition during isometric contraction execution. In gray the EMG trace of opponents pollicis (OP) muscle in one representative subject, for the whole task duration, with 20 s contraction sequences intermingled by 10 s at rest. Light blue line indicates the temporal portions selected for analysis.

subject performed a handgrip, either with left or the right hand separately, against the resistance of a semi-compliant air-bulb, connected to a digital board that recorded the exerted pressure (Interactive Pressure Sensor, InPresS; Tomasevic et al., 2013). Notably, the visual information about the exerted pressure provided as a horizontal segment vertically oscillating on the monitor implies translated feedback, different from the physiological information that we usually have from our visual system while executing a movement, including a weak handgrip.

The four handgrips (about 5 min each) were executed in the same order in all subjects: first with the dominant hand with visual feedback (DxYes), then without (DxNo), thereafter with the non-dominant hand with (SnYes) and without visual feedback (SnNo).

Data analysis

Electro-encephalography data pre-processing

Electro-encephalography data were filtered (1–250 Hz) before the analysis. A semi-automatic fast independent component analysis (fastICA)-based procedure (Barbati et al., 2004) was applied to the whole recordings to identify and remove biological (cardiac, ocular, and muscular) and non-biological (power line, instrumental, and environmental noise) artifacts. For each subject we selected about 180 s of artifact free signal for carrying the analysis. As preliminary step, we selected the bipolar derivations with maximal peak amplitude of cortico-muscular coherence in beta band in each condition (L'Abbate et al., 2022).

Normalized compression distance

The NCD is a quasi-universal metric, in the sense that it has been defined to simultaneously detect all similarities between signals that other effective distances detect separately (Cilibrasi and Vitányi, 2005). In other terms, NCD is based on the concept that two signals are similar if we can significantly "compress" one using the information of the other. NCD captures the dominant similarity over all possible features for every pair of signals compared, up to the stated precision.

We must remember that a lossless compressor acts as an invertible mapping function of a signal into a binary sequence. The length of this binary sequence reveals the amount of compression. Hence, the NCD computed between two signals x and y, i.e., NCD (x,y) is defined as

$$\mathrm{NCD}(x, y) = \frac{C(xy) - \min(C(x),\ C(y))}{\max(C(x),\ C(y))}, \tag{1}$$

where C(xy) denotes the compressed size (length of the binary sequence that has been obtained by applying the compressor C) of the concatenation of x and y, wherein C(x) denotes the compressed size of x, and C(y) denotes the compressed size of y. NCD assumes values between 0 and 1, where 0 indicates maximum similarity and 1 the opposite.

In this work, the compressed size has been measured in terms of number of bits per sample, which is the average number of bits used for coding each sample of the considered signal. We used as compressor C the Huffman coding implemented in Matlab environment (CMncdH). To test the robustness of the proposed measure against the compressor, we computed the CMncd by using the Lempel–Ziv scheme (Lempel and Ziv, 1976) as compressor C. We used the normalized LZ proposed by Zhang et al. (2009) that takes into account the length of the sequence (CMncdLZ) (Zhang et al., 2009).

For each subject and condition (**Figure 2**), we computed the CMncd between the cleaned EEG and EMG signals, with EEG being the selected bipolar channel, for epochs of 180 s length, windowed in segments of 18 s, obtaining 10 estimates for each subject and condition. In some subject we lacked the entire length and a minimum of 6–10 s intervals were included in all subjects.

Statistical analysis

Preliminarily, we tested the stability of the CMncdH estimate by evaluating the variation coefficient of the about ten quantifications in successive 18 s epochs in the same condition, in all subjects and conditions.

The distribution of each variable was checked for normality by Shapiro–Wilk test and homogeneity of variance by Levene test. According to the variable distributions we applied the proper statistical analysis to identify CMncdH/CMncdLZ differences between dominant and non-dominant hand representations and presence and absence of undirect visual feedback. In other terms, once identified whether to apply parametric or non-parametric tests, we analyzed the comparisons across four conditions: *Hemi-Body* (left hemisphere-right hand, right hemisphere-left hand) and *Visual feedback* (Yes, No). We set the significance threshold at 0.05.

Results

CMncdH behavior across conditions

Shapiro–Wilk statistics indicated that the distribution of CMncdH and CMncdLZ measurements across subjects in the four conditions (DxNo, DxYes, SnNo, and SnYes) was not fitting a Gaussian. Furthermore, the Levene tests indicated that CMncdH and CMncdLZ displayed variances not homogeneous across the four conditions. On these bases, we applied non parametric statistical test searching for differences both between absence and presence of visual feedback (within the hemibody; e.g., when using the same hand) and between hemibody, e.g., between dominant and non-dominant hemibody within the same feedback condition (absence or presence).

Huffman compressor

No significant difference was found by comparing the two conditions DxNo and DxYes across subjects ($W = 1653$; $p = 0.112$, **Figure 3A**). A significant difference was found by comparing the two conditions SnNo and SnYes across subjects ($W = 1421$; $p = 0.012$). Significant difference was found between the two conditions DxNo and SnNo across subjects ($W = 1452$; $p = 0.016$). A significant difference was found between the two conditions DxYes and SnYes ($W = 1419$; $p = 0.011$).

Lempel–Ziv compressor

Significant difference was found by comparing the two conditions DxNo and DxYes across subjects ($W = 1262$; $p = 0.0016$, **Figure 3B**). A significant difference was found by comparing the two conditions SnNo and SnYes across subjects ($W = 1488$; $p = 0.024$). No significant difference was found between the two conditions DxNo and SnNo across subjects ($W = 1883$; $p = 0.51$). A significant difference was found between the two conditions DxYes and SnYes ($W = 1378$; $p = 0.007$).

Behavioral quality of fine motor hand control

Execution times of the 9 Hole Peg Test displayed a distribution not differing from a Gaussian, and the ANOVA with *Hand* (right and left) and *Repetition* (1st and 2nd) as within-subject factors indicated a clear *Hand* effect [$F_{(1,15)} = 8.42$, $p = 0.011$] corresponding to quicker execution with the right (16.1 ± 0.4 s) than with the left hand (17.5 ± 0.3 s).

Discussion

Our results show that both CMncdH and CMncdLZ (CMncd considering both) display higher values in absence with respect to presence of visual feedback when executing the left handgrip, reflecting minor synchronization between cortex and muscles when the task requires the integration of transposed visual feedback about the exerted pressure as per the working hypothesis. Moreover, in presence of visual feedback, CMncdH appears sensitive to laterality of movement: it displays higher values for the left than for the right handgrip. As expected, hand control of the non-dominant side expresses minor cortico-muscular synchronization than the dominant one.

Overall, the results tell us that CMncd is sensitive to motor control dexterity, differentiating the dominant vs. non-dominant sides for everyday movements,

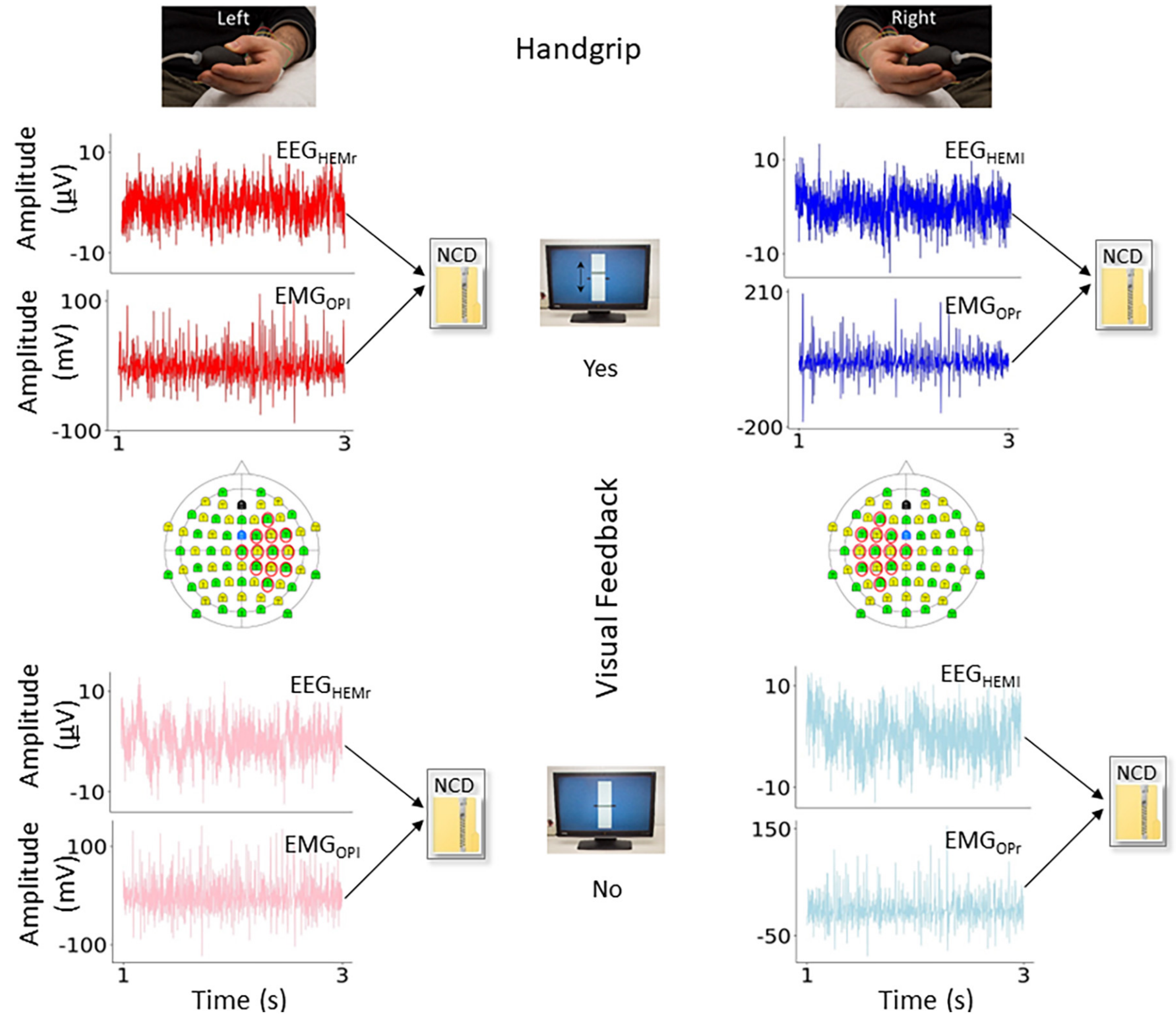

FIGURE 2
Variables of interest. In the four conditions of interest, representation of the functional connectivity measure obtained by normalized compression distance (NCD) from the electro-encephalography (EEG) and electro-myographic (EMG) ongoing signals. In red (left movement) and blue (right movement) the conditions with visual feedback (Yes), and in light red and light blue the conditions without (No). In the topographical representation of the 64-EEG recording channels, we highlighted those considered to estimate the bipolar derivation displaying highest cortico-muscular coherence (CMC) during the task with the contralateral hand, used as criterion to select the EEG representative.

and revealing the difficulty of the non-dominant side to integrate unusual information during an unfamiliar task.

Similarly to CMncd, CMC (L'Abbate et al., 2022) showed sensitivity to visual feedback (**Figure 3C**). Indeed, we observed that the CMC peak in beta band appeared higher in amplitude in the everyday movement in absence of indirect visual feedback. The two measures CMncd and CMC consistently evidence that the unfamiliar task requiring integrating unusual information and focusing attention implies learning mechanisms reflected in a minor cortico-muscular synchronization, that is in a less tuned cortico-muscular communication.

On the other hand, CMncd during everyday movements revealed better synchronizations for the dominant than the non-dominant hand, not emerging in CMC. A possible explanation of higher sensitivity of CMncd is that synchronizations observed frequency by frequency miss synchronizations occurring through different signal patterns.

In planning and implementing motor actions, the gaze plays a crucial role: it both precedes and guides our everyday actions (Jovancevic-Misic and Hayhoe, 2009). When we perform an everyday action we implement eye-motor programmes in parallel with the execution of the spatial shifts of the body segments we are moving (Flanagan and Johansson, 2003). Definitely, it is acknowledged that visual feedback has an essential role for the motor control of

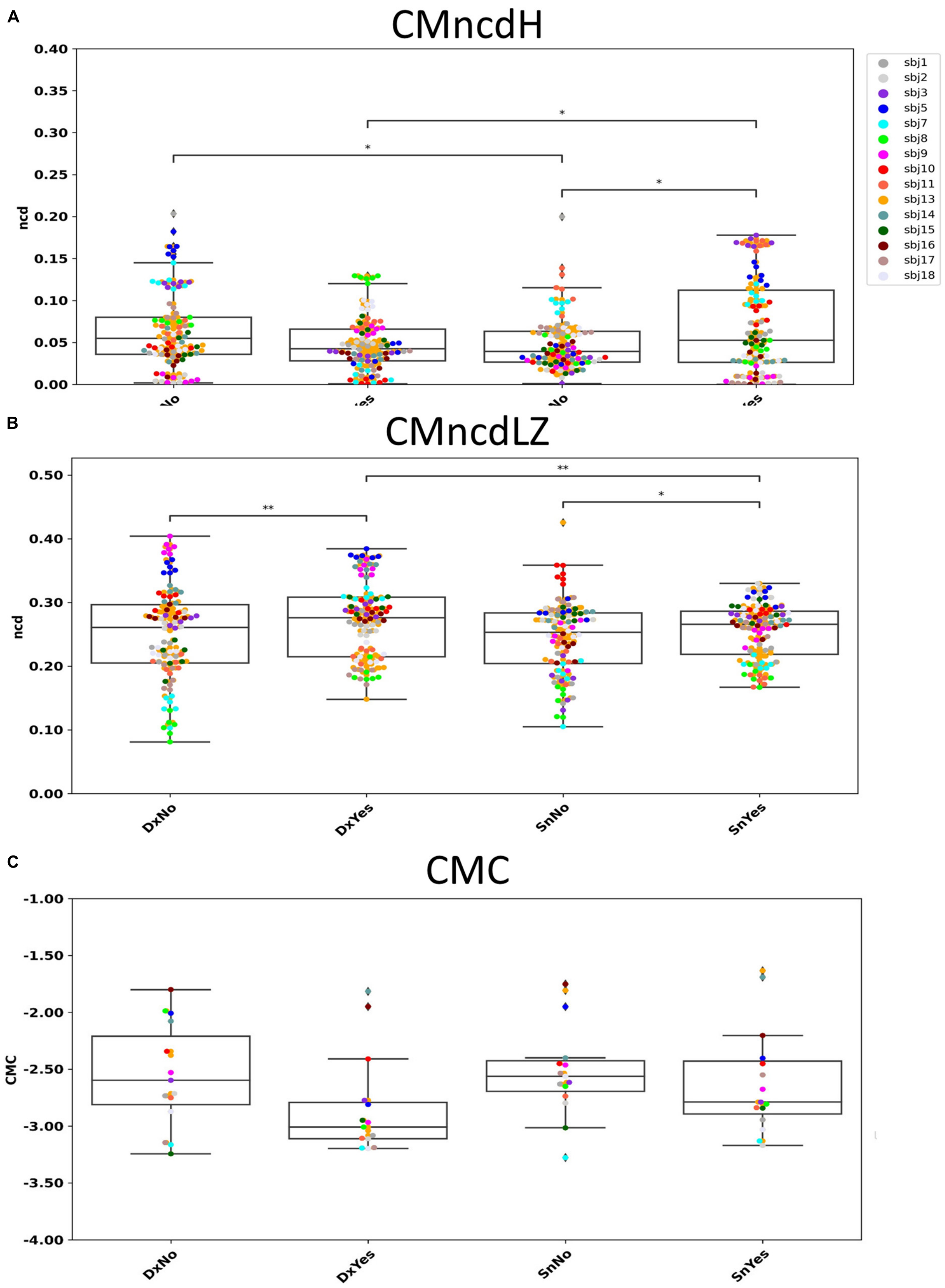

FIGURE 3
CMncdH and CMncdLZ dependence on behavioral condition. Boxplot of CMncdH **(A)** and CMncdLZ **(B)** reporting for each subject the value in 6 estimate intervals in the four conditions. Black lines with asterisks: conditions differing for $p < 0.05$ (1 asterisk) and $p < 0.01$ (2 asterisks). In panel **(C)** we show for comparison single subject data of the study L'Abbate et al. (2022), where we observed a that in absence of visual feedback cortico-muscular coherence (CMC) had higher amplitudes than in presence. Note that higher CMC corresponds to lower CMncd.

hand movements (Saunders and Knill, 2004). The evidence shows that visual feedback is relevant for the on-line control of reaching movements (Saunders and Knill, 2003), grasping movements (Connolly and Goodale, 1999) and object manipulation (Johansson et al., 2001). In the simple handgrip movement exploited in our experiment, the typical physiological condition of everyday life is implemented in the "No" condition. In fact, although people did not look at their hand, the handgrip task looking at the fixed monitor reflects the typical condition in which at the table we eat by looking at each other and without continuously looking at our cutlery. In this situation, the cortico-muscular synchronizations did not differ when moving the dominant or the non-dominant hand.

The task where we provided via the position of the vertically fluctuating horizontal segment information about the executed pressure, is a motor execution quite different from our use of a whatever light tool, for which we calibrate the strength depending on visual and proprioceptive information (Sober and Sabes, 2005). In other terms, our "Yes" condition requires rapid adaptability involving learning mechanisms. In our findings, while the dominant side expressed similar features while executing the everyday movement or the unusual one, the non-dominant hemi-body expressed less cortico-muscular synchronization in approaching the management of novelty. Possibly, CMncd senses the difficulty that less dexterous system encounters to exploit the indirect transposed information with respect the manipulated object.

In our working hypothesis, derived from resting state knowledge, effects of handedness was expected to appear independently of the behavioral test. On the contrary, the effect emerged for movements not belonging to the everyday repertoire, when the two dominant and non-dominant controlling networks were involved in a task with unfamiliar processing requirements. This result leads to reason that while in central networks the resting state emerges with a continuous ongoing neuronal pools activity, the muscles are electrically silent at rest, so that the cortico-muscular synchronization is to be expected much more behaviorally dependent than the intra-cerebral networks' activities.

The human brain, as well as other biological systems, presents asymmetries in structure and function (Toga and Thompson, 2003). It is suggested that lateralization emerged as a function of evolutionary, developmental, hereditary, and experiential factors (Corballis, 2003). Cerebral counterpart of lateralization of motor control was found in relation to skilled actions by EEG (Serrien et al., 2012; Serrien and Sovijärvi-Spapé, 2016) and brain imaging studies (Schluter et al., 2001). Our data strengthen the notion of diverse functional organizations of hemi-body homologue networks devoted to hand control. Indeed, when the subject is due to do a task with a relevant novelty processing component–as it can be adjusting the handgrip pressure according to a visual information distant and independent of the manipulated object–the network controlling the non-dominant left hand shows signs of less tuned coordination with respect to the dominant homolog.

Notably, CMncdH evidenced the dependence on hemi-body dominance also in everyday activities (DxNo vs. SnNo) and CMncdLZ evidenced the dependence on visual feedback also when moving the dominant hand. Further investigations are required to deep understanding of diverse compressors in sensing the physiological properties via NCD.

Tested on the motor-associated synchronization between cortical neuronal activity with that of muscular-sensed spinal moto-neurons, we introduce here the NCD as a measure of synchronization to consider the complex nature of the ongoing neuronal electrical activity, the neurodynamics. In the tested conditions, NCD sensitivity suggests that it can enrich the assessment of communication phenomena inside the nervous system, providing a new window to assess network functional connectivity properties. Because of its definition, NCD can be calculated between activities of different areas, even if collected at different times (Sarasa et al., 2019). This could be very useful when comparing the activities of a specific area at successive times along the lifespan or as an effect of a disease in longitudinal studies. NCD is also suitable for the comparison of signals with different lengths, for example, in the case of activities where artifacts occur in different periods and lead to incongruent epoch rejections (Li and Vitányi, 2008).

In conclusion, we believe that NCD can represent a relevant enrichment tool to assess synchronization phenomena between two nodes, thus enhancing the estimation of functional connectivity within the brain networks that support brain processing.

Data availability statement

The raw data supporting the conclusions of this article will be made available by the authors, without undue reservation.

Ethics statement

The studies involving human participants were reviewed and approved by the Ethical Committee of San Giovanni Calibita Hospital Fatebenefratelli, Rome, Italy. The patients/participants provided their written informed consent to participate in this study.

Author contributions

FT and EG drafted the manuscript. AP, DV, and VB grounded the normalized compression distance theory and algorithm. MA and FP coordinated the analysis on the present data set. LC cured the manuscript writing. MB and JG deepened the clinical perspective and LP the conceptual framework. KA and TL'A shared the neurophysiology-psychotherapy connection. All authors contributed to the final writing.

Funding

This work was supported by POR FESR LAZIO 2014-2020, Prog. 28109, Digital Helpers per e-Communities in Sanità (DHelp4H), 2019, cup B89C20001430002.

Conflict of interest

The authors declare that the research was conducted in the absence of any commercial or financial relationships that could be construed as a potential conflict of interest.

Publisher's note

References

Armonaite, K., Bertoli, M., Paulon, L., Gianni, E., Balsi, M., Conti, L., et al. (2021). Neuronal electrical ongoing activity as cortical areas signature: An insight from MNI intracerebral recording atlas. *Cereb. Cortex* 32, 2895–2906. doi: 10.1093/CERCOR/BHAB389

Axmacher, N., Mormann, F., Fernández, G., Elger, C. E., and Fell, J. (2006). Memory formation by neuronal synchronization. *Brain Res. Rev.* 52, 170–182. doi: 10.1016/J.BRAINRESREV.2006.01.007

Bansal, K., Garcia, J. O., Lauharatanahirun, N., Muldoon, S. F., Sajda, P., and Vettel, J. M. (2021). Scale-specific dynamics of high-amplitude bursts in EEG capture behaviorally meaningful variability. *Neuroimage* 241:118425. doi: 10.1016/J.NEUROIMAGE.2021.118425

Barbati, G., Porcaro, C., Zappasodi, F., Rossini, P. M., and Tecchio, F. (2004). Optimization of an independent component analysis approach for artifact identification and removal in magnetoencephalographic signals. *Clin. Neurophysiol.* 115, 1220–1232. doi: 10.1016/j.clinph.2003.12.015

Borisyuk, R., Borisyuk, G., and Kazanovich, Y. (1998). Synchronization of neural activity and information processing. *Behav. Brain Sci.* 21, 833–833. doi: 10.1017/S0140525X98241768

Brown, P. (2000). Cortical drives to human muscle: The Piper and related rhythms. *Prog. Neurobiol.* 60, 97–108. doi: 10.1016/S0301-0082(99)00029-5

Brown, P., Salenius, S., Rothwell, J. C., and Hari, R. (1998). Cortical correlate of the piper rhythm in humans. *J. Neurophysiol.* 80, 2911–2917. doi: 10.1152/JN.1998.80.6.2911

Broyd, S. J., Demanuele, C., Debener, S., Helps, S. K., James, C. J., and Sonuga-Barke, E. J. S. (2009). Default-mode brain dysfunction in mental disorders: A systematic review. *Neurosci. Biobehav. Rev.* 33, 279–296. doi: 10.1016/J.NEUBIOREV.2008.09.002

Bullmore, E., and Sporns, O. (2012). The economy of brain network organization. *Nat. Rev. Neurosci.* 13, 336–349. doi: 10.1038/nrn3214

Buzsáki, G. (2009). *Rhythms of the brain*. Oxford: Oxford University Press. doi: 10.1093/acprof:oso/9780195301069.001.0001

Buzsáki, G., Logothetis, N., and Singer, W. (2013). Scaling brain size, keeping timing: Evolutionary preservation of brain rhythms. *Neuron* 80, 751–764. doi: 10.1016/j.neuron.2013.10.002

Chen, C. C., Kilner, J. M., Friston, K. J., Kiebel, S. J., Jolly, R. K., and Ward, N. S. (2010). Nonlinear coupling in the human motor system. *J. Neurosci.* 30, 8393–8399. doi: 10.1523/JNEUROSCI.1194-09.2010

Cilibrasi, R., and Vitányi, P. M. B. (2005). Clustering by compression. *IEEE Trans. Inf. Theory* 51, 1523–1545. doi: 10.1109/TIT.2005.844059

Connolly, J. D., and Goodale, M. A. (1999). The role of visual feedback of hand position in the control of manual prehension. *Exp. Brain Res.* 125, 281–286. doi: 10.1007/S002210050684

Corballis, M. C. (2003). From mouth to hand: Gesture, speech, and the evolution of right-handedness. *Behav. Brain Sci.* 26, 199–208. doi: 10.1017/S0140525X03000062

Cottone, C., Porcaro, C., Cancelli, A., Olejarczyk, E., Salustri, C., and Tecchio, F. (2017). Neuronal electrical ongoing activity as a signature of cortical areas. *Brain Struct. Funct.* 222, 2115–2126. doi: 10.1007/S00429-016-1328-4

Daffertshofer, A., and Pietras, B. (2020). "Phase synchronization in neural systems," in *Synergetics*, eds A. Hutt and H. Haken (New York, NY: Springer), 221–233.

Damoiseaux, J. S., Rombouts, S. A. R. B., Barkhof, F., Scheltens, P., Stam, C. J., Smith, S. M., et al. (2006). Consistent resting-state networks across healthy subjects. *Proc. Natl. Acad. Sci. U.S.A.* 103, 13848–13853. doi: 10.1073/PNAS.0601417103

Deco, G., and Corbetta, M. (2011). The dynamical balance of the brain at rest. *Neuroscientist* 17, 107–123. doi: 10.1177/1073858409354384

Deco, G., Jirsa, V. K., and McIntosh, A. R. (2011). Emerging concepts for the dynamical organization of resting-state activity in the brain. *Nat. Rev. Neurosci.* 12, 43–56. doi: 10.1038/nrn2961

Doucet, G. E., Hamlin, N., West, A., Kruse, J. A., Moser, D. A., and Wilson, T. W. (2022). Multivariate patterns of brain-behavior associations across the adult lifespan. *Aging (Albany NY)* 14, 161–194. doi: 10.18632/AGING.203815

Fingelkurts, A. A., Fingelkurts, A. A., and Kähkönen, S. (2005). Functional connectivity in the brain—is it an elusive concept? *Neurosci. Biobehav. Rev.* 28, 827–836. doi: 10.1016/J.NEUBIOREV.2004.10.009

Flanagan, J. R., and Johansson, R. S. (2003). Action plans used in action observation. *Nature* 424, 769–771. doi: 10.1038/nature01861

Fries, P. (2005). A mechanism for cognitive dynamics: Neuronal communication through neuronal coherence. *Trends Cogn. Sci.* 9, 474–480.

Fries, P. (2009). Neuronal gamma-band synchronization as a fundamental process in cortical computation. *Annu. Rev. Neurosci.* 32, 209–224. doi: 10.1146/ANNUREV.NEURO.051508.135603

Gray, C. M. (1994). Synchronous oscillations in neuronal systems: Mechanisms and functions. *J. Comput. Neurosci.* 1, 11–38.

Gray, C. M., König, P., Engel, A. K., and Singer, W. (1989). Oscillatory responses in cat visual cortex exhibit inter-columnar synchronization which reflects global stimulus properties. *Nature* 338, 334–337. doi: 10.1038/338334a0

Gross, J., Kujala, J., Hämäläinen, M., Timmermann, L., Schnitzler, A., and Salmelin, R. (2001). Dynamic imaging of coherent sources: Studying neural interactions in the human brain. *Proc. Natl. Acad. Sci. U.S.A.* 98, 694–699. doi: 10.1073/PNAS.98.2.694

Hlinka, J., Paluš, M., Vejmelka, M., Mantini, D., and Corbetta, M. (2011). Functional connectivity in resting-state fMRI: Is linear correlation sufficient? *Neuroimage* 54, 2218–2225. doi: 10.1016/J.NEUROIMAGE.2010.08.042

Hutchison, R. M., Womelsdorf, T., Allen, E. A., Bandettini, P. A., Calhoun, V. D., Corbetta, M., et al. (2013). Dynamic functional connectivity: Promise, issues, and interpretations. *Neuroimage* 80, 360–378. doi: 10.1016/J.NEUROIMAGE.2013.05.079

Jensen, O., and Mazaheri, A. (2010). Shaping functional architecture by oscillatory alpha activity: Gating by inhibition. *Front. Hum. Neurosci.* 4:186. doi: 10.3389/fnhum.2010.00186

Johansson, R. S., Westling, G., Bäckström, A., and Randall Flanagan, J. (2001). Eye-hand coordination in object manipulation. *J. Neurosci.* 21, 6917–6932. doi: 10.1523/jneurosci.21-17-06917.2001

Jovancevic-Misic, J., and Hayhoe, M. (2009). Adaptive gaze control in natural environments. *J. Neurosci.* 29, 6234–6238. doi: 10.1523/JNEUROSCI.5570-08.2009

Kilner, J. M., Fisher, R. J., and Lemon, R. N. (2004). Coupling of oscillatory activity between muscles is strikingly reduced in a deafferented subject compared with normal controls. *J. Neurophysiol.* 92, 790–796. doi: 10.1152/jn.01247.2003

Kim, J., and Kang, E. (2018). Strength of resting-state functional connectivity associated with performance-adjustment ability. *Behav. Brain Res.* 347, 377–384. doi: 10.1016/J.BBR.2018.02.024

Kristeva, R., Patino, L., and Omlor, W. (2007). Beta-range cortical motor spectral power and corticomuscular coherence as a mechanism for effective corticospinal interaction during steady-state motor output. *Neuroimage* 36, 785–792. doi: 10.1016/J.NEUROIMAGE.2007.03.025

L'Abbate, T., Armonaite, K., Gianni, E., Bertoli, M., Conti, L., Grifoni, J., et al. (2022). Corticomuscular coherence dependence on body side and visual feedback. *Neuroscience* 490, 144–154. doi: 10.1016/j.neuroscience.2022.02.019

Lemon, R. N. (2008). Descending pathways in motor control. *Annu. Rev. Neurosci.* 31, 195–218. doi: 10.1146/annurev.neuro.31.060407.125547

Lempel, A., and Ziv, J. (1976). On the complexity of finite sequences. *IEEE Trans. Inf. Theory* 22, 75–81. doi: 10.1109/TIT.1976.1055501

Li, M., and Vitányi, P. (1990). "Kolmogorov complexity and its applications," in *Algorithms and complexity*, ed. J. V. LEEUWEN (Amsterdam: Elsevier), 187–254. doi: 10.1016/b978-0-444-88071-0.50009-6

Li, M., and Vitányi, P. (2008). *An Introduction to Kolmogorov Complexity and Its Applications*. New York, NY: Springer, doi: 10.1007/978-0-387-49820-1

Liu, J., Sheng, Y., and Liu, H. (2019). Corticomuscular coherence and its applications: A review. *Front. Hum. Neurosci.* 13:100. doi: 10.3389/FNHUM.2019.00100

Mima, T., and Hallett, M. (1999). Corticomuscular coherence: A review. *J. Clin. Neurophysiol.* 16, 501–511. doi: 10.1097/00004691-199911000-00002

Mima, T., Simpkins, N., Oluwatimilehin, T., and Hallett, M. (1999). Force level modulates human cortical oscillatory activities. *Neurosci. Lett.* 275, 77–80. doi: 10.1016/S0304-3940(99)00734-X

Moreno-López, Y., Olivares-Moreno, R., Cordero-Erausquin, M., and Rojas-Piloni, G. (2016). Sensorimotor integration by corticospinal system. *Front. Neuroanat.* 10:24. doi: 10.3389/FNANA.2016.00024

Oldfield, R. C. (1971). The assessment and analysis of handedness: The Edinburgh inventory. *Neuropsychologia* 9, 97–113. doi: 10.1016/0028-3932(71)90067-4

Omlor, W., Patino, L., Hepp-Reymond, M. C., and Kristeva, R. (2007). Gamma-range corticomuscular coherence during dynamic force output. *Neuroimage* 34, 1191–1198. doi: 10.1016/j.neuroimage.2006.10.018

Palva, J. M., Palva, S., and Kaila, K. (2005). Phase synchrony among neuronal oscillations in the human cortex. *J. Neurosci.* 25, 3962–3972. doi: 10.1523/JNEUROSCI.4250-04.2005

Ramayya, A. G., Yang, A. I., Buch, V. P., Burke, J. F., Richardson, A. G., Brandon, C., et al. (2021). Theta synchrony is increased near neural populations that are active when initiating instructed movement. *eNeuro* 8, 1–14. doi: 10.1523/ENEURO.0252-20.2020

Samogin, J., Marino, M., Porcaro, C., Wenderoth, N., Dupont, P., Swinnen, S. P., et al. (2020). Frequency-dependent functional connectivity in resting state networks. *Hum. Brain Mapp.* 41, 5187–5198. doi: 10.1002/HBM.25184

Sarasa, G., Granados, A., and Rodriguez, F. B. (2019). Algorithmic clustering based on string compression to extract P300 structure in EEG signals. *Comput. Methods Programs Biomed.* 176, 225–235. doi: 10.1016/J.CMPB.2019.03.009

Saunders, J. A., and Knill, D. C. (2003). Humans use continuous visual feedback from the hand to control fast reaching movements. *Exp. Brain Res.* 152, 341–352. doi: 10.1007/S00221-003-1525-2

Saunders, J. A., and Knill, D. C. (2004). Visual feedback control of hand movements. *J. Neurosci.* 24, 3223–3234. doi: 10.1523/JNEUROSCI.4319-03.2004

Schluter, N. D., Krams, M., Rushworth, M. F. S., and Passingham, R. E. (2001). Cerebral dominance for action in the human brain: The selection of actions. *Neuropsychologia* 39, 105–113. doi: 10.1016/S0028-3932(00)00105-6

Serrien, D. J., and Sovijärvi-Spapé, M. M. (2016). Manual dexterity: Functional lateralisation patterns and motor efficiency. *Brain Cogn.* 108, 42–46. doi: 10.1016/J.BANDC.2016.07.005

Serrien, D. J., Sovijärvi-Spapé, M. M., and Farnsworth, B. (2012). Bimanual control processes and the role of handedness. *Neuropsychology* 26, 802–807. doi: 10.1037/A0030154

Siebenhühner, F., Wang, S. H., Arnulfo, G., Lampinen, A., Nobili, L., Palva, J. M., et al. (2020). Genuine cross-frequency coupling networks in human resting-state electrophysiological recordings. *PLoS Biol.* 18:e3000685. doi: 10.1371/JOURNAL.PBIO.3000685

Singer, W. (1993). Synchronization of cortical activity and its putative role in information processing and learning. *Annu. Rev. Physiol.* 55, 349–374. doi: 10.1146/annurev.ph.55.030193.002025

Singer, W., and Gray, C. M. (1995). Visual feature integration and the temporal correlation hypothesis. *Annu. Rev. Neurosci.* 18, 555–586. doi: 10.1146/annurev.ne.18.030195.003011

Sober, S. J., and Sabes, P. N. (2005). Flexible strategies for sensory integration during motor planning. *Nat. Neurosci.* 8, 490–497. doi: 10.1038/nn1427

Tan, G., Wang, J., Liu, J., Sheng, Y., Xie, Q., and Liu, H. (2022). A framework for quantifying the effects of transcranial magnetic stimulation on motor recovery from hemiparesis: Corticomuscular Network. *J. Neural Eng.* 19, 026053. doi: 10.1088/1741-2552/AC636B

Tecchio, F., Porcaro, C., Barbati, G., and Zappasodi, F. (2007). Functional source separation and hand cortical representation for a brain–computer interface feature extraction. *J. Physiol.* 580, 703–721.

Tecchio, F., Porcaro, C., Zappasodi, F., Pesenti, A., Ercolani, M., and Rossini, P. M. (2006). Cortical short-term fatigue effects assessed via rhythmic brain–muscle coherence. *Exp. Brain Res.* 174, 144–151.

Toga, A. W., and Thompson, P. M. (2003). Mapping brain asymmetry. *Nat. Rev. Neurosci.* 4, 37–48. doi: 10.1038/nrn1009

Tomasevic, L., Zito, G., Pasqualetti, P., Filippi, M. M., Landi, D., Ghazaryan, A., et al. (2013). Cortico-muscular coherence as an index of fatigue in multiple sclerosis. *Mult. Scler. J.* 19, 334–343.

van Wijk, B. C. M., Beek, P. J., and Daffertshofer, A. (2012). Neural synchrony within the motor system: What have we learned so far? *Front. Hum. Neurosci.* 6:252. doi: 10.3389/FNHUM.2012.00252

Varela, F., Lachaux, J. P., Rodriguez, E., and Martinerie, J. (2001). The brainweb: Phase synchronization and large-scale integration. *Nat. Rev. Neurosci.* 2, 229–239. doi: 10.1038/35067550

Wang, H. E., Bénar, C. G., Quilichini, P. P., Friston, K. J., Jirsa, V. K., and Bernard, C. (2014). A systematic framework for functional connectivity measures. *Front. Neurosci.* 8:405. doi: 10.3389/FNINS.2014.00405

Wang, Y. C., Bohannon, R. W., Kapellusch, J., Garg, A., and Gershon, R. C. (2015). Dexterity as measured with the 9-Hole Peg Test (9-HPT) across the age span. *J. Hand Ther.* 28, 53–60. doi: 10.1016/J.JHT.2014.09.002

Wang, Z., Alahmadi, A., Zhu, D., and Li, T. (2016). "Brain functional connectivity analysis using mutual information," in *Proceedings of the 2015 IEEE global conference on signal and information processing (GlobalSIP)*, Vol. 2015, Orlando, FL, 542–546. doi: 10.1109/GLOBALSIP.2015.7418254

Witham, C. L., Riddle, C. N., Baker, M. R., and Baker, S. N. (2011). Contributions of descending and ascending pathways to corticomuscular coherence in humans. *J. Physiol.* 589, 3789–3800. doi: 10.1113/jphysiol.2011.211045

Wolpert, D. M., Diedrichsen, J., and Flanagan, J. R. (2011). Principles of sensorimotor learning. *Nat. Rev. Neurosci.* 12, 739–751. doi: 10.1038/nrn3112

Womelsdorf, T., and Fries, P. (2007). The role of neuronal synchronization in selective attention. *Curr. Opin. Neurobiol.* 17, 154–160. doi: 10.1016/J.CONB.2007.02.002

Yang, Y., Dewald, J. P., van der Helm, F. C., and Schouten, A. C. (2018). Unveiling neural coupling within the sensorimotor system: Directionality and nonlinearity. *Eur. J. Neurosci.* 48, 2407–2415.

Yang, Y., Solis-Escalante, T., van de Ruit, M., van der Helm, F. C. T., and Schouten, A. C. (2016). Nonlinear coupling between cortical oscillations and muscle activity during isotonic wrist flexion. *Front. Comput. Neurosci.* 10:126. doi: 10.3389/FNCOM.2016.00126

Zhang, Y., Hao, J., Zhou, C., and Chang, K. (2008). Normalized Lempel-Ziv complexity and its application in bio-sequence analysis. *J. Math. Chem.* 464, 1203–1212. doi: 10.1007/S10910-008-9512-2

Frontiers in Neuroscience

Provides a holistic understanding of brain function from genes to behavior

Part of the most cited neuroscience journal series which explores the brain - from the new eras of causation and anatomical neurosciences to neuroeconomics and neuroenergetics.

Discover the latest Research Topics

See more →

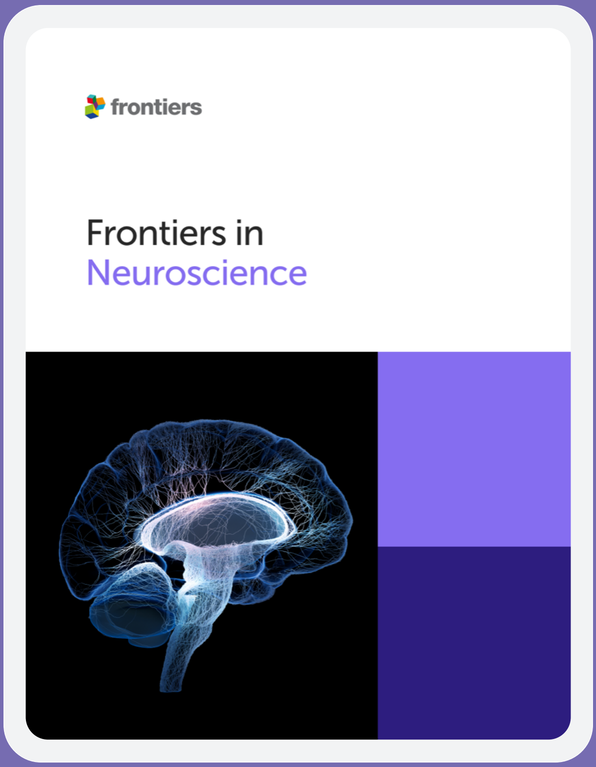

frontiers

Frontiers in
Neuroscience

Frontiers

Avenue du Tribunal-Fédéral 34
1005 Lausanne, Switzerland
frontiersin.org

Contact us

+41 (0)21 510 17 00
frontiersin.org/about/contact